ADVANCED THREE-DIMENSIONAL NONLINEAR ANALYSIS OF REINFORCED CONCRETE STRUCTURES SUBJECTED TO FIRE AND EXTREME LOADS

by

Fady ElMohandes

A thesis submitted in conformity with the requirements
for the degree of Doctor of Philosophy

Department of Civil Engineering
University of Toronto

Advanced Three-Dimensional Nonlinear Analysis of Reinforced Concrete Structures Subjected to Fire and Extreme Loads

Fady ElMohandes

Degree of Doctor of Philosophy

Department of Civil Engineering
University of Toronto

2013

Abstract

With the rise in hazards that structures are potentially subjected to these days, ranging from pre-contemplated terror attacks to accidental and natural disasters, safeguarding structures against such hazards has increasingly become a common design requirement. The extreme loading conditions associated with these hazards renders the concept of imposing generalized codes and standards guidelines for structural design unfeasible. Therefore, a general shift towards performance-based design is starting to dominate the structural design field.

This study introduces a powerful structural analysis tool for reinforced concrete structures, possessing a high level of reliability in handling a wide range of typical and extreme loading conditions in a sophisticated structural framework. VecTor3, a finite element computer program previously developed at the University of Toronto for nonlinear analysis of three-dimensional reinforced concrete structures employing the well-established Modified Compression Field Theory (MCFT), has been further developed to serve as the desired tool.

VecTor3 is extended to include analysis capabilities for extreme loading conditions, advanced reinforced concrete mechanisms, and new material types. For extreme loading conditions, an advanced coupled heat and moisture transfer algorithm is implemented in VecTor3 for the analysis of reinforced concrete structures subjected to fire. This algorithm not only calculates the transient temperature through the depth of concrete members, but also calculates the elevated pore pressure in concrete, which enables the prediction of the occurrence of localized thermally-induced spalling. Dynamic loading conditions are also extended to include seismic loading, in addition to blast and impact loading.

Advancing the mechanisms considered, VecTor3 is developed to include the Disturbed Stress Field Model (DSFM), dowel action and buckling of steel reinforcing bars, geometric nonlinearity effects, strain rate effects for dynamic loading conditions, and the deterioration of mechanical properties at elevated temperatures for fire loading conditions. Finally, the newly-developed Simplified Diverse Embedment Model (SDEM) is implemented in VecTor3 to add analysis capability for steel fibre-reinforced concrete (SFRC).

Various analyses covering a wide range of different structural members and loading conditions are carried out using VecTor3, showing good agreement with experimental results available in the literature. These analyses verify the reliability of the models, mechanisms, and algorithms incorporated in VecTor3.

Acknowledgments

First and foremost, I would like to thank my supervisor, Professor Frank J. Vecchio. His guidance, support, and expert advice have made this study possible, and his patience, composure, and approachability have made it unstressful and quite enjoyable. Working closely with him has truly enriched me technically, professionally, and personally.

I also thank each and every member of my examination committee: Professor D. Paul Gauvreau, Professor Daman K. Panesar, and Professor Shamim A. Sheikh. Their continuous expert guidance and their diligent review of this document are highly appreciated.

I would also like to extend my sincere gratitude to Dr. Michael Simpson for his professional guidance and the entire staff of Consultec Ltd., especially Mr. Alex Ochrym, for the hospitality and professional experience they offered me. The financial support of the Natural Sciences and Engineering Research Council (NSERC), Consultec Ltd., the Department of Civil Engineering of the University of Toronto, and Professor Frank J. Vecchio is gratefully acknowledged as well.

I have made many friends through the years of my studies at the University of Toronto who I would like to thank for making these years as enjoyable as they were beneficial. These friends are David Carnovale, Ivan Chak, Jordon Deluce, Trevor Hrynyk, Akira Jodai, David Johnson, Seong-Cheol Lee, William Luo, Vahid Sadeghian, and Heather Trommels.

Last, but not least, I would like to thank my mother, Nadia, and my sisters, Jermeen and Mirette, for their infinite love and support through the years of my studies. I could not have accomplished this without their constant encouragement.

Table of Contents

List of Tables

List of Figures

Chapter 1
Introduction

1.1 Background

There is a general shift in the structural engineering design field towards performance-based design, rather than blindly satisfying codified requirements. This shift is fuelled by advancements in the construction industry and the escalating need for designing irregular structures with extreme loading conditions. With this shift comes the needed ability to perform structural design based on nonlinear analysis, abandoning decades of strictly abiding by the linear elastic range rules. Also, what makes the shift attainable are advancements in the programming and computational capabilities of computers and their constantly increasing use for structural analysis and design purposes.

Performance-based design finds its real use in the design of structures against extreme loads such as seismic, blast, impact, and fire loading. With the current global increase in the threats of natural disasters, terrorist attacks, and accidental explosions, the safety and functionality of some special structures during such events has become a rather common design requirement in structural design these days. These special structures include critical infrastructure such as water supply structures and electricity power plants, services buildings such as hospitals and police stations, and sensitive structures such as nuclear power plants. Since the irregularities in these types of loading are very wide in range, the general codified guidelines normally fail to cover them all, resulting in ultra-conservative structural designs in some instances and remarkably unsafe ones in others.

One of the least investigated and understood loading conditions of reinforced concrete members is fire loading conditions. According to Wijayasinghe (2011), in the year 2007, a total of 42,753 fires were recorded in the provinces of Alberta, British Columbia, Manitoba, New Brunswick, Nova Scotia, Ontario, and Saskatchewan and the Northwest Territories, combined. Direct property damage from these fires was estimated at a staggering amount of more than 1.5 billion dollars. It is not clear how many of these fire accidents occurred in reinforced concrete structures in particular, nor is it clear how much

of these losses are directly related to reinforced concrete structural damage, repair, or demolishing. Yet, the losses are so high that even if a minor portion relates to reinforced concrete structures, it would make this topic worth investigating. Fire has been known as a major hazard for structures for a long time, with many attempts from researchers around the globe to investigate the behaviour of concrete and steel reinforcing bars under elevated temperatures; yet, our knowledge of this behaviour is still inadequate and inconclusive.

The necessity of studying the behaviour of concrete and steel reinforcing bars under elevated temperatures is not limited to the extreme events of fire only. The nature of some structures involves the subjection of reinforced concrete members to elevated temperatures on a regular basis. These structures include, but are not limited to, nuclear reactor pressure vessels, coal gasification and liquefaction vessels, pressure vessels used in petrochemical industries, and storage tanks for hot crude oil, hot water, and hot clinker (Khoury et al., 1985a).

Concrete is in fact one of the preferred construction materials for such applications because of its good performance under elevated temperature. This is due to its incombustibility and its low thermal conductivity which helps delay the rise in temperature of steel reinforcing bars. Yet, it still suffers significant deterioration in all of its mechanical properties with the rise in temperature. Added to this are the mutual stresses occurring in concrete and steel reinforcing bars due to the differential thermal expansion between the two materials with the rise in temperature. This is actually ironic because one of the advantages in using concrete and steel together for construction is their similar coefficient of thermal expansion at ambient temperatures. Unfortunately, this advantage is lost at elevated temperatures.

Another source of irony is the fact that what is considered to be high-performance concrete at normal temperatures tends to behave more poorly under elevated temperatures, as it loses its compressive strength more rapidly. In addition, high-performance concrete, and high-strength concrete specifically, has a higher risk for the occurrence of explosive spalling when subjected to fire.

Performing effective performance-based design requires the utilization of a robust concrete model. In addition, advanced concrete behavioural properties and mechanisms need to be taken into consideration, such as compression softening, confinement, hysteretic response, tension stiffening, and slippage occurring on the surfaces of cracks. For steel reinforcing bars, buckling, dowel action, and hysteretic response also need to be modelled. Also requiring consideration are the special mechanisms that are particular to specific types of loading, such as strain rate effects for dynamic loading cases (seismic, blast, and impact) and the deterioration of mechanical properties at elevated temperatures for fire loading cases.

A major weakness of the numerous concrete models available for structural analysis is their poor performance in estimating shear stresses and strains or predicting shear failure. This deficiency renders these models extremely unsafe in some cases, because of the sudden unforeseen failures attributed to excessive shear stresses. It should also be noted that accurate modelling of shear mechanisms in concrete is more critical for structures subjected to fire. This is because of the differential expansion between the different concrete members which causes them to place high shear demand on each other as they expand differently. For example, when the floor slabs with their large lateral area expand, they apply additional shear forces on the columns.

1.2 Research Motivation

Due to the increasing interest in designing reinforced concrete structures with high fire resistance, many computer programs were developed over the past few decades with the specific target of modelling reinforced concrete structures subjected to fire. These programs can be classified into three different groups:

Group I:

This group includes programs that solely focus on the transient heat transfer analysis, such as COMPSL (Lie, 1978), HSLAB (Abrahamsson et al., 1979), TASEF (Wickstrom, 1979), and FIRES-T3 (Iding et al., 1996). These programs are quite impractical for structural analysis purposes because they require performing a separate analysis for the

structural aspect; hence, only the final state of the structure can be analyzed. Even with the programs that generate a temperature history profile, users need to perform a structural analysis for each time step in order to achieve a time-stepping structural analysis, which is a very tedious task. However, with regards to their transient heat transfer analysis capabilities, most of these programs perform quite well, and they take into consideration many of the aspects that are normally missed by other universal computer programs.

Group II:

This group includes commercial computer programs which have coupled thermal-structural analysis routines, such as ANSYS®, Abaqus®, and LS-DYNA®. While these programs have the advantage of being capable of handling numerous loading types and conditions, they have the disadvantage of being a "black box", where undisclosed mechanisms are followed and the users have no control over them. For example, Abaqus® User's Manual claims that its tension stiffening formulae implicitly take into account the effects associated with the rebar/concrete interface, such as bond slip between concrete and steel reinforcing bars and dowel action; yet, these mechanisms are not explicitly explained.

Also, the processes of preparing the finite element model, defining the materials, and running the analyses tend to be very complex and time-costly in these programs, as they require the user to define very specific details regarding every aspect of the analysis. For example, Abaqus® requires users to input the heat flux applied on the surface exposed to rise in temperature, rather than simply specify a temperature-time curve. For all these computer programs, users do not have the ability to specify the values of certain temperature-dependant properties, for which intrinsic values are used with no control from the user. This means that limited flexibility is available to the user to define these properties. For the properties that can indeed be specified by users, the user is required to manually enter the points that define the curve of the temperature-dependent property, with no built in standard models to choose from, which, as previously mentioned, makes the process of preparing for the analysis very complex and time-costly.

Group III:

This group includes programs that are dedicated to performing transient heat transfer analysis as a first step then utilizing the temperatures generated to perform structural analysis; examples include BRANZ-TR8 (Wade and Lovatt, 1996), BoFire (Schaumann and Kettner, 2003), SAFIR (Franssen, 2003), and InfoGraph (InfoGraph, 2013). These programs tend to perform the best among the three groups, as they specialize in fire analysis and consider most of the material behaviour details. However, despite the fact that they excel in the transient heat transfer analysis part, the loading types and conditions that they are capable of handling are rather limited. In addition, they typically have numerous weaknesses in their structural analysis capabilities.

The most sophisticated and commonly used programs in this group are SAFIR (Franssen, 2003) and InfoGraph (InfoGraph, 2013). With SAFIR, one of the drawbacks is that while two-dimensional thermal analysis results can be directly passed to the structural analysis using the same model (the same finite element discretization), three-dimensional results cannot be directly followed by structural analysis (Franssen, 2011b). A new model, composed only of truss, beam, and shell elements, has to be generated. Also, users are not allowed to introduce their own material mechanical models for structural analysis (Franssen, 2005), and only linear unloading curves are available for use in hysteretic response (Franssen, 2011a). Another major drawback is that SAFIR uses Bernoulli's beam theory (Bernoulli, 1692); thus, no shear deformations can arise (Franssen, 2011b). Hence, it cannot capture shear failures.

InfoGraph (InfoGraph, 2013), on the other hand, is more sophisticated than SAFIR (Franssen, 2003) on the structural analysis level. It uses a rotating crack model, where shear strains are considered; yet, for solid elements, it only considers bilinear material curves with the Raghava yield criterion (Raghava et al., 1973). Also, geometric nonlinearity effects are not available for all types of loading. In fire scenarios, the shear stiffness of the initial section is used throughout the entire analysis and the response is calculated according to elasticity theory, where loading and unloading follow the same path.

Also, InfoGraph (InfoGraph, 2013) uses an iterative solution, targeting force equilibrium in a load control regime. One of two methods can be followed: the incremental Newton-Raphson method, where the tangential stiffness matrix is calculated based on the internal forces and deformation state, or the modified Newton-Raphson method, where the initial stiffness matrix is used throughout the entire analysis. Therefore, according to the User's Manual, stable convergence necessitates the use of bilinear material curves. Poor convergence is reported for more complex material properties, especially for cracking and tension softening because of the negative tangential stiffness associated with it. This is why tension softening is unavailable for solid elements as well.

Finally, all three groups of computer programs miss numerous features and mechanisms, on both the heat transfer analysis and the structural analysis levels. For example, none considers thermally-induced spalling of concrete subjected to fire. Also, most claim that they implicitly consider bond slip between concrete and steel reinforcing bars, but this cannot be verified. More importantly, all these programs tend to be deficient in estimating shear stresses and strains, which typically results in missing shear failures in shear-critical structures.

This points to the need for developing a new structural analysis tool that utilizes a concrete model with adequate shear-modelling capabilities. This tool should be able to model the advanced mechanisms experienced by concrete and steel and to simulate the conditions of typical and atypical loading profiles, including fire and the ensuing thermally-induced spalling. Stability of convergence and speed should also be ensured for all the iterative processes involved in the analyses carried out by this tool. Therefore, this study was undertaken as an answer to this call.

1.3 Research Scope

As previously mentioned, this study aims at the development of a new structural analysis tool. VecTor3, a finite element computer program developed at the University of Toronto for nonlinear analysis of three-dimensional reinforced concrete structures, has been selected for this purpose. VecTor3 was initially developed by Selby (1990), originally

called SPARCS, where it only included regular eight-noded hexahedral brick elements (right-angled only), with smeared reinforcement only, and with monotonic loading only permitted.

The Modified Compression Field Theory (MCFT), developed by Vecchio and Collins (1986), is the concrete model utilized by VecTor3. MCFT is a well-established model with a long history of corroborated superior performance. Developed based on the results of an intensive experimental program undertaken on a series of panel specimens tested under pure shear and combined shear and normal stresses, the MCFT presents a smeared rotating crack concrete behavioural model that is competently capable of modelling and estimating shear stresses and predicting brittle shear failures. The MCFT uses a total load formulation which provides higher levels of analysis stability and better convergence, as no risk of running into negative stiffnesses exists.

The general scope of this study can be summarized in the further development of VecTor3 to be capable of modelling the advanced behaviour of concrete, to handle a wide range of loading types and conditions, and to model new material types such as steel fibre-reinforced concrete (SFRC).

1.4 Research Objectives

In line with the research scope previously discussed, the following specific objectives have been selected for this study:

1. Adding transient heat transfer analysis capabilities to VecTor3 with all the necessary models of the thermal and mechanical material properties of concrete and steel reinforcing bars that are dependent on temperature. The transient heat transfer analysis is to be coupled with the structural analysis undertaken by VecTor3.

2. Adding the capability to analyze prestrains applied on concrete and steel reinforcing bars, especially thermal expansion strains that are caused by fire exposure. These strains cause additional stresses on restrained structural members as well as additional mutual stresses on both concrete and steel reinforcing bars as they expand differently

at higher temperatures. Also the differential thermal expansion between the zones closer to the surface subjected to fire and the zones lying deeper inside the concrete member contributes to the occurrence of thermally-induced spalling.

3. Adding coupled heat and moisture transfer analysis capabilities to VecTor3 with all the necessary material properties models.

4. Adding the capability to estimate the occurrence of thermally-induced spalling based on the superimposition of the stresses resulting from the high pore pressure inside concrete members subjected to fire, the stresses resulting from the restrained thermal dilatation due to the differential thermal expansion through the depth of concrete members, and the mechanical stresses caused by external loading.

5. Expanding the types of dynamic loads VecTor3 can handle to include earthquakes ground acceleration spectra, in addition to developing the existing impulse loading capabilities to be able to handle a wider range of input data.

6. Improving VecTor3 reinforced concrete behavioural modelling capabilities by adding the Disturbed Stress Field Model (DSFM) (Vecchio, 2000), where shear slippage is permitted on the surface of cracking. The DSFM better predicts the behaviour of reinforced concrete, especially the ductility, but its real strength becomes more apparent for lightly reinforced elements.

7. Adding new eight-noded isoparametric hexahedral elements that can have arbitrary nodes without any limitations on their orientation with respect to each other. These elements serve the purpose of providing more flexibility in modelling any structure with any complicated shape and orientation, as well as accounting for geometric nonlinearity effects (second-order analysis).

8. Adding new elements (link elements) that are capable of modelling the bond slippage between concrete and steel reinforcing bars, allowing for the modelling of typical slippage of smooth and deformed steel reinforcing bars, as well as the unbounded post-tensioning tendons.

9. Developing VecTor3 to account for more advanced material mechanisms for concrete and steel reinforcing bars, such as dowel action and buckling of steel reinforcing bars, strain rate effects for dynamic loading, and the ability to apply specific constraints to groups of nodes on the structure by linking them together with specific displacement relations throughout the analysis to enhance stability and uniformity of loading.

10. Adding the capabilities of modelling steel fibre-reinforced concrete (SFRC) in VecTor3, by adding the Simplified Diverse Embedment Model (SDEM), developed by Lee et al. (2011a, 2011b; 2013a), the tension stiffening behavioural model of concrete matrix in conventionally-reinforced SFRC, developed by Lee et al. (2013b), and the formulae of average crack width in conventionally-reinforced SFRC, developed by Deluce and Vecchio (2013).

11. Minimizing the amount of data required from users by developing VecTor3 to automatically determine many of the general properties of the structure, such as the depths of the different sections in the three directions (required for link elements modelling and for predicting cover splitting failures) and the presence of ties in the different sections to calculate the amount of confinement they provide.

12. Enhancing the overall performance of VecTor3 with regards to convergence stability and speed of analysis.

1.5 Document Outline

This chapter provides background on the analysis of reinforced concrete structures subjected to extreme loads and fire and the research motivation, scope, and objectives, with a brief review on computer programs available for heat transfer analysis and coupled thermal-structural analysis.

Chapter 2 provides details regarding the concrete model used in this study and all the accompanying advanced reinforced concrete mechanisms, together with the procedure used to implement them in the finite element procedure. These mechanisms were implemented in VecTor3 in order to develop its structural analysis capabilities.

Chapter 3 presents and compares the properties of concrete and steel reinforcing bars under elevated temperatures according to the models available in the literature and design codes. The chapter discusses both thermal and mechanical properties. Also, modelling of fire itself, according to the various international standards, is discussed, together with a discussion on some of the phenomena and the physical, chemical, and mechanical changes that concrete experiences when subjected to temperatures as high as those associated with fire exposure. Estimating these properties with the rise in temperature is essential for running coupled heat and structural analyses on reinforced concrete structures.

Chapter 4 discusses the formulation of the time-stepping analysis scheme of modelling reinforced concrete structures subjected to fire. The fundamental theories and concepts required for the analysis of steady and transient heat flow through concrete are explained, and the formulation of the governing differential equations of the analysis is presented. The finite element discretization and its solution procedure are also discussed. This formulation is required for running coupled heat and moisture transfer analyses.

Chapter 5 presents an extensive compilation of various analyses that cover a wide range of different structural members and loading profiles, which aim at corroborating all the models, procedures, and techniques that were incorporated in VecTor3.

Chapter 6 includes the summary and conclusion of this study, together with recommendations for future research that can build on the findings of this study.

Appendix A presents lists of the elements comprising the various matrices derived for the finite element procedures of the coupled heat and moisture transfer analysis for regular eight-noded hexahedral brick elements.

Appendix B presents the material properties that affect the coupled heat and moisture transfer through concrete, which was discussed in Chapter 4.

Appendix C provides a step-by-step calculation procedure for the time-stepping analysis of reinforced concrete structures subjected to fire, together with a flow chart showing the main framework of how this type of analysis is handled within the structural analysis context.

Chapter 2
Structural Modelling Theory and Implementation

2.1 Introduction

In order to capture the realistic behaviour of concrete subjected to various types of loads, typical and extreme, a robust concrete model needs to be utilized along with the consideration of many advanced properties and phenomena related to both concrete and steel reinforcing bars. In this section, the concrete model used in this study and all the accompanying advanced concrete behaviour considerations will be discussed, together with the procedure used to implement them in the finite element procedure.

2.2 Modified Compression Field Theory

The Modified Compression Field Theory (MCFT) is the main basis of all the structural analysis aspects investigated in this study. The MCFT, developed by Vecchio and Collins (1986), is a smeared rotating crack model where cracked concrete is treated as an orthotropic material having specific properties in the principal stress directions perpendicular and parallel to the direction of cracking as shown in Figure 2-1. The MCFT assumes that stresses and strains are uniformly distributed over the element (the panel); likewise for the smeared reinforcement and smeared cracking. It also assumes that the directions of the principal stresses and those of the principal strains are always coincident.

Based on the results of an intensive experimental program undertaken on a series of panel specimens tested under pure shear and combined shear and normal stresses, the MCFT posited constitutive relations for cracked concrete in compression, including compression softening effects, reflecting the observation that the strength and stiffness of cracked concrete are reduced based on the degree of transverse cracking. The MCFT also introduced constitutive relations for cracked concrete in tension that included tension stiffening effects, where the bond between concrete and reinforcement results in the

existence of tensile stresses in concrete between the cracks. In addition, the MCFT investigated equilibrium on the surface of the crack, considering the transfer of tensile stresses across a crack with a local increase in stress in reinforcement at the crack and shear stresses on the surface of the crack resulting from that local increase.

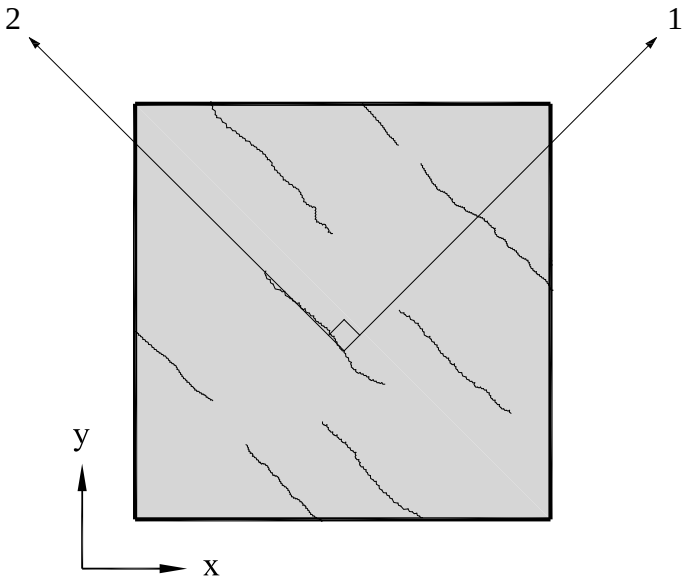

Figure 2-1 Typical element for the Modified Compression Field Theory (MCFT)

Originally developed for membrane elements, the MCFT was later extended by Vecchio and Selby (1991) to model the behaviour of three-dimensional elements as well.

2.3 Disturbed Stress Field Model

The MCFT was extended by Vecchio (2000) to form the Disturbed Stress Field Model (DSFM) in order to account for the shear slip occurring on the surface of the crack in the element which was neglected by the MCFT. In the DSFM, shear slip was permitted on the surface of the crack, allowing a lag to occur between the direction of the principal stress and that of the principal strain. This also eliminated the confusion related to the checking of shear stresses on the surface of the crack that was a crucial part of the MCFT. In addition, the DSFM also presented updated models for compression softening effects and tension stiffening effects.

It was found that for lightly reinforced elements subjected to high levels of shear, the MCFT slightly overestimates strength and stiffness. This is basically caused by the fact that such elements experience high levels of shear slip on the surface of the crack, which the MCFT fails to model. On the other hand, for elements that show no or limited crack rotation, the MCFT tends to underestimate the strength and stiffness. Thus, in general, the DSFM better predicts the behaviour of reinforced concrete, but its accuracy becomes more obvious for lightly reinforced elements. More information about the MCFT and the DSFM can also be found in Wong et al. (2013).

2.4 Finite Element Formulation

Both the MCFT and the DSFM have been implemented in the sophisticated software program suite VecTor (1990), developed at the University of Toronto. As this study focuses mainly on three-dimensional structures, VecTor3, the software utilized for three-dimensional analysis, is the program of interest here. VecTor3 performs nonlinear analysis for reinforced concrete structures based on the MCFT in a total-load secant-stiffness approach. It was initially developed by Selby (1990), originally called SPARCS, where it included regular eight-noded hexahedral brick elements with smeared reinforcement only and only monotonic loading was permitted.

2.4.1 Types of Elements in VecTor3

In order to cover a wide range of structures, VecTor3 has been further developed to include more types of elements. Two types of concrete elements existed in VecTor3: the regular eight-noded hexahedral brick elements and the regular triangular prism six-noded wedge element. Both elements require perfect rectangular faces. For reinforcement, in addition to the smeared reinforcement option, which is the main type of reinforcement included in the development of the MCFT, discrete truss bar elements can also be used. All these elements are shown in Figure 2-2.

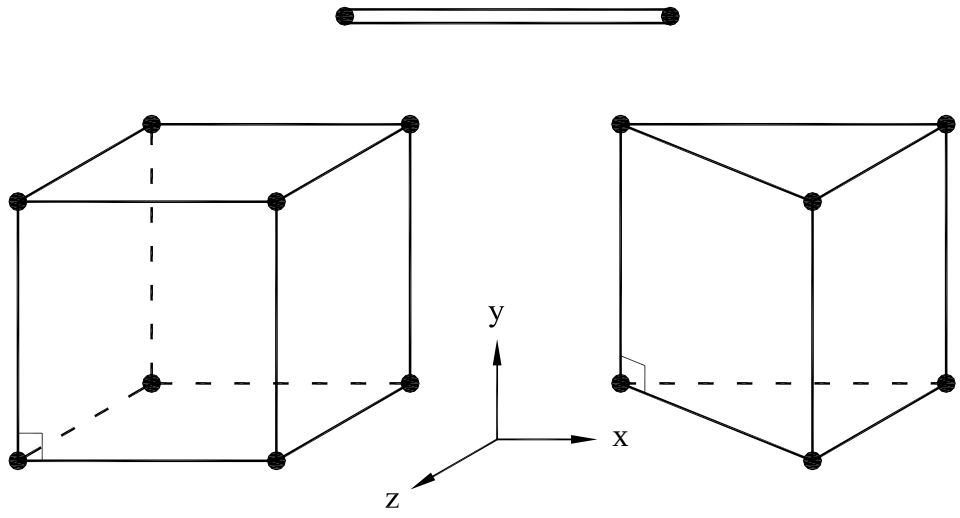

Figure 2-2 Regular eight-noded hexahedral brick element, regular triangular prism six-noded wedge element and discrete truss bar reinforcement element available for use in VecTor3

While these concrete elements are capable of modelling typical regularly-shaped structures, they are unsuited for modelling irregular ones, such as bearing walls with sloped sides, for example, because both concrete element types need to have perfectly rectangular faces. With this need for regular shapes, they also fail to capture the geometric nonlinearity of any structure resulting from large deformations, except by using the Total Lagrangian formulation or the Updated Lagrangian formulation (Bathe, 1982; Crisfield, 1991) with their rigorous calculations. Should geometric nonlinearity be disregarded altogether, it may result in overestimating the overall performance of many types of structures, such as over-predicting the stiffness and load-carrying capacity of a column subjected to lateral loading due to neglecting the P-Δ effects.

This created the need for a new type of element that would provide more flexibility in regard to the shape of structures which can be modelled and that can also handle geometric nonlinearity in a simple straight-forward manner. This is why the isoparametric hexahedral element shown in Figure 2-3 has been developed and added to VecTor3. Unlike the regular hexahedral element, the element is composed of eight arbitrary nodes without any limitations on their orientation with respect to each other. For the finite element solution, the element is transformed from the Cartesian coordinate system to the natural coordinate system as shown in Figure 2-3.

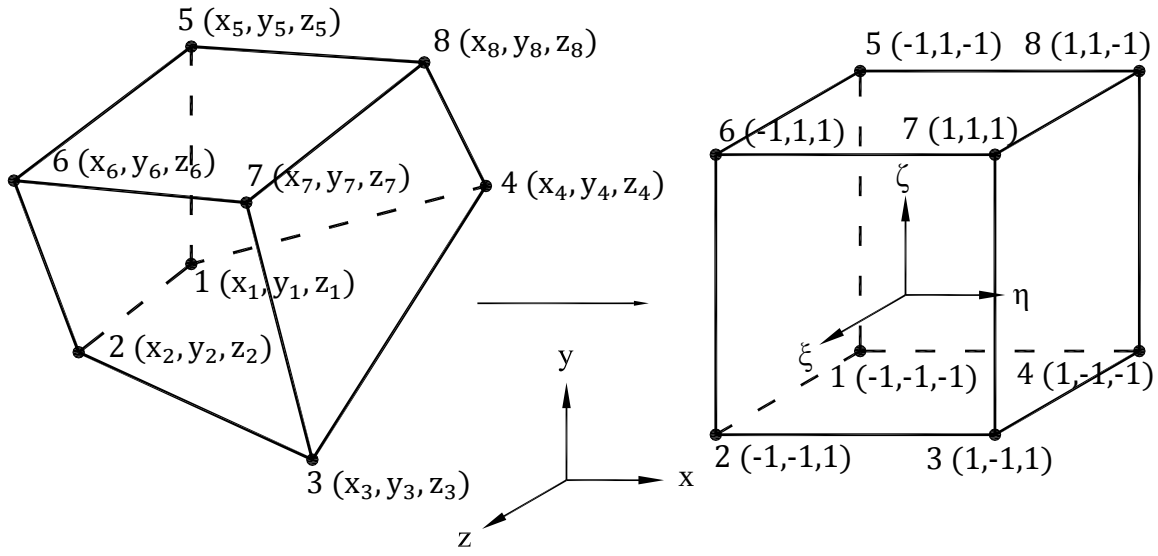

Figure 2-3 Isoparametric hexahexdral element added to VecTor3 and its transformed shape in natural coordinate system

Due to the complexity of the integration calculations required to reach a closed-form stiffness matrix for the element, the Gaussian quadrature rule (Gauss, 1814) is employed. Two Gauss points per direction are used, following the rule that m Gauss points give the exact result of a polynomial integrand of up to an order of $n = 2m - 1$, where the order of the integrand in this case (n) is equal to 3. For two Gauss points, the locations of the points are at $-1/\sqrt{3}$ and $1/\sqrt{3}$ in natural coordinates. Therefore, as shown in Figure 2-4, for this element, a total of eight Gauss points are used for determining the solution of the integrand, with natural coordinates: $(-1/\sqrt{3}, -1/\sqrt{3}, -1/\sqrt{3})$, $(-1/\sqrt{3}, -1/\sqrt{3}, 1/\sqrt{3})$, $(1/\sqrt{3}, -1/\sqrt{3}, 1/\sqrt{3})$, $(1/\sqrt{3}, -1/\sqrt{3}, -1/\sqrt{3})$, $(-1/\sqrt{3}, 1/\sqrt{3}, -1/\sqrt{3})$, $(-1/\sqrt{3}, 1/\sqrt{3}, 1/\sqrt{3})$, $(1/\sqrt{3}, 1/\sqrt{3}, 1/\sqrt{3})$, and $(1/\sqrt{3}, 1/\sqrt{3}, -1/\sqrt{3})$.

Taking advantage of this numerical integration scheme, the strain is calculated at the eight Gauss points and then a weighted average is calculated based on the volume associated with each Gauss point. This means that a more powerful element is formed, allowing for some variation in the value of the strain of the element in the three main directions, even though this variation is just linear.

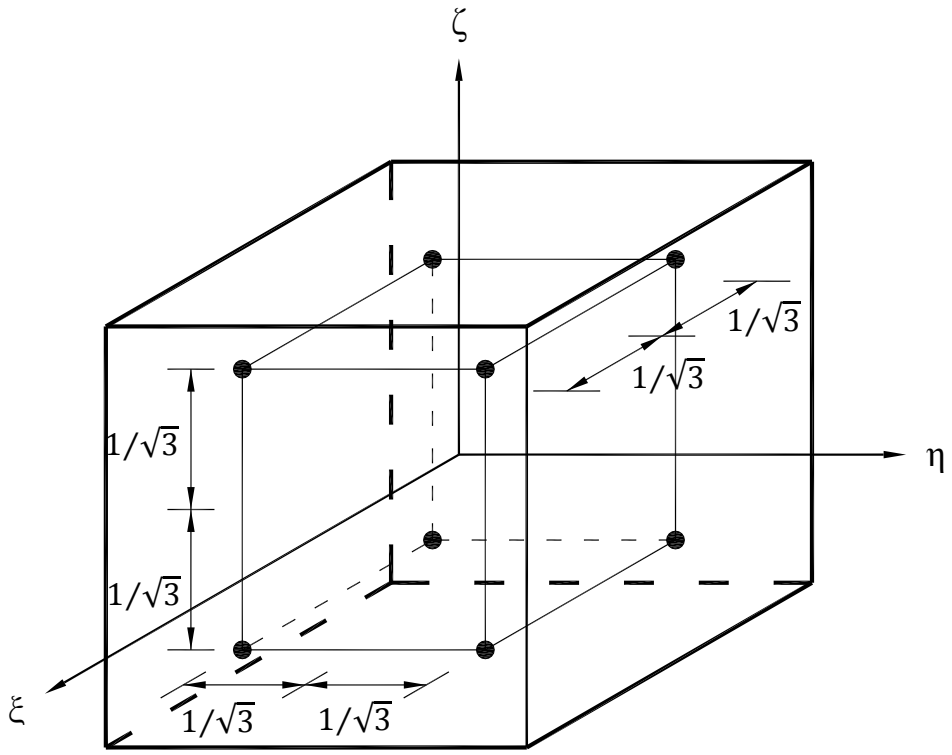

Figure 2-4 The locations of the eight Gauss points in the isoparametric hexahedral element

In order to consider geometric nonlinearity using this type of element, the coordinates of the nodes comprising it are constantly updated, taking into account their new locations based on their displacements. This way, any eccentric loading due to geometric nonlinearity and any P-Δ effects are automatically considered.

2.4.2 Advanced Structural Analysis Modelling in VecTor3

2.4.2.1 Introduction

The MCFT presents a rational theory for the behaviour of uncracked and cracked reinforced concrete. However, while the theory provides a platform for the structural analysis of reinforced concrete structures, many phenomena that reinforced concrete experiences still need to be integrated in this platform to provide a more comprehensive tool capable of analyzing a wide range of reinforced concrete structures in various types of assemblies and subjected to various loading conditions.

The DSFM was implemented in VecTor3 as a part of this study, allowing for modelling shear slip occurring on the surfaces of cracking. Also, VecTor3 was extended on many other levels: element types, constitutive models, and loading conditions. Besides the pre-existing eight-noded regular hexahedral brick elements, the triangular prism six-noded wedge elements, and the discrete truss bar elements, in this study, eight-noded isoparametric hexahedral elements have been developed. These new elements allow for the modelling of a wider range of structures with more complicated shapes and orientations, as well as accounting for the geometric nonlinearity effects (second-order analysis).

For concrete modelling, there are numerous constitutive models previously implemented in VecTor3 for concrete under compression such as Hognestad's parabola (1951), Popovics's curve for normal-strength concrete (1973), Popovics's curve for high-strength concrete presented by Collins and Porasz (1989) as a modification of the curve presented by Thorenfeldt et al. (1987) who, in turn, modified the curve presented by Popovics (1973), and Hoshikuma's curve (1997). For the post-peak phase of the compression stress-strain curve of concrete, the stress-strain curves provided by Saenz (1964) combined with the formulae given by Kwon and Spacone (2002), Park et al. (1982) as a modification of the curve provided by Kent and Park (1971), and Mander et al. (1988) who modified Popovics's curve (1973), are implemented in VecTor3.

Confinement of concrete is also modelled in VecTor3 using the models presented by Richart et al. (1928) and modified by Kupfer et al. (1969), and that provided by Montoya (2003) employing the concept put forth by Ottosen (1979).

Due to the key role that compression softening of concrete plays, where the compressive strength is reduced as a result of transverse tensile straining and cracking, and the special significance given to it in the MCFT, many expressions are implemented in VecTor3 to estimate the compression softening factor such as those given by Vecchio (1982), Vecchio and Collins (1986), Vecchio and Collins (1993), Miyahara et al. (1987) and (1988), Shirai and Noguchi (1989) and Kollegger and Mehlhorn (1990).

Among the models existing in VecTor3 for tension stiffening are those presented by Vecchio (1982) and its modification presented by Collins and Mitchell (1987), Bentz

(2000) and its modification developed by Vecchio and introduced in Sato and Vecchio (2003), and Izumo et al. (1991). For tension softening, besides the simple linear decay approach, the curves presented by Yamamoto (1999), and Hordijk (1991) were also added. As for tension splitting, the model proposed by Vecchio and DeRoo (1995) has been implemented.

For loading capabilities, displacement control and gravity forces have been added as well. Cyclic loading and seismic loading based on the work of Saatci (2007) were also implemented as available options for analyses. With the addition of those types of loading conditions, the need for modelling the hysteretic response of both concrete and reinforcement arose. For concrete, the hysteretic models implemented are those provided by Vecchio (1999) where the loading/unloading curve is linear, its modification where the unloading curve follows the nonlinear curve provided by Ramberg and Osgood (1943). The model presented by Palermo (2002) was also implemented as a part of this study. For reinforcement, the model provided by Seckin (1981) that includes Bauschinger effect (1886) is available in addition to the conventional elastic-plastic model either with or without the strain hardening phenomenon.

Many other additions have been implemented in VecTor3 in this study, such as the development of link elements in order to model the bond between concrete and reinforcement, dowel action of reinforcement, reinforcement prestressing, reinforcement buckling, strain rate effects, geometric nonlinearity effects, element temperature changes, concrete prestrains, ingress pressure in concrete elements, coupled heat and moisture transfer through concrete, spalling of concrete cover and explosive spalling in fire, and steel fibre-reinforced concrete (SFRC) analysis capabilities. Also, the capability to apply constraints in order to link predefined points in a structure with constant relations has been added to VecTor3, enabling users to impose predefined rotations along surfaces as well as assuring uniform load distribution on elements.

The procedures used in VecTor3 for the implementation of some of those models, features, and capabilities will be discussed in this section.

2.4.2.2 Slip Distortion

The main advantage provided by the DSFM over the MCFT is in modelling the shear slips occurring on the surface of the crack, allowing a lag to occur between the directions of the principal stress and those of principal strain. The DSFM was originally developed for two-dimensional membranes which created the need to extend it to three-dimensional solids to be able to implement it in VecTor3. Figure 2-5 shows the slip on the surface of the crack for a two-dimensional membrane. In this case, the slip occurs only in one direction which is the direction of the second principal stress as shown in Figure 2-6.

According to the DSFM, after the shear slip along the crack, δ_s, is calculated using the models that will be discussed later, slip shear strain, γ_s, is calculated according to the following equation:

$$\gamma_s = \frac{\delta_s}{s} \tag{2.1}$$

where s is the average crack spacing. Using Mohr's circle and the orientation of the principal stress, such a strain can be transformed into a slip strain vector in the local Cartesian coordinates of the element. This slip strain vector can, in turn, be dealt with as non-stress-inducing prestrain acting on the concrete element.

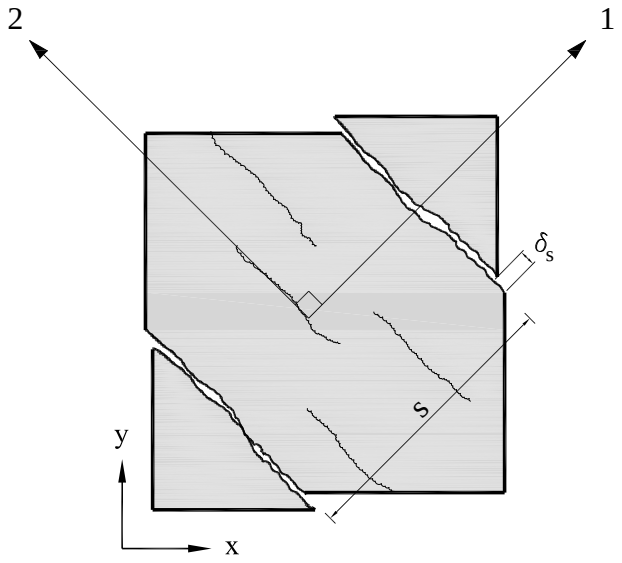

Figure 2-5 Deformation due to slip on the surface of crack for a two-dimensional membrane

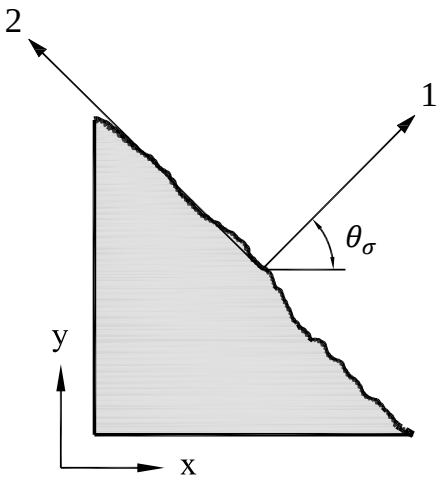

Figure 2-6 Principal directions along the surface of crack for a two-dimensional membrane

However, as shown in Figure 2-7, in the case of three-dimensional solids, the slip occurs over a crack plane rather than a crack line as is the case in two-dimensional membranes. This plane can be represented by two vectors along which shear slip can take place. For the purpose of adopting a procedure that is compatible with the DSFM and its implementation in VecTor3, those vectors are chosen to be in the directions of the second and third principal stress, which means that all slips along the crack are to be analysed into their components in those two directions as shown in Figure 2-8.

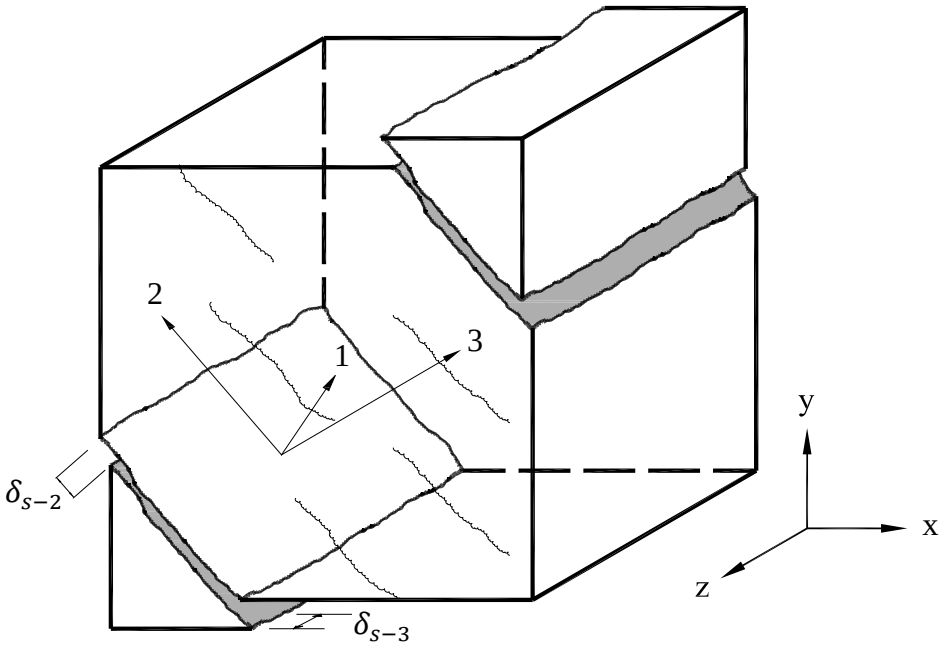

Figure 2-7 Illustration of the crack plane for a three-dimensional solid

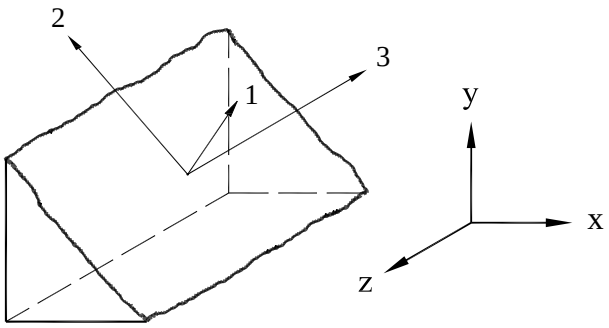

Figure 2-8 Principal directions along the surface of crack for a three-dimensional solid

This imposes the need to determine two separate slips on the crack: one along the direction of the second principal direction, denoted as $\delta_{s_{1-2}}$, and another along the third, denoted as $\delta_{s_{1-3}}$.

There are three different methods that can be used to calculate the slip on the surface of the crack: based on shear stress on the surface of the crack, based on preset constant rotation lag, and based on both shear stress on the crack and rotation lag.

2.4.2.2.1 Slip Based on Shear Stress on the Surface of the Crack

In order to study how slip distortions can be handled in three-dimensional solids, one needs to investigate the way the DSFM represents the transfer of concrete tensile stresses across a crack.

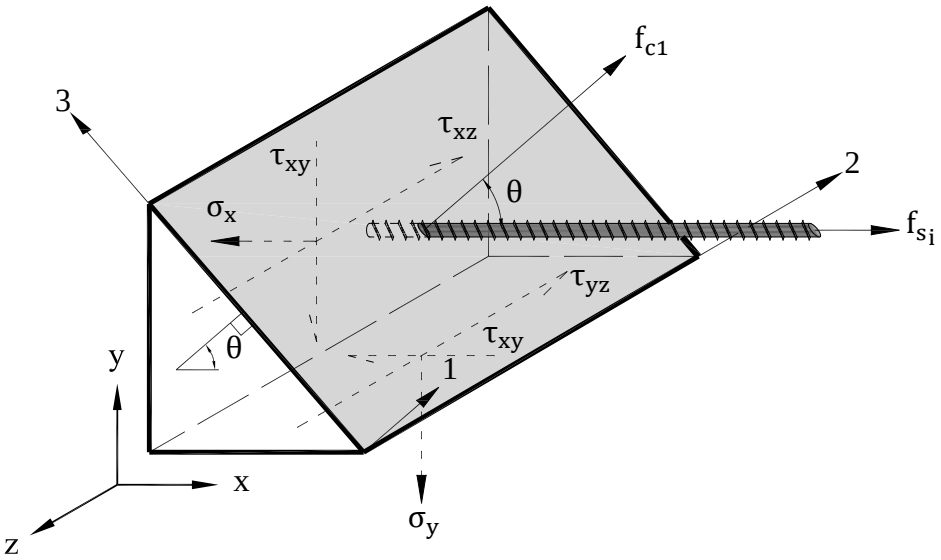

Figure 2-9 Average stresses along a section between the cracks in a three-dimensional reinforced concrete element

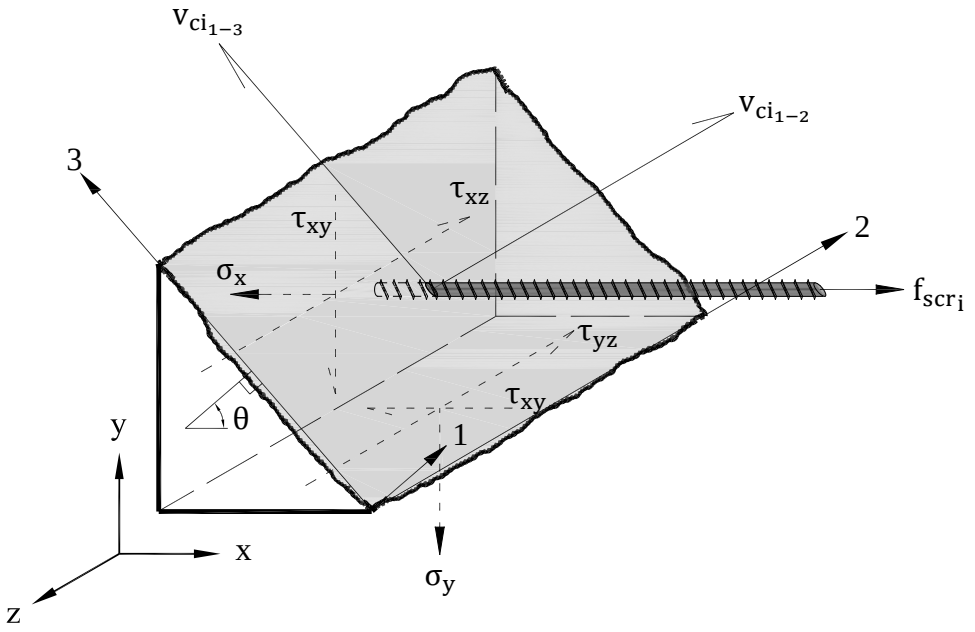

Figure 2-10 Local stresses along the surface of a crack in a three-dimensional reinforced concrete element

Figures 2-9 and 2-10 show how stresses are transformed through a reinforced concrete element on average (between cracks) and through cracks, respectively, where f_{c1} is the first principal tensile stress; f_{s_i} is the average stress in the reinforcing bar or the smeared reinforcement component number i; f_{scr_i} is the stress in such reinforcement across a crack; σ_x, σ_y, and σ_z are the normal stresses in the x, y and z directions, respectively; τ_{xy}, τ_{xz}, and τ_{yz} are the shear stresses on the $x-y$, $x-z$, and $y-z$ surfaces, respectively; and $v_{ci_{1-2}}$ and v_{ci-3} are the shear stresses on the surface of the crack in the second and third principal directions.

With the crack surface forming perpendicular to the first principal tensile stress, comparing Figure 2-9 to Figure 2-10, one can see that for equilibrium to be maintained through the element, an increase in the stress in the reinforcement needs to occur across the crack to make up for the fact that the first principal tensile stresses can no longer be transmitted through the element due to the discontinuity of the concrete particles at the crack. With that local increase in stress in the reinforcement, shear stresses on the surface of the crack arise concurrently to maintain equilibrium on the surface of the crack. Such shear stresses are analyzed into their components in the directions of the second and third principal stress.

Many models are implemented in VecTor3 in order to determine the amount of slip resulting from such shear stresses occurring on the crack, such as Walraven Model (1981), Maekawa Model (1991), and Lai-Vecchio Model (2004). These models relate the shear slips on the surface of cracking in the second principal direction, $\delta_{s_{1-2}}$, and third principal directions, $\delta_{s_{1-3}}$, to the shear stresses occurring on the surface of cracking, $v_{ci_{1-2}}$ and $v_{ci_{1-3}}$ respectively, based on the crack width and the compressive strength of concrete, in addition to the aggregate size in the case of the Maekawa Model and the Lai-Vecchio Model.

As such shear slips on the crack are calculated, they are used to calculate two separate slip shear strains as shown in the two following equations:

$$\gamma_{s_{1-2}} = \frac{\delta_{s_{1-2}}}{s_1} \tag{2.2}$$

$$\gamma_{s_{1-3}} = \frac{\delta_{s_{1-3}}}{s_1} \tag{2.3}$$

where $\gamma_{s_{1-2}}$ and $\gamma_{s_{1-3}}$ are the slip shear strains in the direction of the second and third principal stress respectively and s_1 is the average crack spacing in the direction of the first principal stress; or, in a more general sense, $\gamma_{s_{1-2}}$ and $\gamma_{s_{1-3}}$ are the slip shear strains in two perpendicular directions representing the plane of the crack and s_1 is the average crack spacing in the direction perpendicular to the crack. This general definition becomes useful in the case where the element is cracked in a second direction as well.

It should be noted that calculating shear slips on the surface of cracking in the second principal direction, $\delta_{s_{1-2}}$, and third principal directions, $\delta_{s_{1-3}}$, based on the respective shear stresses occurring on the surface of cracking is an approximation. The exact value of the slip should be a single value based on the vectorial resultant of the shear stresses on the surface of cracking, $v_{ci_{1-2}}$ and $v_{ci_{1-3}}$. Mathematically, combining $\delta_{s_{1-2}}$ and $\delta_{s_{1-3}}$ will obviously not result in the same value. However, this approximation is acceptable for two main reasons.

First, separate values for the slip on the surface of the cracking in the second and third principal directions are required for the calculation of the separate slip shear strains required for the DSFM procedure.

Second, the approximation error is believed to be minor. This is because whilst shear slip along the crack is permitted in any direction over the plane of the crack, it is normally predominant in the direction of the third principal stress with a very little component in the direction of the second principal stress, especially for planar structures.

One can also benefit from this fact, mentioned in the second reason, by ignoring that small component in the second principal direction in the analysis of planar structures in order to achieve a less time-expensive and simpler analysis.

2.4.2.2.2 Slip Based on Preset Constant Rotation Lag

Due to the way the MCFT and the DSFM calculate the shear stresses on the surface of the crack, maintaining equilibrium with the local increase of stress in the reinforcement crossing the crack, the aforementioned models can only estimate slip for reinforced concrete. With plain concrete where the MCFT and the DSFM calculate zero shear stresses on the surface of the crack, those models accordingly calculate zero shear slip on the surface of the crack, which is not how plain concrete behaves in reality.

This created the need for a way to predict shear slip on the surface of the crack without utilizing the state of equilibrium on the surface of the crack. This can be done by specifying a preset constant rotation lag between the post-cracking direction of the principal stress and the post-cracking direction of the principal strain, then calculating the shear slip strain based on that rotation lag. VecTor3 gives the option of specifying a rotation lag of 5, 7.5, 10, or 15 degrees. The procedure of applying the rotation lag starts with determining the direction of the principal strain then applying the rotation lag to it in order to determine the direction of the principal stress. There are two possible planes where the lag can be applied: the plane of the first and second principal stress directions and the plane of the first and third principal stress directions. Yet, the lag can only be applied to one of those two planes, simply because otherwise the mutual orthogonality of

the principal directions would not be maintained. Since it has been found that the slip in the plane of the first and third principal stress directions is more significant, the lag is always applied to that plane, and the second principal direction for both strain and stress will always be common, denoted as σ_2 and ε_2 in Figure 2-11.

The procedure for the application of the lag is an iterative process, where, at first, the projection of the first principal strain direction, ε_1, on the plane of the first and third principal stress directions obtained from the previous iteration (or the previous load step for the first iteration), denoted 'old σ_1' and 'old σ_3' respectively, is determined. That projection is shown in Figure 2-11 and denoted as 'proj ε_1'. The projection is, by definition, perpendicular to the second principal stress/strain direction. Next, another vector is determined with the criteria of having an angle equal to the preset rotation lag with the projection determined in the first step and in the same plane, denoted 'new σ_1'. That vector will represent the first principal stress direction. To determine the third principal stress direction, 'new σ_3', another vector that is normal to the first principal stress direction, 'new σ_1' and the second principal strain/stress direction, and is still on the same plane, will be obtained.

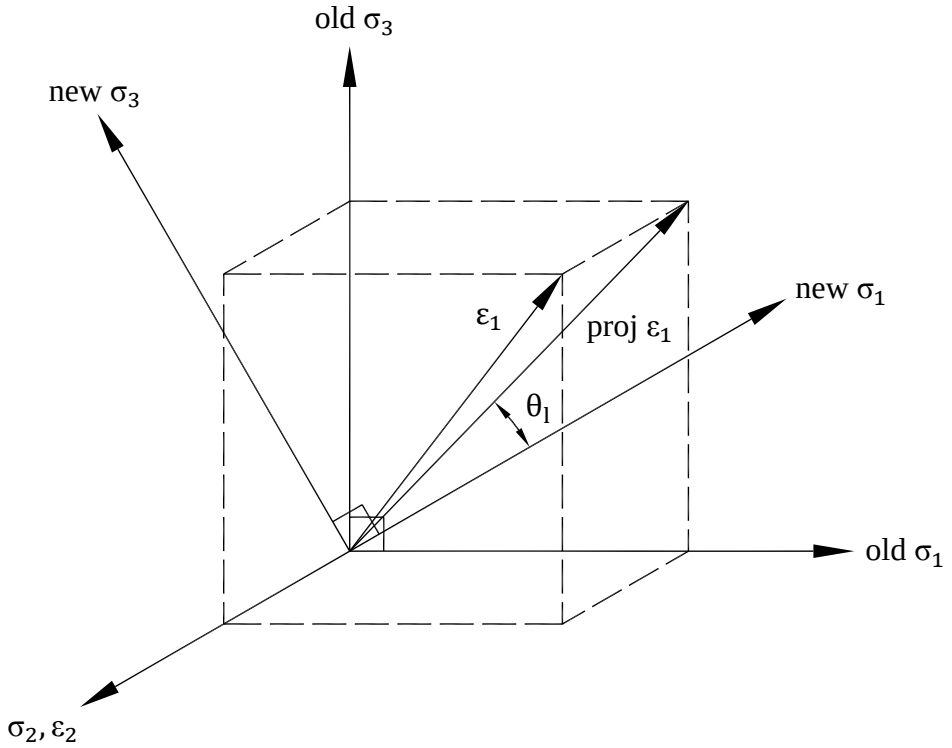

Figure 2-11 Determination of principal stress directions with preset constant lag from principal strain directions

With the principal stress directions calculated, the shear slip strain on the crack, γ_s, can be determined by the transformation of the total strains in the local coordinates to the plane of the crack (plane of the second and third principal stress directions) according to the following matrix transformation:

$$[\gamma] = [T]^T[e][T] \tag{2.4}$$

$$[\gamma] = \begin{bmatrix} \varepsilon_1 & \varepsilon_{12} & \varepsilon_{13} \\ \varepsilon_{12} & \varepsilon_2 & \varepsilon_{23} \\ \varepsilon_{13} & \varepsilon_{23} & \varepsilon_3 \end{bmatrix} \tag{2.5}$$

where

$$[T] = \begin{bmatrix} k_1 & k_2 & k_3 \\ l_1 & l_2 & l_3 \\ m_1 & m_2 & m_3 \end{bmatrix} \tag{2.6}$$

and

$$[e] = \begin{bmatrix} \varepsilon_x & \varepsilon_{xy} & \varepsilon_{xz} \\ \varepsilon_{xy} & \varepsilon_y & \varepsilon_{yz} \\ \varepsilon_{xz} & \varepsilon_{yz} & \varepsilon_z \end{bmatrix} \tag{2.7}$$

where $[\gamma]$ is the total strain matrix in the principal stress directions, $[e]$ is the total strain matrix in the local Cartesian coordinates, $[T]$ is the transformation matrix, k_i, l_i, and m_i represent the direction cosines of the i direction with respect to the x, y, and z directions, respectively, ε_j represents the total strain, and the subscript 'j' represents its direction, with ε_1 representing the total strain in the first principal direction, and ε_{xz} representing the total shear strain in the $x-z$ plane as examples.

Therefore the term that represents the shear slip strain on the surface of the crack, γ_s, is the term ε_{23} and can be calculated using the following expression:

$$\begin{aligned} \gamma_s = k_2k_3\varepsilon_x + l_2l_3\varepsilon_y + m_2m_3\varepsilon_z + k_2l_3\varepsilon_{xy} + k_3l_2\varepsilon_{xy} + k_2m_3\varepsilon_{xz} \\ + k_3m_2\varepsilon_{xz} + l_2m_3\varepsilon_{yz} + l_3m_2\varepsilon_{yz} \end{aligned} \tag{2.8}$$

This shear slip strain on the surface of the crack is then analyzed into its components in the second principal stress direction, γ_{s-2}, and in the third principal stress direction, γ_{s-3}, which can then be applied to the concrete element as a prestrain, as previously explained.

2.4.2.2.3 Slip Based on Shear Stress on the Crack and Rotation Lag

While calculating the shear slip strain on the surface of the crack based on a preset constant rotation lag resolves the problem of unrealistically predicting no shear slip on the surface of the crack in the case of unreinforced concrete when slip is calculated based on shear stress on the surface of the crack, it still has its deficiencies. Using preset constant rotation lag, even for reinforced concrete, can result in acceptable results if an appropriate rotation lag is selected, but only for lower load intensities. When load intensities get higher, the stress-based rotation lag between the principal strain and the principal stress increases. Thus, at such high load intensities, keeping a constant rotation lag would lead to incorrect predictions of slip on the surface of the crack.

Therefore, hybrid models that utilize both shear stress on the surface of the crack and the preset constant rotation lag have been implemented, where the constant lag is used as long as that lag is larger than the stress-based lag calculated between the principal stress and the principal strain. As soon as the real lag surpasses the constant lag, the slip is calculated based on shear stress on the surface of the crack using one of the models mentioned earlier. This means that the rotation lag is always calculated based on the preset constant rotation and based the stress, and the larger lag governs.

Using any of those suggested methods to calculate the shear slip strain on the surface of the crack, it is then transformed into the local coordinates of the element and is treated in the analysis as a non-stress-inducing prestrain.

2.4.2.3 Bond between Concrete and Reinforcement

Both the MCFT and the DSFM assume perfect bond between concrete and reinforcement. While this assumption can be acceptable and imposes an insignificant approximation in some cases, the bond slip can have a very significant effect on the behaviour and failure mode of some types of structures and assemblies such as beam-column assemblies where the bond slip of the longitudinal reinforcement of the beam can be the cause of failure, as well as its significant effect on the seismic behaviour of structures. Hence, the slip of reinforcing bars with respect to concrete had to be modelled

in VecTor3 in order to be able to realistically capture the behaviour of a wider range of structures types, loading conditions, and assembly arrangements. In order to do so, two parts related to the bond had to be modelled: the link elements that connect the concrete elements to the truss bar elements, and the bond stress-slip models that relate the shear stress on the surface of the reinforcing bar to the slip occurring on it.

2.4.2.3.1 Link Elements

The link elements implemented in VecTor3 were developed by Ngo and Scordelis (1967). These are two-noded dimensionless elements that link two coincident nodes. One node would be a component of a concrete element while the other would be a component of a discrete reinforcement truss bar element. Each of the two nodes comprising the link element can displace in any direction, resulting in an element having six degrees of freedom, three per node. Those displacements are governed by three different stiffnesses, one along the direction of the reinforcement truss bar element, K_t, and two others on a plane perpendicular to it, K_{r_1} and K_{r_2}. Those stiffnesses are determined according to any of the bond-slip models that are to be discussed later. Nonetheless, since only the slip along the reinforcement is of interest here, the displacements in the other two perpendicular directions are suppressed by assigning a large value for their stiffnesses. The shape of link element is shown in Figure 2-12.

Hence, the material stiffness matrix of the link element can be calculated according to the following equation:

$$[K] = A_l \begin{bmatrix} K_t & 0 & 0 \\ 0 & K_{r_1} & 0 \\ 0 & 0 & K_{r_2} \end{bmatrix} \tag{2.9}$$

where A_l is the lateral surface area of the portion of the discrete truss bar element tributary to the link element.

The forces on the link element can thus be calculated according to the following relation:

$$[F] = [K][\Delta] \tag{2.10}$$

or
$$\begin{Bmatrix} F_t \\ F_{r_1} \\ F_{r_2} \end{Bmatrix} = A_l \begin{bmatrix} K_t & 0 & 0 \\ 0 & K_{r_1} & 0 \\ 0 & 0 & K_{r_2} \end{bmatrix} \begin{Bmatrix} \Delta_t \\ \Delta_{r_1} \\ \Delta_{r_2} \end{Bmatrix} \quad (2.11)$$

where Δ_t, Δ_{r_1} and Δ_{r_2} are the displacements in the direction tangential to the discrete truss bar element, the first perpendicular direction, and the second perpendicular direction respectively; and F_t, F_{r_1}, and F_{r_2} are the forces in the direction tangential to the discrete truss bar element, the first perpendicular direction, and the second perpendicular direction respectively.

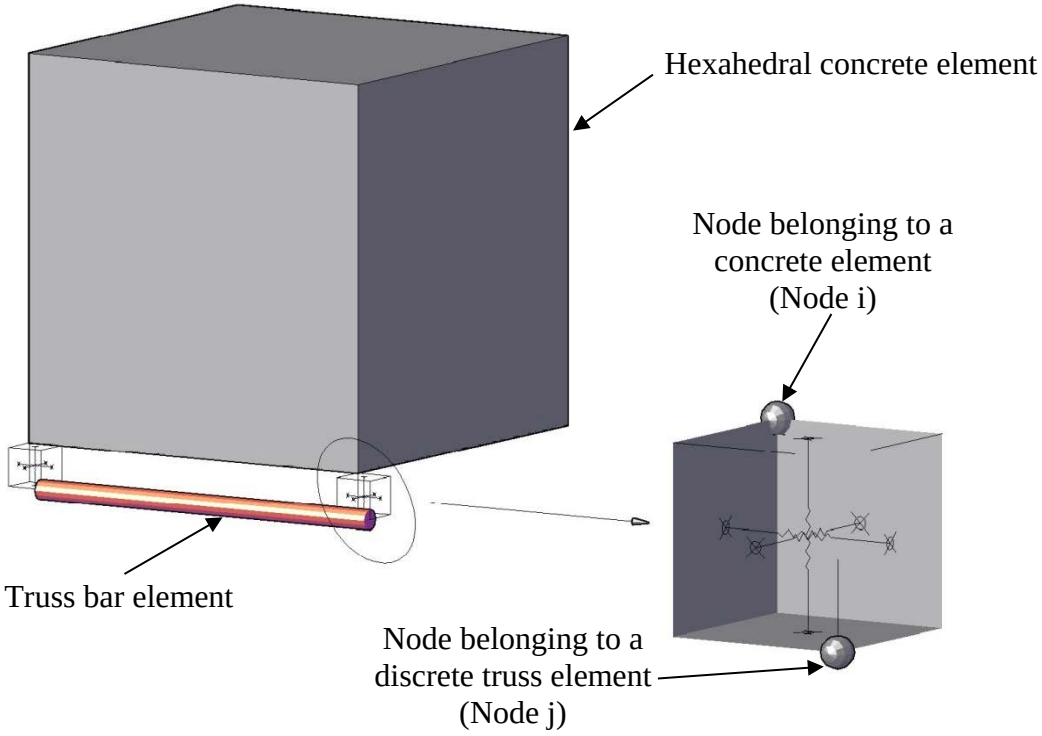

Figure 2-12 Shape of link elements in three dimensions

The displacements of the two nodes comprising the link element have to be analyzed from their components in the x, y and z coordinate system into a coordinate system that has a primary axis going along the axis of the discrete truss bar element, which is given the symbol 't', and two other axes that are perpendicular to it along the surface of the concrete element and are given the symbols 'r_1' and 'r_2'. The relation between the two coordinate systems is shown in Figure 2-13.

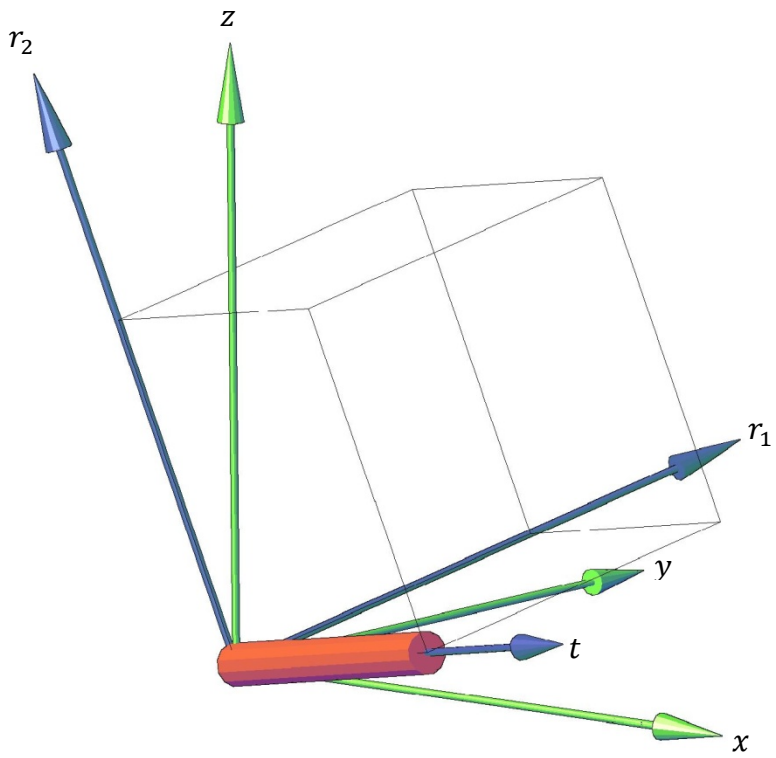

Figure 2-13 The relation between the local coordinate system of the link element and the global coordinate system

Assuming the direction cosines of the t-axis with respect to the x, y, and z axes are k_1, l_1 and, m_1, respectively, and those of the r_1 and r_2 axes are k_2, l_2, and m_2 and k_3, l_3, and m_3, respectively, the deformation of the link element, $[\Delta]$, can be given in terms of the x, y, and z coordinate system according to the relation in Equation (2.12).

$$[\Delta] = [T][r] \tag{2.12}$$

where
$$[r] = [r_{i,x} \quad r_{i,y} \quad r_{i,z} \quad r_{j,x} \quad r_{j,y} \quad r_{j,z}]^T \tag{2.13}$$

and the transformation matrix, $[T]$, is calculated as:

$$[T] = \begin{bmatrix} -k_1 & -l_1 & -m_1 & k_1 & l_1 & m_1 \\ -k_2 & -l_2 & -m_2 & k_2 & l_2 & m_2 \\ -k_3 & -l_3 & -m_3 & k_3 & l_3 & m_3 \end{bmatrix} \tag{2.14}$$

where $r_{i,x}$, $r_{i,y}$, and $r_{i,z}$ are the displacements in the x, y, and z directions for node i, respectively; and $r_{j,x}$, $r_{j,y}$, and $r_{j,z}$ are the displacements in the x, y, and z directions for node j, respectively.

Similarly,

$$\begin{Bmatrix} F_t \\ F_{r_1} \\ F_{r_2} \end{Bmatrix} = [T] \begin{Bmatrix} F_{i,x} \\ F_{i,y} \\ F_{i,z} \\ F_{j,x} \\ F_{j,y} \\ F_{j,z} \end{Bmatrix} \tag{2.15}$$

Since the force is the product of the stiffness and displacement such that:

$$\begin{Bmatrix} F_{i,x} \\ F_{i,y} \\ F_{i,z} \\ F_{j,x} \\ F_{j,y} \\ F_{j,z} \end{Bmatrix} = \left[K_{xyz}\right] \begin{Bmatrix} r_{i,x} \\ r_{i,y} \\ r_{i,z} \\ r_{j,x} \\ r_{j,y} \\ r_{j,z} \end{Bmatrix} \tag{2.16}$$

then, by substituting in Equation (2.10) using Equations (2.12) and (2.15) and comparing to Equation (2.16), $\left[K_{xyz}\right]$ can be calculated as:

$$\left[K_{xyz}\right] = [T]^T[K][T] \tag{2.17}$$

This equation yields a 6×6 stiffness matrix with elements given the notation K_{i-j} where i is the row number and j is the column number as follows:

$$\begin{aligned}
K_{1-1} &= {k_1}^2 K_t + {k_2}^2 K_{r_1} + {k_3}^2 K_{r_2} & K_{3-3} &= {m_1}^2 K_t + {m_2}^2 K_{r_1} + {m_3}^2 K_{r_2} \\
K_{1-2} &= k_1 l_1 K_t + k_2 l_2 K_{r_1} + k_3 l_3 K_{r_2} & K_{3-4} &= -K_{1-3} \\
K_{1-3} &= k_1 m_1 K_t + k_2 m_2 K_{r_1} + k_3 m_3 K_{r_2} & K_{3-5} &= -K_{2-3} \\
K_{1-4} &= -K_{1-1} & K_{3-6} &= -K_{3-3} \\
K_{1-5} &= -K_{1-2} & K_{4-4} &= K_{1-1} \\
K_{1-6} &= -K_{1-3} & K_{4-5} &= K_{1-2} \\
K_{2-2} &= {l_1}^2 K_t + {l_2}^2 K_{r_1} + {l_3}^2 K_{r_2} & K_{4-6} &= K_{1-3} \\
K_{2-3} &= l_1 m_1 K_t + l_2 m_2 K_{r_1} + l_3 m_3 K_{r_2} & K_{5-5} &= K_{2-2} \\
K_{2-4} &= -K_{1-2} & K_{5-6} &= K_{2-3} \\
K_{2-5} &= -K_{2-2} & K_{6-6} &= K_{3-3} \\
K_{2-6} &= -K_{2-3}
\end{aligned}$$

It should be noted here that one can assume perfect bond between concrete and reinforcement by assigning a sufficiently large value to the stiffness of the bond stress-slip curve.

2.4.2.3.2 Bond Stress-Slip Models

While the link elements serve in separating the discrete truss bar elements from the concrete elements, allowing each of them to displace independently and, hence, slip to occur, this amount of slip is yet to be determined. In the same sense that in a typical concrete or steel element, displacement occurs depending on a certain element stiffness and results in the occurrence of stress, in a link element, relative displacement also occurs between the two once-coincident nodes comprising the link element (one node on the discrete truss bar element and the other on the concrete element), known as bond slip, also depending on a certain stiffness and resulting in the occurrence of stress, known as bond stress. Using the same analogy, the stiffness that controls the response of concrete or steel and is calculated from the concrete or steel constitutive model, which is presented in the form of a stress-strain curve, corresponds to the stiffness that controls the slip of the reinforcing bar and is calculated from a constitutive model that is presented in the form of a bond stress-slip curve.

There have been a large number of attempts to provide a reliable model for the bond stress-slip relation, with many of them being relatively successful. In those models, many criteria play an important role in determining the stress resulting from the slip such as the compressive strength of concrete, the concrete cover, the diameter of the reinforcing bar, the type of reinforcing bar, smooth or deformed, the shape of the bar tip (i.e., hooked or unhooked), and the height and spacing of the lugs on the bars.

However, the most significant criterion in determining the stress resulting from the slip is the level of confinement of the bar. This significance goes as far as determining the mode of failure. For confined bars, the bond is stronger and the failure mode is normally a pull-out type of failure, while for unconfined bars, the bond tends to be weaker causing a cover splitting failure to be more dominant. Since there is no decisive line separating the confined and unconfined status of concrete, the confinement pressure factor, β, has been introduced for most of the available models as a factor of the level of confinement of a bar. This factor ranges from zero for the case of unconfined bars and one for the case of fully confined bars. According to CEB-FIP Model Code 1990 (1993), a confinement

pressure of 7.5MPa imposes full confinement for the reinforcing bar. This defines the confinement pressure factor as:

$$\beta = \frac{\sigma}{7.5} \tag{2.18}$$

where σ is the confinement pressure in MPa and β ranges from zero to one. The confinement pressure, σ, can either be computed through the conventional structural analysis procedure, taking advantage of the three-dimensional capabilities of VecTor3, or it can be assumed that once there is a significant slip through the bond, the transverse reinforcement will have yielded at that point and hence the confinement pressure can be assumed to be equal to the transverse reinforcement ratio, ρ_v, multiplied by the yielding stress of that transverse reinforcement, $f_{y,v}$, so that:

$$\sigma = \rho_v f_{y,v} \tag{2.19}$$

Among the models of bond stress-slip available in VecTor3 is the Eligehausen Model, which was developed by Eligehausen et al. (1983) and was the basis for the CEB-FIP Model Code 1990 (1993) as well. The model proposes three sets of equations for three different cases: the fully confined and fully unconfined cases based on the definition previously mentioned and an intermediate case for $0 \leq \beta \leq 1$. The Gan-Vecchio Model, developed by Gan (2000), has the same model for the fully confined case but proposes a different model for the fully unconfined case and subsequently a different model for the intermediate case as well. Based on experimental results, Gan eliminated the bond stress-slip plateau from the case of splitting failure, which was present in the Eligehausen Model, and assumed a steeper decline in the descending branch of the curve. The Eligehausen Model and the Gan-Vecchio Model offer the advantage of modelling the cyclic response of the bond with the option to account for the damage of the bond due to cyclic loading.

Also, the Harajli Model, developed by Harajli and Mukaddam (1988) and the Fujii Model, developed by Morita and Fujii (1982), were implemented in VecTor3. All models, except for the Fujii Model, can account for hooked bars. However, Fujii Model

has the advantage of predicting the type of splitting failure whether side splitting, where the entire concrete cover spalls, or corner splitting, where only the corner tip spalls.

More about these models and their expressions can be found in Wong et al. (2013).

2.4.2.4 Dowel Action of Reinforcement

The Disturbed Stress Field Model (DSFM) models shear slip occurring on the surface of the crack in an element. However, as shown in Figure 2-14, it is expected that such slip can be reduced if the reinforcement happens to be crossing through the crack. This is what creates the need to model the dowel action of reinforcement. This effect can be significant in a case where a small amount of transverse reinforcement is provided, where considering dowel action provides higher shear strength and more ductility for the elements.

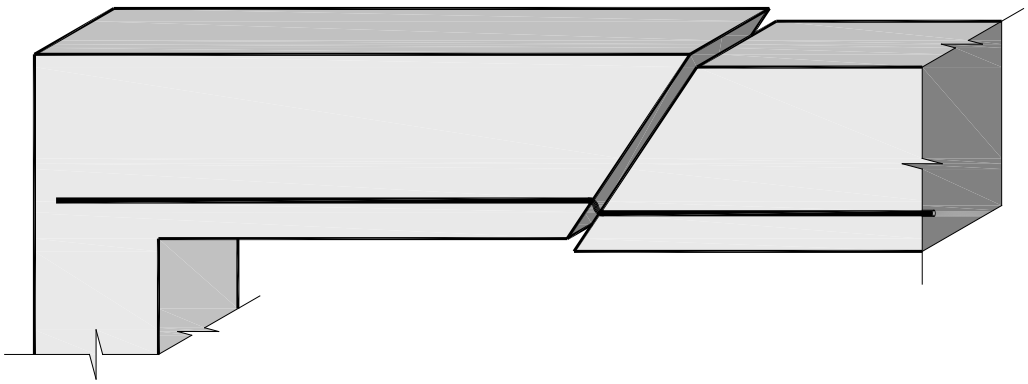

Figure 2-14 Dowel action over a crack slip

Accounting for dowel action basically means accounting for the extra shear resistance gained through the reinforcing bars crossing a crack as that crack slips in a direction perpendicular or inclined with respect to the axis of the bar. Thus, the amount of such resistance increases as the shear slip occurring on the crack increases. That slip, in turn, is caused by the shear stress acting on the surface of the crack and increases as that stress increases.

In order to establish a dowel force-displacement relation, the analysis was done in a way analogous in theory to the analysis of a beam on elastic foundation, developed by Hetényi (1946), with the reinforcement being the beam and the concrete surrounding it being the foundation, as shown in Figure 2-15. The Tassios Model, developed by Vintzeleou and Tassios (1987), proposed a series of expressions to calculate the dowel force as a function of the relative slip displacement along the crack together with the modulus of elasticity of the reinforcement, its moment of inertia, and the relative stiffness of concrete. That relative stiffness corresponds to a series of springs representing the elastic foundation, and depends on its compressive strength, the reinforcing bar diameter, and the clear spacing between the bars. Yet, the reinforcement dowel action is different than beams on elastic foundation in the fact that steel reinforcing bars can yield and that the surrounding concrete can be crushed. This is why Dulacska (1972) proposed a limit on the dowel force at ultimate limit state.

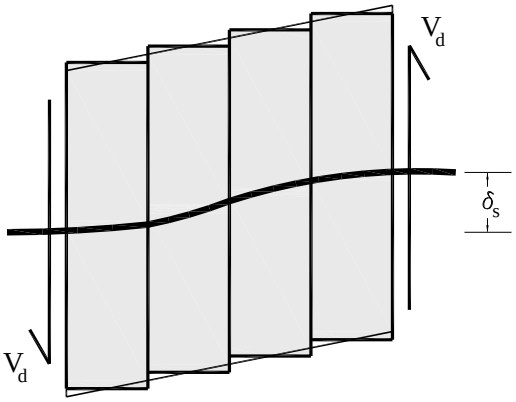

Figure 2-15 Modelling dowel action as a beam on elastic foundation
where V_d is the dowel force and δ_s is the shear slip

Therefore, in order to account for dowel action, the extra shear resistance force needs to be calculated based on the amount of shear slip occurring on the crack, then used to calculate the shear stress resistance due to dowel action. That shear stress resistance is then subtracted from the shear stress occurring on the surface of the crack and the shear slip is recalculated. This procedure shows the iterative aspect of the process.

2.4.2.5 Steel Fibre-Reinforced Concrete

2.4.2.5.1 Introduction

With the rapidly growing use of steel fibre-reinforced concrete (SFRC) in construction, the need for a three-dimensional structural analysis tool, capable of providing reasonable predictions of the behaviour of such a material that is still not totally understood and remains the main interest for numerous researchers, becomes evident. This is why modelling capabilities for SFRC were incorporated in VecTor3. The analysis of plain SFRC and conventionally-reinforced SFRC involves many aspects in which they behave differently from conventional reinforced concrete. The main advantage that SFRC offers is the ductile non-brittle behaviour it shows after cracking due to the contribution of the fibres as they cross the cracks, allowing the transfer of tensile stress through even wide cracks. One main aspect that influences the behaviour of SFRC members and that needs to be investigated and modelled is the tensile stress contribution component of the fibres in the total tensile stress borne by SFRC members. Such a stress contribution is determined by the Simplified Diverse Embedment Model (SDEM), developed by Lee et al. (2011a, 2011b; 2013a). Other significant contributing models include the tension stiffening behaviour of concrete matrix in conventionally-reinforced SFRC, modelled by Lee et al. (2013b) and the average crack width in conventionally-reinforced SFRC, modelled by Deluce and Vecchio (2013). In this section, those aspects will be discussed and the finite element procedure followed for the implementation in VecTor3 will be explained.

2.4.2.5.2 Simplified Diverse Embedment Model (SDEM)

Among the many models available in the literature that have attempted to capture the behaviour of SFRC, the Diverse Embedment Model (DEM), recently developed by Lee et al. (2011a; 2011b), has shown better correlation with experimental results. The model introduced an analysis procedure for the estimation of the tensile stresses attained by the fibres at the cracks for both straight and end-hooked types of fibres.

Due to the complexity of the DEM, incurred by the double numerical integration required for the analysis, Lee et al. (2013a) introduced the Simplified Diverse Embedment Model (SDEM), where the double numerical integration was eliminated by neglecting the estimation of the slip of the fibres on the side of the crack that has the longer fibre embedment length, meaning that the crack width is assumed to be equal to the slip of the fibres on the side of the crack that has the shorter fibre embedment length. In order to account for the over-estimation of the tensile stresses attained by the fibres at the crack resulting from that simplification, Lee et al. introduced the reduction coefficients β_f and β_{eh} to the tensile stresses attained by the fibres at the cracks calculated by solely considering the slip of the fibres on the side of the crack that has a shorter fibre embedment length, where β_f was applied to the frictional bond stress contribution component, f_{st}, and β_{eh} to the mechanical anchorage contribution component, f_{eh}.

The SDEM divides the total tensile stress attained by the fibres crossing a crack into two components: the frictional bond stress contribution component, f_{st}, which both straight and end-hooked fibres exhibit, and the mechanical anchorage contribution component, f_{eh}, which only end-hooked fibres exhibit.

The frictional bond stress contribution component, f_{st}, can be calculated according to the following expression:

$$f_{st} = \alpha_f V_f K_{st} \tau_{f_{max}} \frac{l_f}{d_f}\left(1 - \frac{2w_{cr}}{l_f}\right)^2 \tag{2.20}$$

where

$$K_{st} = \begin{cases} \dfrac{\beta_f}{3}\dfrac{w_{cr}}{s_f} & \text{for } w_{cr} \le s_f \\ 1 - \sqrt{\dfrac{s_f}{w_{cr}}} + \dfrac{\beta_f}{3}\sqrt{\dfrac{w_{cr}}{s_f}} & \text{for } w_{cr} > s_f \end{cases} \tag{2.21}$$

where l_f, d_f, and V_f are the fibre length, diameter, and volumetric ratio, respectively, and α_f is the fibre orientation factor that takes into account the effect of the member size on the general orientation of the fibres in the member and hence its effect on the magnitude of the stresses attained by the fibres. α_f has the value 0.5 for relatively infinite three-dimensional elements where the fibre length is relatively small compared to the size

of the member, which is the case in almost all structural analyses. K_{st} is a factor that represents the average fibre pull-out stresses resulting from the frictional bond stresses along the contact area between the fibre and the concrete; $\tau_{f_{max}}$ is the frictional bond strength of the fibre with the concrete, calculated as $0.396\sqrt{f'_c}$ in MPa based on the studies done by Voo and Foster (2003) and Lee et al. (2011b), where f'_c is the concrete compressive strength; β_f, defined earlier, is analytically determined as 0.67 by correlating the frictional bond stress contribution component calculated by the SDEM to that calculated by the DEM; w_{cr} is the average crack width; and s_f is the slip corresponding to the maximum frictional bond stress for a fibre normal to the crack surface, taken as 0.01 mm according to the suggestions of Naaman and Najm (1991).

The mechanical anchorage stress contribution component, f_{eh}, which is limited to end-hooked fibres only, is calculated according to the following expression:

$$f_{st} = \alpha_f V_f K_{eh} \tau_{eh_{max}} \frac{2(l_i - 2w_{cr})}{d_f} \tag{2.22}$$

where

$$K_{eh} = \begin{cases} \beta_{eh}\left[\frac{2}{3}\frac{w_{cr}}{s_{eh}} - \frac{1}{5}\left(\frac{w_{cr}}{s_{eh}}\right)^2\right] & \text{for } w_{cr} \le s_{eh} \\ 1 + \left(\frac{7\beta_{eh}}{15} - 1\right)\sqrt{\frac{s_{eh}}{w_{cr}}} - \frac{2\left(\sqrt{w_{cr}} - \sqrt{s_{eh}}\right)^2}{l_f - l_i} & \text{for } s_{eh} \le w_{cr} < \frac{l_f - l_i}{2} \\ \left(\frac{l_i - 2w_{cr}}{2l_i - l_f}\right)^2 K_{eh,i} & \text{for } \frac{l_f - l_i}{2} \le w_{cr} < \frac{l_i}{2} \end{cases} \tag{2.23}$$

where K_{eh} is a factor that represents the average fibre pull-out stresses resulting from the mechanical anchorage; $\tau_{eh_{max}}$ is the pull-out strength provided by mechanical anchorage, calculated as $0.429\sqrt{f'_c}$ in MPa based on the studies done by Voo and Foster (2003) and Lee et al. (2011b); l_i is the distance between the mechanical anchorages; β_{eh}, defined earlier, is analytically determined as 0.76 by correlating the frictional bond stress contribution component calculated by the SDEM to that calculated by the DEM; s_{eh} is the slip corresponding to the maximum tensile stresses attained by the fibres due to

mechanical anchorage for a fibre normal to the crack surface, taken as 0.1 mm according to the suggestions of Naaman and Najm (1991).

2.4.2.5.3 Tension Stiffening in Conventionally-Reinforced SFRC

While the literature contains many approaches aimed at evaluating the tension stiffening behaviour of conventionally-reinforced SFRC, including those presented by Abrishami and Mitchell (1997), Chiaia et al. (2009), and Na and Kwak (2011), they are not compatible with the MCFT or the DSFM, or any smeared crack concrete model in general. These approaches evaluate tension stiffening in conventionally-reinforced SFRC by evaluating the difference between the response of the conventionally-reinforced SFRC member and that of a bare bar, thus evaluating the tensile stresses attained by the concrete matrix as a result of its bond with the rebar combined with the tensile stresses attained by the fibres.

Examining the equilibrium on the surface of the crack (as shown in Figure 2-10) and the sections between the cracks (as shown in Figure 2-9) is a key aspect in the MCFT and the DSFM, where the loss of the concrete contribution component in transferring the tensile stresses through the crack is compensated by the local increase in tensile stresses in the reinforcement crossing the crack. This, in turn, results in the occurrence of shear stresses on the surface of the crack. Thus, it is essential that the local stress in the conventional reinforcement crossing the crack be accurately evaluated. However, in the case of conventionally-reinforced SFRC, the fibres crossing the crack also contribute to the compensation for that loss of ability of concrete to transfer the tensile stresses due to cracking. Therefore, the contribution of the fibres crossing the crack has to be separately evaluated so that the local stress in the reinforcement crossing the crack can be evaluated and then the tension stiffening behaviour of concrete can be estimated.

This requirement was satisfied by the DEM, developed by Lee et al. (2011b; 2011a), where the tensile stresses attained by the fibres crossing the crack have been separately evaluated. Employing the DEM, Lee et al. (2013b) managed to estimate the tension stiffening behaviour of concrete in conventionally-reinforced SFRC by removing the

tensile stresses component attained by the conventional reinforcement and the tensile stresses component attained by the fibres from the total tensile stresses borne by the member. Lee et al. modified the conventionally-reinforced concrete tension stiffening model presented by Sato and Vecchio (2003), who, in turn, modified the model presented by Bentz (2000) and presented their tension stiffening model in the following form:

$$f_{c,TS} = \frac{f_{cr}}{1 + \sqrt{3.6 c_f M \varepsilon_{t,avg}}} \tag{2.24}$$

where $$c_f = \begin{cases} 0.6 + \frac{1}{0.058}\left(\frac{l_f}{d_f}\right)^{0.9} \frac{100 V_f}{M^{0.8}} & \text{for SFRC with straight fibres} \\ 0.6 + \frac{1}{0.034}\left(\frac{l_f}{d_f}\right) \frac{(100 V_f)^{1.5}}{M^{0.8}} & \text{for SFRC with end-hooked fibres} \end{cases} \tag{2.25}$$

and $$M = \frac{A_c}{\sum \pi d_{bs_i}} \tag{2.26}$$

where $f_{c,TS}$ is the tensile stress in the concrete matrix of conventionally-reinforced SFRC with tension stiffening behaviour taken into consideration, f_{cr} is the cracking stress of the concrete matrix, c_f is a coefficient that accounts for the effect of the steel fibres, M is the bond parameter calculated as shown in Equation (2.26), and A_c is the cross-sectional area of the concrete effectively bonded with the steel reinforcing bars in mm^2, which, according to CEB-FIP Model Code 1990 (1993), is assumed to be limited to the concrete lying within a distance of $7.5d_{bs_i}$ from the reinforcing bar, where d_{bs_i} is the diameter of the rebar of the i^{th} reinforcing bar series in mm.

Equation (2.26) presents the formula for the calculation of the bond parameter, M, for steel reinforcing bars making a zero angle with the direction of the principal tensile stress. Since this is not the real case, the parameter has to be analyzed to find its component in the direction of the principal tensile stress.

It should be noted that, for the concrete regions that are more than $7.5d_{bs}$ away from the reinforcement, tension softening will govern instead of tension stiffening. For concrete regions that are within this distance, stresses due to tension stiffening and those due to tension softening are both evaluated and then the behaviour offering higher-valued

stresses is assumed to govern. In order to determine the total tensile stresses attained by a member, the tensile stresses attained by the conventional reinforcement, and the tensile stresses due to tension stiffening or due to tension softening are added to the tensile stresses attained by the fibres as calculated using the DEM or the SDEM.

2.4.2.5.4 Average Crack Width in SFRC

There is wide consensus among researchers that, for SFRC members, the post-cracking tensile stresses are directly dependent on the average crack width. This can easily be found in the SDEM formulation previously discussed for both the frictional bond stress contribution component, f_{st}, and the mechanical anchorage contribution component, f_{eh}. Therefore, the ability to accurately determine the average crack width in a member is a vital element in the modelling of SFRC.

Since the average crack width, $w_{cr_{avg}}$, can simply be determined as the product of the member average crack spacing, s_m, and the average tensile strain, ε_1, as shown in Equation (2.27), the real target becomes the determination of the average crack spacing. While the literature offers many models that can be utilized to determine the average crack spacing for conventional reinforced concrete, these models cannot be applied for conventionally-reinforced SFRC. Conventionally-reinforced SFRC members normally show a larger number of cracks, more closely-spaced and smaller in width.

$$w_{cr_{avg}} = s_m \varepsilon_1 \tag{2.27}$$

This is due to the fact that when a crack occurs in a conventionally-reinforced SFRC member, both fibres and conventional reinforcing bars bridge the crack; hence, they both contribute to the transfer of the tensile stresses through the crack. This results in a more efficient transfer of stresses into the concrete matrix in the sections between the cracks than normally happens in conventional reinforced concrete; thus, the concrete matrix in SFRC attains higher stresses causing other cracks to occur between the initial cracks. The result is that more cracks are formed or, in other words, the crack spacing decreases. Also, since, for conventionally-reinforced SFRC members, conventional reinforcement

no longer has to transfer all the tensile stresses through the crack, it will carry less stress than a similar member loaded under the same conditions but with no fibres. With less stress in the reinforcement, there will be lower strain, thus smaller crack width.

Among the models developed to evaluate the crack spacing in conventionally-reinforced SFRC is the model presented by Moffatt (2001). It required the estimation of post-cracking residual tensile stresses in concrete, which has to be done experimentally. This makes the model impractical for typical structural analyses. Also, Dupont and Vandewalle (2003) modified the Eurocode expression (ENV 1992-1-1:1992, 1992) provided for crack spacing for conventional reinforced concrete to be applicable to conventionally-reinforced SFRC. However, the model did not distinguish between the average crack spacings for members having different fibre volumetric ratios, despite the significant effect they have on the average crack spacing and crack width (Deluce, 2011; Deluce and Vecchio, 2013).

Deluce et al. (expected 2013) presented a comprehensive model based on an extensive experimental program undertaken on 47 conventionally-reinforced SFRC members tested under tension. The effects of many parameters were taken into consideration, including the fibre volumetric ratio, length, and aspect ratio and conventional reinforcement ratio and bar diameter. The model modifies the CEB-FIP Model Code (1978) provided for crack spacing for conventional reinforced concrete to be applicable to conventionally-reinforced SFRC as follows:

$$s_m = 2\left(c + \frac{s_b}{10}\right)k_3 + \frac{k_1 k_2}{s_{mi}} \tag{2.28}$$

where

$$s_b = \frac{1}{\sqrt{\sum \frac{4}{\pi}\frac{\rho_{s_i}}{d_{bs_i}}\cos^4\theta_i}} \tag{2.29}$$

and

$$s_{mi} = \sum \frac{\rho_{s_i}}{d_{bs_i}}\cos^2\theta_i + k_f \frac{\alpha_f \min(V_f, 0.015)}{d_f} \tag{2.30}$$

where s_m is the average crack spacing; s_b is the effective spacing between longitudinal bars; s_{mi} is a reinforcement effectiveness parameter; c is the effective concrete cover

taken as 1.5 times the maximum aggregate size in lieu of actual cover dimensions; and $\rho_{s,i}$, $d_{bs,i}$, and θ_i are the conventional reinforcement ratio, conventional reinforcing bar diameter, and the angle between the conventional reinforcing bar and the principal tensile stress for the i^{th} conventional reinforcing bar series, respectively.

Similar to the original CEB-FIP Model Code (1978), the parameter k_1 is a factor that accounts for the bond type of the reinforcing bars, given a value of 0.4 for the deformed bars and 0.8 for the smooth bars and prestressing tendons, and the parameter k_2 is a factor that accounts for the strain conditions in the member where:

$$k_2 = 0.25\frac{\varepsilon_1 + \varepsilon_3}{2\varepsilon_1} \tag{2.31}$$

where ε_1 and ε_3 are the largest and smallest average principal tensile strains in the member respectively.

k_3 is a fibre content factor, determined as follows:

$$k_3 = 1 - \frac{\min(V_f, 0.015)}{0.015}\left(1 - \frac{1}{k_f}\right) \tag{2.32}$$

where k_f is a factor that accounts for fibre effectiveness resulting from the fibre aspect ratio. Dupont and Vandewalle (2003) estimated k_f as:

$$k_f = \frac{l_f}{50d_f} \geq 1.0 \tag{2.33}$$

The limitation of the fibre volumetric ratio, V_f, to 1.5% was introduced to account for the findings of Oh (2011), where SFRC members were tested in direct tension and the effect of the increase of the fibre volumetric ratio to more than 1.5% on the tensile stresses was very limited; this phenomenon is sometimes called fibre saturation.

In order to determine the ultimate capacity of a member, the maximum crack width also has to be determined, since failure typically occurs at the location of the widest crack, being the weakest location in the member. Deluce et al. (expected 2013) presented a

formula to calculate the maximum crack width, $w_{cr_{max}}$, based on the value of the average crack width calculated using Equation (2.27), such that:

$$w_{cr_{max}} = \left(1.7 + 3.4\frac{V_f l_f}{d_f}\right) w_{cr,avg} \tag{2.34}$$

where the factor 1.7 falls in the range that is commonly accepted in relating $w_{cr_{max}}$ to $w_{cr_{avg}}$ for conventional reinforced concrete by many codes (CEB-FIP Model Code, 1978; ENV 1992-1-1:1992, 1992; NS 3473 E, 1992; CEB-FIP Model Code 1990, 1993) and many researchers' experimental results (Clark, 1956; Gergely and Lutz, 1968; Frosch, 1999; Chowdhury and Loo, 2001). The term $3.4\frac{V_f l_f}{d_f}$ accounts for the fact that the maximum crack width significantly increases with the increase in fibre volumetric ratio, V_f, and the fibre aspect ratio, l_f/d_f. Deluce et al. (expected 2013) reported good agreement between this formula and their experimental results, yet the formula is only valid up to the yielding strain of reinforcement at which point normally one crack prevails and dominates over the deformation of the member.

2.4.2.5.5 Three-Dimensional Finite Element Implementation

Employing the previously discussed models and concepts, the analysis of SFRC was implemented in VecTor3. VecTor3, adopting the SDEM, distinguishes between three components in calculating the tensile stresses borne by conventionally-reinforced SFRC members: the tensile stresses attained by the concrete matrix, the tensile stresses attained by the fibres, and tensile stresses attained by the conventional steel reinforcing bars.

In order to implement the SDEM in the DSFM in three-dimensional finite element analysis, one needs to revisit the analysis of the state of equilibrium on the surface of the cracks in a conventionally-reinforced SFRC member as well as the state of equilibrium on the sections between the cracks. With the presence of the fibres in the concrete mix and accounting for the tensile forces in them, Figure 2-9 is transformed into Figure 2-16 and Figure 2-10 into Figure 2-17.

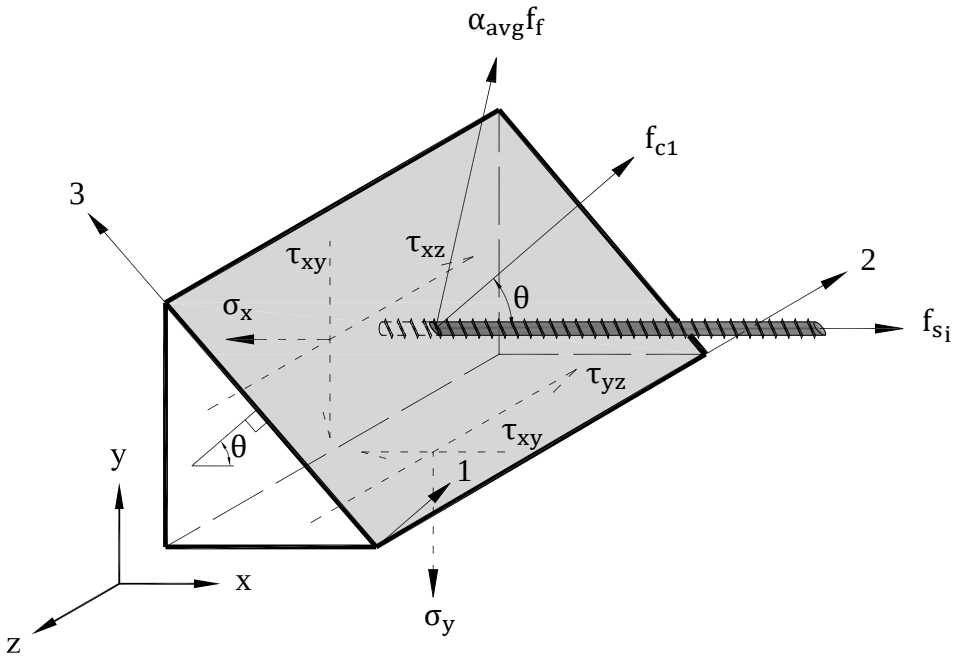

Figure 2-16 Average stresses along a section between the cracks in a three-dimensional conventionally-reinforced SFRC element

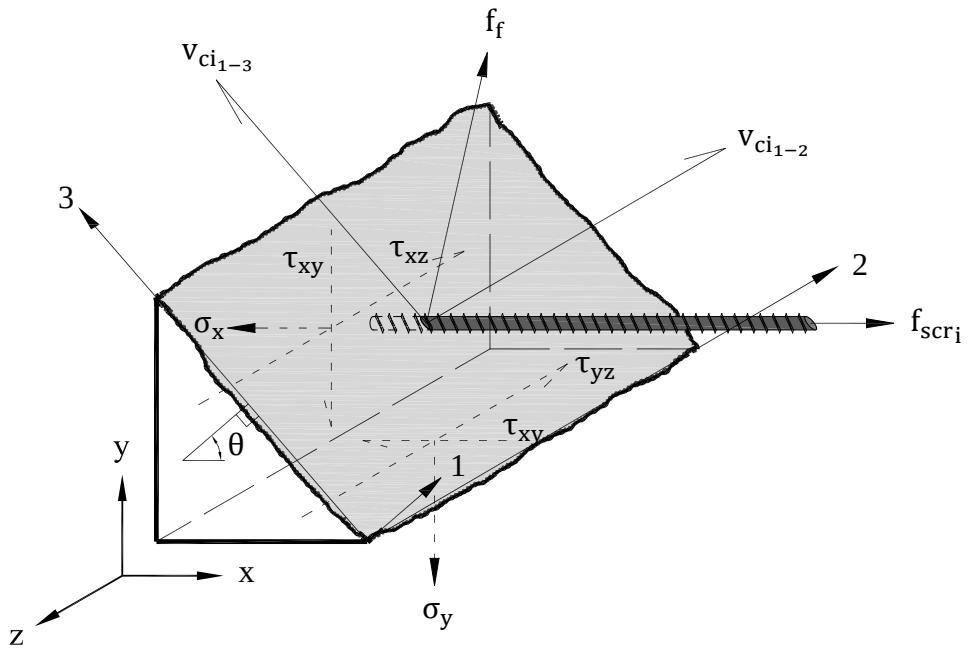

Figure 2-17 Local stresses along the surface of a crack in a three-dimensional conventionally-reinforced SFRC element

Figure 2-16 shows the average stresses acting on a typical section between the cracks. It can be seen that the stresses attained by the fibres between the cracks are calculated by multiplying the stresses attained by the fibres at the cracks, f_f, which are calculated based

on the SDEM, by an averaging factor, α_{avg}. This factor takes into account the dissipation of the tensile stresses in the fibres as the distance from the crack surface increases by averaging the tensile stresses in the fibres through the distance between the cracks (i.e. the crack spacing). Therefore, it can be deduced that this averaging factor is a function of the fibre length and the crack spacing. To determine the value of the average tensile stresses attained by the fibres between the cracks, Lee et al. (2011b) plotted multiple curves for the attenuation of the fibre tensile stresses with the distance from the crack surface for multiple crack widths and calculated the average value of these tensile stresses. They presented an expression for the averaging factor, α_{avg}, that determines the value of the average tensile stresses attained by the fibres between the cracks as a percentage of the average stresses attained by the fibres at the cracks. This expression is presented in Equation (2.35).

$$\alpha_{avg} = \frac{2.0}{5.5}\frac{l_f}{s_m} \quad \leq 1.0 \tag{2.35}$$

In order to study the equilibrium on the surfaces presented in Figures 2-16 and 2-17, one must determine the direction of the average tensile stresses in the fibres. This direction mainly depends on both the crack width and the slip occurring on the surface of the crack. However, as previously discussed, for three-dimensional elements, the slip occurs on a plane of cracking rather than a line of cracking as is the case for two-dimensional elements. Thus, for the purpose of analysis simplicity, the slip is analyzed into two components, one in the second principal stress direction and another in the third principal stress direction.

Thus, the direction of the average tensile stresses in the fibres must be determined using the direction cosines of the vector of the translation occurring at the crack, R_{cr}, which represents the direction of the average tensile stresses attained by the fibres and is calculated as the vectorial resultant of: the slip in the second principal stress direction, $\delta_{s_{1-2}}$, the slip in the third principal stress direction, $\delta_{s_{1-3}}$, and the crack width, w_{cr}, as shown in Figure 2-18. Those direction cosines are calculated with respect to the coordinate system of the principal stress directions.

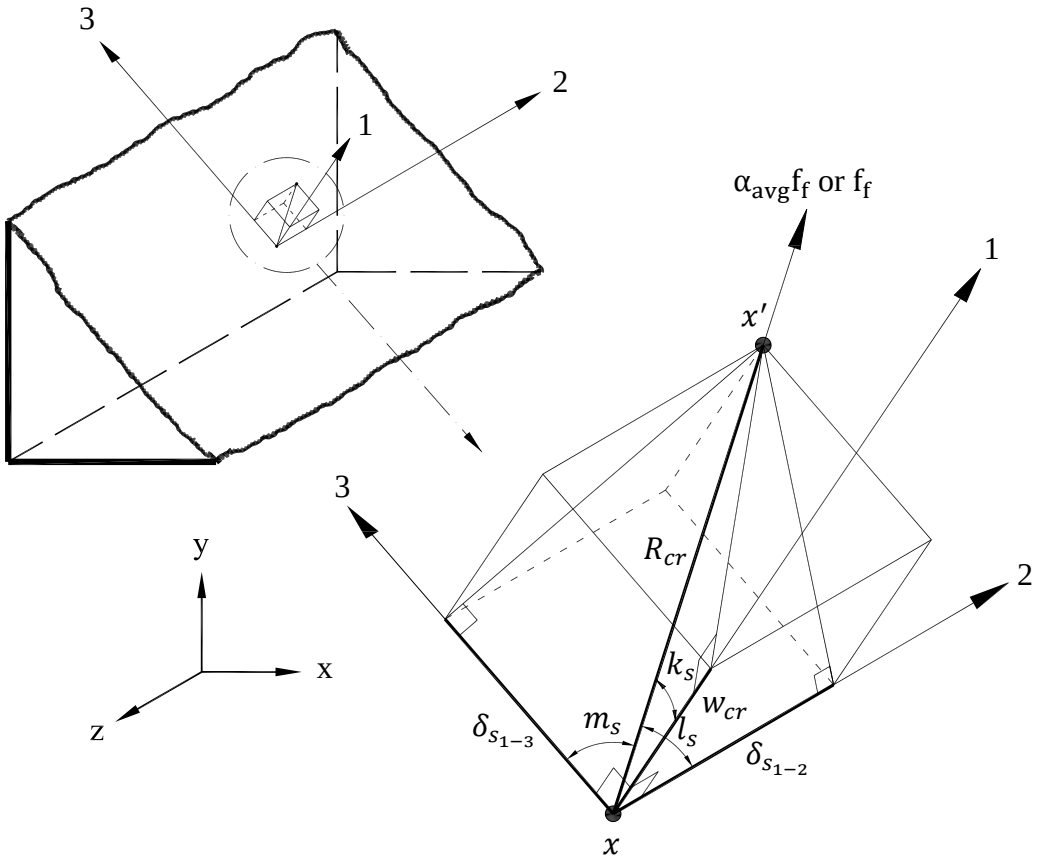

Figure 2-18 The shape of the crack, its width and the slips occurring on its surface in the directions '1 - 2' and '1 – 3'

Therefore, assuming that points x and x', shown in Figure 2-18, were at the exact same location before cracking, and were separated due to cracking to their new shown positions, where the point x is on one surface of the crack and point x' is on the opposite surface, the direction cosines of the average tensile stresses attained by the fibres with respect to the directions of the principal stress can be calculated according to the following expressions:

$$k_s = \frac{w_{cr}}{R_{cr}};\ l_s = \frac{\delta_{s_{1-2}}}{R_{cr}};\ m_s = \frac{\delta_{s_{1-3}}}{R_{cr}} \tag{2.36}$$

where k_s, l_s, and m_s are the direction cosines of the vector representing the direction of the average tensile stresses in the fibres with respect to the first, second, and third principal stress directions, respectively.

With these direction cosines known, the average tensile stress in the fibres - at the crack and at the sections between the cracks - can be analyzed into its components in the coordinate system of the principal stress directions and from that into the Cartesian coordinate system. This process should be iteratively repeated until a convergence of the stresses to a state of equilibrium is reached at the crack and at the sections between the cracks.

In the same way that the increase in tensile stresses in the conventional reinforcement at the crack results in the occurrence of shear stresses on the surface of the crack, so does the tensile stresses in the fibres crossing the crack. Therefore, for equilibrium to be achieved at the crack, an additional component in the shear stresses on the surface of the crack will appear in both the second and third principal directions ($v_{ci_{1-2}}$ and v_{ci-3}).

Another aspect to be considered in the implementation of the SFRC in the finite element formulation is the additional stiffness the fibres impose on a cracked SFRC element. This additional stiffness is calculated as the average tensile stresses in the fibres between the cracks (i.e. as the average tensile stresses in the fibres at the cracks multiplied by the averaging factor, α_{avg}) divided by the strain in the fibres, which can, in turn, be calculated by transforming the principal strain into its components in the direction of the average tensile stress in the fibres.

With that additional stiffness calculated, it is transformed into its components in the coordinate system of the principal stress directions and from that into the Cartesian coordinate system. Then, it can be added to the stiffness of the concrete and the stiffness of the conventional reinforcement, both after being transformed into the Cartesian coordinate system, in order to constitute the compound stiffness of the element.

2.4.2.6 Linked Nodes

In the modelling of structures in finite element analysis, local failure due to modelling errors is very common. For example, when applying concentrated loads or displacements to specific nodes, the elements containing these nodes become vulnerable to local failure. Sometimes, artificial reinforcement or artificial material properties are used to avoid such

failures, but these may affect the overall behaviour of the structure by causing some unreal restraint. One other problem is the approximation involved with the iterative incremental finite element procedure. Since these approximations can occur at any node, for symmetric structures with symmetric loading conditions, such errors may cause the structure to become asymmetric through the analysis. Not only does this cause instability in the numerical analysis, but it may also result in unrealistic stresses caused by secondary moments and geometric nonlinearities.

For this reason, a new feature has been introduced to VecTor3, where nodes can be linked together with specific relations throughout the analysis. This allows two or more groups of nodes to have the same displacements in specific directions, or one group can have displacements of a pre-defined percentage of the displacements of another group. Also, a group of nodes can be kept planar, so sections in beams, for example, can have the same rotation throughout the analysis. In addition to the modelling benefit of this feature, it also helps in the reduction of the software resources required for the analysis. With many degrees of freedom linked together, only one of them is included in the analysis, saving the time and computer memory required to solve more degrees of freedom.

Linking those nodes together can be done using basic manipulation of the matrices involved in the finite element procedure. Considering the typical stiffness equation where the stiffness matrix multiplied by the displacement vector gives the force vector as shown in Equation (2.37), some modifications can be done on this system of linear equations in order to relate some displacements to others.

$$\begin{Bmatrix} \Delta_1 \\ \Delta_2 \\ \Delta_3 \end{Bmatrix} = \begin{bmatrix} K_{1-1} & K_{1-2} & K_{1-3} \\ K_{2-1} & K_{2-2} & K_{2-3} \\ K_{3-1} & K_{3-2} & K_{3-3} \end{bmatrix}^{-1} \begin{Bmatrix} F_1 \\ F_2 \\ F_3 \end{Bmatrix} \tag{2.37}$$

Consider, for example, that displacement Δ_3 needs to be set to α times displacement Δ_2 throughout the analysis. In order to account for this linked displacement, some modifications will have to be made to the stiffness matrix. First, the third column, which is associated with Δ_3 will be multiplied by α and added to the second column, which is associated with Δ_2 as follows:

$$\begin{bmatrix} K_{1-1} & K_{1-2} + \alpha K_{1-3} & K_{1-3} \\ K_{2-1} & K_{2-2} + \alpha K_{2-3} & K_{2-3} \\ K_{3-1} & K_{3-2} + \alpha K_{3-3} & K_{3-3} \end{bmatrix}$$

At this point, the third row and the third column in Equation (2.37) should be omitted and the solution will yield a value for Δ_2, from which Δ_3 can be calculated as $\alpha\Delta_2$. Yet, it can be seen that the resulting stiffness matrix, which was originally symmetric, no longer is. This causes the numerical solution of Equation (2.37) to involve more calculations and thus become more time-consuming. Therefore, in order to restore the symmetry of the stiffness matrix, the third row, which is associated with Δ_3 will also be multiplied by α and added to the second row, which is associated with Δ_2, and then the third row and the third column can be omitted, yielding the following final equation:

$$\begin{Bmatrix} \Delta_1 \\ \Delta_2 \end{Bmatrix} = \begin{bmatrix} K_{1-1} & K_{1-2} + \alpha K_{1-3} \\ K_{2-1} + \alpha K_{3-1} & K_{2-2} + \alpha K_{2-3} + \alpha(K_{3-2} + \alpha K_{3-3}) \end{bmatrix}^{-1} \begin{Bmatrix} F_1 \\ F_2 + \alpha F_3 \end{Bmatrix} \quad (2.38)$$

Solving Equation (2.38), in which the stiffness matrix is symmetric, thus computationally inexpensive, yields a value for the displacement Δ_2. Δ_3 can easily be calculated as $\alpha\Delta_2$, where this relation is imposed throughout the analysis.

Chapter 3
Concrete and Steel Subjected to Fire

3.1 Introduction

Thanks to many decades and even centuries of research, the properties of concrete and steel under normal temperatures are mostly well understood. However, under elevated temperature, our knowledge of these properties is quite inadequate. The applications of studying concrete behaviour under elevated temperatures are not limited to the extreme events of fire only. The nature of some structures involves the subjection of concrete to elevated temperatures on a regular basis. These structures include, but are not limited to, nuclear reactor pressure vessels, coal gasification and liquefaction vessels, pressure vessels used in petrochemical industries, and storage tanks for hot crude oil, hot water, and hot clinker (Khoury et al., 1985a).

Due to the limited amount of research done and the inconsistency of the results available in the literature, the data available at our disposal for analyzing reinforced concrete structures under elevated temperatures are not truly beneficial for analysis purposes. Typically, the available data are only applicable to the materials and conditions of the specimens used. This results in a diverse variety of formulae available to estimate the thermal and structural properties of specific types of concrete and steel reinforcing bars, but the applicability of these formulae to describe all types of concrete and steel reinforcing bars with different constituents and conditions is questionable. This problem is a direct result of the lack of standard testing procedures for the determination of the properties of concrete and steel reinforcing bars under elevated temperatures, which renders the comparison between the results presented by different researchers almost unbeneficial.

In this chapter, many of the properties of concrete and steel under elevated temperatures, as they are currently understood, will be discussed. The data available in the literature and design codes will be presented and compared in an attempt to select the formulae that offer the most reasonable analysis results compared to the available experimental data. In

order to study the different properties of concrete and steel that change due to subjection to elevated temperatures, a distinction is made between thermal properties, which are the properties that affect the heat transfer through concrete, and the mechanical properties, which are the properties that affect the behaviour of concrete and steel under loading.

As a start, modelling of fire itself, according to the various international standards, will be discussed, followed by a discussion of some of the phenomena and the physical, chemical, and mechanical changes that concrete experiences when subjected to temperatures as high as those associated with fire exposure.

3.2 Fire Temperature-Time Curves

Many building codes are shifting nowadays towards performance-based design, especially for conditions that are not covered by building code guidelines such as fire. A crucial component in this performance-based design for fire conditions is the modelling of fire itself, i.e., determining the profile of the increase of temperature with time. Various building codes, standards, and manuals around the world have provided temperature-time curves that model fire for the purpose of structural design. It should be noted that there are many types of fire to be modelled, but the type that is of most concern to structural analysis is the compartment fire or room fire, which is the fire that occurs in enclosed spaces. What is specific to this type of fire is the limited amount of air available for combustion, affecting the fire's ability to attain full temperature capacity, together with the trapping of hot gases. Thus, it is clear how compartment fire is dependent on compartment size, ventilation conditions, and fuel load, with the latter depending on the materials existing in the compartment. These parameters and others impose much complexity in developing fire curves, explaining why many codes have opted to divide fire curves into standard fire curves and parametric fire curves.

Standard fire curves depend only on time, as they develop with time reaching their maximum temperature within a short period of time and then stay almost constant. Among these is the ASTM E119 – 12a (2012) curve, which was originally developed in 1917 and is presented in Equation (3.1). Another curve is the ISO 834-1:1999 (1999)

curve, which was originally developed in 1975, and is presented in Equation (3.2). The ISO 834-1:1999 (1999) curve is one of the most commonly-used curves and was adopted by many building codes and standards around the world, such as the BS 476-20:1987 (1987). The Eurocode (EN 1992-1-2:2004, 2005) presented three curves for three different types of fire, among which only the standard fire curve, which is the same as the ISO 834-1:1999 (1999) curve, concerns typical structural analysis.

The ASTM E119 curve: $$T = 20 + 750\left(1 - e^{-3.79553\sqrt{t}}\right) + 170.41\sqrt{t} \quad (3.1)$$

The ISO 834 curve: $$T = 20 + 345\log_{10}(480t + 1) \quad (3.2)$$

where T is the temperature in ºC, and t is the time from the start of fire in hours. The ASTM E119 – 12a (2012) curve and the ISO 834-1:1999 (1999) curve are compared to each other in Figure 3-1, where it can be seen how the differences are quite minor.

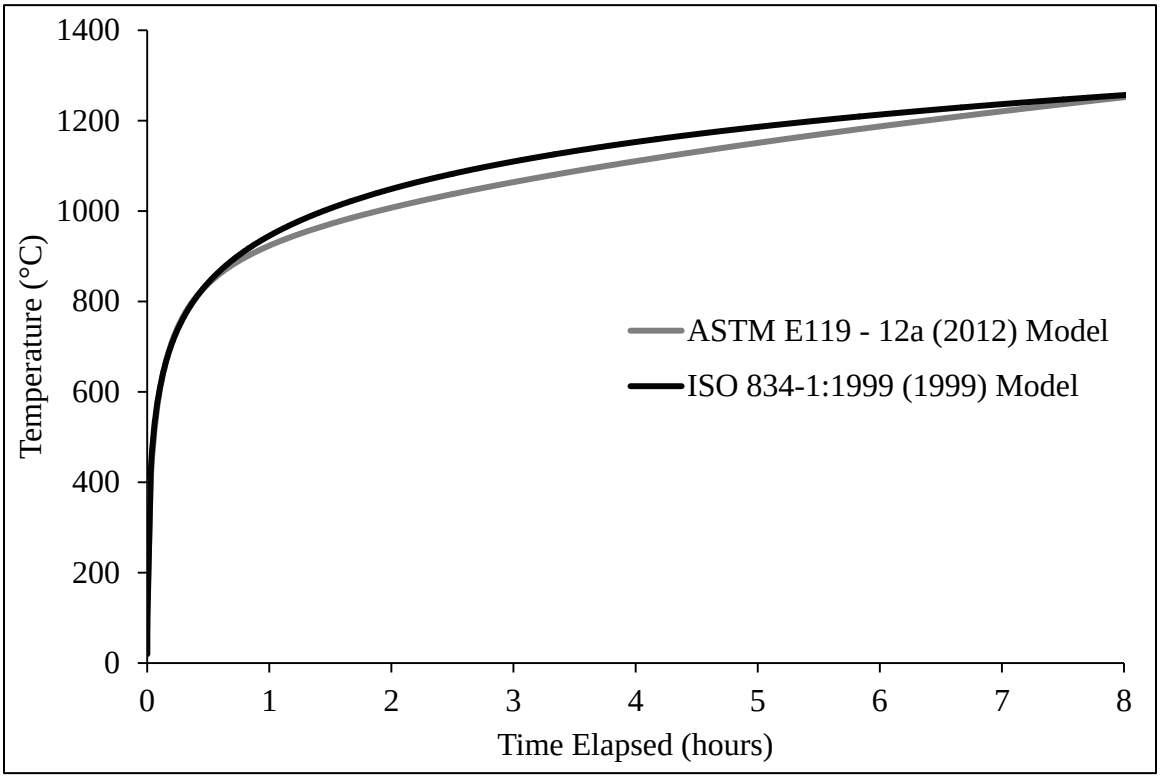

Figure 3-1 Comparison of the standard fire temperature-time curve according to the ASTM E119 – 12a (2012) and the ISO 834-1:1999 (1999)

These two curves are the most commonly used ones, but many other standards and organizations have proposed other curves such as the AS 1530.4-2005 (2005) curve and

the NFPA 251 (2006) curve. Also, the UL 263 (2003), which is similar to the Canadian CAN/ULC S101-07 (2007), presents discrete temperature-time points that create the curve presented by the ASTM E119 – 12a (2012). Added to these are the curve presented by the Rijkswaterstaat (Ministry of Transport) in the Netherlands, the two curves presented by RABT-ZTV in Germany, and the curve presented by the German Federal Railway Office (EBA) also in Germany.

For the decay phase of fire, ISO 834-1:1999 (1999), followed by Eurocode (EN 1992-1-2:2004, 2005), proposed a linear decrease in temperature based on the duration of fire. The following expressions, giving temperature T (in ^{o}C) at a time t (in hours) from the start of fire, were proposed:

$$T = \begin{cases} T_{max} - 625(t - t_f) & \text{for } t_f < 0.5\text{hr} \\ T_{max} - 250(3 - t_f)(t - t_f) & \text{for } 0.5\text{hr} < t_f \leq 2\text{hr} \\ T_{max} - 250(t - t_f) & \text{for } t_f > 2\text{hr} \end{cases} \quad (3.3)$$

where t_f is the time from the start of the fire at which decay starts (in hours), and T_{max} is the temperature corresponding to that time, i.e. the maximum temperature reached before decay starts.

Parametric fire curves, on the other hand, provide a more realistic prediction of the temperature of fire, as they consider the parameters that affect the development of fire that are ignored by standard fire curves, such as the compartment size, its ventilation conditions, presence of openings like doors and windows, fuel load, and the thermal properties of the walls and ceiling of the compartment. The Swedish fire curves that were developed by Magnusson and Thelandersson (1970), and later included in the Swedish Standards (Pettersson et al., 1976) are the most commonly used ones. Also, the Eurocode (EN 1992-1-2:2004, 2005) presented parametric temperature-time curves that are mainly based on the work of Wickström (1985).

In addition to those curves, many researchers have attempted to provide alternative parametric curves, such as the BFD curves presented by Barnett (2002) and the curves proposed by Blagojević and Pešić (2011).

3.3 Phenomena Associated with Heating of Concrete

In order to better understand aspects of the changes that occur in the properties of concrete and steel under elevated temperatures, one needs to first understand many of the phenomena associated with the exposure of concrete and steel to such temperatures. Of these phenomena, the changes in the microstructure of concrete, the thermally-induced spalling phenomenon, and the types of strains associated with elevated temperatures will be discussed.

3.3.1 Concrete Microstructure Changes under Elevated Temperatures

The changes occurring in the microstructure of concrete under elevated temperatures are the direct reason behind the change in its properties. Understanding these changes clarifies the different factors that affect the behaviour of concrete under fire and helps mitigate the loss of vital properties of concrete crucially required to maintain the integrity of any structure. To lay a general outline, the reason behind the deterioration of the concrete properties is a combination of physicochemical changes in the cement matrix, physicochemical changes in the aggregate, and thermal incompatibility between the aggregate and the cement matrix (Naus, 2010). Although we tend to treat concrete as a homogeneous material for structural design purposes (which is in fact how it behaves under normal conditions), it loses this feature as its temperature rises and its different components start to expand, react, and decompose in different manners.

As the temperature of concrete increases, it goes through different phases, each of which affects its microstructure and behaviour in a certain way. In addition, along the entire process, the differential expansion between the different components constituting concrete (cement matrix, sand, coarse aggregate, etc.) causes internal stresses and cracking. Analyses of the phases concrete goes through have been partly introduced as early as the 1920s by Lea and Stradling (1922b; 1922a) and were continued by many other researchers through the following years (Fischer, 1970; Harmathy, 1970; Bažant and Kaplan, 1996; Hertz, 2005).

Up to temperatures of 100ºC to 150ºC, only free water present in the pores of concrete evaporates (Hertz, 2005); hence, very minimal effect is observed on any of its properties,

except for the risk of explosive spalling associated with this phase as will be discussed in Section 3.3.2.1. After this phase, the non-evaporable chemically-bound water present in the calcium silicate hydrates (CSH) in the hydrated cement matrix starts being released, with this process increasing to its peak at around 270ºC (Hertz, 1980). This means that largest portion of the CSH content decomposes around this temperature, which is also accompanied by an endothermic peak.

This phase is associated with a drop ranging from 10% to 15% in the compressive strength of concrete. However, up to this point, the loss in compressive strength, and other concrete properties, is reversible provided that the concrete is not heated beyond this level and is left to cool under normal conditions with no thermal shocks or water cooling (Hertz, 2005). This is because, with time, the CSH in the cement matrix, which was dehydrated due to the high temperature, will react with the water vapour present in the atmosphere and the concrete will regain the strength lost with the dehydration. However, if the heating continues beyond this point, the cement matrix starts to shrink due to dehydration while the aggregate expands due to the high temperature, both causing internal stresses that result in the initiation of microcracks, which are irreversible.

The next phase is the decomposition of calcium hydroxide crystals in the cement matrix into calcium oxide (of smaller volume) and water. This phenomenon occurs between temperatures of 400ºC and 600ºC and reaches its highest intensity at around 535ºC (Harmathy, 1970). The main concern associated with this phase is that besides the negative effect the decomposition of calcium hydroxide crystals has on concrete strength, during the cooling phase of concrete, calcium oxide reacts with the water vapour present in the atmosphere to form new crystals of calcium hydroxide. Since, the volume of calcium hydroxide is about 44% larger than that of calcium oxide (Petzold and Röhrs, 1970), this process causes the previously formed microcracks to widen as the crystals expand, causing further deterioration in the properties of concrete during the cooling phase, which was reported by many researchers (Malhotra, 1956).

Beyond 600ºC, another round of calcium-compound decomposition takes place, peaking at a temperature of around 710ºC and causing further microcracking and further deterioration in the mechanical properties. Harmathy (1970) reported that, at a

temperature of approximately 500ºC, about 70% of the dehydration reaction has been completed and that the CSH are completely depleted at a temperature of approximately 850 ºC.

Since the main cause of the deterioration of concrete under elevated temperatures is the microcracking caused by the internal tensile stresses resulting from the shrinking of some components and the expansion of others, it is understandable why compressively lightly-preloaded concrete experiences less deterioration under elevated temperatures than unloaded concrete. This was experimentally observed and reported by many researchers, including Abrams (1971), Schneider (1976), and Khoury et al. (1985a; 1985b). For microcracks to form, the change in the volume of the aforementioned components has to produce enough tensile stresses to overcome the initial compressive stresses before actual internal tensile stresses can occur.

It is logical to expect the type of aggregate used in the concrete mix to affect the behaviour of concrete under elevated temperatures. This is because different types of aggregates have different chemical composition and different coefficients of expansion, and, as previously mentioned, the deterioration of concrete is caused by the chemical decomposition of its constituents and their differential expansion. For example, it has been found that, for siliceous and calcareous quartz sands, quartz expands 0.85% in volume at about 570ºC due to the $\alpha - \beta$ inversion in its chemical composition (ACI 216R-89, 1989; ACI 221R-96, 1996). For calcareous aggregates such as limestone and dolomites, calcium carbonates begin to break down at around 660ºC to 700ºC, reaching a peak for the reaction at about 800ºC, with all the calcium carbonate completely decomposed at 898ºC, and also magnesium carbonates decompose at temperatures ranging from 740ºC to 840ºC (CEB-FIP Bulletin 38, 2007). On the other hand, igneous-rocks aggregates, such as basalt, perform better than other types of aggregates, with no signs of decomposition or phase change at temperatures as high as 800ºC (Khoury et al., 1985a). They start to show degassing and expansion at temperatures above 1200ºC, going up as high as 1300ºC for some types of igneous rocks (Naus, 2010).

Calcareous aggregates are normally preferred for use in fire-resistant concrete, not only for their chemical stability at higher temperatures compared to other types of aggregate,

but also because their coefficient of expansion is smaller than other types of aggregate and is relatively close to that of the cement matrix. Also, when they decompose, they release carbon dioxide, which acts as a shielding blanket that slows down the heat transfer, and other oxide components that normally have lower thermal conductivity than that of the original carbonate compound, hence slowing down the heat transfer as well (Cather, 2003).

3.3.2 Thermally-Induced Spalling

Despite the advantages that concrete offers as a fire-resistant material, such as being non-combustible and having a relatively low thermal conductivity that helps protect reinforcement from getting too hot too quickly, it still has its disadvantages, among which is the phenomenon of thermally-induced spalling. While spalling during the event of fire has been observed and described by Gary (1916) almost a century ago, it only became a concern in the last few decades with the advancement in the concrete industry and the use of high-strength concrete becoming more common. Ironically, what is considered as high-performance concrete under normal conditions tends to behave more poorly under fire.

Spalling hazards are critical due to the ensuing reduction in the load-bearing cross section and the decrease or even loss of concrete cover, which results in a more rapid rise in temperature in the reinforcement or even the direct contact between steel and fire. This is a major concern because of the dramatic loss of strength steel experiences at high temperatures as will be discussed in Section 3.5.2. Thus, spalling can cause early failure as it expedites the loss of strength and stiffness of reinforced concrete members. Figure 3-2 shows a slab specimen after exposure to fire with the reinforcement exposed due to spalling.

Thermally-induced spalling has been subcategorized by researchers into many types of spalling occurring in many different ways. In this study, however, it will be subcategorized into two main types, namely in the order of occurrence, explosive spalling and surface scaling.

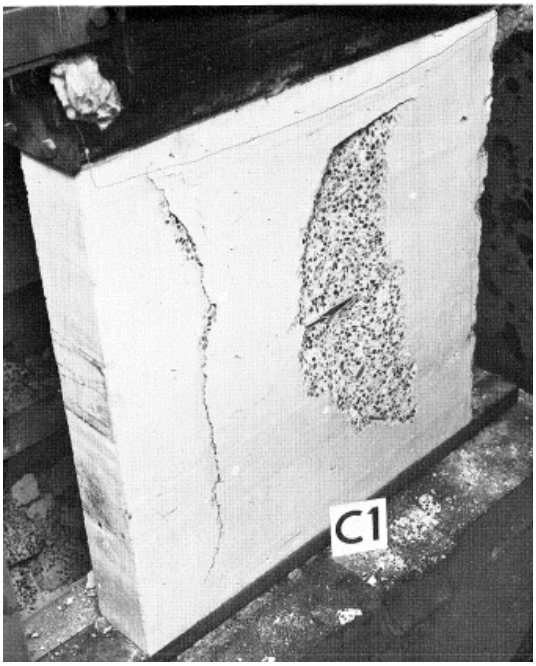

Figure 3-2 A slab specimen subjected to spalling due to exposure to fire (Copier, 1979)

3.3.2.1 Explosive Spalling

Explosive spalling is considered the most significant type of spalling associated with fire exposure of concrete. It has been reported by all researchers to occur in the early stages of heating; some reported its occurrence as early as 5 minutes from the start of fire (Dwaikat and Kodur, 2010) up to a maximum of 50 minutes (Copier, 1983), and at temperatures ranging from 200ºC to 300ºC. It is described as a forcible ejection of large fragments of concrete separating violently and abruptly accompanied by a loud explosive noise. These fragments can be from 100 mm to 300 mm long and 15 mm to 20 mm deep (Malhotra, 1984), although the depth is highly dependent on the reinforcement location as explosive spalling almost never goes past the concrete cover. Gary (1916) reported fragments can be pushed off to distances of 12 m and are capable of causing physical damage on impact.

Explosive spalling has been and is still a major research topic, simply because it is not fully understood yet. This is exacerbated by the fact that the phenomenon is stochastic. For the same batch of concrete, under the same loading and fire conditions, some specimens could experience explosive spalling while others do not (Khoury and

Anderberg, 2000). Many theories have been put forth to rationalize and explain the phenomenon, yet no consensus has been reached. However, despite the uncertainty surrounding its causes, the factors affecting explosive spalling are almost indisputable because they are all based on experimental trials. These factors will be intelligible once those theories are understood.

One of the theories attributes explosive spalling to a phenomenon called “moisture clog” (Harmathy, 1965), or “saturation plug” (England and Khoylou, 1995). When the surface of a concrete member is heated, the temperature of concrete starts rising progressively through the depth of the member. The free water existing inside the pores of concrete starts to evaporate gradually through the thickness as well, as the temperature reaches about 100ºC to 150ºC. The gaseous mixture composed of water vapour and air, driven by the pressure gradient, starts to migrate through the pores of concrete from the hotter regions that have higher pressure near the surface to the cooler ones with lower pressures, either deeper in the member or into the outer atmosphere. Hence, two directions are possible: outwards to the atmosphere or inwards though the depth of the member. Due to the high heating rate and the low permeability of concrete (especially for high-strength concrete), the speed of the evaporation of water surpasses the speed of the gaseous mixture migration, resulting in a pressure build-up in the pores.

Up to this stage, the pressure is still not high enough to cause significant damage to the concrete. However, as previously mentioned, the chemically-bound water present in the CSH in the hydrated cement matrix starts to be released after peaking at temperatures around 270ºC, thus increasing the amount of water available for evaporation and causing higher pressures.

According to Harmathy (1965) and England and Khoylou (1995), the main problem starts when the hot gaseous mixture migrates to the cooler layers of concrete deeper in the member and condenses due to the lower temperatures in these layers, filling and saturating the pores. This saturation forms a blocking front, called “moisture clog” or “saturation plug”, that prevents further migration of the gaseous mixture. At this stage, the gaseous mixture, entrapped between regions having high temperatures and transporting even more gaseous mixture, and regions having moisture clog preventing its

transport past them, causes high pressure in the pores of concrete. This theory claims that this high pore pressure generates tensile stresses in concrete that eventually exceed its tensile strength, causing cracking and violent separation of the outer layers of concrete.

This theory is disputed by the fact that aged concrete (which is practically dry) still experiences explosive spalling. However, dry concrete is devoid of free evaporable water, but non-evaporable chemically-bound water, on the other hand, still exists and can cause the same effect once the temperature required for its release is reached. Another argument is that experiments undertaken by Chapman (1976), Chapman and England (1977), and other researchers have shown pore pressures of a maximum of 1.0 MPa, which is not high enough to cause tensile stresses that would exceed the tensile strength of concrete. However, the concrete used for these tests was normal-strength concrete, while in the case of high-strength concrete with its significantly lower permeability, pore pressures can go up to 2.1 MPa (Phan, 2007), 3.1 MPa (Phan, 2007), 5.0 MPa (Bangi and Horiguchi, 2012), or even 8.0 MPa (Diederichs et al., 1995). Finally, whether this theory is acceptable or not, there is wide consensus that the moisture content of concrete and its permeability have direct relation with the susceptibility of concrete to the occurrence of explosive spalling. Thus, even if this theory is not entirely correct, the pressure build-up is still believed to be at least a partial cause for explosive spalling.

Another theory (Bažant, 1997) argues that the cause behind explosive spalling is the restrained thermal dilatation experienced by the surface layers of concrete subjected to fire. As the temperature of concrete rises progressively through the depth of the member, creating temperature gradients, the outer hotter layers are restrained from expanding by the inner cooler ones. This restraint causes compressive stresses to develop in the outer layers and tension stresses in the inner ones, both parallel to the heated surface. As these stresses rise, combined with the existing stresses due to the loads carried by the member, they are released through brittle fracture of concrete, assisted by the deterioration of concrete strength at higher temperatures; thus, spalling occurs. This theory assumes a secondary role for the pressure build-up, being relatively incapable of causing any damage as the pressure will be immediately released as soon as a crack initiates due to the extra space the crack will present.

The last and most logical theory – also the one adopted in this study – is a combination of both the aforementioned theories. For this theory, the stresses causing explosive spalling are cumulative. The load-induced stresses, the stresses resulting from the differential thermal expansion due to the high temperature gradients resulting from the non-uniform heating, and the stresses resulting from the excessive pressure build-up in the concrete pores due to the moisture clog are all superimposed. When the total stress exceeds the tensile strength of concrete, explosive spalling occurs, acquiring its thrust from the high pore pressure, the rapid rise in thermal gradient stresses, and the brittleness associated with high-strength concrete.

Figure 3-3 shows the changes in the different parameters that contribute to the occurrence of the explosive spalling phenomenon. These parameters are shown within the potentially spalled region and the region beyond it. Examining the figure, the horizontal axis represents the depth through the concrete member from the surface of exposure to fire, where the zero value on the axis (the origin of the axes) represents the surface of fire exposure. The vertical axis represents four different parameters related to explosive spalling, namely, temperature, pore pressure, moisture content, and stress due to restrained thermal expansion. It can be seen that temperature has its maximum value at the surface of fire exposure, and it decreases gradually through the depth of the member until it reaches the initial temperature at deeper concrete layers, which is marked in the figure as the initial state line. This line marks the beginning of the concrete region that has not been affected yet by the fire exposure; hence, all its properties remain at their initial values.

For moisture content in the pores of concrete, Figure 3-3 distinctly marks the three different zones of concrete through the depth of the concrete member exposed to fire. The first zone is the “dry zone” at the surface of fire exposure. Concrete in this zone has lost all its moisture content as time elapsed from the start of fire; hence, it has zero moisture content. The second zone is the “drying zone”, in which concrete is the intermediary state between the dry state and the wet state. In this zone, concrete pores have some moisture that increases steeply through the depth of the concrete member. The end of this zone marks the beginning of the “wet zone”, and more importantly, the moisture clog. At the onset of the wet zone, in which concrete is saturated, the moisture clog appears, showing

a peak in moisture content that gradually decreases to the initial moisture content value at the initial state line. It should be noted that these three distinct zones also describe the states through which concrete passes as it is exposed to fire, where it starts at the wet state then the drying state, and ends at the absolutely dry state.

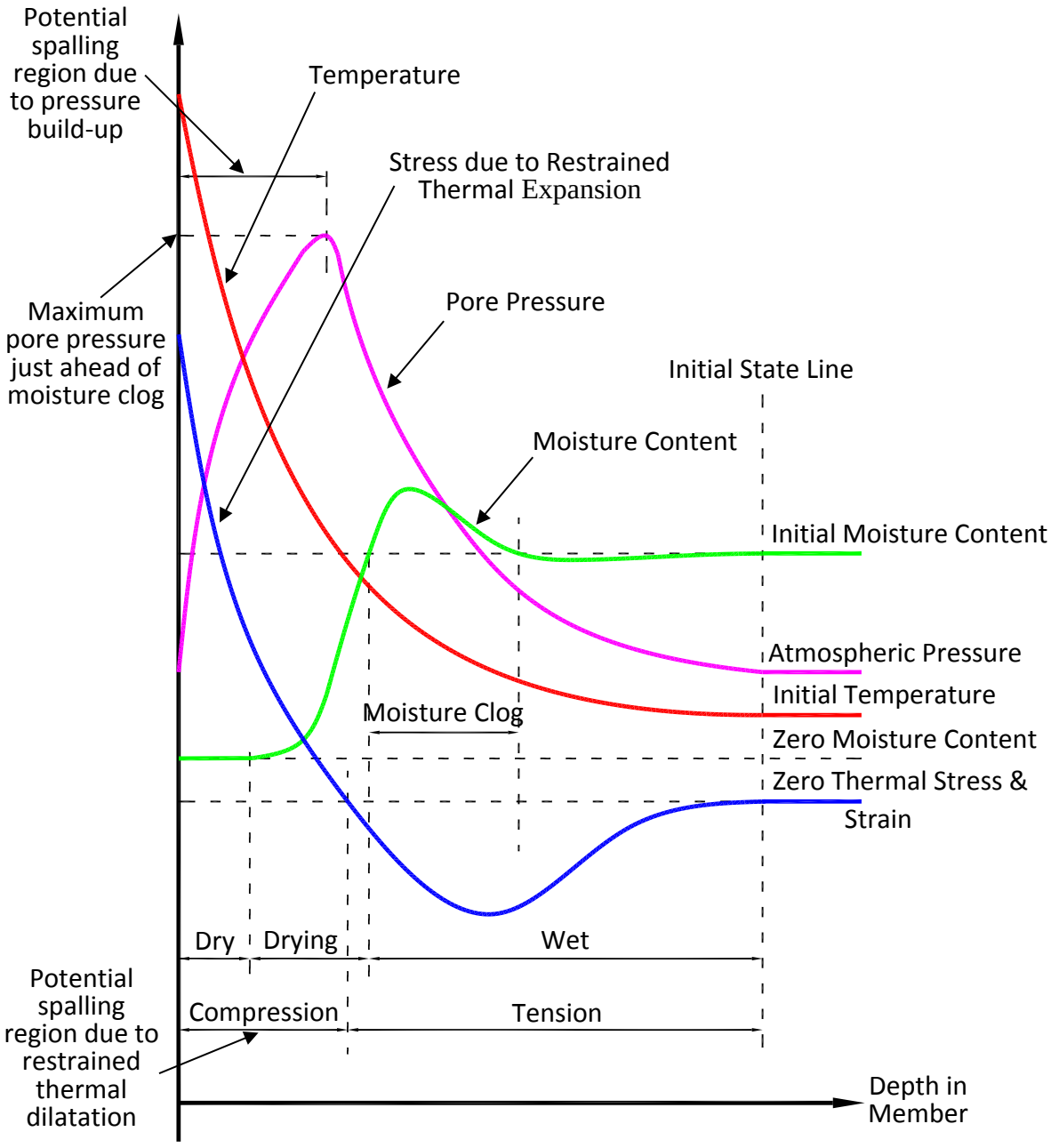

Figure 3-3 Changes in the different parameters that contribute to the explosive spalling phenomenon within the spalled region and the region beyond it

For pore pressure in concrete, Figure 3-3 shows how it steeply increases from its initial value (atmospheric pressure) at the surface exposed to fire to a peak value that occurs just

ahead of the moisture clog. Beyond this peak, the pore pressure gradually decreases until it reaches the initial value (atmospheric pressure) at the initial state line. This peak also marks the region in which explosive spalling is most likely to occur according to the first theory explained earlier, as shown on the figure.

Finally, Figure 3-3 shows the variation of the stresses resulting from the restrained thermal expansion through the depth of the member, which results from the different temperatures and the ensuing different values of thermal expansion strain. It can be seen that the outer region experiences compressive stresses, which decrease gradually to change to tensile stresses in the inner region, which, in turn, decrease gradually until they completely disappear at the initial state line. As explained earlier, the temperatures of the outer region are higher than those of the inner region; hence, higher values of thermal expansion strains in this region are resisted by lower values in the inner region, giving rise to compressive stresses in the outer region and tensile stresses in the inner region. Figure 3-3 also shows that the outer region, where compressive stresses occur due to the restrained thermal dilatation, is the region in which explosive spalling is most likely to occur according to the second theory explained earlier.

Finally, the third theory – previously explained and also the one adopted in this study – proposes adding the stresses resulting from the pressure build-up shown in Figure 3-3 and the stresses resulting from the thermal expansion dilatation, also shown in Figure 3-3, to the stresses resulting from the external loading of the concrete member. What makes this theory possible to adopt is the coupled heat and structural analysis capability presented in this study, which makes such a combined stresses approach viable.

With the phenomenon well explained, the factors affecting it become clear. The following is a brief discussion of the two most influential factors, both of which were deduced though experimental tests and real fire events observation and both of which fit in the theories explained earlier.

1. **Moisture Content:** As the moisture content in concrete increases, the susceptibility to experience explosive spalling increases (Malhotra, 1984). This is expected based on the explanation of the moisture clog theory. Researchers and codes (Malhotra, 1984; BS 8110-2:1985, 1985; Khoury, 2000; Hertz, 2003) have proposed a rule-of-thumb for

the value of moisture content that would safeguard concrete members against explosive spalling. This value is 2% to 3% by weight, 5% by volume or a relative humidity of 75%. While this rule-of-thumb holds for most cases, sometimes it does not (Shuttleworth, 1997) because explosive spalling is a very complex phenomenon that depends on a lot of interacting factors. The rule is only applicable for normal strength concrete and when all the conditions, besides moisture content, are unfavourable for the occurrence of explosive spalling.

2. **Permeability and rate of heating:** The reason these two factors are listed together is that while they both have a very significant effect on explosive spalling, neither of them has an effect exclusive of the other. That is, it is how different they are that determines the susceptibility of concrete to explosive spalling. If they are both too high or both too low, explosive spalling is not likely to occur. The problem arises when the permeability is low and the rate of heating is high. This is because if the rate of heating is high, it causes a high rate of evaporation of water in concrete, and if the permeability is too low to allow the flow of water vapour at this high rate to escape (less than 5×10^{-17} m^2 according to Harmathy (1965)), pressure build-up will occur.

   Since there is no control over the rate of heating, being an intrinsic characteristic of natural fire, permeability of concrete is the property that can be enhanced to mitigate the risks of explosive spalling. However, with the higher permeability that would safeguard concrete against explosive spalling comes lower compressive and tensile strengths and poorer durability. Therefore, there appears to be a trade-off between the performance of concrete under normal temperatures and its performance under elevated temperatures. This also explains why high-strength concrete with its low permeability is more susceptible to explosive spalling. Figure 3-4 shows the extensive spalling occurring in high-strength concrete compared to normal-strength concrete.

In addition to these factors, there are many other factors that were found to play secondary roles. For example, it has been found that members that are heated from two sides, rather than just one side, are more susceptible to spalling (Meyer-Ottens, 1974a, 1974b). This is due to the absence of a path through which water vapour can escape through the section which increases the possibility of the occurrence of pressure build-up.

Figure 3-4 HSC-column (left) showing extensive spalling compared to a similar NSC-column (right) (Kodur and Sultan, 1998)

Another factor is the thickness and the shape of the concrete member. Very thin and very thick members are found to be less susceptible to explosive spalling according to Copier (1979), Copier (1983), and Malhotra (1984). They all specified that members that exceed a thickness of 200 to 300 mm are less susceptible to explosive spalling. Meyer-Ottens (1974a; 1974b) also specified that corners, especially acute-angled ones, are more susceptible to explosive spalling.

All these factors revolve around the idea of the presence of an easy path for the escape of water vapour out of the section so that the pore pressure build-up can be released or not formed at all. Other factors affect the occurrence of explosive spalling indirectly as they affect the two aforementioned most significant factors. Among these are the age of concrete, which affects its moisture content, and the water/cement ratio in the concrete mix, which affects the permeability.

It has also been found that explosive spalling only occurs within the concrete cover and does not go past the reinforcement layer. High load intensities also cause more spalling

because the extra stresses are superimposed over those resulting from pressure build-up and from the temperature gradient, increasing the possibility of tensile stresses to exceed the compromised tensile strength of concrete under fire. For steel fibre-reinforced concrete (FRC), the only advantage it offers towards fighting explosive spalling is the added tensile strength (Hertz, 1984; Sideris et al., 2009). However, this high tensile strength results in a more violent spalling due to the extra amount of energy to be released.

While knowing these factors has helped designers mitigate the explosive spalling risks, one other way that has been widely accepted as an effective way to reduce the risks of explosive spalling is the addition of polypropylene fibres in the concrete mix. Figure 3-5 shows the effect of using polypropylene fibres in the high-strength concrete mix. This discovery was first patented by Miller (1989) in Sweden and Hansen and Davies (1990) for the World Intellectual Property Organization (WIPO), and then was confirmed by many other researchers (Nishida et al., 1995; Breitenbucker, 1996; Bilodeau et al., 1998; Kalifa et al., 2001). The amount of polypropylene fibres that can eliminate or significantly reduce explosive spalling has also been a major research topic with recommendations of 0.05% by weight (Connolly, 1995), 0.10% to 0.15% by volume (Kodur, 1999), and about 0.17% by volume (Shuttleworth, 1997). Merely based on reports provided by various researchers, ACI 213R-03 (2003) suggested that the addition of 0.10% to 0.20% polypropylene fibres in light-weight concrete mixes (supposedly by volume) provides a significant reduction of spalling.

It is commonly accepted by almost all researchers that the reason behind the ability of polypropylene to mitigate the explosive spalling risks is that the fibres melt at relatively low temperatures creating a network of pathways that increase the permeability of concrete, and hence help relieve the pore pressure build-up. However, Khoury and Anderberg (2000) claimed that, based on unpublished microscopic studies, the reason was found to be that the pore pressure build-up is actually relieved due to the presence of significant microcracking around the fibres, even in unheated regions. In addition, they claimed, also based on unpublished studies, that the presence of polypropylene fibres is only beneficial for high-strength concrete of compressive strength of 60 MPa to

110 MPa, but not for ultra-high-strength concrete of strength 150 MPa or greater, which still showed explosive spalling.

Figure 3-5 Spalling extent in HSC with (right) and without (left) polypropylene fibres (Shuttleworth, 1997)

Despite the beneficial effect of adding polypropylene fibres to the concrete mix with respect to explosive spalling, there have been conflicting results regarding their effect on the mechanical properties of concrete. Komonen and Penttala (2003) reported a negative effect for the addition on polypropylene fibres in the concrete mix on the residual compressive and tensile strengths of concrete. This has been confirmed by Sideris et al. (2009) who reported that the addition of polypropylene fibres significantly decreases the residual post-cooling tensile strength. On the other hand, Luo et al. (2000), Xiao and König (2004), and Peng et al. (2008) did not report much difference in either the residual compressive strength or the residual tensile strength between plain concrete and concrete mixed with polypropylene fibres.

Finally, it should be noted that explosive spalling and spalling in general are less serious in real fires than they are in laboratory-controlled furnace tests (Khoury and Anderberg, 2000). This is justified by the fact that the exposure conditions are more severe and load intensities are higher in the tests. Also, a better distribution of heat is achieved with the continuous assemblies in existing structures than with the single members often tested in the furnace tests.

Explosive spalling was reported in many real accidental fires such as those that happened in the railway tunnel of the Great Belt Fixed Link (Storebæltsforbindelsen) in Denmark in 1994 (shown in Figure 3-6), the Channel Tunnel (the Chunnel) between England and France in 1996 (shown in Figure 3-7), Mont Blanc Tunnel in France and Italy in 1999 (shown in Figure 3-8), and Tauern Road Tunnel in Austria. As a matter of fact, explosive spalling is a more major concern in tunnel fires than it is in regular buildings fires. One of the reasons for that is the much higher humidity present in tunnels, compared to regular buildings, which results in higher moisture content in concrete. Another reason is the tendency (or, in most cases, the necessity) to use high-strength concrete with compressive strengths as high as 100 MPa in the construction of tunnels. Such concrete is typically used not only for the higher load bearing capacity it offers, but also for the higher durability resulting from its low permeability, which, in turn, adversely affects the explosive spalling resistance as explained earlier.

Figure 3-6 Damaged concrete in the Great Belt Fixed Link due to fire (Høj et al., 2008)

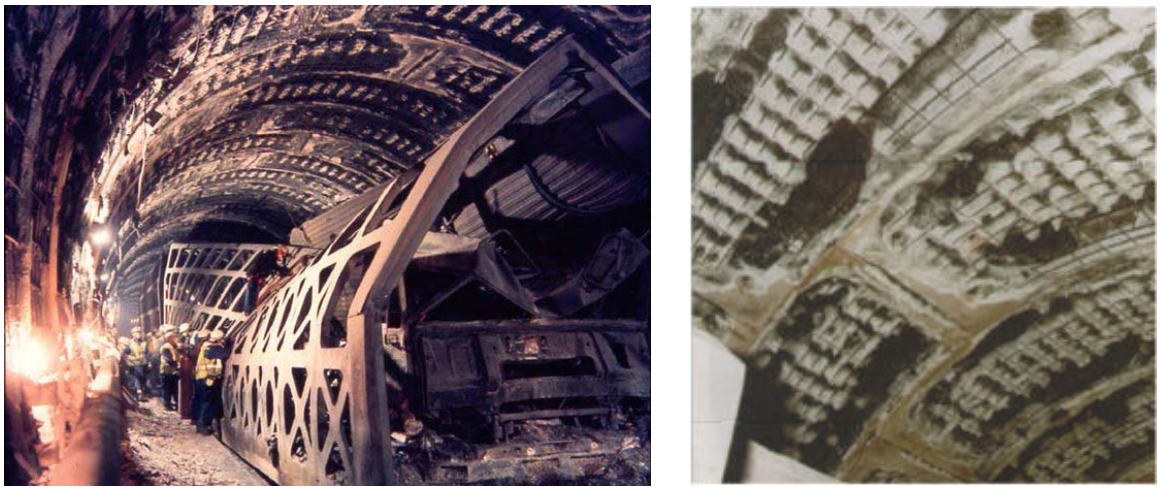

Figure 3-7 Damaged concrete in the Channel Tunnel due to fire (Høj et al., 2008)

Figure 3-8 Damaged concrete in Mont Blanc Tunnel due to fire (Høj et al., 2008)

3.3.2.2 Surface Scaling

This type of spalling involves the gradual progressive loss of the outer surface of concrete. It combines two types of spalling as described by Khoury (2008), namely, sloughing-off and post-cooling spalling. This phenomenon occurs throughout the duration of the fire and even after the fire is extinguished (post-cooling spalling). This

type of spalling happens due to the significant reduction in the concrete strength caused by the previously discussed chemical transitions it goes through during exposure to fire. When the concrete reaches the point where it can no longer carry its own weight, it falls off; hence, surface scaling occurs. This process continues even during the cooling phase of concrete. As previously discussed, one of the products of the dehydration process happening to concrete during exposure to fire is calcium oxide, and during the cooling phase, calcium oxide reacts with the water vapour present in the atmosphere to form new crystals of calcium hydroxide. Since, the volume of calcium hydroxide is about 44% larger than that of calcium oxide (Petzold and Röhrs, 1970), this process causes the microcracks previously formed to widen as the crystals expand, causing further deterioration in the properties of concrete and more surface scaling. It has been reported by many researchers that post-cooling spalling can be very significant.

3.3.3 Strain Associated with Elevated Temperatures

This section presents an overview of the different types of strains that concrete and steel experience when subjected to elevated temperatures. In addition, some of the models available in the literature are presented, discussed, and compared.

3.3.3.1 Concrete Strain

While the types of strain that concrete normally experiences under compression have been well understood for many decades, an additional strain associated with the heating of stressed concrete for the first time has been discovered relatively recently. It has been observed by many researchers, such as Wallo et al. (1965) and Hansen and Eriksson (1966), that in addition to the typical thermal expansion strain, concrete experiences additional irrevocable creep when heated while stressed for the first time, with no similar behaviour for subsequent heating cycles (Nishizawa and Okamura, 1970; 1972).

Fahmi et al. (1972) made the same observation and put forth a mathematical expression for predicting the value of this additional strain. The expression took into account the

effect of temperature, humidity, age, and type of load (compression or torsion). It was not until 1973 that Illston and Sanders (1973) explained this type of strain and called it 'transitional thermal creep'. Anderberg and Thelandersson (1976) called it 'transient strain', described it as "the part of the total strain obtained in stressed concrete under heating that cannot be accounted for otherwise", and developed a special formula for it. Some other researchers combined all components of strain occurring in concrete excluding the stress-inducing strain, and gave the combination the term 'load-induced thermal strain' (LITS).

Transient strain is generally attributed to the chemical changes occurring in the cement matrix; hence, it is independent of the type of aggregate as reported by many researchers (Terro, 1998). Transient strain is also believed to be linearly dependent on the applied stress (or load) and nonlinearly dependent on the temperature of concrete (Illston and Sanders, 1973; Anderberg and Thelandersson, 1976; Khoury et al., 1985a; Schneider, 1986; Diederichs, 1987; Terro, 1998).

Hence, the total strain, $\varepsilon_{c_{tot}}$, occurring in stressed concrete (which is how concrete typically is when the event of fire happens) can be divided into four components as opposed to only three for unstressed concrete. The first component is the stress-inducing strain, ε_{c_σ}, caused by the external loading and controlled by the stress level and the temperature of concrete which changes its mechanical properties. The second component is the thermal expansion strain, $\varepsilon_{c_{th}}$, caused by the expansion resulting from the rise in temperature and only depending on the temperature of concrete. The third component is the typical creep strain, $\varepsilon_{c_{cr}}$, experienced by concrete under long-term loading due to the slipping and dislocation of the microstructure of concrete. This component depends on the stress level, duration of loading, and temperature. However, for this study, only the portion of creep happening through the duration of the fire will be considered, which is normally very small compared to the other strain components due to the relatively short duration of the fire event. The fourth and last component is the transient strain, $\varepsilon_{c_{tr}}$, which is restricted to stressed concrete subjected to elevated temperatures for the first time only. This component depends on the stress level and temperature. These components can be assembled in the following mathematical expression:

$$\varepsilon_{c_{tot}}(\sigma, T, t) = \varepsilon_{c_\sigma}(\sigma, T) + \varepsilon_{c_{th}}(T) + \varepsilon_{c_{cr}}(\sigma, T, t) + \varepsilon_{c_{tr}}(\sigma, T) \quad (3.4)$$

Therefore, a distinction was made between the response of concrete in two different types of tests or fire cases, namely the steady-state test and the transient test. In the steady-state test, concrete is heated to a pre-defined temperature and then loaded under constant temperature to failure, while in the transient test, concrete is loaded to a certain stress intensity (normally low), then heated to a pre-defined temperature and then loaded under constant temperature to failure. The transient strain only appears in the transient test and only in the case of first-time heating.

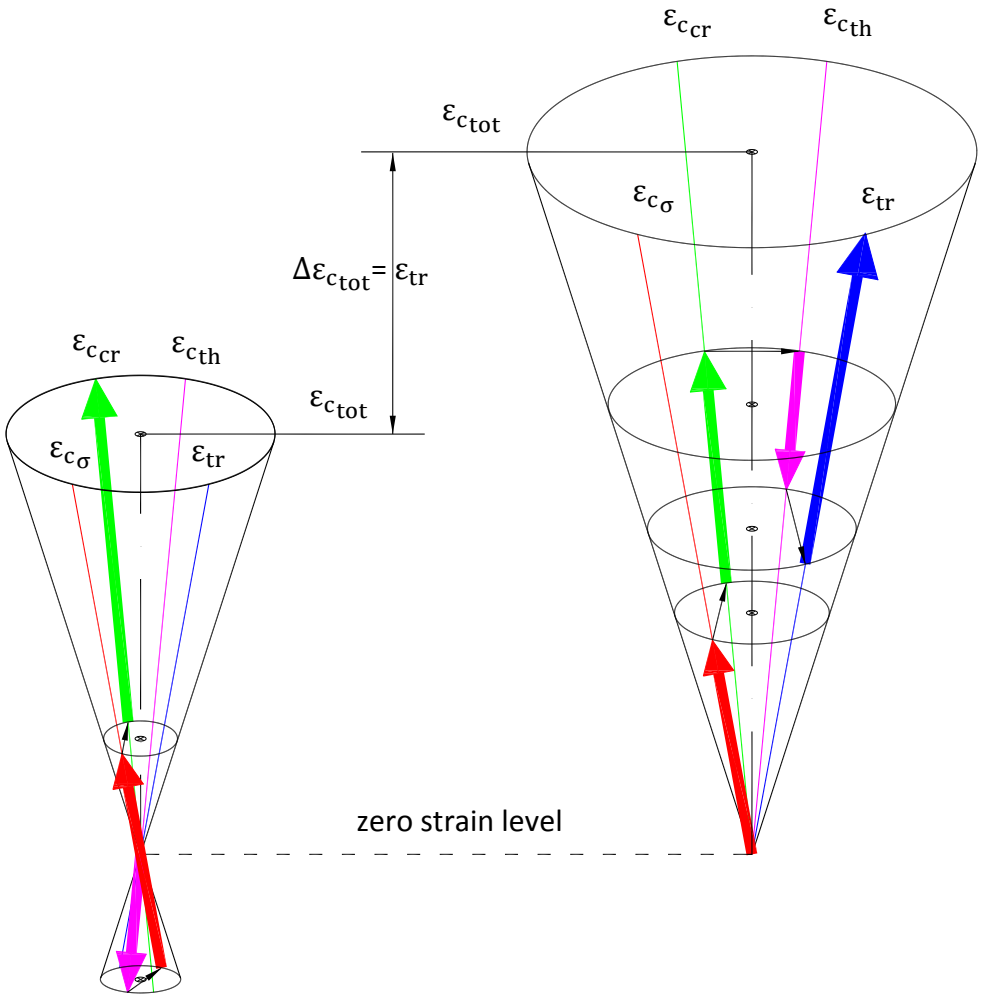

(a) Steady-State Test (b) Transient Test

Figure 3-9 Illustration of the various strains occurring in: (a) the steady-state test and (b) the transient test

Figure 3-9 presents an illustration of the various types of strain occurring in the steady-state test and the transient test for the same pre-defined temperature for concrete under compression, thus starting at the zero strain level and following the arrows, one can see the total of the different strain components in both cases. Note that the thermal expansion strain, $\varepsilon_{c_{th}}$, is in a direction opposite to the other types of strains associated with concrete under compression as it involves expansion. If one sequentially lists the types of strain experienced by concrete in each case, then for the steady-state test, the first strain is an expansion thermal strain, $\varepsilon_{c_{th}}$, followed by the stress-inducing strain, ε_{c_σ}, in the opposite direction as the concrete gets compressed when loaded. If the duration of the fire is long enough, the specimen would experience the typical creep strain, $\varepsilon_{c_{cr}}$, as well. For the transient test, the straining starts with the stress-inducing strain, ε_{c_σ}, then the typical creep strain, $\varepsilon_{c_{cr}}$. The heating starts after this point, causing thermal expansion strain, $\varepsilon_{c_{th}}$, and hence decreasing the total strain. Finally, due to the change in the chemical composition of concrete heated while loaded, the transient strain, ε_{tr}, occurs.

Also note that, in the case of the steady-state test, the initial stress-inducing strain, ε_{c_σ}, is expected to be greater in value relative to its respective value in the transient test due to the decrease in the concrete initial stiffness as it is already heated at that point. However, the stress-inducing strain, ε_{c_σ}, in the transient test, eventually draws level with the stress-inducing strain occurring in the steady-state test as the temperature increases and concrete stiffness gradually decreases with it. Hence, the final values should be similar for this component for both tests.

3.3.3.1.1 Modelling of Transient Strain

Since it has been discovered, transient strain has been the focus of many researchers who followed different approaches in attempting to quantify it along with the other temperature-dependent strains. A brief review of the models available in the literature will be presented in chronological order in this section, starting with the Anderberg and Thelanderson model (1976). This model separated between the four aforementioned components of strain, where the expression for the typical creep strain, $\varepsilon_{c_{cr}}$ is presented

in Equation (3.5). Yet, it was suggested that this component can be neglected due to its small values compared to the other components.

$$\varepsilon_{c_{cr}} = -0.53 \times 10^{-3} \left(\frac{f_{c_T}}{f'_{c_T}}\right)\left(\frac{t}{180}\right)^{0.5} e^{3.04\times10^{-3}(T-20)} \tag{3.5}$$

The thermal strain, $\varepsilon_{c_{th}}$, is determined from thermal expansion curves. The other components are given in the following expressions:

$$\varepsilon_{tr} = -k_{tr}\left(\frac{f_{c_T}}{f'_c}\right)\varepsilon_{c_{th}} \qquad \text{for } T \leq 550℃ \tag{3.6}$$

$$\frac{\partial \varepsilon_{tr}}{\partial T} = -0.0001\left(\frac{f_{c_T}}{f'_c}\right) \qquad \text{for } T > 550℃ \tag{3.7}$$

where f_{c_T} is the stress at a temperature T (which is the same as the stress at normal temperatures (20ºC) because the stress is kept constant throughout the test); f'_{c_T} is the peak compressive stress (compressive strength) at temperature T; f'_c is the peak compressive stress at normal temperatures (20ºC); t is the time in minutes; and k_{tr} is an experimentally determined parameter.

The negative sign in the transient strain expression accounts for the fact that the transient strain, ε_{tr}, is a contraction strain while the thermal strain, $\varepsilon_{c_{th}}$, is an expansion strain. For k_{tr}, Anderberg and Thelandersson ran regression analysis for their experimental results for temperatures up to 550ºC and reported a value of 2.35 for it. From the results of Weigler and Fischer (1968) and Schneider (1973; 1974), k_{tr} was evaluated at 2.00 and 1.80, respectively. Purkiss and Bali (1988) reported that the assumed linear relation between the transient strain, ε_{tr}, and the thermal strain, $\varepsilon_{c_{th}}$, did not show in their tests.

Schneider (1986) combined the transient strain and the typical creep strain together in one term and presented the following expression:

$$\varepsilon_{tr} + \varepsilon_{c_{cr}} = \Phi \frac{f_{c_T}}{E_{c_{i_T}}} \tag{3.8}$$

where $$E_{c_{i_T}} = g(f_{c_T}, T) f(T) E_{c_i} \quad (3.9)$$

where $E_{c_{i_T}}$ is the initial modulus of elasticity at elevated temperatures; f(T) is a reduction factor whose value is given through an experimentally produced plot; and $g(f_{c_T}, T)$ is a function that accounts for the increase in the initial modulus of elasticity, E_{c_i}, due to external loads, and is calculated as follows:

$$g(f_{c_T}, T) = 1 + \frac{f_{c_T}}{f'_c} \frac{T - 20}{100} \quad (3.10)$$

Φ is a creep function calculated according to the following expression:

$$\Phi = g(f_{c_T}, T)\varphi + \frac{f_{c_T}}{f'_c} \frac{T - 20}{100} \quad (3.11)$$

with $\frac{f_{c_T}}{f'_{c_T}}$ capped at 0.3 for Equations (3.10) and (3.11), and φ is a parameter calculated according to the following expression:

$$\varphi = C_1 \tanh \gamma_w (T - 20) + C_2 \tanh \gamma_\circ (T - T_g) + C_3 \quad (3.12)$$

where C_1, C_2, C_3, $\gamma_\circ$, and T_g are constants, defined in Table 3-1, and γ_w is a constant, defined by the following expression:

$$\gamma_w = (0.3w + 2.2) \times 10^{-3} \quad (3.13)$$

where w is the moisture content in % by weight.

Table 3-1 Constants of Schneider Model (1986) for estimating transient strain

Aggregate Type in Concrete Mix	C_1	C_2	C_3	$\gamma_\circ$ ($^oC^{-1}$)	T_g (^oC)
Siliceous	2.60	1.40	1.40	7.5×10^{-3}	700
Calcareous	2.60	2.40	2.40	7.5×10^{-3}	650
Light-weight	2.60	3.00	3.00	7.5×10^{-3}	600

Schneider also presented the formula given in Equation (3.14) in the form of a compliance function to estimate the stress-inducing strain, ε_{c_σ}.

$$\varepsilon_{c_\sigma} = (1 + \kappa)\frac{f_{c_T}}{E_{c_{i_T}}} \tag{3.14}$$

where

$$\kappa = \begin{cases} \dfrac{1}{n-1}\left(\dfrac{f_{c_T}}{f'_{c_T}}\right)^5 \\ or \\ \dfrac{1}{n-1}\left(\dfrac{\varepsilon_\sigma}{\varepsilon'_{c_T}}\right)^n \end{cases} \tag{3.15}$$

where ε'_{c_T} is the strain corresponding to the peak compressive stress, and constant n is assigned a value of 3.0 for normal-weight concrete and 2.5 for light-weight concrete.

Another model was presented by Diederichs (1987), where the stress-inducing strain was calculated based on the initial modulus of elasticity, E_{c_i}, then multiplied by a modification function to account for the change in the modulus of elasticity due to the high temperature and for creep strain and transient strain, so that:

$$\varepsilon_{c_{tot}} - \varepsilon_{c_{th}} = \varepsilon_{c_\sigma} + \varepsilon_{tr} + \varepsilon_{c_{cr}} = \frac{f_{c_T}}{E_{c_i}}\left[1 - \frac{E_{c_i}}{f'_c} f(T)\right] \tag{3.16}$$

where

$$f(T) = [0.0412(T - 20) + 0.172\times10^{-4}(T - 20)^2 + 0.33\times10^{-6}(T - 20)^3]\times10^{-3} \tag{3.17}$$

The same concept was adopted by Khoury et al. (1985b) who introduced the term 'Load-Induced Thermal Strain' (LITS) which included all the components of strain in heated concrete except for the free thermal strain component. Using the concepts and results of Khoury et al. (1985b), Terro (1998) presented a formula for LITS, normalized to a compressive stress of 30% of the peak compressive stress of concrete at normal temperature and an aggregate content percentage, V_a, of 65% by volume, together with formulae to evaluate its value at other stress levels and aggregate contents. The expressions are presented in the following equations:

$$\varepsilon_{c_{tot}} - \varepsilon_{c_{th}} = \text{LITS}\left(T, \frac{f_{c_T}}{f'_c}, V_a\right) \tag{3.18}$$

and $$\text{LITS}(T, 0.3, 65\%) = [A_0 + A_1 T + A_2 T^2 + A_3 T^3 + A_4 T^4] \times 10^{-6} \tag{3.19}$$

where $A_0 = -43.87$, $A_1 = 2.73$, $A_2 = 6.35\times10^{-2}$, $A_3 = -2.19\times10^{-4}$, $A_4 = 2.77\times10^{-6}$, and $\text{LITS}(T, 0.3, 65\%)$ is LITS at a temperature T, compressive stress of 30% of the peak compressive stress of concrete at normal temperature, and an aggregate content of 65% by volume.

Equation (3.18) applies to temperatures up to 590ºC for concrete mixed with all types of aggregate, except for concrete mixed with Thames gravel (siliceous aggregate) which has the following equation for temperatures above 400ºC.

$$\text{LITS}(T, 0.3, 65\%) = 1.48\times10^{-6}[B_0 + B_1 T + B_2 T^2 + B_3 T^3 + B_4 T^4 + B_5 T^5] \tag{3.20}$$

where $B_0 = -1098.50$, $B_1 = 39.21$, $B_2 = -0.43$, $B_3 = 2.44\times10^{-3}$, $B_4 = -6.27\times10^{-6}$, and $B_4 = 5.95\times10^{-9}$.

To calculate LITS for all ranges of stress ratio (f_{c_T}/f'_c) and aggregate content (V_a):

$$\text{LITS}\left(T, \frac{f_{c_T}}{f'_c}, V_a\right) = \left[0.032 + 3.226\frac{f_{c_T}}{f'_c}\right]\text{LITS}(T, 0.3, V_a) \tag{3.21}$$

$$\text{LITS}\left(T, \frac{f_{c_T}}{f'_c}, V_a\right) = \left[3.05\frac{V_a}{100}\right]\text{LITS}\left(T, \frac{f_{c_T}}{f'_c}, 65\%\right) \tag{3.22}$$

where $\text{LITS}\left(T, \frac{f_{c_T}}{f'_c}, V_a\right)$ is LITS at a temperature T, compressive stress of f_{c_T}, and an aggregate content of V_a by volume, $\text{LITS}(T, 0.3, V_a)$ is LITS at a temperature T, compressive stress of 30% of the peak compressive stress of concrete at normal temperatures, and an aggregate content of V_a by volume, and $\text{LITS}\left(T, \frac{f_{c_T}}{f'_c}, 65\%\right)$ is LITS at a temperature T, compressive stress of f_{c_T}, and an aggregate content of 65% by volume.

While the previously discussed models explicitly evaluate the transient strain and account for it in the overall response of concrete, some other models, such as that proposed by the Eurocode (EN 1992-1-2:2004, 2005), include the transient strain implicitly in the stress-strain model they present. This is done by providing the strain corresponding to the peak compressive stress (the total strain excluding the free thermal strain) for different temperatures. Although this approach seems simpler, it has a major flaw. It neglects the irrevocability feature of the transient strain, which creates a significant error in the cases of cyclic loading, cyclic temperature changes, or even one typical cycle of heating and cooling caused by the event of fire followed by extinguishment.

Gernay and Franssen (2011) developed the Explicit Transient Creep Eurocode model (ETC Eurocode model) that discretizes the irrevocable transient strain component from the total strain values presented in the Eurocode (EN 1992-1-2:2004, 2005). For the development of their model, Gernay and Franssen (2011) utilized the commonly accepted theory that transient strain is linearly dependent on the stress applied (Illston and Sanders, 1973; Anderberg and Thelandersson, 1976; Khoury et al., 1985a; Schneider, 1986; Diederichs, 1987; Terro, 1998).

They evaluated the transient strain as the algebraic difference between a strain value that does not include the transient strain and a strain value that includes the transient strain component. The former is linearly calculated using the initial modulus of elasticity (at zero stress state) presented by the previous version of the Eurocode (ENV 1992-1-2:1995, 1996), while the latter is linearly calculated using the initial modulus of elasticity presented by the current version of the Eurocode (EN 1992-1-2:2004, 2005). The model is presented in Equation (3.23), where the components of $\phi(T)$ can easily be calculated using the data presented in ENV 1992-1-2:1995 (1996) and EN 1992-1-2:2004 (2005).

$$\varepsilon_{tr} = \frac{f_{c_T}}{E_{c_{i_{EC2}}}} - \frac{f_{c_T}}{E_{c_{i_{ENV}}}} = \frac{2}{3}\frac{\left(\varepsilon'_{c_{T_{EC2}}} - \varepsilon'_{c_{T_{ENV}}}\right)}{\left(f'_c/f'_{c_T}\right)}\frac{f_{c_T}}{f'_{c_T}} = \phi(T)\frac{f_{c_T}}{f'_{c_T}} \tag{3.23}$$

where $E_{c_{i_{EC2}}}$ and $\varepsilon'_{c_{T_{EC2}}}$ are the initial modulus of elasticity and the strain corresponding to the maximum compressive stress at temperature T according to the current version of the Eurocode (EN 1992-1-2:2004, 2005), respectively, and $E_{c_{i_{ENV}}}$ and $\varepsilon'_{c_{T_{ENV}}}$ are the initial

modulus of elasticity and the strain corresponding to the maximum compressive stress at temperature T according to the previous version of the Eurocode (ENV 1992-1-2:1995, 1996), respectively.

The ETC Eurocode Model was compared to the experimental results presented by Schneider (1982) and showed reasonable correlation. Gernay and Franssen (2011) also presented a complete stress-strain curve for concrete under elevated temperatures that follows the same format as that of the Eurocode (EN 1992-1-2:2004, 2005) but calibrated to their transient strain model.

3.3.3.1.2 Modelling of Thermal Expansion Strain

Thermal expansion strain of concrete is of particular significance due to its general effect on the behaviour of the reinforced concrete member on the macro level. In restrained members, for example, expansion will result in the generation of forces on the member. One more serious concern is the differential thermal expansion between concrete and steel reinforcing bars. While the coefficients of expansion of concrete and steel reinforcing bars are relatively similar for minor temperature changes, they are not so similar under elevated temperatures, which imposes additional mutual stresses on both of them.

There is wide consensus, backed by experimental results, that the "thermal expansion strain" of concrete, $\varepsilon_{c_{th}}$, caused by the expansion resulting from the rise in temperature, is majorly dependent on temperature, the type of aggregate used in the concrete mix, and to some extent, the cement content. In lieu of calculating the strain of materials directly, a coefficient of thermal expansion, α_{th}, is typically used to describe it, as shown in Equation (3.24). It is defined as the strain per unit change in temperature or, in other words, the slope of the thermal strain-temperature curve, and it has a unit of $^{o}C^{-1}$.

$$\alpha_{c_{th}} = \frac{\varepsilon_{c_{th}}}{(T - 20)} \tag{3.24}$$

Thermal expansion of concrete is a rather complex phenomenon, due to the different constituents of concrete with their different coefficients of expansion and the interaction

between them under elevated temperatures. This differential expansion results in the formation of microcracks that further results in more expansion of the total volume.

The phenomenon also includes the changes in the volume of concrete constituents due to the chemical and physical changes they go through as the temperature rises, such as the shrinkage of the cement matrix as the evaporable water and the non-evaporable chemically-bound water are lost with the advancement of the dehydration process.

Thermal expansion of concrete has been studied since the beginning of the twentieth century beginning with Norton (1911). Since aggregate is the main constituent of concrete, it highly dominates its thermal expansion. Griffith (1936) indicated that silica is the material with the highest thermal expansion in the aggregate chemical composition. Hence, the less silica there is in the aggregate, the less the coefficient of expansion it has, and accordingly, the less the coefficient of expansion for the concrete. This means that calcareous aggregates are better aggregates to use than siliceous ones from a thermal expansion point of view, which is also confirmed by BS 8110-2:1985 (1985) and ACI 216R-89 (1989). Schneider and Diederichs (1981a; 1981b) ran experiments on concrete mixed with different types of aggregate and their results show the same trend. More experimental results were also presented by Philleo (1958), Concrete Manual (1963), Harada et al. (1972), Harmathy and Allen (1973), and Hildenbrand et al. (1978).

Another factor that affects the thermal expansion of concrete is the cement content, because the cement paste has a higher coefficient of thermal expansion than that of the aggregate (Bonnell and Harper, 1950). Lastly, it was also reported that moisture content plays some minor role as well, where completely dry and completely saturated concretes show less thermal expansion than partially saturated ones (Bonnell and Harper, 1950). This also means that the age of concrete has some effect on its thermal expansion, as the moisture content decreases with age.

A very influential factor that affects the thermal expansion of concrete is the level of concrete stress, which can be observed in the results provided by Anderberg and Thelandersson (1976). They also reported shrinkage of concrete rather than expansion at temperatures above 800ºC due to the occurrence of the final stages of concrete dehydration around this temperature.

There are many expressions in the literature aimed at evaluating the thermal expansion of concrete, either by evaluating the thermal strain or the coefficient of thermal expansion that would be transformed to thermal strain by multiplying it by the change in temperature as shown in Equation (3.24). The ASCE Manual of Practice (Structural Fire Protection by T. T. Lie, 1992) suggested one common formula for the coefficient of thermal expansion of normal-weight concrete, as presented in Equation (3.25), and a constant value of $7.5\times10^{-6}\,^{o}C^{-1}$ for concrete mixed with light-weight expanded-shale aggregate.

Calcareous and siliceous aggregates: $$\alpha_{c_{th}} = (0.008T + 6) \times 10^{-6} \quad (3.25)$$

For steel fibre-reinforced concrete (SFRC) with fibre volumetric ratio of around 0.5%, Lie and Kodur (1996) provided the formulae presented in Equation (3.26) and Equation (3.27) for the thermal expansion strain, acknowledging its dependency on the type of aggregate used. It should be noted that the formulae were provided to represent the coefficient of thermal expansion, but examining their values, it is believed that they represent the thermal expansion strain.

For concrete mixed with siliceous aggregates:

$$\varepsilon_{c_{th}} = \begin{cases} 0.016 \times 10^{-3}T - 1.15 \times 10^{-3} & \text{for } 20℃ < T \leq 530℃ \\ 0.083 \times 10^{-3}T - 36.4 \times 10^{-3} & \text{for } 530℃ < T \leq 600℃ \\ 13.5 \times 10^{-3} & \text{for } 600℃ < T \leq 1000℃ \end{cases} \quad (3.26)$$

For concrete mixed with calcareous aggregates:

$$\varepsilon_{c_{th}} = \begin{cases} 0.010 \times 10^{-3}T - 1.15 \times 10^{-3} & \text{for } 20℃ < T \leq 750℃ \\ 0.077 \times 10^{-3}T - 51.87 \times 10^{-3} & \text{for } 750℃ < T \leq 1000℃ \end{cases} \quad (3.27)$$

The Eurocode (ENV 1992-1-2:1995, 1996) and its current version (EN 1992-1-2:2004, 2005) gave the following expressions for the thermal expansion strain depending on the type of aggregate as well:

For concrete mixed with siliceous aggregates:

$$\varepsilon_{c_{th}} = \begin{cases} 2.3 \times 10^{-11}T^3 + 9 \times 10^{-6}T - 1.8 \times 10^{-4} & \text{for } T \leq 700℃ \\ 14 \times 10^{-3} & \text{for } 700℃ < T \leq 1200℃ \end{cases} \quad (3.28)$$

For concrete mixed with calcareous aggregates:

$$\varepsilon_{c_{th}} = \begin{cases} 1.4 \times 10^{-11}T^3 + 6 \times 10^{-6}T - 1.2 \times 10^{-4} & \text{for } T \leq 805℃ \\ 12 \times 10^{-3} & \text{for } 700℃ < T \leq 1200℃ \end{cases} \quad (3.29)$$

For concrete mixed with light-weight aggregates:

$$\varepsilon_{c_{th}} = 8 \times 10^{-6}(T - 20) \quad (3.30)$$

Kodur and Sultan (2003) presented the following formulae for high-strength concrete, also dependent on the aggregate type. It should be noted that the formulae were provided to represent the coefficient of thermal expansion, but examining their values, it is believed that they represent the thermal expansion strain.

For concrete mixed with siliceous aggregates:

$$\varepsilon_{c_{th}} = \begin{cases} 11.0 \times 10^{-6}T - 0.20 \times 10^{-3} & \text{for } 20℃ < T \leq 450℃ \\ 36.0 \times 10^{-6}T - 11.5 \times 10^{-3} & \text{for } 450℃ < T \leq 650℃ \\ 11.9 \times 10^{-3} & \text{for } 650℃ < T \leq 1000℃ \end{cases} \quad (3.31)$$

For concrete mixed with calcareous aggregates:

$$\varepsilon_{c_{th}} = \begin{cases} 8.00 \times 10^{-6}T - 0.20 \times 10^{-3} & \text{for } 20℃ < T \leq 450℃ \\ 21.0 \times 10^{-6}T - 6.10 \times 10^{-3} & \text{for } 450℃ < T \leq 920℃ \\ -12.0 \times 10^{-6}T + 24.2 \times 10^{-3} & \text{for } 920℃ < T \leq 1000℃ \end{cases} \quad (3.32)$$

Kodur and Sultan (2003) also provided expressions for the thermal expansion of steel fibre-reinforced high-strength concrete for concrete mixed with different types of aggregate, as shown in Equations (3.33) and (3.34). They reported that the behaviour is similar to plain concrete, except that expansion is greater for temperatures beyond 800ºC,

which they attributed to the continuous expansion of the steel fibres, as opposed to the cessation of expansion for concrete at these temperature levels. These formulae were also provided to represent the coefficient of thermal expansion, but are believed to represent the thermal expansion strain.

For concrete mixed with siliceous aggregates:

$$\varepsilon_{c_{th}} = \begin{cases} 16.0 \times 10^{-6}\mathrm{T} - 1.00 \times 10^{-3} & \text{for } 20℃ < \mathrm{T} \leq 530℃ \\ 87.0 \times 10^{-6}\mathrm{T} - 38.6 \times 10^{-3} & \text{for } 530℃ < \mathrm{T} \leq 600℃ \\ 13.6 \times 10^{-3} & \text{for } 600℃ < \mathrm{T} \leq 1000℃ \end{cases} \quad (3.33)$$

For concrete mixed with calcareous aggregates:

$$\varepsilon_{c_{th}} = \begin{cases} 9.00 \times 10^{-6}\mathrm{T} - 0.20 \times 10^{-3} & \text{for } 20℃ < \mathrm{T} \leq 700℃ \\ 58.0 \times 10^{-6}\mathrm{T} - 34.5 \times 10^{-3} & \text{for } 700℃ < \mathrm{T} \leq 870℃ \\ 16.0 \times 10^{-3} & \text{for } 870℃ < \mathrm{T} \leq 1000℃ \end{cases} \quad (3.34)$$

Kodur and Khaliq (2011) provided different expressions for different types of high-strength concrete, all mixed with calcareous aggregates, as shown in Equation (3.35), Equation (3.36), and Equation (3.37). They also tested steel fibre-reinforced high-strength concrete and noted that steel fibres have no significant effect on the thermal expansion of high-strength concrete with all its types; hence, they recommended the same formulae, presented below, for high-strength concrete and steel fibre-reinforced high-strength concrete as well.

For self-consolidating concrete (SCC):

$$\varepsilon_{c_{th}} = \begin{cases} 10.0 \times 10^{-6}\mathrm{T} - 0.3 \times 10^{-3} & \text{for } 20℃ < \mathrm{T} \leq 200℃ \\ 17.0 \times 10^{-6}\mathrm{T} - 2.0 \times 10^{-3} & \text{for } 200℃ < \mathrm{T} \leq 700℃ \\ 20.0 \times 10^{-6}\mathrm{T} - 5.0 \times 10^{-3} & \text{for } 700℃ < \mathrm{T} \leq 1000℃ \end{cases} \quad (3.35)$$

For fly ash concrete (FAC):

$$\varepsilon_{c_{th}} = \begin{cases} 10.0 \times 10^{-6}T - 0.3 \times 10^{-3} & \text{for } 20℃ < T \leq 200℃ \\ 13.0 \times 10^{-6}T - 1.7 \times 10^{-3} & \text{for } 200℃ < T \leq 600℃ \\ 20.0 \times 10^{-6}T - 5.0 \times 10^{-3} & \text{for } 600℃ < T \leq 1000℃ \end{cases} \quad (3.36)$$

It should be noted that the term '20.0×10^{-6}' in Equation (3.36) is given as '5.0×10^{-6}' in the publication, but it appears to be a typographical mistake.

Kodur and Khaliq (2011) also provided a formula for high-strength concrete with minimal superplasticizer and no water reducer or fly ash over the whole range of temperature increase, as follows:

$$\varepsilon_{c_{th}} = 10.0 \times 10^{-6}T - 5.0 \times 10^{-3} \quad \text{for } 20℃ < T \leq 1000℃ \quad (3.37)$$

3.3.3.2 Steel Strain

For steel reinforcing bars, a strain similar to the transient strain in concrete occurs when the steel is heated while stressed. Since steel does not show any creep at normal temperatures and creep for steel is totally associated with elevated-temperatures, this strain is simply called the creep strain. This type of creep strain has been noticed and studied for metals in general since the 1920s (Tapsell and Clenshaw, 1927). Many researchers have verified and confirmed the phenomenon for both structural steel and steel reinforcing bars, such as Hult (1966) and Harmathy (1967). This means that the total strain of steel under elevated temperatures can be evaluated as:

$$\varepsilon_{s_{tot}}(\sigma, T, t) = \varepsilon_{s_\sigma}(\sigma, T) + \varepsilon_{s_{th}}(T) + \varepsilon_{s_{cr}}(\sigma, T, t) \quad (3.38)$$

where, $\varepsilon_{s_{tot}}$, is the total strain in steel; ε_{s_σ} is the stress-inducing strain, which depends on the stress level and temperature; $\varepsilon_{s_{th}}$ is the thermal expansion strain, which depends on temperature only; and $\varepsilon_{s_{cr}}$ is the creep strain, experienced by steel when heated while stressed, which depends on stress level, temperature, and time.

3.3.3.2.1 Modelling of Steel Creep Strain

Many models were proposed by researchers to explicitly evaluate the steel creep strain such as the models proposed by Dorn (1954), Harmathy (1967), Thor (1973), and Anderberg (1983), together with the theory put forth by Zienkiewicz and Cormeau (1974). Other models just implicitly included the steel creep strain in a stress-strain relation. It was reported by Huang and Tan (2003) that creep strains in steel become pronounced at temperatures higher than 400ºC. However, Crook (1980) reported that, for a short duration of fire (less than three hours), steel reinforcement creep strain can be ignored.

Since fire events normally do not last long enough for the steel creep strain to become significant and since the constitutive models to be used in this study supposedly include the steel creep strain implicitly, no explicit model will be used. Therefore, the only thermal strain to be considered for steel under elevated temperatures in this study is the thermal expansion strain.

3.3.3.2.2 Modelling of Thermal Expansion Strain

Evaluating the thermal expansion of steel is not as complicated as that of concrete, for the simple reason that steel is a homogeneous metal alloy as opposed to concrete with its numerous constituents. Ödeen (1968) reported an almost constant coefficient of thermal expansion, which was also confirmed by Malhotra (1982b) who ran simple tests and claimed a constant value of 1.4×10^{-5} ºC^{-1} for the coefficient of thermal expansion of steel. Anderberg (1983) also reported a linear relation between the thermal expansion of steel and temperature, which means a constant coefficient of thermal expansion. He also reported that this constant value is almost independent of the steel type.

However, the European Convention for Constructional Steelwork (ECCS) (1983), the ASCE Manual of Practice (Structural Fire Protection by T. T. Lie, 1992), and the Eurocode (ENV 1992-1-2:1995, 1996) and its current version (EN 1992-1-2:2004, 2005) disagreed with the constant values assigned for the coefficient of thermal expansion of

steel by others. The ECCS (1983) presented the following expression, where the coefficient of thermal expansion of steel increases linearly with temperature:

$$\alpha_{s_{th}} = (10.0 \times 10^{-3}T + 12.0) \times 10^{-6} \tag{3.39}$$

The ASCE Manual of Practice (Structural Fire Protection by T. T. Lie, 1992) proposed the formulae shown in Equation (3.40) for the coefficient of thermal expansion of steel, where it increases linearly with temperature until 1000ºC, at which point its remains constant thereafter.

$$\alpha_{s_{th}} = \begin{cases} (4.0 \times 10^{-3}T + 12.0) \times 10^{-6} & \text{for } 20℃ < T < 1000℃ \\ 16.0 \times 10^{-6}℃^{-1} & \text{for } T \geq 1000℃ \end{cases} \tag{3.40}$$

For the Eurocode (ENV 1992-1-2:1995, 1996) and its current version (EN 1992-1-2:2004, 2005), the following expressions were presented for the thermal expansion strain of steel:

$$\varepsilon_{s_{th}} = \begin{cases} 0.4 \times 10^{-8}T^2 + 1.2 \times 10^{-5}T - 2.416 \times 10^{-4} & \text{for } 20℃ < T < 750℃ \\ 1.1 \times 10^{-2} & \text{for } 750℃ < T \leq 860℃ \\ 2.0 \times 10^{-5}T - 6.2 \times 10^{-3} & \text{for } 860℃ < T \leq 1200℃ \end{cases} \tag{3.41}$$

3.3.3.3 Models Assessment and Comparison

This section presents a comparison between the different models available in the literature for thermal expansion strain and shows how significantly different they are. In order to do that, Figure 3-10, Figure 3-11, and Figure 3-12 are presented to show the models for the thermal expansion strain of concrete mixed with siliceous aggregates, concrete mixed with calcareous aggregates, and steel reinforcing bars, respectively.

Comparing the models presented in each figure, one can notice the significant differences among them. Also, comparing the thermal expansion strain of concrete and steel reinforcing bars, it can be noticed that they can vary significantly from each other at higher temperatures. This differential thermal expansion is particularly of high significance because of the mutual stresses it causes in both concrete and steel reinforcing bars.

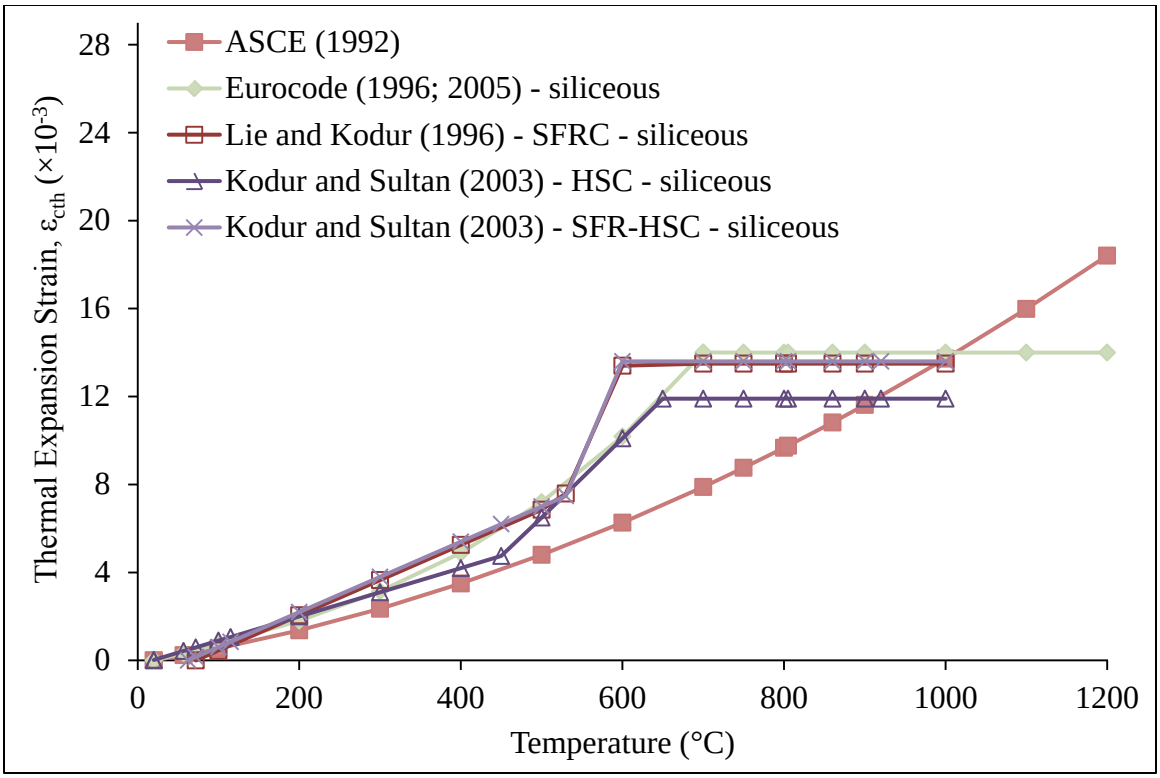

Figure 3-10 Thermal expansion strain of concrete mixed with siliceous aggregates at different temperatures based on available models

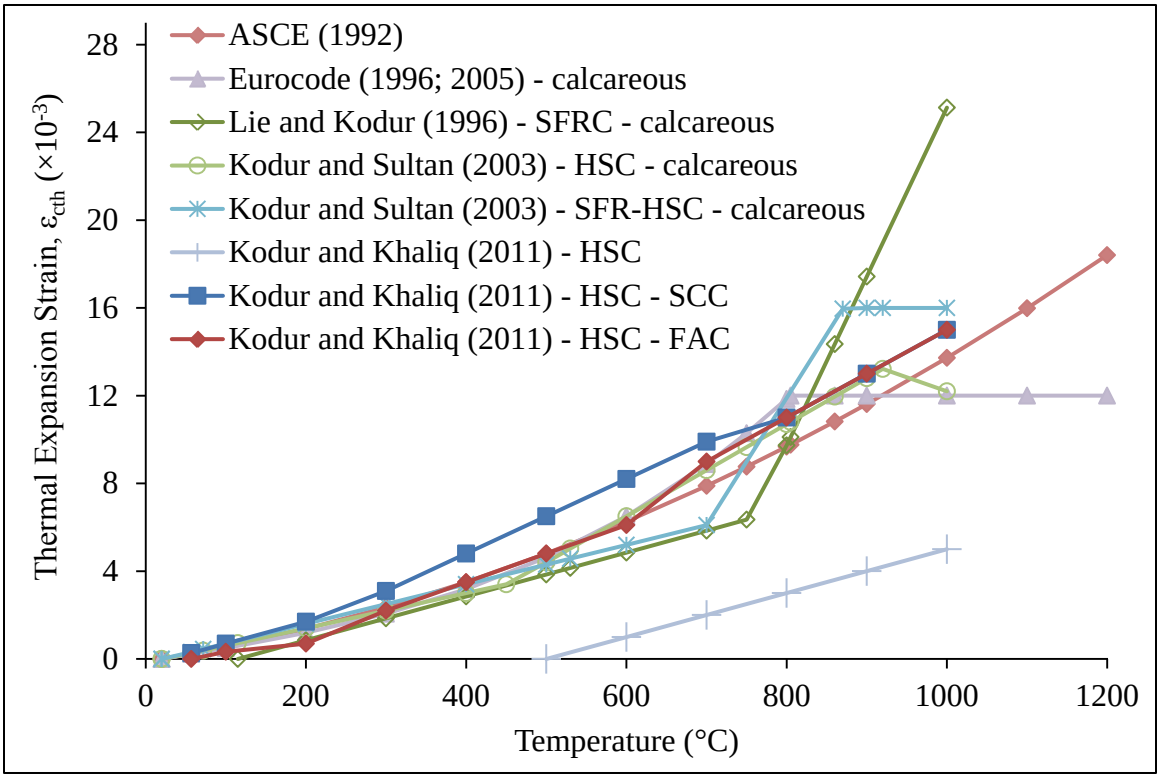

Figure 3-11 Thermal expansion strain of concrete mixed with calcareous aggregates at different temperatures based on available models

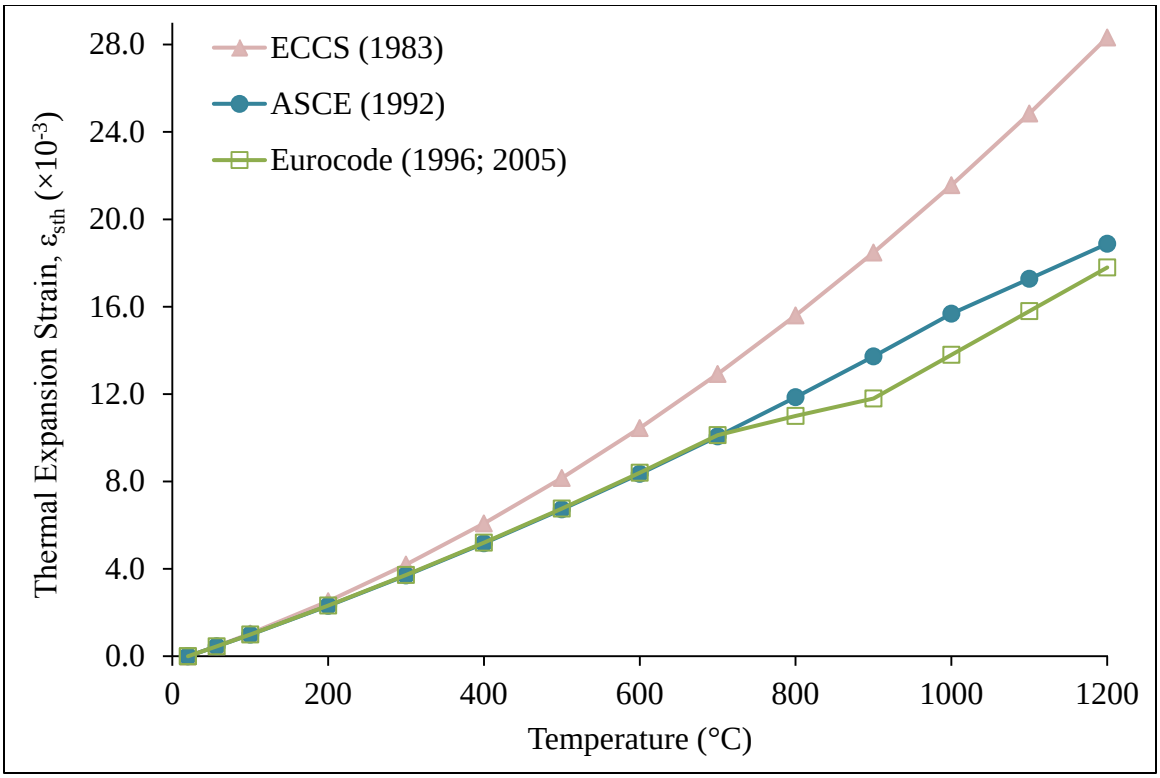

Figure 3-12 Thermal expansion strain of steel reinforcing bars at different temperatures based on available models

3.4 Properties Related to Heat and Moisture Transfer

In Chapter 4, the procedure followed for the analysis of heat and moisture transfer through concrete is discussed. Many properties of concrete, water, and air control the transfer, with most of these properties changing with temperature. In this section, the thermal properties of concrete will be discussed and evaluated. The thermal properties of water and air are discussed in Appendix B. The thermal properties of steel reinforcing bars, on the other hand, play a minimal role in the transfer of heat and moisture through the depth of reinforced concrete members; hence, they will not be discussed.

3.4.1 Properties of Concrete

The properties of concrete that control heat transfer through concrete are the thermal conductivity, k, the density, ρ_c, and the specific heat capacity, c_{p_c}. For coupled heat and

moisture transfer calculations, other properties also contribute to the process, such as the porosity, ϕ, and the permeability, K. Many research programs have been dedicated to the estimation of these properties under elevated temperatures. The properties controlling the heat transfer can be combined in one relation that defines a thermal property known as the thermal diffusivity, α, as shown in Equation (3.42). Thermal diffusivity defines the rate at which heat is conducted through a material in transient thermal processes, and it has an SI unit of m^2/sec. It is sometimes described as a measure of the thermal inertia of the material.

$$\alpha = \frac{k}{\rho_c c_{p_c}} \tag{3.42}$$

Also, the product of the density, ρ_c, and the specific heat capacity, c_{p_c}, which is in the denominator of Equation (3.42) is equal to the heat capacity of the material, C_c, which is commonly evaluated rather than evaluating its constituents individually.

3.4.1.1 Thermal Conductivity

Defined as the heat flux transmitted under a unit temperature gradient, or the amount of heat flowing per second per unit area under unit temperature gradient, the thermal conductivity is the property that defines the ability of material to conduct heat. While high thermal conductivity is a desirable concrete property for normal temperatures as it results in lower thermal gradients, in the case of concrete subjected to elevated temperatures, low thermal conductivity is typically sought. This is because, in the event of fire, the concrete cover acts as a protection layer for reinforcing bars, where the slower the heat reaches the steel reinforcing bars, the longer the member can withstand fire.

Being a heterogeneous material, concrete has a thermal conductivity that directly depends on its constituents. Listing these constituents in a descending order according to their thermal conductivity, aggregate comes first, followed by cement, water, and finally air, which has a very low thermal conductivity (Khoury, 1983). This presents a good idea of the factors that affect the thermal conductivity of concrete, such as the aggregate-cement ratio which causes higher thermal conductivity as it increases. Since increasing the water-cement ratio causes higher porosity (i.e. causes more air voids), it results in lower thermal

conductivity. Added to these factors are the pore volume and distribution, which significantly affects the conductivity, and the age of concrete, which only affects the thermal conductivity in the sense that the moisture content decreases with age and the thermal conductivity decreases with moisture increase.

The significance of experimentally determining the thermal conductivity of concrete under elevated temperatures has been noted as early as the beginning of the twentieth century, when Norton (1911) designed a special testing apparatus specifically for this purpose. Generally, experimental results show that thermal conductivity of concrete decreases with temperature. Since aggregate comprises 60% to 80% of the concrete volume, it has been the main focus of most of the research conducted on the thermal conductivity of concrete. Birch and Clark (1940) presented the values of the thermal conductivity of different types of rock normally used as aggregate over a range of temperatures of 0ºC to 500ºC, presenting conclusions that have been confirmed by almost all researchers thereafter. They reported that siliceous aggregates have the highest thermal conductivity, followed by calcareous aggregates and finally light-weight aggregates, which have the least thermal conductivity, obviously because of their high porosity.

Harmathy and Allen (1973) presented the experimental results of the National Research Council of Canada (NRC), showing an upper and lower limit for the thermal conductivity of three different mixes of normal-weight concrete. In addition, they showed the much lower thermal conductivity of light-weight concrete using the results of 13 different concrete mixes. Their results also show the same conclusion for the performance of different types of aggregates as previously mentioned.

Studying the results of Harmathy (1970), Harada et al. (1972), Hundt (1976), and many others, Schneider et al. (1982) reached the conclusion that the decrease of thermal conductivity with the increase in temperature is attributed to the fact that the moisture content is at its highest level at low temperatures, but as temperature rises, water evaporates and is substituted by air, which has much lower thermal conductivity. This is followed by the loss of non-evaporable chemically-bound water, which results in even

lower thermal conductivity. In addition, as cracks form in concrete due to fire, the air gaps increase; hence, the thermal conductivity decreases.

There are many expressions available in the literature to analytically model the thermal conductivity of concrete under elevated temperatures. Valore (1980) focused on concrete mixed with light-weight aggregates, where he plotted the experimental results of the National Bureau of Standards, published by Kluge et al. (1949), the U.S. Bureau of Reclamation, published by Price and Cordon (1949), and the University of Minnesota, published by Rowley and Algren (1937), and developed the following expression for the thermal conductivity of concrete as a function of its dry density:

$$k = 0.072e^{1.25\times10^{-3}w} \tag{3.43}$$

where the thermal conductivity, k, in Equation (3.43) and all the models to follow is in $W/m℃$ and w is the oven-dry density of concrete in kg/m^3.

The ASCE Manual of Practice (Structural Fire Protection by T. T. Lie, 1992) also recognized the significant effect of the type of aggregate on the thermal conductivity of concrete under elevated temperatures and presented the following expressions:

For concrete mixed with siliceous aggregates:

$$k = \begin{cases} -0.625\times10^{-3}T + 1.5 & \text{for } 20℃ < T \leq 800℃ \\ 1.0 & \text{for } T > 800℃ \end{cases} \tag{3.44}$$

For concrete mixed with calcareous aggregates:

$$k = \begin{cases} 1.355 & \text{for } 20℃ < T \leq 293℃ \\ -1.241\times10^{-3}T + 1.7162 & \text{for } T > 293℃ \end{cases} \tag{3.45}$$

For concrete mixed with pure quartz aggregate:

$$k = \begin{cases} -0.850\times10^{-3}T + 1.9 & \text{for } 20℃ < T \leq 800℃ \\ 1.22 & \text{for } T > 800℃ \end{cases} \tag{3.46}$$

For concrete mixed with light-weight expanded shale aggregate:

$$k = \begin{cases} -0.39583 \times 10^{-3}T + 0.925 & \text{for } 20℃ < T \leq 600℃ \\ 0.6875 & \text{for } T > 600℃ \end{cases} \quad (3.47)$$

Lie and Kodur (1996) presented the formulae shown in Equations (3.48) and (3.49) for steel fibre-reinforced concrete (SFRC) with fibre volumetric ratio of around 0.5%, pointing out that the steel fibres increase the thermal conductivity to a small extent and justified this increase by the fact that the thermal conductivity of steel is about 50 times that of concrete.

For SFRC mixed with siliceous aggregates:

$$k = \begin{cases} -7.0 \times 10^{-3}T + 3.22 & \text{for } 20℃ < T \leq 200℃ \\ -2.1 \times 10^{-3}T + 2.24 & \text{for } 200℃ < T \leq 400℃ \\ 1.40 & \text{for } 400℃ < T \leq 1000℃ \end{cases} \quad (3.48)$$

For SFRC mixed with calcareous aggregates:

$$k = \begin{cases} -1.775 \times 10^{-3}T + 2.000 & \text{for } 20℃ < T \leq 500℃ \\ -0.579 \times 10^{-3}T + 1.402 & \text{for } 500℃ < T \leq 1000℃ \end{cases} \quad (3.49)$$

The previous version of the Eurocode (ENV 1992-1-2:1995, 1996) presented the following expressions for different types of aggregate:

For concrete mixed with siliceous aggregates:

$$k = 2.0 - 0.24\left(\frac{T}{120}\right) + 0.012\left(\frac{T}{120}\right)^2 \qquad \text{for } 20℃ < T \leq 1200℃ \quad (3.50)$$

For concrete mixed with calcareous aggregates:

$$k = 1.6 - 0.16\left(\frac{T}{120}\right) + 0.008\left(\frac{T}{120}\right)^2 \qquad \text{for } 20℃ < T \leq 1200℃ \quad (3.51)$$

For concrete mixed with light-weight aggregates:

$$k = \begin{cases} 1.0 - \dfrac{T}{1600} & \text{for } 20℃ < T \leq 800℃ \\ 0.5 & \text{for } 800℃ < T \leq 1200℃ \end{cases} \tag{3.52}$$

However, the current version of the Eurocode (EN 1992-1-2:2004, 2005) proposed similar expressions as those proposed by its predecessor but as upper and lower limits for the thermal conductivity of concrete under elevated temperatures without specifying a certain type of aggregate as follows:

$$k = \begin{cases} 2.00 - 0.2451\left(\dfrac{T}{100}\right) + 0.0107\left(\dfrac{T}{100}\right)^2 & \text{for upper limit} \\ 1.36 - 0.1360\left(\dfrac{T}{100}\right) + 0.0057\left(\dfrac{T}{100}\right)^2 & \text{for lower limit} \end{cases} \tag{3.53}$$

with these expressions being valid for a range of temperatures of 20ºC to 1000ºC. For concrete mixed with light-weight aggregates, it kept the same expression presented by its predecessor.

Shin et al. (2002) tested Korean concrete, which they claimed to be similar in its chemical composition to basaltic concrete in the United States of America, under temperatures ranging between 20ºC and 1100 ºC. They presented the following expression for the thermal conductivity of concrete at elevated temperatures as a curve fit for their results:

$$k = 1.36469 \times 10^{-6}T^2 - 2.56908 \times 10^{-3}T + 2.24266 \tag{3.54}$$

Also, Kodur and Sultan (2003) presented the following expressions for the thermal conductivity of high-strength concrete under elevated temperatures, depending on aggregate type:

For concrete mixed with siliceous aggregates:

$$k = -1.1 \times 10^{-3}T + 2.00 \qquad \text{for } 20℃ < T \leq 1000℃ \tag{3.55}$$

For concrete mixed with calcareous aggregates:

$$k = \begin{cases} -1.3 \times 10^{-3}T + 2.00 & \text{for } 20℃ < T \leq 300℃ \\ -2.0 \times 10^{-3}T + 2.21 & \text{for } 300℃ < T \leq 1000℃ \end{cases} \quad (3.56)$$

It should be noted that one year later, Kodur et al. (2004) presented revised formulae, multiplying all those formulae by a factor of 0.85.

Kodur and Sultan (2003) also studied the effect of temperature on the thermal conductivity of steel fibre-reinforced high-strength concrete with fibre volumetric ratio of around 0.5%, where they reported that thermal conductivity becomes constant at higher temperatures. This can be attributed to the narrower cracks associated with SFRC, which result in smaller air gaps and hence higher conductivity. Kodur and Sultan (2003) presented expressions for thermal conductivity of steel fibre-reinforced high-strength concrete as follows:

For concrete mixed with siliceous aggregates:

$$k = \begin{cases} -3.4 \times 10^{-3}T + 2.50 & \text{for } 20℃ < T \leq 200℃ \\ -2.1 \times 10^{-3}T + 2.24 & \text{for } 200℃ < T \leq 400℃ \\ 1.40 & \text{for } 400℃ < T \leq 1000℃ \end{cases} \quad (3.57)$$

For concrete mixed with calcareous aggregates:

$$k = \begin{cases} -1.6 \times 10^{-3}T + 1.80 & \text{for } 20℃ < T \leq 500℃ \\ -0.4 \times 10^{-3}T + 1.20 & \text{for } 500℃ < T \leq 1000℃ \end{cases} \quad (3.58)$$

Kodur and Khaliq (2011) provided different expressions for the thermal conductivity of different types of high-strength concrete, all mixed with calcareous aggregates, under elevated temperatures as follows:

For self-consolidating concrete (SCC):

$$k = \begin{cases} -4.5 \times 10^{-3}T + 3.12 & \text{for } 20℃ < T \leq 400℃ \\ 4.4 \times 10^{-3}T - 0.58 & \text{for } 400℃ < T \leq 450℃ \\ -2.5 \times 10^{-3}T + 3.00 & \text{for } 450℃ < T \leq 800℃ \end{cases} \quad (3.59)$$

For fly ash concrete (FAC):

$$k = \begin{cases} -4.5 \times 10^{-3}T + 3.00 & \text{for } 20℃ < T \leq 400℃ \\ 11.1 \times 10^{-3}T - 3.12 & \text{for } 400℃ < T \leq 450℃ \\ -2.5 \times 10^{-3}T + 2.60 & \text{for } 450℃ < T \leq 800℃ \end{cases} \quad (3.60)$$

Kodur and Khaliq (2011) also provided the formulae presented in Equation (3.61) for high-strength concrete with minimal superplasticizer and no water reducer or fly ash.

$$k = \begin{cases} -3.3 \times 10^{-3}T + 2.50 & \text{for } 20℃ < T \leq 400℃ \\ 5.5 \times 10^{-3}T - 1.00 & \text{for } 400℃ < T \leq 450℃ \\ -2.0 \times 10^{-3}T + 2.30 & \text{for } 450℃ < T \leq 800℃ \end{cases} \quad (3.61)$$

It should be noted that the expressions provided by Kodur and Khaliq (2011) were originally discontinuous at 400ºC and the expressions presented here for the temperature range between 400ºC and 450ºC were added to make the models continuous.

The formulae available in the literature are plotted in Figure 3-13 and Figure 3-14 for concrete mixed with siliceous aggregates and calcareous aggregates, respectively. The scatter of the experimental results and the wide variation in the formulae is comprehensible, due to the fact that the thermal conductivity of concrete is highly dependent on the moisture content, combined with the lack of standard testing mechanisms to make the experimental results presented by different researchers comparable.

Finally, for the residual thermal conductivity of concrete after cooling, Ödeen and Nordström (1972) presented results showing that thermal conductivity of concrete remains constant at the value reached at the maximum temperature of heating before cooling starts.

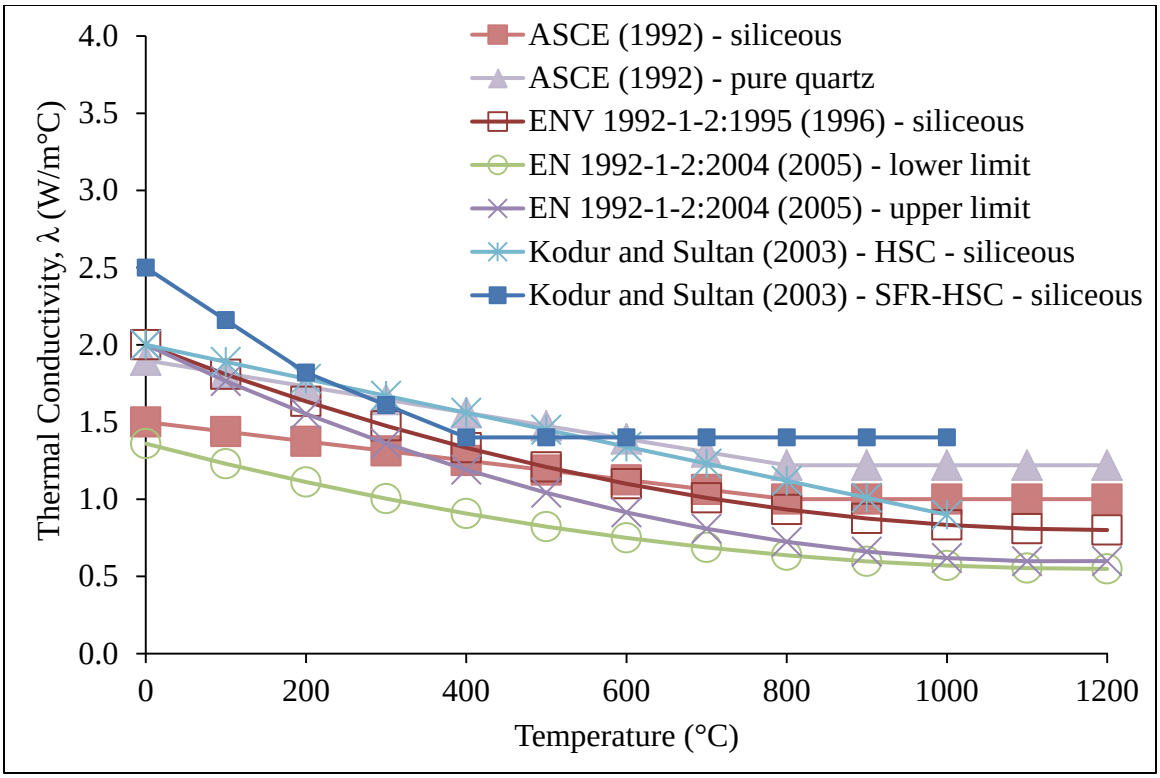

Figure 3-13 Thermal Conductivity of concrete mixed with siliceous aggregates at different temperatures based on available models

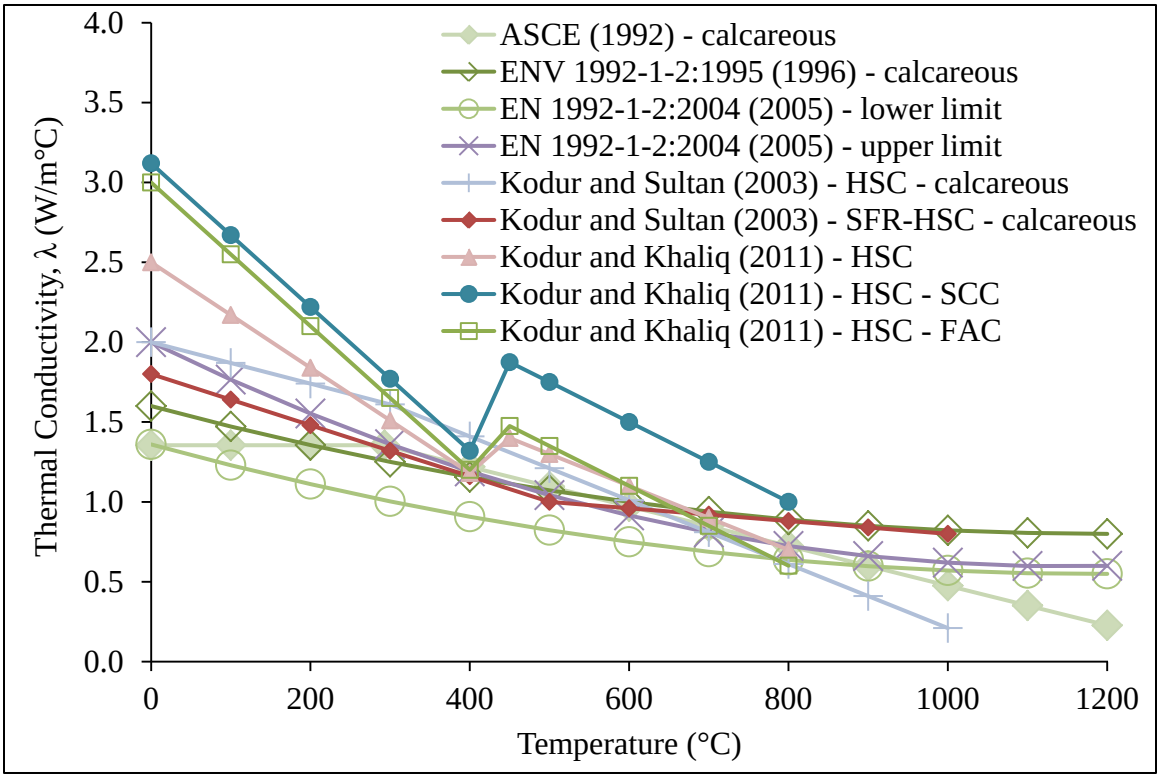

Figure 3-14 Thermal Conductivity of concrete mixed with calcareous aggregates at different temperatures based on available models

3.4.1.2 Density

Generally, the density of concrete decreases with increased temperature. This is attributed to many factors, such as the increase in volume due to thermal expansion and the decomposition of the concrete components causing rise to more voids, hence increasing the porosity. The main significance of evaluating the density of concrete under elevated temperatures lies in its role in determining the heat capacity. The experimental results presented by Harmathy (1970), Harmathy and Allen (1973), Hildenbrand et al. (1978), and Schneider (1982) show similar patterns for the decrease of density of concrete with temperature. Other researchers studied the loss of mass or weight with temperature instead, such as Lie and Kodur (1996), Saad et al. (1996), Gajda et al. (1997), and Kodur and Sultan (2003).

At lower temperatures, the loss of free evaporable water is the main driver for the decline of density for temperatures up to 100ºC to 150ºC, with the extent of decline directly proportional to the moisture content of concrete. This is followed by the loss of non-evaporable chemically-bound water, causing more loss in density at temperatures around 200ºC. For higher temperatures, the decrease in density is due to the decomposition of calcium hydroxide at temperatures between 400ºC and 600ºC.

Up to this point, the decrease in density is minor, but at temperatures between 600ºC and 800ºC, concrete mixed with calcareous aggregates experiences a steep decline in density, due to the decarbonation of calcium carbonate. For concrete mixed with siliceous aggregates, a similar decline, but to a less extent, occurs at temperatures around 700ºC, mainly attributed to the high thermal expansion of quartz at this temperature rather than to chemical changes. Comparing the loss of mass of concrete mixed with siliceous aggregates to the decline of its density, one can notice that this steep decline in density is due to high thermal expansion and not loss of mass. As for concrete mixed with basalt, the decrease in density is much less than with other types of aggregate, mainly due to the low thermal expansion of basalt (Schneider and Diederichs (1981a, 1981b). Quantitatively, the decline of density can go up to around 40% of the normal-temperature density at temperatures above 800ºC.

A few researchers have measured the density of concrete at elevated temperatures and presented formulae for evaluating it for analysis purposes, but the majority of researchers opted to simply evaluate and present formulae for the loss of mass instead.

Lie and Kodur (1996) presented the following formulae for the mass loss of steel fibre-reinforced concrete (SFRC) with fibre volumetric ratio of around 0.5%, pointing out no significant effect for the presence of the steel fibres:

For concrete mixed with siliceous aggregates:

$$\frac{m}{m_o} = -39.92 \times 10^{-6}T + 0.9987 \qquad \text{for } 20℃ < T \leq 1000℃ \tag{3.62}$$

For concrete mixed with calcareous aggregates:

$$\frac{m}{m_o} = \begin{cases} -0.065 \times 10^{-3}T + 1.000 & \text{for } 20℃ < T \leq 700℃ \\ -2.350 \times 10^{-3}T + 2.600 & \text{for } 700℃ < T \leq 800℃ \\ -0.015 \times 10^{-3}T + 0.720 & \text{for } 800℃ < T \leq 1000℃ \end{cases} \tag{3.63}$$

where m and m_o are the mass of concrete at temperature T and at normal temperatures, respectively.

As previously mentioned, Shin et al. (2002) tested Korean concrete, which they claimed to be similar in its chemical composition to basaltic concrete in the United States of America, under temperatures ranging between 20ºC and 1100 ºC. They presented the following expression for the density of concrete at elevated temperatures as a curve fit for their results:

$$\rho_c = 189.575 \times 10^{-6}T^2 - 0.39802T + 2259.62 \tag{3.64}$$

For high-strength concrete, Kodur and Sultan (2003) presented the following formulae:

For concrete mixed with siliceous aggregates:

$$\frac{m}{m_o} = -0.05 \times 10^{-3}T + 1.000 \qquad \text{for } 20℃ < T \leq 1000℃ \tag{3.65}$$

For concrete mixed with calcareous aggregates:

$$\frac{m}{m_o} = \begin{cases} -0.06 \times 10^{-3}T + 1.003 & \text{for } 20℃ < T \leq 600℃ \\ -2.64 \times 10^{-3}T + 2.551 & \text{for } 600℃ < T \leq 700℃ \\ -0.01 \times 10^{-3}T + 0.710 & \text{for } 700℃ < T \leq 1000℃ \end{cases} \quad (3.66)$$

They also presented the following formulae for the mass loss of steel fibre-reinforced high-strength concrete with fibre volumetric ratio of around 0.5%:

For concrete mixed with siliceous aggregates:

$$\frac{m}{m_o} = -0.04 \times 10^{-3}T + 1.000 \qquad \text{for } 20℃ < T \leq 1000℃ \quad (3.67)$$

For concrete mixed with calcareous aggregates:

$$\frac{m}{m_o} = \begin{cases} -0.06 \times 10^{-3}T + 1.003 & \text{for } 20℃ < T \leq 700℃ \\ -1.79 \times 10^{-3}T + 2.214 & \text{for } 700℃ < T \leq 785℃ \\ -0.01 \times 10^{-3}T + 0.817 & \text{for } 785℃ < T \leq 1000℃ \end{cases} \quad (3.68)$$

The Eurocode (EN 1992-1-2:2004, 2005) neglected the significant difference in change in density between concrete mixed with calcareous aggregates and that mixed with siliceous aggregates and presented the following universal formula:

$$\frac{\rho_c}{\rho_{c_o}} = \begin{cases} 1.00 & \text{for } 20℃ < T \leq 115℃ \\ 1.00 - 0.02\dfrac{(T-115)}{85} & \text{for } 115℃ < T \leq 200℃ \\ 0.98 - 0.03\dfrac{(T-200)}{200} & \text{for } 200℃ < T \leq 400℃ \\ 0.95 - 0.07\dfrac{(T-400)}{800} & \text{for } 400℃ < T \leq 1200℃ \end{cases} \quad (3.69)$$

where ρ_{c_o} is the density of concrete at normal temperatures.

The models available for the density at elevated temperatures are plotted against each other in Figure 3-15 and Figure 3-16 for concrete mixed with siliceous and calcareous aggregates, respectively, showing the wide inconsistency of the values offered by the various models.

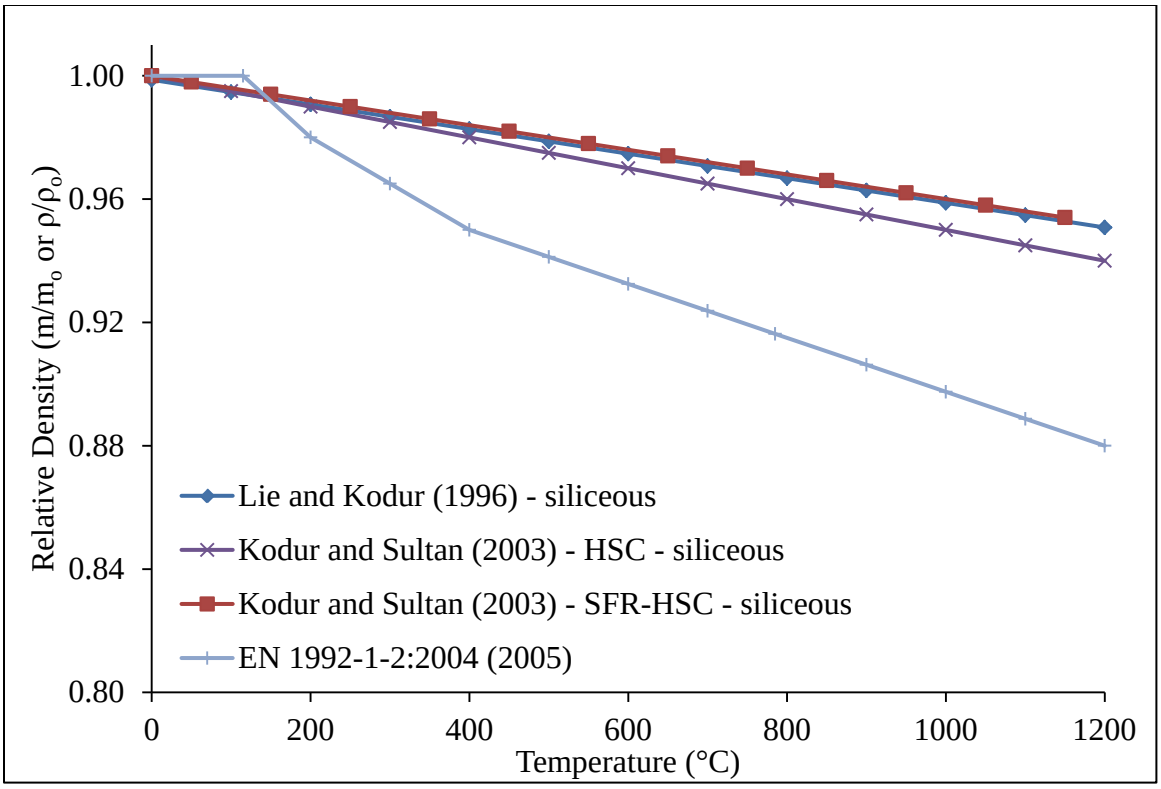

Figure 3-15 Density of concrete mixed with siliceous aggregates at different temperatures based on available models

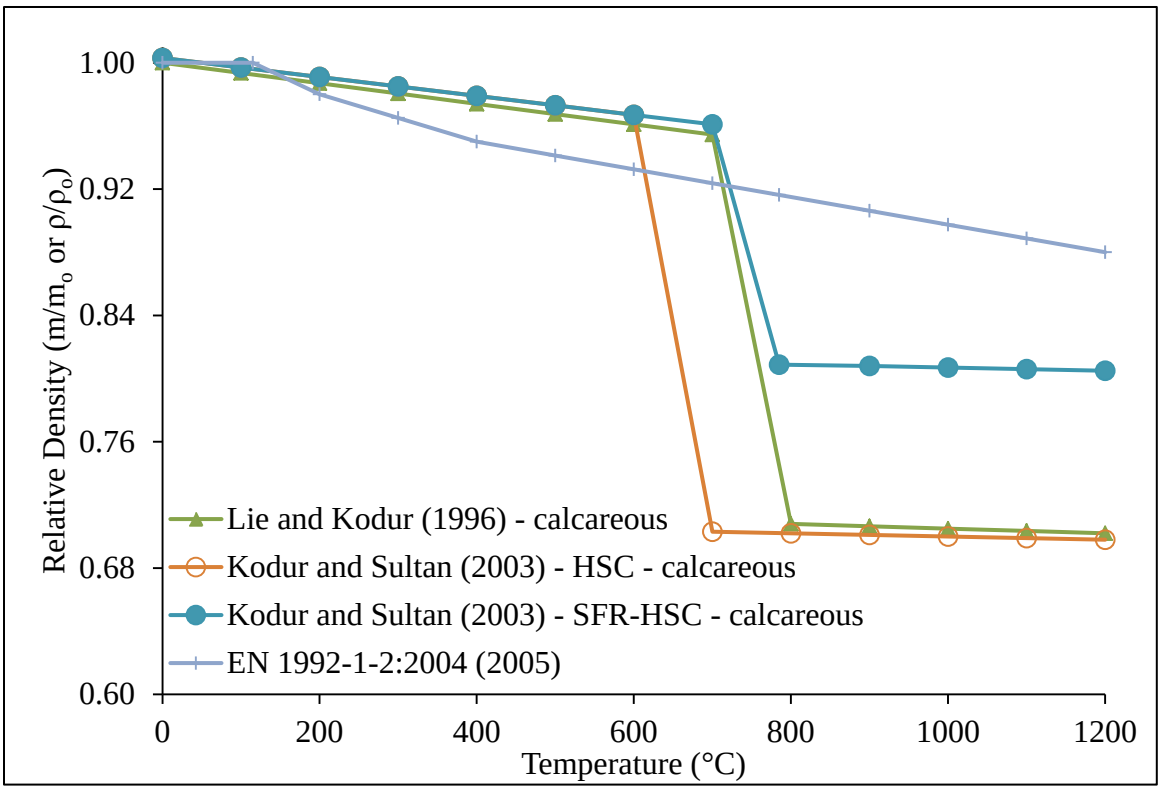

Figure 3-16 Density of concrete mixed with calcareous aggregates at different temperatures based on available models

3.4.1.3 Specific Heat Capacity

Specific heat capacity, commonly called specific heat, is defined as the amount of heat energy required to raise the temperature of a unit mass by a unit temperature; hence, it has an SI unit of J/kg℃. Through its definition, it can be deduced that this property is highly dependent on the reactions undergone by concrete with the rise in temperature, and whether these reactions are endothermic or exothermic. Most of these reactions, such as the vaporization of free water, the release of chemically-bound water, the decomposition of carbon hydroxide, and the $\alpha - \beta$ inversion in chemical composition, are endothermic. This is why the specific heat of concrete increases with temperature, as endothermic reactions require extra heat energy in order to take place.

Therefore, one of the major factors affecting the increase of specific heat of concrete with temperature is the mix proportions, specifically the cement content. The experimental results of different types of cement paste presented by Harmathy (1983) show a minor peak in the plot of the specific heat capacity of cement paste versus temperature at temperatures between 100ºC and 150ºC, corresponding with the loss of evaporable water, followed by a much higher peak at temperatures between 400ºC and 450ºC, corresponding with the decomposition of carbon hydroxide.

Another factor that plays a role in the increase of specific heat of concrete with temperature is the moisture content. At normal temperatures, high moisture content results in higher specific heat. However, this role ends by an abrupt increase in specific heat resulting from the rapid evaporation of evaporable water at temperatures around 200ºC. As previously mentioned, the results presented by Harmathy (1983) show this effect. Also, Schneider (1988) reported that for temperatures below 200ºC, wet concretes show a specific heat nearly twice as high as oven-dried concretes.

The results showing the effect of the type of aggregate on the specific heat of concrete at elevated temperatures are rather conflicting. The results presented by Harmathy and Allen (1973), Collet and Tavernier (1976), and Hildenbrand et al. (1978) show that the type of aggregate used in the concrete mix has little influence on the increase of specific heat at elevated temperatures of up to 800ºC. The results presented by Ödeen (1968) show that no significant increase in specific heat occurs in the case of concrete mixed

with granite aggregate. Yet, it is should be noted that specific heat of concrete is not as highly affected by the type of aggregate used as are other thermal properties of concrete. What is unarguable though is the occurrence of an abrupt increase in specific heat of concrete mixed with calcareous aggregates at temperatures above 800ºC, which is commonly attributed to the decarbonization reaction that the aggregate undergoes.

The evaluation of the specific heat of concrete is complicated and involves many parameters that may affect the results. Many researchers have attempted to develop expressions to predict the specific heat capacity of concrete at elevated temperatures. Some have presented their formulae for the specific heat and the density of concrete separately, while others chose to present formulae for the heat capacity, C_c, which is the product of the specific heat, c_{p_c}, and the density, ρ_c, as previously mentioned. Normally, these formulae represent the properties of completely dry concrete. In all the models to follow c_{p_c} is calculated in J/kg℃ and C_c, or $\rho_c c_{p_c}$, is calculated in $J/m^3℃$.

The ASCE Manual of Practice (Structural Fire Protection by T. T. Lie, 1992) recognized the abrupt rises in the specific heat at temperatures between 400ºC and 600ºC for all types of aggregate used in the concrete mix and the higher rise at temperatures around 800ºC for concrete mixed with calcareous aggregates. It also recognized the lower specific heat of concrete mixed with light-weight aggregates. It presented the expressions shown in Equation (3.70), Equation (3.71), and Equation (3.72) for the heat capacity, which Lie and Kodur (1996) also recommended for steel fibre-reinforced concrete with fibre volumetric ratio of around 0.5%.

For concrete mixed with siliceous aggregates:

$$\rho_c c_{p_c} = \begin{cases} (0.005T + 1.7) \times 10^6 & \text{for } 20℃ < T \leq 200℃ \\ 2.7 \times 10^6 & \text{for } 200℃ < T \leq 400℃ \\ (0.013T - 2.5) \times 10^6 & \text{for } 400℃ < T \leq 500℃ \\ (-0.013T + 10.5) \times 10^6 & \text{for } 500℃ < T \leq 600℃ \\ 2.7 \times 10^6 & \text{for } T > 600℃ \end{cases} \quad (3.70)$$

For concrete mixed with calcareous aggregates:

$$\rho_c c_{p_c} = \begin{cases} 2.566 \times 10^6 & \text{for } 20℃ < T \leq 400℃ \\ (0.1765T - 68.034) \times 10^6 & \text{for } 400℃ < T \leq 410℃ \\ (-0.05043T + 25.00671) \times 10^6 & \text{for } 410℃ < T \leq 445℃ \\ 2.566 \times 10^6 & \text{for } 445℃ < T \leq 500℃ \\ (0.01603T - 5.44881) \times 10^6 & \text{for } 500℃ < T \leq 635℃ \\ (0.16635T - 100.90225) \times 10^6 & \text{for } 635℃ < T \leq 715℃ \\ (-0.22103T + 176.07343) \times 10^6 & \text{for } 715℃ < T \leq 785℃ \\ 2.566 \times 10^6 & \text{for } T > 785℃ \end{cases} \quad (3.71)$$

For concrete mixed with expanded shale (light-weight) aggregate:

$$\rho_c c_{p_c} = \begin{cases} 1.930 \times 10^6 & \text{for } 0℃ < T \leq 400℃ \\ (0.0772T - 28.95) \times 10^6 & \text{for } 400℃ < T \leq 420℃ \\ (-0.1029T + 46.706) \times 10^6 & \text{for } 420℃ < T \leq 435℃ \\ 1.930 \times 10^6 & \text{for } 435℃ < T \leq 600℃ \\ (0.03474T - 18.9140) \times 10^6 & \text{for } 600℃ < T \leq 700℃ \\ (-0.1737T + 126.994) \times 10^6 & \text{for } 700℃ < T \leq 720℃ \\ 1.930 \times 10^6 & \text{for } T > 720℃ \end{cases} \quad (3.72)$$

On the other hand, the previous version of the Eurocode (ENV 1992-1-2:1995, 1996) neglected the difference between the change in specific heat for concrete mixed with siliceous aggregates and that for concrete mixed with calcareous aggregates, which is mainly the abrupt rise around 800ºC for concrete mixed with calcareous aggregates due to the decarbonation reaction of the aggregate. However, it recognized the negligible effect of temperature on the specific heat of concrete mixed with light-weight aggregate and assigned a constant value of 840 J/kg℃ for it throughout the whole temperature range up to 1000ºC.

The Eurocode (ENV 1992-1-2:1995, 1996) also recognized the effect of the moisture content represented in the abrupt rise in specific heat around 115ºC due to the rapid evaporation of evaporable water at this temperature. Therefore, it specified Equation (3.73) for the specific heat of concrete under elevated temperatures for a moisture content of 0%, which does not have this rise because of the absence of moisture, and presented different values for the value of the specific heat at a temperature of 115ºC depending on the moisture content as shown in Equation (3.74).

For concrete mixed with siliceous or calcareous aggregates, with 0% moisture content:

$$c_{p_c} = 900 + 80\left(\frac{T}{120}\right) - 4\left(\frac{T}{120}\right)^2 \qquad \text{for } 20℃ < T \leq 1000℃ \tag{3.73}$$

For concrete mixed with siliceous or calcareous aggregates, with a moisture content of u% by weight, a peak of the following values occurs at 115ºC:

$$c_{p_{c_{peak}}} = \begin{cases} 1875 & \text{for } u = 2\% \\ 2750 & \text{for } u = 4\% \end{cases} \tag{3.74}$$

The current version of the Eurocode (EN 1992-1-2:2004, 2005) kept the same constant value for the specific heat of concrete mixed with light-weight aggregates. For concrete mixed with other types of aggregate, it considered the same parameters as its predecessor but provided different formulae, as follows:

For concrete mixed with siliceous or calcareous aggregates, with 0% moisture content:

$$c_{p_c} = \begin{cases} 900 & \text{for } 20℃ < T \leq 100℃ \\ 900 + (T - 100) & \text{for } 100℃ < T \leq 200℃ \\ 1000 + (T - 200)/2 & \text{for } 200℃ < T \leq 400℃ \\ 1100 & \text{for } 400℃ < T \leq 1200℃ \end{cases} \tag{3.75}$$

For concrete mixed with siliceous or calcareous aggregates, with a moisture content of u% by weight, a peak of the following value occurs at 115ºC:

$$c_{p_{c_{peak}}} = \begin{cases} 1470 & \text{for } u = 1.5\% \\ 2020 & \text{for } u = 3.0\% \\ 5600 & \text{for } u = 10.0\% \end{cases} \tag{3.76}$$

Using the different values of the peak specific heat capacity occurring at 115ºC for the different moisture contents of concrete provided by both ENV 1992-1-2:1995 (1996) and EN 1992-1-2:2004 (2005), the following equation was reached through curve-fitting to relate the peak specific heat capacity to any moisture of content:

$$c_{p_{c_{peak}}} = c_{p_c} + 470\,T \tag{3.77}$$

Shin et al. (2002) presented a formula for the thermal diffusivity of concrete under elevated temperature (in m^2/sec) rather than an explicit expression for the specific heat capacity. As previously mentioned the formula is a curve fit for their experimental results of concrete specimens that they claimed to be similar in its chemical composition to basaltic concrete in the United States of America. In order to use this formula, the expression presented in Equation (3.42), which relates all the thermal properties to each other, should be used in conjunction with the other formulae presented by Shin et al. (2002) for the thermal conductivity and density of concrete at elevated temperatures, presented in Equation (3.54) and Equation (3.64), respectively.

$$\alpha = (9.16391 \times 10^{-7}T^2 - 1.36982 \times 10^{-3}T + 0.909062) \times 10^{-6} \tag{3.78}$$

For high-strength concrete, Kodur and Sultan (2003) reported the same phenomena and peaks that normal-strength concrete undergoes. For high-strength concrete mixed with siliceous aggregates, they presented the same formulae presented by the ASCE Manual of Practice (Structural Fire Protection by T. T. Lie, 1992), while for that mixed with calcareous aggregates the following formulae were proposed:

$$\rho_c c_{p_c} = \begin{cases} 2.450 \times 10^6 & \text{for } 20℃ < T \leq 400℃ \\ (-0.0260T + 12.850) \times 10^6 & \text{for } 400℃ < T \leq 475℃ \\ (0.0143T - 6.295) \times 10^6 & \text{for } 475℃ < T \leq 650℃ \\ (0.1894T - 120.11) \times 10^6 & \text{for } 650℃ < T \leq 735℃ \\ (-0.2630T + 212.40) \times 10^6 & \text{for } 735℃ < T \leq 800℃ \\ 2.000 \times 10^6 & \text{for } 800℃ < T \leq 1000℃ \end{cases} \tag{3.79}$$

Despite the limited influence that steel fibres have on the heat capacity of steel fibre-reinforced high-strength concrete compared to plain concrete, Kodur and Sultan (2003) presented special formulae to predict the heat capacity for SFR-HSC with fibre volumetric ratio of around 0.5% as follows:

For concrete mixed with siliceous aggregates:

$$\rho_c c_{p_c} = \begin{cases} (0.006T + 1.6) \times 10^6 & \text{for } 20℃ < T \leq 100℃ \\ 2.2 \times 10^6 & \text{for } 100℃ < T \leq 400℃ \\ (0.011T - 2.2) \times 10^6 & \text{for } 400℃ < T \leq 500℃ \\ (-0.011T + 8.8) \times 10^6 & \text{for } 500℃ < T \leq 600℃ \\ 2.2 \times 10^6 & \text{for } T > 600℃ \end{cases} \quad (3.80)$$

For concrete mixed with calcareous aggregates:

$$\rho_c c_{p_c} = \begin{cases} 3.81 \times 10^6 & \text{for } 20℃ < T \leq 400℃ \\ (-0.0165T + 10.41) \times 10^6 & \text{for } 400℃ < T \leq 475℃ \\ (0.0079T - 1.182) \times 10^6 & \text{for } 475℃ < T \leq 625℃ \\ (0.2333T - 142.06) \times 10^6 & \text{for } 625℃ < T \leq 700℃ \\ (-0.1800T + 147.25) \times 10^6 & \text{for } 700℃ < T \leq 800℃ \\ 3.25 \times 10^6 & \text{for } 800℃ < T \leq 1000℃ \end{cases} \quad (3.81)$$

Kodur and Khaliq (2011) studied the heat capacity of different types of high-strength concrete, mixed with calcareous aggregates, under elevated temperatures along with the effect of steel fibres, polypropylene fibres, and a mixture of both. They reported minimal effect of both types of fibres for temperatures up to 400ºC and a slight increase up to 600ºC. At temperatures between 600ºC and 800ºC, they reported that the heat capacity of concrete keeps increasing with temperature, attributing this to how steel fibres cause narrower cracks, which means smaller air gaps in concrete and hence higher heat capacity. Yet, for the same temperature range, polypropylene fibres decompose, leaving air gaps in the space they occupied, resulting in a drop in the heat capacity of concrete. Kodur and Khaliq (2011) presented the formulae shown in Equation (3.82),

Equation (3.83), and Equation (3.84), reflecting their findings. The temperature ranges of some of the equations have been modified from the original values in order to make the models continuous.

For self-consolidating concrete (SCC) without polypropylene fibres:

$$\rho_c c_{p_c} = \begin{cases} (1.0 \times 10^{-3} T + 2.4) \times 10^6 & \text{for } 20℃ < T \leq 360℃ \\ (6.0 \times 10^{-3} T + 0.6) \times 10^6 & \text{for } 360℃ < T \leq 800℃ \end{cases} \quad (3.82)$$

For self-consolidating concrete (SCC) with polypropylene fibres:

$$\rho_c c_{p_c} = \begin{cases} (1.0 \times 10^{-3} T + 2.4) \times 10^6 & \text{for } 20℃ < T \leq 400℃ \\ (6.0 \times 10^{-3} T + 0.6) \times 10^6 & \text{for } 400℃ < T \leq 625℃ \\ (-10.0 \times 10^{-3} T + 10.6\ ) \times 10^6 & \text{for } 625℃ < T \leq 800℃ \end{cases} \quad (3.83)$$

For fly ash concrete (FAC):

$$\rho_c c_{p_c} = \begin{cases} (0.4 \times 10^{-3} T + 2.7) \times 10^6 & \text{for } 20℃ < T \leq 393℃ \\ (6.5 \times 10^{-3} T + 0.3) \times 10^6 & \text{for } 393℃ < T \leq 647℃ \\ (1.4T \times 10^{-3} + 3.6) \times 10^6 & \text{for } 647℃ < T \leq 800℃ \end{cases} \quad (3.84)$$

Kodur and Khaliq (2011) also provided formulae for high-strength concrete with minimal superplasticizer and no water reducer or fly ash, with and without polypropylene fibres as shown in Equation (3.85) and Equation (3.86).

For high-strength concrete without polypropylene fibres:

$$\rho_c c_{p_c} = \begin{cases} (0.2 \times 10^{-3} T + 2.4) \times 10^6 & \text{for } 20℃ < T \leq 400℃ \\ (4.3 \times 10^{-3} T + 1.0) \times 10^6 & \text{for } 400℃ < T \leq 800℃ \end{cases} \quad (3.85)$$

For high-strength concrete with polypropylene fibres:

$$\rho_c c_{p_c} = \begin{cases} (0.2 \times 10^{-3}T + 2.4) \times 10^6 & \text{for } 20℃ < T \leq 400℃ \\ (4.3 \times 10^{-3}T + 1.0) \times 10^6 & \text{for } 400℃ < T \leq 650℃ \\ (-9.0 \times 10^{-3}T + 9.1) \times 10^6 & \text{for } 650℃ < T \leq 800℃ \end{cases} \quad (3.86)$$

Figure 3-17 and Figure 3-18 show the various models available in the literature for the specific heat capacity at elevated temperatures for concrete mixed with siliceous and calcareous aggregates, respectively. For the models presented by Kodur and Sultan (2003), where the heat capacity is calculated, the corresponding models for the density of concrete at elevated temperatures, also provided by Kodur and Sultan (2003) are used to calculate the specific heat capacity. As for the models provided by Kodur and Khaliq (2011), a constant value of 2400 kg/m^3 is used for the density of concrete, due to the lack of a corresponding model for the density of concrete with polypropylene fibres at elevated temperatures.

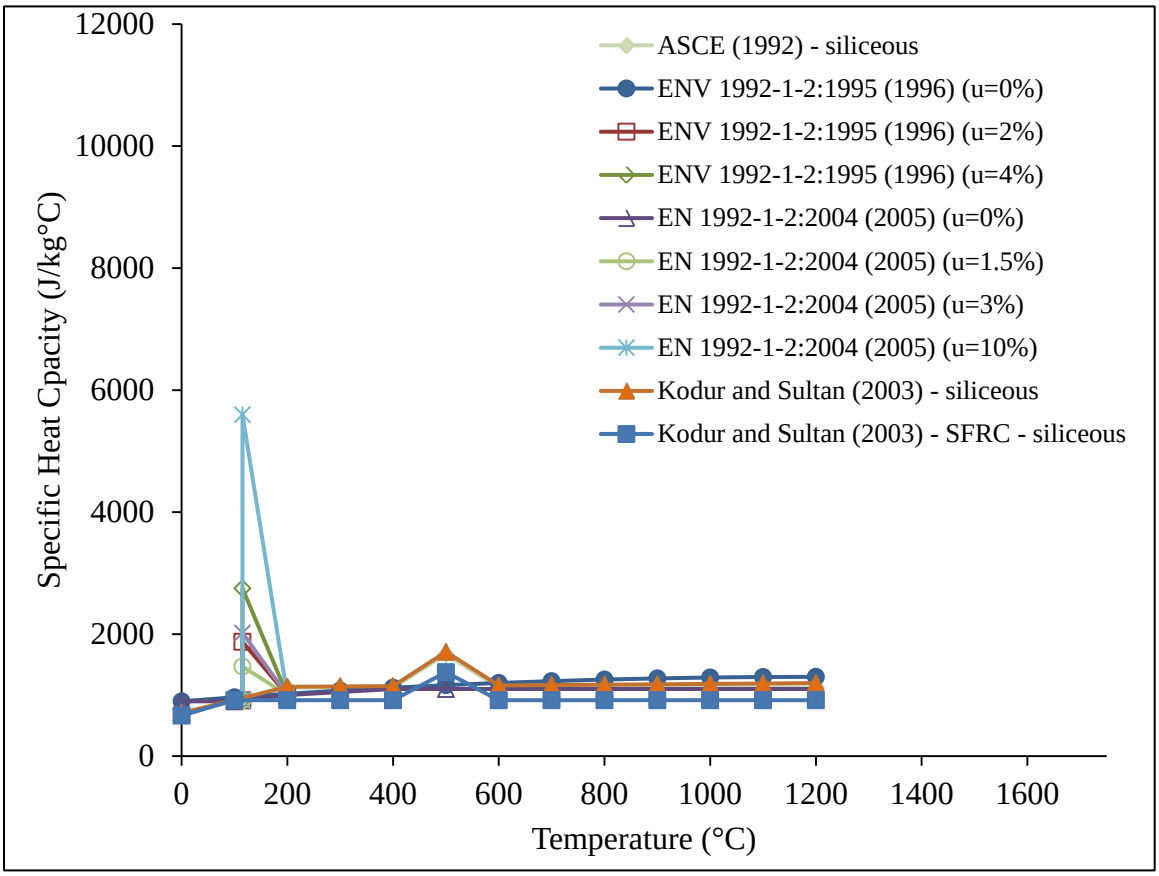

Figure 3-17 Specific heat capacity of concrete mixed with siliceous aggregates at different temperatures based on available models

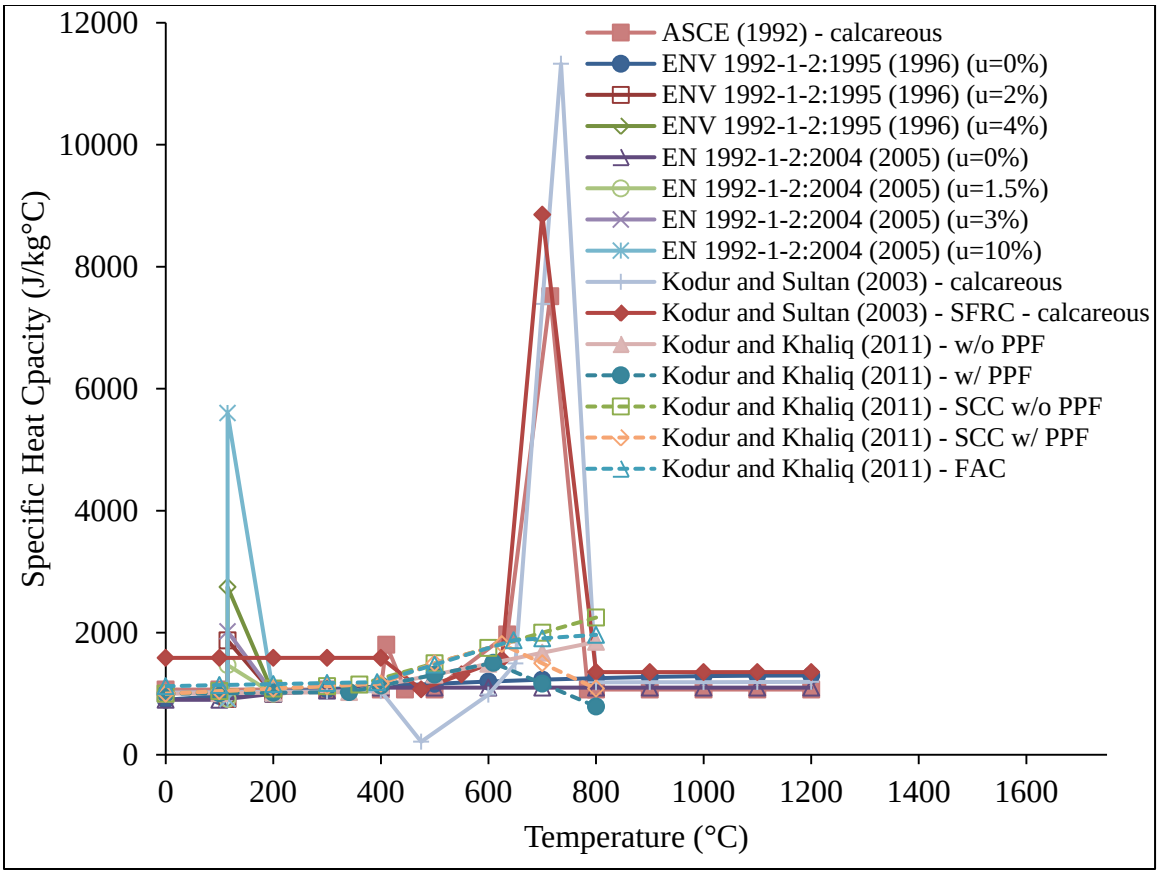

Figure 3-18 Specific heat capacity of concrete mixed with calcareous aggregates at different temperatures based on available models

3.4.1.4 Porosity and Permeability

As previously discussed in Section 3.3.1, concrete experiences extensive changes on the micro level as its temperature rises. According to Fischer (1970), Harmathy (1970), Bažant and Kaplan (1996), and Hertz (2005), for temperatures up to 100ºC to 150ºC, only the free water present in the pores of concrete evaporates; hence, very minimal effect is observed in any of its properties. Beyond this point, the non-evaporable chemically-bound water starts being released by the decomposition of the CSH in the hydrated cement matrix. With this decomposition and the decomposition of many other compounds in concrete as the temperature rises, additional pore spaces are created, hence the porosity, ϕ, of concrete increases (which also decreases the density of concrete as discussed in Section 0).

Numerous test results are available in the literature, but the wide scatter, as shown in Figure 3-19, makes it extremely difficult to reach a specific general relation between the porosity and the rise in temperature. The test results presented by Harmathy (1970) show an increase of around 40% in porosity with a rise in temperature from 105ºC to 850ºC. Saad et al. (1996) showed that the porosity doubled from 100ºC to 600ºC. Kalifa et al. (2001) reported an increase of less than 10% for a rise in temperature from 105ºC to 400ºC. Komonen and Penttala (2003)'s results showed that the porosity of portland cement paste more than doubled when heated from 20ºC to 1000ºC. Zadražil et al. (2004) reported that the porosity of concrete more than tripled as it was heated to 900ºC. Lion et al. (2005) measured an increase in the connected porosity of concrete of 15.8% when heated to 150ºC and 16.9% when heated to 250 ºC.

Some results are very extreme, such as those presented by Annerel and Taerwe (2007; 2008) who reported porosities at 700ºC that are as high as ten times the initial porosity. Also, Heikal (2008) reported an increase of about 170% in porosity for portland cement paste heated from 105ºC to 600ºC. Noumowé et al. (2009) compared the increase in porosity for high-strength concrete to that of normal-strength concrete and showed a more pronounced increase in porosity in the latter with the increase in temperature. While normal-strength concrete showed an increase of around 140% being heated from 20ºC to 600ºC, high-strength concrete only showed an increase of around 90%.

Despite this scatter, many researchers have attempted to reach a general formula for the porosity at different temperatures. Gawin et al. (1999) exploited the results of the several types of concrete presented by Schneider and Herbst (1989) and related the porosity of concrete to temperature through the linear relation presented in Equation (3.87), where the constant 'A_ϕ' determined the relation according to the type of concrete.

$$\phi = \phi_o + A_\phi (T - T_o) \tag{3.87}$$

where ϕ_o and T_o are the initial porosity and initial temperature of concrete, respectively, and T is the temperature of concrete. For B35-concrete, ϕ_o and A_ϕ were evaluated as 0.0600 and 195×10^{-6} ºC^{-1}, respectively, for concrete mixed with siliceous gravel; 0.0870

and 163×10^{-6} ºC^{-1}, respectively, for concrete mixed with limestone; and 0.0802 and 170×10^{-6} ºC^{-1}, respectively, for concrete mixed with basalt.

Another model was proposed by Toumi and Resheidat (2010), where a linear relation was proposed for temperatures up to 500ºC and a logarithmic function for temperatures higher than 500ºC, as shown in Equation (3.88).

$$\phi = \begin{cases} (13.1 \times 10^{-3}\mathrm{T} + 5.6929) \times 10^{-2} & \text{for } \mathrm{T} \leq 500℃ \\ (1.3978e^{3.7\times10^{-3}\mathrm{T}}) \times 10^{-2} & \text{for } \mathrm{T} > 500℃ \end{cases} \quad (3.88)$$

These models, as well as various test results, are plotted in Figure 3-19, normalized with respect to the initial porosities at ambient temperatures.

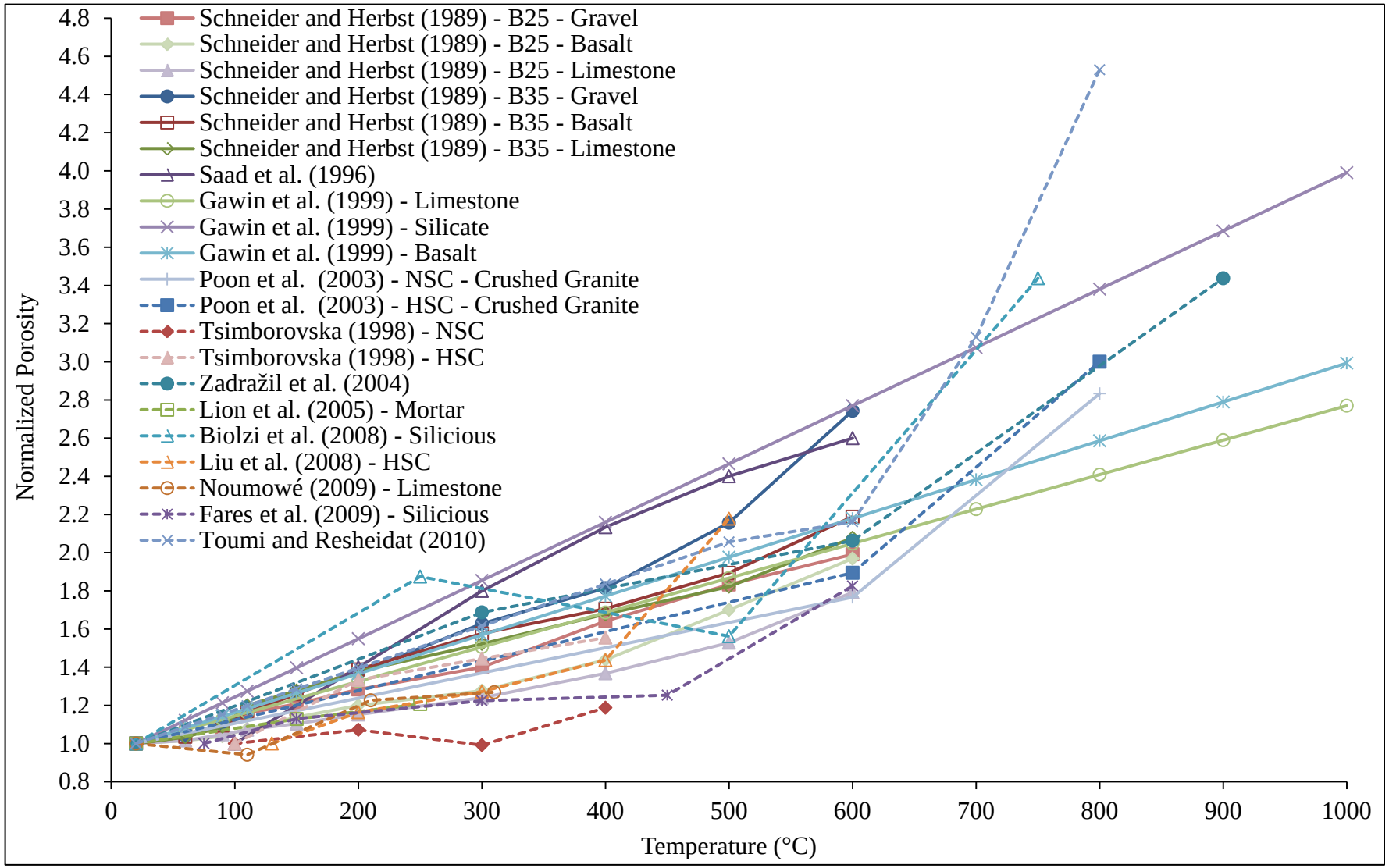

Figure 3-19 Normalized porosity of concrete at different temperatures based on experimental results and available models

The permeability of concrete, K, which mainly depends on the porosity and the pore structure (connectivity of pores), also increases with a rise in temperature. This is caused by the increase in porosity, the arising microcracks and the additional cracking caused by the elevated pore pressure (Gawin et al., 2002). However, the amount of this increase is not proportional to the increase in porosity as one would expect. An interesting finding was first reported by Bažant and Thonguthai (1978) through tests undertaken at Northwestern University, whose results are shown in Figure 3-20. While, at normal temperatures, the permeability of concrete depends on the porosity and the pore structure, for temperatures over 100ºC, it escalates by two orders of magnitude, an increase that is not associated by any tangible increase in porosity. This means that the mobility of water through the pores of concrete increases, with no change in the total volume of pores. Similar results were reached by other researchers, such as Schneider and Herbst (1989), England and Khoylou (1995), Kalifa et al. (2001), Zeiml et al. (2008), and Galek et al. (2010).

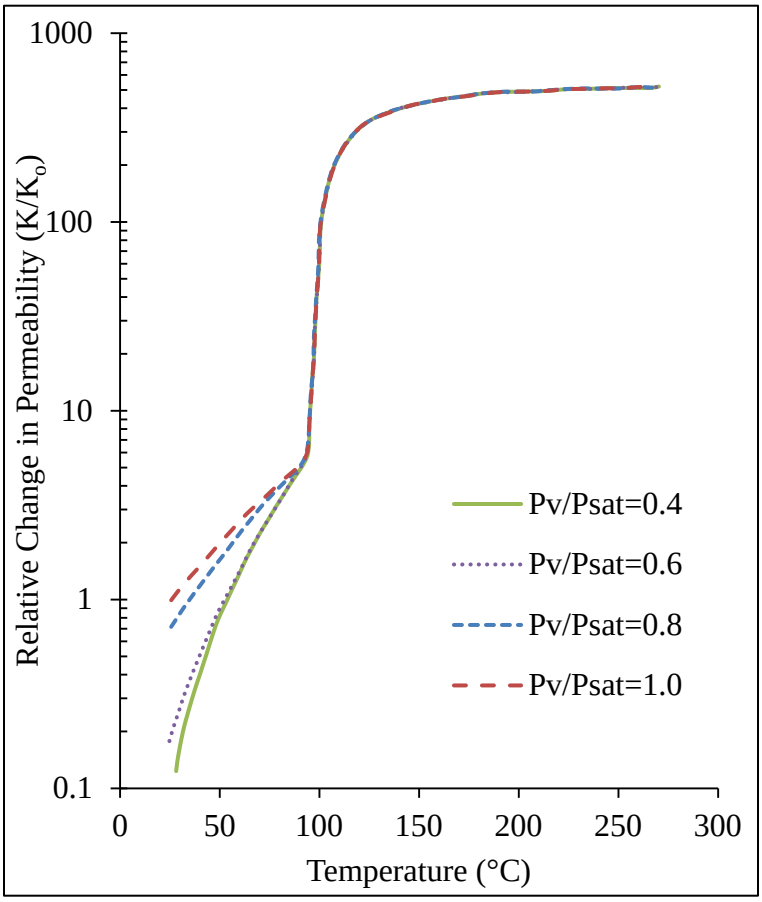

Figure 3-20 Relative change in permeability with rise in temperature (Bažant and Thonguthai, 1978), where K_o is the initial permeability, P_v is the partial pressure of water vapour, and P_{sat} is the saturation pressure of water vapour at the respective temperature

While there is no experimentally-verified explanation for this phenomenon, Bažant and Thonguthai (1978) brought forth a hypothesis that this increase is caused by the smoothening of initially-very-rough pore surfaces due to the rise in temperature, which reduces the surface energy. This means that, with the rise in temperature, the average width of the necks connecting the pores together and governing the passage through them increases, which facilitates the flow of water. This hypothesis accounts for the striking increase in permeability with almost constant porosity.

For modelling this increase, various approaches have been adopted. Gawin et al. (1999) used the results presented by Schneider and Herbst (1989) to develop the following expression, where they took into account the dependence of permeability on the temperature and pore pressure.

$$K = K_o 10^{A_K(T-T_o)} \left(\frac{P_G}{P_\infty}\right)^{B_K} \tag{3.89}$$

where K_o is the initial permeability of concrete at normal temperatures; T_o is the initial temperature (20ºC); and P_∞ and P_G are the pressures of the gaseous mixture in concrete pores at normal temperatures (atmospheric pressure) and at current temperatures, respectively. A_K and B_K are constants. For the results of B35-concrete presented by Schneider and Herbst (1989), Gawin et al. (1999) proposed a value of 1.5×10^{-15} for K_o, 0.005 for A_K, and 0.368 for B_K.

However, the expression presented in Equation (3.89) was extended by Gawin et al. (2002) to include the effect of the mechanical damage arising in concrete with the rise in temperature based on the expression proposed by Bary (1996) to reach the following expression:

$$K = K_o 10^{A_K(T-T_o)} \left(\frac{P_G}{P_\infty}\right)^{B_K} 10^{D.A_D} \tag{3.90}$$

where A_D is a material constant that was evaluated for concrete by Bary (1996) at 4.0 and D is a damage parameter ranging from 0 to 1.

Tenchev et al. (2001) proposed the expression presented in Equation (3.91) assuming that the porosity increases equally in all directions and that the permeability is proportional to

this increase of the cross section of the pores. This approach obviously underestimates the permeability at temperatures above 100ºC.

$$K = K_o \left(\frac{\phi}{\phi_o}\right)^{2/3} \tag{3.91}$$

The increase in both porosity and permeability of concrete due to a rise in temperature is irreversible, meaning that the residual porosity and permeability of concrete after cooling are equal to those at the highest temperature reached.

It should be noted that the permeability discussed in this section is the intrinsic (or absolute) permeability of concrete. Intrinsic permeability is a property of a material that theoretically depends only on its microstructure and is independent of the permeant (fluid). On the other hand, the effective permeability is a measure of the permeability of a porous material for one fluid phase when the material is saturated with more than one fluid. Finally, the relative permeability, denoted in this study as K_i, is a dimensionless measure of the permeability of a specific phase (liquid water for $i = L$ or gaseous mixture consisting of water vapour and air for $i = G$). It is used in the analysis of multiphase flow through porous material and is calculated as the ratio of the effective permeability of that phase to the absolute permeability. In Chapter 4, the use of the intrinsic permeability and the effective permeability in the coupled heat and moisture analysis is explained.

For determining the value of the relative permeability of the gaseous mixture, K_G, Tenchev et al. (2001) proposed the expression presented in Equation (3.92).

$$K_G = 1 - s \tag{3.92}$$

where s is the degree of saturation of concrete, given the following expression by Scheidegger (1957):

$$s = \frac{\varepsilon_L}{\phi} \tag{3.93}$$

Where ε_L is the volume fraction of liquid water, which will be defined in Equation (4.13).

For the relative permeability of the liquid phase, K_L, Tenchev et al. (2001) relied on the observation of Scheidegger (1957) that the partial pressure of the liquid phase, P_L, is about one hundredth of the pressure of the gaseous mixture, P_G. Scheidegger (1957)

attributed this small percentage to the surface tension of liquid water in the capillaries of porous material. To account for this fact, Tenchev et al. (2001) assigned a value of 0.01 to the relative permeability of the liquid phase.

Therefore, $$K_L = 0.01 \tag{3.94}$$

However, a more precise approach, commonly used in coupled heat and moisture transfer analysis, is based on the Mualem (1976) model, which van Genuchten (1980) used to develop the expression presented in Equation (3.95) for the relative permeability of the liquid phase:

$$K_L = \sqrt{s}\left[1 - \left(1 - s^{1/m}\right)^m\right]^2 \tag{3.95}$$

where the coefficient m was evaluated by Baroghel-Bouny et al. (1999), who introduced the coefficient $b = 1/m$ and assigned it a value of 2.2748 for concrete.

Luckner et al. (1989) used the same model to develop the following expression for the relative permeability of the gaseous mixture:

$$K_G = \sqrt{1 - s}\left(1 - s^{1/m}\right)^{2m} \tag{3.96}$$

Davie et al. (2006) ran a sensitivity model on the use of Equation (3.92) and Equation (3.96) to determine the relative permeability of the gaseous mixture and reported little effect of using either of them on the overall results.

3.5 Mechanical Properties

The mechanical properties of reinforced concrete are highly affected by elevated temperatures. They have been the focus of numerous research programs, starting with Lea (1920), who studied the factors affecting the deterioration of concrete strength at elevated temperatures. Lea was followed by many other researchers, also interested in concrete strength, until 1957, when Saemann and Washa (1957) extended the scope of research to also include the effect of elevated temperatures on the modulus of elasticity, tensile strength, modulus of rupture, and toughness of concrete. For steel, Cross et al.

(1948), Simmons and Cross (1952), and Larson and Miller (1952) were among the first researchers studying the mechanical properties of steel under elevated temperatures. Since the behaviour of neither concrete nor steel under elevated temperatures is fully investigated up to the present, research in this topic is still ongoing. In this section, many of the mechanical properties of concrete and steel under elevated temperatures will be discussed.

3.5.1 Properties of Concrete

When studying the behaviour of concrete under elevated temperatures, one needs to realize that concrete at such temperatures behaves in a very different way than it does under normal temperatures, which makes the task more complicated than simply applying some modifications to the models available for concrete under normal temperatures. Exacerbating the problem is the way that researchers typically test concrete under elevated temperatures in order to develop models that capture its behaviour. Both the steady-state test and the transient test, previously described, do not represent the state of concrete at the occurrence of fire. In the event of fire, a member would be loaded to its service load level and then it is heated. The temperature is never kept constant at any point and this is specifically important because this variation in heat causes the differential expansion of concrete layers, which causes internal stresses. These stresses, in turn, cause cracking and spalling, which significantly affect the behaviour of concrete.

Studying the behaviour of concrete under elevated temperatures is not an easy task, due to the large number of parameters that play a role in determining such behaviour. While the behaviour of concrete under normal temperatures is affected in a specific way by confinement, for example, confinement has a different effect on concrete under elevated temperatures. It indeed enhances the performance of concrete as it does under normal temperatures, but to a different extent. Also, the behaviour of preloaded concrete under elevated temperatures differs from that of unloaded concrete, with the effect of high temperatures decreasing with the increase in the amount of loading.

This makes the study much more complicated than studying the behaviour of concrete under normal temperatures, because one needs to test concrete under elevated temperatures taking all the parameters that affect concrete under normal temperatures into account, such as confinement, compression softening, cyclic loading hysteresis, tension stiffening, and tension softening among others. All this needs to be done at different temperatures and for different intensities of loading. Besides, as previously discussed, the behaviour of concrete under elevated temperatures also depends on its density, moisture content, porosity, permeability, aggregate type, and many other parameters that affect the microstructure of concrete causing microcracking to occur under elevated temperatures. This adds more variables that also need to be taken into account.

In the following sections, many of the mechanical properties of concrete under elevated temperatures will be discussed, along with various models available in the literature to predict them. In addition, since it has been found that the effect of fire on concrete is irreversible, meaning that concrete does not recover its original pre-fire properties after it cools (Malhotra, 1956; Weigler and Fischer, 1972; Mohamedbhai, 1983), the post-fire residual properties will be discussed.

3.5.1.1 Concrete under Compression

Concrete compressive strength under elevated temperatures has received the largest share of interest in the literature among all other concrete properties. This is understandable, since compressive strength is often used as an indicator to many other concrete properties. Since the main target of this study is the modelling of reinforced concrete for structural analysis, a reliable constitutive model that represents the behaviour of concrete during the event of fire (at elevated temperatures) is a necessity. Another constitutive model for the behaviour of concrete after the event of fire, when it cools (residual strength), is one other main target.

A constitutive model, represented in a stress-strain relation, has three main parameters: a peak compressive stress (compressive strength), a corresponding strain, and an initial

modulus of elasticity. In order to produce a constitutive model for concrete during or after the event of fire, two approaches can be followed. The first is to apply modification factors to the aforementioned parameters, and use the stress-strain models already available for concrete under normal temperatures, while the second approach is to propose new models dedicated to concrete under elevated temperatures.

Although the second approach intuitively sounds as if it would result in better simulation of the actual behaviour of concrete, the wide scatter of the experimental results available in the literature and the ensuing very different constitutive models and modification factors developed have made the choice a very challenging task. The same challenge is also faced when a structure is being modelled, and a constitutive model needs to be selected. With all the parameters affecting the behaviour of concrete and with each researcher using different types of aggregate and from different sources, different mix proportions, moisture contents, hydration levels of cement, levels of sustained loads, and sealed or unsealed concrete, the choice of a specific model seems random. One way to make a selection, albeit very impractical, is to select the model whose researcher's specimens characteristics best resemble the concrete to be used in the structure being modelled.

A chronological summary of some of the modification factors, following the first approach, will be presented first. Then, following the second approach, some of the comprehensive constitutive models dedicated to modelling concrete under elevated temperatures will be presented as well.

3.5.1.1.1 Compressive Strength

It has been plainly reported by numerous researchers through the years that concrete compressive strength deteriorates with the rise of temperature; see Lea (1920), Lea and Stradling (1922b; 1922a), Grün and Beckmann (1930), Malhotra (1956), Harmathy and Berndt (1966), Furumura (1966), Fischer (1970), Abrams (1971), Purkiss and Dougill (1973), and Hertz (1980). It has been reported by Schneider (1988) that some properties of concrete have minimal or no influence on the effect of fire on compressive strength,

such as the original compressive strength (which is proven to be only true for normal-strength concrete), type of cement, and the water-cement ratio. On the other hand, some other properties were found to highly affect the compressive strength at elevated temperatures, such as the type of aggregate, where the use of siliceous aggregates causes the most strength loss, the aggregate-cement ratio, where lean mixes (with lower cement contents) maintain their strengths more than rich mixes (with higher cement contents) do, and the amount of sustained load, where higher load intensities help concrete maintain its strength under relatively high temperatures. The reason why these parameters affect the intensity of the deterioration of concrete was explained in Section 3.3.1, where the phenomena associated with the subjection of concrete to fire were investigated.

The rate of heating plays an important role as well, but this can be ignored since the rate of heating is constant in most tests and, in reality, is consistent with the natural rate of heating that fire causes. A distinction should also be recognized between normal-strength concrete and high-strength concrete, where the latter exhibits much higher deterioration in strength with higher temperatures and the effect becomes more severe as the strength increases. This is due to the added internal stresses due to internal pore pressure resulting from the trapping of air, water, and water vapour inside pores of high-strength concrete, being smaller in size than those found in normal-strength concrete, as explained in Section 3.3.2.

Bažant and Chern (1987) plotted the experimental results presented by Furumura (1970), Purkiss and Dougill (1973), Anderberg and Thelandersson (1976), and Schneider (1982); and they used the bilinear curve presented in Equation (3.97) to reach the best fit.

$$\frac{f'_{c_T}}{f'_c} = \begin{cases} 1.00 - 0.1786 \times 10^{-3} T & \text{for } T \leq 350℃ \\ 0.9375 - 1.713 \times 10^{-3}(T - 350) & \text{for } 350℃ \leq T \leq 800℃ \end{cases} \quad (3.97)$$

where f'_{c_T}, f'_c are the peak compressive stress (compressive strength) in MPa at temperature T (ºC) and at normal temperatures (20ºC), respectively.

Li and Guo (1993) proposed a simple expression for the cube characteristic strength of concrete at elevated temperatures in MPa, f'_{c-cu_T} as a function of its value at normal temperatures, f'_{c-cu}, as follows:

$$f'_{c-cu_T} = \frac{f'_{c-cu}}{1 + 2.4(T-20)^6 \times 10^{-17}} \tag{3.98}$$

Among the models that only proposed modification factors for compressive strength for concrete during fire, with no modification factors for other parameters, is the previous version of the Eurocode (ENV 1992-1-2:1995, 1996). It presented the expression shown in Equation (3.99) as a conservative guideline for normal-strength concrete mixed with siliceous aggregates, with the recommendation of using more accurate modification factors if available. The material properties at normal temperatures (20ºC) were to be assessed according to the Eurocode (ENV 1992-1-1:1992, 1992).

where
$$\frac{f'_{c_T}}{f'_c} = \begin{cases} 1.0 & \text{for } T \leq 100℃ \\ \dfrac{1600 - T}{1500} & \text{for } 100℃ < T \leq 400℃ \\ \dfrac{900 - T}{625} & \text{for } 400℃ < T \leq 900℃ \\ 0.0 & \text{for } 900℃ < T \leq 1200℃ \end{cases} \tag{3.99}$$

The Eurocode (ENV 1992-1-2:1995, 1996) also gave a separate curve in its Annex A, with different guidelines for the peak compressive stress and the corresponding strain. Yet, the same curve was included in the main body of the current version of the Eurocode (EN 1992-1-2:2004, 2005), but the modification factors were changed.

Chang and Jau (2001) further updated the model presented by Lie et al. (1986) to the expression given in Equation (3.100) and claimed better correlation between their experimental results and their proposed model.

$$\frac{f'_{c_T}}{f'_c} = \begin{cases} 1 - 0.001T & \text{for } T \leq 500℃ \\ 1.6046 + (1.3T^2 - 2817T) \times 10^{-6} & \text{for } T > 500℃ \end{cases} \tag{3.100}$$

Li and Purkiss (2005) provided the following expression for the compressive strength of concrete mixed with siliceous aggregates:

$$\frac{f'_{c_T}}{f'_c} = 0.00165\left(\frac{T}{100}\right)^3 - 0.03\left(\frac{T}{100}\right)^2 + 0.025\left(\frac{T}{100}\right) + 1.002 \qquad (3.101)$$

The model proposed by Hertz (2005) took into consideration the effect of the type of aggregate used in the mix on the compressive strength of concrete under elevated temperatures. To develop his model, Hertz utilized his own experimental results and the results of 400 test series comprising approximately 3000 specimens from the literature. The model assumes one common formula for the modification factors of all the concrete and steel reinforcement properties. The formula is an equation of an S-shaped curve that describes each concrete or reinforcement property by using the respective values for the variables in it. The common formula is:

$$\xi(T) = k + \frac{1-k}{\left[1 + \left(\frac{T}{T_1}\right) + \left(\frac{T}{T_2}\right)^2 + \left(\frac{T}{T_8}\right)^8 + \left(\frac{T}{T_{64}}\right)^{64}\right]} \qquad (3.102)$$

where $\xi(T)$ is the ratio between the material property at a given temperature T and its respective value at 20ºC, i.e. f'_{c_T}/f'_c in the case of concrete compressive strength; k is the ratio between the minimum and the maximum value of the property (for example, k equals zero for compressive strength, since the minimum value of the compressive strength is zero, which occurs at very high temperatures); and T_1, T_2, T_8, and T_{64} are the parameters, with the unit ºC, that describe the curve for each specific property. For the compressive strength during the event of fire, Table 3-2 presents the values of these parameters for the different types of concrete depending on the aggregate type used in the mix.

Table 3-2 Parameters defining compressive strength of concrete at elevated temperatures for Equation (3.102**)**

Aggregate Type in Concrete Mix	k	T_1	T_2	T_8	T_{64}
Siliceous	0.00	15,000	800	570	100,000
Light-weight	0.00	100,000	1,100	800	940
Other Types	0.00	100,000	1,080	690	1,000

The term 'Other Types' refers to all the other types of aggregate, such as granite, basalt, limestone, and sea gravel. Based on the experimental results presented by Hertz (2005), Khoury et al. (2002), and Persson (2003), Hertz (2005) found that, for all the specimen mixed with these types of aggregate, the reduction in compressive strength during and after the event of fire and the standard deviation of this reduction are nearly the same. Therefore, they were all gathered in one group having the same curve.

3.5.1.1.2 Strain Corresponding to Peak Compressive Stress

The value of the strain corresponding to the peak compressive stress is crucial for the composition of a constitutive model that represents the behaviour of concrete under compression under elevated temperatures. As previously discussed in Section 3.3.3.1, there are many components that compose the total strain of concrete under elevated temperatures, all of which also contribute to the total value of strain corresponding to peak compressive stress. It is widely established that the value of the strain corresponding to peak compressive stress increases as temperature increases, especially for temperatures above 200ºC. This was reported by many researchers, such as Furumura (1966), Purkiss and Dougill (1973), Schneider (1976), Anderberg and Thelandersson (1976), and many others.

There are two approaches in determining the value of the total strain corresponding to the peak compressive stress. The first one is the explicit approach, where the formulae and procedures presented in Section 3.3.3.1.1 are utilized to determine the values of transient strain and creep strain components which are, in turn, added to the strain corresponding to the peak compressive stress. The second approach is the implicit one, where the formulae presented in this section are utilized to determine the total value of the strain corresponding to the peak compressive stress; then, to account for its irrevocability, the transient strain component is calculated using the formulae presented in Section 3.3.3.1.1 and then separated. Both approaches lead to similar results, but the second approach is more practical because it allows for the use of a wider choice of constitutive models of concrete, specifically developed for modelling concrete subjected to elevated temperatures.

Bažant and Chern (1987) plotted the experimental results provided by Furumura (1970), Purkiss and Dougill (1973), Anderberg and Thelandersson (1976), and Schneider (1982) for the total strain corresponding to the peak compressive stress and used the bilinear curve presented in Equation (3.103) to reach the best fit.

$$\varepsilon'_{c_T} = \begin{cases} 6.4 \times 10^{-6}\mathrm{T} + 2.16 \times 10^{-3} & \text{for } \mathrm{T} \leq 600℃ \\ 0.015 \times 10^{-3}\mathrm{T} - 3.00 \times 10^{-3} & \text{for } 600℃ \leq \mathrm{T} \leq 800℃ \end{cases} \quad (3.103)$$

where ε'_{c_T} is the total strain corresponding to the peak compressive stress at a temperature T (ºC), excluding thermal expansion strain, ε_{th}.

Li and Purkiss (2005) compared the values of the strain corresponding to the peak compressive stress (the total strain excluding the free thermal strain) based on the models of transient and creep strain components presented by Anderberg and Thelanderson model (1976) and Schneider model (1986), and based on the total strain values presented by the current version of the Eurocode (EN 1992-1-2:2004, 2005) at increments of 100ºC. From this comparison, they developed an empirical formula for the strain corresponding to the maximum stress. The formula is based on the Anderberg and Thelanderson model (1976) for temperatures up to 350ºC, and on the average of the three aforementioned models for temperatures beyond that. The formula is presented in Equation (3.104).

$$\varepsilon'_{c_T} - \varepsilon_{th} = 2\frac{f'_c}{E_{c_i}} + 0.21 \times 10^{-4}(\mathrm{T} - 20) - 0.9 \times 10^{-8}(\mathrm{T} - 20)^2 \quad (3.104)$$

where E_{c_i} is the initial modulus of elasticity at normal temperatures (20ºC).

3.5.1.1.3 Initial Modulus of Elasticity

Saemann and Washa (1957) were possibly the first researchers to consider the effect of fire on the initial modulus of elasticity of concrete among many other properties of concrete that were not tackled before. They, as well as all other subsequent researchers, have reported a decline in the modulus of elasticity of concrete with a rise of temperature.

For the sake of computational accuracy and stability, the initial modulus of elasticity of concrete under elevated temperatures should be evaluated based on the stress-strain curve used. However, many researchers and codes of practice have attempted to provide separate formulae to model the decline of the modulus of elasticity of concrete at elevated temperatures, such as Schneider (1986) who presented Equation (3.9) and the bilinear curve fit that Bažant and Chern (1987) presented based on the experimental results of Furumura (1970), Purkiss and Dougill (1973), Anderberg and Thelandersson (1976), and Schneider (1982). The expressions describing the curve fit are presented in Equation (3.105).

$$\frac{E_{c_i T}}{E_{c_i}} = \begin{cases} -1.256 \times 10^{-3} T + 1.00 & \text{for } T \leq 650℃ \\ -0.565 \times 10^{-3} (T - 650) + 0.1837 & \text{for } 650℃ \leq T \leq 800℃ \end{cases} \quad (3.105)$$

where $E_{c_i T}$ is the initial modulus of elasticity at a temperature T (°C).

Based on experimental results from tests carried out in China, Lu (1989) presented the following expressions, where he employed the commonly used approach of assuming the initial modulus of elasticity to be equal to the secant modulus at $0.4 f'_{c_T}$:

$$\frac{E_{c_i T}}{E_{c_i}} = \begin{cases} -1.50 \times 10^{-3} T + 1.00 & \text{for } T \leq 300℃ \\ -0.84 \times 10^{-3} T + 0.87 & \text{for } 300℃ < T \leq 700℃ \\ 0.28 & \text{for } T > 700℃ \end{cases} \quad (3.106)$$

Li and Guo (1993), also from China, presented the following expression:

$$\frac{E_{c_i T}}{E_{c_i}} = \begin{cases} 1.0 & \text{for } T \leq 60℃ \\ -0.84 \times 10^{-3} T + 0.83 & \text{for } 60℃ \leq T \leq 700℃ \end{cases} \quad (3.107)$$

Also, Li and Purkiss (2005) employed the experimental data published by Purkiss (1996) and the current version of the Eurocode (EN 1992-1-2:2004, 2005) to develop the following formula:

$$\frac{E_{c_i T}}{E_{c_i}} = \begin{cases} 1.0 & \text{for } T \leq 60℃ \\ \dfrac{800 - T}{740} & \text{for } 60℃ \leq T \leq 800℃ \end{cases} \quad (3.108)$$

3.5.1.1.4 Compressive Stress-Strain Constitutive Models

In this section, the stress-strain curves that were developed by researchers and building codes of practice specifically to model the behaviour of concrete under elevated temperatures, following the second approach previously discussed in Section 3.5.1.1, will be presented.

In 1985, Lie and Lin (1985) used the results obtained from testing twelve column specimens under fire, along with the results obtained from the tests run by Schneider and Haksever (1976), to develop a model that simulates the behaviour of normal-strength concrete under fire. The model is presented in Equation (3.109), Equation (3.110), and Equation (3.111). In order to account for the transient creep strain (discussed in Section 3.3.3.1.1), Lie and Lin (1985) utilized the work done by Schneider and Haksever (1976) to modify the stress-strain curve by shifting it to higher strains as the temperature goes higher. Lie also adopted this model in the ASCE Manual of Practice (Structural Fire Protection by T. T. Lie, 1992).

$$f_{c_T} = \begin{cases} f'_{c_T}\left[1 - \left(\dfrac{\varepsilon'_{c_T} - \varepsilon_{c_T}}{\varepsilon'_{c_T}}\right)^2\right] & \text{for } \varepsilon_{c_T} \le \varepsilon'_{c_T} \\ f'_{c_T}\left[1 - \left(\dfrac{\varepsilon_{c_T} - \varepsilon'_{c_T}}{3\varepsilon'_{c_T}}\right)^2\right] & \text{for } \varepsilon_{c_T} > \varepsilon'_{c_T} \end{cases} \tag{3.109}$$

where $$\frac{f'_{c_T}}{f'_c} = \begin{cases} 1.0 & \text{for } T \le 450℃ \\ 2.011 - 2.353\dfrac{T - 20}{1000} & \text{for } 450℃ < T \le 874℃ \\ 0.0 & \text{for } T > 874℃ \end{cases} \tag{3.110}$$

$$\varepsilon'_{c_T} = 0.0025 + (6.0T + 0.04T^2) \times 10^{-6} \tag{3.111}$$

where f_{c_T} is the stress corresponding to a strain ε_{c_T} at a temperature T (ºC).

Lie and Kodur (1996) modified this formula for modelling steel fibre-reinforced concrete, keeping the same curve but changing the parameters, so that:

$$\frac{f'_{c_T}}{f'_c} = \begin{cases} 1.0 - 0.769 \times 10^{-3}(T - 20) & \text{for } T \leq 150℃ \\ 1.1 & \text{for } 150℃ < T \leq 400℃ \\ 2.011 - 2.353\dfrac{T - 20}{1000} & \text{for } T > 400℃ \end{cases} \quad (3.112)$$

and $$\varepsilon'_{c_T} = 0.003 + (7.0T + 0.05T^2) \times 10^{-6} \quad (3.113)$$

With high-strength concrete becoming more popular with time, and with the awareness of its different response to elevated temperatures, the need to develop new constitutive models for high-strength concrete under elevated temperatures evolved. Therefore, based on experimental results, Cheng et al. (2004) developed a model for high-strength concrete by modifying the model presented by Lie and Lin (1985), which was presented by Kodur et al. (2004) as:

$$f_{c_T} = \begin{cases} f'_{c_T}\left[1 - \left(\dfrac{\varepsilon'_{c_T} - \varepsilon_{c_T}}{\varepsilon'_{c_T}}\right)^H\right] & \text{for } \varepsilon_{c_T} \leq \varepsilon'_{c_T} \\ f'_{c_T}\left[1 - \left(\dfrac{30\left(\varepsilon_{c_T} - \varepsilon'_{c_T}\right)}{(130 - f'_c)\varepsilon'_{c_T}}\right)^2\right] & \text{for } \varepsilon_{c_T} > \varepsilon'_{c_T} \end{cases} \quad (3.114)$$

where $$\frac{f'_{c_T}}{f'_c} = \begin{cases} 1.0625 - 3.125 \times 10^{-3}(T - 20) & \text{for } T < 100℃ \\ 0.75 & \text{for } 100℃ \leq T < 400℃ \\ 1.33 - 1.45 \times 10^{-3}T & \text{for } 400℃ \leq T < 917℃ \\ 0.00 & \text{for } T \geq 917℃ \end{cases} \quad (3.115)$$

$$\varepsilon'_{c_T} = 0.0018 + (6.7f'_c + 6.0T + 0.03T^2) \times 10^{-6} \quad (3.116)$$

and $$H = 2.28 - 0.012f'_c \quad (3.117)$$

It should be noted that the term ‘0.0018’ in Equation (3.116) is given as ‘0.018’ in the publication, but it appears to be a typographical mistake.

Terro (1998) presented the relation presented in Equation (3.118) for the stress-strain curve of concrete under elevated temperatures, in addition to the formulae he presented

for the strain components associated with elevated temperatures, discussed in Section 3.3.3.1.1.

$$f_{c_T} = \frac{E_{c_{i_T}} \varepsilon_{c_T}}{1 + \left(\varepsilon_{c_T} / \varepsilon'_{c_T}\right)^2} \tag{3.118}$$

He also suggested that $E_{c_{i_T}}$ should be calculated as twice the secant modulus at the peak compressive stress, i.e. $2f'_{c_T}/\varepsilon'_{c_T}$. For the value of the peak compressive stress and the corresponding strain, Terro considered that concrete loaded to relatively low compressive stresses (up to 20% of its compressive strength at normal temperatures) shows less compressive strength deterioration at elevated temperatures of up to 600ºC for concrete mixed with basalt and limestone aggregate and 650ºC for all other types of aggregate (Abrams, 1971; Schneider, 1976; Khoury et al., 1985a; 1985b).

Due to the lack of experimental results to reach reliable conclusions, Terro assumed that for pre-loaded concrete with stress levels higher than 20% of the compressive strength at normal temperatures, there will be no further enhancement in the ability of concrete to hinder the deterioration in compressive strength. While this is most likely not correct, it is a more conservative assumption, lest compressive strengths higher than the actual ones should be predicted for concrete with higher pre-loading stress levels. One other agreed upon fact is that with high pre-loading stress levels, the deterioration of concrete with the rise in temperature becomes more pronounced, due to the pre-existence of microcracks in the highly-stressed concrete, which would expedite the deterioration under elevated temperatures.

Therefore, for the peak compressive stress (compressive strength) at different stress levels, Terro proposed a simple linear interpolation scheme. He suggested using the experimental results of the compressive strength at pre-defined elevated temperatures at no pre-loading stress ($f_{c_T}/f'_c = 0$) and the compressive strength at the same temperatures at a pre-loading stress of 20% of the compressive strength of concrete at normal temperatures (i.e., $f_{c_T}/f'_c = 0.2$). Then, for stress levels between 0 and 20% of the compressive strength of concrete at normal temperatures (i.e., $0 < f_{c_T}/f'_c < 0.2$), linear

interpolation should be done between these two values, where a maximum stress level of 20% is assumed.

Based on the results provided by Schneider (1982), Terro presented expressions for the value of the strain corresponding to the peak compressive stress at no pre-loading stress ($f_{c_T}/f'_c = 0$), denoted $\varepsilon'_{c_o}(T)$, and shown in Equation (3.119), and at a pre-loading stress of 10% of compressive strength at normal temperatures ($f_{c_T}/f'_c = 0.1$), denoted $\varepsilon'_{c_1}(T)$, and shown in Equation (3.120). For a pre-loading stress of 20% of compressive strength at normal temperatures ($f_{c_T}/f'_c = 0.2$) and above, he assumed a constant value for the strain corresponding to the peak compressive stress of 0.002 irrespective of the temperature, denoted $\varepsilon'_{c_2}(T)$. Terro assumed a second order interpolation scheme, as a function in f_{c_T}/f'_c, for all its values ranging from 0 to 0.1 and from 0.1 to 0.2. The expression used is given in Equation (3.121). All temperatures, T, in the following expressions are in ^oC.

For $f_{c_T}/f'_c = 0$ $$\varepsilon'_{c_o}(T) = C_0 + C_1 T + C_2 T^2 + C_3 T^3 \quad (3.119)$$

with $C_0 = 2.05 \times 10^{-3}$, $C_1 = 3.08 \times 10^{-6}$, $C_2 = 6.17 \times 10^{-9}$, and $C_3 = 6.58 \times 10^{-12}$.

For $f_{c_T}/f'_c = 0.1$: $$\varepsilon'_{c_1}(T) = D_0 + D_1 T + D_2 T^2 + D_3 T^3 \quad (3.120)$$

with $D_0 = 2.03 \times 10^{-3}$, $D_1 = 1.27 \times 10^{-6}$, $D_2 = 2.17 \times 10^{-9}$, and $D_3 = 1.64 \times 10^{-12}$.

For $0 < f_{c_T}/f'_c < 0.2$: $$\varepsilon'_{c_T}\left(T, f_{c_T}/f'_c\right) = N_0 \varepsilon'_{c_o} + N_1 \varepsilon'_{c_1} + N_2 \varepsilon'_{c_2} \quad (3.121)$$

with $$N_0 = 2L_i\left(L_i - \frac{1}{2}\right),\ N_1 = 4L_i L_j, \text{ and } N_2 = 2L_j\left(L_j - \frac{1}{2}\right) \quad (3.122)$$

and $$L_i = 1 - 5\frac{f_{c_T}}{f'_c} \text{ and } L_j = 5\frac{f_{c_T}}{f'_c} \quad (3.123)$$

Terro also presented the following expression for the ultimate strain at crushing, ε_{crush}:

$$\varepsilon_{crush} = 4.942 \times 10^{-3} - 6.995 \times 10^{-5} f'_{c_T} + 3.993 \times 10^{-7} {f'_{c_T}}^2 \quad (3.124)$$

As the amount of research revolving around the behaviour of concrete under elevated temperatures increased, the conclusion became apparent that a single model cannot be applied to concrete mixed with all types of aggregate. Therefore, the Eurocode (EN 1992-

1-2:2004, 2005) updated the models previously suggested in its former edition (ENV 1992-1-2:1995, 1996), with a new model specifically dedicated to concrete under elevated temperatures recognizing the different behaviour of concrete mixed with different types of aggregate. The Eurocode (EN 1992-1-2:2004, 2005) proposed the following equation as the main expression for the stress-strain curve:

$$f_{c_T} = \frac{3\varepsilon_{c_T} f'_{c_T}}{\varepsilon'_{c_T}\left[2 + \left(\varepsilon_{c_T}/\varepsilon'_{c_T}\right)^3\right]} \qquad \text{for } \varepsilon_{c_T} < \varepsilon'_{c_T} \tag{3.125}$$

Equation (3.125) presents the ascending part of the stress-strain curve. For the descending part, the Eurocode (EN 1992-1-2:2004, 2005) proposed either using the same expression or a linear relation that connects the peak stress, f'_{c_T}, to the ultimate strain, ε_{cu_T}, whose values were also provided by the Eurocode (EN 1992-1-2:2004, 2005) at different temperatures.

Table 3-3 Parameters of stress-strain relation of normal-strength concrete at elevated temperature

Temperature (°C)	Siliceous Aggregates			Calcareous Aggregates			Light-Weight Aggregates		
	f'_{c_T}/f'_c	ε'_{c_T}	ε_{cu_T}	f'_{c_T}/f'_c	ε'_{c_T}	ε_{cu_T}	f'_{c_T}/f'_c	ε'_{c_T}	ε_{cu_T}
20	1.00	0.0025	0.0200	1.00	0.0025	0.0200	1.00	To be obtained from experimental tests	To be obtained from experimental tests
100	1.00	0.0040	0.0225	1.00	0.0040	0.0225	1.00		
200	0.95	0.0055	0.0250	0.97	0.0055	0.0250	1.00		
300	0.85	0.0070	0.0275	0.91	0.0070	0.0275	1.00		
400	0.75	0.0100	0.0300	0.85	0.0100	0.0300	0.88		
500	0.60	0.0150	0.0325	0.74	0.0150	0.0325	0.76		
600	0.45	0.0250	0.0350	0.60	0.0250	0.0350	0.64		
700	0.30	0.0250	0.0375	0.43	0.0250	0.0375	0.52		
800	0.15	0.0250	0.0400	0.27	0.0250	0.0400	0.40		
900	0.08	0.0250	0.0425	0.15	0.0250	0.0425	0.28		
1000	0.04	0.0250	0.045	0.06	0.0250	0.0450	0.16		
1100	0.01	0.0250	0.0475	0.02	0.0250	0.0475	0.04		
1200	0.00	–	–	0.00	–	–	0.00		

For the values of f'_{c_T}, ε'_{c_T}, and ε_{cu_T}, the Eurocode (EN 1992-1-2:2004, 2005) provided Table 3-3 that lists certain modification factors to be applied to the compressive strength at normal temperatures (20ºC), the corresponding strain, and the ultimate strain, respectively. The table also provides different factors for concrete mixed with each of siliceous, calcareous, and light-weight aggregates.

Table 3-4 Reduction factors for the compressive strength of high-strength concrete at elevated temperature

Temperature (ºC)	Class 1	Class 2	Class 3
20	1.000	1.000	1.000
50	1.000	1.000	1.000
100	0.900	0.750	0.750
200	0.900	0.750	0.700
250	0.900	0.750	0.675
300	0.850	0.750	0.650
400	0.750	0.750	0.450
500	0.600	0.600	0.300
600	0.450	0.450	0.250
700	0.300	0.300	0.200
800	0.150	0.150	0.150
900	0.080	0.113	0.080
1000	0.040	0.075	0.040
1100	0.010	0.038	0.010
1200	0.000	0.000	0.000

For high-strength concrete, Table 3-4 was presented, based on the experimental results of Diederichs et al. (1995), Clayton and Lennon (2000), and Lennon et al. (2002). The table provides reduction factors for the compressive strength of high-strength concrete, which has been subcategorized into three classes, namely:

1. Class 1 for concrete C55/67 and C60/75
2. Class 2 for concrete C70/85 and C80/95
3. Class 3 for concrete C90/105

where the strength notation Ca/b refers to a concrete grade of characteristic cylinder strength of ‘a’ MPa and characteristic cube strength of ‘b’ MPa.

Moftah (2008) suggested using the stress-strain curve proposed by Park et al. (1982), or that proposed by Mander et al. (1988) after replacing the peak compressive stress and the corresponding strain under normal temperatures with their corresponding values under elevated temperatures, calculated using the formula presented by Hertz (2005) in Equation (3.102) for the peak compressive stress and the formulae presented by Terro (1998) in Equation (3.119), Equation (3.120), and Equation (3.121) for the corresponding strain.

Aslani and Bastami (2011) modified the stress-strain relation developed by Carreira and Chu (1985) for concrete under normal temperatures, in order to develop their own constitutive model for concrete under elevated temperatures under compression. The model is presented in Equation (3.126) where $E_{c_{T_s}}$ represents the secant modulus of elasticity at the peak compressive stress at a specific elevated temperature, calculated as $f'_{c_T}/\varepsilon'_{c_T}$.

$$f_{c_T} = \frac{\beta_{m_T}\left(\varepsilon_{c_T}/\varepsilon'_{c_T}\right)f'_{c_T}}{\beta_{m_T} - 1 + \left(\varepsilon_{c_T}/\varepsilon'_{c_T}\right)^{\beta_{m_T}}} \tag{3.126}$$

where
$$\beta_{m_T} = \begin{cases} \left[1.02 - 1.17\left(\frac{E_{c_{T_s}}}{E_{c_i}}\right)\right]^{-0.74} & \text{for } \varepsilon_{c_T} \le \varepsilon'_{c_T} \\ \left[1.02 - 1.17\left(\frac{E_{c_{T_s}}}{E_{c_i}}\right)\right]^{-0.74} + (a + 28b) & \text{for } \varepsilon_{c_T} > \varepsilon'_{c_T} \end{cases} \tag{3.127}$$

$$a = 2.7\left(12.4 - 1.66 \times 10^{-2} f'_{c_T}\right)^{-0.46} \tag{3.128}$$

and
$$b = 0.83e^{\left(-91.1/f'_{c_T}\right)} \tag{3.129}$$

It should be noted that the term ’91.1’ in Equation (3.129) was given as ‘911’ in the publication, but it appears to be a typographical mistake.

Aslani and Bastami (2011) also ran regression analyses on existing experimental data and developed formulae for the parameters describing the stress-strain curve of concrete under elevated temperatures. Equation (3.130) shows the formulae presented for the compressive strength of normal-strength concrete; Equation (3.131) and Equation (3.132) show the formulae for high-strength concrete mixed with siliceous aggregates; Equation (3.133) shows the formulae for high-strength concrete mixed with calcareous aggregates; and Equation (3.134) shows the formulae for high-strength concrete mixed with light-weight aggregates.

For normal-strength concrete:

$$\frac{f'_{cT}}{f'_c} = \begin{cases} 1.012 - 0.0005T \leq 1.0 & \text{for } T \leq 100℃ \\ 0.985 + 0.0002T - 2.235\times10^{-6}T^2 + 8\times10^{-10}T^3 & \text{for } 100℃ < T \leq 800℃ \\ 0.440 - 0.0004T & \text{for } 800℃ < T \leq 1000℃ \\ 0.000 & \text{for } T > 1000℃ \end{cases} \quad (3.130)$$

For high-strength concrete mixed with siliceous aggregates of compressive strength (f'_c) ranging between 55 MPa and 80 MPa:

$$\frac{f'_{cT}}{f'_c} = \begin{cases} 1.010 - 0.00068T \leq 1.0 & \text{for } T \leq 200℃ \\ 0.935 + 0.00026T - 2.13\times10^{-6}T^2 + 8\times10^{-10}T^3 & \text{for } 200℃ < T \leq 400℃ \\ 0.900 + 0.00020T - 2.13\times10^{-6}T^2 + 8\times10^{-10}T^3 & \text{for } 400℃ < T \leq 800℃ \\ 0.440 - 0.0004T & \text{for } 800℃ < T \leq 1000℃ \\ 0.000 & \text{for } T > 1000℃ \end{cases} \quad (3.131)$$

For high-strength concrete mixed with siliceous aggregates of compressive strength (f'_c) ranging between 80 MPa and 110 MPa:

$$\frac{f'_{c_T}}{f'_c} = \begin{cases} 0.800 - 0.0005T \leq 1.0 & \text{for } T \leq 500℃ \\ 0.960 - 0.0008T - 5.170\times10^{-7}T^2 + 4\times10^{-10}T^3 & \text{for } 500℃ < T \leq 800℃ \\ 0.440 - 0.0004T & \text{for } 800℃ < T \leq 1000℃ \\ 0.000 & \text{for } T > 1000℃ \end{cases} \quad (3.132)$$

For concrete mixed with calcareous aggregates:

$$\frac{f'_{c_T}}{f'_c} = \begin{cases} 1.01 - 0.0006T \leq 1.0 & \text{for } T \leq 200℃ \\ 1.0565 - 0.0017T + 5.0\times10^{-6}T^2 - 5.0\times10^{-9}T^3 & \text{for } 200℃ < T \leq 900℃ \\ 0.00 & \text{for } T > 900℃ \end{cases} \quad (3.133)$$

For concrete mixed with light-weight aggregates:

$$\frac{f'_{c_T}}{f'_c} = \begin{cases} 1.01 - 0.00037T \leq 1.0 & \text{for } T \leq 300℃ \\ 1.0491 - 0.00036T + 1.0\times10^{-6}T^2 - 2.0\times10^{-9}T^3 & \text{for } 300℃ < T \leq 900℃ \\ 0.000 & \text{for } T > 900℃ \end{cases} \quad (3.134)$$

The formula presented for the initial modulus of elasticity of concrete under elevated temperatures is shown in Equation (3.135). Although it has not been explicitly mentioned, judging by the high values of the initial modulus of elasticity of concrete under elevated temperatures calculated using Equation (3.135), it seems it was developed for preloaded concrete, rather than unloaded concrete.

$$\frac{E_{c_i T}}{E_{c_i}} = \begin{cases} 1.000 & \text{for } T \leq 100℃ \\ 1.015 - 1.54\times10^{-3}T + 2.0\times10^{-7}T^2 + 3.0\times10^{-10}T^3 & \text{for } 100℃ < T \leq 1000℃ \\ 0.000 & \text{for } T > 1000℃ \end{cases} \quad (3.135)$$

3.5.1.1.5 Post-Cooling Behaviour

The post-cooling behaviour of concrete is without doubt a more significant topic of research than the behaviour of concrete at elevated temperatures during the event of fire

itself. This is because the continuous development in fire detection and fighting technologies has managed to keep the duration of fire incidents to the minimum, except for a limited number of incidents when the automatic fire fighting systems fail or in locations with challenging accessibility, such as tunnels or high-rise buildings. After the fire is out, there come the more challenging questions of whether the structure is safe to enter and use or not, and what needs to be done with the structure: retrofitting or demolishing.

As previously explained in Section 3.3.1, the properties of concrete deteriorate even more drastically after cooling from a fire event. This observation was reported by many researchers through the years, such as Malhotra (1956), Abrams (1971), Hertz (1984), Hertz (1991; 1992), Papayianni and Valiasis (1991), Sullivan and Sharshar (1992), Morita et al. (1992), Nassif et al. (1995), Furumura et al. (1995), Felicetti et al. (1996), and Noumowé et al. (1996).

The results from these researchers show a lot of scatter compared to each other. However, a general trend can be deduced from their results; that is, that for concrete exposed to relatively low temperature rise of less than 200ºC, the compressive strength is recoverable to a high extent after cooling. This is not applicable to the modulus of elasticity which does not recover its pre-heating value. For temperatures higher than 200ºC, the residual compressive strength of concrete after cooling, f'_{c_R}, is even less than the compressive strength it attained at the elevated temperature. The reason is the continuously increasing internal stress resulting from the continuous restrained thermal dilatation that occurs during fire and carries on during the cooling phase, in addition to the volume increase associated with the rehydration of the calcium oxide in the cement matrix as explained in Section 3.3.1.

Another point of general consensus among researchers concerns the factors that affect the residual compressive strength. All researchers reported that the residual compressive strength decreases as the maximum temperature to which the concrete was exposed increases. In addition, the cooling regime plays a very important role on the residual properties of concrete. Smith (1983) focused on the effects of many factors on the residual compressive strength. He, among others, reported that the longer the duration of

exposure to fire, and the higher the maximum temperature reached during exposure, the less the residual compressive strength. He also reported that soaking concrete that has been exposed to a temperature of 300ºC for two hours in water results in a residual compressive strength that is 10% less than that of concrete that has been soaked in water for one hour only.

This extended deterioration due to rapid water cooling is commonly explained by the rise of internal stresses due to a thermal shock that concrete experiences when exposed to water while hot. Luo et al. (2000) focused on this topic, where they compared water cooling to furnace cooling for different types of concrete. They reported that, in general, the residual compressive strength of concrete cooled using water is less than that of concrete naturally cooled to room temperature in air. This difference decreases when exposure of concrete to fire reaches higher temperatures. They also reported that steel fibres reduced the deterioration of the residual concrete strength, but not polypropylene fibres, which are sometimes used to help prevent explosive spalling as explained in Section 3.3.2.1.

Peng et al. (2008) also studied the effect of the cooling regime on the residual properties of concrete, comparing natural cooling to spraying the concrete surface with water for durations ranging from 5 to 60 minutes, and to quenching in water. They confirmed that, in general, water cooling caused more deterioration in the concrete properties than natural cooling. The deterioration is more pronounced as the duration of exposure to water increases, where it was reported that the effect of a water-spraying time of 30 minutes was equivalent to complete quenching in water.

Nassif (2002) focused on the residual initial modulus of elasticity and the effect of the cooling regime on it, rather than the residual compressive strength. One conclusion he reached was that spraying concrete exposed to a temperature of 320ºC with water results in about twice the reduction in its initial modulus of elasticity compared to that caused by extending the duration of thermal exposure for two more hours.

Despite the amount of research undertaken on this topic, constitutive models that simulate the post-cooling residual behaviour of concrete are very scarce. One of them was presented by Lie et al. (1986) where the experimental results provided by Abrams

(1971) and Whinnett (1978) were used to develop the following expressions for the residual compressive strength of concrete based on the maximum temperature reached during exposure to fire, T_{max}:

$$\frac{f'_{c_R}}{f'_c} = \begin{cases} -1.00 \times 10^{-3} T_{max} + 1.000 & \text{for } T_{max} \leq 500℃ \\ -1.75 \times 10^{-3} T_{max} + 1.375 & \text{for } 500℃ < T_{max} \leq 700℃ \\ 0 & \text{for } T_{max} > 700℃ \end{cases} \quad (3.136)$$

It can be noticed that the model presented by Lie et al. (1986) assumed absolutely no residual strength for concrete which reached a maximum temperature higher than 700°C, which causes the discontinuity of the model. Therefore, in this study, a minimum value of 15% of f'_c is kept for concrete in this range to ensure the continuity of the model over all temperatures.

As previously discussed, Hertz (2005) utilized his own experimental results and the results of 400 test series comprising approximately 3000 specimens from the literature to develop one common formula, presented in Equation (3.102), for the modification factors of all the concrete and steel reinforcement properties. In this case, ξ(T) represents the ratio between the residual compressive strength after cooling to a temperature T and its respective value at 20ºC, i.e. f'_{c_R}/f'_c.

For the residual compressive strength after the event of fire, Table 3-6 presents the values of the parameters defining the S-shaped curve presented in Equation (3.102) for the different types of concrete depending on the aggregate type used in the mix.

Table 3-5 Parameters defining residual compressive strength of concrete after the event of fire for Equation (3.102**)**

Aggregate Type in Concrete Mix	k	T_1	T_2	T_8	T_{64}
Siliceous	0.00	3,500	600	480	680
Light-weight	0.00	4,000	650	830	930
Other Types	0.00	10,000	780	490	100,000

The term 'Other Types' was explained in Table 3-2.

Chang et al. (2006) tested 108 specimens mixed with siliceous aggregates heated up to temperatures ranging from 100ºC to 800ºC to provide formulae for the different parameters describing the behaviour of concrete in compression following the exposure to elevated temperatures. Two expressions were proposed for the residual compressive strength:

$$\frac{f'_{c_R}}{f'_c} = 1.008 + \frac{T_{max}}{450 \ln\left(T_{max}/5800\right)} \geq 0.0 \qquad \text{for } T_{max} \leq 800℃ \tag{3.137}$$

or

$$\frac{f'_{c_R}}{f'_c} = \begin{cases} -0.55 \times 10^{-3} T_{max} + 1.01 & \text{for } T_{max} \leq 200℃ \\ -1.25 \times 10^{-3} T_{max} + 1.15 & \text{for } 200℃ \leq T_{max} \leq 800℃ \end{cases} \tag{3.138}$$

They also proposed an expression for the increase in the strain corresponding to the peak compressive stress, ε'_{c_R}, as follows:

$$\frac{\varepsilon'_{c_R}}{\varepsilon'_c} = \begin{cases} 1.0 & \text{for } T_{max} \leq 200℃ \\ (-0.1 f'_c + 7.7)\left[\frac{e^K}{1+e^K} - 0.0219\right] + 1.0 & \text{for } 200℃ < T_{max} \leq 800℃ \end{cases} \tag{3.139}$$

where

$$K = 10.0 \times 10^{-3} T_{max} - 5.8 \tag{3.140}$$

Two different formulae were also presented for the residual initial modulus of elasticity, E_{c_R}, based on the regression analysis they ran. The formulae are presented in Equation (3.141) and Equation (3.142).

$$\frac{E_{c_R}}{E_{c_i}} = \begin{cases} -1.65 T_{max} \times 10^{-3} + 1.033 & \text{for } T_{max} \leq 125℃ \\ \dfrac{1}{1.2 + 18(1.5 \times 10^{-3} T_{max})^{4.5}} & \text{for } 125℃ \leq T_{max} \leq 800℃ \end{cases} \tag{3.141}$$

or

$$\frac{E_{c_R}}{E_{c_i}} = -1.65 \times 10^{-3} T_{max} + 1.033 \qquad \text{for } T_{max} \leq 600℃ \tag{3.142}$$

Finally, Chang et al. (2006) proposed a post-cooling constitutive model for the stress-strain curve of concrete based on the general curve introduced by Tsai (1988). The model is shown in Equation (3.143).

$$f_{c_R} = \frac{M\left(\varepsilon_{c_T}/\varepsilon'_{c_T}\right)f'_{c_R}}{1 + \left(M + \frac{n}{n-1}\right)\left(\varepsilon_{c_T}/\varepsilon'_{c_T}\right) + \left(\frac{1}{n-1}\right)\left(\varepsilon_{c_T}/\varepsilon'_{c_T}\right)^n} \tag{3.143}$$

with

$$M = \frac{E_{c_R}}{E_{c_{R_s}}} \tag{3.144}$$

$$n = n_o\left(\frac{M}{M_o}\right)^{1.014+0.7\times10^{-3}T_{max}} \tag{3.145}$$

$$n_o = \frac{f'_c}{12} + 0.77 \quad \geq 1.0 \tag{3.146}$$

$$M_o = \frac{E_{c_i}}{E_{c_s}} \tag{3.147}$$

where E_{c_s} is the secant modulus of elasticity at the peak compressive stress at normal temperatures, calculated as f'_c/ε'_c, and $E_{c_{R_s}}$ is the respective residual value after fire exposure and cooling, calculated as $f'_{c_R}/\varepsilon'_{c_R}$. Chang et al. (2006) suggested using the expression given by Mander et al. (1988) to calculate E_{c_i}, such that $E_{c_i} = 5000\sqrt{f'_c}$, where f'_c is in MPa in all the equations.

This model is supposed to represent both heated and unheated concrete, where f'_{c_R}, ε'_{c_R}, E_{c_R}, $E_{c_{R_s}}$, M, and n become f'_c, ε'_c, E_{c_i}, E_{c_s}, M_o, and n_o, respectively, for unheated concrete.

3.5.1.1.6 Models Assessment and Comparison

At this point, with the numerous models discussed for concrete under compression, a comparison is due. Since each of these models was developed based on one or more research programs, it will be assumed that each of them represents its respective research

program; hence, they will be compared to each other, rather than being compared to the experimental results. Also, this study is concerned with the structural analysis aspect of these models, more than it is concerned with the material properties aspect.

Figure 3-21 shows a comparison of models for compressive strength of concrete mixed with siliceous aggregates at elevated temperatures, according to the ones dedicated to normal-strength concrete mixed with siliceous aggregates (Li and Purkiss (2005), Hertz (2005), the Eurocode (EN 1992-1-2:2004, 2005), and Aslani and Bastami (2011)) along with the models that are available for concrete regardless of the type of aggregate (Bažant and Chern (1987), Li and Guo (1993), the Eurocode (ENV 1992-1-2:1995, 1996), and the ASCE Manual of Practice (Structural Fire Protection by T. T. Lie, 1992)).

Similarly, Figures 3-18 and 3-19 show comparisons of the compressive strength of concrete mixed with calcareous aggregates and light-weight aggregates at elevated temperatures, respectively. Both figures include the models that do not consider the aggregate type (Bažant and Chern (1987), Li and Guo (1993), the Eurocode (ENV 1992-1-2:1995, 1996), the ASCE Manual of Practice (Structural Fire Protection by T. T. Lie, 1992)) together with the models of Hertz (2005), the Eurocode (EN 1992-1-2:2004, 2005), and Aslani and Bastami (2011) for normal-strength concrete mixed with calcareous aggregates for Figure 3-22, and for normal-strength concrete mixed with light-weight aggregates for Figure 3-23.

Figure 3-24 presents the same comparison for high-strength concrete, according to Cheng et al. (2004), the Eurocode (EN 1992-1-2:2004, 2005) with its three classes depending on the compressive strength of concrete at normal temperatures, and Aslani and Bastami (2011) with its two strength ranges for high-strength concrete mixed with siliceous aggregates.

For the shape of the stress-strain curve and how different researchers assumed different constitutive models, additional comparisons are presented in Figures 3-21, 3-22, and 3-23. Here, the various models discussed previously for the compressive constitutive models for normal-strength concrete of 30 MPa strength under a temperature of 100ºC are compared for concrete mixed with siliceous aggregates, calcareous aggregates, and light-weight aggregates, respectively. For high-strength concrete, Figures 3-24, 3-25, and

3-26 show similar comparisons for the compressive constitutive models of strengths 60 MPa, 80 MPa, and 90 MPa, respectively, under a temperature of 100ºC.

The same comparison is presented for a temperature of 300ºC in Figures 3-27, 3-28, and 3-29 for normal-strength concrete, and in Figures 3-30, 3-31, and 3-32 for high-strength concrete. For a temperature of 500ºC, Figures 3-33, 3-34, and 3-35 show the stress-strain curves for normal-strength concrete, and Figures 3-36, 3-37, and 3-38 show those for high-strength concrete. Finally, for 800ºC, Figures 3-39, 3-40, and 3-41 show the stress-strain curves for normal-strength concrete, and Figures 3-42, 3-43, and 3-44 show those for high-strength concrete.

For the models that only provided formulae for the compressive strength without providing a constitutive model for the stress-strain curve, Hognestad's parabola (1951) was used along with the strain corresponding to maximum compressive stress formula provided by the ASCE Manual of Practice (Structural Fire Protection by T. T. Lie, 1992) for normal-strength concrete and that provided by Cheng et al. (2004) for high-strength concrete.

These figures show a staggering variation in the stress-strain curve shape and the compressive strength and the corresponding strain especially at higher temperatures for normal-strength concrete. While this observation has been previously discussed and justified in Section 3.5.1.1, it still imposes great difficulty on the criteria based on which a certain model would be preferred to the other.

Finally, Figure 3-49 shows a comparison of the residual compressive strength of concrete after cooling.

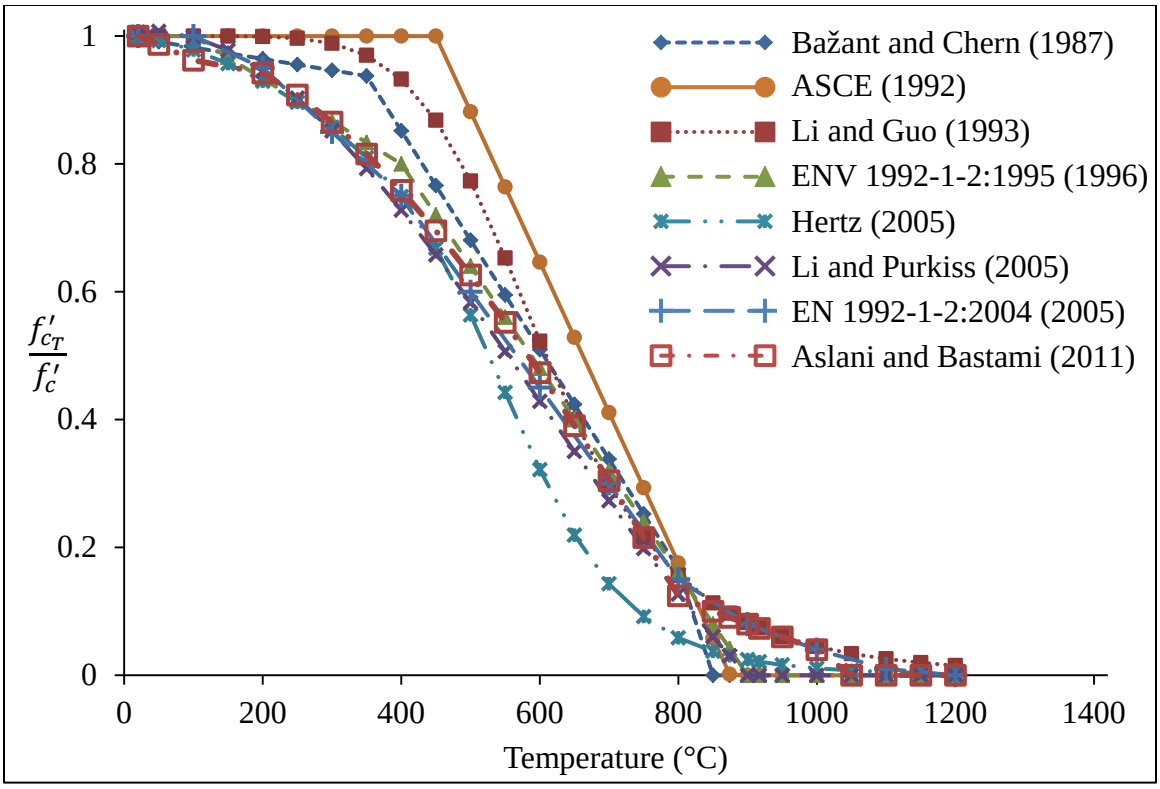

Figure 3-21 Comparison of models for compressive strength of concrete mixed with siliceous aggregates at elevated temperatures

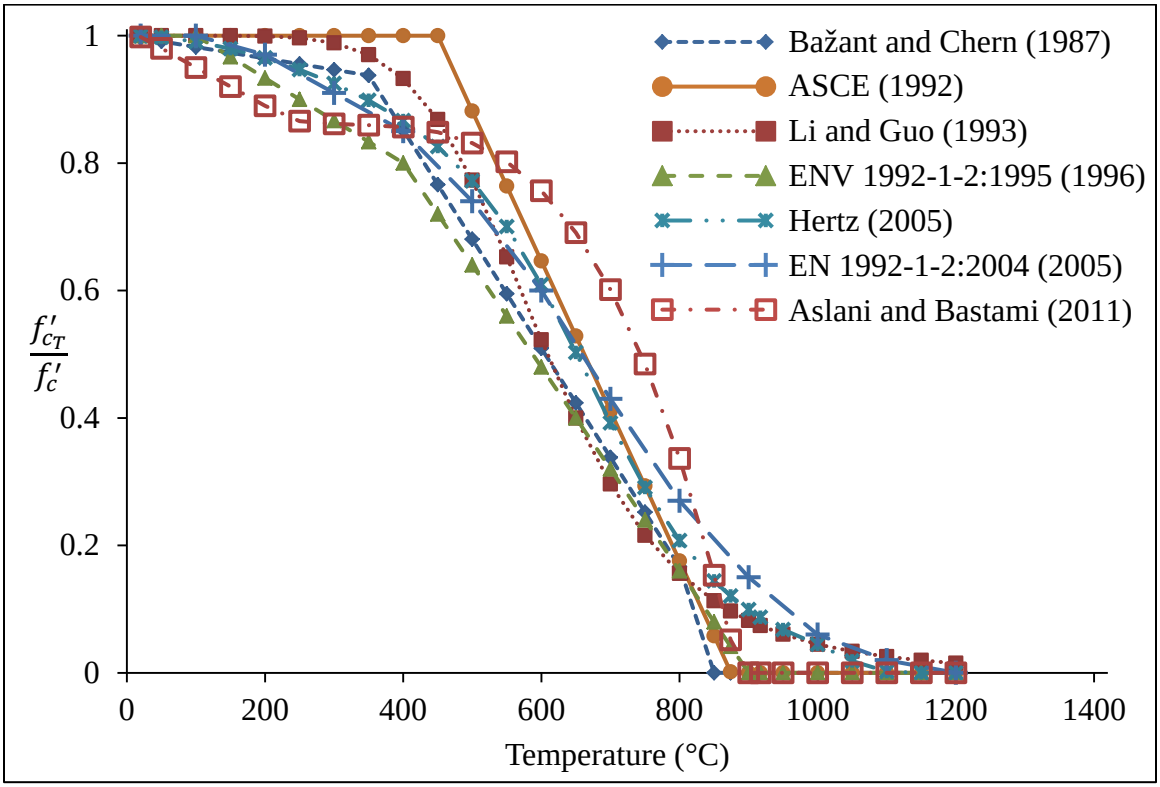

Figure 3-22 Comparison of models for compressive strength of concrete mixed with calcareous aggregates at elevated temperatures

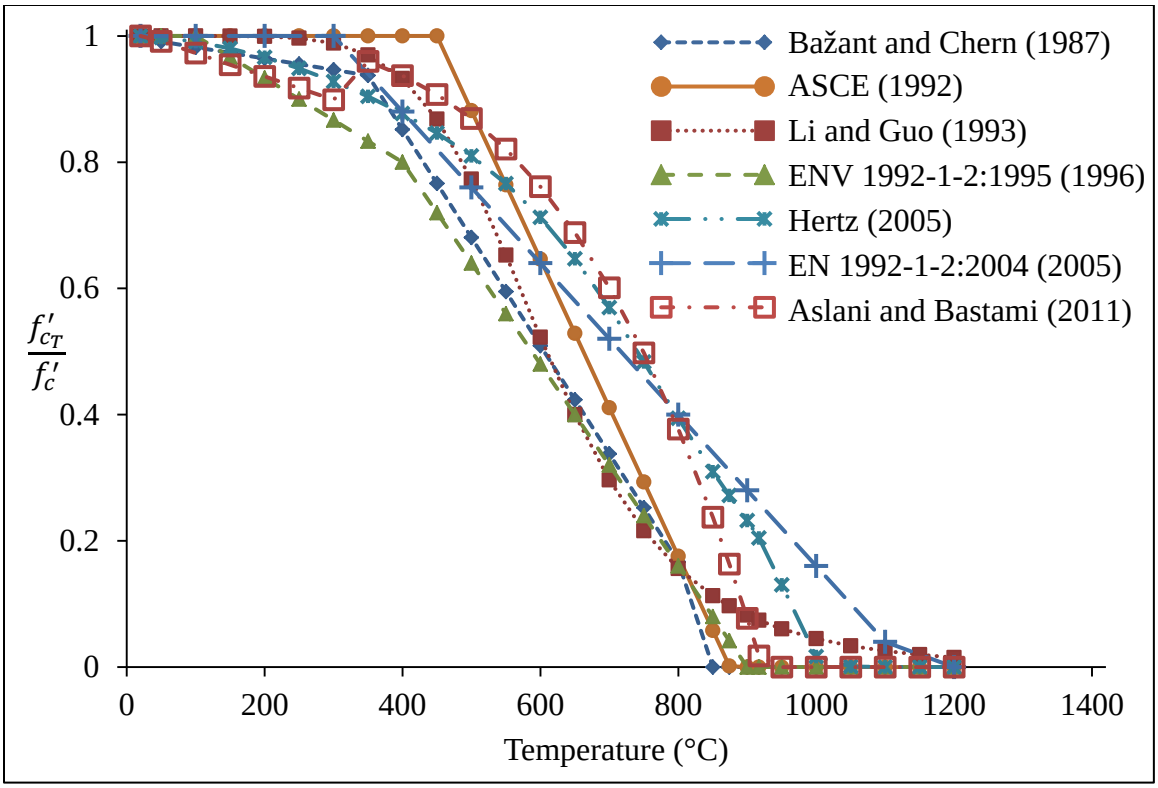

Figure 3-23 Comparison of models for compressive strength of concrete mixed with light-weight aggregates at elevated temperatures

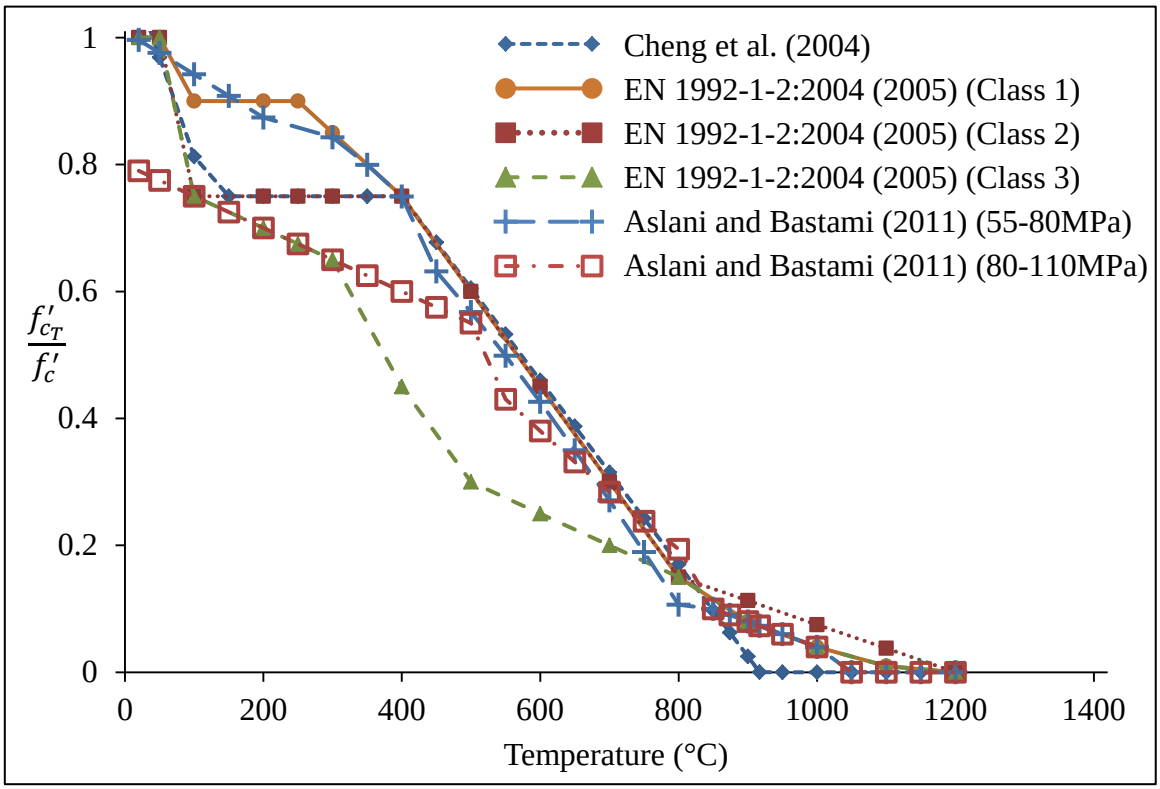

Figure 3-24 Comparison of models for compressive strength of high-strength concrete at elevated temperatures

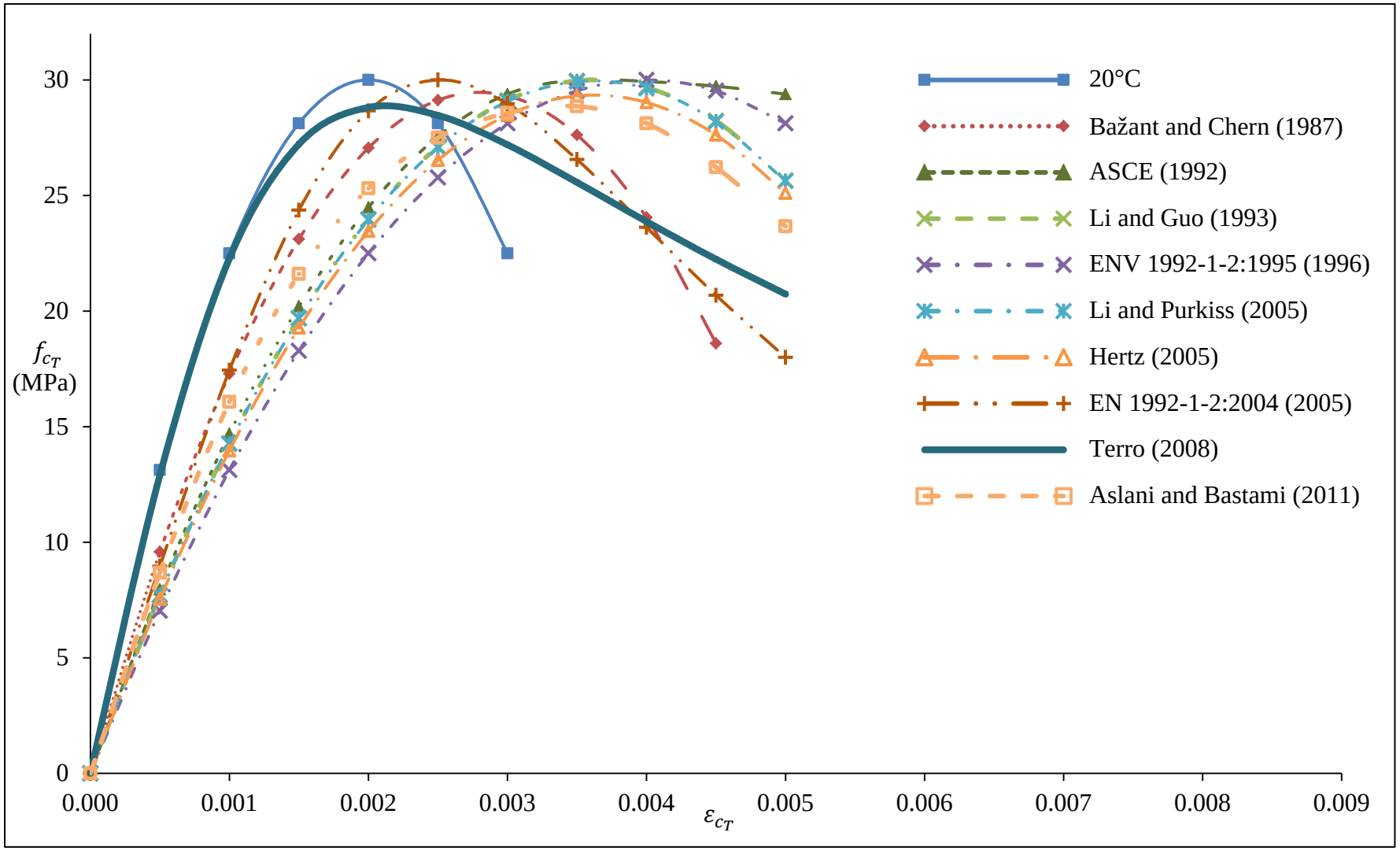

Figure 3-25 Comparison of models for stress-strain curves of normal-strength concrete of 30 MPa strength mixed with siliceous aggregates at 100°C

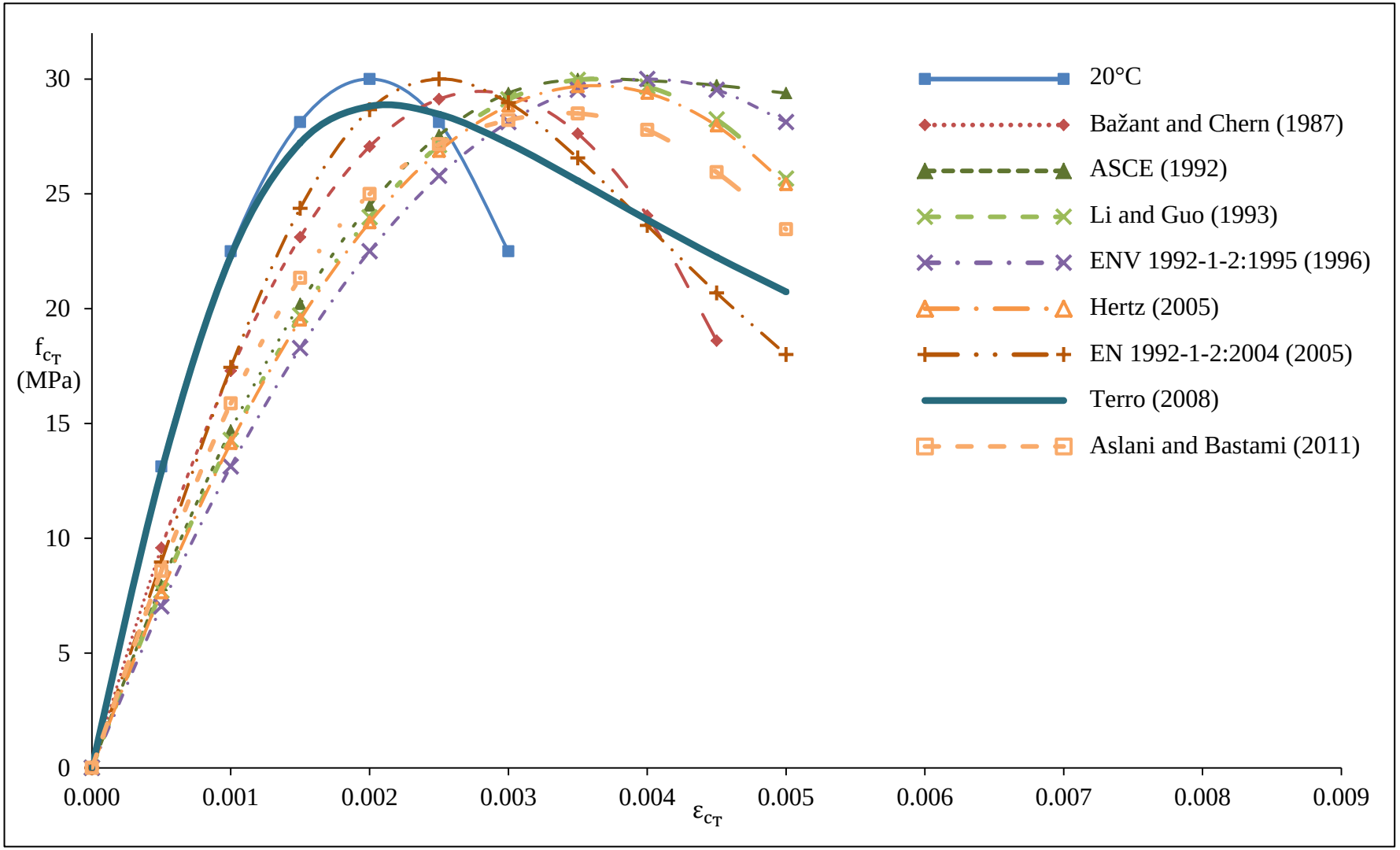

Figure 3-26 Comparison of models for stress-strain curves of normal-strength concrete of 30 MPa strength mixed with calcareous aggregates at 100°C

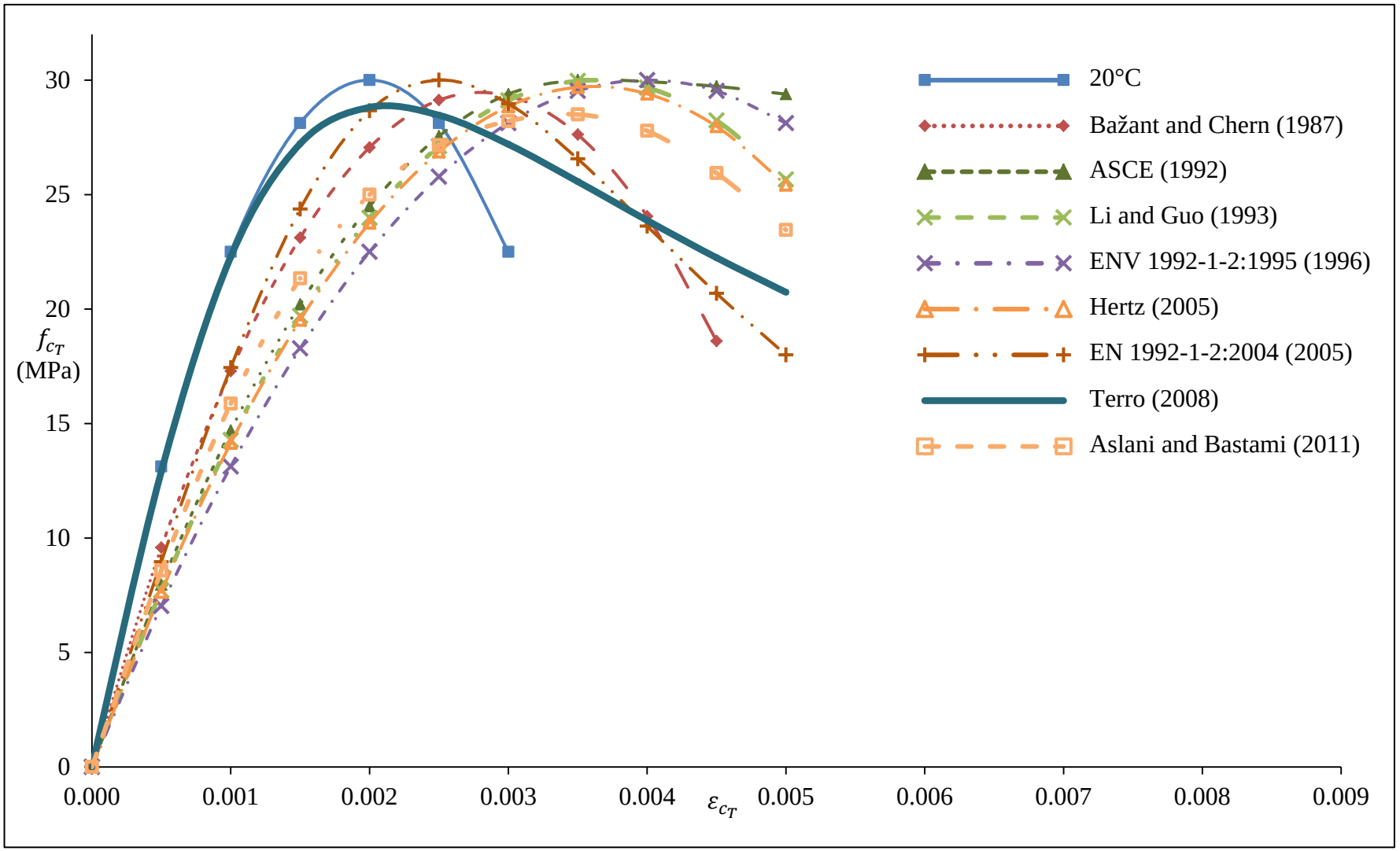

Figure 3-27 Comparison of models for stress-strain curves of normal-strength concrete of 30 MPa strength mixed with light-weight aggregates at 100°C

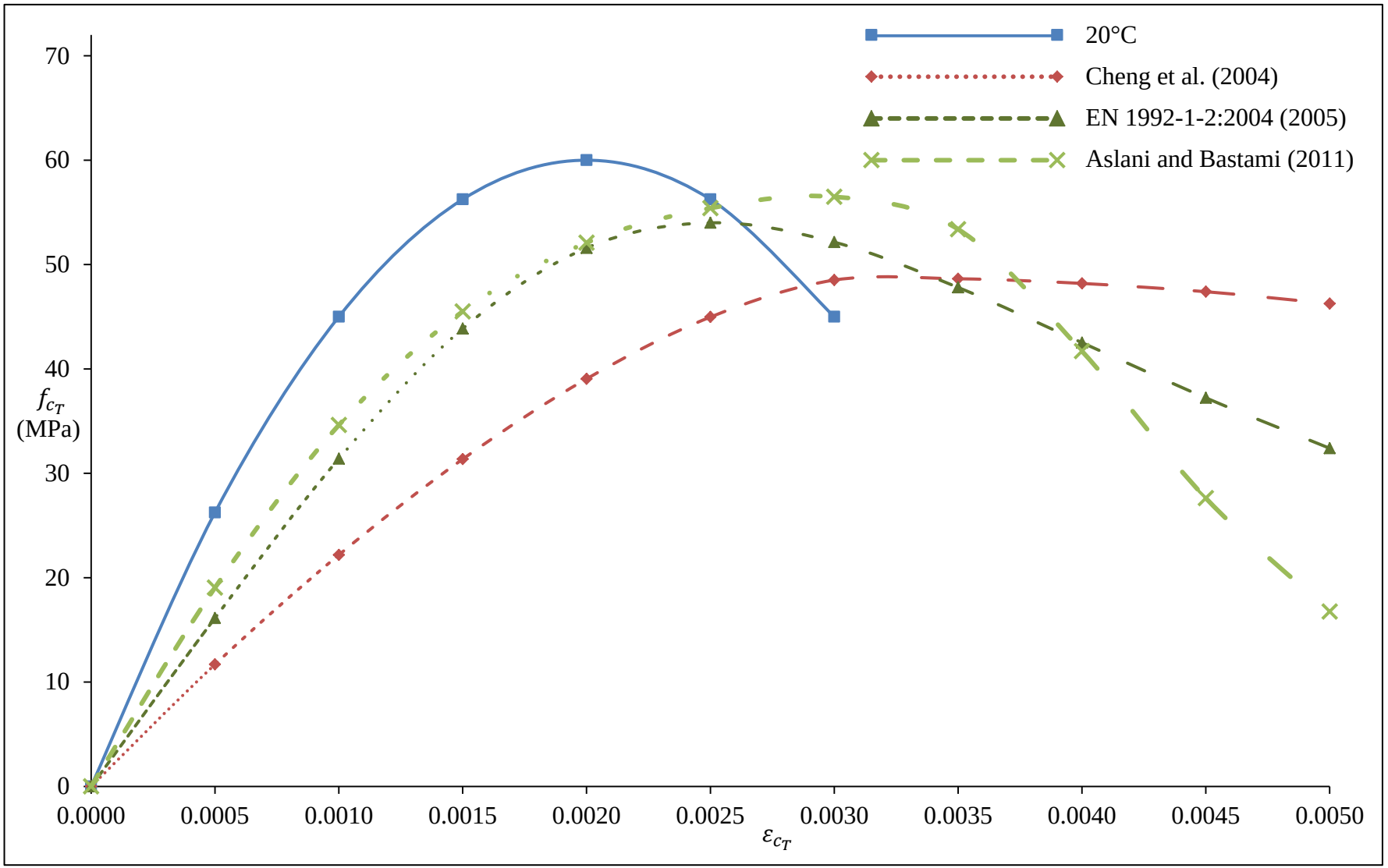

Figure 3-28 Comparison of models for stress-strain curves of high-strength concrete of 60 MPa strength at 100°C

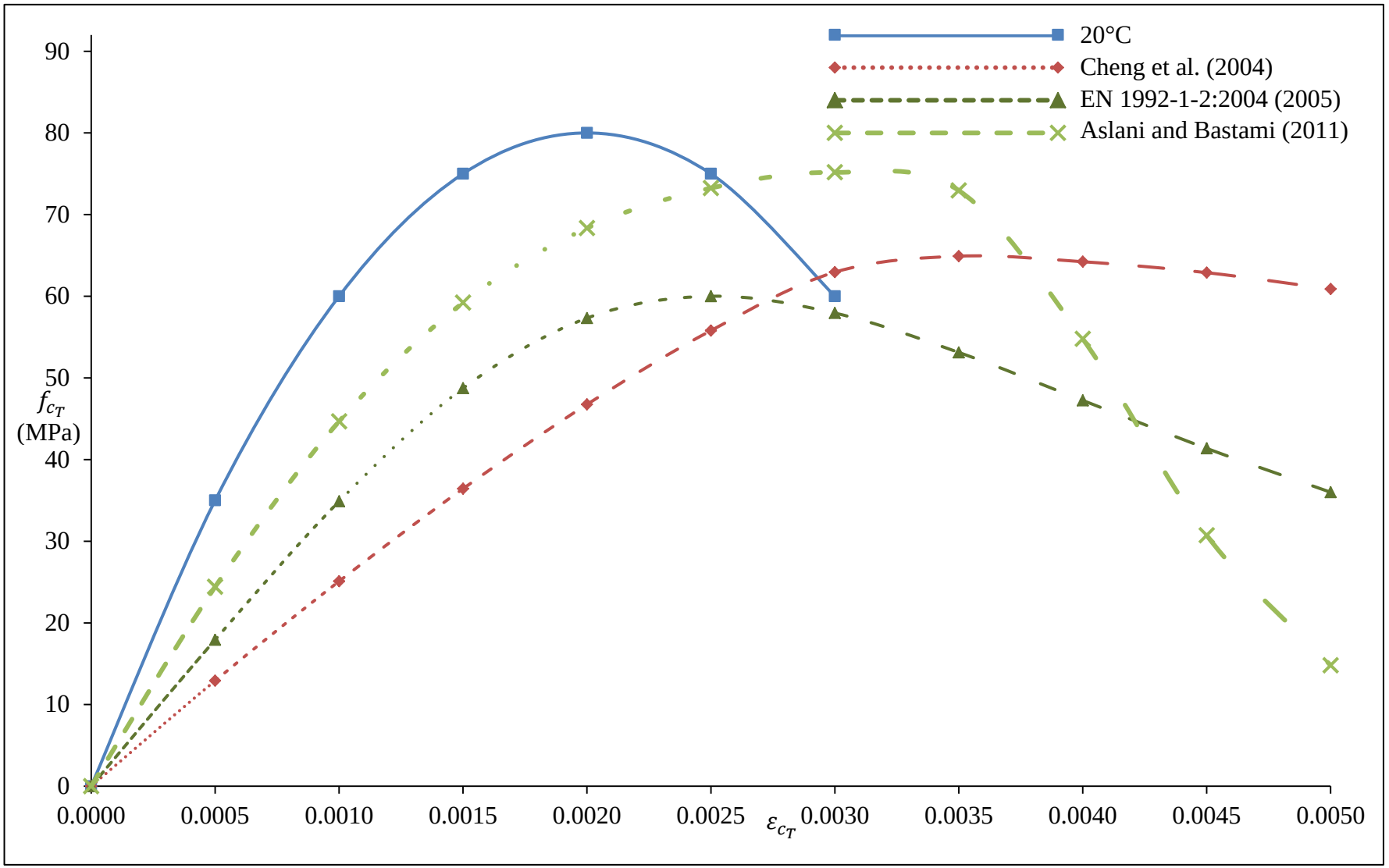

Figure 3-29 Comparison of models for stress-strain curves of high-strength concrete of 80 MPa strength at 100°C

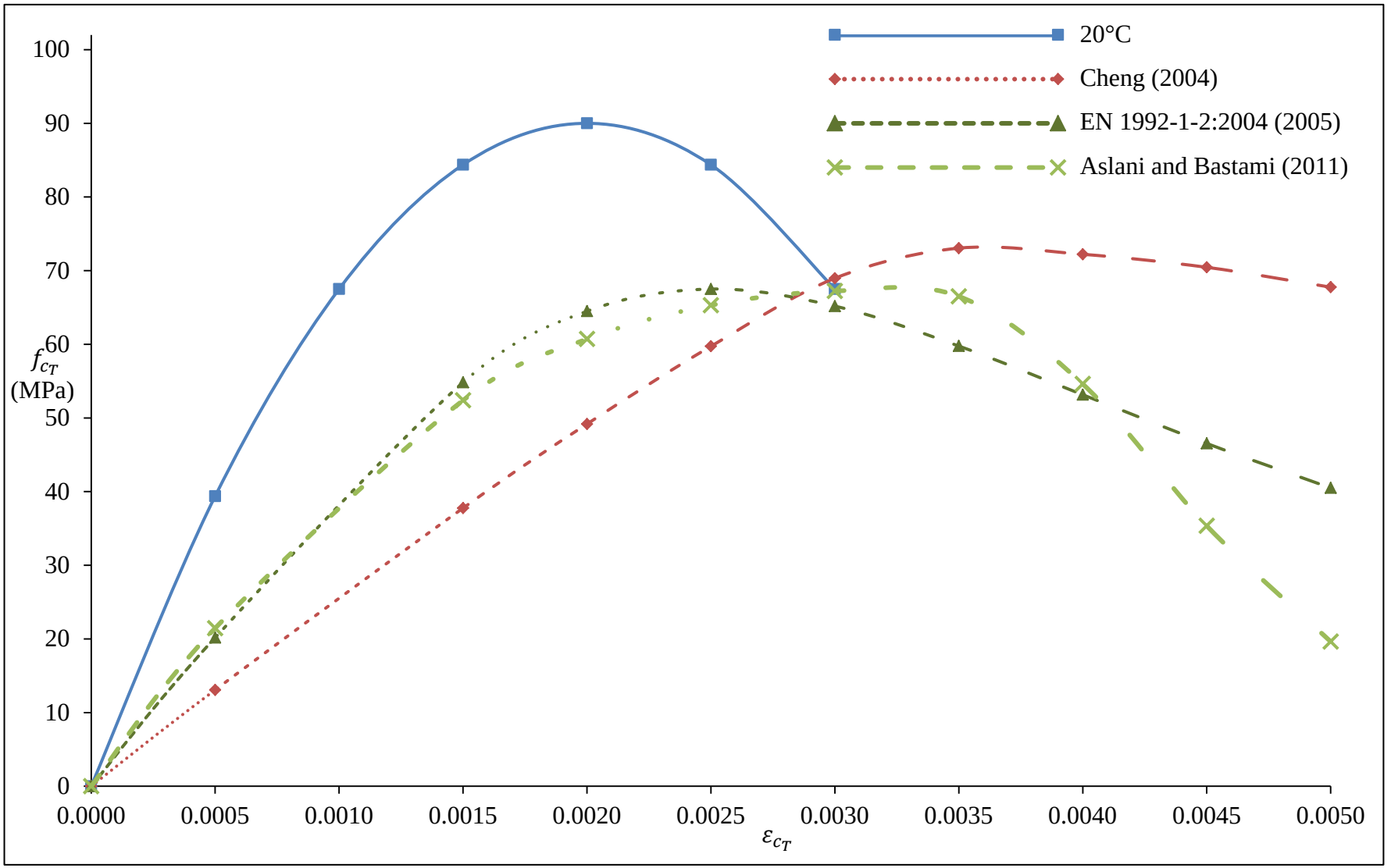

Figure 3-30 Comparison of models for stress-strain curves of high-strength concrete of 90 MPa strength at 100°C

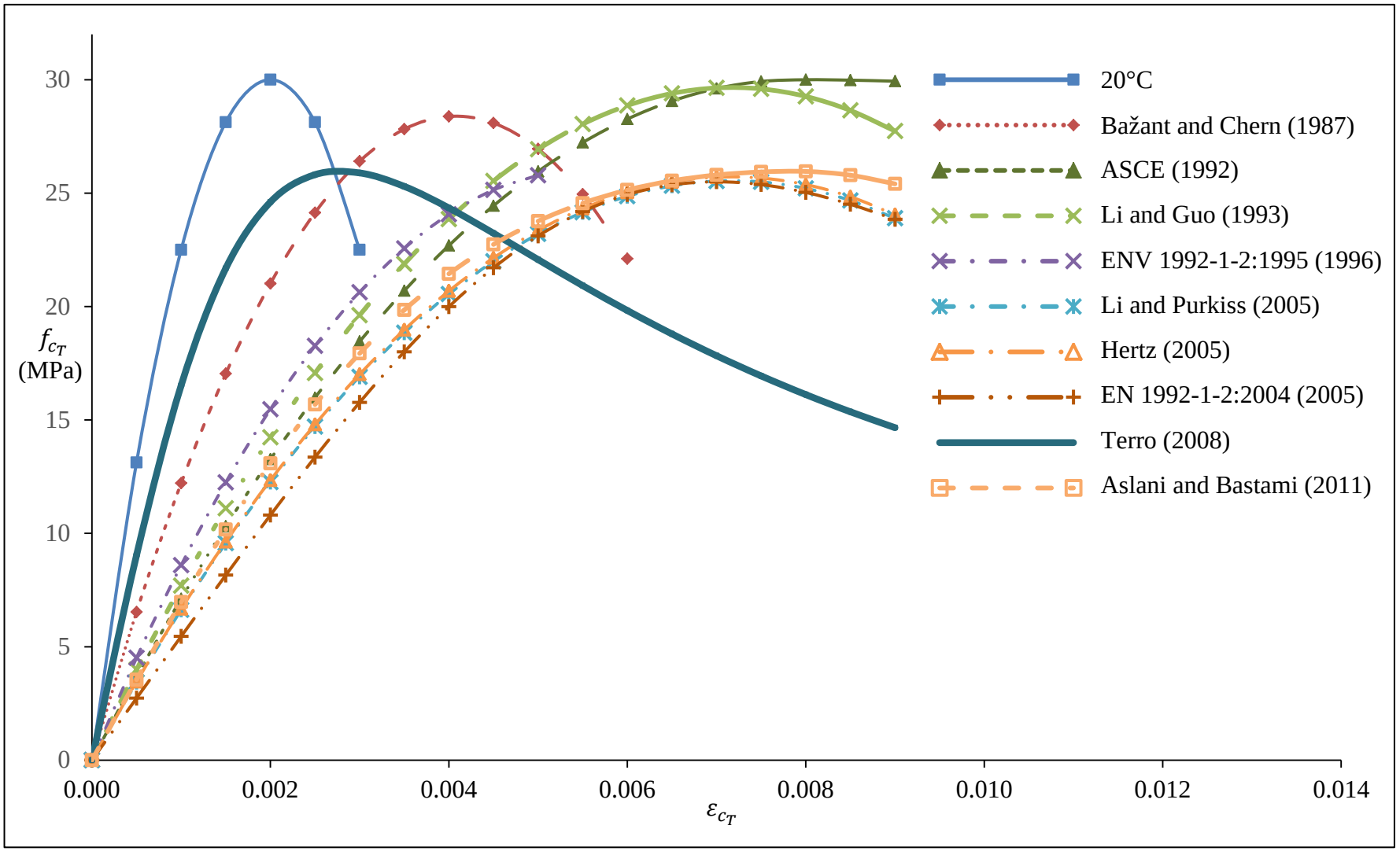

Figure 3-31 Comparison of models for stress-strain curves of normal-strength concrete of 30 MPa strength mixed with siliceous aggregates at 300°C

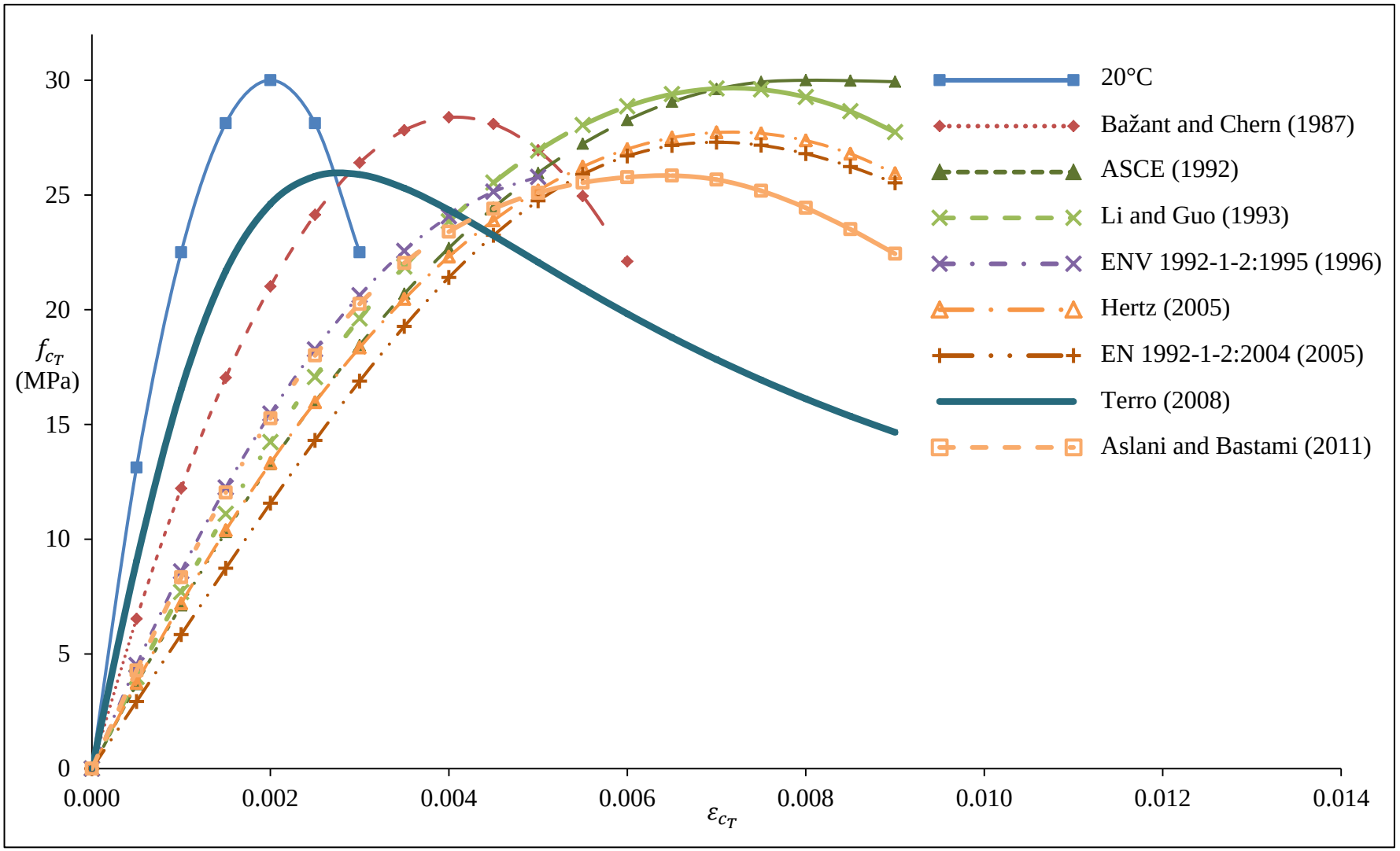

Figure 3-32 Comparison of models for stress-strain curves of normal-strength concrete of 30 MPa strength mixed with calcareous aggregates at 300°C

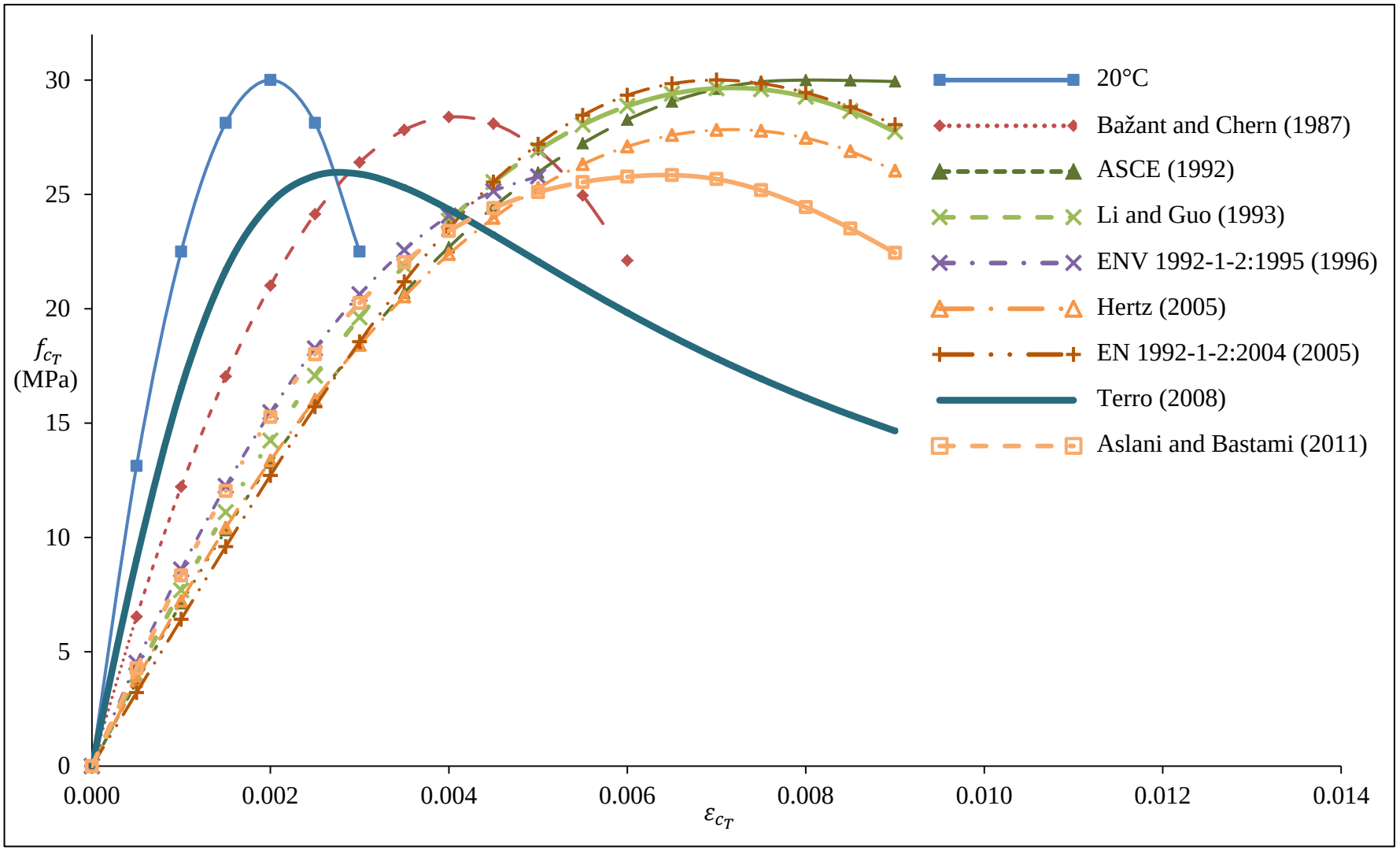

Figure 3-33 Comparison of models for stress-strain curves of normal-strength concrete of 30 MPa strength mixed with light-weight aggregates at 300°C

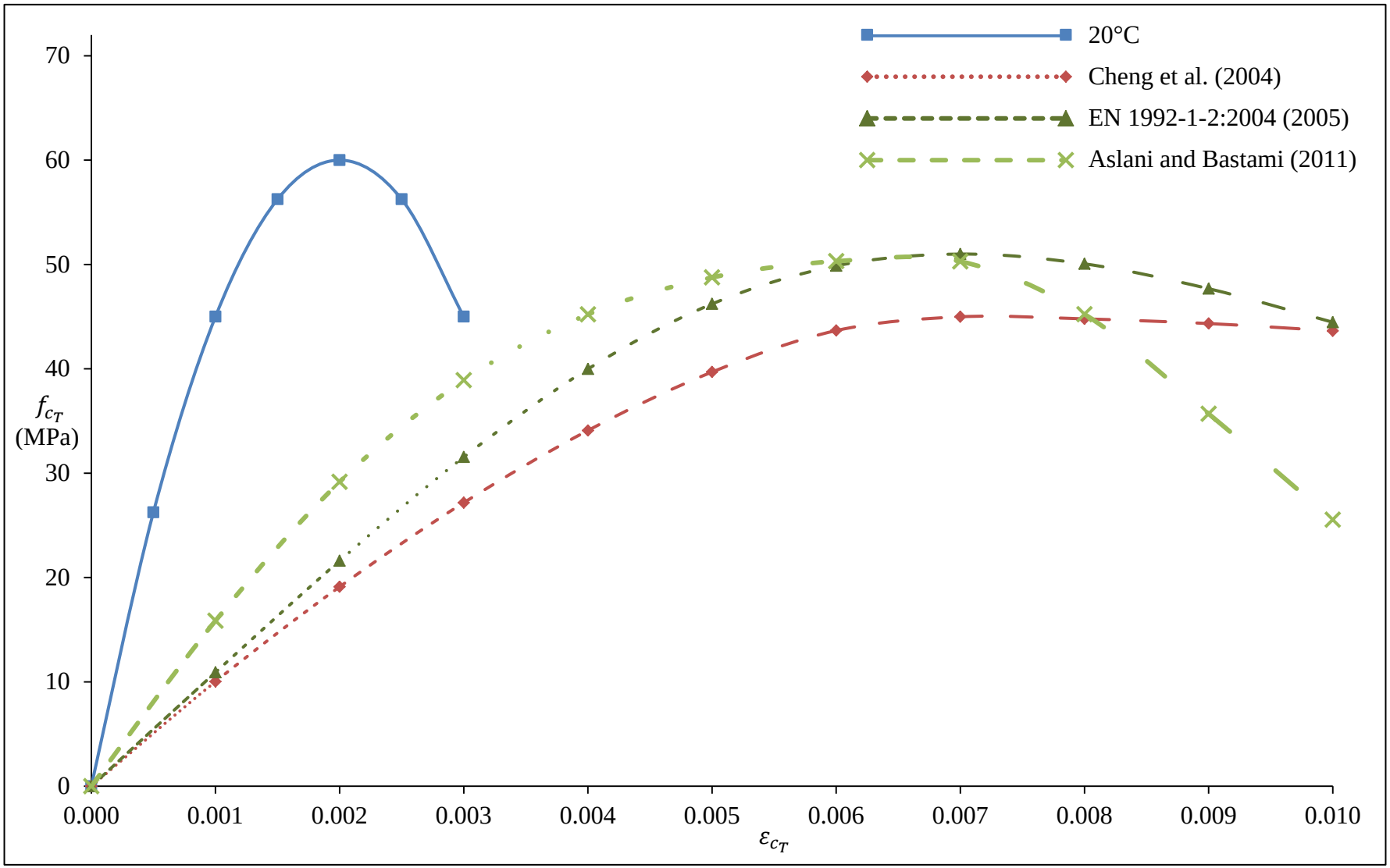

Figure 3-34 Comparison of models for stress-strain curves of high-strength concrete of 60 MPa strength at 300°C

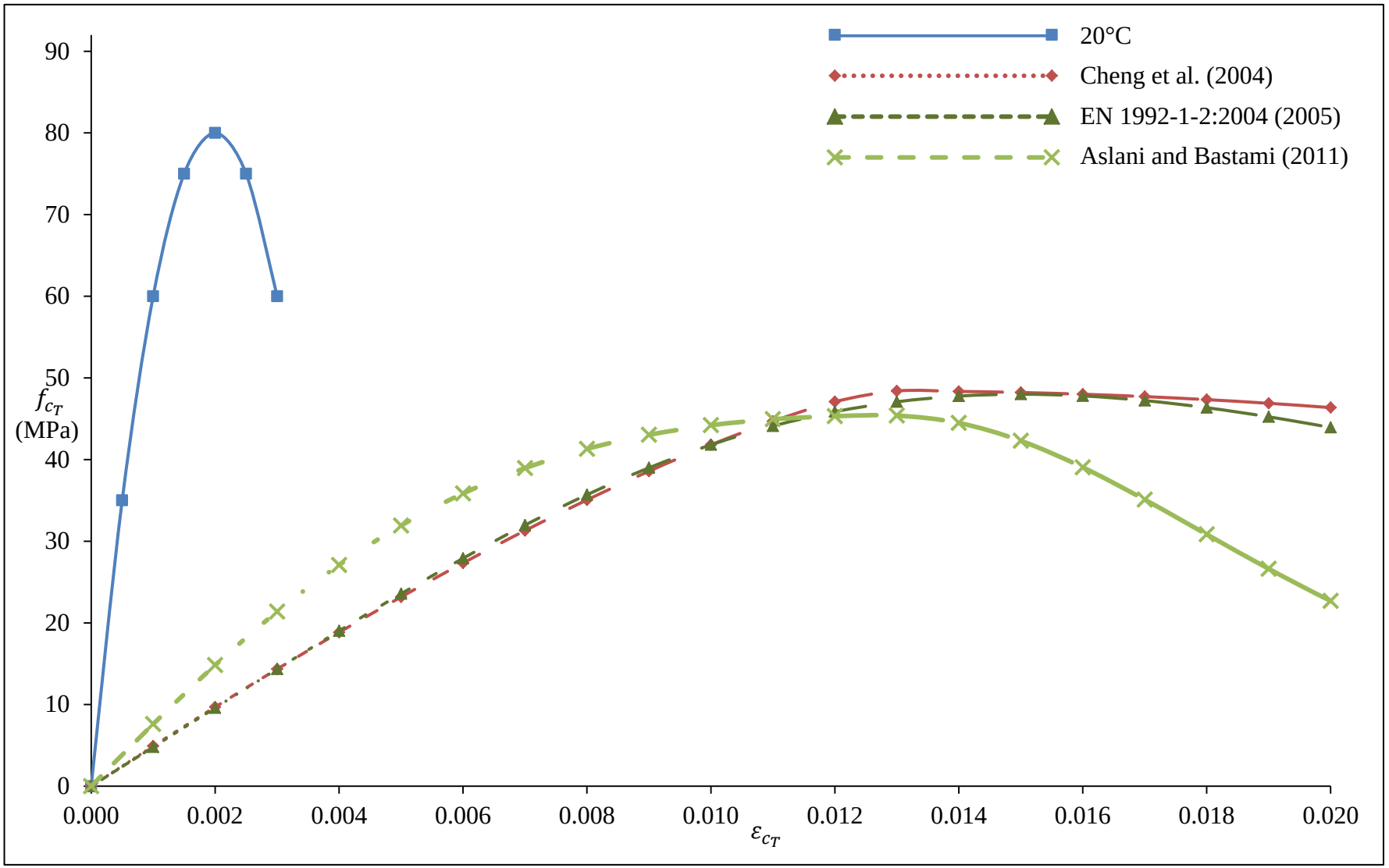

Figure 3-35 Comparison of models for stress-strain curves of high-strength concrete of 80 MPa strength at 300°C

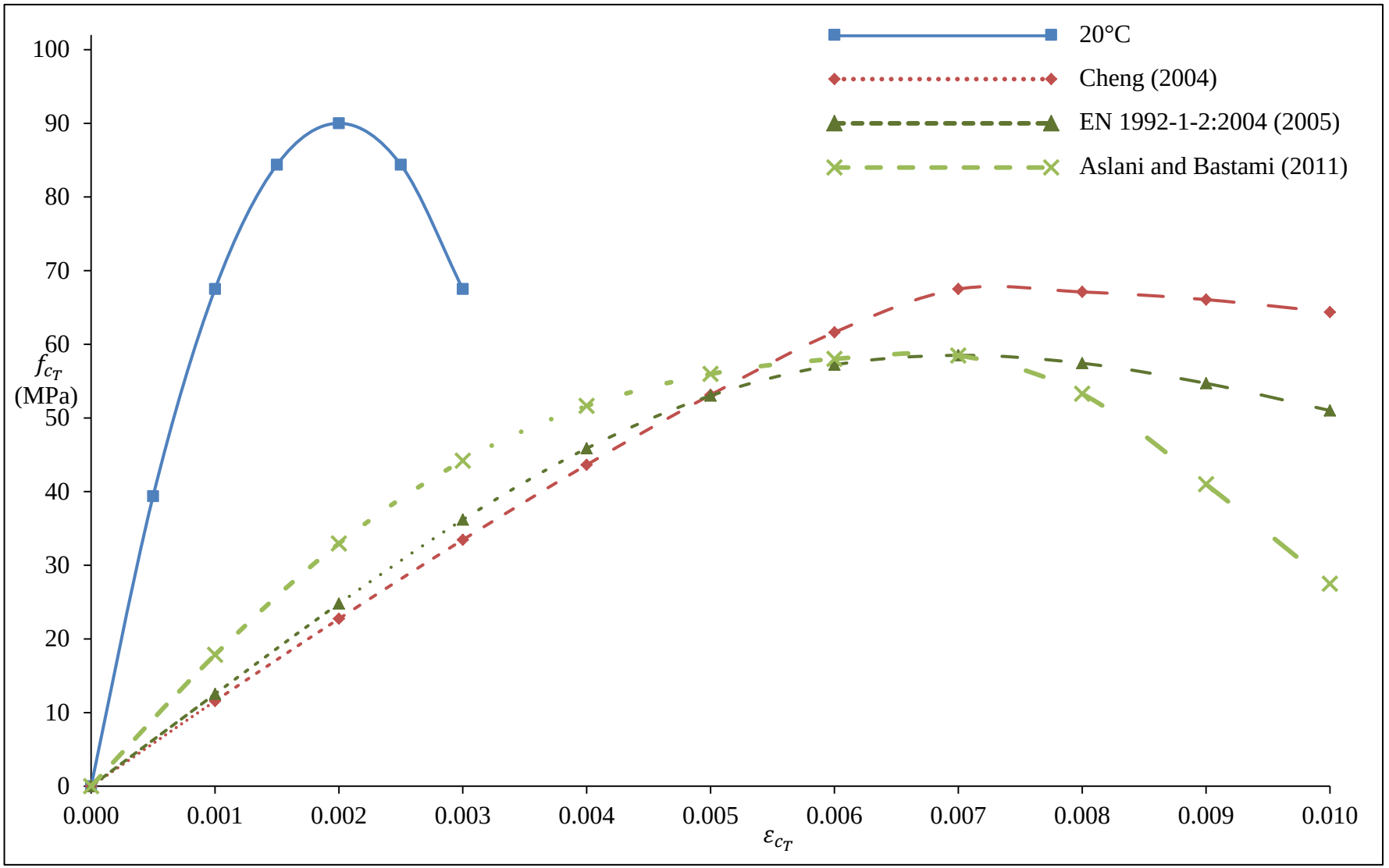

Figure 3-36 Comparison of models for stress-strain curves of high-strength concrete of 90 MPa strength at 300°C

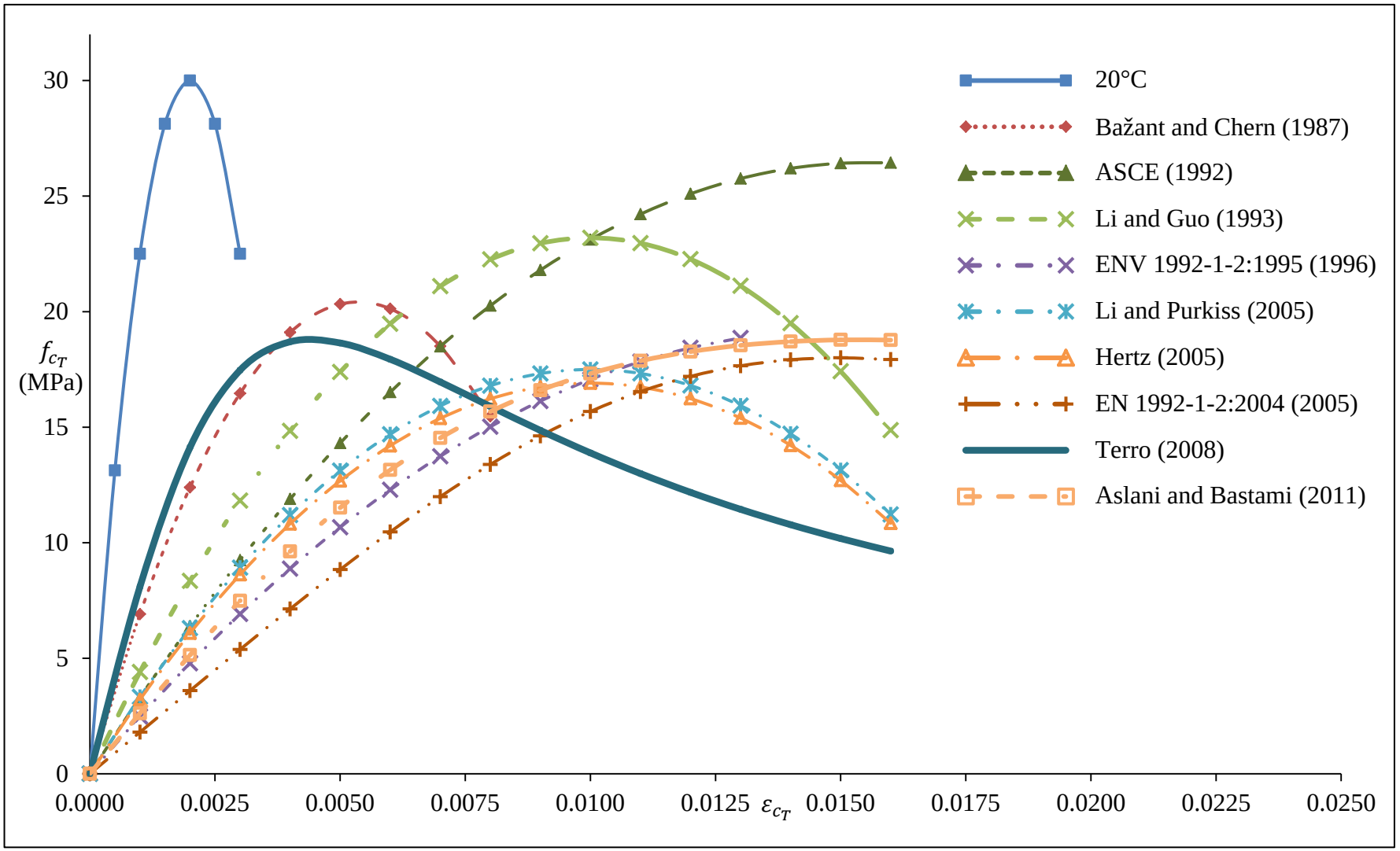

Figure 3-37 Comparison of models for stress-strain curves of normal-strength concrete of 30 MPa strength mixed with siliceous aggregates at 500°C

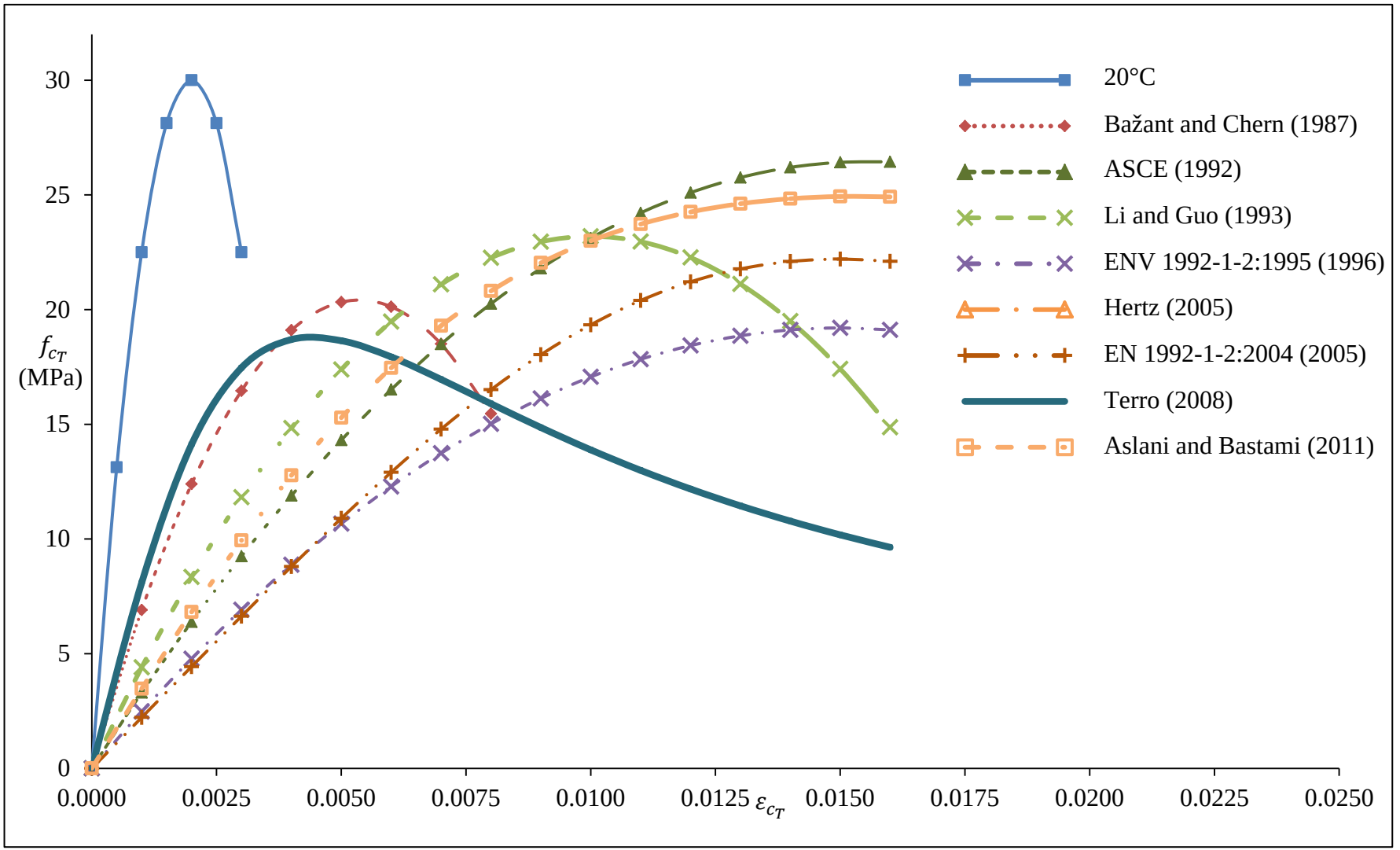

Figure 3-38 Comparison of models for stress-strain curves of normal-strength concrete of 30 MPa strength mixed with calcareous aggregates at 500°C

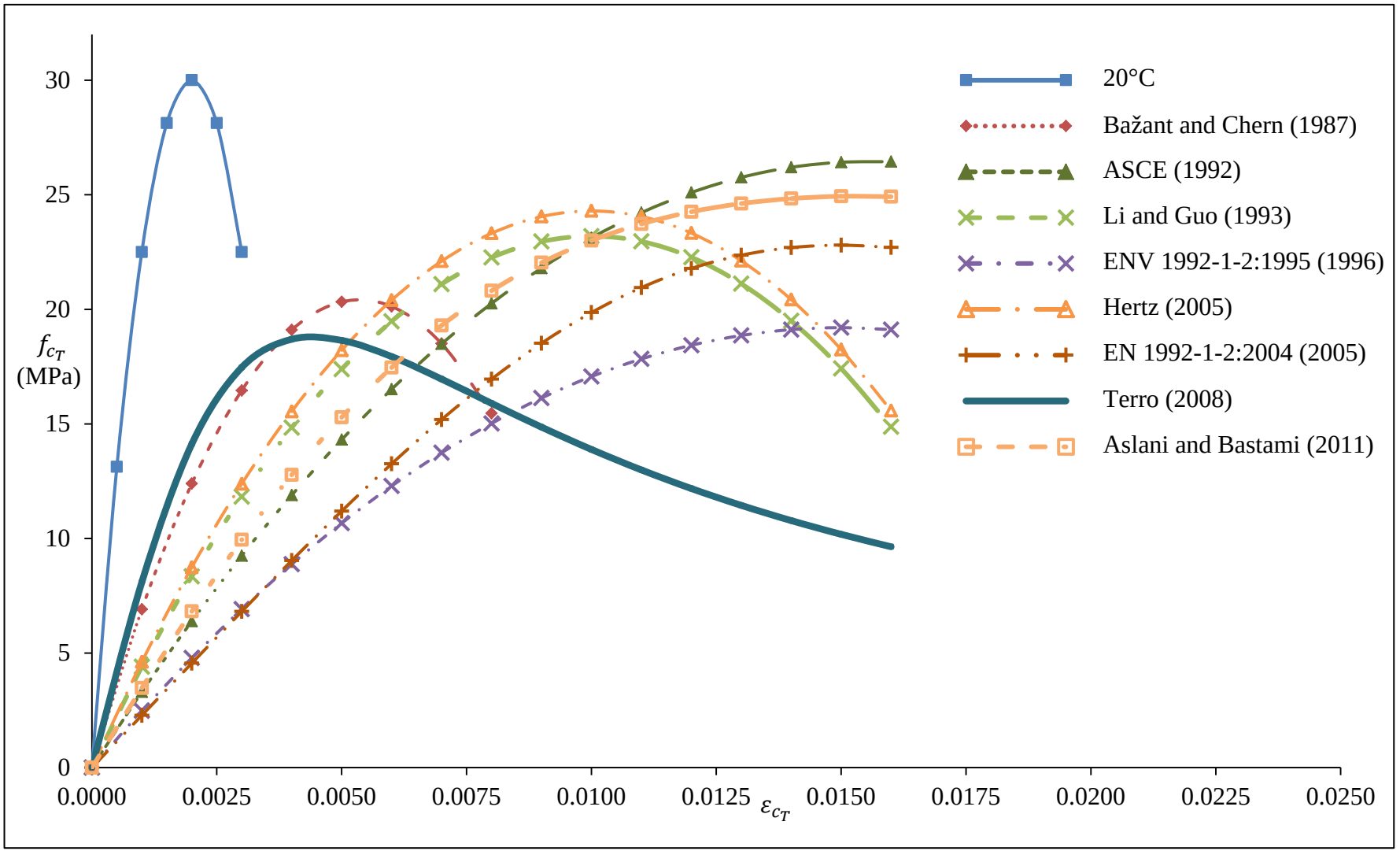

Figure 3-39 Comparison of models for stress-strain curves of normal-strength concrete of 30 MPa strength mixed with light-weight aggregates at 500°C

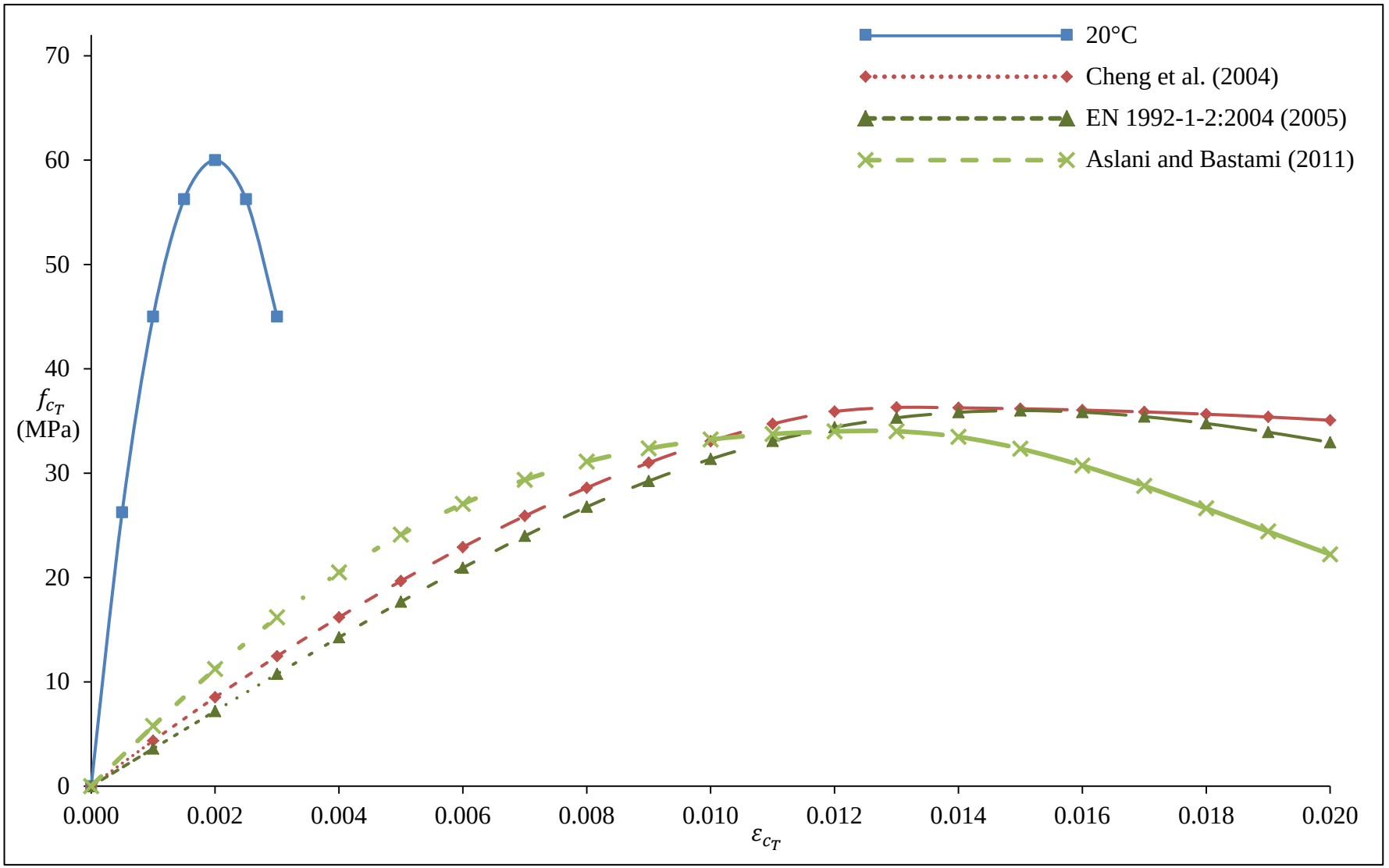

Figure 3-40 Comparison of models for stress-strain curves of high-strength concrete of 60 MPa strength at 500°C

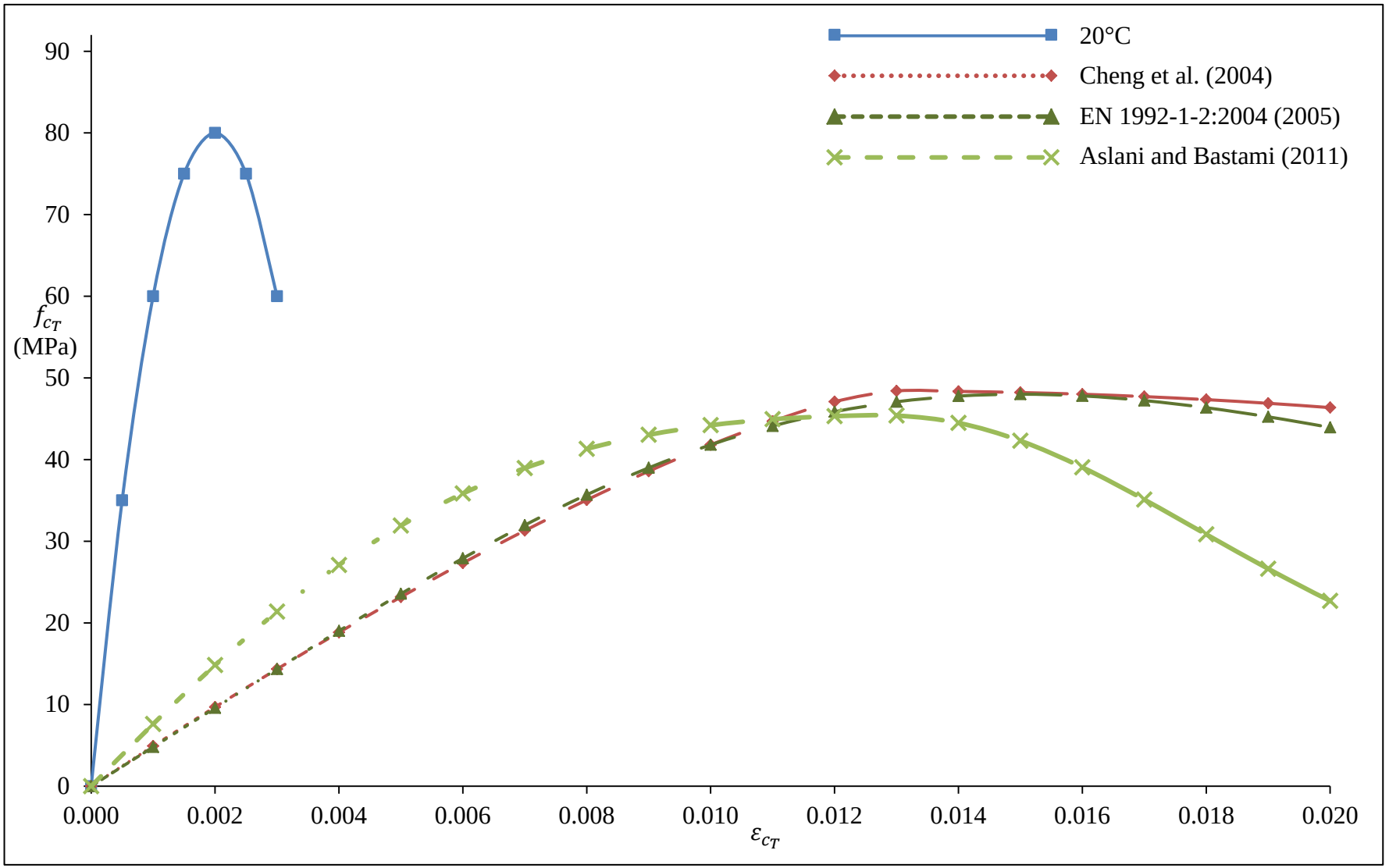

Figure 3-41 Comparison of models for stress-strain curves of high-strength concrete of 80 MPa strength at 500°C

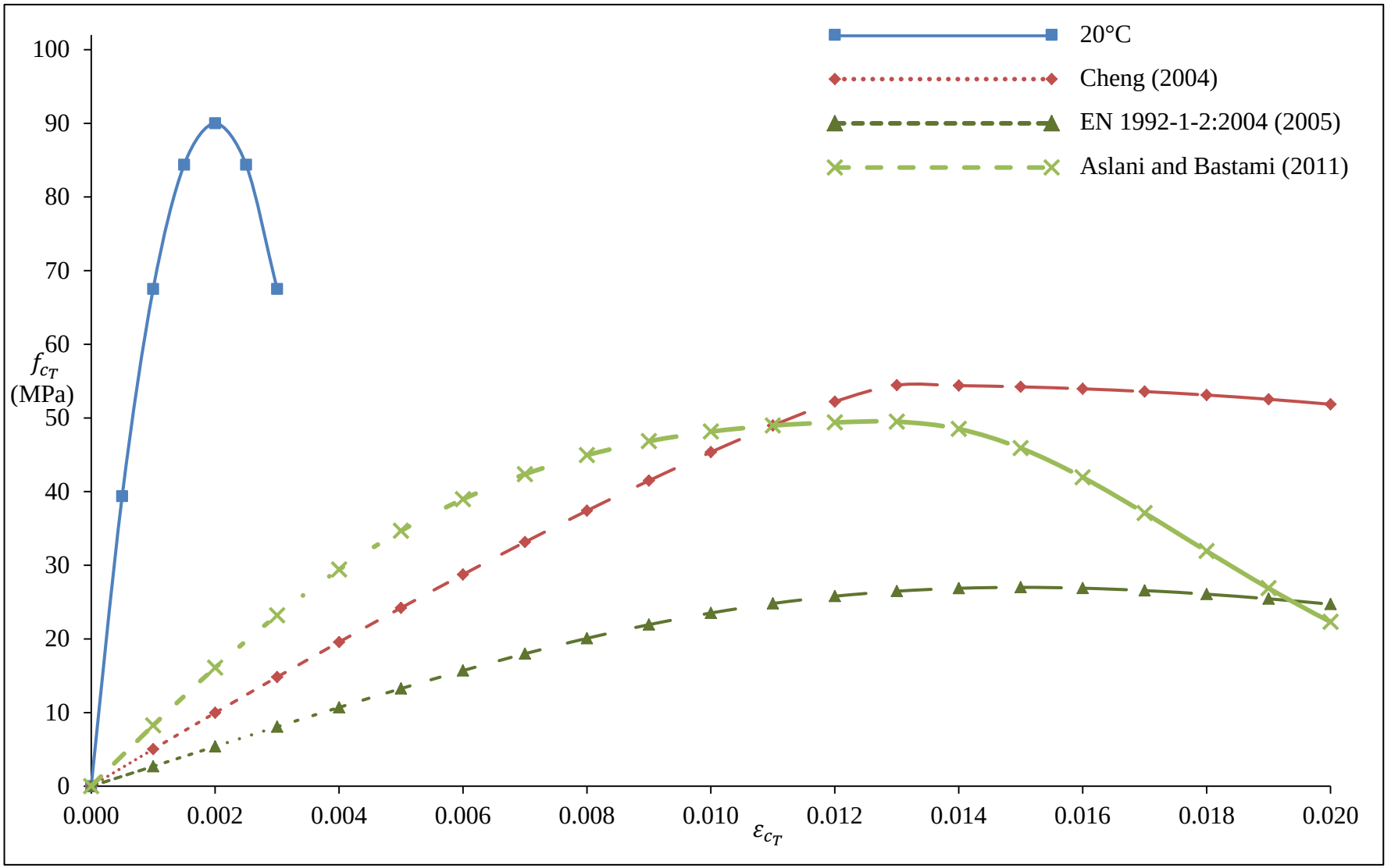

Figure 3-42 Comparison of models for stress-strain curves of high-strength concrete of 90 MPa strength at 500°C

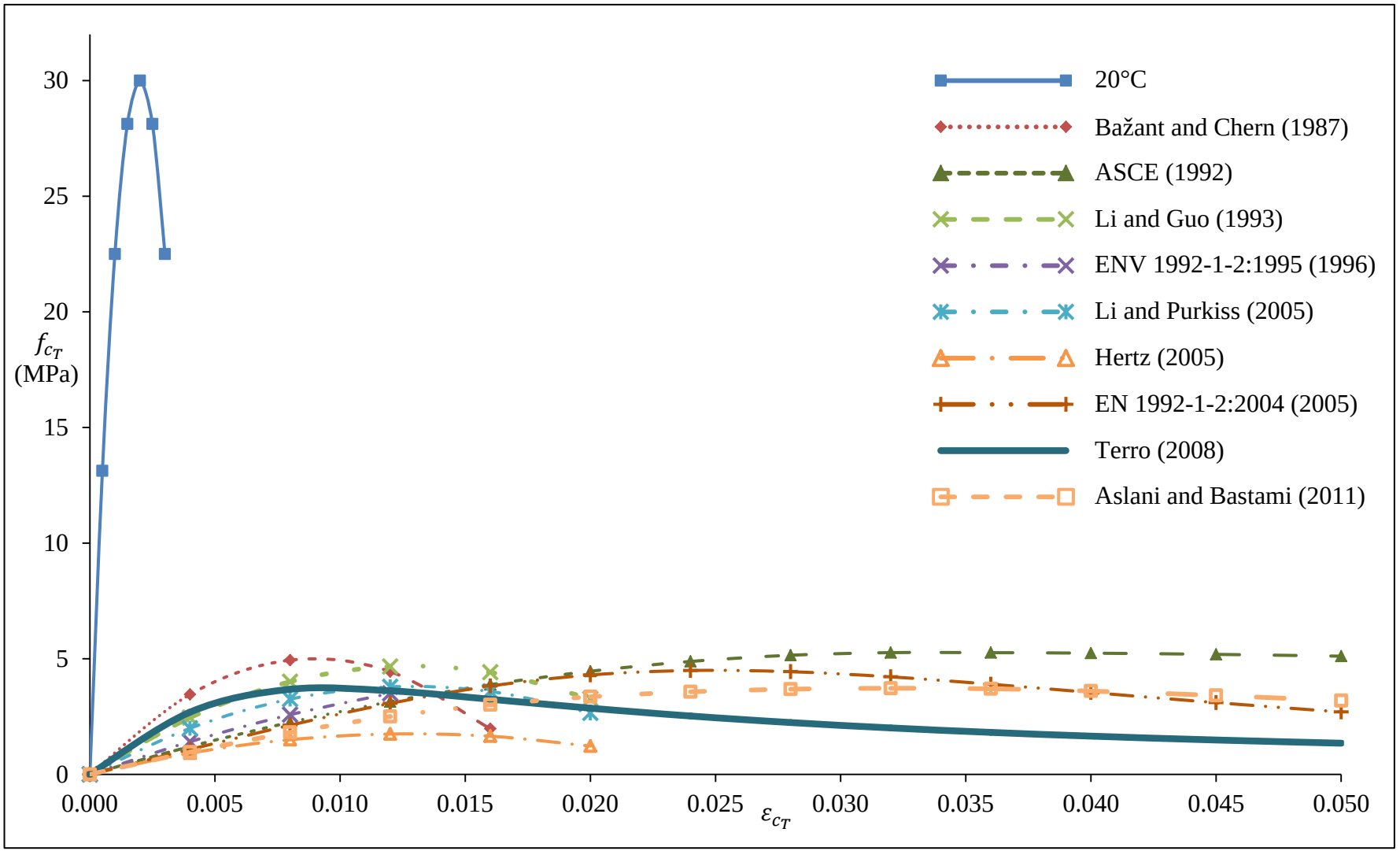

Figure 3-43 Comparison of models for stress-strain curves of normal-strength concrete of 30 MPa strength mixed with siliceous aggregates at 800°C

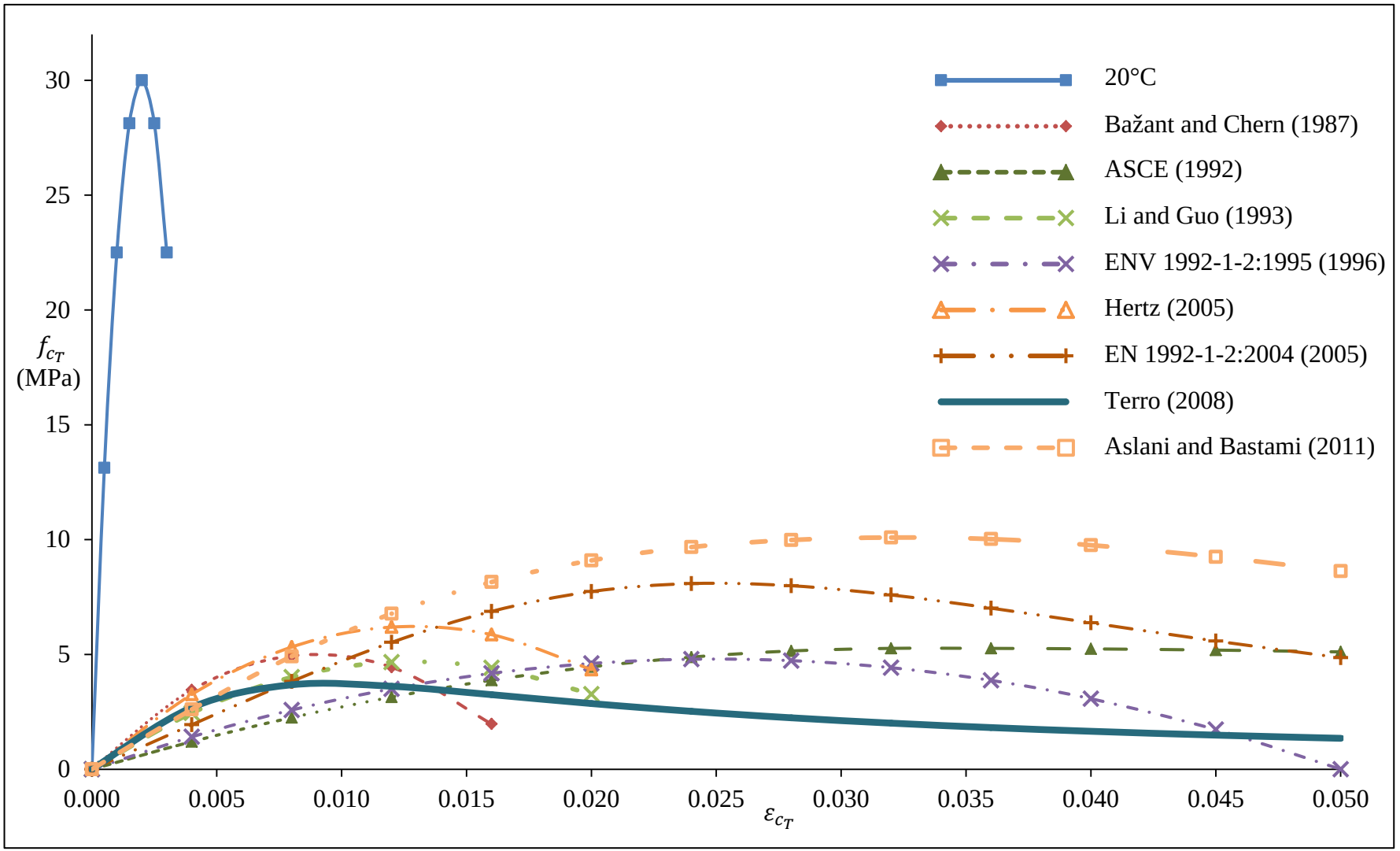

Figure 3-44 Comparison of models for stress-strain curves of normal-strength concrete of 30 MPa strength mixed with calcareous aggregates at 800°C

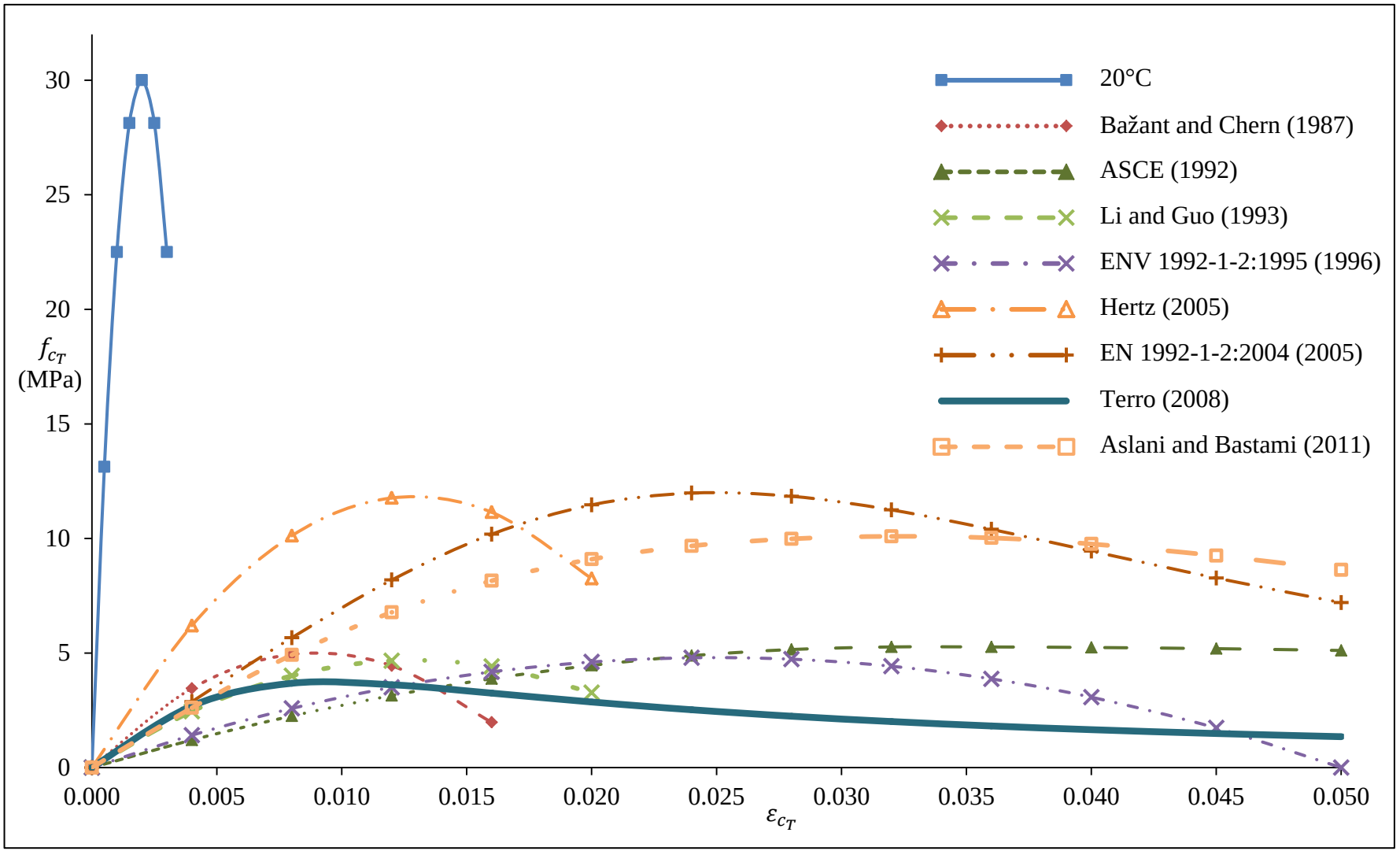

Figure 3-45 Comparison of models for stress-strain curves of normal-strength concrete of 30 MPa strength mixed with light-weight aggregates at 800°C

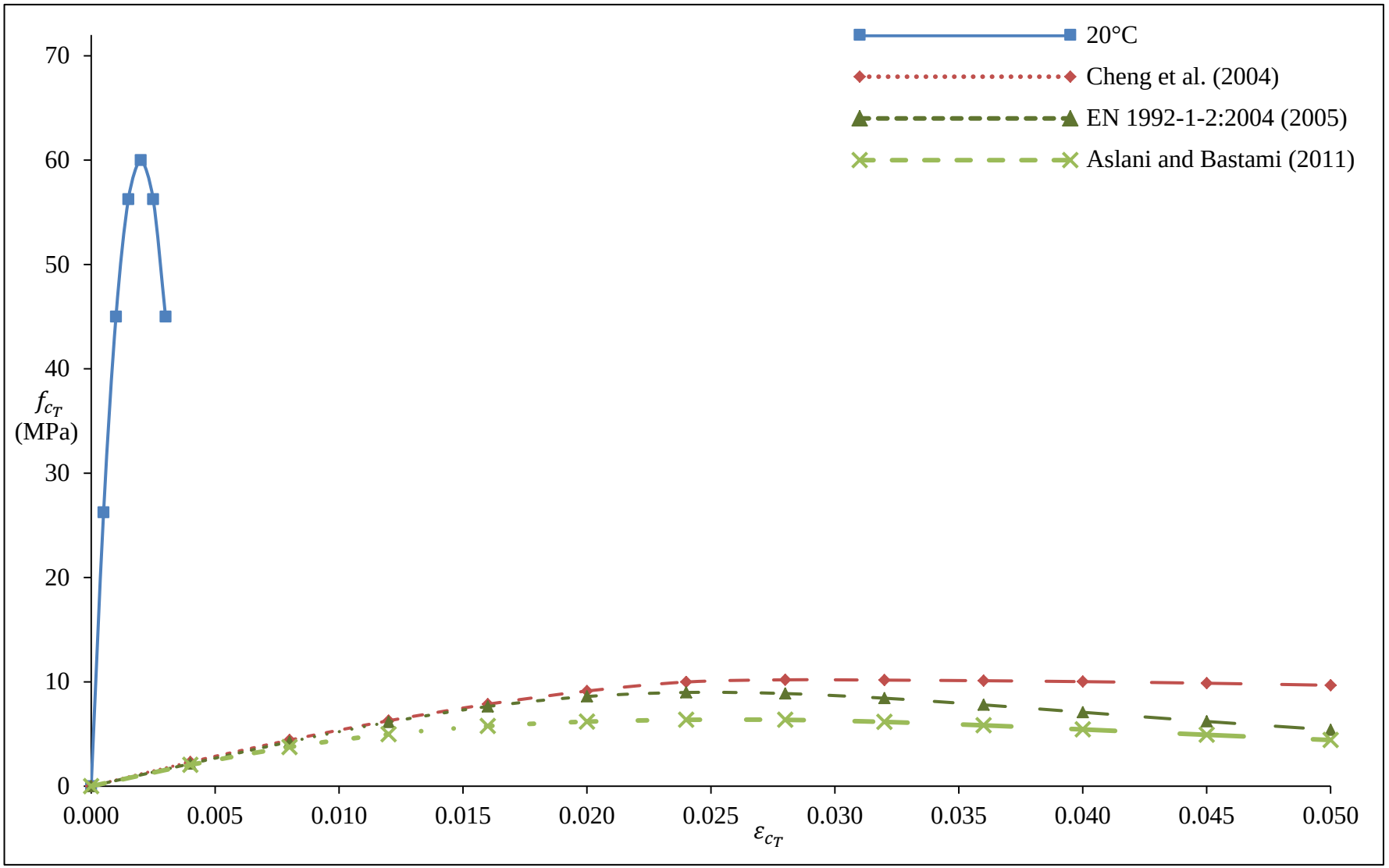

Figure 3-46 Comparison of models for stress-strain curves of high-strength concrete of 60 MPa strength at 800°C

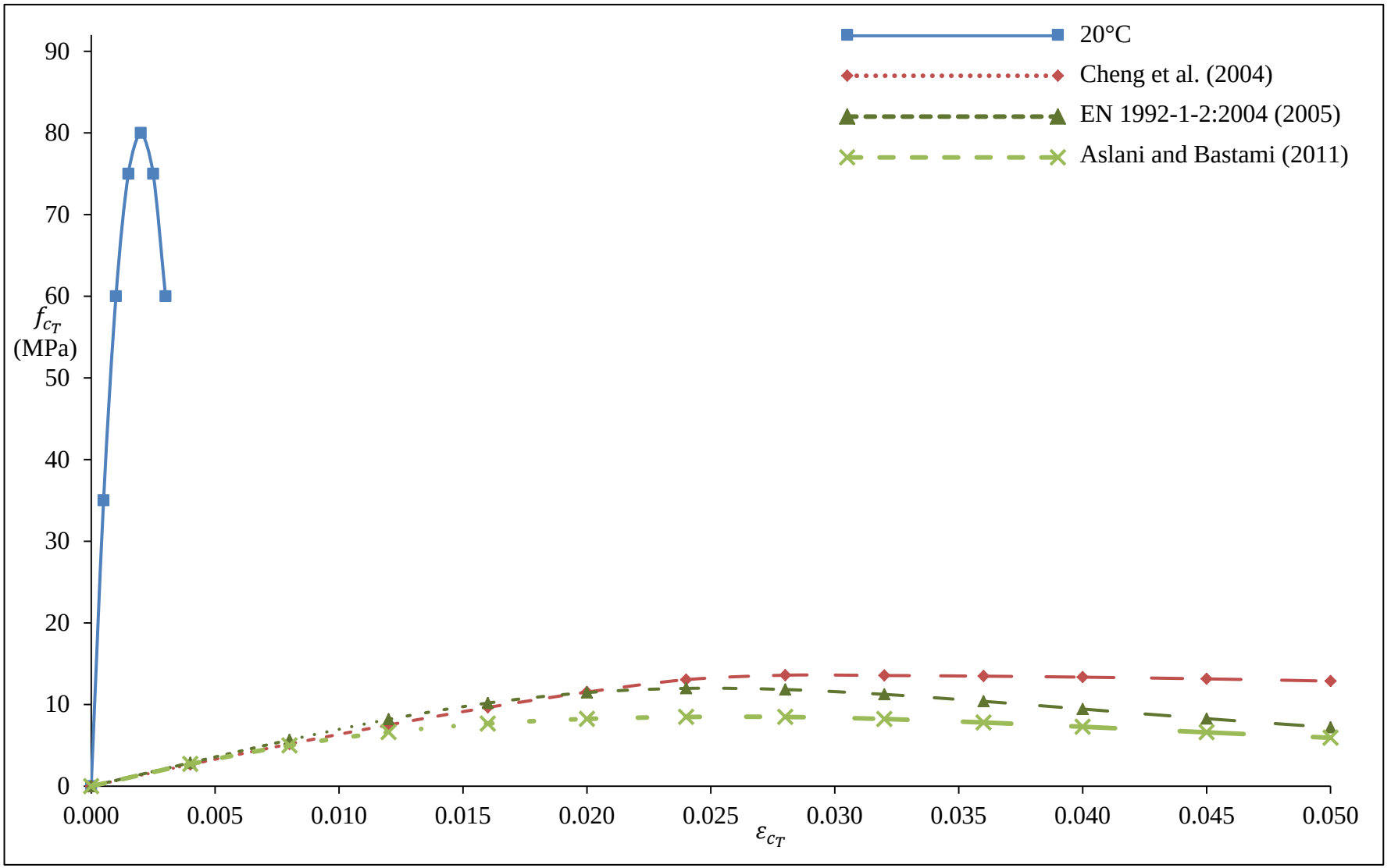

Figure 3-47 Comparison of models for stress-strain curves of high-strength concrete of 80 MPa strength at 800°C

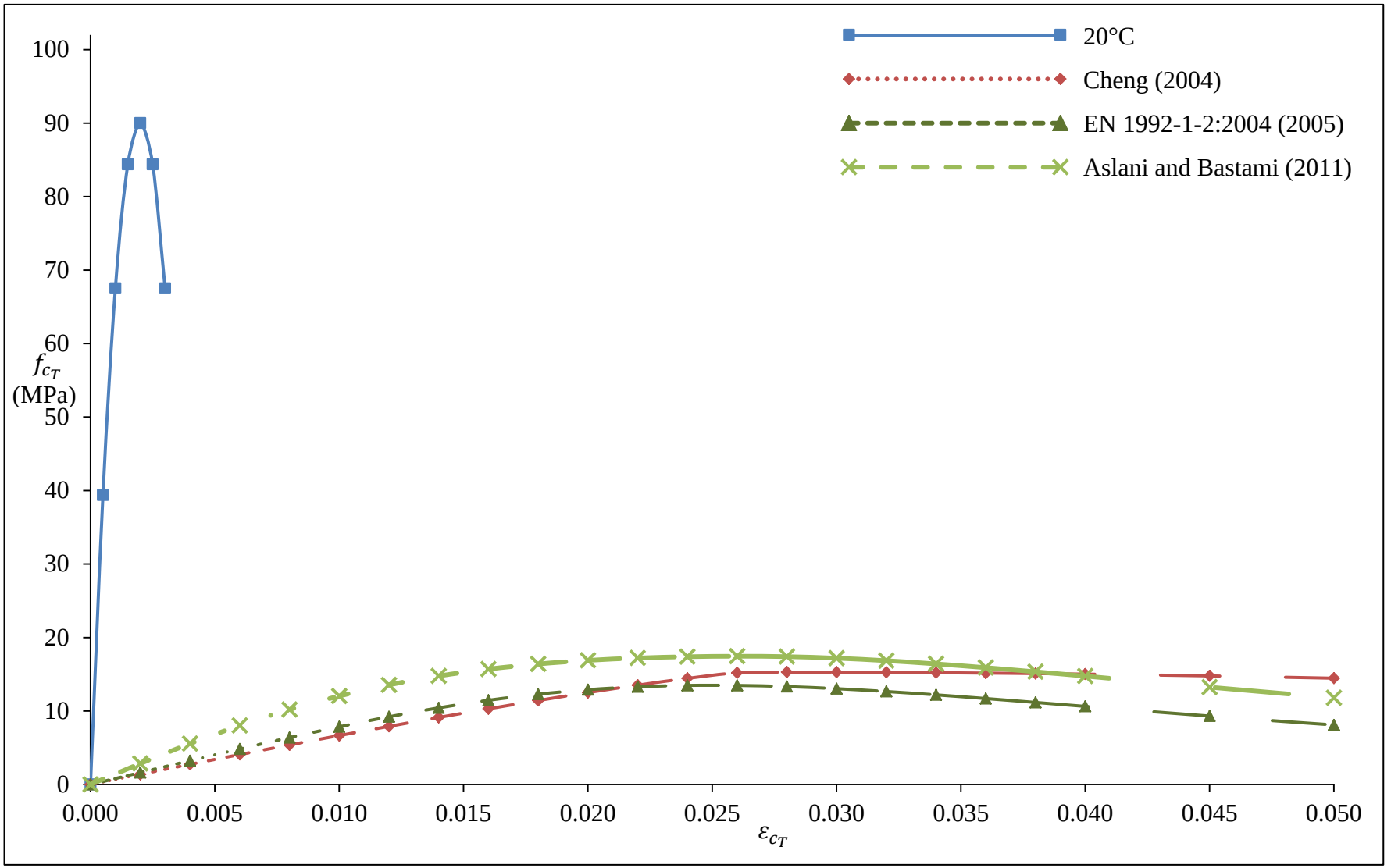

Figure 3-48 Comparison of models for stress-strain curves of high-strength concrete of 90 MPa strength at 800°C

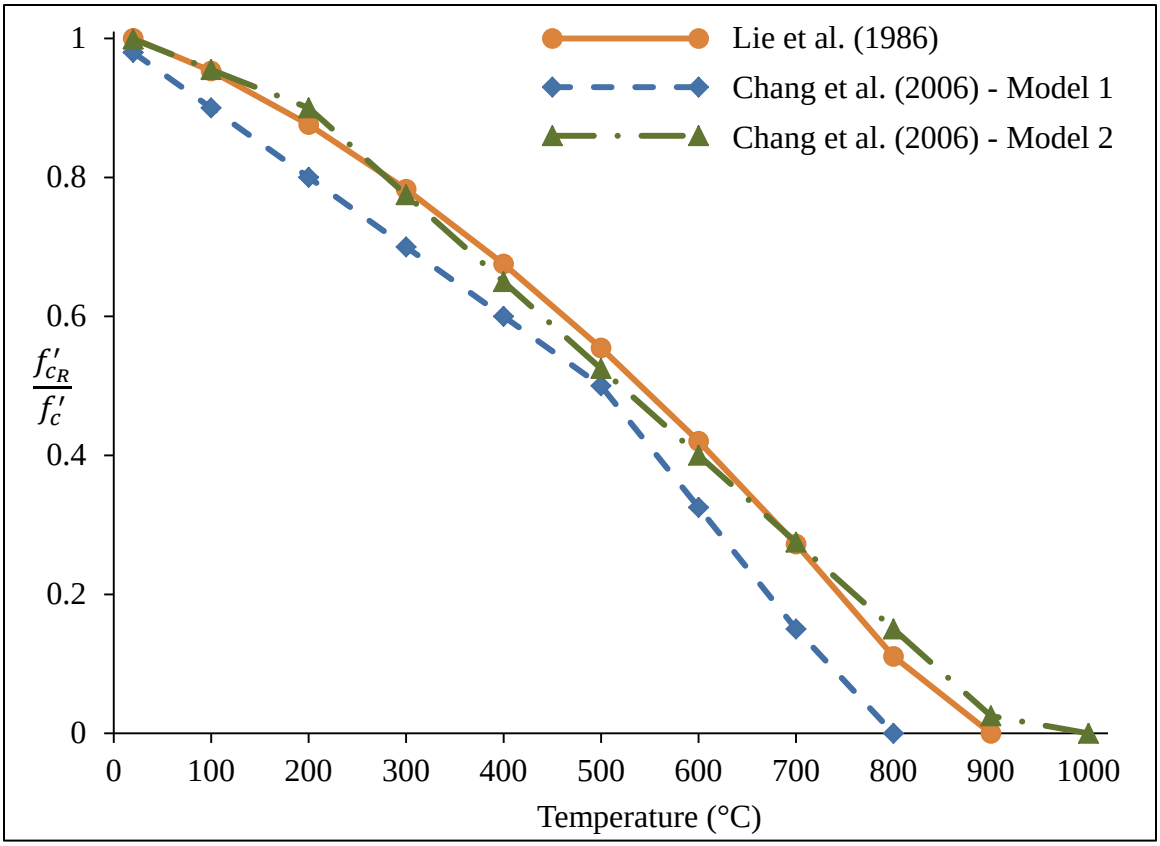

Figure 3-49 Comparison of models for residual compressive strength of concrete after cooling

3.5.1.2 Concrete under Tension

In general, fire has a more drastic effect on the tensile strength of concrete than it has on the compressive strength (Harada et al., 1972). There are much less data in the literature on the properties of concrete in tension under elevated temperatures. Among the first research programs studying this topic was that undertaken by Zoldners (1960), who ran flexural strength tests for concrete under elevated temperatures. More experimental results were presented by Campbell-Allen and Desai (1967), Thelandersson (1972), Anderberg (1976), Bresler et al. (1976), Papayianni and Valiasis (1991), Felicetti et al. (1996), Noumowé et al. (1996), Chan et al. (1999), and Xu et al. (2003).

The difficulty in experimentally determining the tensile strength of concrete (using direct tension, bending, or splitting tests), even under normal temperatures, has obstructed the

advancement in developing reliable constitutive models that represent concrete behaviour in tension under elevated temperatures. Added to this problem is the lack, if not the complete absence, of information regarding the advanced phenomena concrete experiences when subjected to tension under elevated temperatures, such as tension softening, tension splitting, and tension stiffening for reinforced concrete.

As explained in Section 3.5.1.1 regarding the availability of two approaches for determining the constitutive model describing concrete under elevated temperatures in compression, the same two approaches have been employed for determining the constitutive model describing concrete under elevated temperatures in tension as well. Section 3.5.1.2.1 presents the first approach, where the parameters defining the stress-strain curve are evaluated for concrete under elevated temperatures in tension, while typical stress-strain curves for concrete under normal temperatures are used. For the second approach, Section 3.5.1.2.2 presents complete constitutive models that simulate the behaviour of concrete under elevated temperatures in tension.

3.5.1.2.1 Tensile Strength (Cracking Stress)

Despite the limited amount of data available, Naus (2010) attempted to find a trend in the tensile behaviour of concrete under elevated temperatures as he collected and reviewed the works of Lankard et al. (1971), Harada et al. (1972), Carette et al. (1982), Faiyadh and Al-Ausi (1989), Nagao and Nakane (1991), Noumowé et al. (1996), Guo and Waldron (2000), Ravindrarajah et al. (2002), Zhang et al. (2002), Balendran et al. (2003), Li et al. (2004), Potha Raju et al. (2004), Haddad et al. (2008), and Tanyildizi and Coskun (2008). He reached some definite conclusions, such as the significant effect that the aggregate type and the concrete mix proportions have on the tensile strength of concrete under elevated temperatures, compared to the minimal effect of the heating rate.

The results of Harada et al. (1972) and Schneider (1988) showed that, at a temperature of 500 ºC, concrete mixed with calcareous aggregates lost about twice as much of its tensile strength as what was lost by concrete mixed with siliceous aggregates. Also, lean concrete (concrete with lower cement contents) was found to better maintain its strength

at elevated temperatures than rich concrete (concrete with higher cement contents). This is consistent with the effect of aggregate-cement ratio on compressive strength, yet contradictory to the observations of Thelandersson (1972), who reported that tensile strength under elevated temperatures decreases as the aggregate-cement ratio decreases. The experimental results of Harada et al. (1972) and Carette et al. (1982) show how significant the duration of fire exposure is on the tensile strength of concrete.

Finally, the strength of concrete has been reported to have no effect on the extent of the deterioration of the tensile strength under elevated temperatures. This means that, aside from the explosive spalling risks, the tensile strength of high-strength concrete will deteriorate in the same way as normal-strength concrete (Phan, 1996). Also, Sideris et al. (2009) reported that, in fibre-reinforced concrete, steel fibres slightly enhanced the performance of concrete behaviour in tension under elevated temperatures, while polypropylene fibres, which are sometimes used to help prevent explosive spalling as explained in Section 3.3.2.1, significantly decrease the residual post-cooling tensile strength.

Despite these findings, most researchers who attempted to model concrete under elevated temperatures in tension have ignored the factors that affect it. In fact, there has been a common assumption that the behaviour is solely dependent on temperature. As a result of the lack of more accurate data, the behaviour of concrete under elevated temperatures is normally assumed to follow the same path of the behaviour under normal temperatures. Therefore, the tensile stress-strain curve of concrete under elevated temperatures is assumed to be linear up to the cracking stress with a slope equal to the initial modulus of elasticity in compression at the same temperature, then a descending branch incorporating tension softening/stiffening, modelled using the models available in the literature for normal temperatures, is assumed until failure.

Anderberg (1976) specified a constant temperature-independent cracking strain of 0.004. However, from the plots he provided, it can be observed that the strain he described as the cracking strain is not the cracking strain as defined today; it is the failure strain.

Bažant and Chern (1987) plotted the experimental results provided by Thelandersson (1972) for the tensile strength of concrete under elevated temperatures and used the trilinear relation presented in Equation (3.148) to reach the best fit.

$$\frac{f'_{t_T}}{f'_t} = \begin{cases} 1.01052 - 0.526 \times 10^{-3}T & \text{for } T \leq 400℃ \\ 1.8 - 2.5 \times 10^{-3}T & \text{for } 400℃ < T \leq 600℃ \\ 0.6 - 0.5 \times 10^{-3}T & \text{for } 600℃ < T \leq 1200℃ \end{cases} \quad (3.148)$$

Where f'_t and f'_{t_T} are the tensile strengths (cracking stress) at normal temperatures (20ºC) and at temperature T (ºC), respectively.

Li and Guo (1993) suggested a simple expression for the tensile strength under elevated temperatures as follows:

$$\frac{f'_{t_T}}{f'_t} = 1.0 - 0.001T \qquad \text{for } T \leq 1000℃ \quad (3.149)$$

Probably because of the lack of a better model, as a conservative approach, the Eurocode (ENV 1992-1-2:1995, 1996) and its current version (EN 1992-1-2:2004, 2005) assumed that concrete completely loses its tensile strength at a temperature of 600ºC, presenting the following expression to determine it:

$$\frac{f'_{t_T}}{f'_t} = \begin{cases} 1.0 & \text{for } T \leq 100℃ \\ 1.0 - \dfrac{T - 100}{500} & \text{for } 100℃ < T \leq 600℃ \end{cases} \quad (3.150)$$

Song et al. (2007) also provided the expression presented in Equation (3.151) for the same purpose.

$$\frac{f'_{t_T}}{f'_t} = 0.9798 - 0.001T \qquad \text{for } T \leq 979.8℃ \quad (3.151)$$

Moftah (2008) recommended using the same reduction factor used for the compressive strength of concrete under elevated temperatures for the tensile strength at the same temperature as shown in Equation (3.152). He also recommended using the same

reduction factor of the concrete-steel bond strength at elevated temperatures for the post-cracking branch of the stress-strain curve at the same temperature.

$$f'_{t_T} = \frac{f'_{c_T}}{f'_c}\left[0.33\lambda\sqrt{f'_c}\right] \tag{3.152}$$

where λ is the factor accounting for the density of concrete according to CSA 23.3-04 (2004).

Dwaikat and Kodur (2009) argued that employing the model presented by the Eurocode (ENV 1992-1-2:1995, 1996) and its current version (EN 1992-1-2:2004, 2005) leads to unrealistic prediction of spalling at relatively low temperatures (below 600ºC), because the model postulates that concrete completely loses its tensile strength at a temperature of 600ºC. Therefore, they provided the model presented in Equation (3.153) as a modification of the Eurocode model, where a small value is maintained for the tensile strength of concrete for temperatures up to 1200ºC. This model is also preferred for analytical finite element computer programs, as it avoids the computational instabilities that my result from analyzing the response of concrete with absolutely no tensile strength.

where

$$\frac{f'_{t_T}}{f'_t} = \begin{cases} 1.0 & \text{for } T < 100℃ \\ \dfrac{600 - T}{500} & \text{for } 100℃ \le T < 550℃ \\ \dfrac{1200 - T}{6500} & \text{for } 550℃ \le T < 1200℃ \\ 0.00 & \text{for } T \ge 1200℃ \end{cases} \tag{3.153}$$

3.5.1.2.2 Tensile Stress-Strain Constitutive Models

For providing a complete constitutive model describing concrete under elevated temperatures in tension, Terro (1998) adopted the same curve recommended by Anderberg (1976) together with a value of $0.1f'_{c_T}$ for the cracking stress. Terro's curve can be defined using the expression provided in Equation (3.154).

$$f_{t_T} = \begin{cases} E_{c_T}\varepsilon_{c_T} & \text{for } \varepsilon_{c_T} \le \varepsilon_{cr} \\ f'_{t_T}\left[\dfrac{0.004 - \varepsilon_{c_T}}{0.004 - \varepsilon_{cr}}\right] & \text{for } \varepsilon_{cr} < \varepsilon_{c_T} < 0.004 \\ 0 & \text{for } \varepsilon_{c_T} > 0.004 \end{cases} \quad (3.154)$$

where f_{t_T} is the tensile stress at a temperature T (ºC); ε_{c_T} is the corresponding tensile strain; and ε_{cr} is the cracking strain corresponding to the cracking stress, f'_{t_T}, at a slope equal to the compressive initial modulus of elasticity at a specific temperature, i.e., $\varepsilon_{cr} = f'_{t_T}/E_{c_T}$.

Aslani and Bastami (2011) also presented a complete stress-strain curve that represents the behaviour of concrete under elevated temperatures in tension. Equation (3.155) describes the curve and Equation (3.156) shows the expressions given for calculating the cracking stress.

$$f_{t_T} = \begin{cases} E_{c_T}\varepsilon_{c_T} & \text{for } \varepsilon_{c_T} \le \varepsilon_{cr} \\ f'_{t_T}\left(\dfrac{\varepsilon_{c_T}}{\varepsilon_{cr}}\right)^{0.75} & \text{for } \varepsilon_{c_T} > \varepsilon_{cr} \end{cases} \quad (3.155)$$

where the cracking strain, ε_{cr}, is calculated the same way it is for Terro's model in Equation (3.154) (i.e. $\varepsilon_{cr} = f'_{t_T}/E_{c_T}$) and the cracking stress, f'_{t_T}, can be calculated using the following expressions:

$$\frac{f'_{t_T}}{f'_t} = \begin{cases} 1.02 - 0.98 \times 10^{-3}T \le 1.0 & \text{for } T \le 100℃ \\ 0.965 - 0.1 \times 10^{-3}T - 9 \times 10^{-7}T^2 \\ \qquad -3 \times 10^{-9}T^3 + 3.2 \times 10^{-12}T^4 & \text{for } 100℃ < T \le 900℃ \\ 0 & \text{for } T > 900℃ \end{cases} \quad (3.156)$$

3.5.1.2.3 Post-Cooling Behaviour

The results of Harada et al. (1972) and Carette et al. (1982) showed that concrete tends to lose more of its tensile strength as it cools, meaning that the residual tensile strength is

normally less than the tensile strength at the maximum temperature reached. Also, the experimental results presented by Balendran et al. (2003) and Peng et al. (2008) showed the effect of the cooling rate on the residual tensile strength. Similar to residual compressive strength, higher cooling rates cause more deterioration in the residual post-cooling tensile strength.

For the residual tensile strength after cooling, f'_{t_R}, Xie and Qian (1998) provided two separate expressions: one of them is a second-order curve, as shown in Equation (3.157), and the other is a bilinear curve, as shown in Equation (3.158).

$$\frac{f'_{t_R}}{f'_t} = \left[2.08\left(\frac{T_{max}}{100}\right)^2 - 2.666\left(\frac{T_{max}}{10}\right) + 104.79\right] \times 10^{-2} \quad \text{for } T \leq 700℃ \tag{3.157}$$

and

$$\frac{f'_{t_R}}{f'_t} = \begin{cases} 0.58\left[1.0 - \frac{T_{max}}{300}\right] + 0.42 & \text{for } T_{max} \leq 300℃ \\ 0.20\left[1.0 - \frac{T_{max}}{300}\right] + 0.42 & \text{for } 300℃ < T_{max} \leq 700℃ \end{cases} \tag{3.158}$$

Chang et al. (2006) also attempted to provide an expression for the estimation of the residual tensile strength. Their trilinear curve is presented in Equation (3.159).

and

$$\frac{f'_{t_R}}{f'_t} = \begin{cases} 1.05 - 0.0025T_{max} & \text{for } T_{max} \leq 100℃ \\ 0.8 & \text{for } 100℃ < T_{max} \leq 200℃ \\ 1.02 - 0.0011T_{max} & \text{for } 200℃ < T_{max} \leq 800℃ \end{cases} \tag{3.159}$$

3.5.1.2.4 Models Assessment and Comparison

In order to compare between the different models available in the literature and show how significantly different they are, Figures 3-46 and 3-47 are presented to show these models for the tensile strength of concrete at elevated temperatures and the residual tensile strength after cooling, respectively.

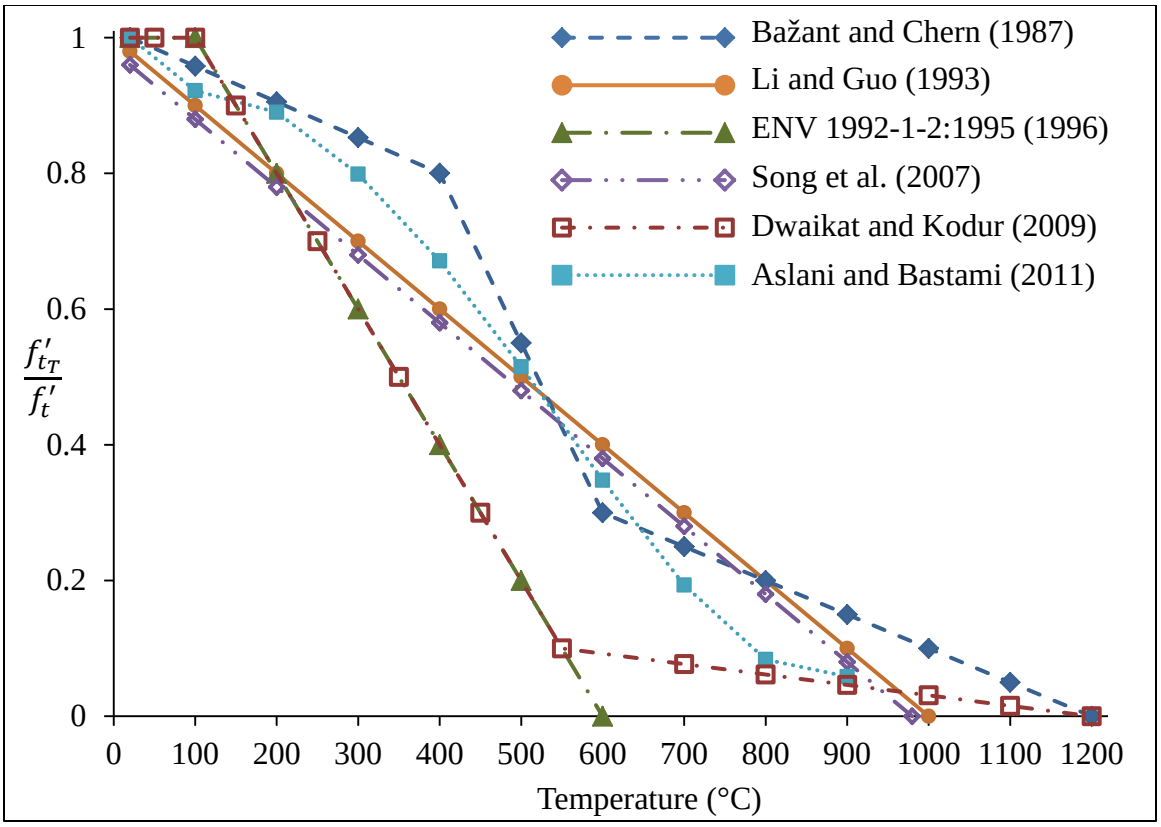

Figure 3-50 Comparison of models for tensile strength of concrete at elevated temperatures

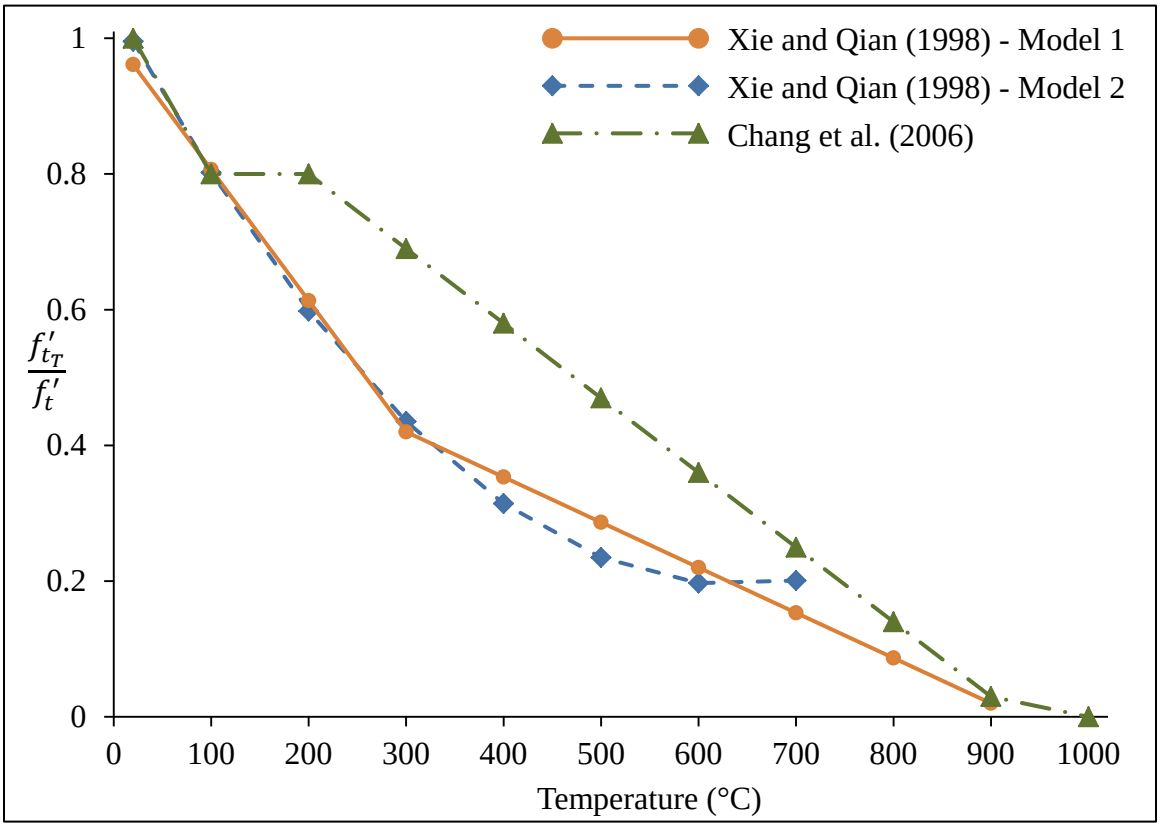

Figure 3-51 Comparison of models for residual tensile strength of concrete after cooling

3.5.2 Properties of Steel Reinforcing Bars

In general, the consistency and manufacturing quality control associated with steel reinforcing bars make studying its mechanical properties much easier than concrete, whether at normal temperatures or at elevated temperatures. Being a metal alloy, steel will become softer and more malleable with temperature despite the fact that for this to happen it requires relatively high temperatures (above 400ºC). Melting should not be a major concern in case of natural fires, as steel typically begins to melt at temperatures above 1100ºC. The melting point is generally around 1400ºC, with this value decreasing as the carbon content increases.

3.5.2.1 Steel Reinforcing Bars under Compression and Tension

The most interesting aspect of the mechanical behaviour of steel reinforcing bars under elevated temperatures is the absence of a distinct yielding plateau and the occurrence of the strain hardening phenomenon throughout the entire plastic range, starting at temperatures of 100ºC (Harmathy and Stanzak, 1970; ECCS, 1983; Custer and Meacham, 2000).

Some researchers reported an insignificant effect of fire on the mechanical properties of steel up to temperatures of 200ºC (Custer and Meacham, 2000; Zheng et al., 2007), while others extended the observation up to 300ºC (Harmathy and Stanzak, 1970; Takeuchi et al., 1993). After this point, both the proportional limit stress and Young's modulus significantly decrease with the rising temperature, while the yielding stress maintains its value for temperatures as high as 400ºC (Takeuchi et al., 1993). This has been reported by many researchers, such as Harmathy and Stanzak (1970), Lie and Stanzak (1974), Malhotra (1982a), Holmes et al. (1982), and Xiao and König (2004).

Numerous models have been developed through many years of research to present a stress-strain curve for steel reinforcing bars under elevated temperatures, represented by three main defining parameters: the proportional limit, f_{p_T}, the yielding stress, f_{y_T}, and Young's Modulus, E_{s_T}. Some models ignored the nonlinear transitional part of the curve and assumed the bilinear curve typically used to model steel reinforcing bars under

normal temperatures for modelling steel reinforcing bars under elevated temperatures as well. One of the oldest models available in the literature is the one presented by Brockenbrough (1970), who proposed a formula for the yielding stress under elevated temperatures, f_{y_T}, which is given in Equation (3.160), and another for Young's Modulus under elevated temperatures, E_{s_T}, which is given in Equation (3.161).

$$\frac{f_{y_T}}{f_y} = \begin{cases} 1.0 - \dfrac{T - 100}{5833} & \text{for } 100°F < T < 800°F \\ (-2.75T^2 + 4{,}200T - 720{,}000) \times 10^{-6} & \text{for } 800°F < T < 1200°F \end{cases} \tag{3.160}$$

$$\frac{E_{s_T}}{E_s} = \begin{cases} 1.0 - \dfrac{T - 100}{5000} & \text{for } 100°F < T < 700°F \\ (-1.111T^2 + 1333T + 500{,}000) \times 10^{-6} & \text{for } 700°F < T < 1200°F \end{cases} \tag{3.161}$$

where f_y and E_s are the yield stress and Young's modulus at normal temperatures (20°C), respectively.

Also, the Centre Technique Industriel de la Construction Métallique (CTICM) (1982) presented the following formulae:

$$\frac{f_{y_T}}{f_y} = \begin{cases} 1.0 + \dfrac{T}{900\ln(T/1750)} & \text{for } T \leq 600°C \\ \dfrac{340(1.0 - T/1000)}{T - 240} & \text{for } 600°C < T < 1000°C \end{cases} \tag{3.162}$$

$$\frac{E_{s_T}}{E_s} = \begin{cases} 1.0 + \dfrac{T}{2000\ln(T/1100)} & \text{for } T \leq 600°C \\ \dfrac{690(1.0 - T/1000)}{T - 53.5} & \text{for } 600°C < T < 1000°C \end{cases} \tag{3.163}$$

Dounas and Golrang (1982) proposed the constitutive model given in Equation (3.164). It should be noted that this model was originally developed for structural steel, which

typically behaves slightly better than steel reinforcing bars under elevated temperatures (Tao et al., 2012).

$$\frac{f_{s_T}}{f_y} = \begin{cases} \varepsilon_{s_T} E(T) & \text{for } \varepsilon_{s_T} \leq \varepsilon_1 \\ 2\beta + b\left[1 - \left((0.03 - \varepsilon_{s_T})/a\right)^2\right]^{1/2} & \text{for } \varepsilon_1 < \varepsilon_{s_T} \leq 2\alpha \\ b + 2\beta + \left(\varepsilon_{s_T} - 0.03\right)/(0.85 \times 10^{-3} T + 0.0123) & \text{for } \varepsilon_{s_T} > 2\alpha \end{cases} \quad (3.164)$$

where
$$E(T) = \begin{cases} -0.194T + 404 & \text{for } T \leq 200℃ \\ -0.590T + 483 & \text{for } 200℃ < T \leq 700℃ \end{cases} \quad (3.165)$$

$$\varepsilon_1 = 0.00217,\ 2\alpha = 0.03,\ 2\beta = 0.88 - 2T/1820 \quad (3.166)$$

$$a = 0.0283 \quad (3.167)$$

and
$$b = \begin{cases} -0.60 \times 10^{-3} T + 0.730 & \text{for } T \leq 500℃ \\ -1.45 \times 10^{-3} T + 1.155 & \text{for } 500℃ < T \leq 700℃ \end{cases} \quad (3.168)$$

where f_{s_T} is the stress in the steel bar at temperature T (ºC); ε_{s_T} is the corresponding strain; $E(T)$ is a reduction factor for the slope of the linear elastic part of the curve; 2α represents the strain of the centre point of the ellipse that constitutes the nonlinear transitional part of the curve as shown in Figure 3-52; while 2β represents the corresponding reduction factor at that strain, and a and b are the radii of this ellipse.

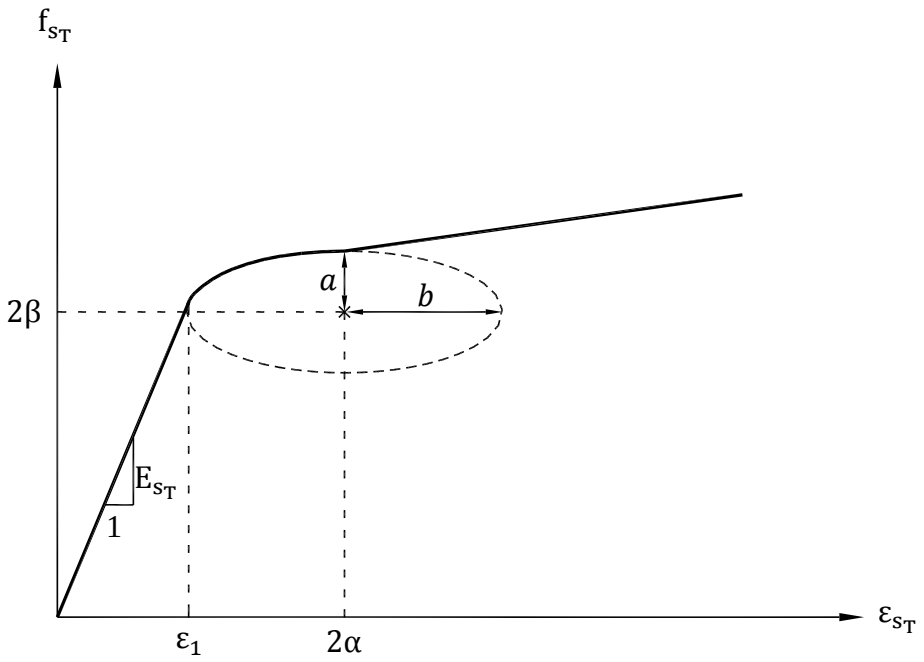

Figure 3-52 Linear-elliptic idealization of stress-strain curve of structural steel as presented by Dounas and Golrang (1982)

Another model available in the literature is the European Convention for Constructional Steelwork (ECCS) (1983) model, which presented a formula for the reduction factor of the yield stress of structural steel, as given in Equation (3.169), and another for Young's modulus, as given in Equation (3.170).

$$\frac{f_{y_T}}{f_y} = \begin{cases} 1.0 + \dfrac{T}{767\ln(T/1750)} & \text{for } T \le 600℃ \\ \dfrac{108(1.0 - T/1000)}{T - 440} & \text{for } 600℃ < T < 1000℃ \end{cases} \tag{3.169}$$

$$\frac{E_{s_T}}{E_s} = \begin{cases} -17.2\times10^{-12}T^4 + 11.8\times10^{-9}T^3 - \\ \qquad 34.5\times10^{-7}T^2 + 15.9\times10^{-5}T + 1.0 & \text{for } T \le 600℃ \\ \text{undefined} & \text{for } T > 600℃ \end{cases} \tag{3.170}$$

Saab (1990) attempted to satisfy the BS 5950-8:1990 (1990) data, reaching the following expressions:

$$\frac{f_{y_T}}{f_y} = \begin{cases} 0.987 - 0.034\dfrac{T}{350} & \text{for } 80℃ < T \leq 400℃ \\ 1.553 - 0.155\dfrac{T}{100} & \text{for } 400℃ < T \leq 550℃ \\ 2.340 - 0.220\dfrac{T}{70} & \text{for } 550℃ < T \leq 600℃ \\ 1.374 - 0.078\dfrac{T}{50} & \text{for } 600℃ < T \leq 690℃ \\ 1.120 - 0.128\dfrac{T}{100} & \text{for } 690℃ < T \leq 800℃ \end{cases} \tag{3.171}$$

For Young's Modulus at elevated temperatures, Saab (1990) also attempted to satisfy the BS 5950-8:1990 (1990) stress-strain-temperature data relations, where he employed the expressions presented by Sharples (1987), reaching the following expressions:

$$\frac{E_{s_T}}{E_s} = \begin{cases} 1.0 - 2.8\left(\dfrac{T-20}{1485}\right)^2 & \text{for } 80℃ < T < 550℃ \\ 1.0 - 3.0\left(\dfrac{T-20}{1463}\right)^2 & \text{for } 550℃ < T < 800℃ \end{cases} \tag{3.172}$$

Lie (1992) proposed two different models, which he adopted in the ASCE Manual of Practice (Structural Fire Protection by T. T. Lie, 1992). The first model, which is recommended as the more conservative option, is presented in Equation (3.173).

$$f_{s_T} = \begin{cases} \dfrac{f(T,0.001)}{0.001}\varepsilon_{s_T} & \text{for } \varepsilon_{s_T} \leq \varepsilon_p \\ \dfrac{f(T,0.001)}{0.001}\varepsilon_p + f\left(T,\left(\varepsilon_{s_T} - \varepsilon_p + 0.001\right)\right) - f(T,0.001) & \text{for } \varepsilon_{s_T} > \varepsilon_p \end{cases} \tag{3.173}$$

where

$$\varepsilon_p = 4 \times 10^{-6} f_y \tag{3.174}$$

$$f(T,0.001) = (50 - 0.04T)\left(1 - e^{(-30+0.03T)\sqrt{0.001}}\right) \times 6.9 \tag{3.175}$$

and

$$f\left(T,\left(\varepsilon_{s_T} - \varepsilon_p + 0.001\right)\right) = (50 - 0.04T)\left(1 - e^{(-30+0.03T)\sqrt{\varepsilon_{s_T} - \varepsilon_p + 0.001}}\right) \times 6.9 \tag{3.176}$$

where ε_p is the proportional limit strain, which is independent of temperature in this model.

The other model Lie (1992) presented in the ASCE Manual of Practice (Structural Fire Protection by T. T. Lie, 1992) for the stress-strain curve of steel reinforcing bars under elevated temperatures provides temperature-dependent formulae for the proportional limit strain, ε_{p_T}, the yield stress, f_{y_T}, and Young's modulus, E_{s_T}. The model is presented in Equation (3.177).

$$f_{s_T} = \begin{cases} E_{s_T}\varepsilon_{s_T} & \text{for } \varepsilon_{s_T} \le \varepsilon_{p_T} \\ \left(12.5\varepsilon_{s_T} + 0.975\right)f_{y_T} - \dfrac{12.5\left(f_{y_T}\right)^2}{E_{s_T}} & \text{for } \varepsilon_{s_T} > \varepsilon_{p_T} \end{cases} \tag{3.177}$$

where

$$\varepsilon_{p_T} = \frac{0.975f_{y_T} - 12.5\left(f_{y_T}\right)^2/E_{s_T}}{E_{s_T} - 12.5f_{y_T}} \tag{3.178}$$

For this model, Lie (1992) proposed the formulae presented by the Centre Technique Industriel de la Construction Métallique (CTICM) (1982) for the reduction factors f_{y_T}/f_y and E_{s_T}/E_s, which were presented in Equation (3.162) and Equation (3.163) respectively.

The previous version of the Eurocode (ENV 1992-1-2:1995, 1996) provided expressions for the reduction factor of the yield stress of steel reinforcing bars, k_{y_T}, where $k_{y_T} = f_{y_T}/f_y$, depending on the stress conditions. Separate formulae were presented for steel reinforcing bars under tension, which are shown in Equation (3.179), and steel reinforcing bars under compression, which are shown in Equation (3.180).

For tension reinforcement:

$$k_{y_T} = \begin{cases} 1.0 & \text{for } T \le 350℃ \\ \dfrac{6650 - 9T}{3500} & \text{for } 350℃ < T \le 700℃ \\ \dfrac{1200 - T}{5000} & \text{for } 700℃ < T \le 1200℃ \end{cases} \tag{3.179}$$

$$\text{For compression reinforcement: } k_{y_T} = \begin{cases} 1.0 & \text{for } T \leq 100℃ \\ \dfrac{1100 - T}{1000} & \text{for } 100℃ < T \leq 400℃ \\ \dfrac{8300 - 12T}{5000} & \text{for } 400℃ < T \leq 650℃ \\ \dfrac{1200 - T}{5500} & \text{for } 650℃ < T \leq 1200℃ \end{cases} \tag{3.180}$$

Another rather more complicated model was proposed by Poh (2001), which included a linear elastic part, an upper yield peak, a yield plateau and a nonlinear strain hardening part.

The current version of the Eurocode (EN 1992-1-2:2004, 2005) presented a different approach for describing the stress-strain curve of steel under elevated temperatures. The extent of the linear elastic part decreases as the temperature rises, followed by a softer more ductile curve. The linear elastic part ends at the proportional limit stress, f_{p_T}, then a nonlinear transitional curve starts and continues until the yielding stress plateau occurs, as shown in Figure 3-53. The model is presented in Equation (3.181).

$$f_{s_T} = \begin{cases} E_{s_T}\varepsilon_{s_T} & \text{for } \varepsilon_{s_T} \leq \varepsilon_{p_T} \\ f_{p_T} - c + \dfrac{b}{a}\sqrt{a^2 - \left(\varepsilon_{y_T} - \varepsilon_{s_T}\right)^2} & \text{for } \varepsilon_{p_T} < \varepsilon_{s_T} < \varepsilon_{y_T} \\ f_{y_T} & \text{for } \varepsilon_{y_T} < \varepsilon_{s_T} < \varepsilon_{t_T} \\ f_{y_T}\left[1 - \left(\dfrac{\varepsilon_{s_T} - \varepsilon_{t_T}}{\varepsilon_{u_T} - \varepsilon_{t_T}}\right)\right] & \text{for } \varepsilon_{t_T} < \varepsilon_{s_T} < \varepsilon_{u_T} \\ 0.00 & \text{for } \varepsilon_{s_T} > \varepsilon_{u_T} \end{cases} \tag{3.181}$$

$$\text{where} \qquad \varepsilon_{p_T} = f_{p_T}/E_{s_T},\ \varepsilon_{y_T} = 0.02,\ \varepsilon_{t_T} = 0.15, \text{and } \varepsilon_{u_T} = 0.20 \tag{3.182}$$

$$\text{and} \qquad a^2 = \left(\varepsilon_{y_T} - \varepsilon_{p_T}\right)\left(\varepsilon_{y_T} - \varepsilon_{p_T} + \frac{c}{E_{s_T}}\right) \tag{3.183}$$

$$b^2 = c(\varepsilon_{y_T} - \varepsilon_{p_T})E_{s_T} + c^2 \tag{3.184}$$

$$c = \frac{(f_{y_T} - f_{p_T})^2}{(\varepsilon_{y_T} - \varepsilon_{p_T})E_{s_T} - 2(f_{y_T} - f_{p_T})} \tag{3.185}$$

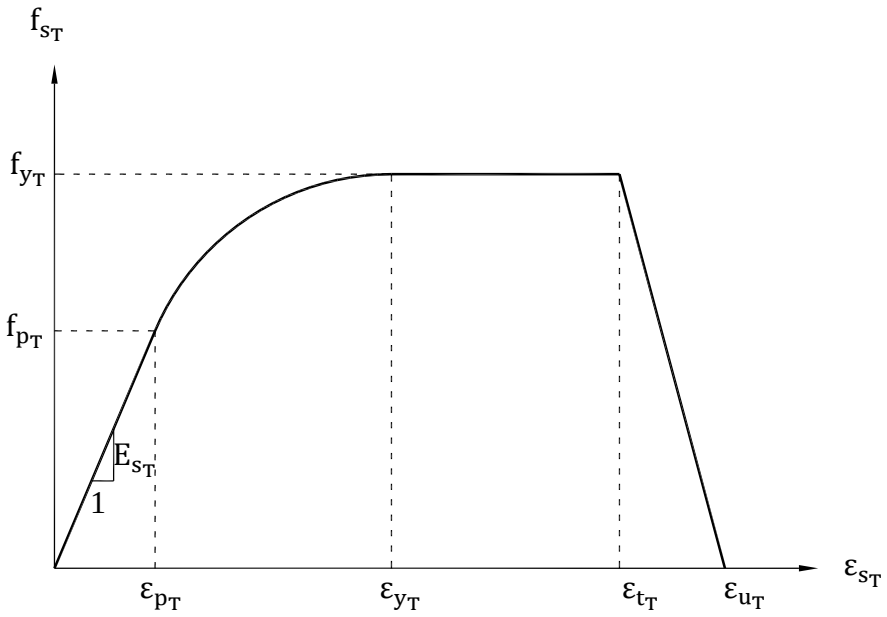

Figure 3-53 The Eurocode stress-strain curve for steel at elevated temperatures

The strains defining the stress-strain curve at elevated temperatures are the proportional limit strain, ε_{p_T}, the yielding strain at elevated temperatures, ε_{y_T}, the limiting strain for yield strength at elevated temperatures, ε_{t_T}, and the ultimate strain at elevated temperatures, ε_{u_T}. The reduction factors required for calculating f_{p_T}, f_{y_T}, and E_{s_T} are k_{p_T}, k_{y_T}, and k_{E_T}, respectively, and are presented in Table 3-6, where:

$$f_{p_T} = k_{p_T} f_y, \quad f_{y_T} = k_{y_T} f_y, \quad \text{and } E_{s_T} = k_{E_T} E_s \tag{3.186}$$

Table 3-6 Reduction factors for the strength of high-strength concrete at elevated temperature

Temperature (ºC)	Yield Stress (k_{y_T})	Proportional Limit Stress (k_{p_T})	Slope of the Linear Elastic Range (k_{E_T})
20	1.0000	1.0000	1.0000
100	1.0000	1.0000	1.0000
200	1.0000	0.8070	0.9000
300	1.0000	0.6130	0.8000
400	1.0000	0.4200	0.7000
500	0.7800	0.3600	0.6000
600	0.4700	0.1800	0.3100
700	0.2300	0.0750	0.1300
800	0.1100	0.0500	0.0900
900	0.0600	0.0375	0.0675
1000	0.0400	0.0250	0.0450
1100	0.0200	0.0125	0.0225
1200	0.0000	0.0000	0.0000

3.5.2.2 Post-Cooling Behaviour

As a metal and a homogeneous material, steel outperforms concrete at regaining its pre-heating strength. The experimental results provided by Smith et al. (1981), Edwards and Gamble (1986), Topçu and Karakurt (2008), Felicetti et al. (2009), and Tao et al. (2012) show almost a complete recovery of the initial yield and ultimate strength for steel reinforcing bars heated up to 500ºC, and a loss of 20% to 30% in both, if heated to 650ºC to 850ºC (CEB-FIP Bulletin 45, 2008).

Due to this good recovery, and due to the fact that a reasonable thickness of the concrete cover would prevent the temperature of steel reinforcing bars from rising much beyond 500ºC, the residual strength of steel after fire exposure has not been investigated extensively. However, Tao et al. (2012) have recently developed a model for this purpose, where they collected data from 380 experimental results from 18 publications

and ran nonlinear regression analysis to develop a model that represents the stress-strain curve of steel reinforcing bars after fire exposure.

The model is a modification of the formulation that was originally proposed by Mander (1983) for steel under normal temperatures, where the effect of preheating has been taken into account. The model is presented in Equation (3.187). It divides the stress-strain curve into four different stages: the elastic stage, the plastic stage, the strain-hardening stage, and the necking and failure stage, as shown in Figure 3-54.

$$f_{s_R} = \begin{cases} E_{s_R}\varepsilon_{s_R} & \text{for } \varepsilon_{s_R} \le \varepsilon_{y1_R} \\ f_{y_R} & \text{for } \varepsilon_{y1_R} < \varepsilon_{s_R} < \varepsilon_{y2_R} \\ f_{f_R} - \left(f_{f_R} - f_{y_R}\right)\left(\dfrac{\varepsilon_{f_R} - \varepsilon_{s_R}}{\varepsilon_{f_R} - \varepsilon_{y2_R}}\right)^{p} & \text{for } \varepsilon_{y2_R} < \varepsilon_{s_R} < \varepsilon_{f_R} \\ f_{f_R} & \text{for } \varepsilon_{s_R} > \varepsilon_{f_R} \end{cases} \tag{3.187}$$

where

$$\varepsilon_{y1_R} = \frac{f_{y_R}}{E_{s_R}} \tag{3.188}$$

$$\frac{\varepsilon_{y2_R}}{\varepsilon_{y1_R}} = \begin{cases} 15 & \text{for } f_y \le 300℃ \\ 15 - 0.018\left(f_y - 300\right) & \text{for } 300 \text{ MPa} < f_y < 800 \text{ MPa} \end{cases} \tag{3.189}$$

$$\frac{\varepsilon_{f_R}}{\varepsilon_{y1_R}} = \begin{cases} 100 & \text{for } f_y \le 300℃ \\ 100 - 0.15\left(f_y - 300\right) & \text{for } 300 \text{ MPa} < f_y < 800 \text{ MPa} \end{cases} \tag{3.190}$$

$$p = E_{p_R}\left(\frac{\varepsilon_{f_R} - \varepsilon_{y2_R}}{f_{f_R} - f_{y_R}}\right) \tag{3.191}$$

$$E_{p_R} = 0.03E_{s_R} \tag{3.192}$$

$$\frac{f_{y_R}}{f_y} = \begin{cases} 1.0 & \text{for } T_{max} \le 500℃ \\ 1.0 - 5.82 \times 10^{-4}(T_{max} - 500) & \text{for } T_{max} > 500℃ \end{cases} \tag{3.193}$$

$$\frac{f_{f_R}}{f_f} = \begin{cases} 1.0 & \text{for } T_{max} \leq 500℃ \\ 1.0 - 4.85 \times 10^{-4}(T_{max} - 500) & \text{for } T_{max} > 500℃ \end{cases} \quad (3.194)$$

$$\frac{E_{s_R}}{E_s} = \begin{cases} 1.0 & \text{for } T_{max} \leq 500℃ \\ 1.0 - 1.30 \times 10^{-4}(T_{max} - 500) & \text{for } T_{max} > 500℃ \end{cases} \quad (3.195)$$

where ε_{s_R} is the strain in pre-heated steel and f_{s_R} is the corresponding stress; ε_{y1_R} is the yielding strain and f_{y_R} is the corresponding stress; ε_{y2_R} is the strain at the onset of the strain hardening phase; ε_{f_R} is the strain at the conclusion of the strain hardening phase and the onset of the necking and failure phase; p is a parameter that determines the shape of the strain-hardening stage; E_{s_R} is the initial modulus of elasticity and E_{p_R} is the tangential stiffness at the onset of strain hardening, i.e. at a strain of ε_{y2_R}.

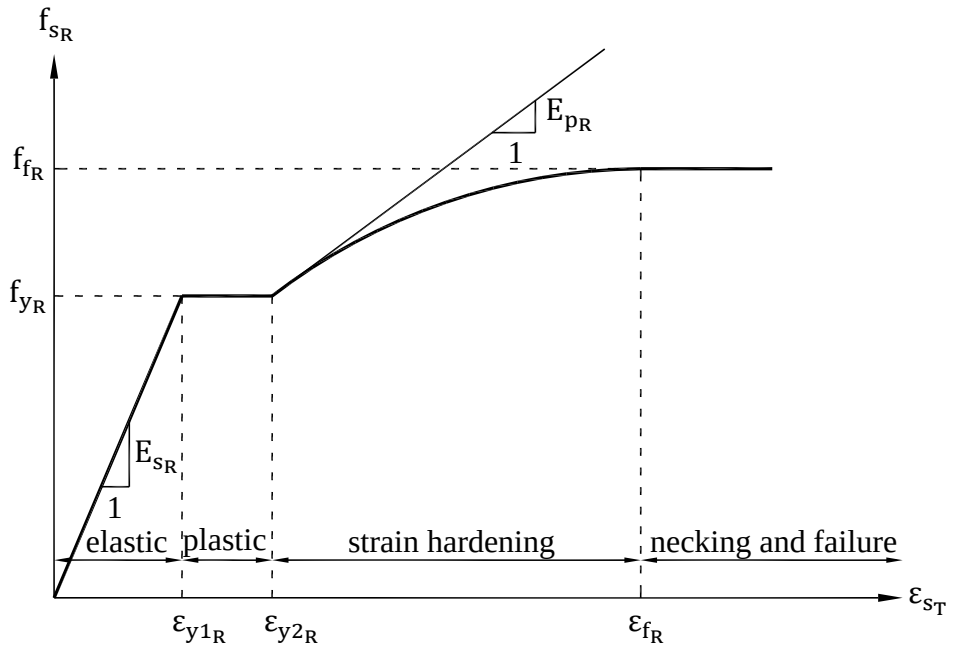

Figure 3-54 The Tao et al. (2012) residual stress-strain curve for preheated steel

The stress that concludes the strain-hardening stage and starts the necking and failure stage at normal temperatures, f_f, is not always known so it can be used to calculate the corresponding residual value, f_{f_R}, using Equation (3.194). Thus, Tao et al. (2012)

collected the data of 148 experimental results from 30 publications to develop Equation (3.196) to calculate f_f by knowing the yielding stress at normal temperatures, f_y.

$$\frac{f_f}{f_y} = 1.6 - 9.17 \times 10^{-4}(f_y - 200) \quad \text{for } 200 \text{ MPa} < f_y < 800 \text{ MPa} \quad (3.196)$$

3.5.2.3 Models Assessment and Comparison

Despite the relative simplicity of determining the behaviour of steel under elevated temperatures compared to concrete and despite the consistency of steel as a material produced with high levels of quality control, the models discussed for the behaviour of steel under elevated temperatures show very significant variation. This is shown in Figure 3-55 for the yield/proportional stress of steel under elevated temperatures and Figure 3-56 for Young's modulus of steel under elevated temperatures.

Figures 3-53, 3-54, 3-55, and 3-56 show comparisons of models for stress-strain curves of steel reinforcing bars of yield stress of 400 MPa and ultimate stress of 600 MPa at temperatures of 100°C, 300°C, 500°C, 800°C, respectively. 'EN 1992-1-2:2004, 2005 bilinear idealization' refers to the stress-strain curve generated by using the reduction factors presented by the Eurocode (EN 1992-1-2:2004, 2005) in the typical idealized bilinear steel stress-strain curve with strain hardening taken into account.

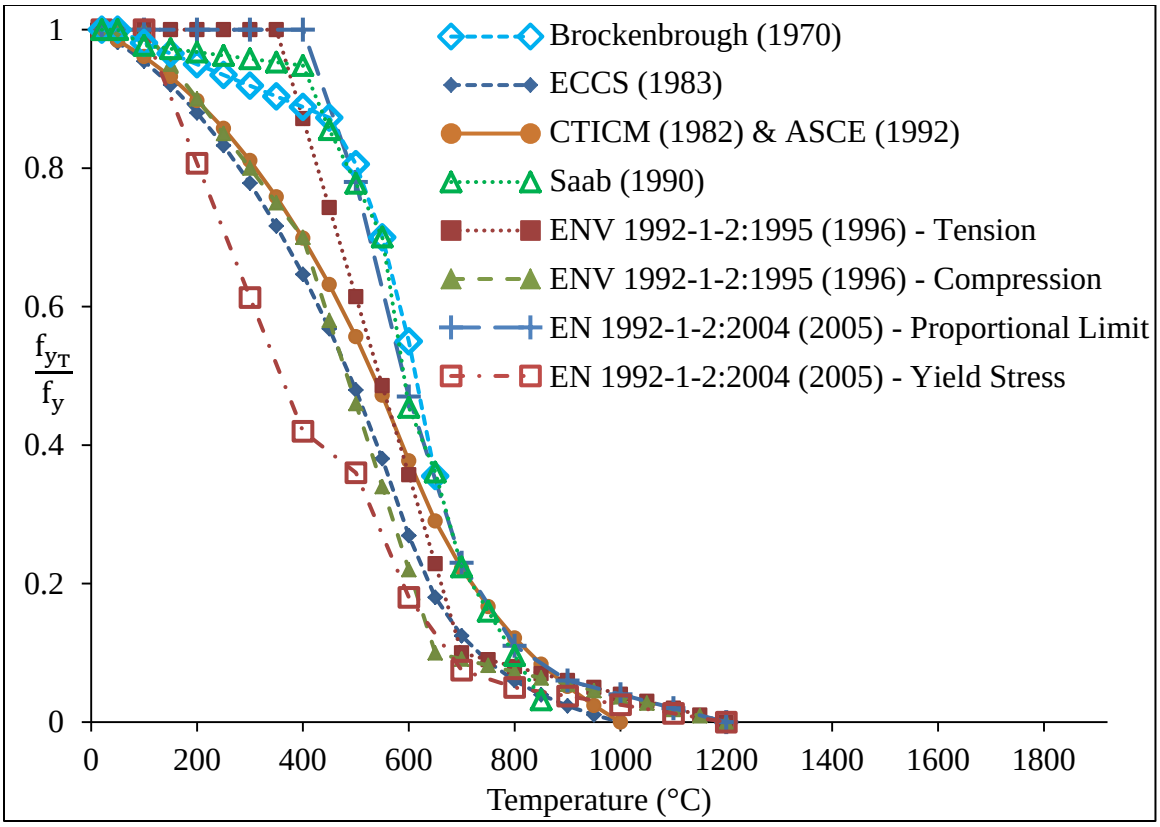

Figure 3-55 Comparison of models for steel yield stress at elevated temperatures

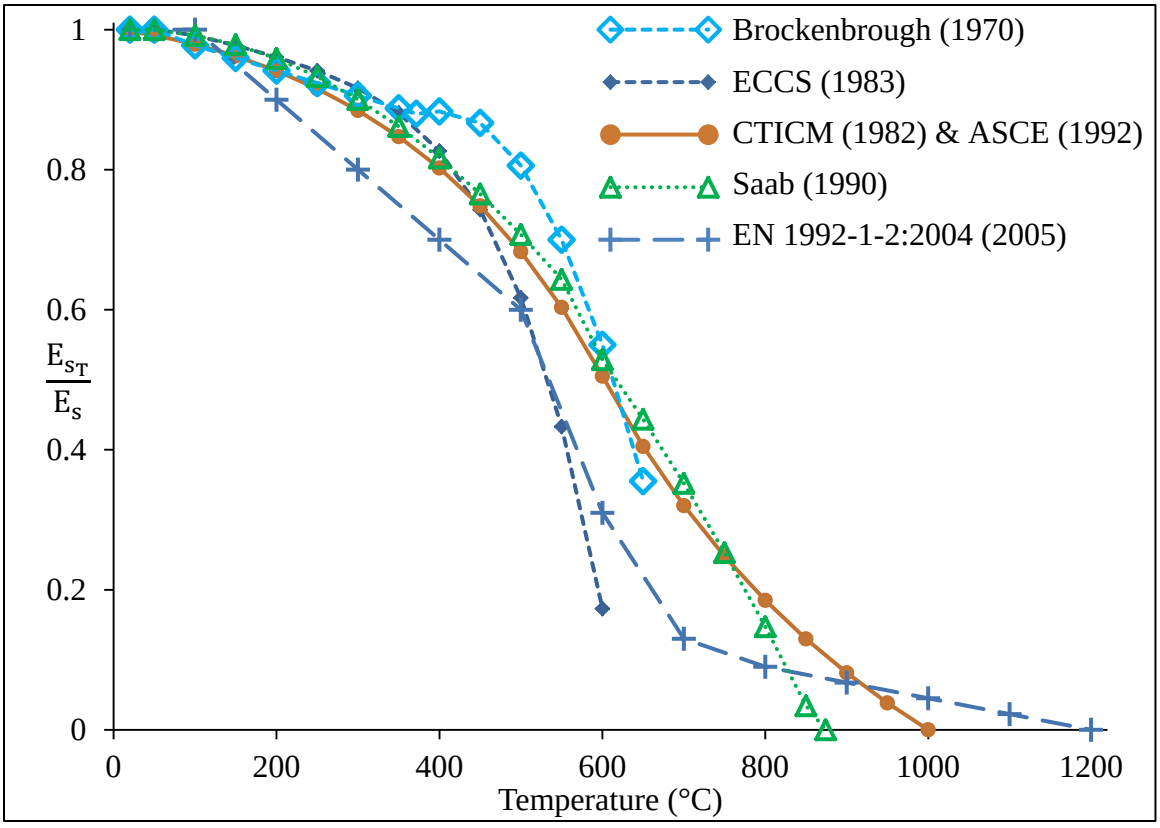

Figure 3-56 Comparison of models for steel Young's modulus at elevated temperatures

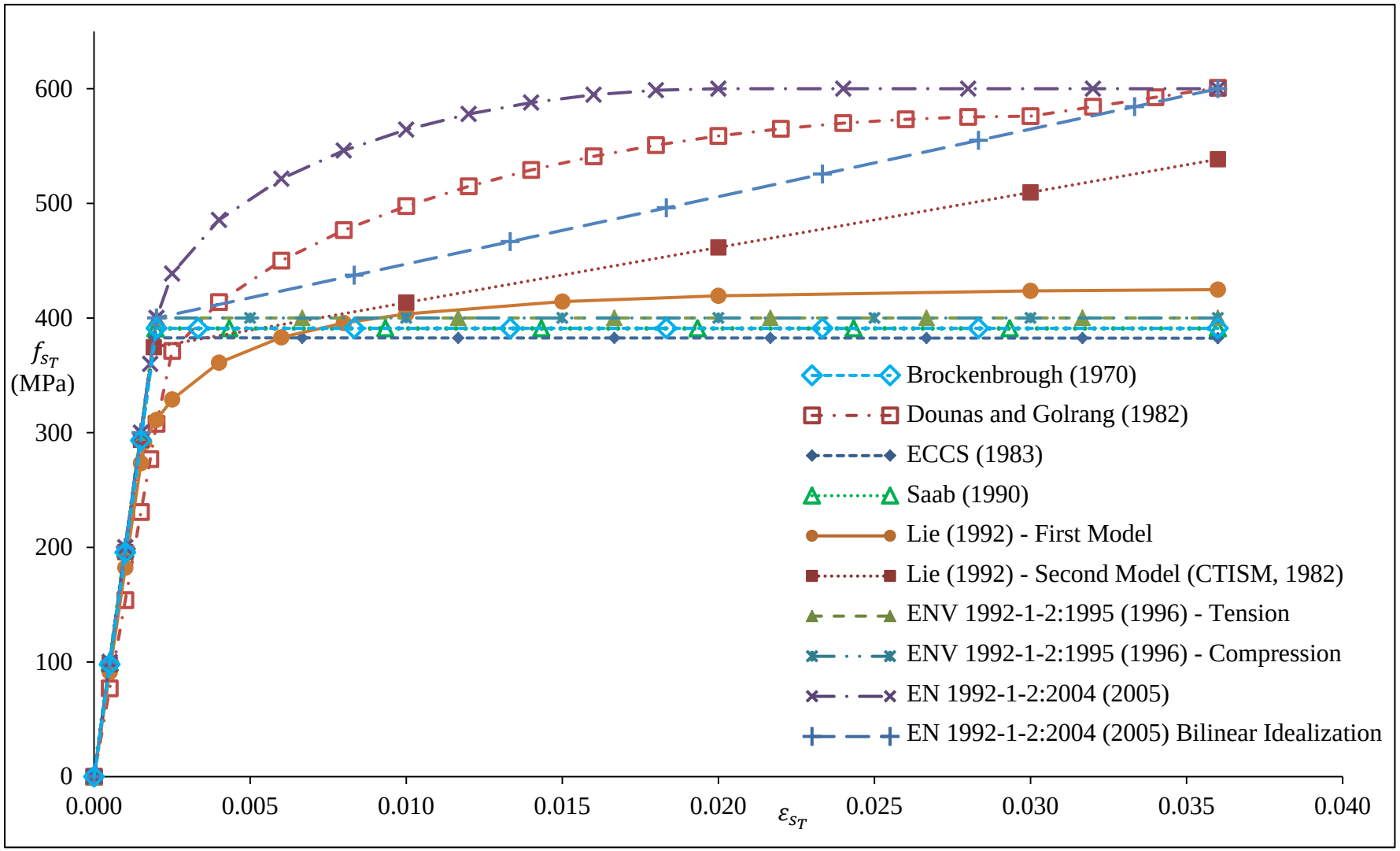

Figure 3-57 Comparison of models for stress-strain response of steel reinforcing bars at 100°C for bars having a yield stress of 400 MPa and an ultimate stress of 600 MPa

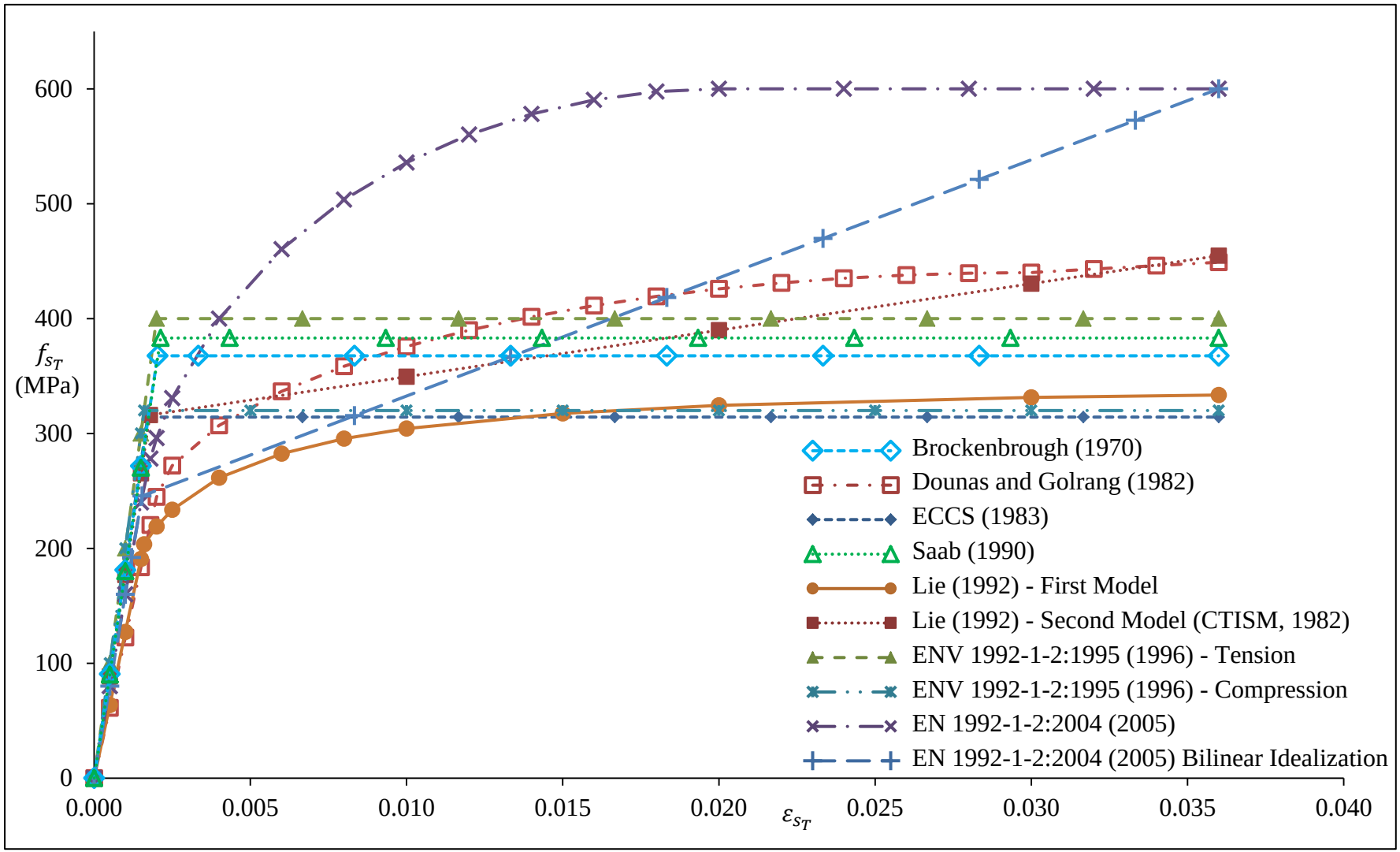

Figure 3-58 Comparison of models for stress-strain response of steel reinforcing bars at 300°C for bars having a yield stress of 400 MPa and an ultimate stress of 600 MPa

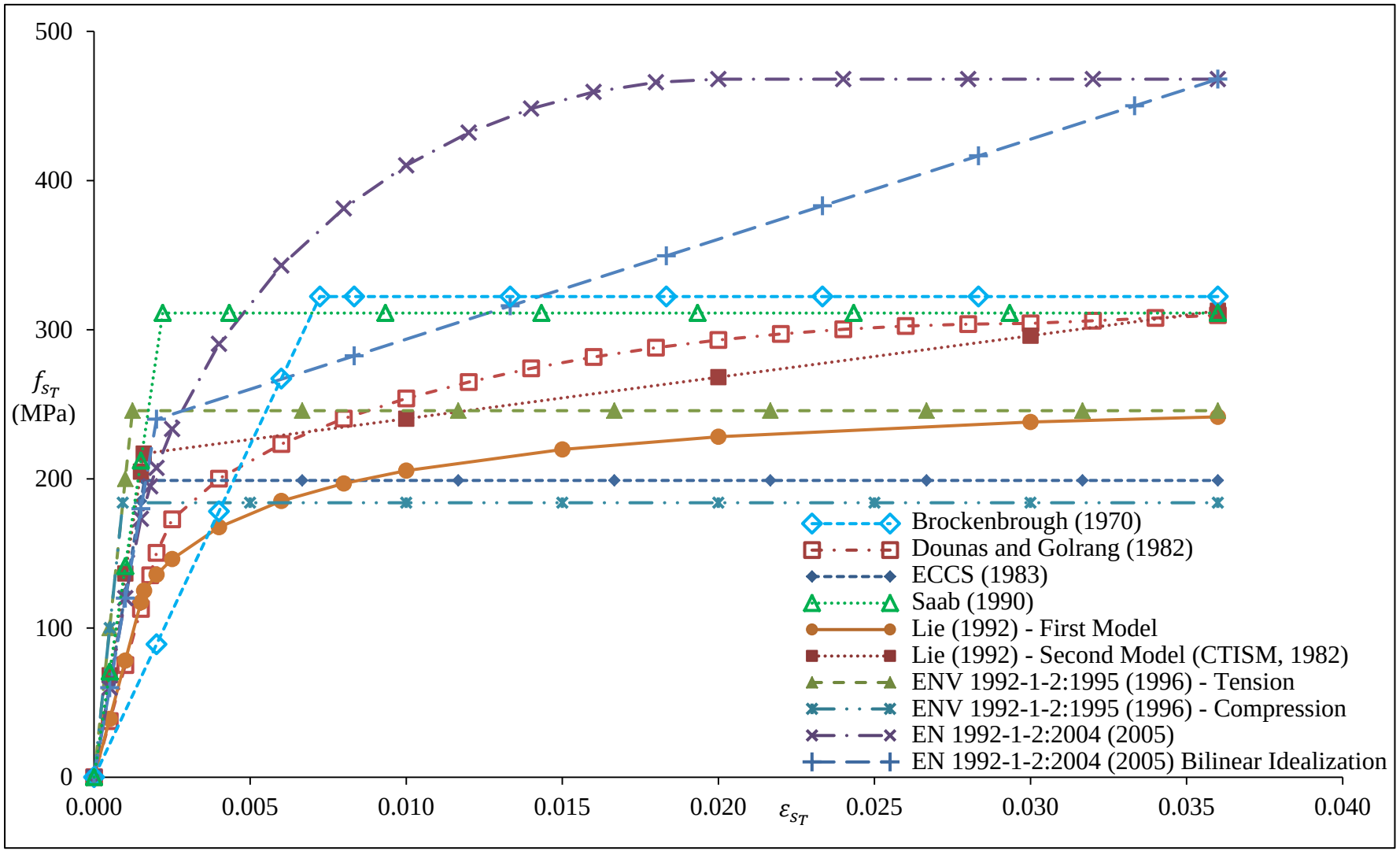

Figure 3-59 Comparison of models for stress-strain response of steel reinforcing bars at 500°C for bars having a yield stress of 400 MPa and an ultimate stress of 600 MPa

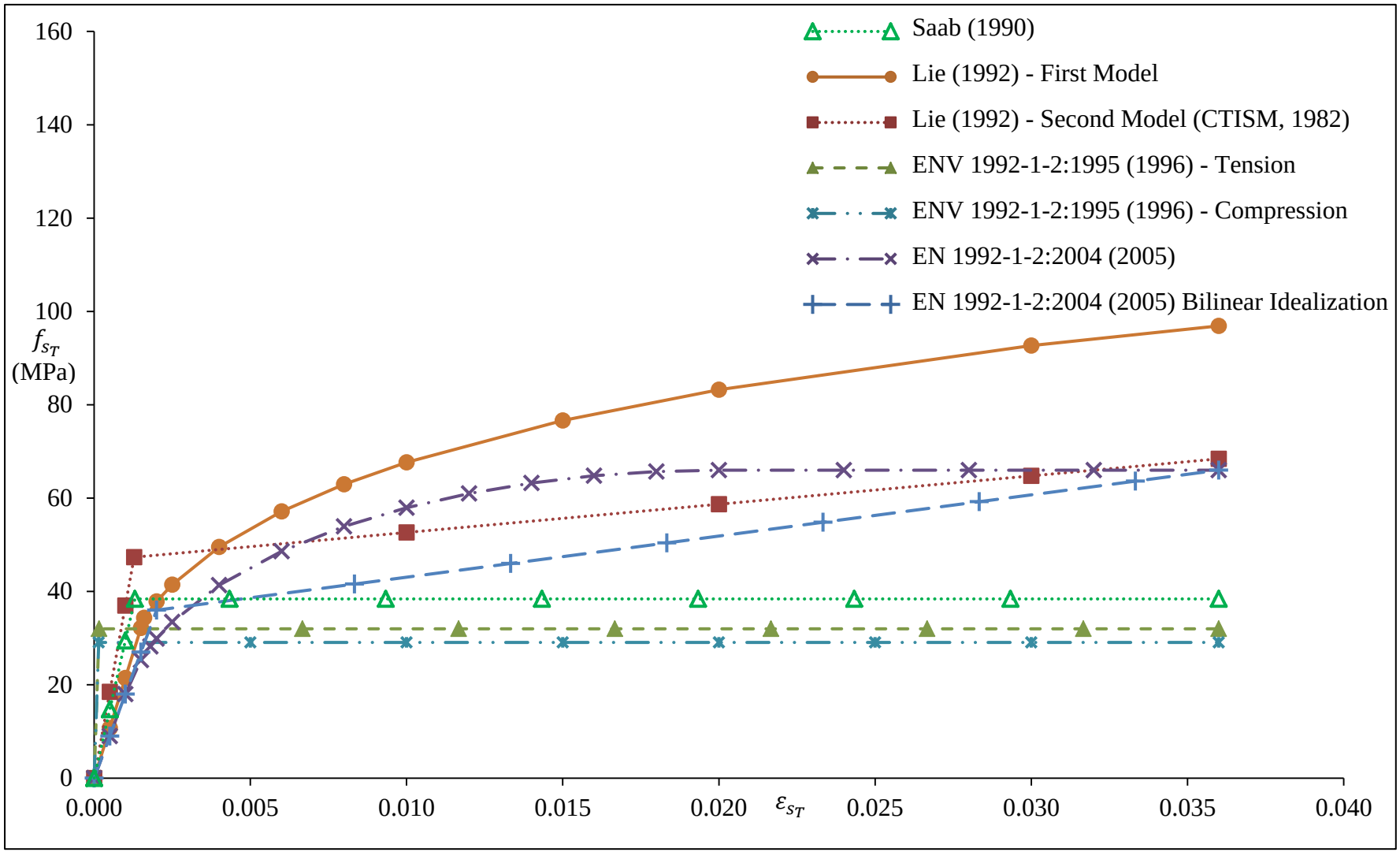

Figure 3-60 Comparison of models for stress-strain response of steel reinforcing bars at 800°C for bars having a yield stress of 400 MPa and an ultimate stress of 600 MPa

3.6 Models Implementation into VecTor3

A fairly exhaustive discussion of the models available in the literature for the thermal and mechanical properties of concrete and steel under elevated temperatures and after cooling (residual properties) has been presented in this chapter. This is in addition to the models available in the literature for the strain associated with elevated temperatures for concrete and steel as well. These models have been compared to each other in the form of an extensive set of plots, depicting a general picture of how different these models are from each other.

Yet, it remains essential to run a more comprehensive comparison and to have the ability to estimate the effect of using these different models on the overall behaviour of reinforced concrete structures under elevated temperatures, on the thermal transfer analysis level and on the structural analysis level. Therefore, all these models have been implemented in VecTor3. This provides the ability to perform multiple coupled heat and structural analyses using different combinations of models for the various properties affecting the behaviour of reinforced concrete structures under elevated temperatures. The results of these analyses can be compared to each other in order to detect the effect that each of those models has on the overall results.

The following are lists of the models and options that have been implemented in VecTor3 for the fire temperature time curve, the thermal expansion strain for both concrete and steel reinforcing bars, the thermal properties of concrete, and the mechanical properties of both concrete and steel reinforcing bars under elevated temperatures.

Fire temperature time curve:

1. Constant temperature (for steady-state heat transfer analysis)
2. User-input model using three key points
3. The ASTM E119 – 12a (2012) model
4. The ISO 834-1:1999 (1999) model

Thermal expansion strain of concrete:

1. The ASCE Manual of Practice (Structural Fire Protection by T. T. Lie, 1992)
2. Lie and Kodur (1996) - for SFRC
3. The Eurocode (ENV 1992-1-2:1995, 1996)
4. The Eurocode (EN 1992-1-2:2004, 2005)
5. Kodur and Sultan (2003) - for HSC
6. Kodur and Sultan (2003) - for SFR-HSC
7. Kodur and Khaliq (2011) - for HSC

Thermal expansion strain of steel:

1. The European Convention for Constructional Steelwork (ECCS) (1983)
2. The ASCE Manual of Practice (Structural Fire Protection by T. T. Lie, 1992)
3. The Eurocode (ENV 1992-1-2:1995, 1996)
4. The Eurocode (EN 1992-1-2:2004, 2005)

Thermal properties of concrete:

Density:

1. Lie and Kodur (1996) - for SFRC
2. Shin et al. (2002)
3. Kodur and Sultan (2003) - for HSC
4. Kodur and Sultan (2003) - for SFR - HSC
5. The Eurocode (EN 1992-1-2:2004, 2005)

Thermal conductivity:

1. The ASCE Manual of Practice (Structural Fire Protection by T. T. Lie, 1992)
2. The Eurocode (ENV 1992-1-2:1995, 1996)
3. Lie and Kodur (1996) - for SFRC
4. Shin et al. (2002)
5. Kodur and Sultan (2003) - for HSC
6. Kodur and Sultan (2003) - for SFR - HSC

7. Kodur et al. (2004) - for HSC
8. The Eurocode (EN 1992-1-2:2004, 2005)
9. Kodur and Khaliq (2011) - for HSC

Specific heat capacity:

1. The ASCE Manual of Practice (Structural Fire Protection by T. T. Lie, 1992)
2. The Eurocode (ENV 1992-1-2:1995, 1996)
3. Shin et al. (2002)
4. Kodur and Sultan (2003) - for HSC
5. Kodur and Sultan (2003) - for SFR - HSC
6. The Eurocode (EN 1992-1-2:2004, 2005)
7. Kodur and Khaliq (2011) - for HSC

Porosity:

1. Gawin et al. (1999)
2. Toumi and Resheidat (2010)

Permeability:

1. Gawin et al. (1999)
2. Tenchev et al. (2001)

Modification factors of the mechanical properties of concrete:

Compressive strength:

1. No modification factor
2. Lie and Lin (1985) - the ASCE Manual of Practice (Structural Fire Protection by T. T. Lie, 1992)
3. Bažant and Chern (1987)
4. Li and Guo (1993)
5. The Eurocode (ENV 1992-1-2:1995, 1996)
6. Lie and Kodur (1996) - for SFRC

7. Chang and Jau (2001) - for siliceous aggregates
8. Cheng et al. (2004) - for HSC
9. The Eurocode (EN 1992-1-2:2004, 2005)
10. Li and Purkiss (2005)
11. Hertz (2005)
12. Aslani and Bastami (2011)

Residual compressive strength:

1. No modification factor
2. Lie et al. (1986)
3. Hertz (2005)
4. Chang et al. (2006) - Model 1
5. Chang et al. (2006) - Model 2

Strain corresponding to peak compressive stress:

1. No modification factor
2. Lie and Lin (1985) - the ASCE Manual of Practice (Structural Fire Protection by T. T. Lie, 1992)
3. Bažant and Chern (1987)
4. The Eurocode (ENV 1992-1-2:1995, 1996)
5. Lie and Kodur (1996) - for SFRC
6. Cheng et al. (2004) - for HSC
7. The Eurocode (EN 1992-1-2:2004, 2005)
8. Li and Purkiss (2005)

Residual strain corresponding to peak compressive stress:

1. No modification factor
2. Chang et al. (2006)

Initial modulus of elasticity:

1. No modification factor
2. Modification factor of peak compressive stress / Modification factor of strain corresponding to peak compressive stress

3. Bažant and Chern (1987)
4. Lu (1989)
5. Li and Guo (1993)
6. Li and Purkiss (2005)
7. Aslani and Bastami (2011)

Residual initial modulus of elasticity strength:

1. No modification factor
2. Chang et al. (2006) - Model 1
3. Chang et al. (2006) - Model 2

Stress-strain curve under elevated temperatures:

1. No modification factor
2. Lie and Lin (1985) - the ASCE Manual of Practice (Structural Fire Protection by T. T. Lie, 1992)
3. Cheng et al. (2004) - for HSC
4. The Eurocode (EN 1992-1-2:2004, 2005)
5. Aslani and Bastami (2011)

Tensile strength:

1. No modification factor
2. Bažant and Chern (1987)
3. Li and Guo (1993)
4. The Eurocode (ENV 1992-1-2:1995, 1996)
5. The Eurocode (EN 1992-1-2:2004, 2005)
6. Song et al. (2007)
7. Moftah (2008)
8. Dwaikat and Kodur (2009)
9. Aslani and Bastami (2011)

Residual tensile strength:

1. No modification factor

2. Xie and Qian (1998) - Model 1
3. Xie and Qian (1998) - Model 2
4. Chang et al. (2006)

Modification factors of the mechanical properties of steel reinforcing bars:

Yield stress:

1. No modification factor
2. Brockenbrough (1970)
3. The Centre Technique Industriel de la Construction Métallique (CTICM) (1982) - the ASCE Manual of Practice (Structural Fire Protection by T. T. Lie, 1992)
4. The European Convention for Constructional Steelwork (ECCS) (1983)
5. Saab (1990)
6. The Eurocode (ENV 1992-1-2:1995, 1996) - loading based
7. The Eurocode (ENV 1992-1-2:1995, 1996) - tension model
8. The Eurocode (ENV 1992-1-2:1995, 1996) - compression model
9. The Eurocode (EN 1992-1-2:2004, 2005)

Ultimate stress:

1. No modification factor
2. The Eurocode (EN 1992-1-2:2004, 2005)

Young's modulus:

1. No modification factor
2. Brockenbrough (1970)
3. The Centre Technique Industriel de la Construction Métallique (CTICM) (1982) - the ASCE Manual of Practice (Structural Fire Protection by T. T. Lie, 1992)
4. The European Convention for Constructional Steelwork (ECCS) (1983)
5. Saab (1990)
6. The Eurocode (EN 1992-1-2:2004, 2005)

These models can be selected in the coupled heat and structural analysis in VecTor3 in any combination. In addition, all the models relating to the typical structural analysis of reinforced concrete structures under normal temperatures and the advanced mechanisms of concrete and steel that are available in VecTor3 (as previously mentioned) can be selected in any combination as well. This provides a wide platform for a comprehensive parametric study on the global effect of all these models on the overall behaviour of reinforced concrete structures under elevated temperatures.

Chapter 4
Heat Transfer Analysis Computational Theory

4.1 Introduction

In this chapter, the formulation for a time-stepping analysis scheme aiming at modelling reinforced concrete structures subjected to fire will be discussed. A step-by-step calculation procedure for the analysis is presented in Appendix C, together with a flow chart showing the main framework of how this type of analysis is handled within the structural analysis context.

The fundamental theories and concepts required for the analysis of steady and transient heat flow through concrete will be discussed, followed by the formulation of the governing differential equations of the analysis and their discretization for the purpose of the finite element solution. Finally, the solution procedure for the finite difference time discretization will be discussed.

4.2 Governing Fundamental Laws and Principles of Physics

In order to reach the set of differential equations required to analyze the transient transfer of heat alone, or heat and moisture coupled together, through concrete, many fundamental laws and principles of physics must be employed. One main principle that has many applications and is heavily used in the formulations presented in this section is the law of conservation of mass, established by the French chemist Antoine Lavoisier in 1774. Based on this law, the laws of water conservation, water vapour conservation, and air conservation were derived. These laws and their application in the formulation of the governing differential equations are discussed in this section.

- The law of water conservation

Utilizing the fact that the amount of water in the system remains constant throughout the entire transfer process, the rate of change (or the gain) of the mass of liquid water per unit

volume of concrete, $\bar{\rho}_L$, should always be equal to the summation of the gradient of the mass flux of liquid water per unit area of concrete, ∇J_L, which is the liquid water transferred by convection (a loss of mass), the rate of evaporation of liquid water per unit volume of concrete, $\dot{E}_L$, (another loss of mass), and the rate of change of the mass of liquid water resulting from the dehydration of the water chemically bound in the cement paste of concrete, $\bar{\rho}_D$, (a gain of mass). This law can be presented in the equation form as:

$$\frac{\partial \bar{\rho}_L}{\partial t} = -\nabla J_L - \dot{E}_L + \frac{\partial \bar{\rho}_D}{\partial t} \tag{4.1}$$

- The law of water vapour conservation

For water vapour, the rate of change (or the gain) of the mass of water vapour per unit volume of concrete, $\bar{\rho}_V$ should always be equal to the summation of the gradient of the mass flux of water vapour per unit area of concrete, ∇J_V, which is the water vapour transferred by convection (a loss of mass), and the rate of evaporation of liquid water per unit volume of concrete, $\dot{E}_L$, which is considered as a gain in mass in the case of water vapour as opposed to being a loss of mass in the case of liquid water as previously mentioned. Expressing this concept in equation form yields Equation (4.2).

$$\frac{\partial \bar{\rho}_V}{\partial t} = -\nabla J_V + \dot{E}_L \tag{4.2}$$

- The law of air conservation

In the case of air, as there is no change in form as in the case of water (changing from liquid to vapour), the law of conservation only involves the rate of change (or the gain) of the mass of dry air per unit volume of concrete, $\bar{\rho}_A$, being equal to the gradient of the mass flux of dry air per unit area of concrete, ∇J_A, which is the air lost by convection (a loss of mass). In equation form:

$$\frac{\partial \bar{\rho}_A}{\partial t} = -\nabla J_A \tag{4.3}$$

- The law of energy conservation

This law, first documented and formulated by Mayer et al. (1929), requires that the rate of change of energy per unit volume of concrete should always be equal to the summation of the rate of change of energy consumed through thermal conduction, which

is given by the gradient of the heat flux density of concrete, $\vec{q}$, the rate of change in energy consumed through convection (or fluid flow), the rate of change of energy consumed for the evaporation of liquid water, and the rate of change of energy consumed in releasing the chemically-bound water in the cement paste of concrete. Hence,

$$\rho_T c_T \frac{\partial T}{\partial t} = -\nabla(\vec{q}) - (\rho_T c_T v)\nabla T - \lambda_E \dot{E}_L - \lambda_D \frac{\partial \bar{\rho}_D}{\partial t} \tag{4.4}$$

where ρ_T and c_T are the density and specific heat capacity of concrete with all its constituents under elevated temperatures (dry skeleton, liquid water, water vapour, and air), respectively; v is the velocity of transport of fluid through concrete; T is temperature; t is time; and λ_E and λ_D are the specific heat of evaporation and the specific heat of dehydration of chemically-bound water, respectively.

However, according to Fourier's law (Fourier, 1822), or the law of heat conduction, the rate of change of energy consumed through thermal conduction can be related to the thermal conductivity of concrete, k, according to the following relation:

$$\vec{q} = -k\nabla T \tag{4.5}$$

which converts Equation (4.4) into the form:

$$\rho_T c_T \frac{\partial T}{\partial t} = -\nabla(-k\nabla T) - (\rho_T c_T v)\nabla T - \lambda_E \dot{E}_L - \lambda_D \frac{\partial \bar{\rho}_D}{\partial t} \tag{4.6}$$

Also, the term $(\rho_T c_T v)$ is a collective term describing the energy transported by the flow of fluid through the porous material (concrete) and is calculated as:

$$(\rho_T c_T v) = \bar{\rho}_L c_{p_L} v_L + \bar{\rho}_V c_{p_V} v_V + \bar{\rho}_A c_{p_A} v_A \tag{4.7}$$

where c_{p_L}, c_{p_V} and c_{p_A} are the specific heat capacities of liquid water, water vapour, and dry air, respectively, and v_L, v_V, and v_A are the velocities of transport of liquid water, water vapour and dry air, respectively.

However, in this study, that energy component will be combined with the energy consumed through thermal conduction, $\vec{q}$, substituting $-\nabla(-k\nabla T) - (\rho_T c_T v)\nabla T$ with $-\nabla(-k_{eff}\nabla T)$ where k_{eff} will describe the effective thermal conductivity of concrete measured experimentally so it combines the energy consumed for conduction as well as that consumed for convection for the current moisture content of concrete.

Therefore $$-\nabla(-k\nabla T) - (\rho_T c_T v)\nabla T = -\nabla(-k_{eff}\nabla T) \quad (4.8)$$

Having discussed the previous governing laws and principles, two cases of transient flow analysis can be considered depending on the type of results required from the analysis: coupled heat and moisture transfer analysis and thermal transfer analysis with its cases of conduction and convection.

4.3 Coupled Heat and Moisture Transfer Analysis

4.3.1 Introduction

This section discusses in detail the theory, governing equations, and finite element implementation for the procedure of heat and moisture transfer analysis through concrete. This process is a coupled process governed by temperature, pressure, and moisture gradients as driving forces, yielding the temperature, T, the pressure of gaseous mixture, P_G, and the mass of water vapour phase per unit volume of the gaseous mixture, $\tilde{\rho}_V$, through the depth of concrete as outputs. The formulations presented in this section are composed of original contributions of the author, in addition to a combination of the works of Tenchev et al. (2001) and Davie et al. (2006).

4.3.2 Governing Differential Equations

In addition to all the laws and principles discussed previously, it should also be noted at this point that the pressure of the gaseous mixture in concrete, P_G, is the summation of the partial pressures of the air and water vapour comprising the gaseous mixture, P_A and P_V, respectively; hence,

$$P_G = P_A + P_V \quad (4.9)$$

The same concept also applies to the masses of the fluids so that

$$\tilde{\rho}_G = \tilde{\rho}_A + \tilde{\rho}_V \quad (4.10)$$

where $\tilde{\rho}_G$, $\tilde{\rho}_L$, $\tilde{\rho}_V$ are the masses of the gaseous, liquid water, and water vapour phases per unit volume of the gaseous mixture, respectively. This, consequently, means that v_V and

v_A are equal and can be substituted in Equation (4.7) by the collective term 'v_G' as the velocity of transport for the whole gaseous mixture.

Another term to be introduced here is ε, which represents the volume fraction of a particular phase, meaning that ε is the ratio of the volume of a particular phase to the entire volume of concrete.

Hence, $$\bar{\rho}_A = \varepsilon_G \tilde{\rho}_A \tag{4.11}$$

and $$\bar{\rho}_V = \varepsilon_G \tilde{\rho}_V \tag{4.12}$$

Also $$\varepsilon_L = \frac{\bar{\rho}_L}{\rho_L} \tag{4.13}$$

where ρ_L is the density of water and ε_G and ε_L are the volume fractions of the gaseous mixture and liquid water respectively, with their sum equal to the porosity of concrete, ϕ.

Thus $$\phi = \varepsilon_L + \varepsilon_G \tag{4.14}$$

Now, by substituting for $\bar{\rho}_A$ from Equation (4.11) in Equation (4.3), the following equation is obtained:

$$\frac{\partial(\varepsilon_G \tilde{\rho}_A)}{\partial t} = -\nabla J_A \tag{4.15}$$

By adding Equations (4.1) and (4.2), eliminating the rate of evaporation of liquid water per unit volume of concrete, $\dot{E}_L$, and substituting for $\bar{\rho}_V$ from Equation (4.12), the following equation can be reached:

$$\frac{\partial(\varepsilon_G \tilde{\rho}_V)}{\partial t} + \frac{\partial \bar{\rho}_L}{\partial t} - \frac{\partial \bar{\rho}_D}{\partial t} = -\nabla(J_V + J_L) \tag{4.16}$$

Finally, by substituting for the rate of evaporation of liquid water per unit volume of concrete, $\dot{E}_L$, from Equation (4.1) into Equation (4.4), one reaches the following expression:

$$\rho_T c_T \frac{\partial T}{\partial t} - \lambda_E \frac{\partial \bar{\rho}_L}{\partial t} + (\lambda_D + \lambda_E) \frac{\partial \bar{\rho}_D}{\partial t} = \nabla(k \nabla T) + \lambda_E \nabla J_L - (\rho_T c_T v) \nabla T \tag{4.17}$$

The three governing differential equations for the coupled heat and moisture transfer through concrete are thus deduced and represented in Equations (4.15), (4.16), and (4.17).

These three equations shall be solved for three unknowns: the temperature, T, the pressure of gaseous mixture, P_G, and the mass of water vapour per unit volume of the gaseous mixture, $\tilde{\rho}_V$. All these unknowns will be calculated through the depth of concrete. In the following sections the procedure for the solution will be presented.

4.3.3 Simplifying the Governing Equations System

In order to solve the system of governing equations presented in the previous section, some additional laws and principles will need to be discussed and employed. The following is a summary of the most significant ones that will be needed for the solution procedure:

- Fick's Law of Diffusion

The law, presented by Fick (1855), states that the flux of diffusion goes from the regions with high concentration to those with lower concentration, in an amount proportional to the concentration gradient. Hence, if J_A and J_V are the mass fluxes of air and water vapour per unit area of concrete, respectively, they can be computed using the following expression:

$$J_A = -D_{AV}\nabla\bar{\rho}_A \tag{4.18}$$

$$J_V = -D_{AV}\nabla\bar{\rho}_V \tag{4.19}$$

where D_{AV} is the mass diffusivity (or diffusion coefficient) of air or water vapour in concrete, defined in Appendix B.

In addition to the one term in Equations (4.18) and (4.19), another component of the mass flux is added in the form $\bar{\rho}_A v_A$ and $\bar{\rho}_V v_V$ establishing the following expression for the flux of diffusion:

$$J_A = \bar{\rho}_A v_A - D_{AV}\nabla\bar{\rho}_A \tag{4.20}$$

and

$$J_V = \bar{\rho}_V v_V - D_{AV}\nabla\bar{\rho}_V \tag{4.21}$$

Similarly,

$$J_L = \bar{\rho}_L v_L \tag{4.22}$$

where the term resulting from Fick's law of diffusion obviously does not appear in the case of the liquid water flux in Equation (4.22).

• Darcy's Law

This law, presented by Darcy (1856), postulates that the rate of discharge of a fluid through a porous medium from one region to another is proportional to its dynamic viscosity and the gradient of the pressure between these two regions as follows:

$$v_L = -\frac{K_L}{\mu_L}\nabla P_L \tag{4.23}$$

$$v_G = -\frac{K_G}{\mu_G}\nabla P_G = v_A = v_V \tag{4.24}$$

where v_i is the rate of discharge (or the velocity of discharge) of the fluid, K_i is the relative permeability of concrete for the fluid, μ_i is the dynamic viscosity of the fluid and ∇P_i is the pressure gradient. The subscripts L and G respectively denote the properties of liquid water and the total gaseous mixture consisting of water vapour and air. In this analysis, the pressure of liquid water, P_L, and that of the gaseous mixture, P_G, are assumed to be the same.

$$P_L = P_G \tag{4.25}$$

• Ideal Gas Law

This law, first presented by French engineer and physicist Émile Clapeyron in 1834, relates the gas state to its pressure, volume, and temperature. While the law has many forms, the one that will be used in this study has the following form:

$$P_V = R_V \tilde{\rho}_V T \tag{4.26}$$

$$P_A = R_A \tilde{\rho}_A T \tag{4.27}$$

where R_V and R_A are the specific gas constants of water vapour and dry air, evaluated at 461.5 J/kg°K and 287 J/kg°K, respectively (Çengel, 1998); T is in °K.

Having discussed this set of laws and principles, they will be employed in the following section to transform the differential governing Equations (4.15), (4.16), and (4.17) to more solvable forms for the purpose of obtaining the simplest procedure for finite element analysis.

Each term in Equations (4.15), (4.16), and (4.17) will be simplified by rearranging it to be represented in terms of T, P_G, and $\tilde{\rho}_V$ for the finite element element procedure as follows:

1. Mass Flux of Dry Air:

Substituting for v_A from Equation (4.24) in Equation (4.20),

$$J_A = \bar{\rho}_A \left(-\frac{K_G}{\mu_G}\nabla P_G\right) - D_{AV}\nabla\bar{\rho}_A \tag{4.28}$$

Substituting for $\bar{\rho}_A$ from Equation (4.11), Equation (4.28) will take the following form:

$$J_A = \varepsilon_G\tilde{\rho}_A \left(-\frac{K_G}{\mu_G}\nabla P_G\right) - \varepsilon_G\tilde{\rho}_G D_{AV}\nabla\left(\frac{\tilde{\rho}_A}{\tilde{\rho}_G}\right) \tag{4.29}$$

Since
$$\nabla\left(\frac{\tilde{\rho}_A}{\tilde{\rho}_G}\right) = \nabla\left(\frac{\tilde{\rho}_G - \tilde{\rho}_V}{\tilde{\rho}_G}\right) = -\nabla\left(\frac{\tilde{\rho}_V}{\tilde{\rho}_G}\right) \tag{4.30}$$

While
$$\nabla\left(\frac{\tilde{\rho}_V}{\tilde{\rho}_G}\right) = \frac{\tilde{\rho}_G\nabla\tilde{\rho}_V - \tilde{\rho}_V\nabla\tilde{\rho}_G}{(\tilde{\rho}_G)^2} \tag{4.31}$$

Substituting for $\tilde{\rho}_G$ from Equation (4.10),

$$\begin{aligned}\nabla\left(\frac{\tilde{\rho}_V}{\tilde{\rho}_G}\right) &= \frac{(\tilde{\rho}_A + \tilde{\rho}_V)\nabla\tilde{\rho}_V - (\tilde{\rho}_V)\nabla(\tilde{\rho}_A + \tilde{\rho}_V)}{(\tilde{\rho}_G)^2} \\ &= \frac{\tilde{\rho}_A\nabla\tilde{\rho}_V - \tilde{\rho}_V\nabla\tilde{\rho}_A}{(\tilde{\rho}_G)^2}\end{aligned} \tag{4.32}$$

While from Equation (4.27):

$$\tilde{\rho}_A = \frac{P_A}{R_A T} \tag{4.33}$$

Substituting for P_A from Equation (4.9):

$$\tilde{\rho}_A = \frac{P_G - P_V}{R_A T} = \frac{P_G}{R_A T} - \frac{P_V}{R_A T} \tag{4.34}$$

Substituting for P_V from Equation (4.26):

$$\tilde{\rho}_A = \frac{P_G}{R_A T} - \frac{R_V\tilde{\rho}_V}{R_A} \tag{4.35}$$

Therefore,
$$\nabla\tilde{\rho}_A = \frac{T\nabla P_G - P_G\nabla T}{R_A T^2} - \frac{R_V}{R_A}\nabla\tilde{\rho}_V \tag{4.36}$$

Rearranging: $$\nabla\tilde{\rho}_A = \left(-\frac{P_G}{R_A T^2}\right)\nabla T + \left(\frac{1}{R_A T}\right)\nabla P_G + \left(-\frac{R_V}{R_A}\right)\nabla\tilde{\rho}_V \quad (4.37)$$

Substituting in Equation (4.32) and rearranging:

$$\nabla\left(\frac{\tilde{\rho}_V}{\tilde{\rho}_G}\right) = \left(\frac{\tilde{\rho}_V P_G}{(\tilde{\rho}_G)^2 R_A T^2}\right)\nabla T + \left(-\frac{\tilde{\rho}_V}{(\tilde{\rho}_G)^2 R_A T}\right)\nabla P_G + \left(\frac{\tilde{\rho}_A}{(\tilde{\rho}_G)^2} + \frac{\tilde{\rho}_V R_V}{(\tilde{\rho}_G)^2 R_A}\right)\nabla\tilde{\rho}_V \quad (4.38)$$

Using Equation (4.30) and rearranging:

$$\nabla\left(\frac{\tilde{\rho}_A}{\tilde{\rho}_G}\right) = \left(-\frac{\tilde{\rho}_V P_G}{(\tilde{\rho}_G)^2 R_A T^2}\right)\nabla T + \left(\frac{\tilde{\rho}_V}{(\tilde{\rho}_G)^2 R_A T}\right)\nabla P_G + \left(-\frac{\tilde{\rho}_A}{(\tilde{\rho}_G)^2} - \frac{\tilde{\rho}_V R_V}{(\tilde{\rho}_G)^2 R_A}\right)\nabla\tilde{\rho}_V \quad (4.39)$$

Substituting in Equation (4.29) and rearranging:

$$-J_A = \left(-\frac{\varepsilon_G D_{AV}\tilde{\rho}_V P_G}{\tilde{\rho}_G R_A T^2}\right)\nabla T + \left(\frac{K_G}{\mu_G}\varepsilon_G\tilde{\rho}_A + \frac{\varepsilon_G D_{AV}\tilde{\rho}_V}{\tilde{\rho}_G R_A T}\right)\nabla P_G + \left(-\frac{\varepsilon_G D_{AV}}{\tilde{\rho}_G}\left(\tilde{\rho}_A + \tilde{\rho}_V\frac{R_V}{R_A}\right)\right)\nabla\tilde{\rho}_V \quad (4.40)$$

Therefore $$-J_A = K_{AT}\nabla T + K_{AP}\nabla P_G + K_{AV}\nabla\tilde{\rho}_V \quad (4.41)$$

2. Mass Flux of Water Vapour:

Substituting for v_V from Equation (4.24) in Equation (4.19):

$$J_V = \bar{\rho}_V\left(-\frac{K_G}{\mu_G}\nabla P_G\right) - D_{AV}\nabla\bar{\rho}_V \quad (4.42)$$

Substituting for $\bar{\rho}_V$ from Equation (4.12), Equation (4.42) will take the following form:

$$J_V = \varepsilon_G\tilde{\rho}_V\left(-\frac{K_G}{\mu_G}\nabla P_G\right) - \varepsilon_G\tilde{\rho}_G D_{AV}\nabla\left(\frac{\tilde{\rho}_V}{\tilde{\rho}_G}\right) \quad (4.43)$$

Substituting for $\nabla\left(\frac{\tilde{\rho}_V}{\tilde{\rho}_G}\right)$ from Equation (4.38) and rearranging:

$$J_V = \left(\frac{-\varepsilon_G D_{AV}\tilde{\rho}_V P_G}{\tilde{\rho}_G R_A T^2}\right)\nabla T + \left(\frac{\varepsilon_G D_{AV}\tilde{\rho}_V}{\tilde{\rho}_G R_A T} - \varepsilon_G\tilde{\rho}_V\frac{K_G}{\mu_G}\right)\nabla P_G + \left(-\frac{\varepsilon_G D_{AV}}{\tilde{\rho}_G}\left(\tilde{\rho}_A + \tilde{\rho}_V\frac{R_V}{R_A}\right)\right)\nabla\tilde{\rho}_V \quad (4.44)$$

Rearranging

$$-J_V = \left(\frac{\varepsilon_G D_{AV} \tilde{\rho}_V P_G}{\tilde{\rho}_G R_A T^2}\right)\nabla T + \left(\varepsilon_G \tilde{\rho}_V \frac{K_G}{\mu_G} - \frac{\varepsilon_G D_{AV} \tilde{\rho}_V}{\tilde{\rho}_G R_A T}\right)\nabla P_G + \left(\frac{\varepsilon_G D_{AV}}{\tilde{\rho}_G}\left(\tilde{\rho}_A + \tilde{\rho}_V \frac{R_V}{R_A}\right)\right)\nabla \tilde{\rho}_V \quad (4.45)$$

Therefore $$-J_V = K_{MT}\nabla T + K_{VP}\nabla P_G + K_{MV}\nabla \tilde{\rho}_V \quad (4.46)$$

3. Mass Flux of Liquid Water:

By substituting for v_L from Equation (4.23) in Equation (4.22):

$$J_L = -\bar{\rho}_L \frac{K_L}{\mu_L}\nabla P_L \quad (4.47)$$

From Equation (4.25) $$-J_L = \left(\bar{\rho}_L \frac{K_L}{\mu_L}\right)\nabla P_G \quad (4.48)$$

Therefore $$-J_L = (0)\nabla T + K_{LP}\nabla P_G + (0)\nabla \tilde{\rho}_V \quad (4.49)$$

4. Time Derivative of the Mass of Dry Air per Unit Volume of Concrete:

From the basic differentiation principles:

$$\frac{\partial(\varepsilon_G \tilde{\rho}_A)}{\partial t} = \varepsilon_G \frac{\partial \tilde{\rho}_A}{\partial t} + \tilde{\rho}_A \frac{\partial \varepsilon_G}{\partial t} \quad (4.50)$$

Calculating the time derivative of $\tilde{\rho}_A$ from Equation (4.35) and rearranging:

$$\frac{\partial \tilde{\rho}_A}{\partial t} = \left(-\frac{P_G}{R_A T^2}\right)\frac{\partial T}{\partial t} + \left(\frac{1}{R_A T}\right)\frac{\partial P_G}{\partial t} + \left(-\frac{R_V}{R_A}\right)\frac{\partial \tilde{\rho}_V}{\partial t} \quad (4.51)$$

Calculating the time derivative of ε_G from Equation (4.14):

$$\frac{\partial \varepsilon_G}{\partial t} = \frac{\partial \phi}{\partial t} - \frac{\partial \varepsilon_L}{\partial t} \quad (4.52)$$

Therefore, $$\frac{\partial \varepsilon_G}{\partial t} = \frac{\partial \phi}{\partial T}\frac{\partial T}{\partial t} - \frac{\partial \varepsilon_L}{\partial t} \quad (4.53)$$

By calculating the time derivative of ε_L from Equation (4.13),

$$\frac{\partial \varepsilon_L}{\partial t} = \frac{\partial \left(\frac{\bar{\rho}_L}{\rho_L}\right)}{\partial t} = \frac{1}{{\rho_L}^2}\left(\rho_L \frac{\partial \bar{\rho}_L}{\partial t} - \bar{\rho}_L \frac{\partial \rho_L}{\partial t}\right) \tag{4.54}$$

And since $\bar{\rho}_L$ is a function of both T and $\tilde{\rho}_V$, then

$$\frac{\partial \bar{\rho}_L}{\partial t} = \frac{\partial \bar{\rho}_L}{\partial T}\frac{\partial T}{\partial t} + \frac{\partial \bar{\rho}_L}{\tilde{\rho}_V}\frac{\partial \tilde{\rho}_V}{\partial t} \tag{4.55}$$

By substituting in Equation (4.54),

$$\frac{\partial \varepsilon_L}{\partial t} = \frac{1}{{\rho_L}^2}\left(\rho_L\left(\frac{\partial \bar{\rho}_L}{\partial T}\frac{\partial T}{\partial t} + \frac{\partial \bar{\rho}_L}{\tilde{\rho}_V}\frac{\partial \tilde{\rho}_V}{\partial t}\right) - \bar{\rho}_L \frac{\partial \rho_L}{\partial t}\right) \tag{4.56}$$

Rearranging:
$$\frac{\partial \varepsilon_L}{\partial t} = \left(\frac{1}{\rho_L}\frac{\partial \bar{\rho}_L}{\partial T} - \frac{\bar{\rho}_L}{{\rho_L}^2}\frac{\partial \rho_L}{\partial T}\right)\frac{\partial T}{\partial t} + \left(\frac{1}{\rho_L}\frac{\partial \bar{\rho}_L}{\tilde{\rho}_V}\right)\frac{\partial \tilde{\rho}_V}{\partial t} \tag{4.57}$$

Substituting in Equation (4.53):

$$\frac{\partial \varepsilon_G}{\partial t} = \left(\frac{\partial \phi}{\partial T} - \frac{1}{\rho_L}\frac{\partial \bar{\rho}_L}{\partial T} + \frac{\bar{\rho}_L}{{\rho_L}^2}\frac{\partial \rho_L}{\partial T}\right)\frac{\partial T}{\partial t} + \left(-\frac{1}{\rho_L}\frac{\partial \bar{\rho}_L}{\tilde{\rho}_V}\right)\frac{\partial \tilde{\rho}_V}{\partial t} \tag{4.58}$$

Substituting for $\frac{\partial \tilde{\rho}_A}{\partial t}$ from Equation (4.51) and for $\frac{\partial \varepsilon_G}{\partial t}$ from Equation (4.58) in Equation (4.50) and rearranging:

$$\begin{aligned}\frac{\partial(\varepsilon_G \tilde{\rho}_A)}{\partial t} = {} & \left(\tilde{\rho}_A \frac{\partial \phi}{\partial T} - \frac{\tilde{\rho}_A}{\rho_L}\frac{\partial \bar{\rho}_L}{\partial T} + \frac{\tilde{\rho}_A \bar{\rho}_L}{{\rho_L}^2}\frac{\partial \rho_L}{\partial T} - \frac{\varepsilon_G P_G}{R_A T^2}\right)\frac{\partial T}{\partial t} + \left(\frac{\varepsilon_G}{R_A T}\right)\frac{\partial P_G}{\partial t} \\ & + \left(-\varepsilon_G \frac{R_V}{R_A} - \frac{\tilde{\rho}_A}{\rho_L}\frac{\partial \bar{\rho}_L}{\tilde{\rho}_V}\right)\frac{\partial \tilde{\rho}_V}{\partial t}\end{aligned} \tag{4.59}$$

Therefore
$$\frac{\partial(\varepsilon_G \tilde{\rho}_A)}{\partial t} = C_{AT}\frac{\partial T}{\partial t} + C_{AP}\frac{\partial P_G}{\partial t} + C_{AV}\frac{\partial \tilde{\rho}_V}{\partial t} \tag{4.60}$$

5. Time Derivative of the Mass of Water Vapour per Unit Volume of Concrete:

$$\frac{\partial(\varepsilon_G \tilde{\rho}_V)}{\partial t} = \varepsilon_G \frac{\partial \tilde{\rho}_V}{\partial t} + \tilde{\rho}_V \frac{\partial \varepsilon_G}{\partial t} \tag{4.61}$$

Substituting for $\frac{\partial \varepsilon_G}{\partial t}$ from Equation (4.58) and rearranging:

$$\frac{\partial(\varepsilon_G \tilde{\rho}_V)}{\partial t} = \left(\tilde{\rho}_V \frac{\partial \phi}{\partial t} - \frac{\tilde{\rho}_V}{\rho_L}\frac{\partial \bar{\rho}_L}{\partial T} + \frac{\tilde{\rho}_V \bar{\rho}_L}{{\rho_L}^2}\frac{\partial \rho_L}{\partial T}\right)\frac{\partial T}{\partial t} + \left(\varepsilon_G - \frac{\tilde{\rho}_V}{\rho_L}\frac{\partial \bar{\rho}_L}{\tilde{\rho}_V}\right)\frac{\partial \tilde{\rho}_V}{\partial t} \tag{4.62}$$

With all the components simplified, and rearranged to be in terms of T, P_G, and $\tilde{\rho}_V$, they can be assembled for the analysis procedure required to solve the differential governing equations previously derived.

Starting with Equation (4.15), the term $\frac{\partial(\varepsilon_G \tilde{\rho}_A)}{\partial t}$ can be substituted from Equation (4.60) and the term J_A from Equation (4.41); hence

$$C_{AT}\frac{\partial T}{\partial t} + C_{AP}\frac{\partial P_G}{\partial t} + C_{AV}\frac{\partial \tilde{\rho}_V}{\partial t} = \nabla(K_{AT}\nabla T + K_{AP}\nabla P_G + K_{AV}\nabla \tilde{\rho}_V) \tag{4.63}$$

Similarly, in Equation (4.16), $\frac{\partial(\varepsilon_G \tilde{\rho}_V)}{\partial t}$ will be substituted from Equation (4.62), $\frac{\partial \bar{\rho}_L}{\partial t}$ from Equation (4.55), J_V from Equation (4.46), and J_L from Equation (4.49). In addition, the chain rule will be utilized as follows:

$$\frac{\partial \bar{\rho}_D}{\partial t} = \frac{\partial \bar{\rho}_D}{\partial T}\frac{\partial T}{\partial t} \tag{4.64}$$

After rearranging, the equation will have the following form:

$$\begin{aligned}\left(\tilde{\rho}_V \frac{\partial \phi}{\partial T} - \frac{\tilde{\rho}_V}{\rho_L}\frac{\partial \bar{\rho}_L}{\partial T} + \frac{\tilde{\rho}_V \bar{\rho}_L}{{\rho_L}^2}\frac{\partial \rho_L}{\partial T} + \frac{\partial \bar{\rho}_L}{\partial T} - \frac{\partial \bar{\rho}_D}{\partial T}\right)\frac{\partial T}{\partial t} + \frac{(0)(\partial P_G)}{\partial t} \\ + \left(\varepsilon_G - \frac{\tilde{\rho}_V}{\rho_L}\frac{\partial \bar{\rho}_L}{\tilde{\rho}_V} + \frac{\partial \bar{\rho}_L}{\tilde{\rho}_V}\right)\frac{\partial \tilde{\rho}_V}{\partial t} = \nabla(K_{MT}\nabla T + (K_{VP} + K_{LP})\nabla P_G + K_{MV}\nabla \tilde{\rho}_V)\end{aligned} \tag{4.65}$$

or
$$C_{MT}\frac{\partial T}{\partial t} + C_{MP}\frac{\partial P_G}{\partial t} + C_{MV}\frac{\partial \tilde{\rho}_V}{\partial t} = \nabla(K_{MT}\nabla T + K_{MP}\nabla P_G + K_{MV}\nabla \tilde{\rho}_V) \tag{4.66}$$

Finally, using Equations (4.48), (4.55) and (4.64), Equation (4.17) can be rearranged to:

$$\begin{aligned}\left(\rho_T c_T + (\lambda_D + \lambda_E)\frac{\partial \bar{\rho}_D}{\partial T} - \lambda_E \frac{\partial \bar{\rho}_L}{\partial T}\right)\frac{\partial T}{\partial t} + \left(-\lambda_E \frac{\partial \bar{\rho}_L}{\tilde{\rho}_V}\right)\frac{\partial \tilde{\rho}_V}{\partial t} \\ = \nabla\left(k\nabla T + \left(-\lambda_E \bar{\rho}_L \frac{K_L}{\mu_L}\right)\nabla P_G\right) - (\rho Cv)\nabla T\end{aligned} \tag{4.67}$$

Therefore
$$C_{TT}\frac{\partial T}{\partial t}+C_{TP}\frac{\partial P_G}{\partial t}+C_{TV}\frac{\partial \tilde{\rho}_V}{\partial t} = \nabla(K_{TT}\nabla T+K_{TP}\nabla P_G+K_{TV}\nabla\tilde{\rho}_V)-(\rho Cv)\nabla T \tag{4.68}$$

Putting Equations (4.63), (4.66), and (4.68) in the matrix form, the following equation is obtained:

$$\begin{bmatrix} C_{TT} & C_{TP} & C_{TV} \\ C_{AT} & C_{AP} & C_{AV} \\ C_{MT} & C_{MP} & C_{MV} \end{bmatrix}\frac{\partial}{\partial t}\begin{Bmatrix} T \\ P_G \\ \tilde{\rho}_V \end{Bmatrix} = \nabla\left(\begin{bmatrix} K_{TT} & K_{TP} & K_{TV} \\ K_{AT} & K_{AP} & K_{AV} \\ K_{MT} & K_{MP} & K_{MV} \end{bmatrix}\nabla\begin{Bmatrix} T \\ P_G \\ \tilde{\rho}_V \end{Bmatrix}\right)-\begin{bmatrix} (\rho Cv) & 0 & 0 \\ 0 & 0 & 0 \\ 0 & 0 & 0 \end{bmatrix}\nabla\begin{Bmatrix} T \\ P_G \\ \tilde{\rho}_V \end{Bmatrix} \tag{4.69}$$

or
$$C_E\frac{\partial x_E}{\partial t}=\nabla(K_E\nabla x_E)-Kv_E\nabla x_E \tag{4.70}$$

where the expressions for the coefficients C_{TT}, C_{TP}, C_{TV}, C_{AP}, C_{AV}, C_{MT}, C_{MP}, C_{MV}, K_{TT}, K_{TP}, K_{TV}, K_{AT}, K_{AP}, K_{AV}, K_{MT}, K_{MP}, and K_{MV} are presented in Table 4-1.

However, as previously explained, with the use of k_{eff} as shown in Equation (4.8), Equations (4.69) and (4.70) can be reduced to:

$$\begin{bmatrix} C_{TT} & C_{TP} & C_{TV} \\ C_{AT} & C_{AP} & C_{AV} \\ C_{MT} & C_{MP} & C_{MV} \end{bmatrix}\frac{\partial}{\partial t}\begin{Bmatrix} T \\ P_G \\ \tilde{\rho}_V \end{Bmatrix} = \nabla\left(\begin{bmatrix} K_{TT} & K_{TP} & K_{TV} \\ K_{AT} & K_{AP} & K_{AV} \\ K_{MT} & K_{MP} & K_{MV} \end{bmatrix}\nabla\begin{Bmatrix} T \\ P_G \\ \tilde{\rho}_V \end{Bmatrix}\right) \tag{4.71}$$

and
$$C_E\frac{\partial x_E}{\partial t}=\nabla(K_E\nabla x_E) \tag{4.72}$$

Equation (4.72) represents the final set of differential equations required for the finite element solution of the coupled heat and mass transient flow through concrete.

Table 4-1 Coefficients governing the coupled heat and moisture transfer analysis

$C_{TT} = \rho_T c_T + (\lambda_D + \lambda_E)\frac{\partial \bar{\rho}_D}{\partial T} - \lambda_E \frac{\partial \bar{\rho}_L}{\partial T}$	$K_{TT} = k_{eff}$
$C_{TP} = 0$	$K_{TP} = -\lambda_E \bar{\rho}_L \frac{K_L}{\mu_L}$
$C_{TV} = -\lambda_E \frac{\partial \bar{\rho}_L}{\tilde{\rho}_V}$	$K_{TV} = 0$
$C_{AT} = \tilde{\rho}_A \frac{\partial \phi}{\partial t} - \frac{\tilde{\rho}_A}{\rho_L}\frac{\partial \bar{\rho}_L}{\partial T} + \frac{\tilde{\rho}_A \bar{\rho}_L}{{\rho_L}^2}\frac{\partial \rho_L}{\partial T} - \frac{\varepsilon_G P_G}{R_A T^2}$	$K_{AT} = -\frac{\varepsilon_G D_{AV} \tilde{\rho}_V P_G}{\tilde{\rho}_G R_A T^2}$
$C_{AP} = \frac{\varepsilon_G}{R_A T}$	$K_{AP} = \frac{K_G}{\mu_G}\varepsilon_G \tilde{\rho}_A + \frac{\varepsilon_G D_{AV} \tilde{\rho}_V}{\tilde{\rho}_G R_A T}$
$C_{AV} = -\varepsilon_G \frac{R_V}{R_A} - \frac{\tilde{\rho}_A}{\rho_L}\frac{\partial \bar{\rho}_L}{\tilde{\rho}_V}$	$K_{AV} = -\frac{\varepsilon_G D_{AV}}{\tilde{\rho}_G}\left(\tilde{\rho}_A + \tilde{\rho}_V \frac{R_V}{R_A}\right)$
$C_{MT} = \tilde{\rho}_V \frac{\partial \phi}{\partial T} - \frac{\tilde{\rho}_V}{\rho_L}\frac{\partial \bar{\rho}_L}{\partial T} + \frac{\tilde{\rho}_V \bar{\rho}_L}{{\rho_L}^2}\frac{\partial \rho_L}{\partial T} + \frac{\partial \bar{\rho}_L}{\partial T} - \frac{\partial \bar{\rho}_D}{\partial T}$	$K_{MT} = \frac{\varepsilon_G D_{AV} \tilde{\rho}_V P_G}{\tilde{\rho}_G R_A T^2}$
$C_{MP} = 0$	$K_{MP} = \varepsilon_G \tilde{\rho}_V \frac{K_G}{\mu_G} - \frac{\varepsilon_G D_{AV} \tilde{\rho}_V}{\tilde{\rho}_G R_A T} + \bar{\rho}_L \frac{K_L}{\mu_L}$
$C_{MV} = \varepsilon_G - \frac{\tilde{\rho}_V}{\rho_L}\frac{\partial \bar{\rho}_L}{\tilde{\rho}_V} + \frac{\partial \bar{\rho}_L}{\tilde{\rho}_V}$	$K_{MV} = \frac{\varepsilon_G D_{AV}}{\tilde{\rho}_G}\left(\tilde{\rho}_A + \tilde{\rho}_V \frac{R_V}{R_A}\right)$

4.3.4 Boundary Conditions

The boundary conditions for the coupled heat and moisture transfer through concrete in fire will have specific components related to the variables that need to be determined through the analysis which are the temperature, T, the pressure of gaseous mixture, P_G, and the mass of water vapour per unit volume of the gaseous mixture, $\tilde{\rho}_V$, through the depth of concrete.

All the boundary conditions will be associated with the surface exposed to fire; hence, they will be determined in terms of "n", the unit vector normal to the boundary surface exposed to fire in the outward direction.

1. Temperature Boundary Condition

This boundary condition is governed by the energy balance (energy conservation) on the boundary surface, where the energy going from within the body to the boundary surface should always be equal to that going outside the body to the surrounding atmosphere through the same boundary surface. Therefore, the total of the amount of heat energy transferred by conduction from inside the body to the boundary surface, $k\frac{\partial T}{\partial n}$, the amount of heat energy consumed in the evaporation of liquid water through the boundary surface, $\lambda_E J_L n$, and the amount of heat energy dissipated into the surrounding atmosphere though convection, $h(T - T_\infty)$, should all sum up to zero as shown in Equation (4.73). This relation assumes that the mass of the gaseous mixture, composed of air and water vapour, transferred to the boundary surface from inside the body is equal to that dissipated into the surrounding atmosphere. Thus, the heat energy gained by the boundary surface through that transfer is equal to the heat energy lost to the surrounding atmosphere through the same boundary surface.

$$k\frac{\partial T}{\partial n} + \lambda_E J_L n + h(T - T_\infty) = 0 \tag{4.73}$$

where h is the combined convective and radiative heat transfer coefficients on the boundary surface, as shown in Equation (4.74), and T_∞ is the temperature of the surrounding atmosphere.

$$h = h_q + h_r \tag{4.74}$$

where h_q and h_r are the convective and radiative heat transfer coefficients of concrete.

Assuming that the boundary surface of concrete will be completely dry prior to exposure to fire or shortly after, the flux of liquid water, J_L, can be set to zero, converting Equation (4.73) to the final expression for the temperature boundary conditions, where k can be substituted with K_{TT} as discussed earlier.

Therefore $$\frac{\partial T}{\partial n} = -\frac{h}{K_{TT}}(T - T_{\infty}) \tag{4.75}$$

2. Pressure of Gaseous Mixture Boundary Condition

Since the boundary surface is exposed to the surrounding atmosphere, the pressure of any gas existing on it should be equal to the atmospheric pressure. This yields the pressure of gaseous mixture of concrete boundary conditions as follows:

$$P_G = P_{\infty} \tag{4.76}$$

3. Mass of Water Vapour per Unit Volume of the Gaseous Mixture Boundary Condition

Similar to the conservation of energy on the boundary surface discussed earlier, this boundary condition arises from the conservation of mass on the boundary surface, meaning that the flux of water vapour transferring to the boundary surface from within the body shall always be equal to mass of water vapour dissipated to the surrounding atmosphere per unit area of the boundary surface in one second.

Therefore $$J_V n = \beta\left(\tilde{\rho}_V - \tilde{\rho}_{V_{\infty}}\right) \tag{4.77}$$

where β is the water vapour transfer coefficient and $\tilde{\rho}_{V_{\infty}}$ is the mass of water vapour per unit volume of the gaseous mixture on the boundary surface.

Substituting for J_V from Equation (4.46) and converting the gradient over volume to be over surface:

$$-\left(K_{MT}\frac{\partial T}{\partial n} + K_{VP}\frac{\partial P_G}{\partial n} + K_{MV}\frac{\partial \tilde{\rho}_V}{\partial n}\right) = \beta\left(\tilde{\rho}_V - \tilde{\rho}_{V_{\infty}}\right) \tag{4.78}$$

From Equation (4.76), one can deduce that the gradient of the pressure of the gaseous mixture on the boundary surface will always be equal to zero.

$$\frac{\partial P_G}{\partial n} = 0 \tag{4.79}$$

Substituting for $\frac{\partial T}{\partial n}$ and $\frac{\partial P_G}{\partial n}$ from Equations (4.75) and (4.79), respectively, in Equation (4.78) and rearranging, one reaches the following expression:

$$\frac{\partial \tilde{\rho}_V}{\partial n} = \frac{K_{MT}}{K_{MV}K_{TT}} h(T - T_\infty) - \frac{1}{K_{VV}} \beta\left(\tilde{\rho}_V - \tilde{\rho}_{V_\infty}\right) \tag{4.80}$$

Equation (4.80) represents the third boundary condition for the analysis.

Combining Equation (4.79) with the two other boundary conditions presented in Equations (4.75) and (4.80) in a matrix form, the following equation can be reached:

$$\begin{Bmatrix} \frac{\partial T}{\partial n} \\ \frac{\partial \tilde{\rho}_V}{\partial n} \end{Bmatrix} = \begin{bmatrix} K_{TT} & 0 \\ K_{MT} & K_{MV} \end{bmatrix}^{-1} \begin{Bmatrix} hT_\infty \\ \beta\tilde{\rho}_{V_\infty} \end{Bmatrix} - \begin{bmatrix} K_{TT} & 0 \\ K_{MT} & K_{MV} \end{bmatrix}^{-1} \begin{bmatrix} h & 0 \\ 0 & \beta \end{bmatrix} \begin{Bmatrix} T \\ \tilde{\rho}_V \end{Bmatrix} \tag{4.81}$$

While these two boundary conditions ($\frac{\partial T}{\partial n}$ and $\frac{\partial \tilde{\rho}_V}{\partial n}$) are applied as driving forces in the analysis, the third boundary condition presented in Equation (4.76) is applied as a preset value for the pressure of gaseous mixture at the surface of concrete.

4.3.5 Finite Element Formulation and Procedure

Using the Galerkin weighted residual method (Galerkin, 1915), the weak form of Equation (4.69) has been obtained. The weak form is an integral form of the equation which requires a weaker continuity on the field variables (Liu and Quek, 2003). The use of the weak form produces a set of discretized system equations that are easier to solve. The standard finite element approximation procedure is applied to discretize the variables that need to be calculated (T, P_G, and $\tilde{\rho}_V$) and express them in terms of their nodal components. The discrete system resulting from these operations can be represented in the following first-order differential equation:

$$\mathbf{C}\frac{\partial \mathbf{x}}{\partial t} + \mathbf{K}\mathbf{x} = \mathbf{F} \tag{4.82}$$

where
$$\mathbf{C} = \sum_{E=1}^{N_E} \int_{\Omega} (N^T C_E N) d\Omega \tag{4.83}$$

$$\mathbf{K} = \sum_{E=1}^{N_E} \int_{\Omega} (\nabla N^T K_E \nabla N + N^T K v_E \nabla N) d\Omega + \int_{\Gamma} \left(N^T K_E F_{K_E} N\right) d\Gamma \tag{4.84}$$

or according to Equation (4.8), Kv_E can be omitted when using the effective thermal conductivity of concrete, k_{eff}, experimentally determined at the current moisture content, which can easily be done:

$$\mathbf{K} = \sum_{E=1}^{N_E} \int_{\Omega} (\nabla N^T K_E \nabla N) d\Omega + \int_{\Gamma} \left(N^T K_E F_{K_E} N\right) d\Gamma \tag{4.85}$$

$$\mathbf{F} = \sum_{E=1}^{N_E} \int_{\Gamma} \left(N^T K_E F_{\infty_E}\right) d\Gamma \tag{4.86}$$

and
$$\mathbf{x} = \sum_{E=1}^{N_E} x_E \tag{4.87}$$

where C_E, K_E, Kv_E, and x_E are defined in Equation (4.70); N_E is the number of elements in the system; E is the element number; N is the shape functions matrix; Ω is the whole domain; and Γ is the domain of the boundary surface exposed to fire.

Also,
$$F_{K_e} = \begin{bmatrix} K_{TT} & 0 \\ K_{MT} & K_{MV} \end{bmatrix}^{-1} \begin{bmatrix} h & 0 \\ 0 & \beta \end{bmatrix} \xrightarrow{\text{expanded to}} \begin{bmatrix} \frac{h}{K_{TT}} & 0 & 0 \\ 0 & 0 & 0 \\ -\frac{K_{MT} h}{(K_{TT} K_{MV})} & 0 & \frac{\beta}{K_{MV}} \end{bmatrix} \tag{4.88}$$

and
$$F_{\infty_e} = \begin{bmatrix} K_{TT} & 0 \\ K_{MT} & K_{MV} \end{bmatrix}^{-1} \begin{Bmatrix} hT_{\infty} \\ \beta \tilde{\rho}_{V_{\infty}} \end{Bmatrix} \xrightarrow{\text{expanded to}} \begin{Bmatrix} \frac{h}{K_{TT}} T_{\infty} \\ 0 \\ -\frac{K_{MT} h}{(K_{TT} K_{MV})} T_{\infty} + \frac{\beta}{K_{MV}} \tilde{\rho}_{V_{\infty}} \end{Bmatrix} \tag{4.89}$$

4.3.6 Three-Dimensional Finite Element Formulation

In this section, the finite element formulation required for the three-dimensional analysis is presented. The exact formulation for the regular hexahedral (brick) eight-noded elements shown in Figure 4-1 will be presented as a straight-forward example, although the procedure for the isoparametric element and other element types is similar. The procedure presented by Liu and Quek (2003) has been used and extended for the purposes of the coupled heat and moisture transfer analysis.

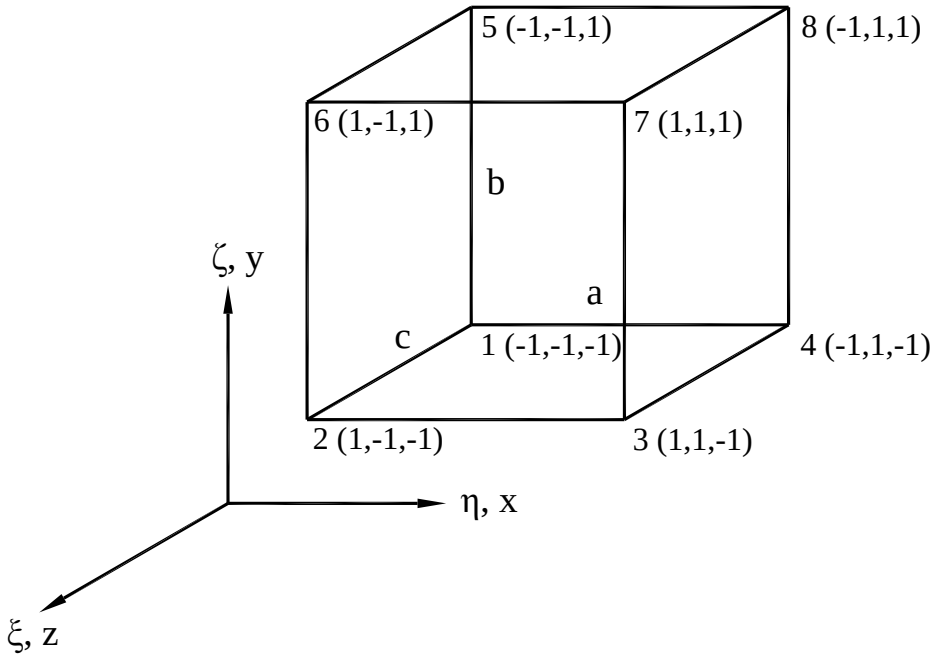

Figure 4-1 Three-dimensional regular hexahedral (brick) eight-noded element

The shape functions for the element in local natural coordinates can be given as:

$$N_i = \frac{1}{8}(1 + \eta\eta_i)(1 + \zeta\zeta_i)(1 + \xi\xi_i) \tag{4.90}$$

where ξ_i, η_i and ζ_i are the local natural coordinates of node i. This function can be expanded in the following form:

$$\begin{aligned} N_1 &= \frac{1}{8}(1-\eta)(1-\zeta)(1-\xi) \\ N_2 &= \frac{1}{8}(1-\eta)(1-\zeta)(1+\xi) \\ N_3 &= \frac{1}{8}(1+\eta)(1-\zeta)(1+\xi) \end{aligned} \tag{4.91}$$

$$N_4 = \frac{1}{8}(1+\eta)(1-\zeta)(1-\xi)$$
$$N_5 = \frac{1}{8}(1-\eta)(1+\zeta)(1-\xi)$$
$$N_6 = \frac{1}{8}(1-\eta)(1+\zeta)(1+\xi)$$
$$N_7 = \frac{1}{8}(1+\eta)(1+\zeta)(1+\xi)$$
$$N_8 = \frac{1}{8}(1+\eta)(1+\zeta)(1-\xi)$$

In order to apply these shape functions to Equations (4.83), (4.84), and (4.86), they are assembled in the shape functions matrix as follows:

$$N = [\mathbf{N_1} \quad \mathbf{N_2} \quad \mathbf{N_3} \quad \mathbf{N_4} \quad \mathbf{N_5} \quad \mathbf{N_6} \quad \mathbf{N_7} \quad \mathbf{N_8}] \tag{4.92}$$

$$\mathbf{N_i} = \begin{bmatrix} N_i & 0 & 0 \\ 0 & N_i & 0 \\ 0 & 0 & N_i \end{bmatrix} \tag{4.93}$$

where $\mathbf{i} = 1,2,\cdots,8$

∇N can also be calculated according to the following relation:

$$\nabla N = [\nabla\mathbf{N_1} \quad \nabla\mathbf{N_2} \quad \nabla\mathbf{N_3} \quad \nabla\mathbf{N_4} \quad \nabla\mathbf{N_5} \quad \nabla\mathbf{N_6} \quad \nabla\mathbf{N_7} \quad \nabla\mathbf{N_8}] \tag{4.94}$$

where
$$\nabla\mathbf{N_i} = \begin{bmatrix} \frac{\partial}{\partial x} & 0 & 0 \\ 0 & \frac{\partial}{\partial x} & 0 \\ 0 & 0 & \frac{\partial}{\partial x} \\ \frac{\partial}{\partial y} & 0 & 0 \\ 0 & \frac{\partial}{\partial y} & 0 \\ 0 & 0 & \frac{\partial}{\partial y} \\ \frac{\partial}{\partial z} & 0 & 0 \\ 0 & \frac{\partial}{\partial z} & 0 \\ 0 & 0 & \frac{\partial}{\partial z} \end{bmatrix} \begin{bmatrix} N_i & 0 & 0 \\ 0 & N_i & 0 \\ 0 & 0 & N_i \end{bmatrix} = \begin{bmatrix} \frac{\partial N_i}{\partial x} & 0 & 0 \\ 0 & \frac{\partial N_i}{\partial x} & 0 \\ 0 & 0 & \frac{\partial N_i}{\partial x} \\ \frac{\partial N_i}{\partial y} & 0 & 0 \\ 0 & \frac{\partial N_i}{\partial y} & 0 \\ 0 & 0 & \frac{\partial N_i}{\partial y} \\ \frac{\partial N_i}{\partial z} & 0 & 0 \\ 0 & \frac{\partial N_i}{\partial z} & 0 \\ 0 & 0 & \frac{\partial N_i}{\partial z} \end{bmatrix} \tag{4.95}$$

However, since the shape functions are presented in natural coordinates, ξ_i, η_i, and ζ_i, the chain rule of partial differentiation will be employed to calculate their derivatives with respect to the Cartesian coordinate system, thus

$$\begin{aligned}\frac{\partial N_i}{\partial x} &= \frac{\partial N_i}{\partial \xi}\frac{\partial N_\xi}{\partial x} + \frac{\partial N_i}{\partial \eta}\frac{\partial N_\eta}{\partial x} + \frac{\partial N_i}{\partial \zeta}\frac{\partial N_\zeta}{\partial x} \\ \frac{\partial N_i}{\partial y} &= \frac{\partial N_i}{\partial \xi}\frac{\partial N_\xi}{\partial y} + \frac{\partial N_i}{\partial \eta}\frac{\partial N_\eta}{\partial y} + \frac{\partial N_i}{\partial \zeta}\frac{\partial N_\zeta}{\partial y} \\ \frac{\partial N_i}{\partial z} &= \frac{\partial N_i}{\partial \xi}\frac{\partial N_\xi}{\partial z} + \frac{\partial N_i}{\partial \eta}\frac{\partial N_\eta}{\partial z} + \frac{\partial N_i}{\partial \zeta}\frac{\partial N_\zeta}{\partial z}\end{aligned} \tag{4.96}$$

or

$$\begin{Bmatrix} \frac{\partial N_i}{\partial \eta} \\ \frac{\partial N_i}{\partial \zeta} \\ \frac{\partial N_i}{\partial \xi} \end{Bmatrix} = J \begin{Bmatrix} \frac{\partial N_i}{\partial x} \\ \frac{\partial N_i}{\partial y} \\ \frac{\partial N_i}{\partial z} \end{Bmatrix} \tag{4.97}$$

where J is defined as:

$$J = \begin{bmatrix} \frac{\partial x}{\partial \eta} & \frac{\partial y}{\partial \eta} & \frac{\partial z}{\partial \eta} \\ \frac{\partial x}{\partial \zeta} & \frac{\partial y}{\partial \zeta} & \frac{\partial z}{\partial \zeta} \\ \frac{\partial x}{\partial \xi} & \frac{\partial y}{\partial \xi} & \frac{\partial z}{\partial \xi} \end{bmatrix} \tag{4.98}$$

and is called the Jacobian matrix.

Returning back to the basic definition of the shape functions where

$$x = N_1x_1 + N_2x_2 + N_3x_3 + N_4x_4 + N_5x_5 + N_6x_6 + N_7x_7 + N_8x_8 \tag{4.99}$$

Thus $$\frac{\partial x}{\partial \eta} = \frac{\partial N_1}{\partial \eta}x_1 + \frac{\partial N_2}{\partial \eta}x_2 + \frac{\partial N_3}{\partial \eta}x_3 + \frac{\partial N_4}{\partial \eta}x_4 + \frac{\partial N_5}{\partial \eta}x_5 + \frac{\partial N_6}{\partial \eta}x_6 + \frac{\partial N_7}{\partial \eta}x_7 + \frac{\partial N_8}{\partial \eta}x_8 \tag{4.100}$$

Employing Equation (4.100) and applying the same concept for the y and z coordinates in Equation (4.98), the following expression is reached:

$$J = \begin{bmatrix} \frac{\partial N_1}{\partial \eta} & \frac{\partial N_2}{\partial \eta} & \frac{\partial N_3}{\partial \eta} & \frac{\partial N_4}{\partial \eta} & \frac{\partial N_5}{\partial \eta} & \frac{\partial N_6}{\partial \eta} & \frac{\partial N_7}{\partial \eta} & \frac{\partial N_8}{\partial \eta} \\ \frac{\partial N_1}{\partial \zeta} & \frac{\partial N_2}{\partial \zeta} & \frac{\partial N_3}{\partial \zeta} & \frac{\partial N_4}{\partial \zeta} & \frac{\partial N_5}{\partial \zeta} & \frac{\partial N_6}{\partial \zeta} & \frac{\partial N_7}{\partial \zeta} & \frac{\partial N_8}{\partial \zeta} \\ \frac{\partial N_1}{\partial \xi} & \frac{\partial N_2}{\partial \xi} & \frac{\partial N_3}{\partial \xi} & \frac{\partial N_4}{\partial \xi} & \frac{\partial N_5}{\partial \xi} & \frac{\partial N_6}{\partial \xi} & \frac{\partial N_7}{\partial \xi} & \frac{\partial N_8}{\partial \xi} \end{bmatrix} \begin{bmatrix} x_1 & y_1 & z_1 \\ x_2 & y_2 & z_2 \\ x_3 & y_3 & z_3 \\ x_4 & y_4 & z_4 \\ x_5 & y_5 & z_5 \\ x_6 & y_6 & z_6 \\ x_7 & y_7 & z_7 \\ x_8 & y_8 & z_8 \end{bmatrix} \tag{4.101}$$

where

$$\frac{\partial N_1}{\partial \eta} = -\frac{1}{8}(1-\zeta)(1-\xi) \quad \frac{\partial N_1}{\partial \zeta} = -\frac{1}{8}(1-\eta)(1-\xi) \quad \frac{\partial N_1}{\partial \xi} = -\frac{1}{8}(1-\eta)(1-\zeta)$$
$$\frac{\partial N_2}{\partial \eta} = -\frac{1}{8}(1-\zeta)(1+\xi) \quad \frac{\partial N_2}{\partial \zeta} = -\frac{1}{8}(1-\eta)(1+\xi) \quad \frac{\partial N_2}{\partial \xi} = \frac{1}{8}(1-\eta)(1-\zeta)$$
$$\frac{\partial N_3}{\partial \eta} = \frac{1}{8}(1-\zeta)(1+\xi) \quad \frac{\partial N_3}{\partial \zeta} = -\frac{1}{8}(1+\eta)(1+\xi) \quad \frac{\partial N_3}{\partial \xi} = \frac{1}{8}(1+\eta)(1-\zeta)$$
$$\frac{\partial N_4}{\partial \eta} = \frac{1}{8}(1-\zeta)(1-\xi) \quad \frac{\partial N_4}{\partial \zeta} = -\frac{1}{8}(1+\eta)(1-\xi) \quad \frac{\partial N_4}{\partial \xi} = -\frac{1}{8}(1+\eta)(1-\zeta)$$
$$\frac{\partial N_5}{\partial \eta} = -\frac{1}{8}(1+\zeta)(1-\xi) \quad \frac{\partial N_5}{\partial \zeta} = \frac{1}{8}(1-\eta)(1-\xi) \quad \frac{\partial N_5}{\partial \xi} = -\frac{1}{8}(1-\eta)(1+\zeta)$$
$$\frac{\partial N_6}{\partial \eta} = -\frac{1}{8}(1+\zeta)(1+\xi) \quad \frac{\partial N_6}{\partial \zeta} = \frac{1}{8}(1-\eta)(1+\xi) \quad \frac{\partial N_6}{\partial \xi} = \frac{1}{8}(1-\eta)(1+\zeta)$$
$$\frac{\partial N_7}{\partial \eta} = \frac{1}{8}(1+\zeta)(1+\xi) \quad \frac{\partial N_7}{\partial \zeta} = \frac{1}{8}(1+\eta)(1+\xi) \quad \frac{\partial N_7}{\partial \xi} = \frac{1}{8}(1+\eta)(1+\zeta)$$
$$\frac{\partial N_8}{\partial \eta} = \frac{1}{8}(1+\zeta)(1-\xi) \quad \frac{\partial N_8}{\partial \zeta} = \frac{1}{8}(1+\eta)(1-\xi) \quad \frac{\partial N_8}{\partial \xi} = -\frac{1}{8}(1+\eta)(1+\zeta)$$

Employing the fact that for a regular hexahedral element as the one shown in Figure 4-1, $x_1 = x_2 = x_5 = x_6$, $x_3 = x_4 = x_7 = x_8$, $y_1 = y_2 = y_3 = y_4$, $y_5 = y_6 = y_7 = y_8$, and $z_2 = z_3 = z_6 = z_7$, in Equation (4.101), J is reduced to:

$$J = \begin{bmatrix} \frac{x_4 - x_1}{2} & 0 & 0 \\ 0 & \frac{y_5 - y_1}{2} & 0 \\ 0 & 0 & \frac{z_2 - z_1}{2} \end{bmatrix} \tag{4.102}$$

But as shown in Figure 4-1, $x_4 - x_1 = a$, $y_5 - y_1 = b$ and $z_2 - z_1 = c$.

Therefore
$$J = \begin{bmatrix} \frac{a}{2} & 0 & 0 \\ 0 & \frac{b}{2} & 0 \\ 0 & 0 & \frac{c}{2} \end{bmatrix} \tag{4.103}$$

Substituting in Equation (4.97)
$$\begin{Bmatrix} \frac{\partial N_i}{\partial \eta} \\ \frac{\partial N_i}{\partial \zeta} \\ \frac{\partial N_i}{\partial \xi} \end{Bmatrix} = \begin{Bmatrix} \left(\frac{a}{2}\right)\frac{\partial N_i}{\partial x} \\ \left(\frac{b}{2}\right)\frac{\partial N_i}{\partial y} \\ \left(\frac{c}{2}\right)\frac{\partial N_i}{\partial z} \end{Bmatrix} \tag{4.104}$$

Therefore, from Equation (4.95),

$$\nabla \mathbf{N_i} = \begin{bmatrix} \left(\frac{2}{a}\right)\frac{\partial N_i}{\partial \eta} & 0 & 0 \\ 0 & \left(\frac{2}{a}\right)\frac{\partial N_i}{\partial \eta} & 0 \\ 0 & 0 & \left(\frac{2}{a}\right)\frac{\partial N_i}{\partial \eta} \\ \left(\frac{2}{b}\right)\frac{\partial N_i}{\partial \zeta} & 0 & 0 \\ 0 & \left(\frac{2}{b}\right)\frac{\partial N_i}{\partial \zeta} & 0 \\ 0 & 0 & \left(\frac{2}{b}\right)\frac{\partial N_i}{\partial \zeta} \\ \left(\frac{2}{c}\right)\frac{\partial N_i}{\partial \xi} & 0 & 0 \\ 0 & \left(\frac{2}{c}\right)\frac{\partial N_i}{\partial \xi} & 0 \\ 0 & 0 & \left(\frac{2}{c}\right)\frac{\partial N_i}{\partial \xi} \end{bmatrix} \tag{4.105}$$

Returning to Equations (4.83) and (4.84), in order to calculate the terms $\int_\Omega (N^T C_E N) d\Omega$ and $\int_\Omega (\nabla N^T K_E \nabla N) d\Omega$, $d\Omega$ will be substituted with $dx.dy.dz$ which is equal to $\det[J].d\eta.d\zeta.d\xi$. Also, for calculating $\int_\Omega (\nabla N^T K_E \nabla N) d\Omega$, K_E will have to be extrapolated into the following form:

$$K_E = \begin{bmatrix} K_{TT} & K_{TP} & K_{TV} & 0 & 0 & 0 & 0 & 0 & 0 \\ K_{AT} & K_{AP} & K_{AV} & 0 & 0 & 0 & 0 & 0 & 0 \\ K_{MT} & K_{MP} & K_{MV} & 0 & 0 & 0 & 0 & 0 & 0 \\ 0 & 0 & 0 & K_{TT} & K_{TP} & K_{TV} & 0 & 0 & 0 \\ 0 & 0 & 0 & K_{AT} & K_{AP} & K_{AV} & 0 & 0 & 0 \\ 0 & 0 & 0 & K_{MT} & K_{MP} & K_{MV} & 0 & 0 & 0 \\ 0 & 0 & 0 & 0 & 0 & 0 & K_{TT} & K_{TP} & K_{TV} \\ 0 & 0 & 0 & 0 & 0 & 0 & K_{AT} & K_{AP} & K_{AV} \\ 0 & 0 & 0 & 0 & 0 & 0 & K_{MT} & K_{MP} & K_{MV} \end{bmatrix} \tag{4.106}$$

Both $\int_\Omega (N^T C_E N) d\Omega$ and $\int_\Omega (\nabla N^T K_E \nabla N) d\Omega$ can be calculated as 24×24 matrices whose elements are given in Appendix A.

For the matrices produced from the integration over the boundary surface (i.e. the surface exposed to fire), $\int_\Gamma \left(N^T K_E F_{K_E} N\right) d\Gamma$ and $\int_\Gamma \left(N^T K_E F_{\infty_E} N\right) d\Gamma$, they can be any combination of any of six matrices representing the six surfaces of the hexahedral element that can be exposed to fire. From Figure 4-1, it can be seen that the six surfaces can be represented as: $\eta = -1, \eta = +1, \zeta = -1, \zeta = +1, \xi = -1,$ and $\xi = +1$. The corresponding matrices for each of those cases are given in Appendix A.

4.4 Thermal Transfer Analysis

4.4.1 Introduction

Due to the fact that the solution of coupled heat and moisture transfer involves the use of asymmetric matrices, the procedure is normally computationally expensive. For this reason, in this section, the solution of heat transfer analysis will be introduced so it can be used whenever the results of the transfer of water vapour through concrete and the pressure in its pores are not of great value. This occurs, for example, when spalling of concrete, or explosive spalling to be more precise, is not a concern, as is the case for very porous normal-strength concrete.

4.4.2 Governing Differential Equations

Only the law of energy conservation as presented in Equation (4.6) and modified using Equation (4.8) will come into play in the case of heat transfer analysis, as shown in the following form:

$$\rho_c c_{p_c} \frac{\partial T}{\partial t} - \nabla(-k_{eff} \nabla T) = 0 \tag{4.107}$$

where the rate of change of energy consumed for the evaporation of liquid water, $\lambda_E \dot{E}_L$, and the rate of change of energy consumed for releasing the chemically-bound water in the cement paste of concrete, $\lambda_D \frac{\partial \bar{\rho}_D}{\partial t}$, are ignored. Also, note that the term '$\rho_T c_T$', which denotes the heat capacity of concrete with all its phases (dry skeleton, liquid water, water vapour and air), is substituted by the term '$\rho_c c_{p_c}$', which denotes the heat capacity of completely dry concrete.

Equation (4.107) represents the only governing equation required for transient heat transfer analysis.

4.4.3 Boundary Conditions

The boundary conditions for the case of heat transfer analysis depend on the type of heat transfer: conduction or convection.

In the case of heat conduction analysis, a heat source is applied to the surface of concrete; that is, the temperature of the surface of concrete is known and the profile of the distribution of temperature of concrete through the depth of concrete from the surface subjected to the heat source inward is to be calculated. It should be noted that this is not the case of fire. In this case, the boundary conditions are introduced as preset temperatures at the surface of concrete, without introducing any driving forces to the analysis.

On the other hand, the case of fire is the case of heat convection analysis, where only the temperature of the atmosphere around the concrete surface is known and not the temperature of the surface itself. In this case, the boundary conditions are introduced as driving forces in the system, based on Equation (4.75) alone.

4.4.4 Finite Element Formulation and Procedure

As previously discussed for the coupled heat and moisture transfer analysis, the Galerkin weighted residual method (Galerkin, 1915) has been used to obtain the weak form of Equation (4.107) as explained in Section 4.3.5. Following the same procedure, the temperature, T, is descretized and expressed in terms of the nodal components and the discrete system is expressed in the following first-order differential equation:

$$\mathbf{C_T}\frac{\partial \mathbf{T}}{\partial \mathrm{t}} + \mathbf{K_T T} = \mathbf{F_T} \tag{4.108}$$

where

$$\mathbf{C_T} = \sum_{\mathrm{E}=1}^{\mathrm{N_E}} \int_{\Omega} \left({N_T}^{\mathrm{T}} \rho_c c_{p_c} N_T \right) \mathrm{d}\Omega \tag{4.109}$$

In the case of heat conduction,

$$\mathbf{K_T} = \sum_{E=1}^{N_E} \int_{\Omega} \left(\nabla N_T{}^T K_{TE} \nabla N_T\right) d\Omega \tag{4.110}$$

and

$$\mathbf{F} = 0 \tag{4.111}$$

While in the case of heat convection,

$$\mathbf{K_T} = \sum_{E=1}^{N_E} \int_{\Omega} \left(\nabla N_T{}^T K_{TE} \nabla N_T\right) d\Omega + \int_{\Gamma} \left(N_T{}^T h N_T\right) d\Gamma \tag{4.112}$$

$$\mathbf{F_T} = \sum_{E=1}^{N_E} \int_{\Gamma} \left(N_T{}^T h T_{\infty}\right) d\Gamma \tag{4.113}$$

where

$$K_{TE} = \begin{bmatrix} K_{TT} & 0 & 0 \\ 0 & K_{TT} & 0 \\ 0 & 0 & K_{TT} \end{bmatrix} \tag{4.114}$$

4.4.5 Three-Dimensional Finite Element Formulation

For the regular hexahedral (brick) element shown in Figure 4-1, the same shape functions discussed in Section 4.3.6 will be used here. However, the matrices will be reduced to allow for the calculation of temperature alone, hence the shape functions matrix will be given as:

$$N_T = [N_1 \quad N_2 \quad N_3 \quad N_4 \quad N_5 \quad N_6 \quad N_7 \quad N_8] \tag{4.115}$$

and ∇N_T will also be calculated according to the following expression:

$$\nabla N_T = [\nabla \mathbf{N_{T_1}} \quad \nabla \mathbf{N_{T_2}} \quad \nabla \mathbf{N_{T_3}} \quad \nabla \mathbf{N_{T_4}} \quad \nabla \mathbf{N_{T_5}} \quad \nabla \mathbf{N_{T_6}} \quad \nabla \mathbf{N_{T_7}} \quad \nabla \mathbf{N_{T_8}}] \tag{4.116}$$

where $$\nabla \mathbf{N_{T_i}} = \begin{Bmatrix} \frac{\partial}{\partial x} \\ \frac{\partial}{\partial y} \\ \frac{\partial}{\partial z} \end{Bmatrix} N_i = \begin{Bmatrix} \frac{\partial N_i}{\partial x} \\ \frac{\partial N_i}{\partial y} \\ \frac{\partial N_i}{\partial z} \end{Bmatrix} \quad (4.117)$$

where $\mathbf{i} = 1,2,\cdots 8$

Both $\int_\Omega \left(N_T{}^T \rho C N_T\right) d\Omega$ and $\left(\nabla N_T{}^T K_{TE} \nabla N_T\right)$ produce 8×8 matrices whose elements are given in Appendix A. For the case of heat convection, the matrices $\int_\Gamma \left(N_T{}^T h N_T\right) d\Gamma$ and $\int_\Gamma \left(N_T{}^T h T_\infty\right) d\Gamma$ can be any combination of any of six matrices representing the six surfaces of the hexahedral element that can be exposed to fire as shown in Figure 4-1. The corresponding matrices for each of those cases are given in Appendix A.

4.5 Finite Difference Time Discretization

Having all the components of Equation (4.82) or Equation (4.108) assembled, the finite difference method is used for time discretization to solve the differential equation (Huang and Usmani, 1994; Reddy and Gartling, 2010). In this study, the generalized mid-point family of methods is used for the solution, such that:

$$\left[\frac{C_{n+\alpha}}{\Delta t} + \alpha K_{n+\alpha}\right](x_{n+1}) = \left[\frac{C_{n+\alpha}}{\Delta t} - (1-\alpha) K_{n+\alpha}\right](x_n) + (F_{n+\alpha}) \quad (4.118)$$

where n represents the n^{th} time step and the subscript $n + \alpha$ represents the property at time $(t_n + \alpha \Delta t)$ and condition $(1 - \alpha)x_n + \alpha x_{n+1}$. Depending on the value of α, from 0 to 1, Equation (4.118) yields different members of the generalized mid-point family as follows:

$\alpha = 0$ Forward Euler (Forward Difference) Method

$\alpha = \frac{1}{2}$ Crank-Nicolson (Mid-point) Method

$\alpha = \frac{2}{3}$ Galerkin Method

$\alpha = 1$ Backward Euler (Backward Difference) Method

Each of these methods presents some advantage over the others. The Forward Euler (Forward Difference) Method, for example, is an explicit method and, hence, more straightforward with low computational cost per time step. Yet, it is conditionally stable, which ultimately results in much longer computational time due to the need to use smaller time steps to achieve a stable analysis. On the other hand, implicit methods ($\alpha > 0$), are stable over a wider range of time steps, sometimes unconditionally stable as in the case of Crank-Nicolson (Mid-point) Method, but they are computationally expensive per time step.

4.6 Steady State vs. Transient Flow

While all the past discussions focused primarily on the transient flow of heat or coupled heat and moisture through concrete with time, the analysis of the steady state, where the time required for the transfer to be complete has elapsed and the system has become thermally static, is also of some interest in some cases. For cases where the rate of rise in temperature is low, where the source of heat is not fire, steady state analysis provides enough data for the structural analysis; yet, it is much less computationally expensive.

For the steady state analysis, the time differential component in Equation (4.82), which is $\mathbf{C}\,\partial\mathbf{x}/\partial t$, and in Equation (4.108) , which is $\mathbf{C_T}\,\partial\mathbf{T}/\partial t$, will be reduced to zero, since $\partial\mathbf{x}/\partial t$ and $\partial\mathbf{T}/\partial t$ become equal to zero due to the fact that $\mathbf{x}$ and $\mathbf{T}$ will not change with time any more. The rest of the components and the solution procedure remain the same.

It should be noted that the steady state should only be performed for heat transfer analysis, but not for coupled heat and moisture analysis. This is simply because the steady state of coupled heat and moisture analysis is similar to the steady state of heat transfer analysis, because at the steady state, which is reached after a prolonged amount of time, the pore pressure will be back to the atmospheric pressure and any clogged moisture will be released as well. However, a steady state analysis for coupled heat and moisture will still take much longer time to analyze and much more computer resources will be needed; therefore there is no need for such analysis to be performed.

Chapter 5
Analysis Verification Studies

5.1 Introduction

This chapter presents an extensive compilation of various analyses performed that cover a wide range of structural members and loading profiles, aimed at corroborating the models, procedures, and techniques that were incorporated in VecTor3, as previously explained and discussed.

Some models implicitly affect the analytical results of any type of structure or loading, such as slip distortion in the Disturbed Stress Field Model (DSFM), the bond between concrete and steel reinforcing bars, dowel action in steel reinforcing bars, linking the displacements of predetermined nodes to each other, and geometric nonlinearity effects. Therefore, no analysis will be specifically dedicated to the corroboration of these features; yet, their effect will be shown and discussed throughout the analyses presented in this section.

On the other hand, special corroboration analyses for the models that were developed and incorporated in this study that involve specific material types and loading conditions will be explicitly presented. These include the modelling of steel fibre-reinforced concrete (SFRC), cyclic and dynamic loading conditions, thermal loading under fire conditions, and the estimation of pore pressure inside concrete subjected to fire for the purpose of predicting the occurrence of spalling.

For all the analyses presented in this section, the same models, procedures, and techniques have been utilized, in order to have a consistent basis for the comparisons. The following is a list of these default models:

For thermal analyses:

Three groups of standards were used and compared to each other, namely, the ASCE Manual of Practice (Structural Fire Protection by T. T. Lie, 1992), the former version of the Eurocode (ENV 1992-1-2:1995, 1996), and its current version (EN 1992-1-2:2004,

2005). The sources of the models used in each group for the different thermal and mechanical properties at elevated temperatures are shown in Table 5-1 for concrete and in Table 5-2 for steel reinforcing bars, where substitutive models were used for properties that did not have a specific model in a certain group.

Table 5-1 Models used for the properties of concrete for the thermal analyses carried out in this study

Property	ASCE Manual of Practice (1992)	Eurocode (ENV 1992-1-2:1995, 1996)	Eurocode (EN 1992-1-2:2004, 2005)
Thermal Expansion Strain	ASCE Manual of Practice (1992)	Eurocode (ENV 1992-1-2:1995, 1996)	Eurocode (EN 1992-1-2:2004, 2005)
Density	Eurocode (EN 1992-1-2:2004, 2005)	Eurocode (EN 1992-1-2:2004, 2005)	Eurocode (EN 1992-1-2:2004, 2005)
Thermal Conductivity	ASCE Manual of Practice (1992)	Eurocode (ENV 1992-1-2:1995, 1996)	Eurocode (EN 1992-1-2:2004, 2005)
Specific Heat Capacity	ASCE Manual of Practice (1992)	Eurocode (ENV 1992-1-2:1995, 1996)	Eurocode (EN 1992-1-2:2004, 2005)
Compressive Strength	ASCE Manual of Practice (1992)	Eurocode (ENV 1992-1-2:1995, 1996)	Eurocode (EN 1992-1-2:2004, 2005)
Strain Corresponding to Peak Stress	ASCE Manual of Practice (1992)	Eurocode (ENV 1992-1-2:1995, 1996)	Eurocode (EN 1992-1-2:2004, 2005)
Tensile Strength	Dwaikat and Kodur (2009)	Dwaikat and Kodur (2009)	Dwaikat and Kodur (2009)

For the tensile strength of concrete at elevated temperatures, the model presented by Dwaikat and Kodur (2009), which is a modification of the model presented by the Eurocode (EN 1992-1-2:2004, 2005), was used in the three groups of standards. The reason is that this model retains a small part of the tensile strength of concrete up to a temperature of 1200°C, which avoids computational problems arising from analyzing concrete with absolutely no tensile strength.

For the post-fire residual mechanical properties of concrete, the models presented by Chang et al. (2006) for the residual peak compressive stress (compressive strength), the corresponding strain, and the cracking stress (tensile strength) were used.

Table 5-2 Models used for the properties of steel reinforcing bars for the thermal analyses carried out in this study

Property	ASCE Manual of Practice (1992)	Eurocode (ENV 1992-1-2:1995, 1996)	Eurocode (EN 1992-1-2:2004, 2005)
Thermal Expansion Strain	ASCE Manual of Practice (1992)	Eurocode (ENV 1992-1-2:1995, 1996)	Eurocode (EN 1992-1-2:2004, 2005)
Yield Stress	ASCE Manual of Practice (1992)	Eurocode (ENV 1992-1-2:1995, 1996)	Eurocode (EN 1992-1-2:2004, 2005)
Steel Ultimate Stress	Eurocode (EN 1992-1-2:2004, 2005)	EN 1992-1-2:2004, 2005	Eurocode (EN 1992-1-2:2004, 2005)
Steel Young's Modulus	ASCE Manual of Practice (1992)	Eurocode (EN 1992-1-2:2004, 2005)	Eurocode (EN 1992-1-2:2004, 2005)

For the post-fire residual mechanical properties of steel, full recovery of the properties at normal temperatures was assumed for the reasons explained in Section 3.5.2.2.

Other properties relating to the heat transfer analysis that were used include 25 $W/m^2°C$ for the convective heat transfer coefficient of concrete, h_q, according to the Eurocode (EN 1991-1-2:1992, 1993) and 0.7 for the emissivity of concrete, e, according to the Eurocode (EN 1992-1-2:2004, 2005). e is used to calculate the radiative heat transfer coefficient, h_r, as shown in Equation (B.33). The initial density of concrete was taken as 2400 kg/m^3.

For the properties relating to the coupled heat and moisture transfer analysis, in addition to the models and values used for the properties of concrete in heat transfer analysis as mentioned above, the following models and values were used:

For porosity: the model presented by Gawin et al. (1999) was used, with an initial value of 0.08.

For permeability: the model presented by Tenchev et al. (2001) was used, with an initial value of 5×10^{-17} m^2.

Many other properties and models that were used in the coupled heat and moisture transfer analysis are discussed in Appendix B and Appendix C.

For structural analyses:

For concrete:

Compression ascending curve:	Hognestad's parabola (1951) for normal-strength concrete and Popovics's curve (1973) for high-strength concrete (compressive strength of more than 45MPa)
Compression post-peak curve:	Modified Park-Kent model (Kent and Park, 1971; Park et al., 1982) for normal-strength concrete and Popovics's curve (1973) for high-strength concrete (compressive strength of more than 45 MPa)
Compression softening factor:	Vecchio 1992-A (Vecchio and Collins, 1993)
Tension stiffening model:	Modified Bentz (A modification the model presented by Bentz (2000), developed by Vecchio, and introduced by Sato and Vecchio (2003))
Tension softening model:	Bilinear
FRC post-crack tension model:	SDEM (Monotonic) (Lee et al., 2011a, 2011b, 2013a).
Confinement strength model:	Kupfer / Richart (developed by Richart et al. (1928) and modified by Kupfer et al. (1969))
Concrete dilatation model:	Variable - Kupfer (Kupfer et al. (1969))
Cracking criterion:	Mohr-Coulomb (Stress) (Coulomb, 1776; Mohr, 1900)
Crack shear check for MCFT:	Vecchio-Collins 1986 (Vecchio and Collins, 1986)
Crack width check:	Crack Limit (Agg/2.5) (nominal aggregate size/2.5)
Concrete-steel bond model:	Eligehausen Model (Eligehausen et al., 1983)
Hysteresis model:	Linear w/ Offsets (Vecchio, 1999)
Slip distortion model:	Walraven (Monotonic) (Walraven and Reinhardt, 1981)
Strain rate effects model:	fib2010 (fib Model Code 2010 (2012))

For steel:

Hysteresis model:	Seckin (w/ Bauschinger) (model provided by Seckin (1981) and includes Bauschinger effect (1886))
Rebar dowel action model:	Tassios (Crack Slip) (Vintzeleou and Tassios, 1987)
Rebar buckling model:	Refined Dhakal-Maekawa (Dhakal and Maekawa, 2002)
Strain rate effects model:	CEB (1988)

General features:

Structural damping:	Rayleigh Damping (Rayleigh, 1877)
Previous load history:	Considered
Geometric nonlinearity:	Considered

5.2 Steel Fibre-Reinforced Concrete

This section tests the capabilities of VecTor3 in analytically modelling steel fibre-reinforced concrete members as discussed in Section 2.4.2.5, employing the Simplified Diverse Embedment Model (SDEM), discussed in Section 2.4.2.5.2, special tension stiffening model, discussed in Section 2.4.2.5.3, and special average crack width, as discussed in Section 2.4.2.5.4. For this purpose, two experimental series have been chosen: Susetyo panels and Semelawy slabs.

5.2.1 Susetyo Panels

These steel fibre-reinforced concrete panels were tested by Susetyo (2009) using the unique Panel Element Tester, first used in 1979 (Vecchio and Collins, 1986), at the University of Toronto. The experimental program was aimed at investigating the feasibility of steel fibres replacing conventional shrinkage reinforcement minimum requirements for concrete structures.

For this purpose, ten 890×890×70 mm concrete panels were tested under in-plane pure shear stress, with the varying parameters of fibre volume content, concrete compressive strength, and fibre type (pertaining to fibre geometric and material properties). In order to exclude conventional reinforcement as an effective parameter in the behaviour of the panels, the reinforcement ratio was kept constant among all specimens. One direction was reinforced by forty D8 deformed wires, with a total cross-sectional area of 2063 mm^2, equivalent to a reinforcement ratio of 3.31%. The other direction was kept unreinforced. The reason why the panel was relatively heavily reinforced in one direction was to ensure that the panels would maintain adequate post-cracking resistance, in order to capture the post-cracking behaviour without risking premature failure.

Of the ten panels, two were conventionally reinforced concrete control panels with no fibres. Therefore, only the results of the eight SFRC panels are presented here. The analytical results generated by VecTor3 are compared to both the experimental results and the analytical results of VecTor2. VecTor2 is the well-established nonlinear finite element program for the analysis of two-dimensional reinforced concrete membrane

structures, also developed at the University of Toronto. It employs the exact same models that are employed by VecTor3.

The panel test series involved two different concrete compressive strengths, f'_c, of 50 MPa and 80 MPa, denoted in the panels' names as C1 and C2, respectively. They also tested three different values of fibre volume contents, V_f: 0.5%, 1.0%, and 1.5%, denoted as V1, V2, and V3, respectively. Finally, they tested two different fibre types, denoted F1 and F2. Table 5-3 lists the various parameters of the panels of the test series. The fibres used were end-hooked fibres manufactured by Dramix®, having the properties shown in Table 5-4, where l_f, d_f, and f_{uf} are the fibre length, diameter and ultimate tensile strength, respectively.

Table 5-3 Parameters of Susetyo panels test series

Panel Name	f'_c (MPa)		Fibre Type	V_f (%)
	Design	Actual		
C1F1V1	50.0	51.4	RC80/50-BN	0.5
C1F1V2	50.0	53.4	RC80/50-BN	1
C1F1V3	50.0	49.7	RC80/50-BN	1.5
C1F2V3	50.0	59.7	RC80/30-BP	1.5
C1F3V3	50.0	45.5	RC65/35-BN	1.5
C2F1V3	80.0	79.0	RC80/50-BN	1.5
C2F2V3	80.0	76.5	RC80/30-BP	1.5
C2F3V3	80.0	62.0	RC65/35-BN	1.5

Table 5-4 Properties of the Dramix® steel fibres used in Susetyo panels

Fibre Type	Code in Panel Name	l_f (mm)	d_f (mm)	Aspect Ratio (l_f/d_f)	f_{uf} (MPa)
RC80/50-BN	F1	50	0.62	81	1050
RC80/30-BP	F2	30	0.38	79	2300
RC65/35-BN	F3	35	0.55	64	1100

The panels were modelled in both VecTor2 and VecTor3 as one element with smeared reinforcement, with the specimens' dimensions and loading conditions inducing in-plane pure shear stress in the element, as shown in Figure 5-1. In VecTor2, a regular four-noded rectangular element was used, while in VecTor3, the regular eight-noded hexahedral element was used. Each arrow in Figure 5-1 represents a concentrated nodal force, where half the force is applied on each face of the element in case of VecTor3. The loads were increased in fixed increments, causing an in-plane pure shear stress increment of 0.016 MPa per load stage.

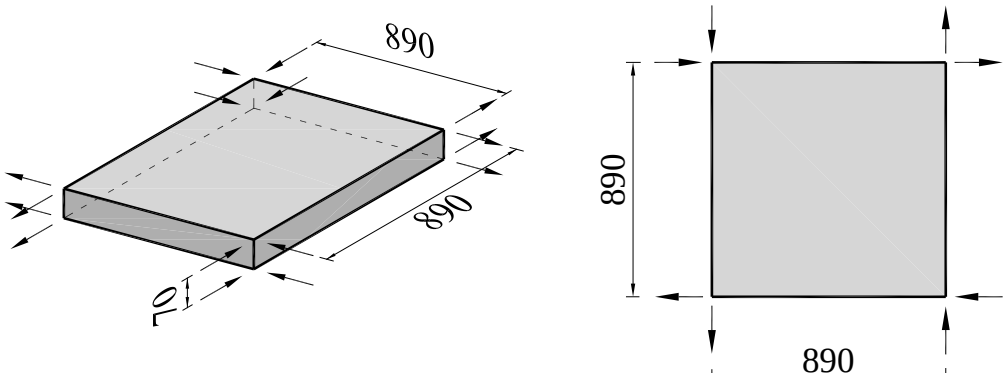

Figure 5-1 Shape of the one-element model of Susetyo panels as modelled in VecTor3 (left) and VecTor2 (right)

The results of the analyses are presented in Figure 5-2 for the eight SFRC panels. It can be observed that the results generated by VecTor3 are almost identical to those generated by VecTor2, and they both show reasonable correlation with the reported experimental results. This supports both the accuracy and stability of the calculation procedure of VecTor3 as it provides almost the same results as the well-established VecTor2 for these two-dimensional panels. The results also support the adequacy of the previously discussed SDEM, tension stiffening model, and average crack width calculations in estimating the behaviour of SFRC with various concrete compressive strengths, fibre volume contents, and fibre types.

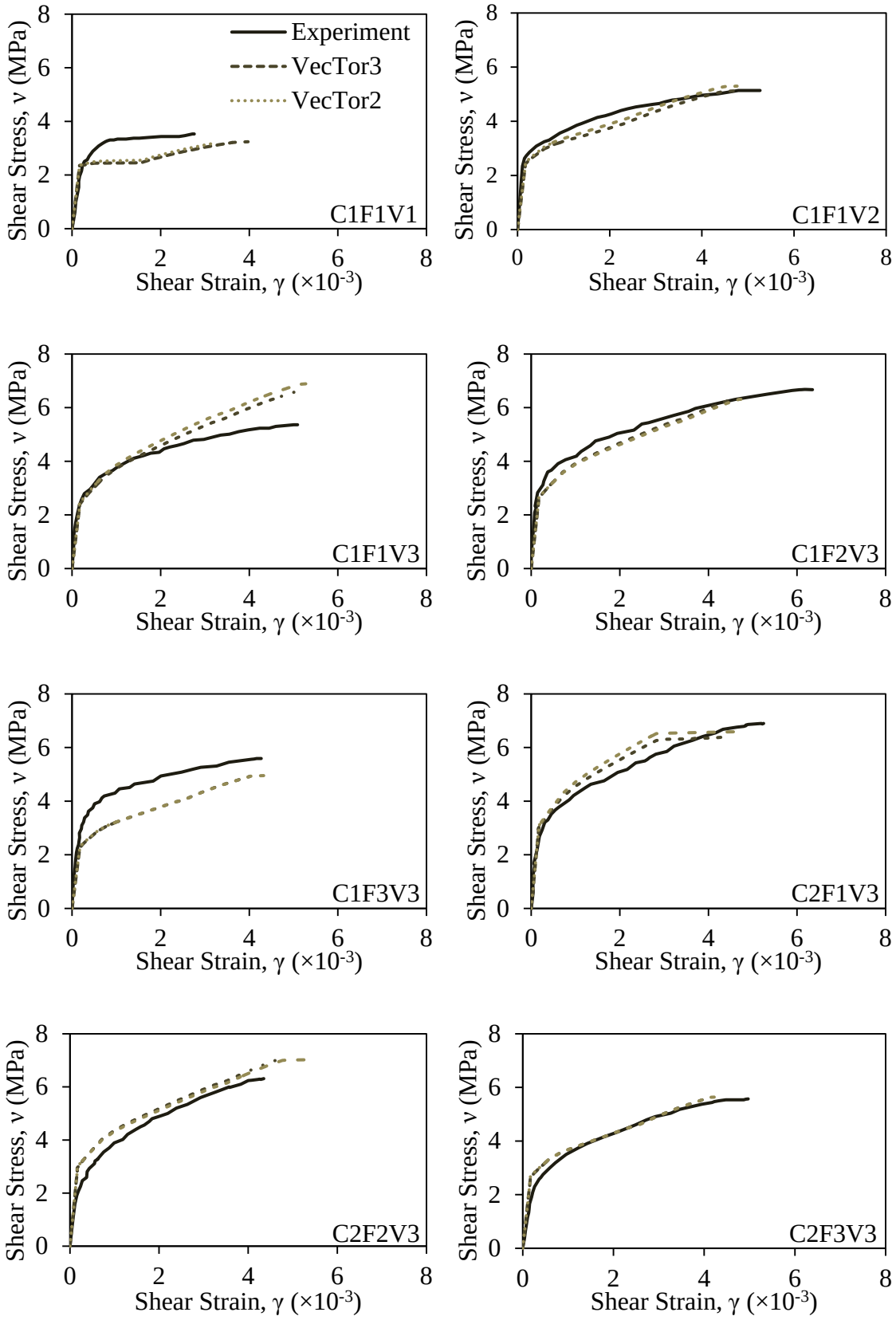

Figure 5-2 Comparison between the experimental results of the Susetyo panels and the analytical results generated by VecTor2 and VecTor3

5.2.2 Semelawy Slabs

While the Susetyo panels demonstrated the efficiency of VecTor3 and the models incorporated within it at accurately representing the behaviour of SFRC on the micro level, there remains the necessity to test their adequacy on the macro level. Therefore, the Semelawy slabs were chosen to provide this test.

The Semelawy slabs were tested at the University of Toronto as a part of an experimental program aimed at testing the behaviour of externally post-tensioned unreinforced concrete slabs against punching shear failure. With the shift towards post-tensioning reinforced concrete bridges in order to decrease their depths, the risk of failure due to punching shear is increased. The experimental program was undertaken in two phases. Phase I was carried out by Semelawy (2007) and it included three plain concrete slabs, denoted P-1, P-2, and P-3, and two steel fibre-reinforced concrete (SFRC) slabs, denoted F-1 and F-2. Phase II was carried out by Mostafaei et al. (2011), and it included two more SFRC slabs, denoted F-3 and F-4.

Since the purpose of these analyses is the corroboration of the ability of VecTor3 to model SFRC under complex three-dimensional conditions, only F-1, F-2, F-3 and F-4 were modelled and analyzed. The specimens were two-way slabs, with dimensions of 1500×1500×127 mm. The main varying parameters among the slabs were the fibre volume content, V_f, and the post-tensioning force. The compressive strength of concrete was kept within a narrow range for all the slabs, varying between 48.6 MPa and 59.9 MPa, and none of the slabs contained conventional reinforcement. Table 5-5 shows the general properties of the specimens. The fibres used were Dramix® RC-80/50-BP high-carbon wire fibres. These are end-hooked fibres with a length of 50 mm, a diameter of 0.6 mm (aspect ratio of 83), and a minimum ultimate tensile strength of 2000 MPa.

The slabs were externally post-tensioned using eight equally-tensioned 32 mm diameter Dywidag bars in each direction, with four of them extending above the slab and four below it. To avoid the occurrence of concentrated stresses at the edges of the slabs at the locations of post-tensioning, four C130 × 10 steel channels, 204 mm in length each, were placed along each of the four sides of the slabs. The forces in the post-tensioned Dywidag bars were transmitted through a special mechanism from the bars to relatively stiff plates

which were bearing against 44 mm diameter bars welded to the steel channels attached to the slabs, as shown in Figure 5-3.

Table 5-5 Properties of the Semelawy slabs

Slab Name	f'_c (MPa)	V_f (%)	Post-Tensioning Force (kN)	
			N-S direction	E-W direction
F-1	59.9	1.0	1148	1135
F-2	54.8	1.0	861	1110
F-3	56.2	1.0	779	780
F-4	48.6	1.5	1167	962

The slabs were supported by 44 mm diameter steel rods positioned along each of the sides at 75 mm from the edges, creating a simply supported two-way slab with a span of 1350 mm in each direction. In an attempt to simulate the actual support conditions of bridge slabs, no restraint against upward displacements was provided, allowing the occurrence of potential uplifting around the edges as the slabs deflect downwards at the centre under loading.

The slabs were loaded vertically, through a loading plate of dimensions 200×200×50 mm, at the centre until failure. With increased loading, the bending and cracking of the slabs caused them to elongate, which, in turn, led to the rise of additional tensioning in the post-tensioning bars and resulted in additional post-tensioning forces in the slabs. The values of the post-tensioning forces in each direction for slabs F-1, F-2, F-3, and F-4 are plotted against the corresponding vertical central concentrated load in Figures 5-4, 5-5, 5-6, and 5-7, respectively.

All slabs failed due to punching shear, as designed. The values of the failure loads are presented in Table 5-6, together with the values of the total post-tensioning forces which were initially applied and those corresponding to the peak load applied (P_{max}) in both N-S and E-W directions.

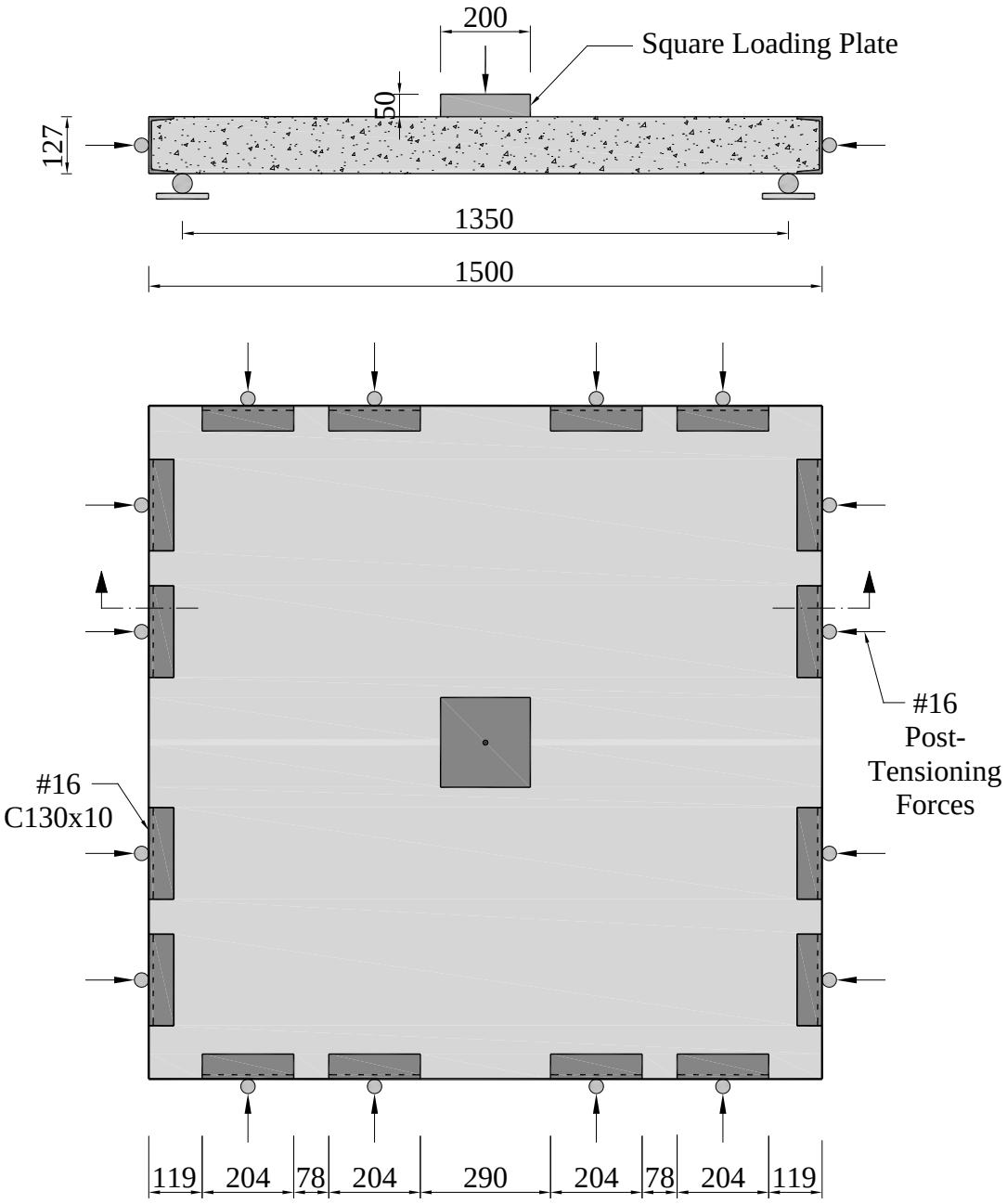

Figure 5-3 General outline of Semelawy slabs
(dimensions in mm)

Table 5-6 Failure loads (P_{max}) and post-tensioning forces for Semelawy slabs

Slab Name	P_{max} (kN)	P/T Force in N-S Dir. (kN)		P/T Force in E-W Dir. (kN)	
		Initial	at P_{max}	Initial	at P_{max}
F-1	503	1148	1423	1135	1377
F-2	457	861	1230	1110	1231
F-3	419	779	971	780	839
F-4	527	1167	1443	962	1105

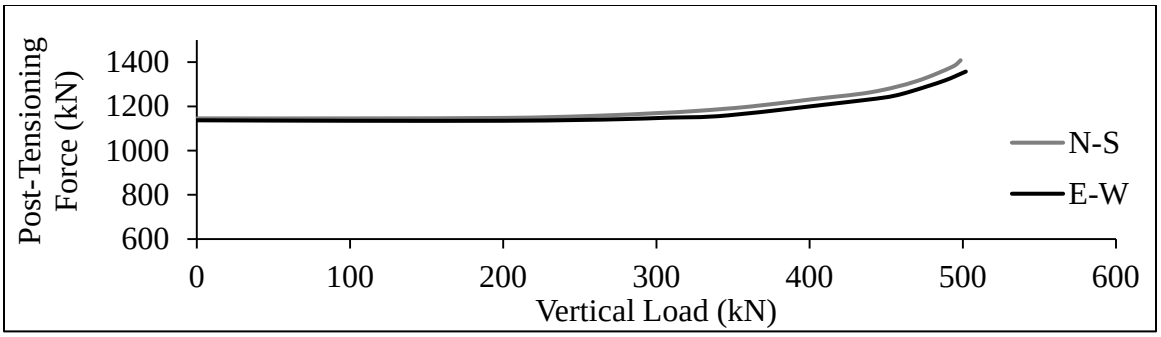

Figure 5-4 Post-tensioning forces in the north-south (N-S) and east-west (E-W) directions for Semelawy slab F-1

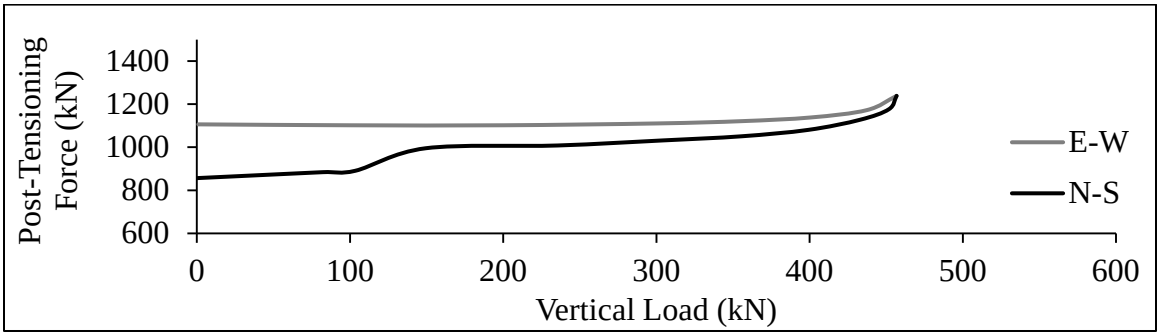

Figure 5-5 Post-tensioning forces in the north-south (N-S) and east-west (E-W) directions for Semelawy slab F-2

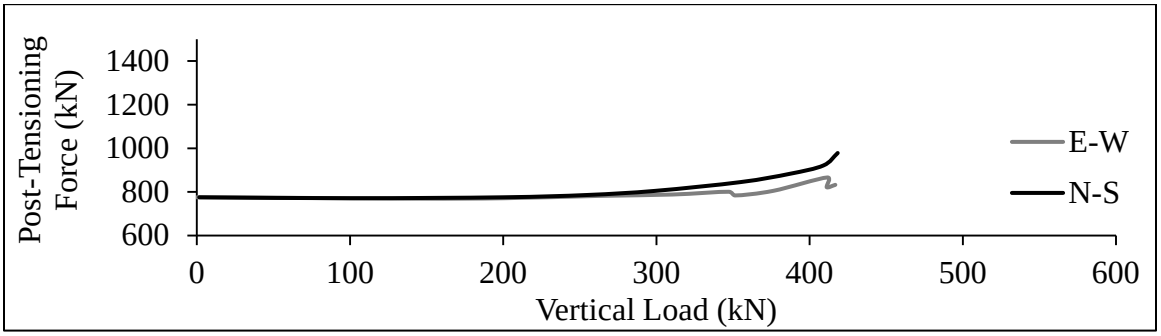

Figure 5-6 Post-tensioning forces in the north-south (N-S) and east-west (E-W) directions for Semelawy slab F-3

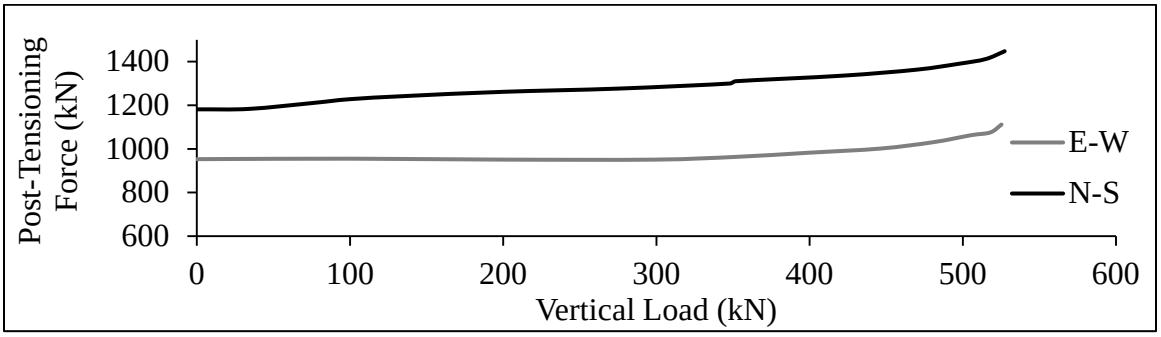

Figure 5-7 Post-tensioning forces in the north-south (N-S) and east-west (E-W) directions for Semelawy slab F-4

Taking advantage of the geometric and loading symmetry of the slabs, only one quarter of each slab was modelled in VecTor3. A total of 4410 elements were used to discretize the slab in the finite element model, as shown in Figure 5-8. They were discretized into ten 12.7 mm elements through the depth. Through the length and width, they were discretized into two elements of 37.5 mm, nine elements of 47.22 mm, and ten elements of 25 mm at the centre, allowing for a denser mesh around the centre in order to capture the behaviour more precisely. Isoparametric hexahedral elements were used, in order to have the ability to consider geometric nonlinearity.

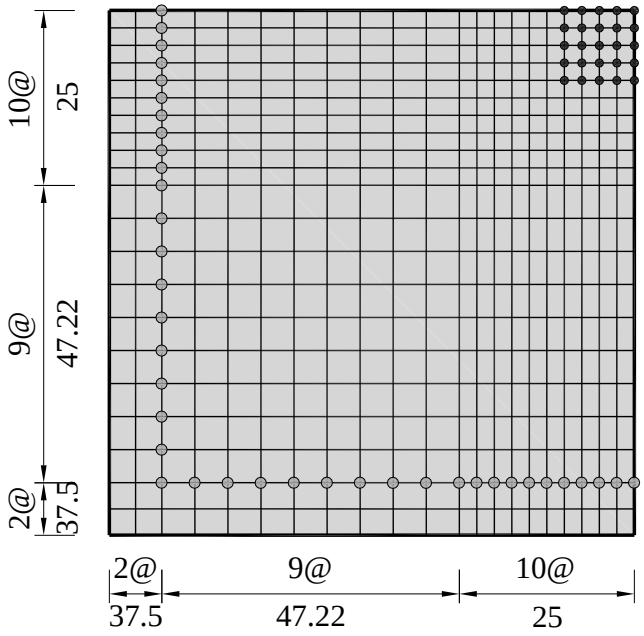

Figure 5-8 Finite element discretization of the quarter slab model analyzed in VecTor3 (dimensions in mm)

For vertical restraint in the downward direction to be applied without any upward restraint, regular supports could not be used. Instead, the slab supports were modelled using a special type of discrete reinforcement truss bar that has high stiffness in compression, but has no stiffness in tension. Hence, these bars created vertical support for the slabs against downward displacement, while allowing them to freely displace upwards. The axes of symmetry were restrained in the direction perpendicular to each of them to simulate the conditions and behaviour of the whole slab with the quarter model actually analyzed.

In modelling the vertical load, the slabs were loaded uniformly in the region below the centre loading plate, as shown in Figure 5-9, in a displacement control procedure with a

step of 0.5 mm. Also, the post-tensioning forces were applied uniformly along the edges of the slabs (not shown in Figure 5-9). To account for the rise in the post-tensioning forces as displacements increased, as noted earlier, additional post-tensioning forces were applied gradually in both directions through the analysis, following the experimental profiles shown in Figures 5-4 to 5-7.

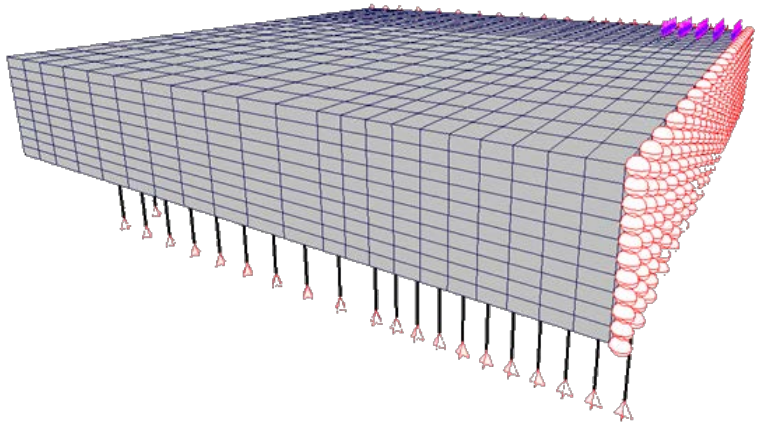

Figure 5-9 Finite element model of Semelawy slabs showing the support conditions and the vertical loading

Figure 5-10 shows plots for the mid-point vertical displacement against vertical load for F-1, F-2, F-3, and F-4. The mid-point vertical displacement plotted is the relative vertical displacement at the upper face of the slab at its centre with respect to the vertical displacement at the upper face of the slab at its corner support, which displaces upwards as the slabs are loaded, as explained earlier.

The analytical results show good correlation with the experimental results in terms of the initial stiffness, the peak load, and to a lesser extent, the ductility represented in the displacement at failure. For the peak load, a mean analytical to experimental ratio of 0.96 was achieved, with a coefficient of variation of 6%, while for the mid-point vertical displacement at failure, the mean analytical to experimental ratio was 1.01, with a coefficient of variation of 11%.

VecTor3 managed to capture the punching shear failure mode for all slabs. Figure 5-11 shows colour-coded contours for the vertical displacement at the time of failure for a typical Semelawy slab. The region below the loading plate appears to have separated from the rest of the slab, which, in turn, returned back to its original unloaded condition, retaining the residual displacements only.

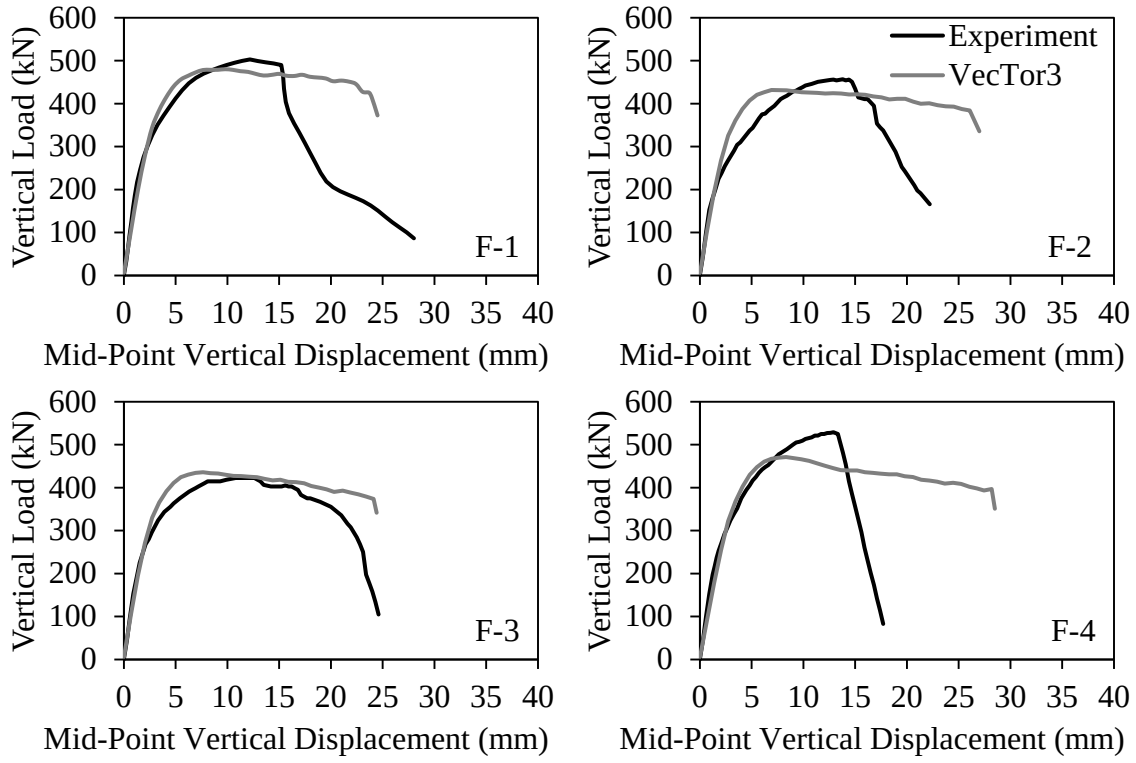

Figure 5-10 Experimental and analytical load-deflection plots for the Semelawy slabs

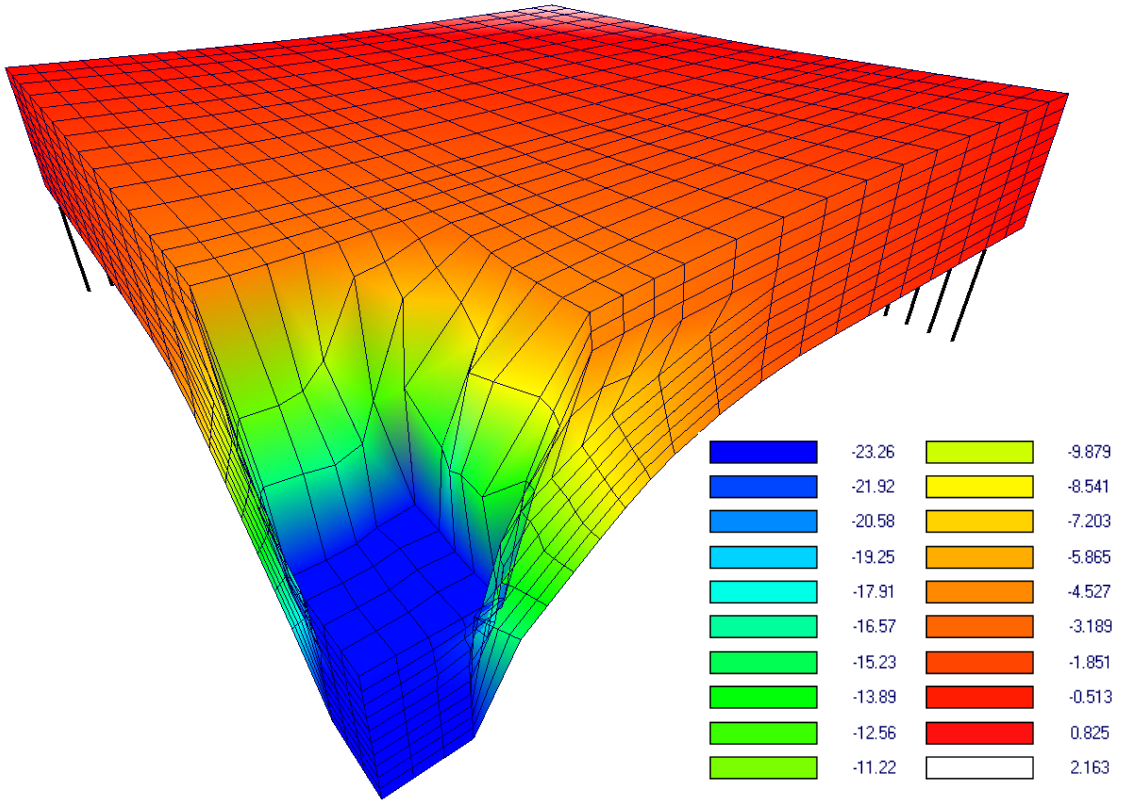

Figure 5-11 Colour-coded contours for the vertical displacement of a typical Semelawy slab at failure (displacements are in mm); slab F-1 shown

5.3 Cyclic Loading

Due to the complicated instrumentation requirements of conducting seismic tests on reinforced concrete structures, testing them under quasi-static reversed cyclic lateral loading instead has always been a more feasible option chosen by many researchers. In addition, cyclic loading provides a good means of testing many, if not all, the advanced mechanisms that reinforced concrete experiences.

Since many of these advanced mechanisms have been implemented in VecTor3 and incorporated within the MCFT and DSFM framework, a corroboration study of these models became necessary. For this purpose, cyclic loading analyses of shear-critical reinforced concrete shear walls, tested by Palermo (2002), have been carried out and compared to experimental results. The hysteretic response of concrete and steel, dowel action of steel reinforcing bars, geometric nonlinearity effects, and slip distortions are the most significant mechanisms that are put to the test in this section.

5.3.1 Palermo Shear Walls

Palermo (2002) tested two similar large-scale wide-flanged squat shear walls, with different axial loading, under cyclic lateral loading. The walls' behaviour was dominated by shear mechanisms, which makes them ideal for testing the MCFT and the DSFM, where their reliability in capturing shear mechanisms can be shown. Also, their wide flanges make them an ideal test for VecTor3, where its three-dimensional analysis capabilities can be utilized.

The walls, denoted DP1 and DP2, were 2020 mm high, with a web 2885 mm long and 75 mm thick, connecting to a flange 3045 mm wide at each end. The thickness of the flange was 95 mm for DP1 and 100 mm for DP2. Both walls rested on a relatively stiff slab with dimensions 4415x4000x620 mm. With these slabs clamped to the laboratory rigid floor, they simulated fixed foundations conditions. Another relatively stiff slab, with dimensions 4415x4000x640 mm, framed the top of both walls as well. These top slaps helped to evenly distribute the lateral and axial loads across the walls.

The web and the flanges were reinforced with D6 reinforcing bars. Horizontally, the bars were spaced at 140 mm in two layers within the web and the flanges. Vertically, the bars were spaced at 130 mm in two layers in the web and in the part of the flanges connecting to the web. For the outer parts of the flanges, the reinforcing bars were spaced at 355 mm in two layers. To ensure relatively stiff upper and lower slabs, these elements were reinforced with No. 30 reinforcing bars spaced at 350 mm in each direction. Table 5-7 provides the properties of both the D6 and No. 30 bars, and Table 5-8 and Table 5-9 give the properties of concrete and the reinforcement ratio of each zone of DP1 and DP2, respectively. Figure 5-12 shows the dimensions and the reinforcement layout of the walls.

Table 5-7 Properties of D6 and No.30 reinforcing bars used in Palermo shear walls DP1 and DP2

Type	Nominal Diameter (mm)	f_{s_y} (MPa)	E_s (MPa)	f_{s_u} (MPa)	ε_{s_u} $(\times 10^{-3})$
D6	7.0	605	190,250	652	46.875
No. 30	29.9	550	220,000	696	36.316

In Table 5-7, f_{s_y} is the yield stress, E_s is Young's modulus, f_{s_u} is the ultimate stress, and ε_{s_u} is the ultimate strain.

Table 5-8 Concrete properties and reinforcement ratios of the different parts of Palermo shear wall DP1

Part	f'_c (MPa)	ε'_c $(\times 10^{-3})$	E_c (MPa)	ρ_h (%)	ρ_v (%)	
Web	21.7	-2.04	25,900	0.737	0.794	
Flange	21.7	-2.04	25,900	0.582	Inner	0.627
					Outer	0.230
Top slab	43.9	-1.93	43,700	0.625	0.625	
Bottom slab	34.7	-1.90	36,900	0.650	0.650	

Table 5-9 Concrete properties and reinforcement ratios of the different parts of Palermo shear wall DP2

Part	f'_c (MPa)	ε'_c ($\times 10^{-3}$)	E_c (MPa)	ρ_h (%)	ρ_v (%)	
Web	18.8	-2.12	18,580	0.737	0.794	
Flange	18.8	-2.12	18,580	0.553	Inner	0.596
					Outer	0.218
Top slab	38.0	-1.96	37,570	0.625	0.625	
Bottom slab	34.7	-1.90	36,900	0.650	0.650	

In Tables 5-8 and 5-9, f'_c is the concrete compressive strength (peak stress), ε'_c is the strain corresponding to the peak compressive stress, E_c is the concrete initial stiffness, and ρ_h and ρ_v are the reinforcement ratios in the horizontal and vertical directions, respectively.

Both shear walls were subjected to quasi-static reversed cyclic lateral loading. The test followed a displacement control protocol with increments of 1 mm from one displacement step to the next, with two repetitions at each displacement step. The lateral loading profile is shown in Figure 5-13. The displacement was applied at two points 1600 mm from the edges of the top slab, at mid-depth, in the direction along the axis of the web. Figure 5-12 shows the locations of the loading points. For the axial loading, in addition to the weight of the top slab, which amounted to 260 kN, DP1 was subjected to an additional downward axial load of 940 kN; DP2 had no additional axial load. This means that that the total axial load to which DP1 was subjected was 1200 kN, as opposed to 260 kN for DP2. In both cases, the axial load was kept constant throughout the test.

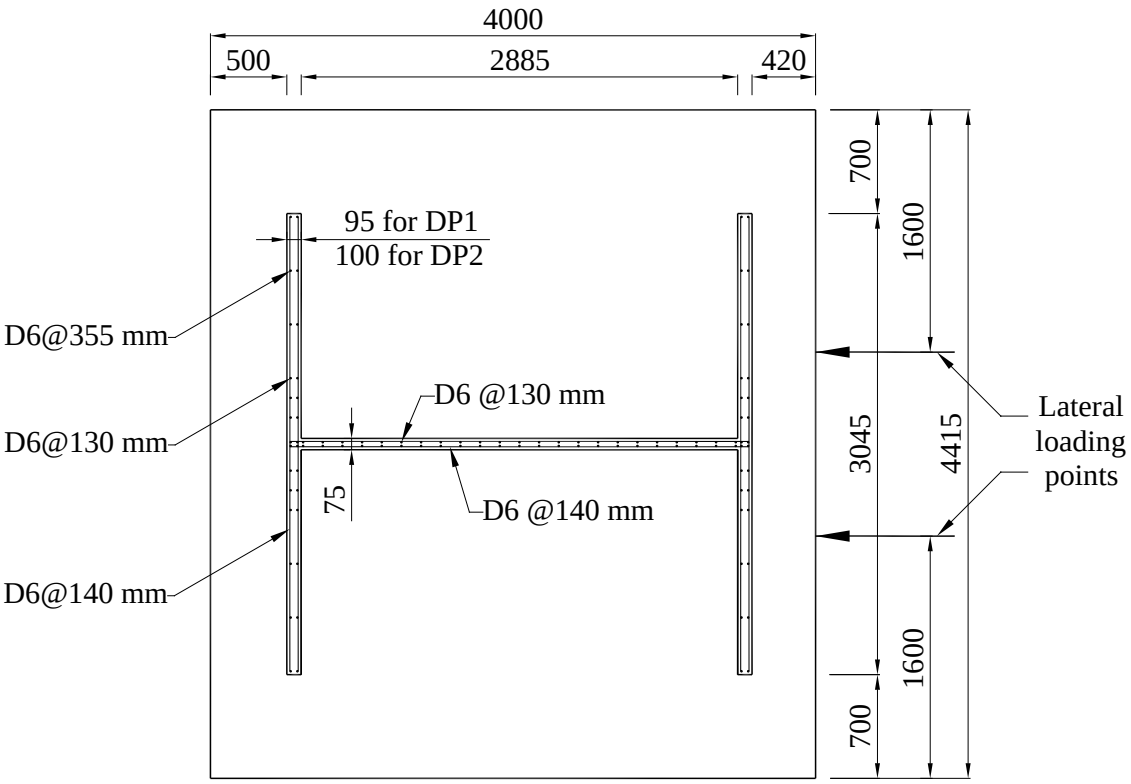

Figure 5-12 The dimensions (in mm) and reinforcement layout of Palermo shear walls DP1 and DP2

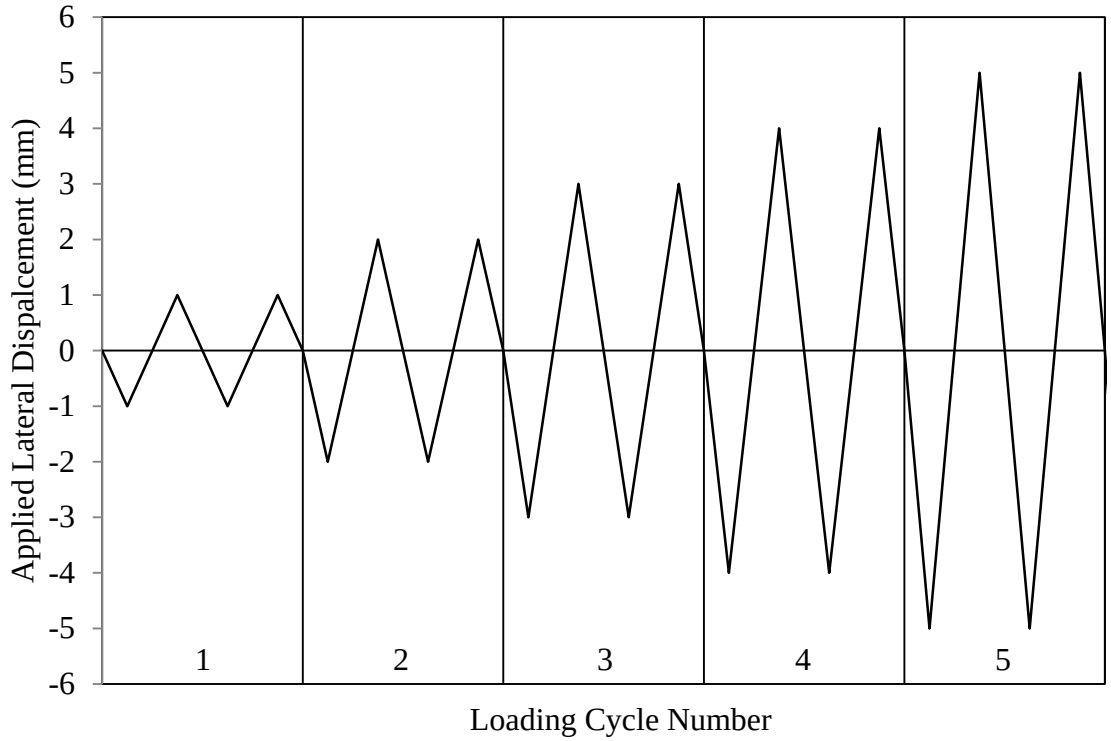

Figure 5-13 Lateral displacement loading profile for Palermo shear walls DP1 and DP2

With DP1, the test was terminated at the completion of displacement cycle number 15, i.e., the cycle applying a displacement of 15 mm at the top slab. At this point, a considerable part of the post-peak response of the shear wall had been exhausted and the wall's lateral loading capacity was reduced to approximately 45% of its maximum capacity of 1298 kN. As for DP2, the test continued until failure, which occurred in displacement cycle number 10 during the first excursion to 10 mm, which it could not attain. The maximum lateral load capacity attained by DP2 was 879 kN.

Figures 5-14 and 5-15 show the experimental load-displacement results of the lateral displacement applied on the top slab and the corresponding lateral load for DP1 and DP2, respectively. Figures 5-16 and 5-17 show the crack pattern and the degree of damage sustained by the web and the flange of DP1, respectively, at the termination of the test. It can be noticed that the entire web experienced severe shear cracking, and the flanges showed significant flexural cracks, which were more extensive at the connection to the web.

Figures 5-18 and 5-19 show the crack pattern and the degree of damage sustained by the web and the flange of DP2, respectively, at failure, which occurred during the first excursion to 10 mm as previously mentioned. In general, DP2 showed a cracking and damage behaviour very similar to that of DP1, except for the failure mode, which involved sudden sliding along a shear plane that formed across the web slightly beneath the top slab, as seen in Figure 5-18.

Taking advantage of the symmetric layout of the geometry and loading profile of the walls along the web, only one half of each wall was modelled using VecTor3. The web was modelled as one element through the thickness, 37.5 mm wide representing half the thickness of the web, and thirty-two elements, each 90.16 mm long, through the length. The flanges were modelled as one element through the thickness, 95 mm wide for DP1 and 100 mm wide for DP2. Through their length, they were modelled as sixteen elements, 92.8 mm long each, and a seventeenth element, 37.5 mm in length at the intersection with the web (the centre of the wall). The cross section of the model is shown in Figure 5-20. The entire walls were discretized into twenty elements through the height. The top and bottom slabs discretization effectively followed that of the web and the flanges.

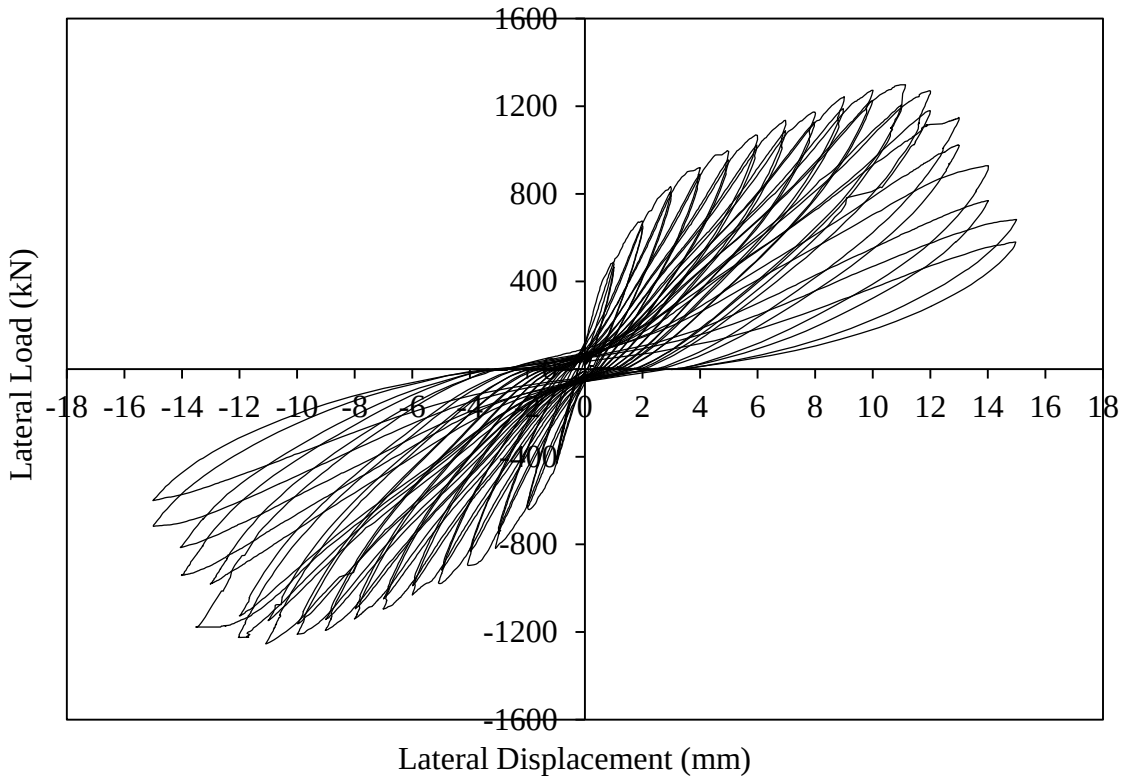

Figure 5-14 Experimental load-displacement results of Palermo shear wall DP1

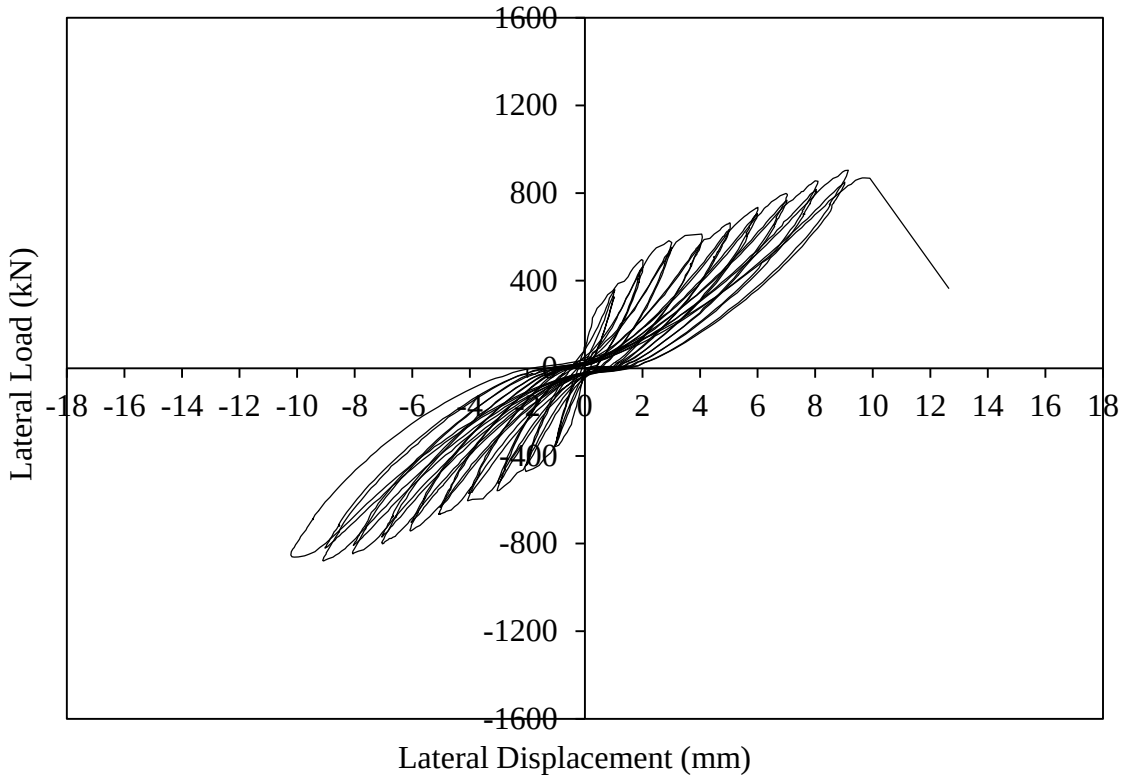

Figure 5-15 Experimental load-displacement results of Palermo shear wall DP2

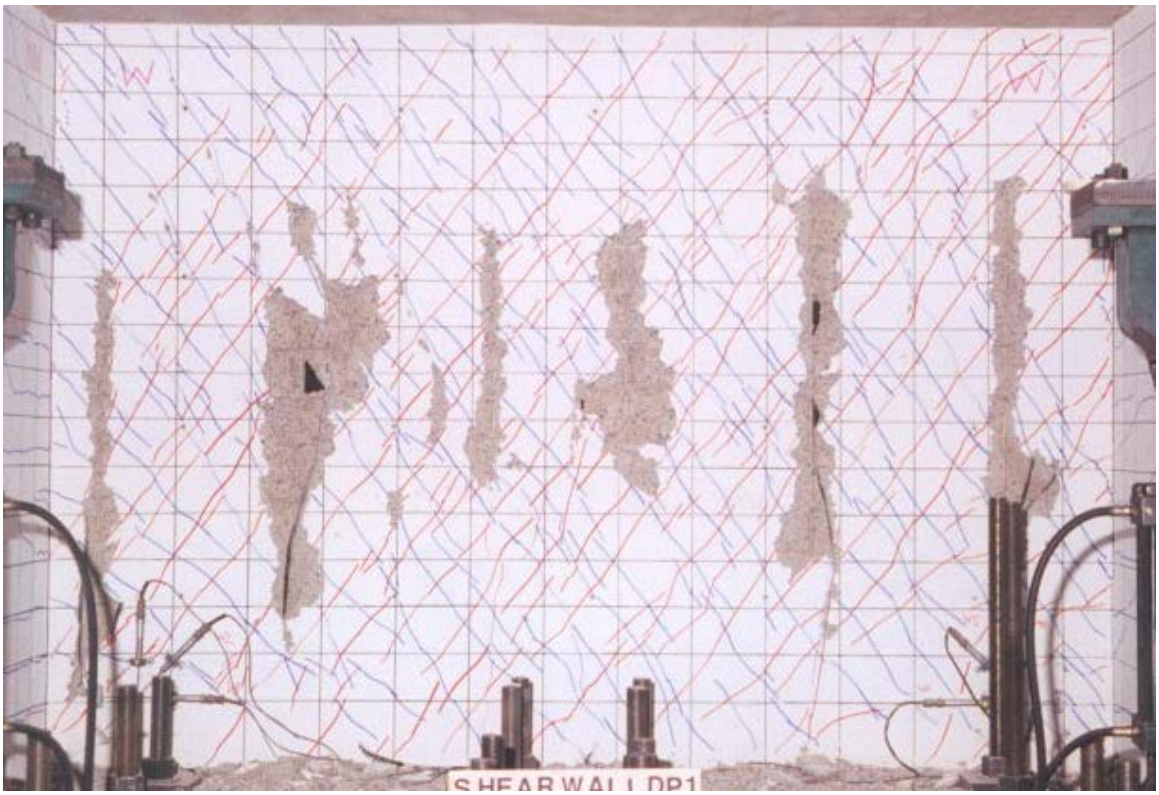

Figure 5-16 Crack pattern and damage sustained by the web of Palermo shear wall DP1 at the termination of the test (Palermo, 2002)

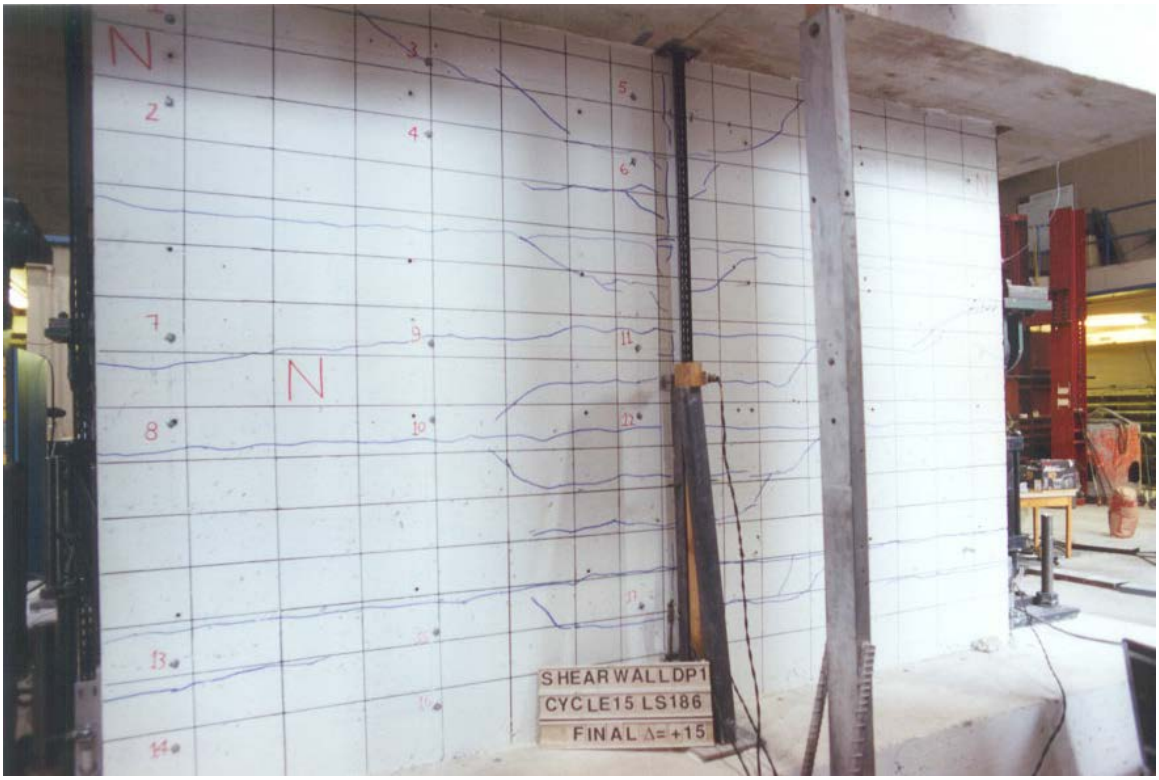

Figure 5-17 Crack pattern and damage sustained by the flange of Palermo shear wall DP1 at the termination of the test (Palermo, 2002)

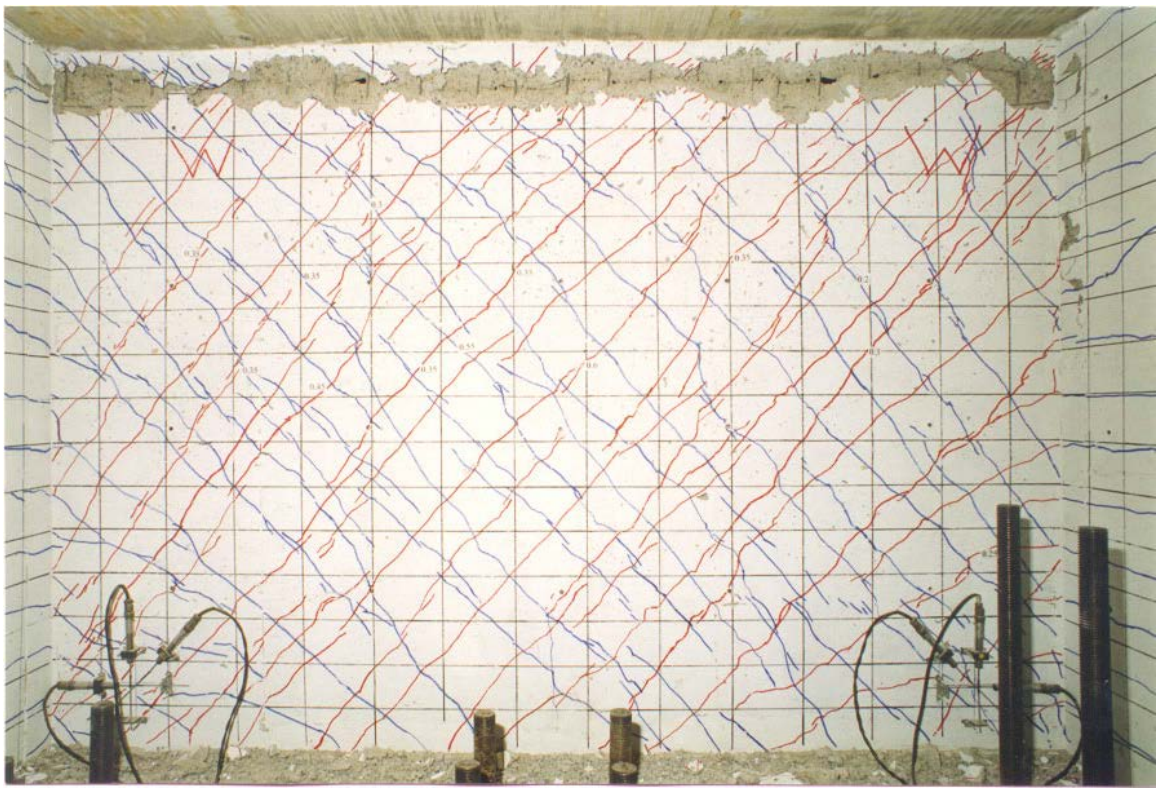

Figure 5-18 Crack pattern and damage sustained by the web of Palermo shear wall DP2 at the termination of the test (Palermo, 2002)

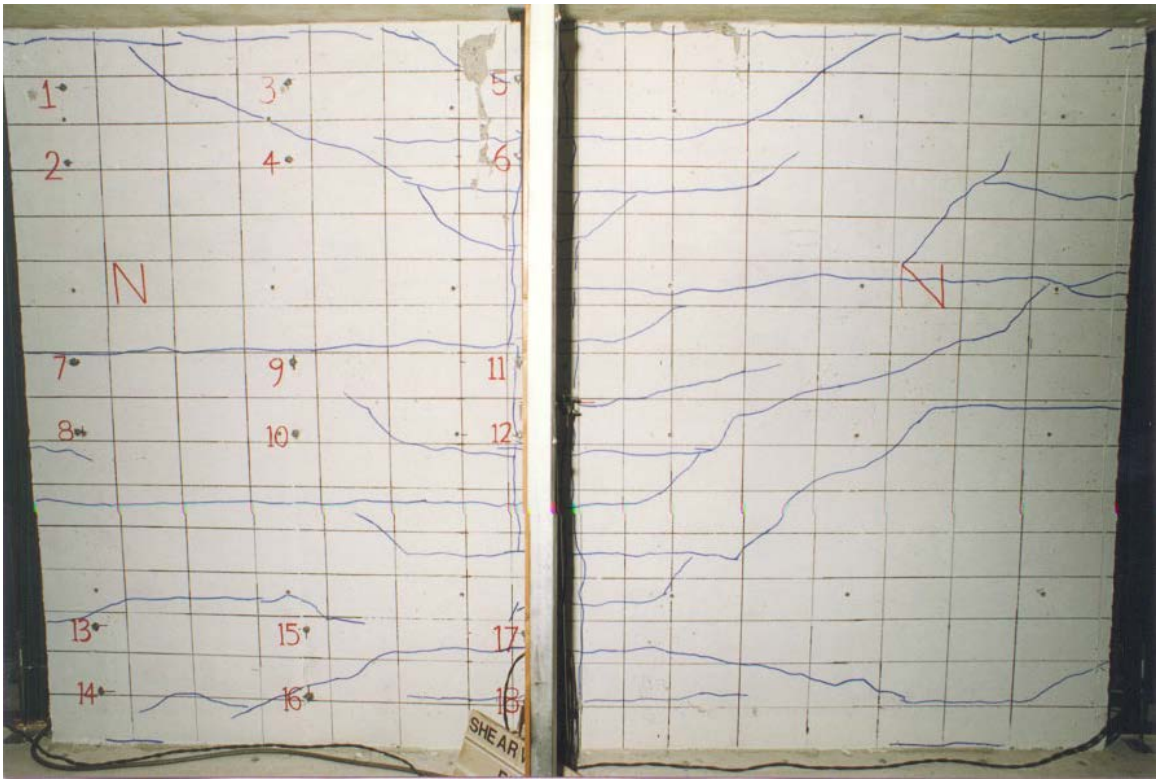

Figure 5-19 Crack pattern and damage sustained by the flange of Palermo shear wall DP2 at the termination of the test (Palermo, 2002)

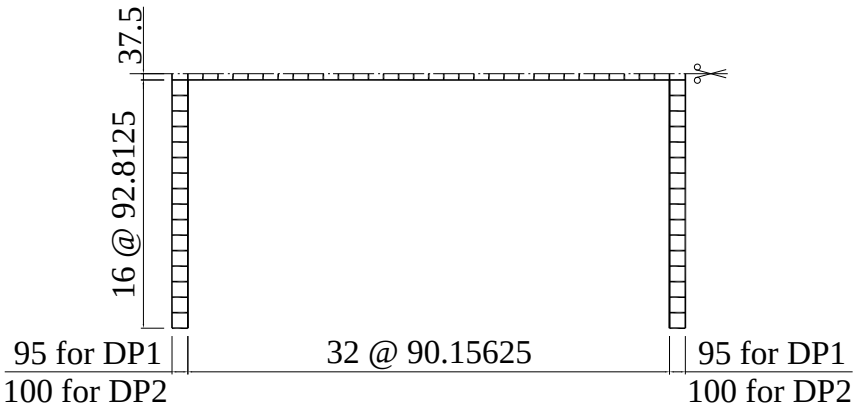

Figure 5-20 Cross section of VecTor3 model for Palermo shear walls DP1 and DP2 (dimensions in mm)

The bottom slab was restrained in all three directions at the base to simulate total foundation fixity, while the nodes lying on the surface of symmetry were restrained in the direction perpendicular to the surface to simulate the conditions and behaviour of the whole shear wall. All reinforcement was modelled as smeared reinforcement, dividing the flange into two separate zones to account for the variation in reinforcement near the edges. Figure 5-21 shows the overall shape of the finite element model analyzed by VecTor3 with the various concrete material properties and reinforcement ratios indicated by different colours. Note that the top and bottom slabs were trimmed to the boundaries of the shear wall. The reason behind that was to minimize the analysis time. However, both slabs were still significantly stiff relative to the shear walls in order to fulfil their purpose.

Lateral displacement loading was applied at the location at which it was applied in the test, at increments of 0.25 mm. Since DP1 and DP2 were tested after 183 days and 168 days from casting, respectively, accounting for concrete shrinkage effects was necessary. Therefore, an overall strain of -0.4×10^{-3} was applied to the body of the wall.

Figures 5-22 and 5-23 show the analytical load-displacement results of the lateral displacement applied on the top slab for DP1 and DP2, respectively, calculated using VecTor3. For DP1, a maximum lateral load capacity of 1381 kN was found, which is about 6% over the capacity achieved experimentally (1289 kN). The post-peak response was also well captured. Figure 5-24 shows the cracking pattern and residual displacement

of DP1 at the termination of the analysis at the completion of displacement cycle number 15. Comparing Figures 5-16 and 5-17 to Figure 5-24, it can be seen that VecTor3 managed to reasonably simulate the cracking pattern with the shear cracking in the web in addition to the flexural cracking at the flanges becoming more extensive at the part connecting to the web.

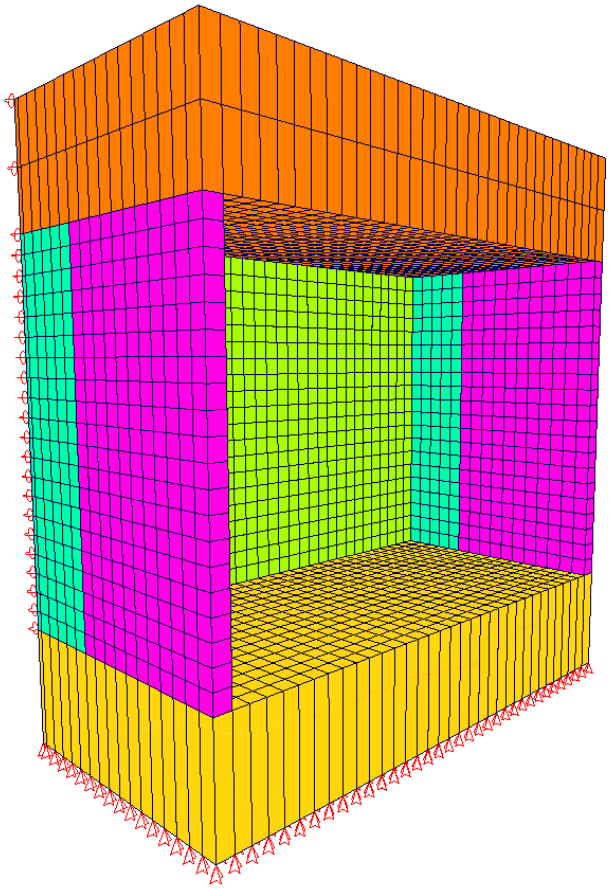

Figure 5-21 Finite element model of Palermo shear walls DP1 and DP2, analyzed by VecTor3 with different colours for different concrete material properties and different reinforcement ratios

For DP2, the failure occurring during the test at the first excursion to 10 mm was not observed in the analysis, where the shear wall showed a more ductile behaviour. However, it should be noted that, experimentally, DP2 failed at the construction joint between the top of the wall and the top slab, where possibly a weak layer of concrete and construction defects existed. The maximum lateral load capacity estimated by VecTor3 was 778 kN, which is about 13% less than the maximum capacity of 879 kN which was achieved experimentally. The analysis was stopped at the completion of displacement cycle number 16, during which the lateral load capacity significantly decreased.

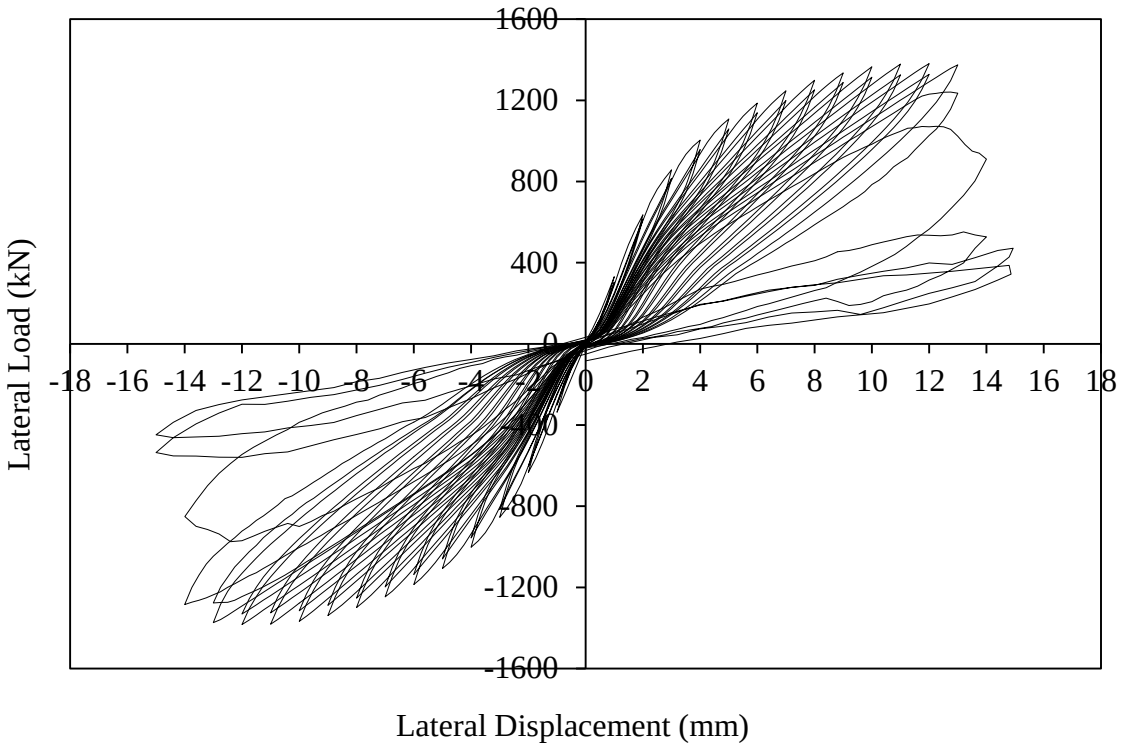

Figure 5-22 Analytical load-displacement results of Palermo shear wall DP1 using VecTor3

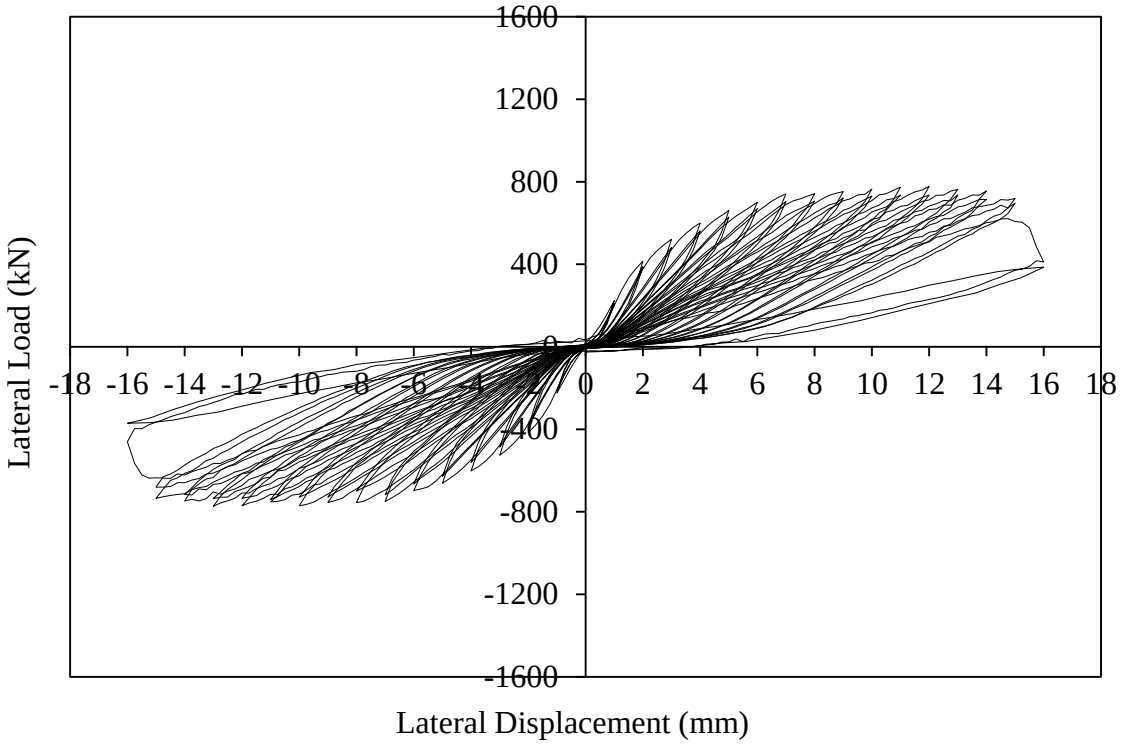

Figure 5-23 Analytical load-displacement results of Palermo shear wall DP2 using VecTor3

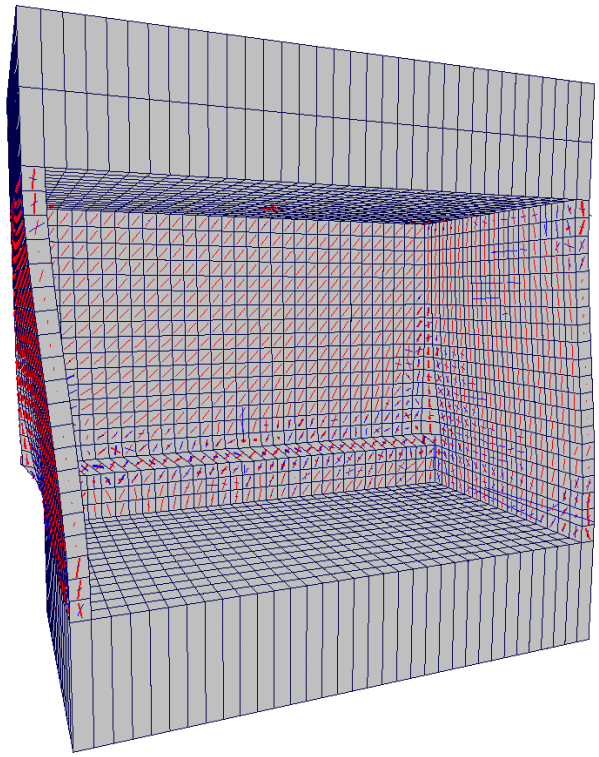

Figure 5-24 Palermo shear walls DP1 and DP2 at the termination of the analysis using VecTor3

Since a major objective of this experimental program was to investigate the three-dimensional effects of wide-flanged walls, the walls were analyzed using VecTor2, which was previously described in Section 5.2.1. VecTor2 is the two-dimensional equivalent to VecTor3; hence it makes a suitable comparison medium to investigate the three-dimensional effects of Palermo shear walls. The exact same material properties and analysis models were used in the VecTor2 analyses. For modelling the flanges, the total reinforcement was smeared through the entire width, amounting to a uniform reinforcement ratio of 0.375% as opposed to the two different reinforcement ratios of 0.627% and 0.230% that were modelled in VecTor3.

Examining the results of the VecTor2 analysis for DP1 shown in Figure 5-25, it can be seen that VecTor2 captures the maximum lateral load capacity of DP1 slightly more accurately than VecTor3. It estimates the capacity as 1254 kN as opposed to the experimental value of 1298 kN, with a difference of about 3%. However, VecTor2 fails to capture the post-peak response of the wall as accurately as VecTor3, which results in overestimating the residual capacity of the shear wall at the termination of the test. This is

an expected effect of modelling the shear wall in two dimensions rather than three dimensions. In two-dimensional analysis, the entire width of the flanges is assumed to be effectively contributing to the capacity of the wall, which is not entirely correct. The parts of the flanges connecting to the web are much stiffer than the outer parts and hence they contribute to the capacity of the wall more than the outer parts, which barely make any contribution near the tips. This is why the wall tends to retain its capacity at higher lateral displacement loading when analyzed using VecTor2.

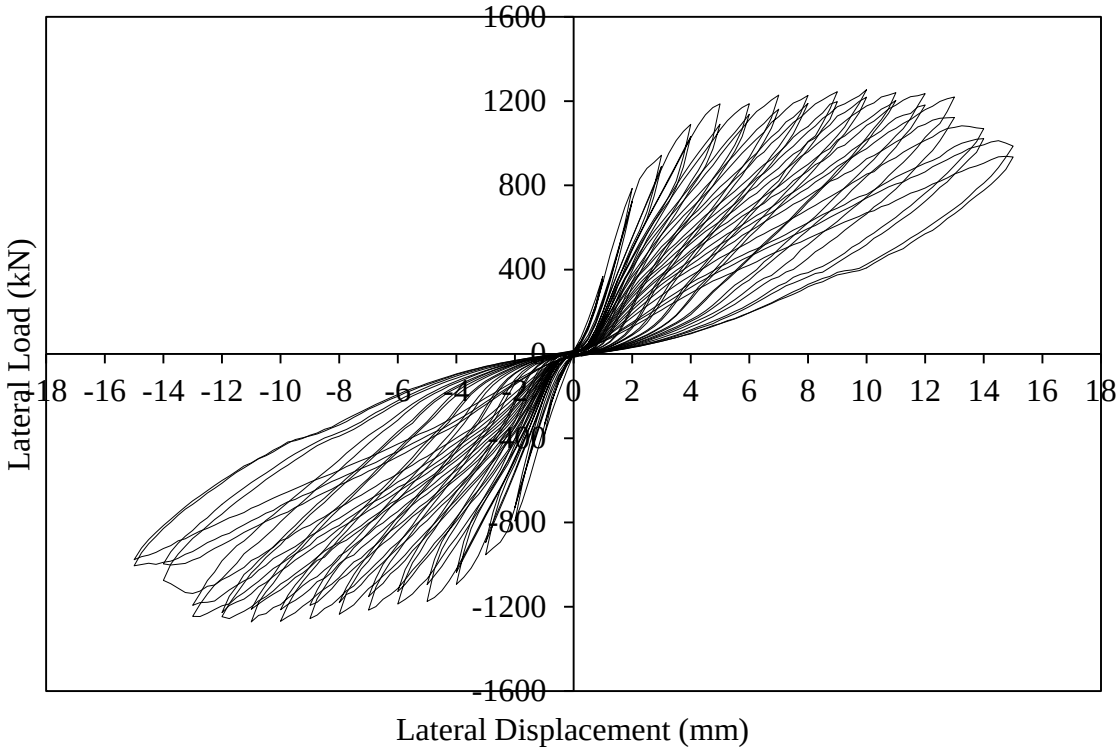

Figure 5-25 Analytical load-displacement results of Palermo shear wall DP1 using VecTor2

For DP2, VecTor2 also fails to predict the abrupt failure that occurred experimentally. One more interesting observation is the overestimation of the lateral load capacity of the shear wall, which came to about 1058 kN as opposed to the experimental result of 879 kN, which is an overestimation of more than 20%. Also, the residual lateral load capacity at the termination of the analysis was significantly higher than that estimated by VecTor3. Both observations fall in line with the results obtained from the analysis of DP1, and the difference in the behaviour estimation between VecTor2 and VecTor3 also follows the same explanation discussed for DP1. The analytical load-displacement results for DP2 obtained from VecTor2 are presented in Figure 5-26.

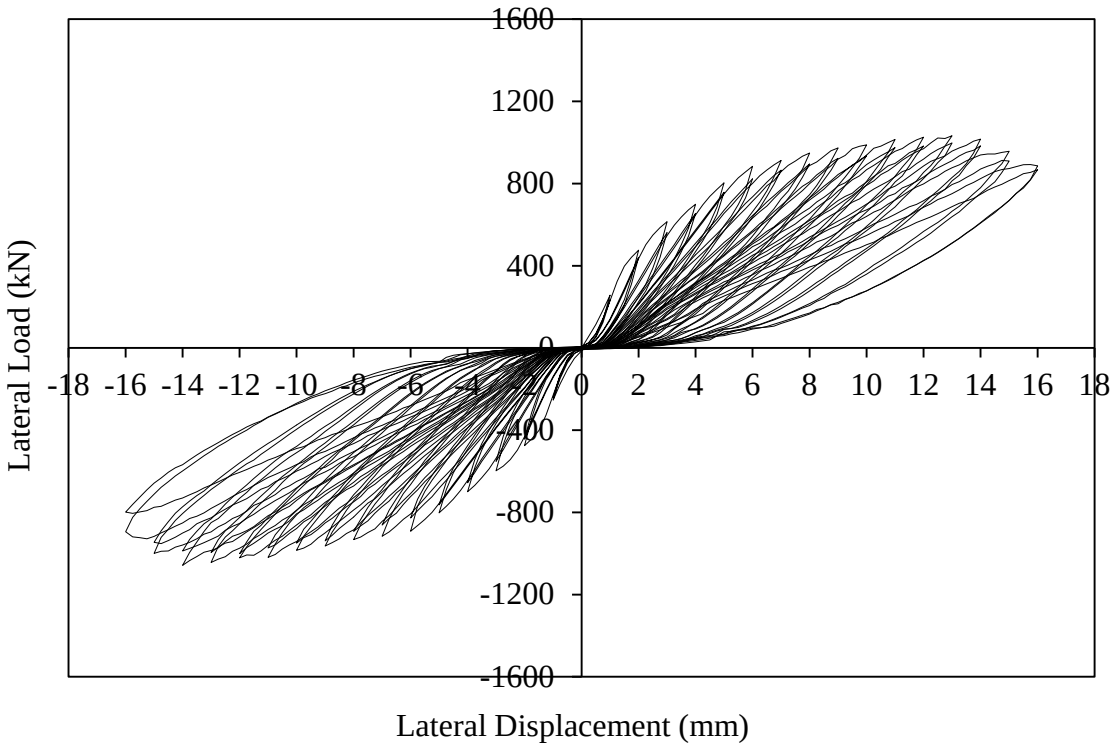

Figure 5-26 Analytical load-displacement results of Palermo shear wall DP2 using VecTor2

5.4 Dynamic Loading

This section presents a verification study for the dynamic analysis capabilities incorporated in VecTor3. In addition to the advanced concrete and steel mechanisms that govern the overall behaviour of reinforced concrete structures under monotonic loading, and the mechanisms that affect the behaviour under cyclic loading, some mechanisms are specific to the dynamic loading conditions of seismic, impact, and blast. Among these mechanisms are the strain rate effects which have proven to play an important role in the behaviour of reinforced concrete structures, as they alter the mechanical properties of both concrete and steel.

Due to the rise in terrorist attacks and explosions threatening critical infrastructure and services buildings, or at least the increase of threats, blast loading is increasingly becoming a major research topic in the structural engineering field. Therefore, a blast test of a two-way fully-fixed reinforced concrete slab, tested by Jacques (2011), has been chosen for a verification analysis of VecTor3 to analyze these loading conditions.

5.4.1 Jacques Slab

Jacques (2011) undertook a research program aiming at developing fibre-reinforced polymer (FRP) retrofit methodologies for blast-damaged structural members. The program involved the testing of thirteen reinforced concrete wall and slab specimens divided into five companion sets with one-way/two-way and simply-supported/fully-clamped support conditions. The specimens were subjected to simulated explosions generated at the University of Ottawa Shock Tube Testing Facility.

Since the program's main focus was the investigation of fibre reinforced polymer (FRP) retrofit, most of the specimens were constructed with FRP sheets covering their surfaces. The specimen chosen for this corroboration study, Specimen SC5-C was an unretrofitted control specimen from Companion Set 5, which also had an identical slab retrofitted with carbon fibre reinforced polymer (CFRP). SC5-C was a two-way fully-clamped slab with nominal dimensions of 2440×2440×75 mm. The slab was reinforced with two meshes of eleven evenly-spaced 6.3 mm diameter non-deformed (plain) steel reinforcing bars in both directions, one at the top and the other at the bottom, with a clear concrete cover of 6 mm. This provided a total reinforcement ratio of 0.375% for the slab section. The reinforcing bars had 180-degree hooks at both their ends, with an outer diameter of 63 mm and a hook length of 150 mm, ensuring sufficient development length within the support region. These hooks should have provided a reasonable amount of bond between concrete and steel reinforcing bars to compensate for the fact that non-deformed reinforcing bars were used. The dimensions and reinforcement layout of SC5-C are shown in Figure 5-27.

The slab was constructed using 10 mm crushed limestone aggregate, with a target slump of 100 mm. On the day of the test, the compressive strength was measured at 49.5 MPa, based on the average of at least three standard cylinders. The non-deformed steel reinforcing bars had a yield stress of 580 MPa at a yield strain of 0.0028 mm/mm (Young's modulus of 207,143 MPa). The ultimate strength of the bars was 670 MPa at an ultimate strain of 0.196 mm/mm. The material properties of the bars were determined based on an average of four tensile coupon tests.

Fully-fixed support conditions were achieved by clamping the specimen between the shock tube test frame and a specially constructed rigid steel frame assembled from four 152×152×6.4 mm hollow steel sections, as shown in Figure 5-28. The slab had a final clear span of 2132 mm.

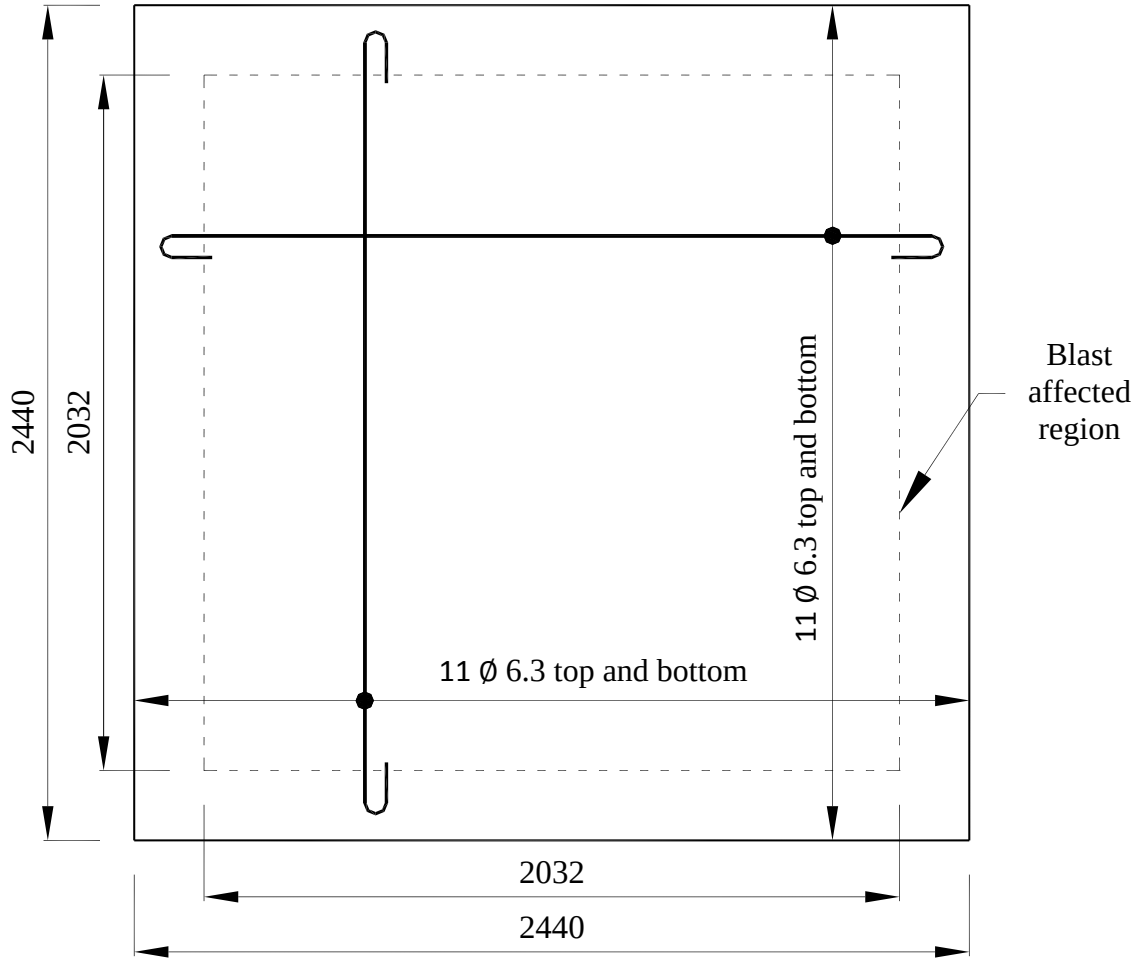

Figure 5-27 Jacques specimen CS5-C dimensions and reinforcement layout (dimensions in mm)

Specimen CS5-C was subjected to seven shock tests with varying driving pressures, but only the first three were analyzed using VecTor3 and presented in this section. A summary of the reflected pressure properties and the response of the slab for the first three shock waves are presented in Table 5-10, where 'VT3' denotes VecTor3 results.

Figure 5-28 Fully-fixed support conditions of Jacques specimen CS5-C (Jacques, 2011)

Table 5-10 Reflected pressure properties and the response of Jacques specimen CS5-C

Shot #	Reflected Pressure (kPa)	Positive Phase Duration (ms)	Reflected Impulse (kPa.ms)	Period (ms)		First Peak Deflection (mm)		Residual Deflection (mm)	
				Test	VT3	Test	VT3	Test	VT3
1	8.2	5	24.7	16	18	0.53	0.57	0	0
2	17.2	14	142.7	29	30	3.51	3.80	1.6	0.13
3	26.7	15.4	219.6	35	35	6.69	7.49	0	0.15

For the finite element discretization, only one-quarter of the slab was modelled, taking advantage of the geometric and loading symmetry. The quarter-slab was discretized into 4232 elements, with ten 7.5 mm elements through the depth and twenty-three 48 mm elements through the length and width. Isoparametric hexahedral elements were used, in order to have the ability to consider geometric nonlinearity. For the support conditions, the nodes on the edges were restrained in all three directions to simulate the fully-clamped experimental support conditions. The nodes lying on the axes of symmetry were restrained in their perpendicular direction to simulate the behaviour of the whole

structure. Steel reinforcing bars were modelled as discrete truss bars meshes at 7.5 mm from the top and bottom surfaces. This resulted in a clear cover of 4.35 mm as opposed to the actual 6 mm clear cover. Figure 5-29 presents the finite element model used for the analysis of Jacques specimen CS5-C, showing the support conditions and the steel reinforcing bars of the top and bottom meshes going along the axis of symmetry.

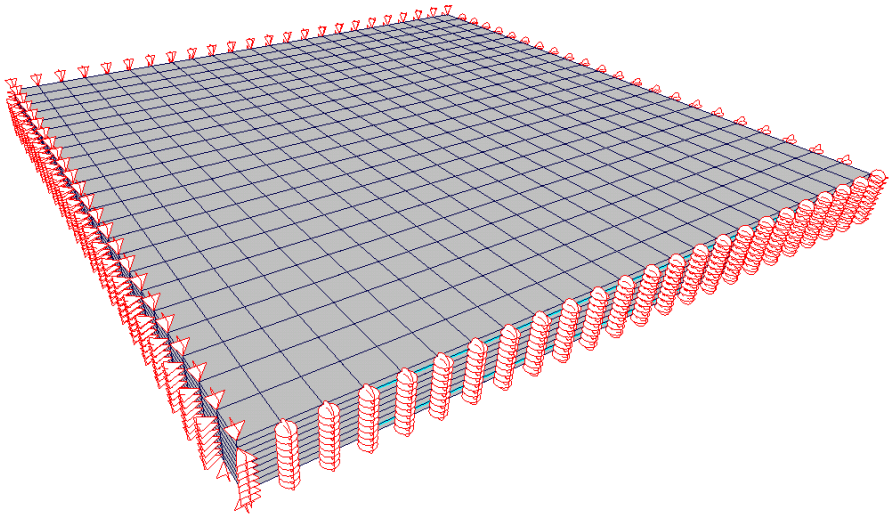

Figure 5-29 Finite element model of the analysis of Jacques specimen CS5-C

Figures 5-31, 5-33, and 5-35 show the reflected pressure profiles of Shot #1, Shot #2, and Shot #3, respectively, for Jacques specimen CS5-C, which were closely matched in the loading profiles used in the finite element analysis. The pressure was used to calculate concentrated loads on the nodes on the top surface of the slab, based on the nominal area around each node.

The finite element analysis was carried out with a time step of 0.1 ms, which is much smaller than the widely-accepted recommendation of using one tenth of the period for such analyses. For analyzing the multiple shots, the damaged state of the slab had to be preserved to act as the initial state for the subsequent shot. For this to be done, the analysis carried out for each shot continued until the slab oscillations almost fully damped out, then the strain histories were saved in a file that acted as a 'seed' to start the analysis of the subsequent shot from. Also, after the damping of the slab oscillations, the residual displacement could be checked and saved.

The slab did not suffer any damage or cracking due to Shot #1, which was the case for the VecTor3 analysis as well. Since the reflected pressure was small for this shot, the

concrete in the slab remained in the linear elastic range. However, for Shot #2, Jacques (2011) reported that "small cracks began to appear on the surface of the specimen, although these appeared to be random in nature". VecTor3 estimated the cracking pattern shown in Figure 5-30 (a) after Shot #2. While the cracks are small, as reported by Jacques (2011), they do not appear to be random in nature. Flexural cracks can be seen at the centre of the slab and around the supports, which is a typical expected cracking pattern for a fully-clamped two-way slab under bending. Jacques (2011) also reported no additional cracking or damage due to Shot #3, which is rather doubtful, since Shot #2 caused a peak displacement of 3.51 mm, while Shot #3 caused 6.69 mm, making it illogical that no additional cracking, or at least widening of the existing cracks, occurred. VecTor3 estimated more damage due to Shot #3, as shown in Figure 5-30 (b).

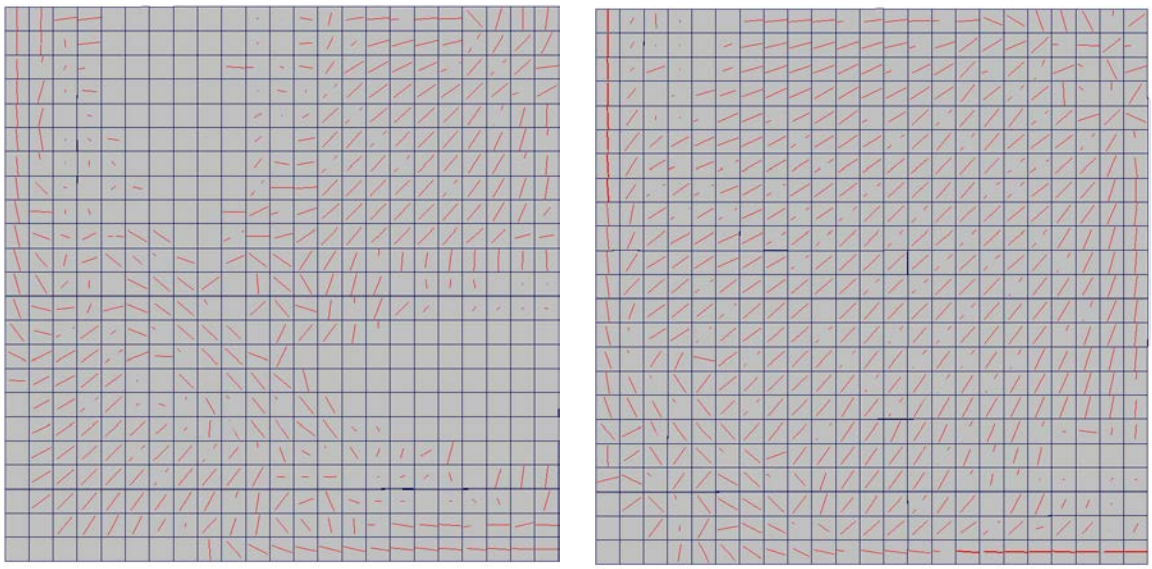

Figure 5-30 Residual cracks pattern after Shot #2 (a) and Shot #3 (b) for Jacques specimen CS5-C

Figures 5-32, 5-34, and 5-36 show the experimental and analytical mid-point displacement for Jacques specimen CS5-C due to Shot #1, Shot #2, and Shot #3, respectively. The analytical results show a good correlation with the experimental results, where the mean analytical to experimental ratio for the period for the three shots analyzed is 1.05, with a coefficient of variation of 6%. For the first peak mid-point deflection, the mean analytical to experimental ratio is 1.09, with a coefficient of variation of 2%.

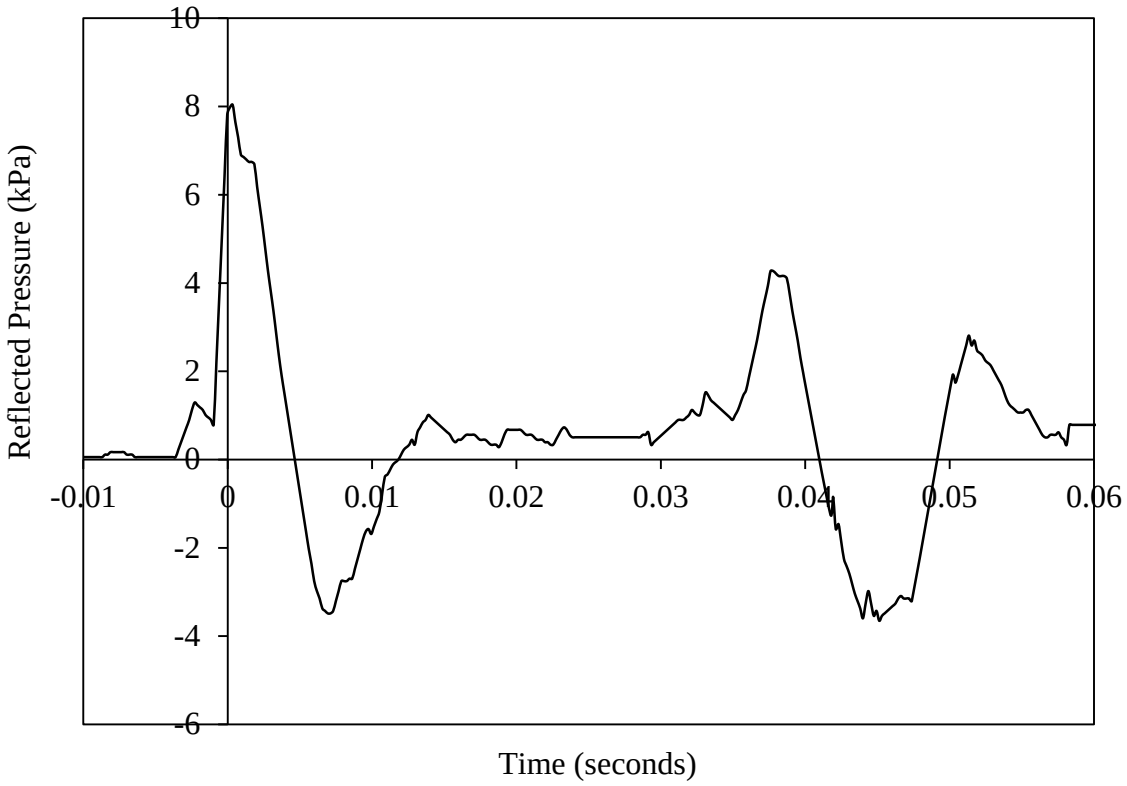

Figure 5-31 Reflected pressure profile of Shot #1 for Jacques specimen CS5-C

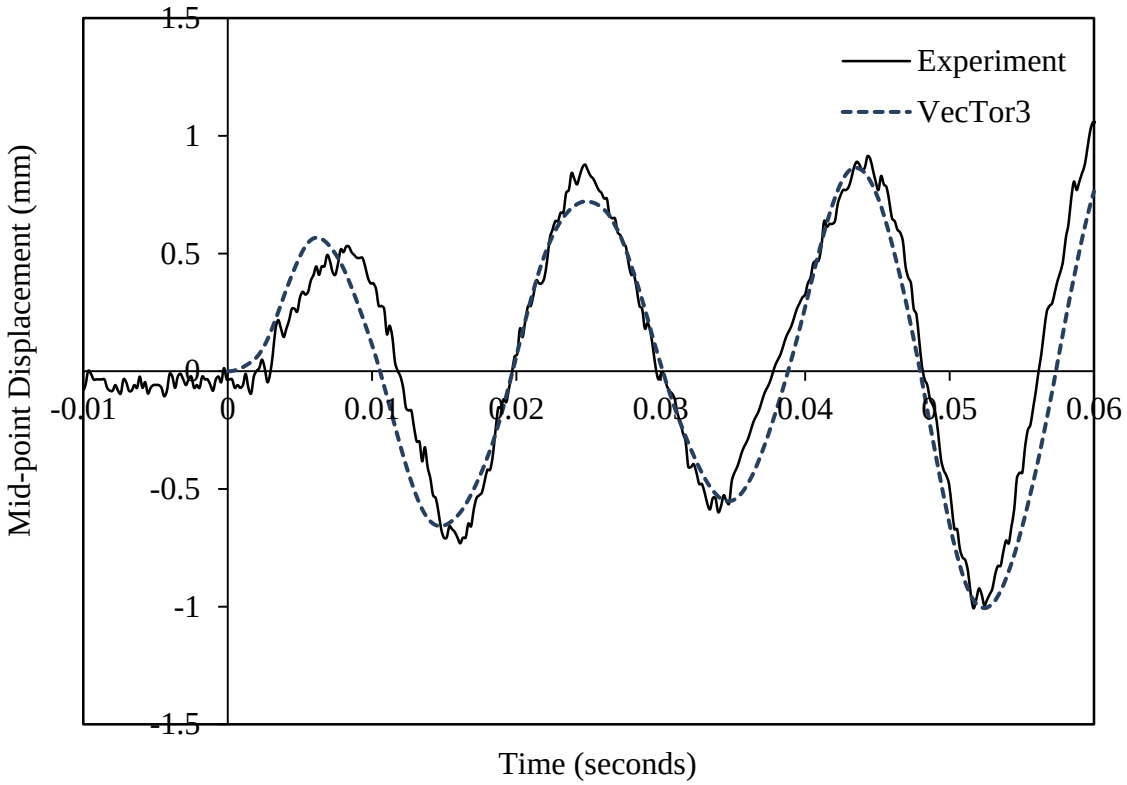

Figure 5-32 Experimental and analytical mid-point displacement due to Shot #1 for Jacques specimen CS5-C

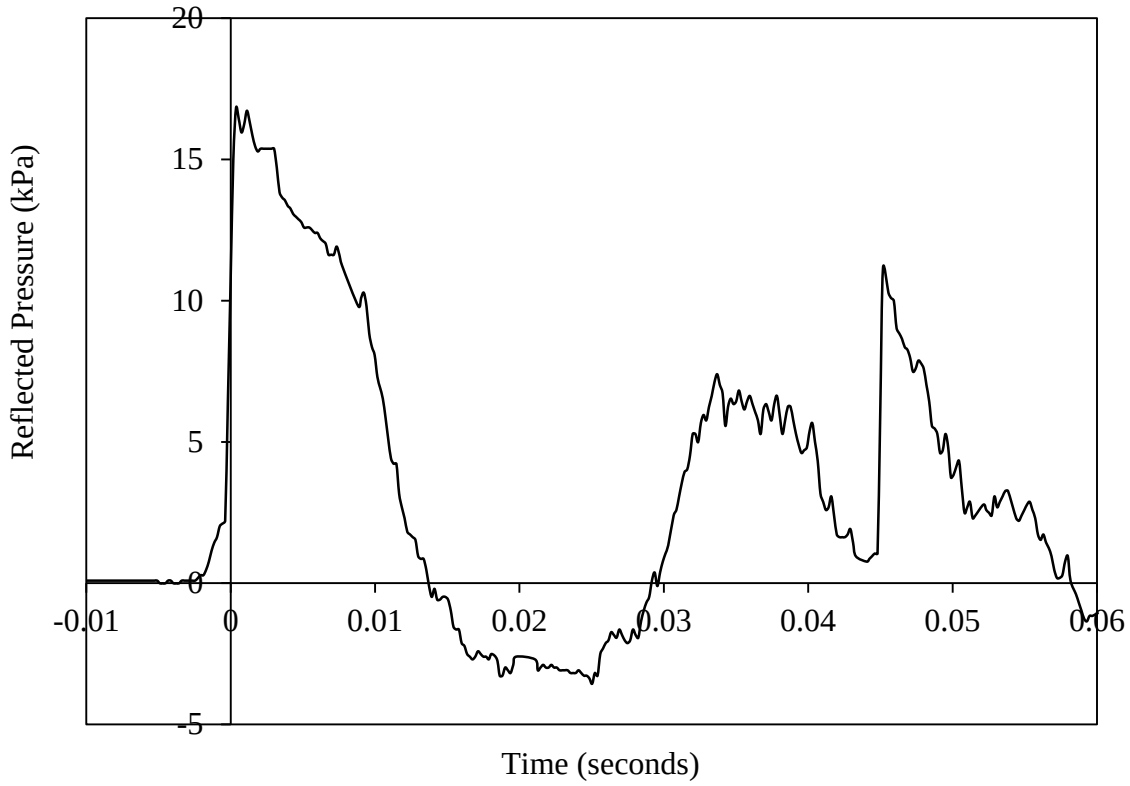

Figure 5-33 Reflected pressure profile of Shot #2 for Jacques specimen CS5-C

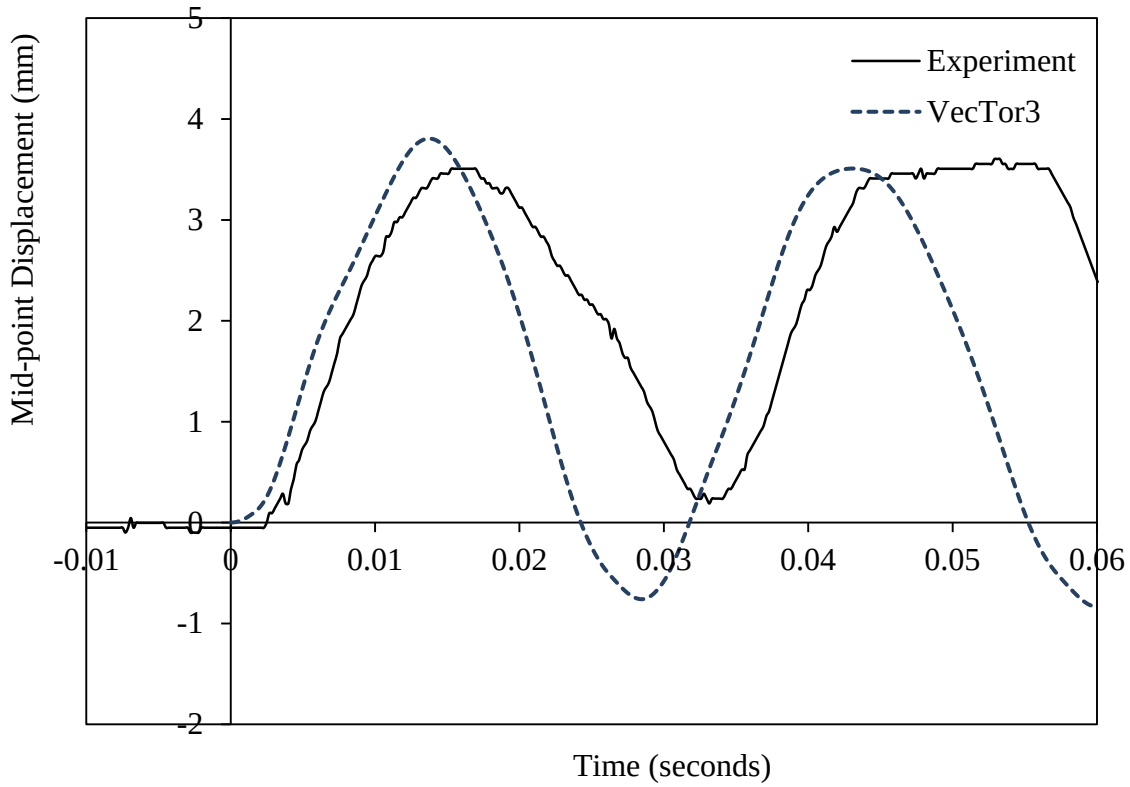

Figure 5-34 Experimental and analytical mid-point displacement due to Shot #2 for Jacques specimen CS5-C

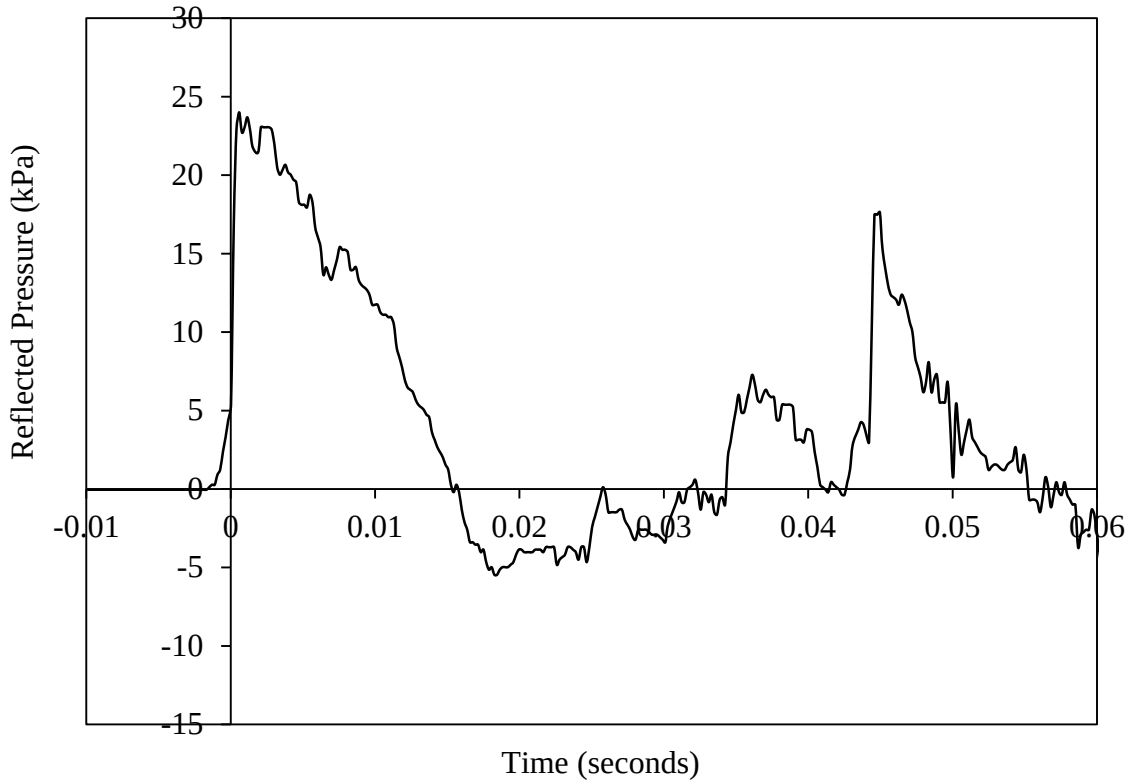

Figure 5-35 Reflected pressure profile of Shot #3 for Jacques specimen CS5-C

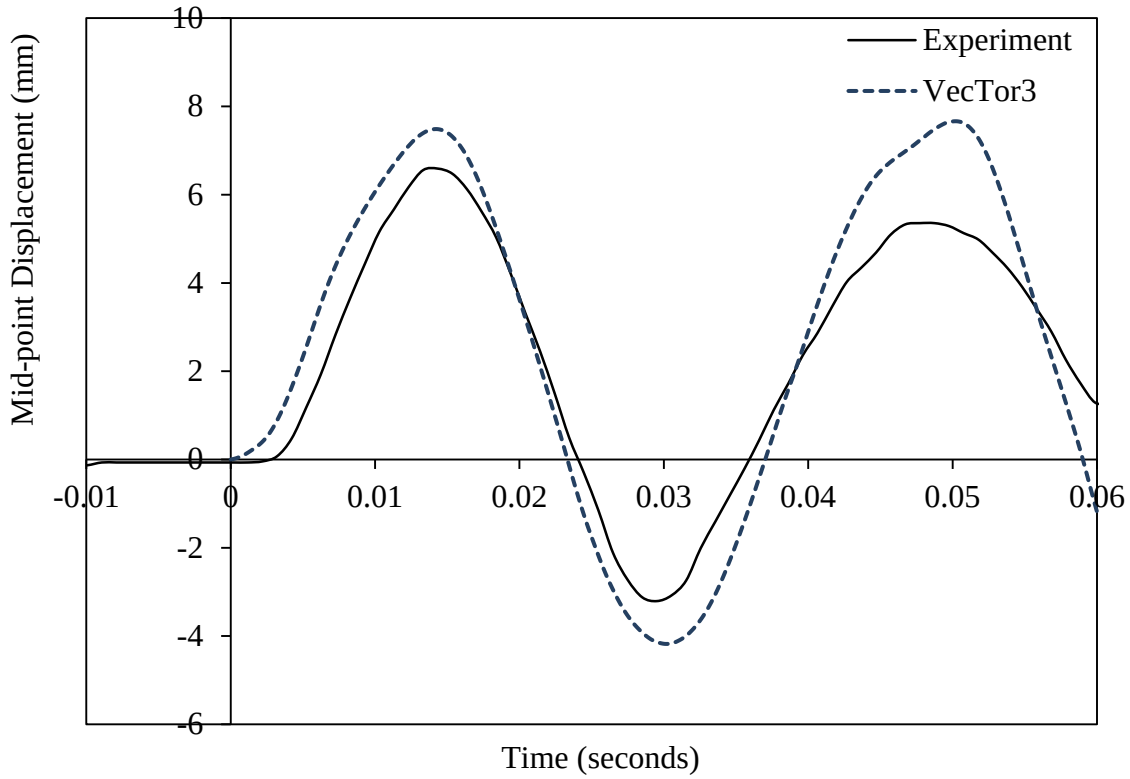

Figure 5-36 Experimental and analytical mid-point displacement due to Shot #3 for Jacques specimen CS5-C

Examining Figures 5-32, 5-34, and 5-36, one can notice generally good correlation between the analytical and experimental results. For Shot #1, the exceptionally good correlation is due to the precision of any analysis falling within the linear elastic behaviour of concrete, where a very limited contribution from the advanced concrete mechanisms exists. However, this excellent correlation proves the reliability of the dynamic analysis procedure used by VecTor3 for the analysis.

The experimental results for Shot #2 show a short plateau at the second peak, as shown in Figure 5-34, which was probably caused by some relaxation or local damage. This plateau was not captured by VecTor3. Also, the VecTor3 results show a higher second peak in the response of Shot #3, as shown in Figure 5-36, which is probably caused by the spike in reflected pressure, seen in Figure 5-35. This higher peak did not appear experimentally. This may be due to the fact that the two pressure sensors used to measure the reflected pressure were located along the bottom and side walls of the expansion section of the shock tube, 50 mm away from the specimens. Therefore, it is possible that some discrepancy would occur between the measured reflected pressure and the actual reflected pressure that hit the slab.

Residual deformations were reasonably estimated by VecTor3 for Shot #1 and Shot #3. However, for Shot #2, where significant damage occurred, residual deformations were significantly underestimated. This can be attributed to the fact that localized plastic strains of steel reinforcing bars crossing the cracking surfaces are not accounted for in the analysis.

5.5 Thermal Loading

Since one of the major objectives of this research is to investigate and model the behaviour of reinforced concrete structures under fire, additional corroboration studies have been undertaken to investigate the capability of VecTor3 in this regard, and to evaluate the adequacy of the currently available models. In an attempt to simulate the actual conditions of concrete when subjected to fire, three different cases were investigated through three experimental series conducted by the National Research Council Canada (NRC):

Case I: The behaviour of reinforced concrete columns under sustained loading during the event of fire, investigated through the experimental series of Columns 1 to 12 (Lie and Lin, 1983).

Case II: The behaviour of reinforced concrete columns under sustained axial loading during the event of fire taking into account the effect of the lateral expansion of slabs, investigated through the testing of Column 1582 (Mostafaei et al., 2012).

Case III: The post-fire behaviour and capacity of reinforced concrete structures, investigated through the experimental series of Columns A and B (Lie et al., 1986)

All three series were conducted on geometrically and structurally identical full-scale column specimens, although the concrete mix and level of loading were different. The columns had a 305 mm square cross section, and a height of 3810 mm. They were reinforced using four 25 mm diameter longitudinal steel reinforcing bars at the four corners with a clear cover of about 48 mm, tied using 10 mm diameter ties at a spacing of 305 mm. Figure 5-37 shows the cross section of a typical specimen and Figure 5-38 shows the reinforcement of the columns in an isometric view.

The compressive strength of concrete varied among the different specimens. For the steel reinforcing bars, it appears that only one test was carried out for all the specimens, where the yield stress and the ultimate strength of the longitudinal bars were reported as 444 MPa and 730 MPa, respectively, and the yield stress and the ultimate strength of the ties were reported as 427 MPa and 671 MPa, respectively.

The simulation of natural fire conditions in the three experimental series was done in the NRC Column Furnace Facility, shown in Figure 5-39, following the ASTM E119 – 12a (2012) model (which is similar to the CAN/ULC S101-07 (2007) model) for the ascending temperature branch (fire development phase) and the ISO 834-1:1999 (1999) model for the descending temperature branch (fire decay phase). For all three experimental series, thermocouples were used to measure the temperatures of concrete and steel at different locations through the depth and height of the columns throughout the entire duration of the tests.

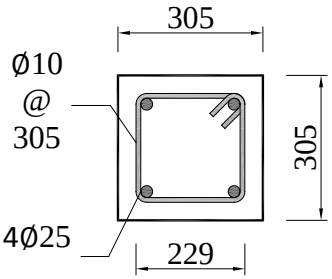

Figure 5-37 Cross section of a typical NRC column specimen (dimensions in mm)

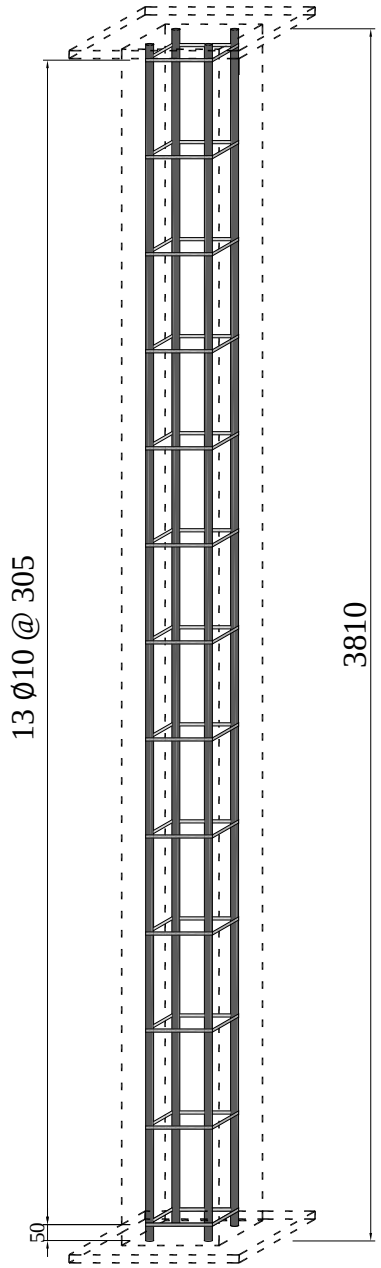

Figure 5-38 Reinforcement of a typical NRC column specimen in an isometric view (dimensions in mm)

Figure 5-39 NRC Column Furnace Facility (Mostafaei et al., 2012)

In VecTor3, the thermal loading analysis procedure is composed of two separate analysis stages: the heat transfer analysis stage (or the coupled heat and moisture transfer analysis for more accurate results and prediction of spalling) and the structural analysis stage. The analysis process is time stepped, where the results are generated for predefined time steps. The heat transfer analysis is performed first, generating the temperatures at all the nodes composing the structure. Since the thermal properties of concrete are dependent on

its temperature, this analysis becomes iterative. These temperatures are then used to estimate the temperature of each element based on an average of the temperatures of the nodes comprising it. The element temperatures are then used to estimate thermal expansion strain and the various mechanical properties as discussed in Chapter 3. Finally, the thermal expansion strain is applied as a pre-loading strain, in addition to the external loading conditions of the structural element. Another iterative process is then started for the structural analysis stage until equilibrium is satisfied.

5.5.1 Heat Transfer Analysis

The first step required in the corroboration study is to evaluate the heat transfer analysis capabilities of VecTor3 and the adequacy of the models provided by the ASCE Manual of Practice (Structural Fire Protection by T. T. Lie, 1992), the former version of the Eurocode (ENV 1992-1-2:1995, 1996), and its current version (EN 1992-1-2:2004, 2005) for estimating the thermal properties of concrete at elevated temperatures. This check aims at testing the standards' evaluation of the various thermal properties of concrete and their ability to provide a reliable means for heat transfer analysis. The analyses discussed in this section involve the heat transfer analysis stage only, without the structural analysis stage.

To be able to compare the experimentally measured temperatures to the analytically estimated ones, a special finite element mesh was used in a separate heat transfer analysis in order to ensure the occurrence of a mesh node at the location of each thermocouple through the section of the specimens. Also, only one-quarter of the section was analyzed since the section is symmetric in two directions, and the model had only one element, 25 mm thick in the vertical direction, since the heat transfer analysis is two-dimensional through the thickness of the column. Figure 5-40 shows the finite element mesh, where the element discretization distances are the same in both directions. It also shows the locations of the thermocouples installed through the section of the column specimens, shown as black circles.

The model was subjected to the ASTM E119 – 12a (2012) model (which is similar to the CAN/ULC S101-07 (2007) model) for the ascending temperature branch (fire development phase) and the ISO 834-1:1999 (1999) model for the descending temperature branch (fire decay phase) along all the edges. Figure 5-41 shows a typical temperature distribution through the quarter cross section as estimated by VecTor3.

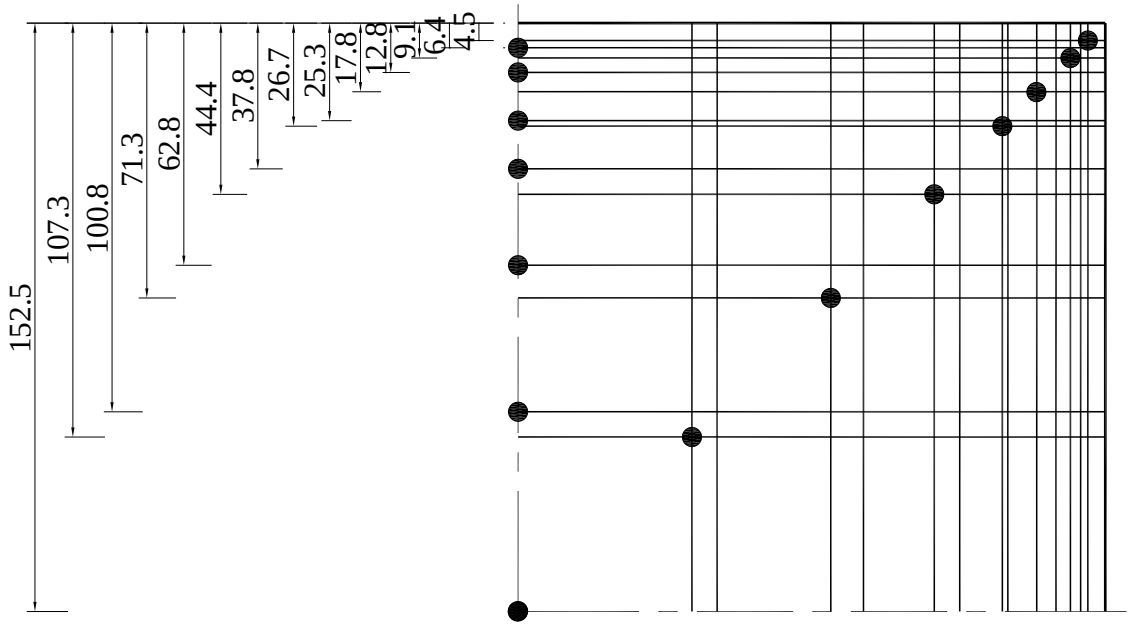

Figure 5-40 Finite element mesh of heat transfer analysis and locations of thermocouples (dimensions in mm)

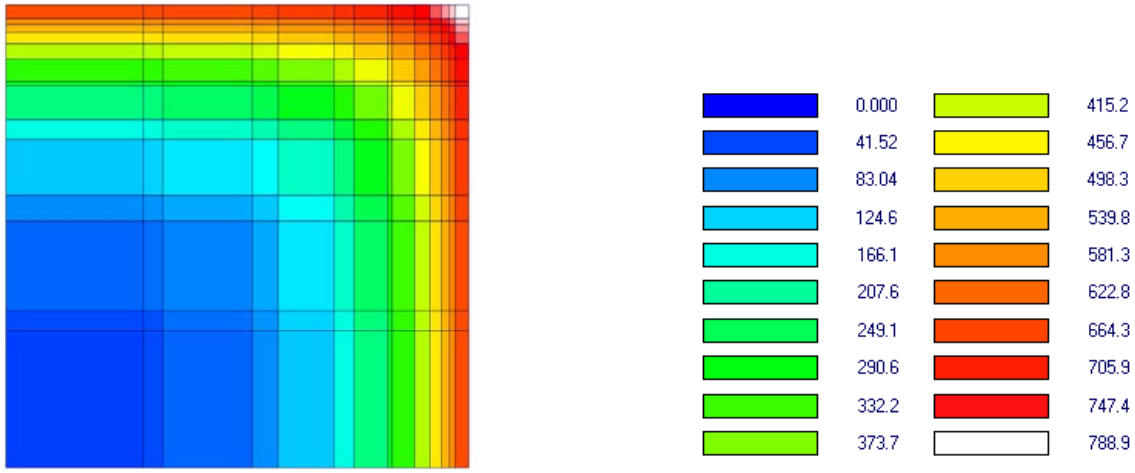

Figure 5-41 Typical temperature distribution through the quarter cross section after 30 minutes as calculated by VecTor3 with the legend indicating temperatures in ºC

The temperatures of three thermocouples were chosen for comparison to the analytical results: at 25.3 mm from the surface, at 62.8 mm (the location of the steel bars), and at 152.5 mm (the centre of the columns). Since the ASCE Manual of Practice (Structural Fire Protection by T. T. Lie, 1992) and the former version of the Eurocode (ENV 1992-1-2:1995, 1996) provide different models for thermal properties of concrete mixed with calcareous aggregates and concrete mixed with siliceous aggregates, the analysis results for both cases are presented for comparison. The current version of the Eurocode (EN 1992-1-2:2004, 2005), however, does not distinguish between concrete mixed with different types of aggregate, hence, only one curve is shown.

As explained in Section 3.4.1.3, another major difference between the models is that the former version of the Eurocode (ENV 1992-1-2:1995, 1996) and the current version (EN 1992-1-2:2004, 2005) recognize the effect of the moisture content of concrete on its specific heat capacity, while the ASCE Manual of Practice (Structural Fire Protection by T. T. Lie, 1992) does not. Therefore, separate analyses were undertaken for three different moisture contents in concrete: 0% (absolutely dry), 4%, and 10% by weight.

Among the three NRC experimental series to be discussed, two were mixed with calcareous aggregates (Columns 10 to 12 and Column 1582) and one was mixed with siliceous aggregates (Columns A and B). The results of the heat transfer analyses are presented in two sets of plots, divided according to the type of aggregate used in the concrete mix, as follows.

5.5.1.1 Calcareous-Aggregates Specimens

The first set of plots gathers the experimental series of Columns 10 to 12 and the experimental series of Column 1582. Calcareous aggregates were used in the concrete mix, and the specimens were kept in the fire-simulating furnace until failure of the specimen occurred. The relative humidity at the centre of Columns 10, 11, 12, and 1582 on the day testing was reported as 75%, 75%, 76%, and 72.8%, respectively, which is equivalent to a moisture content of 3.16%, 3.16%, 3.20%, and 3.07% by weight,

respectively. The analytical results of concrete mixed with siliceous aggregates are also presented in these plots just for the sake of comparison.

For Column 1582, for monitoring the temperature of concrete through the depth of the column, a group of thermocouples was installed at the locations shown in Figure 5-40 at mid-height of the column. For Columns 10, 11 and 12, four groups of thermocouples were installed, also at the locations shown in Figure 5-40, at three levels through the height of the columns. A group of thermocouples was installed at one quarter of the height of the column from the top and another at the same distance from the bottom. Two other groups of thermocouples were installed at mid-height of the column at two diagonally opposite quadrants of the square cross section. The results shown here represent the average measurements of the thermocouples at the same location for the four groups.

Figures 5-42, 5-43, and 5-44 show the results of the analysis for concrete with 0% moisture content (absolutely dry) at depths of 25.3 mm, 62.8 mm, and 152.5 mm, respectively. Figures 5-45, 5-46, and 5-47 show the results at the same depths, respectively, for concrete with 4% moisture content by weight, and Figures 5-48, 5-49, and 5-50 show the results, also at the same depths, for concrete with 10% moisture content by weight.

Examining the experimental results of the specimens included in this set of plots, one can notice that the results of Columns 10, 11, and 12 are relatively similar, while the results of Column 1582 are different. This can be attributed to the fact that Columns 10, 11, and 12 were cast and tested as a part of one test series; hence, the same materials and same test technique were used, while Column 1582 was a part of a different series that was cast and tested many years later. Also, as will be explained in Section 5.5.2.2, Column 1582 was subjected to lateral loading, which caused significant spalling of the concrete cover over the entire face that was subjected to tension. This would effectively cause the higher temperatures that can be observed in the plots.

Another major observation is how all the models produce relatively similar results for concrete with low levels of moisture content, except for the models provided by the ASCE Manual of Practice (1992) for concrete mixed with calcareous aggregates. Yet, at

higher levels of moisture content, the models provided by ENV 1992-1-2:1995 (1996) and EN 1992-1-2:2004 (2005) produce results different than those produced by the models provided by the ASCE Manual of Practice (1992), which do not incorporate the effect of moisture content of concrete on its specific heat capacity.

Finally, it can be observed that the models provided by the ASCE Manual of Practice (1992) for concrete mixed with calcareous aggregates manage to accurately estimate the temperature of concrete at shallow depths from the surface, where the level of moisture content of concrete does not play a significant role. However, with a more comprehensive look at the results of the analyses of concrete with a moisture content of 4% by weight, which is around the same moisture content in concrete on the day of testing for all the specimens, it becomes evident that the models provided by the latest version of the Eurocode (EN 1992-1-2:2004, 2005) are the ones most capable of estimating the experimental temperatures. The Eurocode (EN 1992-1-2:2004, 2005) also manages to capture the kink in the plot at 100 ºC caused by the evaporation of the evaporable water inside the concrete, as explained in Chapter 3, which can be seen clearly in Figure 5-47.

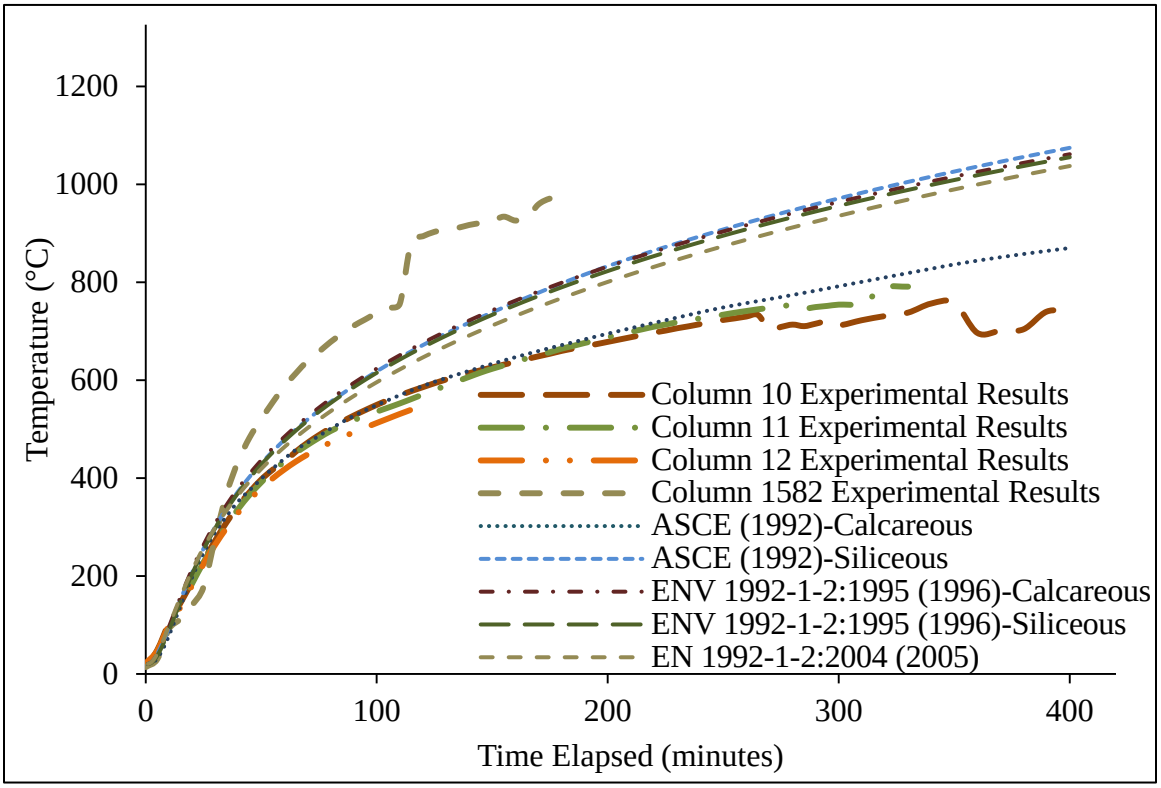

Figure 5-42 Temperature change at a depth of 25.3 mm for NRC Columns 10, 11, 12, and 1582 calculated using different models for absolutely dry concrete

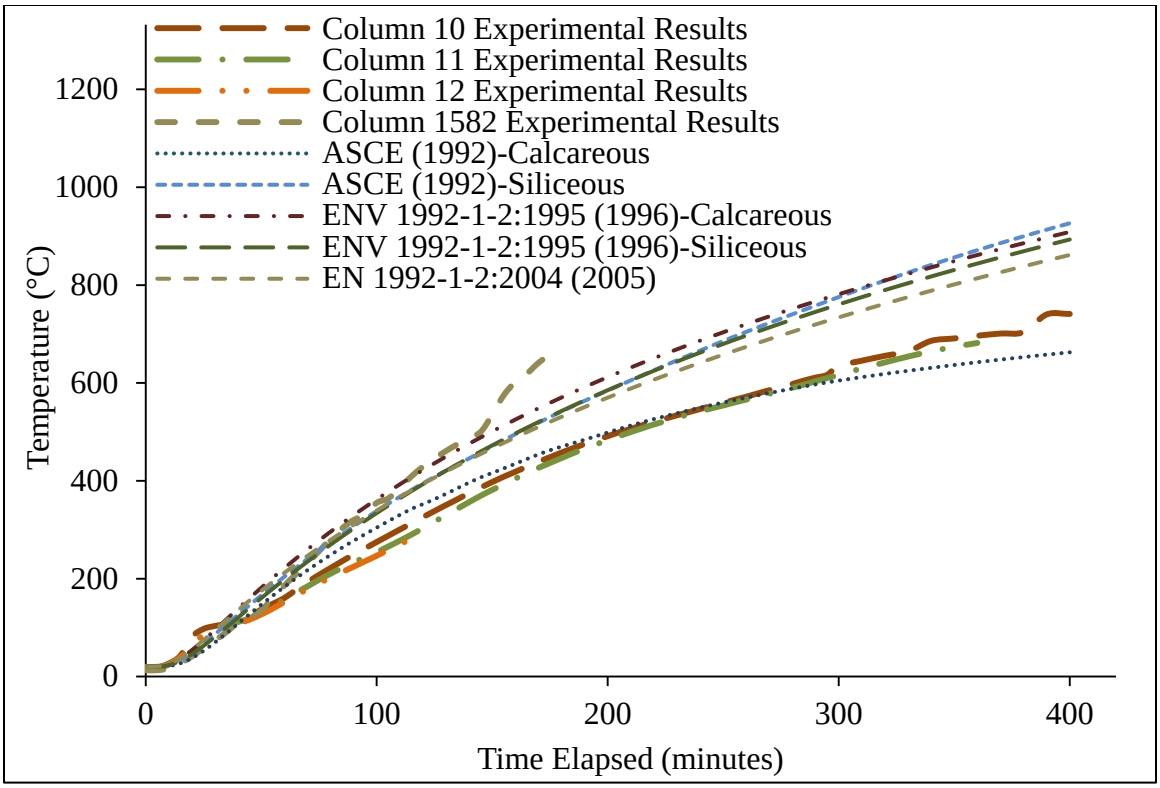

Figure 5-43 Temperature change at a depth of 62.8 mm for NRC Columns 10, 11, 12, and 1582 calculated using different models for absolutely dry concrete

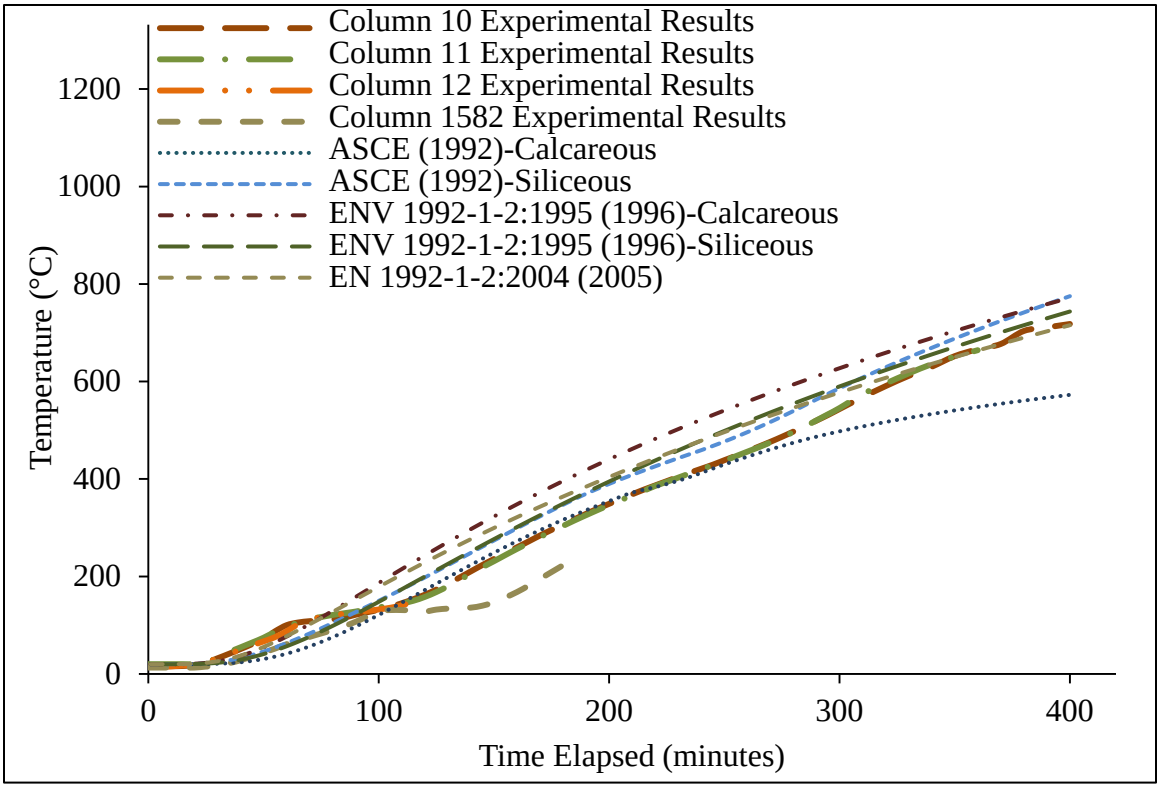

Figure 5-44 Temperature change at a depth of 152.5 mm for NRC Columns 10, 11, 12, and 1582 calculated using different models for absolutely dry concrete

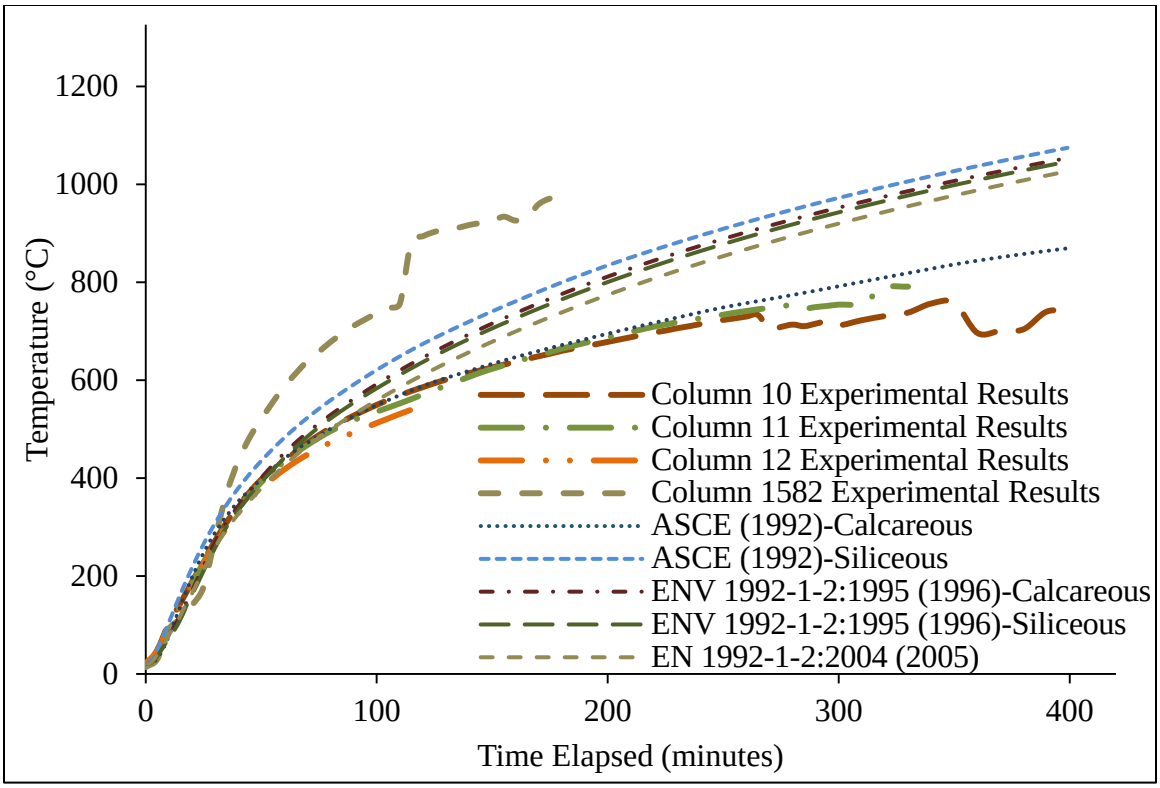

Figure 5-45 Temperature change at a depth of 25.3 mm for NRC Columns 10, 11, 12, and 1582 calculated using different models for concrete with moisture content of 4% by weight

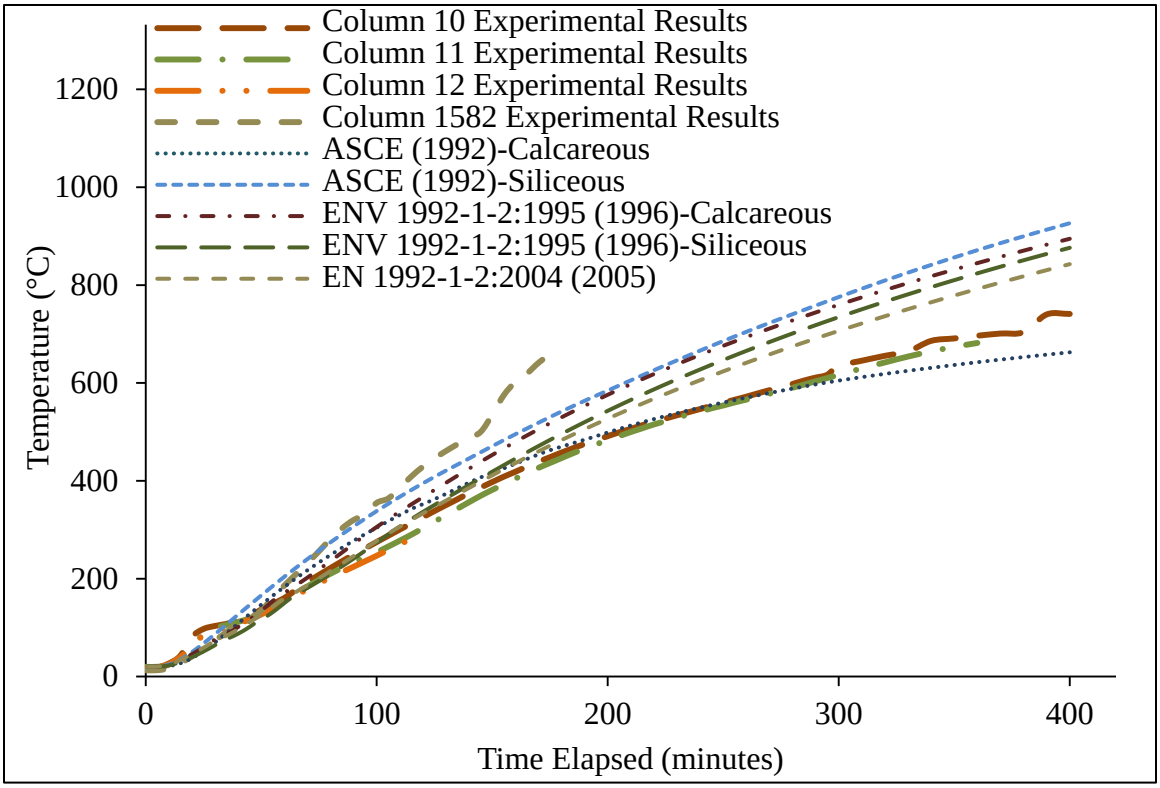

Figure 5-46 Temperature change at a depth of 62.8 mm for NRC Columns 10, 11, 12, and 1582 calculated using different models for concrete with moisture content of 4% by weight

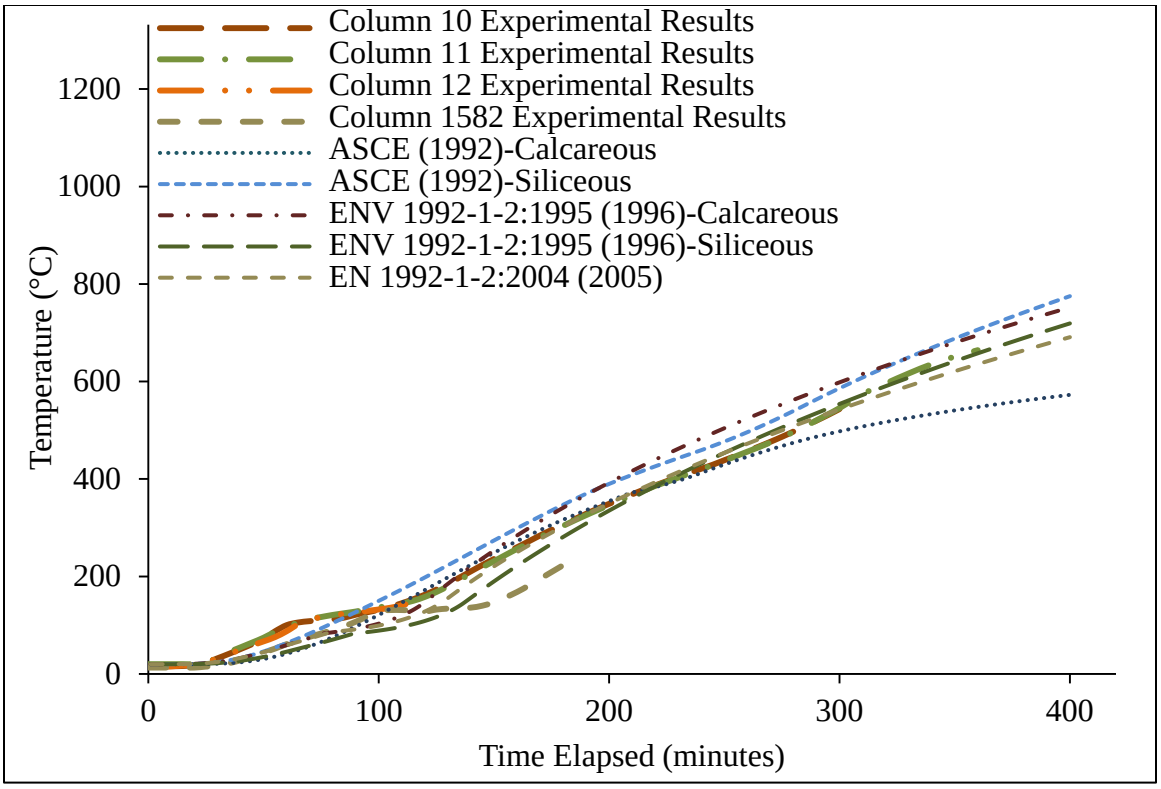

Figure 5-47 Temperature change at a depth of 152.5 mm for NRC Columns 10, 11, 12, and 1582 calculated using different models for concrete with moisture content of 4% by weight

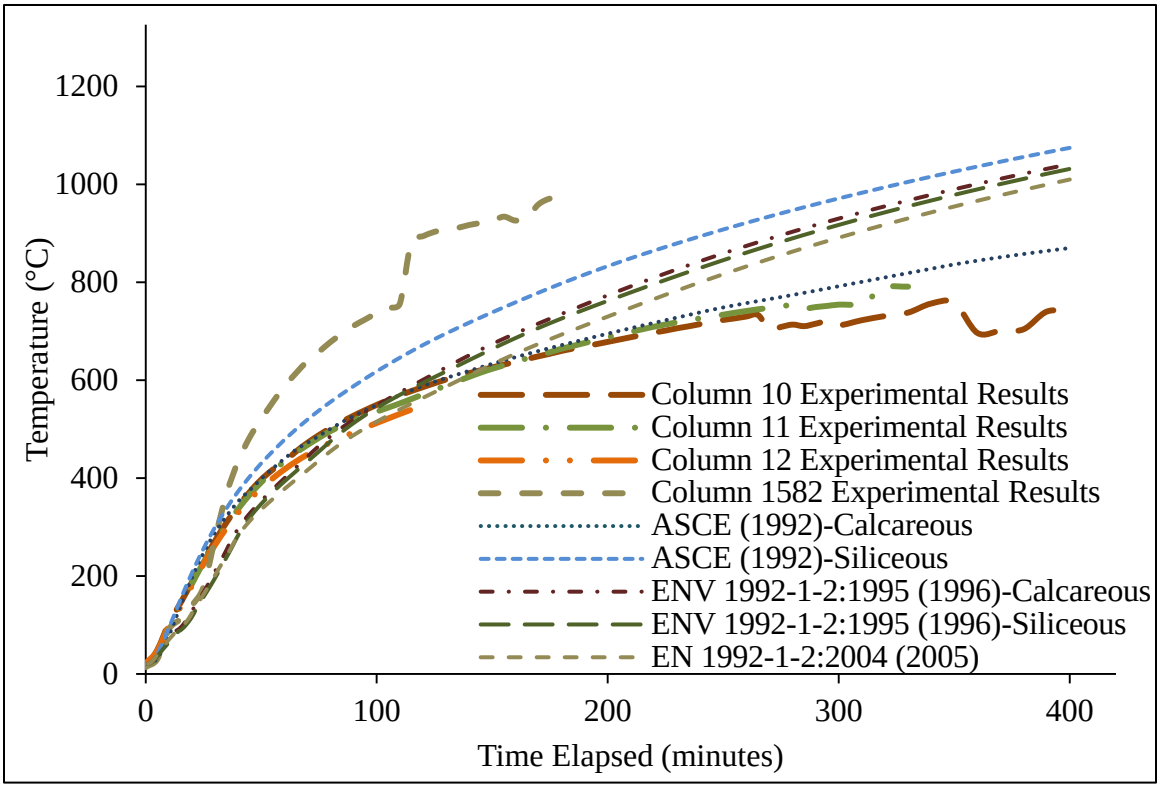

Figure 5-48 Temperature change at a depth of 25.3 mm for NRC Columns 10, 11, 12, and 1582 calculated using different models for concrete with moisture content of 10% by weight

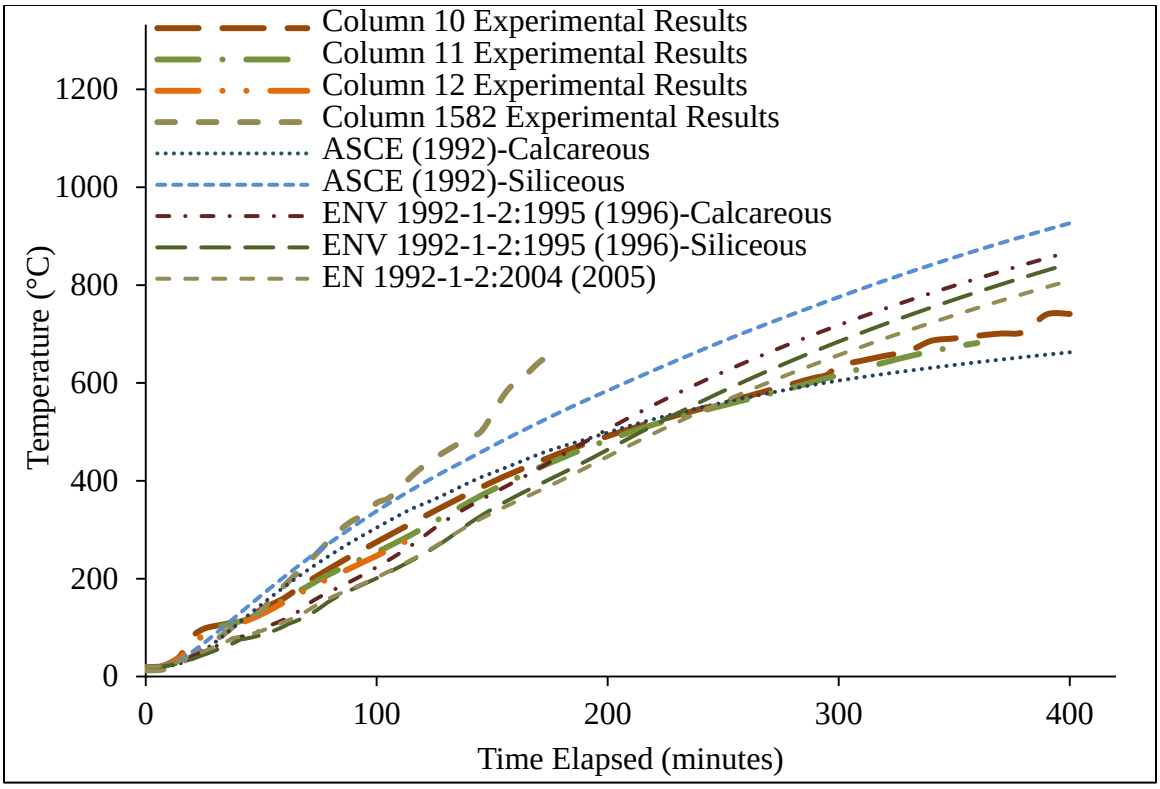

Figure 5-49 Temperature change at a depth of 62.8 mm for NRC Columns 10, 11, 12, and 1582 calculated using different models for concrete with moisture content of 10% by weight

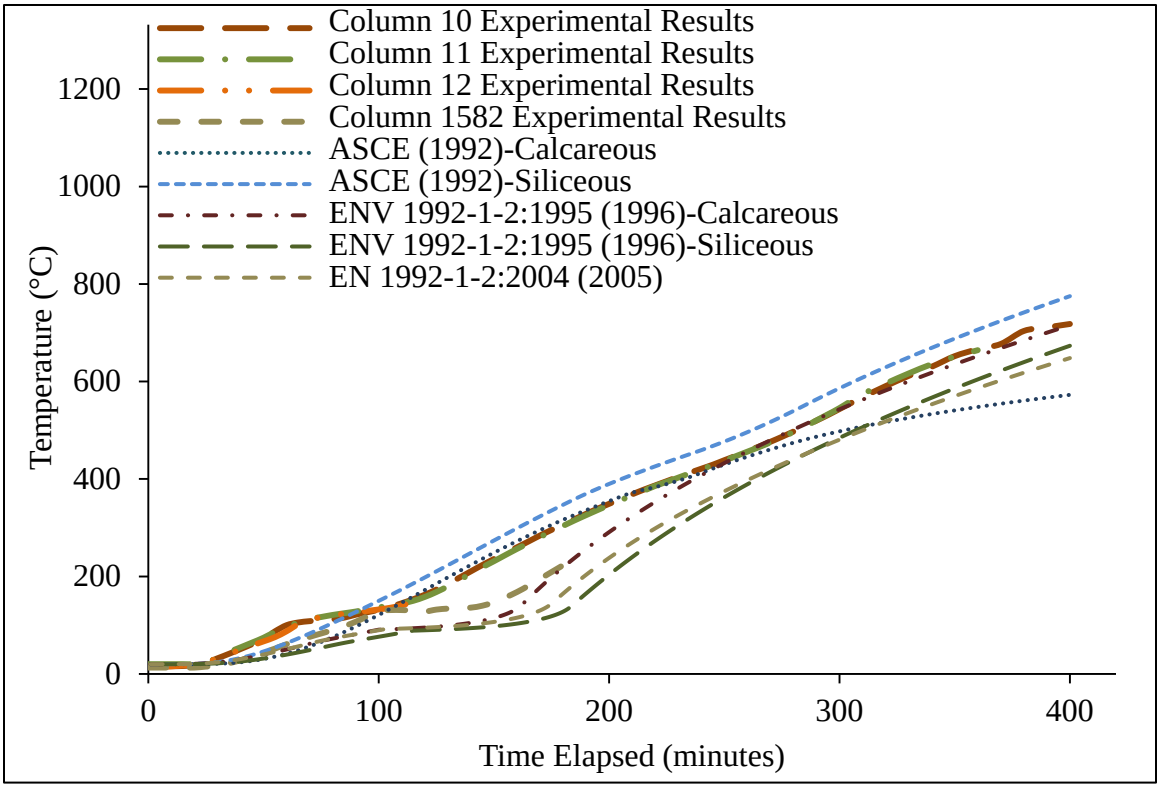

Figure 5-50 Temperature change at a depth of 152.5 mm for NRC Columns 10, 11, 12, and 1582 calculated using different models for concrete with moisture content of 10% by weight

5.5.1.2 Siliceous-Aggregates Specimens

The second set of plots is for the experimental series of Columns A and B, where siliceous aggregates were used and the specimens were kept in the fire-simulating furnace for the limited period of time of one hour for Column A and two hours for Column B, then left to cool for twenty-four hours. The relative humidity at the centre of Columns A and B on the day of testing was reported as 87% and 82%, respectively, which is equivalent to a moisture content of 3.66% and 3.45% by weight, respectively.

The analytical results for concrete mixed with calcareous aggregates are also presented in these plots just for the sake of comparison. Also, the analytical estimates of the temperatures presented by Lie et al. (1986), denoted "NRC Estimate", are presented. These were calculated using the models presented by the ASCE Manual of Practice (1992) in a finite difference method, based on the procedure presented by Lie and Allen (1972) and Lie et al. (1984).

Figures 5-51, 5-52, and 5-53 show the results of the analysis of Column A for concrete with 0% moisture content (absolutely dry) at depths of 25.3 mm, 62.8 mm, and 152.5 mm, respectively. Figures 5-54, 5-55, and 5-56 show the results at the same depths, respectively, for concrete with 4% moisture content by weight, and Figures 5-57, 5-58, and 5-59 show the results, also at the same depths, for concrete with 10% moisture content by weight. For Column B, Figures 5-60 to 5-68 show the results in the same order as those presented for Column A.

Examining the experimental results of the specimens included in this set of plots, one can reach the same conclusion reached through the results of the first set of plots; that is, that the models presented by the latest version of the Eurocode (EN 1992-1-2:2004, 2005) are the ones most capable of estimating the experimental results for the specific moisture content of concrete on the day of testing. This is based on the comparison of the maximum temperatures measured at the various depths through the column section with their respective values estimated by VecTor3 at a moisture content of 4% by weight, which is around the same moisture content in concrete on the day of testing for both specimens.

However, it appears that all the models presented tend to significantly underestimate the post-peak temperatures, although the NRC model underestimates it to a lower extent. Since the NRC estimates were based on analyses using the models presented by the ASCE Manual of Practice (1992), yet these estimates differ from the analytical results calculated in this study using the same models, one might assume that the models are not responsible for this difference. Lie et al. (1986) stated that measurements were made of the furnace temperatures during the fire exposure and the cooling periods until the average furnace temperature reached near ambient temperatures, yet they failed to report these temperatures. Therefore, one may guess that the reason for the difference between the analytical and experimental results can be attributed to a possible difference between the actual furnace temperatures and the ISO 834-1:1999 (1999) model that was used in the analysis for the descending temperature branch (fire decay phase).

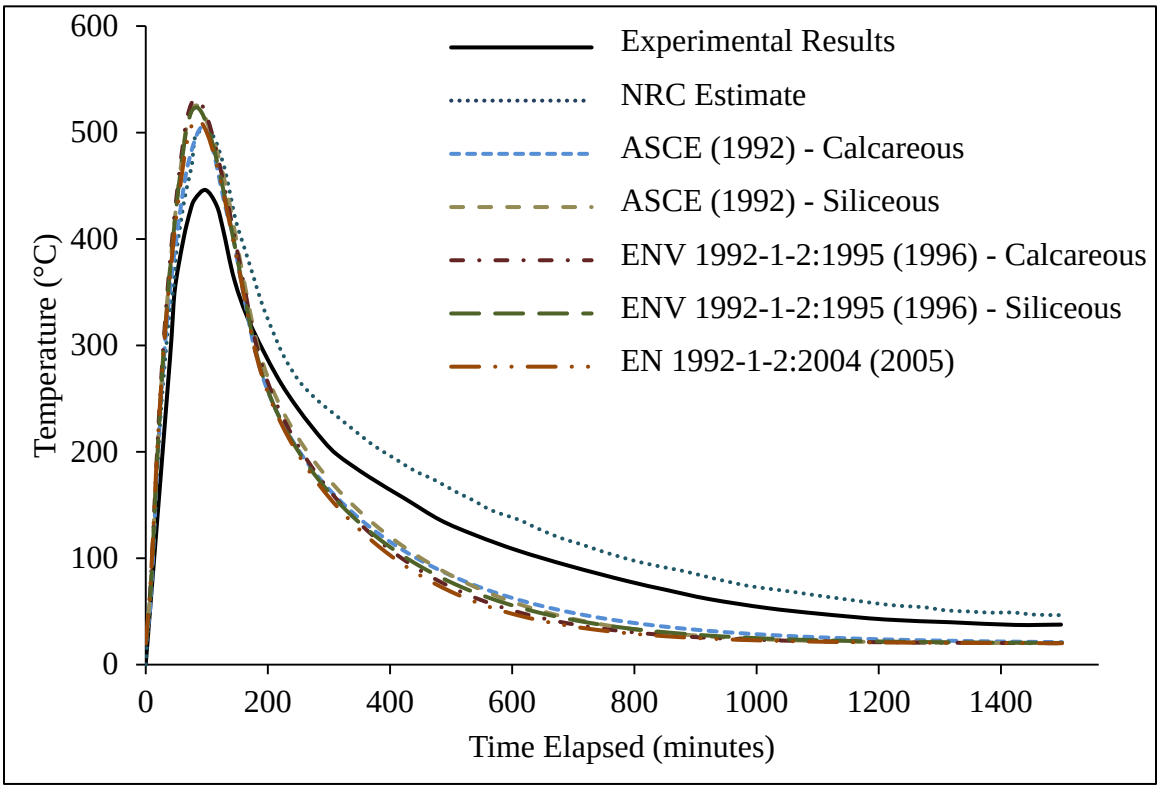

Figure 5-51 Temperature change at a depth of 25.3 mm for NRC Column A calculated using different models for absolutely dry concrete

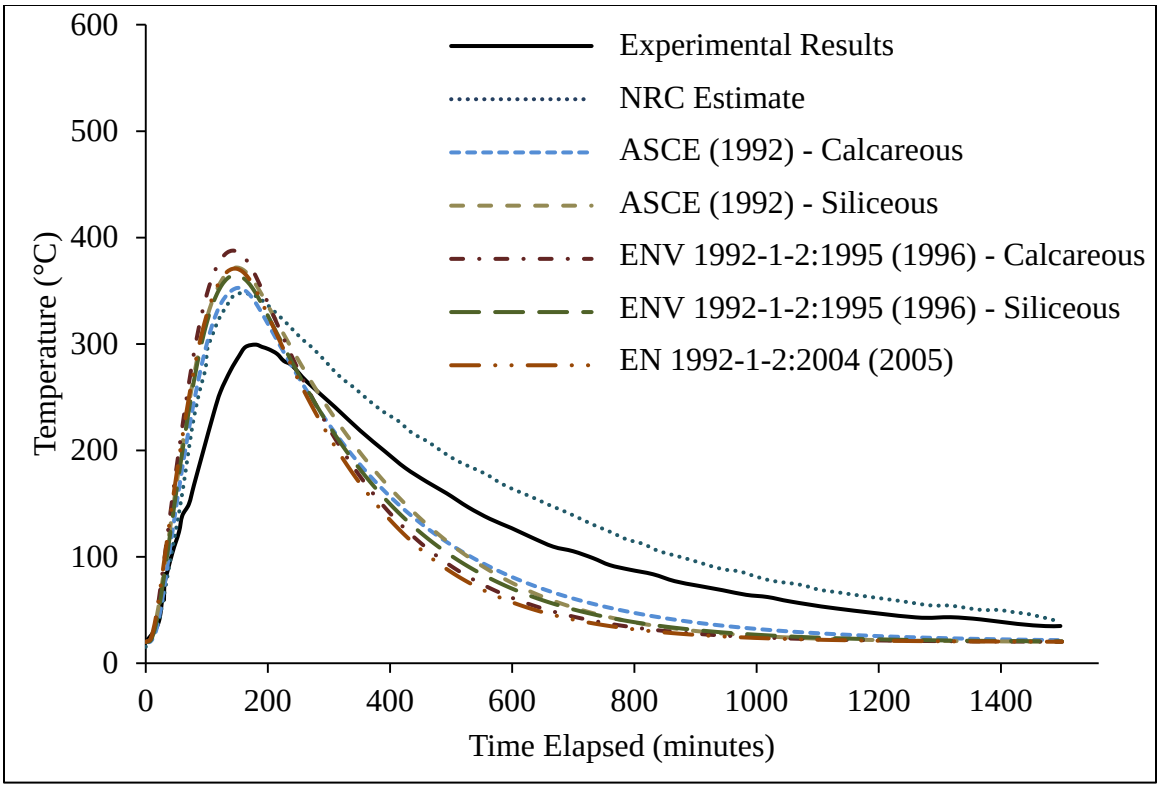

Figure 5-52 Temperature change at a depth of 62.8 mm for NRC Column A calculated using different models for absolutely dry concrete

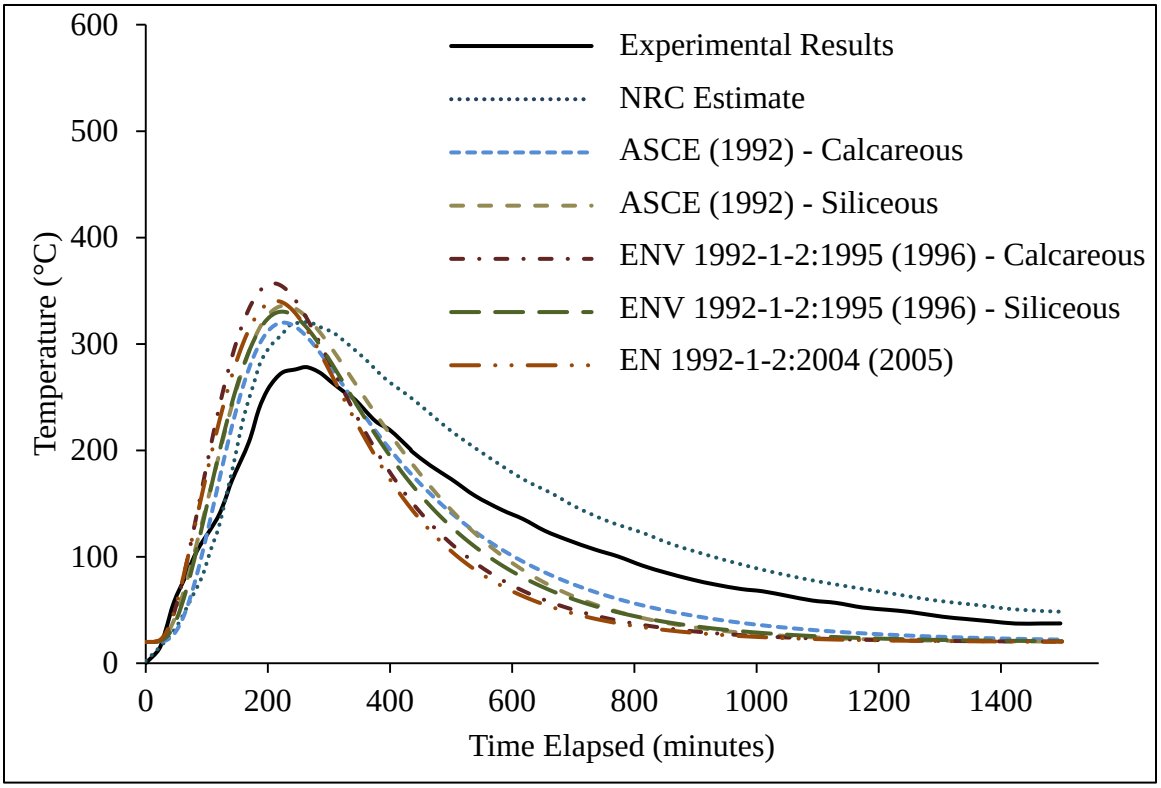

Figure 5-53 Temperature change at a depth of 152.5 mm for NRC Column A calculated using different models for absolutely dry concrete

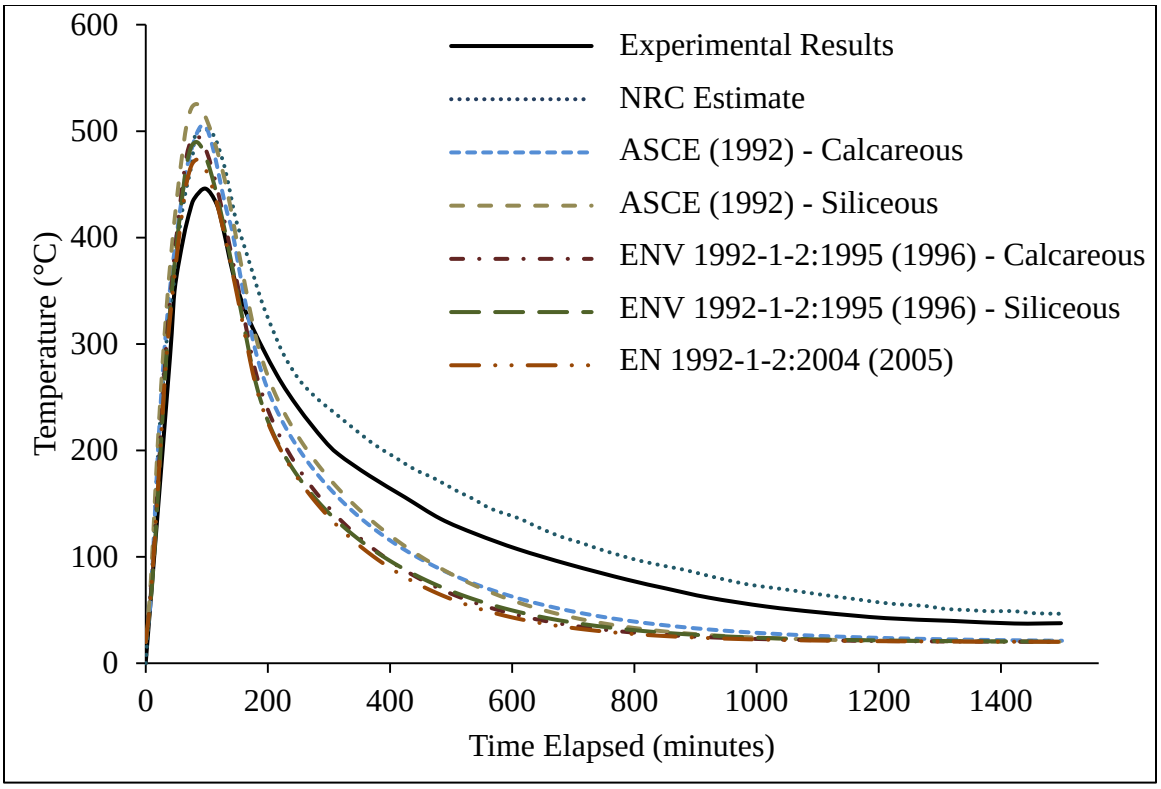

Figure 5-54 Temperature change at a depth of 25.3 mm for NRC Column A calculated using different models for concrete with moisture content of 4% by weight

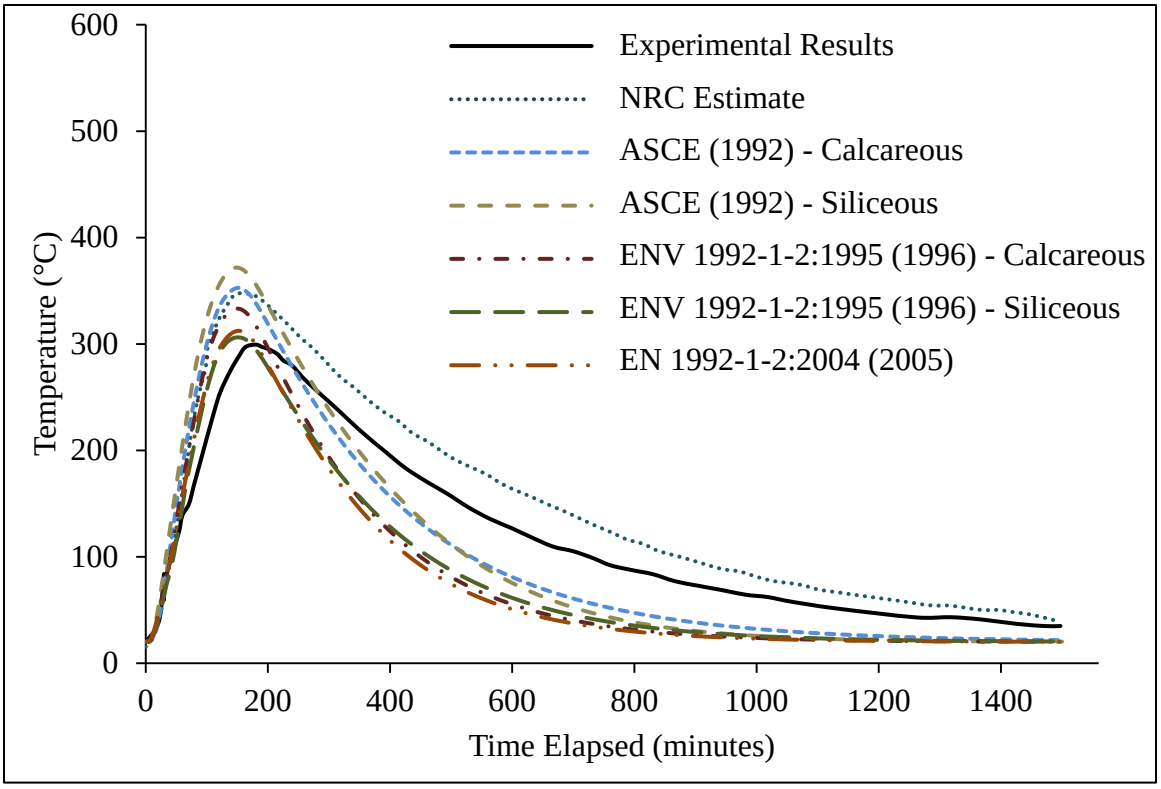

Figure 5-55 Temperature change at a depth of 62.8 mm for NRC Column A calculated using different models for concrete with moisture content of 4% by weight

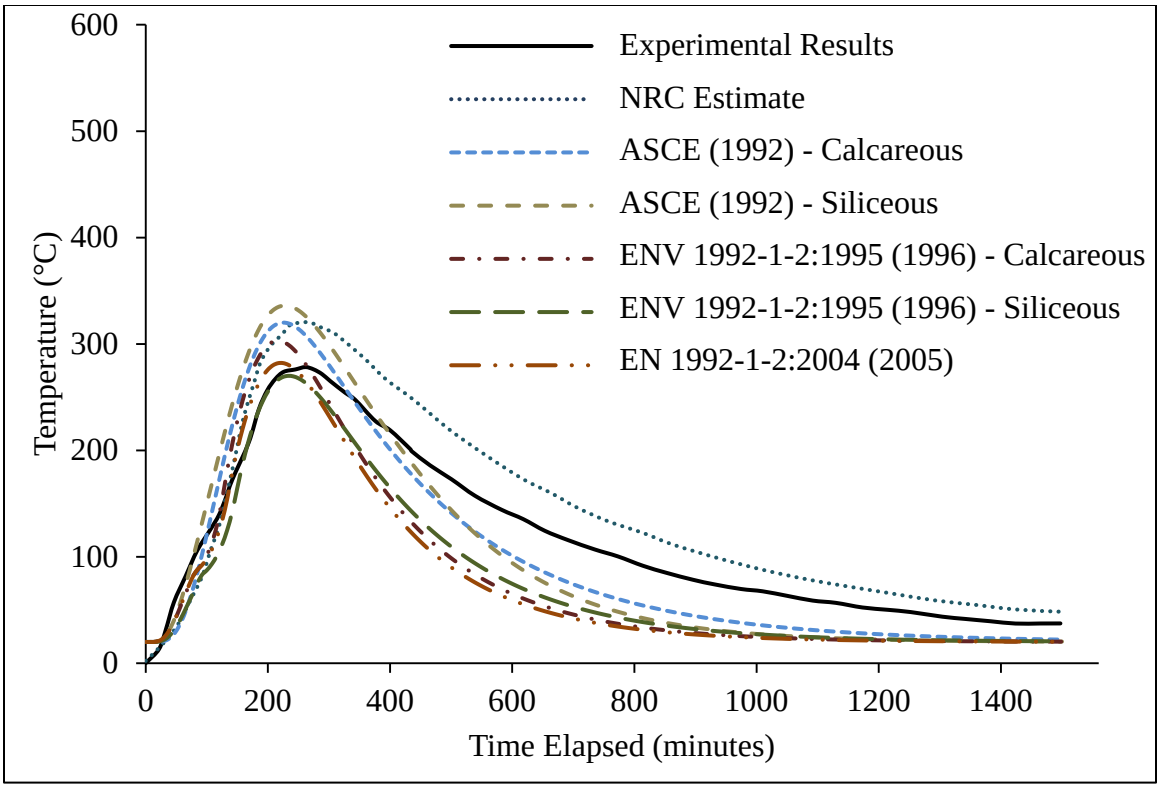

Figure 5-56 Temperature change at a depth of 152.5 mm for NRC Column A calculated using different models for concrete with moisture content of 4% by weight

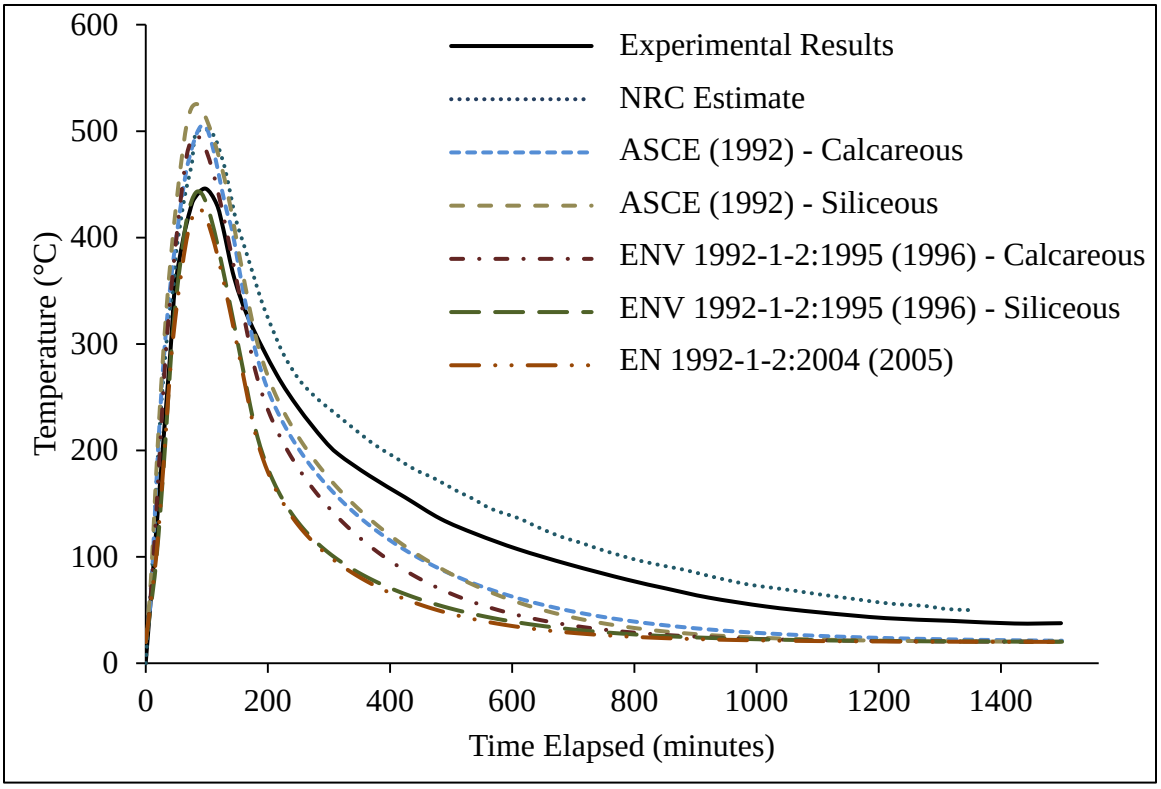

Figure 5-57 Temperature change at a depth of 25.3 mm for NRC Column A calculated using different models for concrete with moisture content of 10% by weight

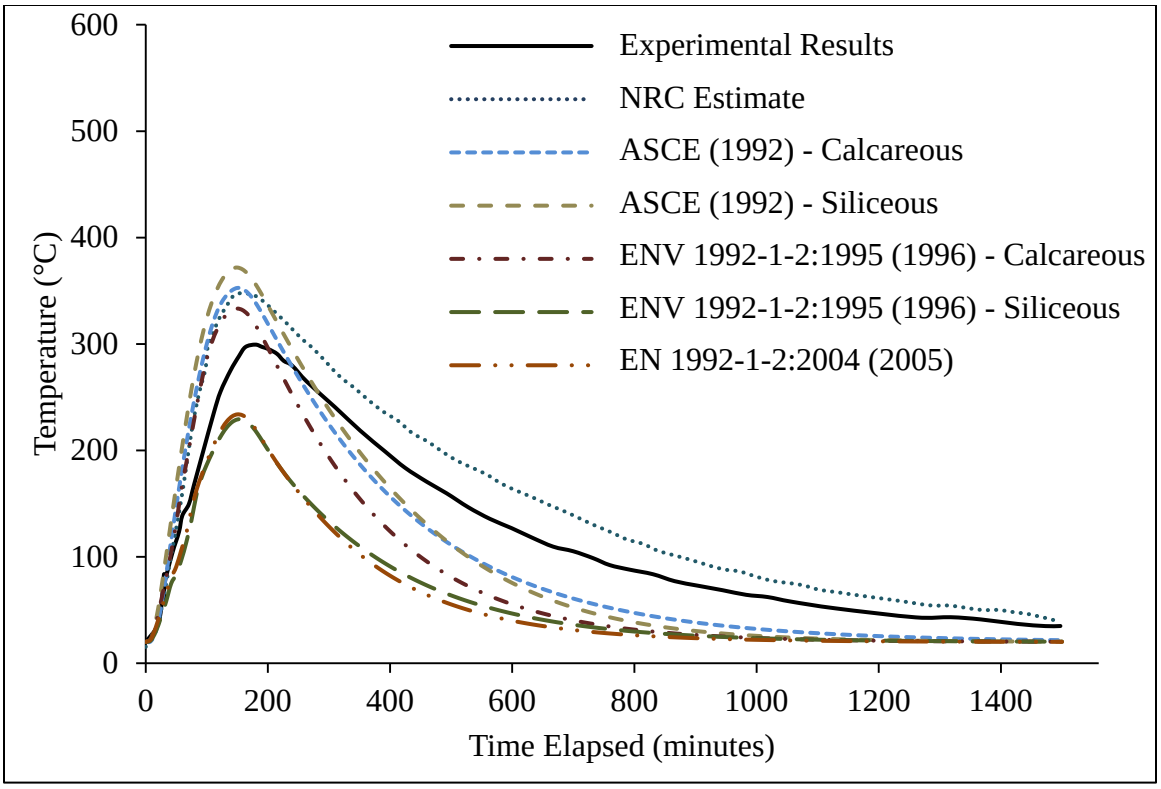

Figure 5-58 Temperature change at a depth of 62.8 mm for NRC Column A calculated using different models for concrete with moisture content of 10% by weight

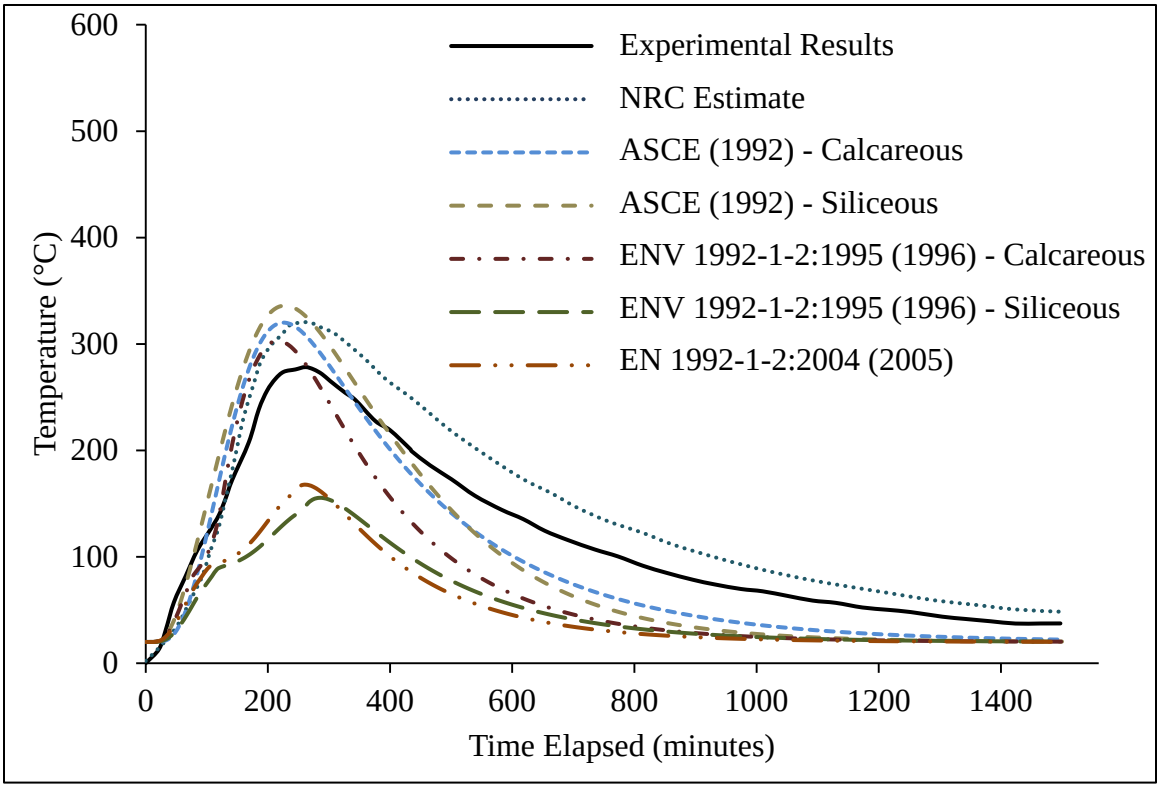

Figure 5-59 Temperature change at a depth of 152.5 mm for NRC Column A calculated using different models for concrete with moisture content of 10% by weight

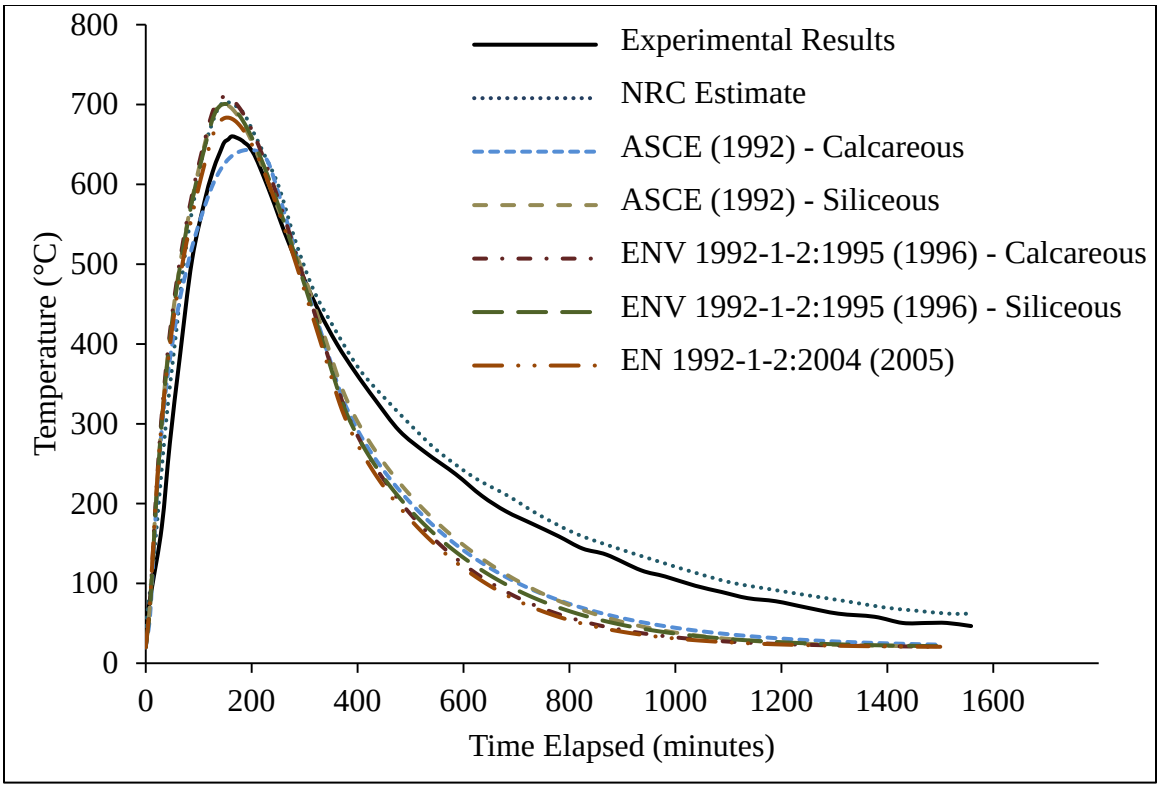

Figure 5-60 Temperature change at a depth of 25.3 mm for NRC Column B calculated using different models for absolutely dry concrete

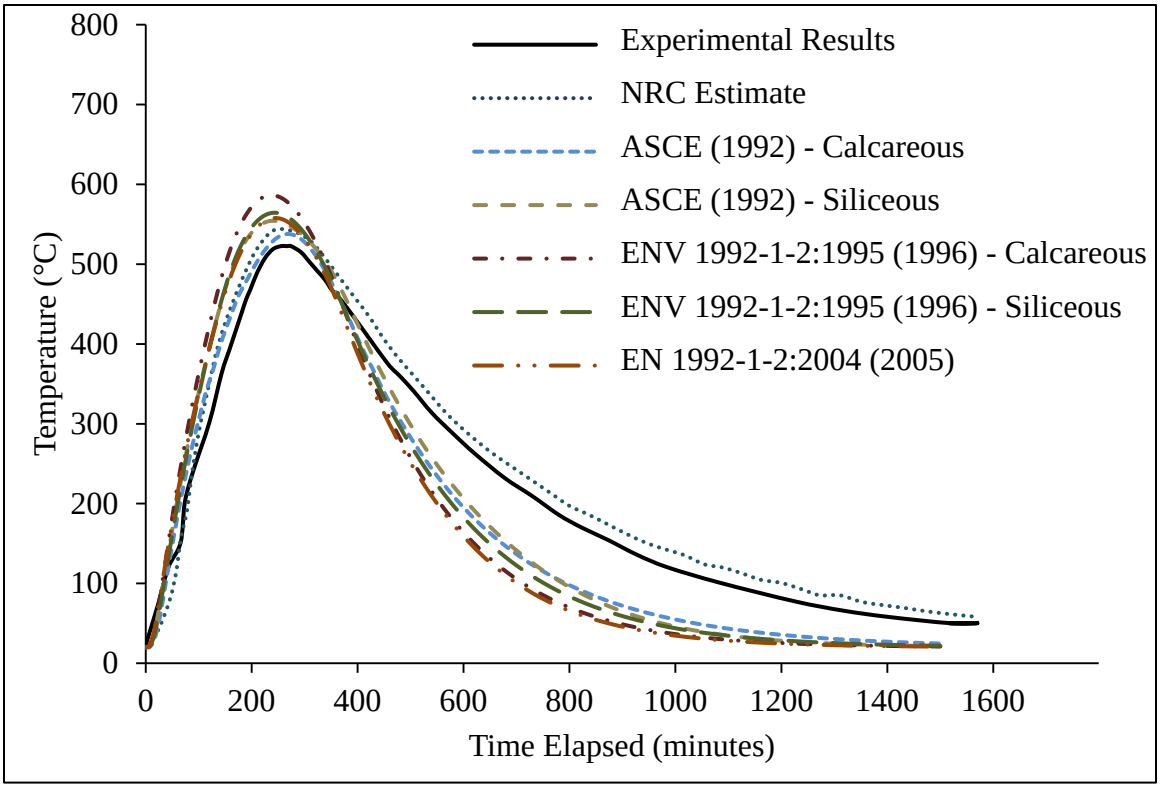

Figure 5-61 Temperature change at a depth of 62.8 mm for NRC Column B calculated using different models for absolutely dry concrete

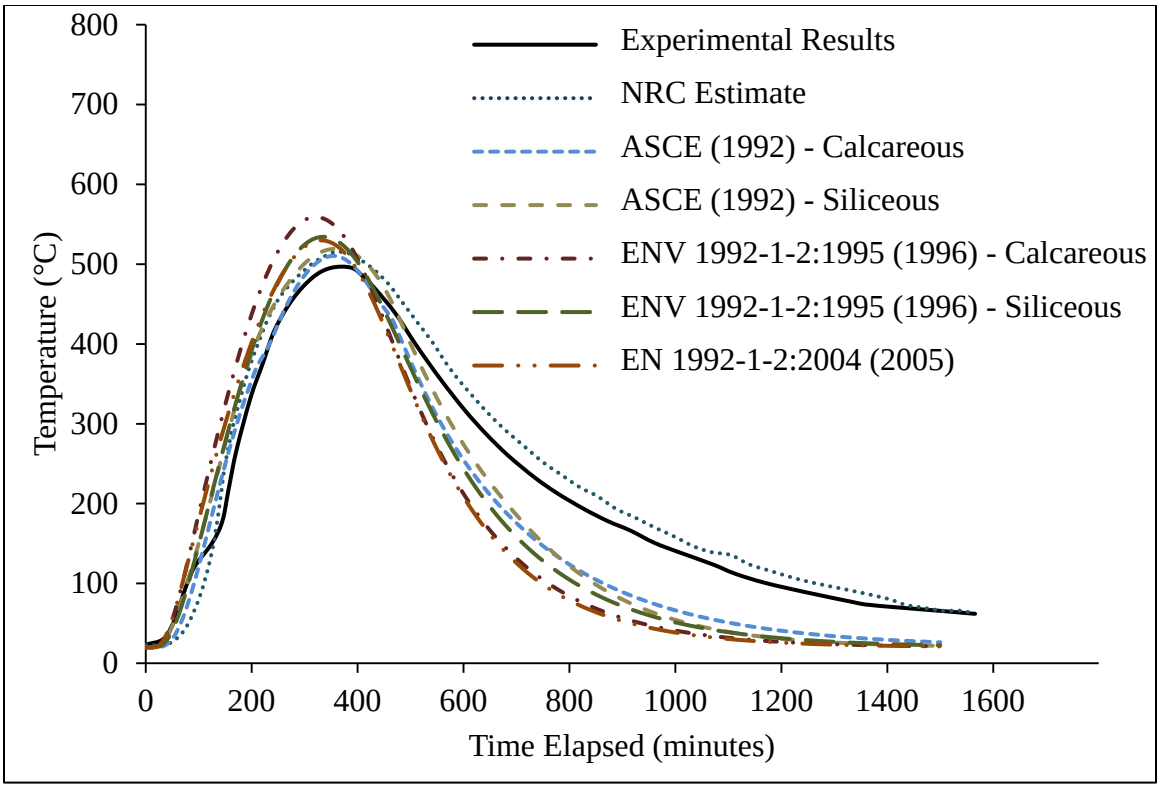

Figure 5-62 Temperature change at a depth of 152.5 mm for NRC Column B calculated using different models for absolutely dry concrete

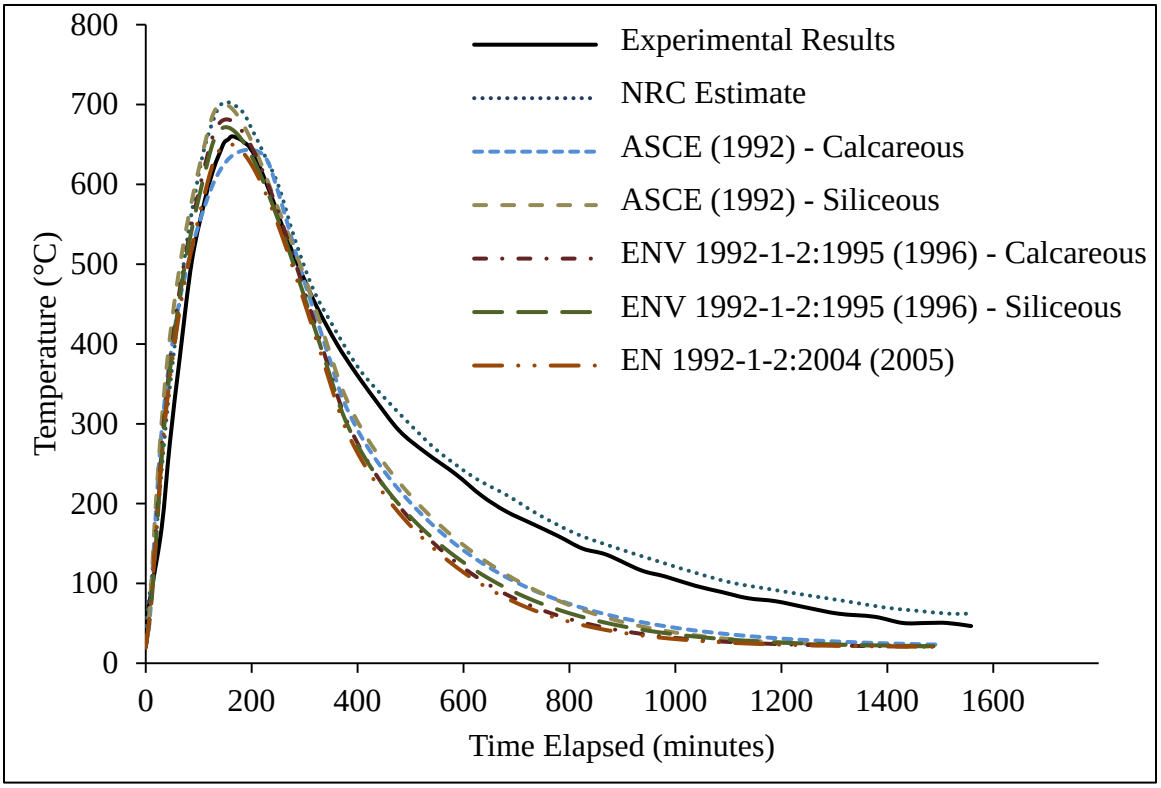

Figure 5-63 Temperature change at a depth of 25.3 mm for NRC Column B calculated using different models for concrete with moisture content of 4% by weight

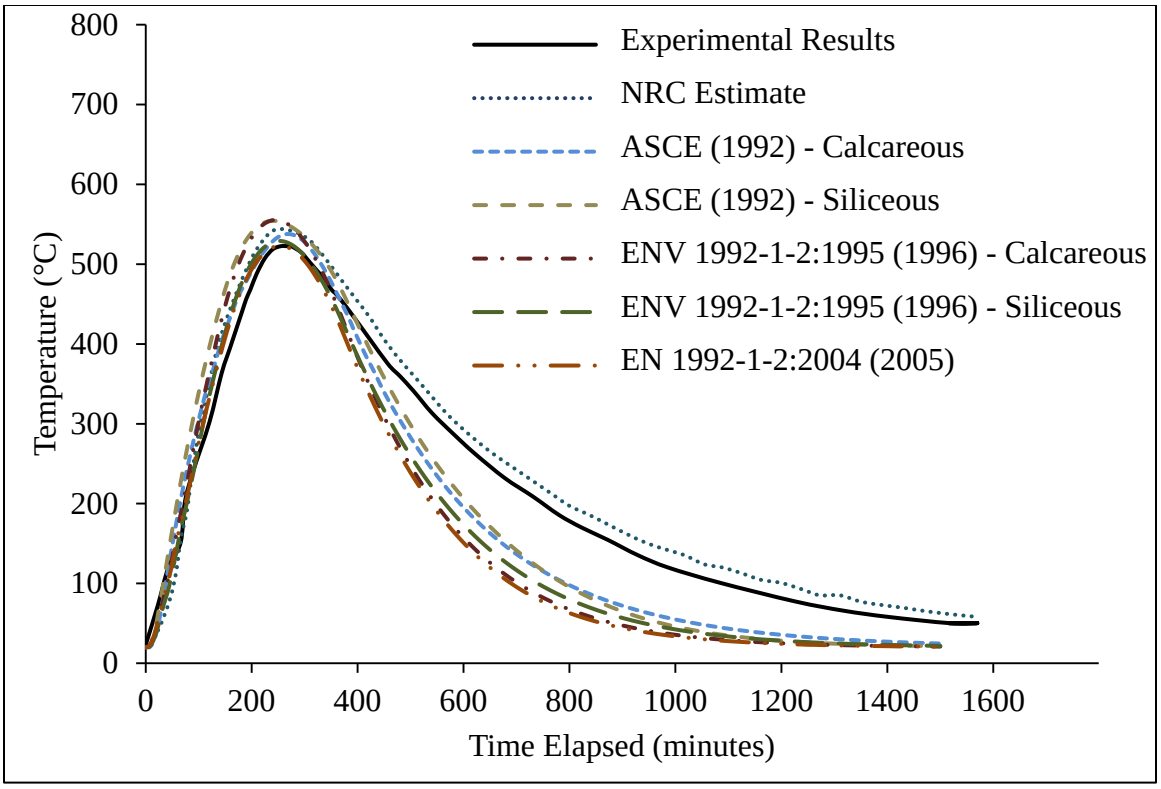

Figure 5-64 Temperature change at a depth of 62.8 mm for NRC Column B calculated using different models for concrete with moisture content of 4% by weight

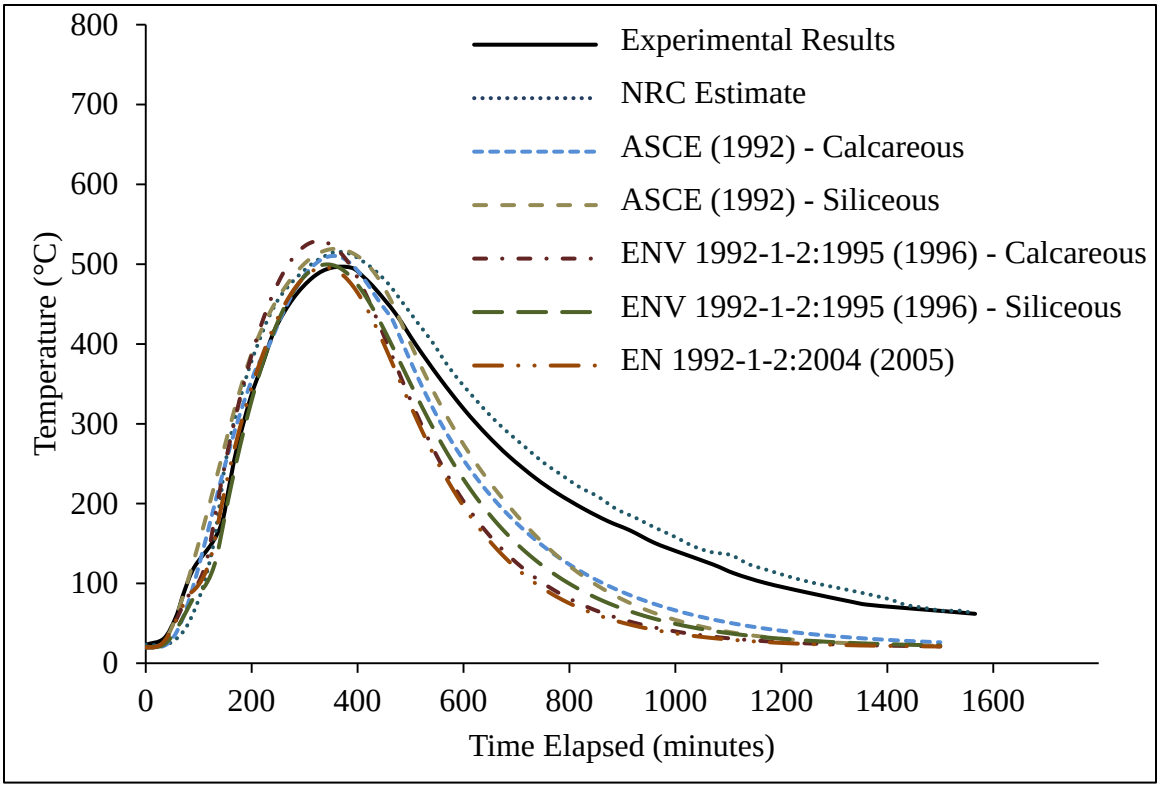

Figure 5-65 Temperature change at a depth of 152.5 mm for NRC Column B calculated using different models for concrete with moisture content of 4% by weight

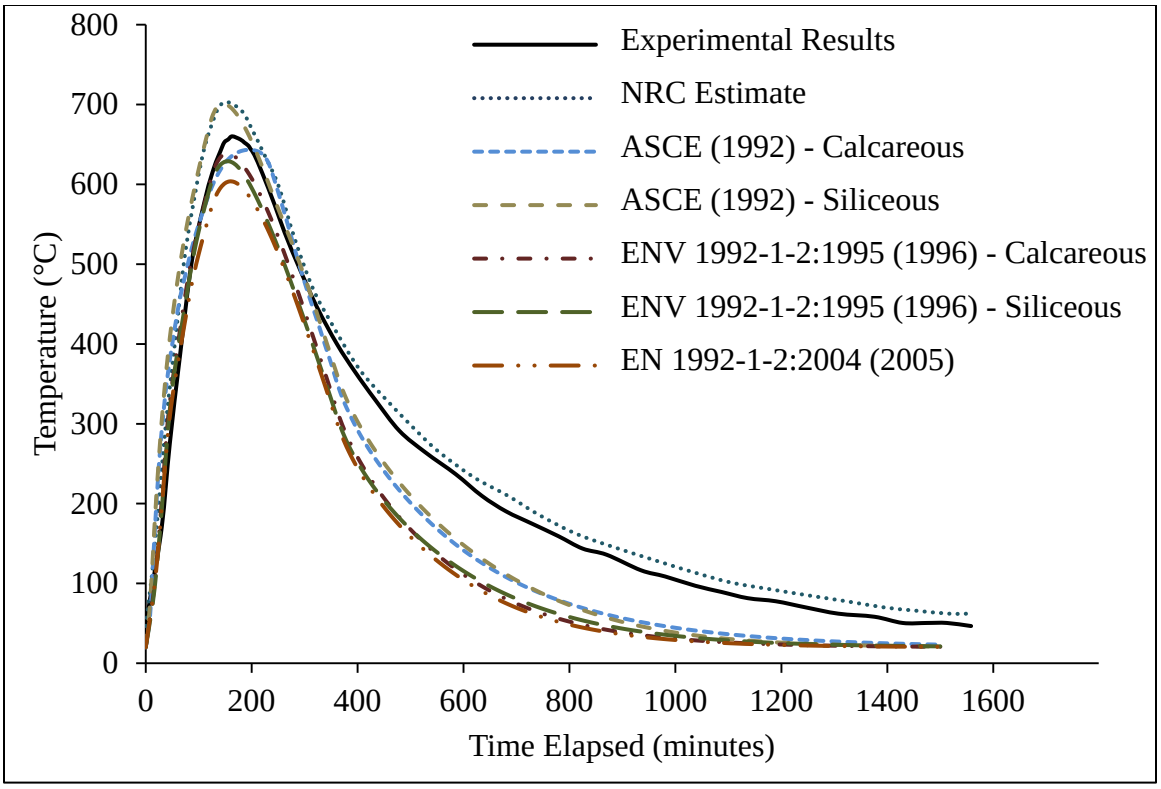

Figure 5-66 Temperature change at a depth of 25.3 mm for NRC Column B calculated using different models for concrete with moisture content of 10% by weight

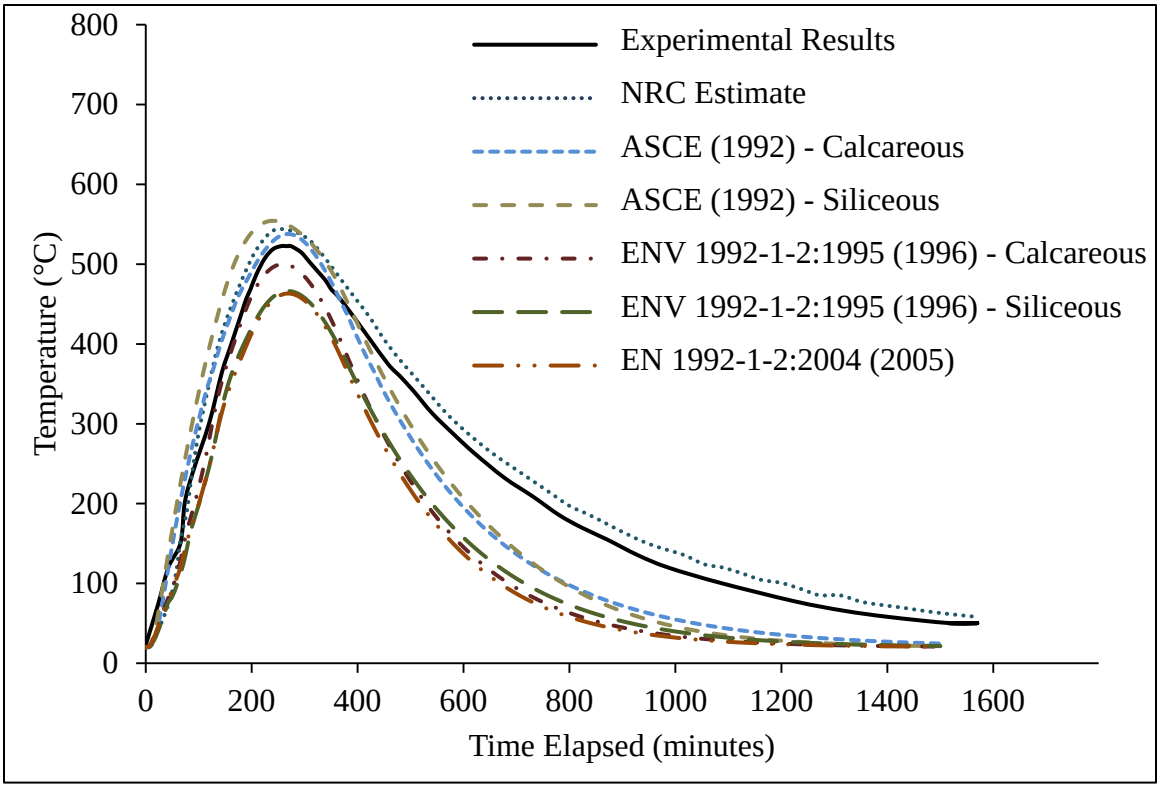

Figure 5-67 Temperature change at a depth of 62.8 mm for NRC Column B calculated using different models for concrete with moisture content of 10% by weight

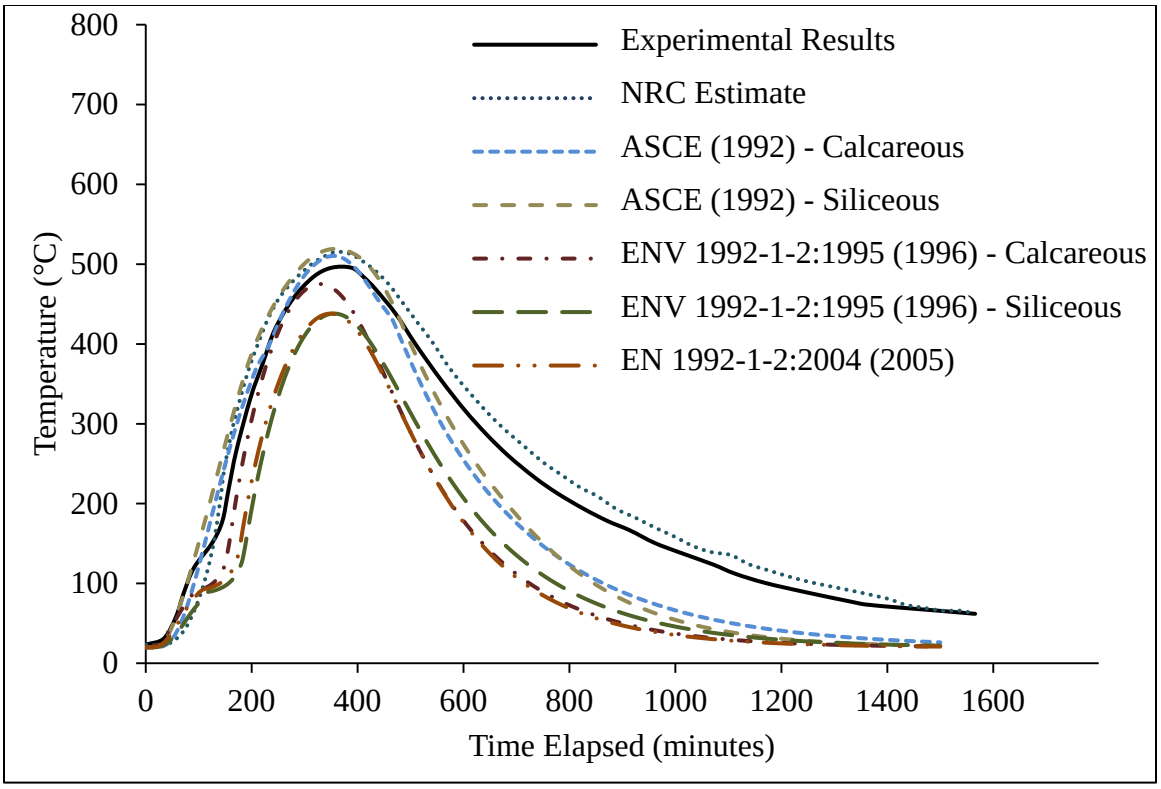

Figure 5-68 Temperature change at a depth of 152.5 mm for NRC Column B calculated using different models for concrete with moisture content of 10% by weight

5.5.2 Heat Transfer and Structural Analysis

It was found in the previous section that the models provided by the current version of the Eurocode (EN 1992-1-2:2004, 2005) produce the best estimation of the temperatures through the depth of concrete, compared to their counterparts in the other two codes. This applies to concrete mixed with both siliceous and calcareous aggregates; hence, it applies to the three experimental series chosen for corroborating the analytical procedure followed in this study. Another major conclusion is the significant effect of the moisture content of concrete on the temperatures developed throughout the columns depths. Therefore, neglecting the moisture content of concrete would lead to highly inaccurate estimates of temperatures, which would, in turn, lead to inaccurate estimation of the mechanical properties of concrete and steel as well as their thermal expansion strains. On the structural level, these inaccuracies my lead to erroneous results represented in an inaccurate overall structural response or even an incorrect failure mode.

With these conclusions in mind, the corroboration of the structural analysis stage is presented in the next three subsections for the three experimental series chosen in this study. For all three analyses, the heat transfer analysis stage has been undertaken using the models provided by the current version of the Eurocode (EN 1992-1-2:2004, 2005) and the moisture content of concrete has been assigned a value of 4%. As previously explained, the structural analysis stage is undertaken at the end of the heat transfer analysis stage at each time step.

Since the mechanical properties of the steel reinforcing bars are very sensitive to temperature, a different mesh was used for the corroboration study in this section. The mesh chosen for this study involved more finite elements in the concrete cover area of the columns near the longitudinal reinforcing bars in order to ensure an accurate estimation of the temperatures of the bars. Also, in order to ensure a stable and accurate structural analysis, better aspect ratios for the elements were chosen. The exact mesh used for the analysis of each experimental series varied depending on the loading conditions and will be discussed later.

This step of the corroboration study aims at evaluating the structural analysis capabilities of VecTor3 for thermally loaded reinforced concrete members and the adequacy of the models provided by the ASCE Manual of Practice (Structural Fire Protection by T. T. Lie, 1992), the former version of the Eurocode (ENV 1992-1-2:1995, 1996), and its current version (EN 1992-1-2:2004, 2005). This check is meant to test their evaluation of the various mechanical properties of both concrete and steel, together with the thermal strain and the ability of these models to provide a reliable means for the structural analysis stage of the thermal loading analysis.

5.5.2.1 NRC Columns 10, 11, and 12

These three columns were cast and tested by Lie and Lin (1983) as part of an experimental series of twelve columns in a joint study on the fire performance of reinforced concrete columns by the National Research Council Canada and the Portland Cement Association. The columns were constructed using calcareous aggregates and had

the typical section described earlier and shown in Figures 5-37 and 5-38. Table 5-11 gives the compressive strength of concrete, f_c', on the day of testing and the level of loading of the three specimens. The compressive strength of concrete was determined based on one cylinder for Column 10 and two cylinders for each of Column 11 and Column 12. The steel reinforcing bars had the properties mentioned earlier.

The test involved loading the columns to the target axial load as indicated in Table 5-11, then, one hour later, subjecting them to the CAN/ULC S101-07 (2007) standard temperature-fire curve in the testing furnace until failure. The level of loading of the specimens as a percentage of their ultimate capacity at normal temperatures was calculated and presented in Table 5-11, based on a monotonic loading analysis carried out using VecTor3 for the each specimen.

Table 5-11 Properties of material and loading of Columns 10, 11, and 12

Specimen	f_c' (MPa)	Axial Load (kN)	Loading Level (%)
Column 10	40.9	800	20.4
Column 11	36.9	1067	29.7
Column 12	39.95	1778	46.7

For all three specimens, compression failure was reported to be accompanied with a crushing sound, faint for Column 10, loud for Column 11, and completely absent for Column 12. Also, according to the photographs provided, it appears all the specimens suffered from excessive spalling. However, the time the photographs were taken is unknown; therefore, it is unclear at what stage this spalling occurred and whether it happened during or after the fire exposure.

For the finite element discretization used for the analysis of these columns, only one-quarter of the column section was modelled, taking advantage of the double symmetry of the geometrical, structural, and loading properties. The mesh used was symmetric, with twelve 5.04 mm thick elements, through the depth of the concrete cover to the longitudinal reinforcing bars, and five 18.4 mm thick elements for the core region. The mesh is shown in Figure 5-69, together with the location of the steel reinforcing bar, which is shown as a black circle (not to scale).

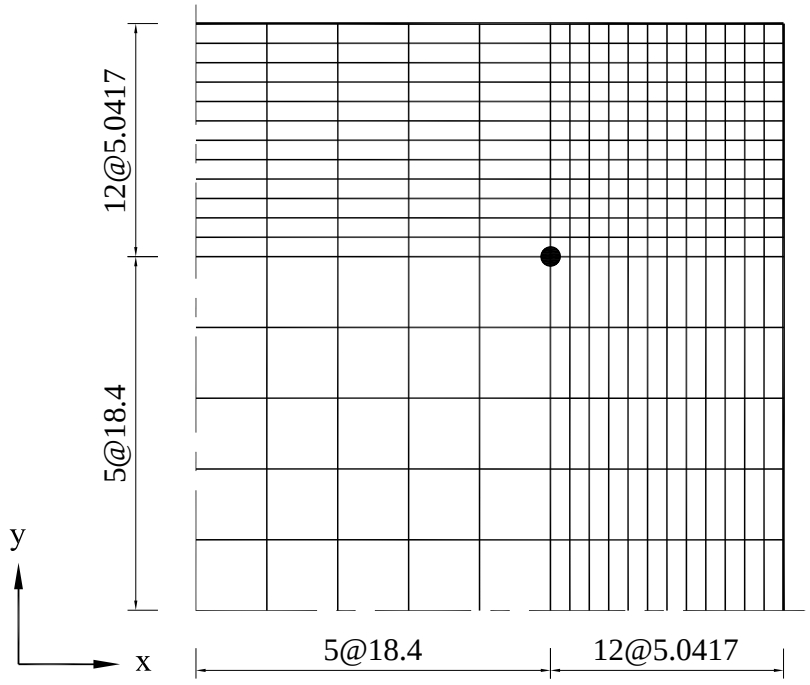

Figure 5-69 Finite element discretization of the cross section of NRC Columns 10, 11, and 12 for structural analysis and the steel reinforcing bar location (dimensions in mm)

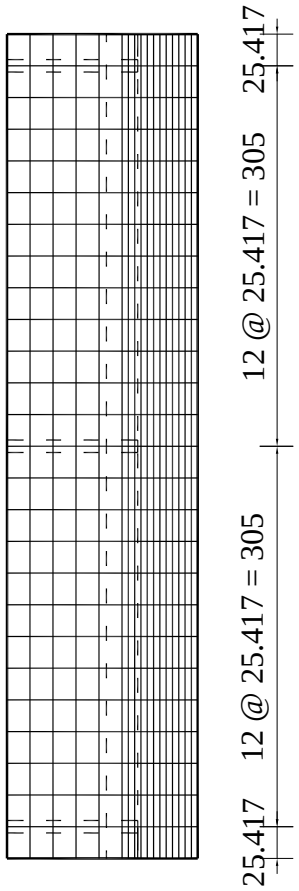

Figure 5-70 Finite element discretization along the height of NRC Columns 10, 11, and 12 (dimensions in mm)

In order to achieve a less time-costly analysis, only a short segment of the columns was modelled along the height. To ensure the capture of concrete confinement effects, two intervals enclosed by three ties were modelled, as shown in Figure 5-70, where 26 elements, with a height of 25.42 mm each, were used through the height of the modelled part of the columns. The ties were spaced at 305 mm, i.e., a tie at every 12 layers of elements along the height.

The axial load was applied at the top of the column at the centre of the cross section. The models were restrained in all directions at their bases, and the planes of symmetry were restrained in the direction perpendicular to them as shown in Figure 5-71. The axial load was kept constant until failure and a time step of 60 seconds was used for the analysis. The models provided by the current version of the Eurocode (EN 1992-1-2:2004, 2005) were used for the thermal analysis, as explained earlier.

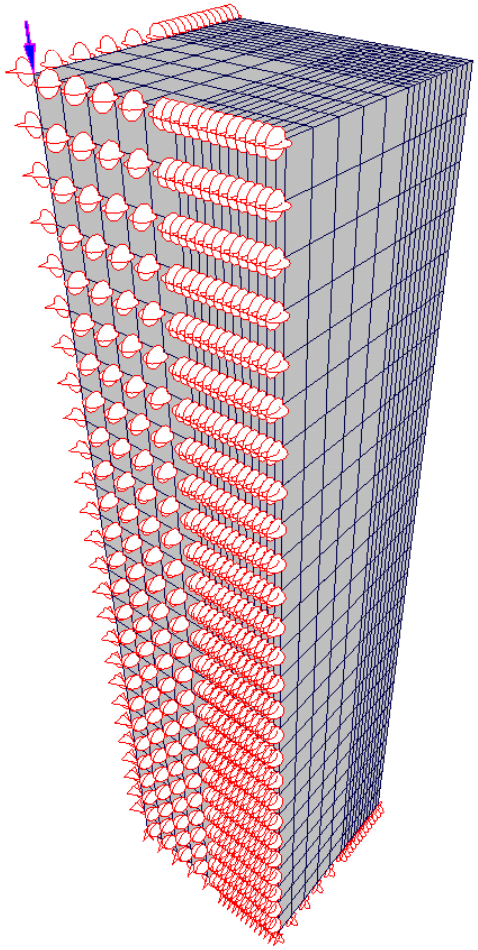

Figure 5-71 The loading and support conditions of the finite element model of Columns 10, 11, and 12

To ensure a uniform axial loading of the column, replicating the function of the steel loading plate used in the experiment, the nodes at this load loading plate location were linked together to displace equally in the vertical direction using the procedure explained in Section 2.4.2.6. Also, in order to ensure a stable analysis, all the nodes on each elevation were linked to displace equally in the vertical direction as well. For the same purpose, taking advantage that the quarter cross section analyzed is also symmetric about its diagonal, the nodes on each elevation were linked together around the line of symmetry. This means that the displacement in the x-direction of a specific node on one side is always equal to the displacement in the y-direction for the mirrored node about the diagonal axis of symmetry on the other side. This ensured that the section remained symmetric throughout the analysis, avoiding unrealistic response caused by secondary moments and geometric nonlinearities

Figures 5-72, 5-73, and 5-74 show the experimental results of the vertical displacement at the top of the columns with time, together with the analytical results estimated by VecTor3 using the models provided by the ASCE Manual of Practice (Structural Fire Protection by T. T. Lie, 1992), the former version of the Eurocode (ENV 1992-1-2:1995, 1996), and its current version (EN 1992-1-2:2004, 2005). A positive displacement means expansion along the height of the specimen, and a negative displacement means contraction. For the analytical results, the vertical displacements produced by VecTor3 have been proportioned to account for the entire length of the column rather than the partial model that has been analyzed. All the displacements shown only represent the change in height from the start of the fire, neglecting the initial displacements resulting from the axial load that was applied an hour prior to the fire exposure.

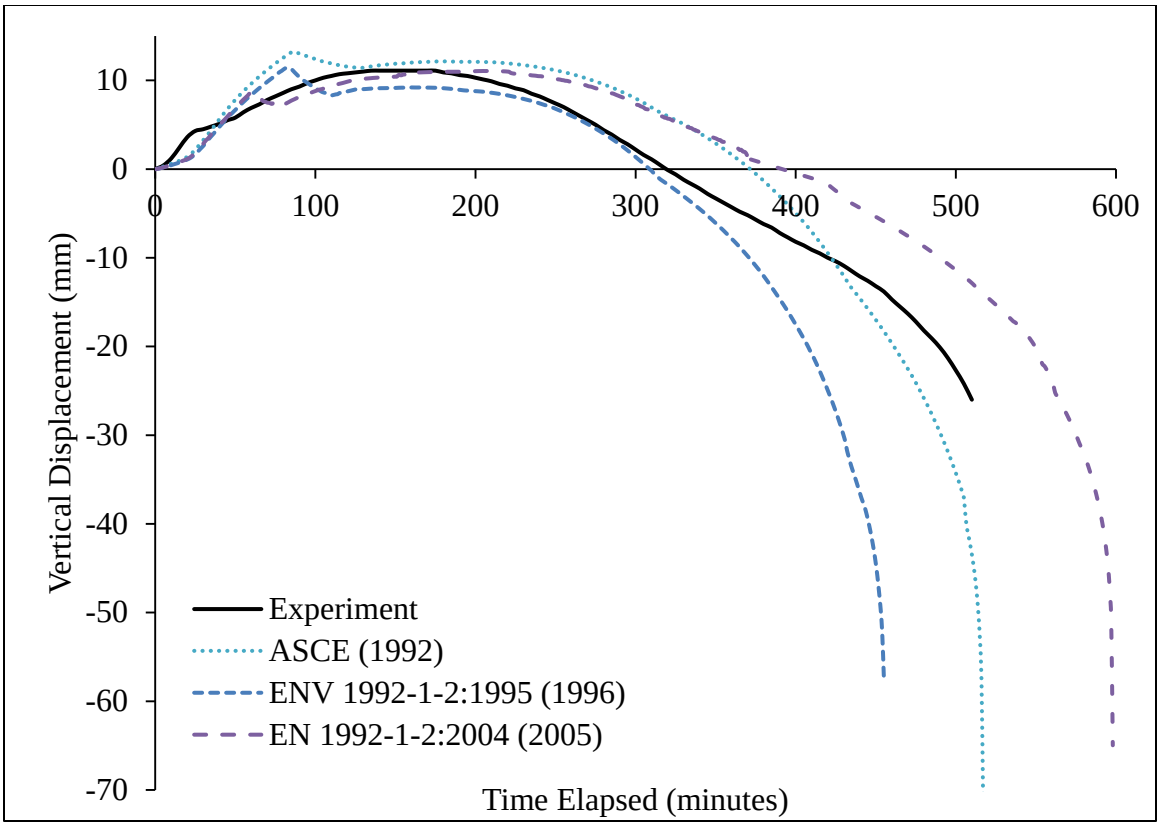

Figure 5-72 Vertical displacement of Column 10 from the start of fire to failure

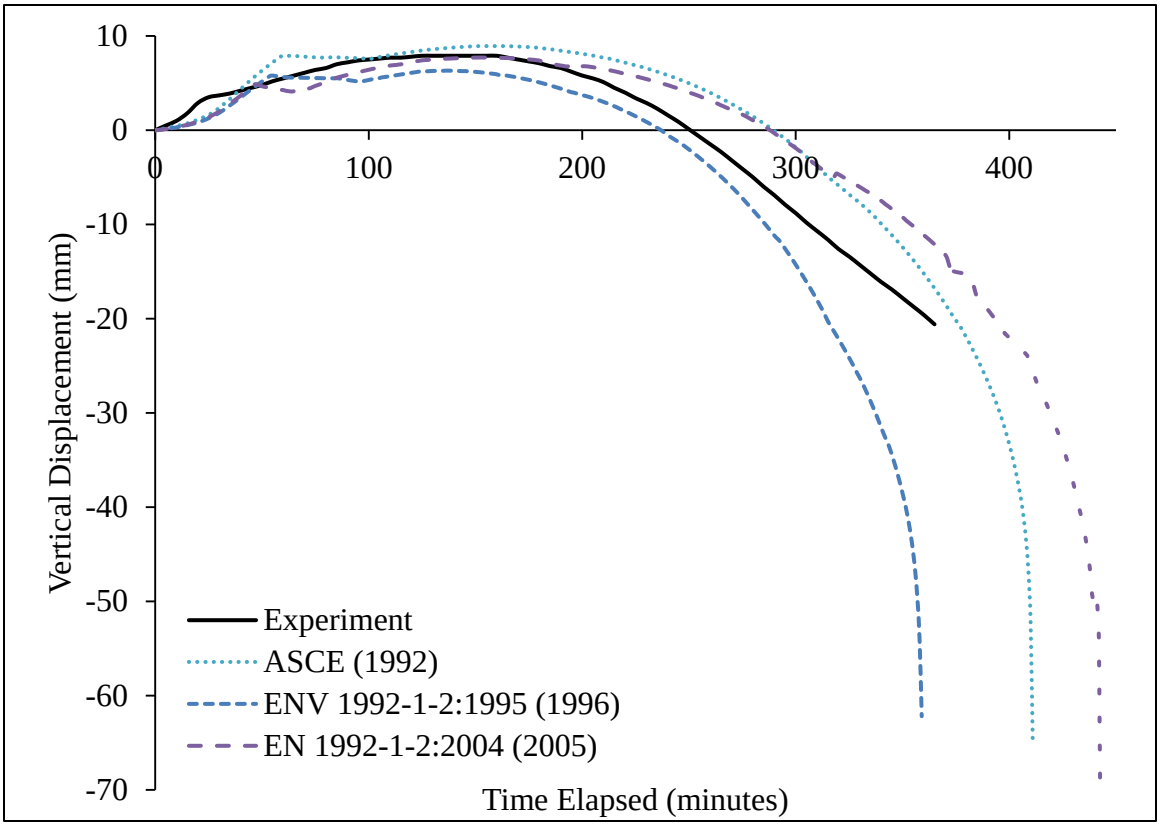

Figure 5-73 Vertical displacement of Column 11 from the start of fire to failure

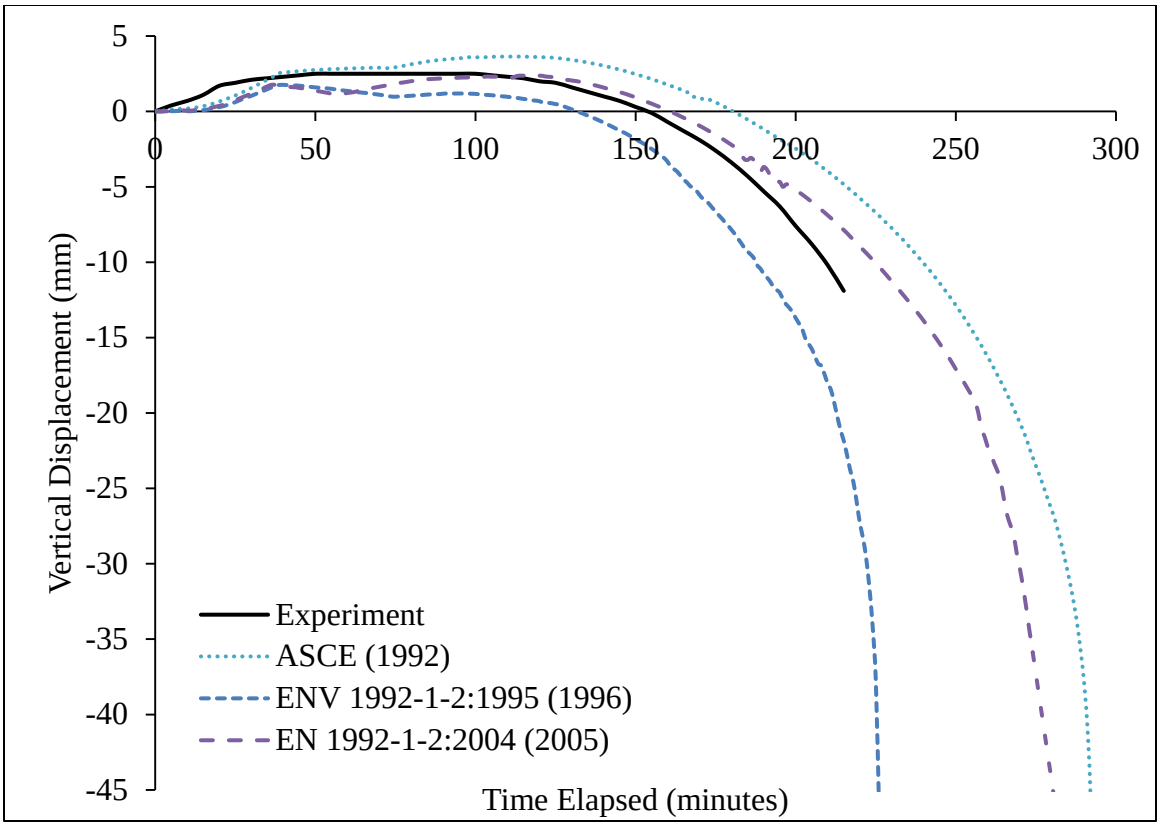

Figure 5-74 Vertical displacement of Column 12 from the start of fire to failure

The deformation of the specimens is governed by a balance between the thermal expansion of steel and concrete and the deterioration of their stiffnesses. In general, regardless of the level of axial loading the specimen is subjected to, the specimen expands during the first part of the test, where the behaviour is mainly dominated by the thermal strains, while the reduction of the stiffnesses of steel and concrete is not substantial at lower temperatures. In this part, one can notice a kink in the time-displacement plot, which is caused by the yielding of steel reinforcing bars, as the yield stress declines with the increase in temperature.

The expansion reaches a peak after a certain period of time, and then decreases as time passes. After reaching the peak expansion, the stiffnesses of concrete and steel are compromised to the extent that the contraction displacement resulting from the axial loading exceeds the expansion displacement resulting from the increase in temperature. As time passes and the temperatures of the concrete and steel increase, their stiffnesses keep declining until a certain point where their strengths are not sufficient to withstand the axial loads and the specimen fails.

When inspecting the results, two aspects are of major importance: the maximum displacement reached and, more importantly, the time from the start of fire to failure. Note that these two main points of interest do not occur concurrently. The experimental results show that Column 10 failed after 8 hours and 30 minutes, experiencing a maximum expansion of 11.1 mm, Column 11 failed after 6 hours and 5 minutes, with a maximum expansion of 7.9 mm, and Column 12 failed after 3 hours and 35 minutes, with a maximum expansion of 2.5 mm.

Table 5-12 shows the maximum expansion displacement reached, "d", and the time from the start of fire to failure, "t", for Columns 10, 11, and 12. For the maximum expansion displacement reached, all the models seem to estimate it reasonably, with a general trend of underestimation in case of ENV 1992-1-2:1995 (1996), with a mean analytical to experimental ratio of 0.85 and a coefficient of variation of 20%. In case of ASCE Manual of Practice (1992), there is a general trend of overestimation, with a mean analytical to experimental ratio of 1.26 and a coefficient of variation of 14%. The EN 1992-1-2:2004 (2005), on the other hand, managed to capture the maximum expansion displacement reached more precisely, with a mean analytical to experimental ratio of 0.97 and a coefficient of variation of 2%.

Table 5-12 Experimental and Analytical results of Columns 10, 11, and 12

Specimen	Experimental Results		ASCE Manual of Practice (1992)		ENV 1992-1-2:1995 (1996)		EN 1992-1-2:2004 (2005)	
	d (mm)	t (min)	d (mm)	t (min)	d (mm)	t (min)	d (mm)	t (min)
Column 10	11.10	510	12.15	517	9.21	455	11.06	598
Column 11	7.90	365	8.94	411	6.32	359	7.71	443
Column 12	2.50	215	3.65	295	1.77	228	2.37	294

However, EN 1992-1-2:2004 (2005) does not estimate the time from the start of fire to failure within a reasonable range of accuracy, giving an unsafe overestimation with a mean analytical to experimental ratio of 1.25 and a coefficient of variation of 8%. The ASCE Manual of Practice (1992) also overestimates the time to failure with a mean analytical to experimental ratio of 1.17 and a coefficient of variation of 16%. The models that manage to capture the time of failure more precisely are the ones provided by ENV

1992-1-2:1995 (1996), estimating it with a mean analytical to experimental ratio of 0.98 and a coefficient of variation of 9%.

5.5.2.2 NRC Column 1582

This test, carried out by Mostafaei et al. (2012), is the first of its kind. It involved testing a full-scale column specimen for fire resistance assessment under both axial and lateral loads. While testing columns for fire resistance under axial loads is rather common, simultaneous lateral loading is not. This type of loading profile aims at imitating the loading conditions of columns as parts of buildings, rather than individual members. A column in a building exposed to fire would experience lateral displacement due to the differential thermal expansion of the slabs it connects to at its top and bottom. In a reinforced concrete bridge, bent girders would have the same effect on the columns.

This test represents a part of a general objective of the National Research Council Canada (NRC) towards a more realistic fire resistance assessment method that takes into account the interaction of reinforced concrete members subjected to fire with the structural system of the whole building. This interaction is normally neglected by most researchers, who tend to test individual reinforced concrete members, such as beams, slabs, or columns. The obvious reason behind this is the exorbitant cost required for constructing a full-scale reinforced concrete building and applying fire in one compartment to test this interaction.

In order to estimate the lateral displacement acting on the column specimen, the commercial thermal analysis program SAFIR (Franssen, 2003) was used to carry out a finite element analysis for the six-storey prototype building shown in Figure 5-75, for which a compartment fire scenario was assumed. The building had six 9-metre spans in one direction and four 5-metre spans in the other. Each of the six storeys was 3.8 m high, resulting in a total height of 22.8 m for the entire building. The compartment selected for the fire scenario was on the first floor in one of the middle spans of one of the shorter edges as shown in Figure 5-75. The compartment was exposed to the CAN/ULC S101-07 (2007) standard temperature-fire curve. Column 1582, shown in Figure 5-75, was

selected for the experimental testing as a worst case scenario, with the maximum axial and lateral load combination.

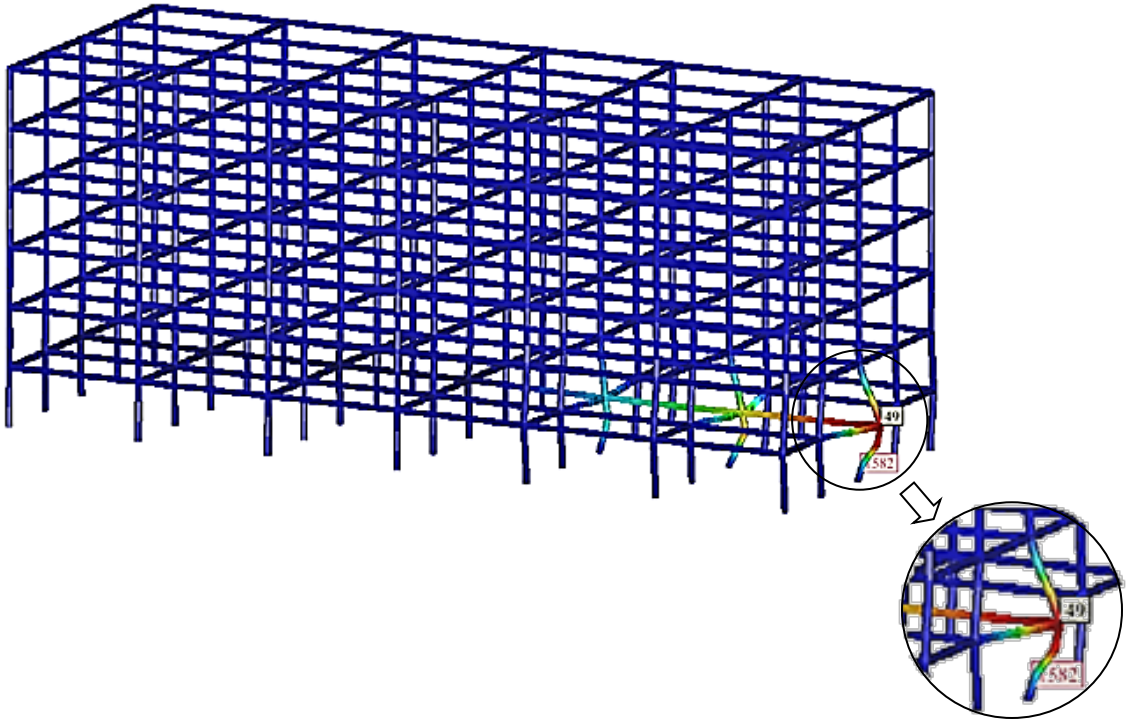

Figure 5-75 Finite element model analyzed using SAFIR (Franssen, 2003) with a magnification of the fire compartment and the lateral displacement in NRC Column 1582 (adapted from Mostafaei et al. (2012))

The same typical specimen shown in Figures 5-37 and 5-38 was used, with the same steel reinforcement material properties. The concrete was mixed using calcareous aggregates and had a compressive strength of 55 MPa, based on three cylinder compression tests carried out on the day of testing. The column was tested in the NRC column furnace, where it was loaded to an axial load of 1590 kN, applied from the bottom, prior to the start of fire. This axial loading amounted to 31.1% of the column capacity, based on a monotonic loading analysis of the column carried out using VecTor3. To allow for longer fire exposure duration, the lateral displacement applied to the top of the column was approximated and capped at 50 mm, following the profile shown in Figure 5-76. The rotation was restrained at both ends of the column.

The temperature of the furnace was set to follow the CAN/ULC S101-07 (2007) standard temperature-fire curve and was monitored throughout the test. The setup of the test required that the column's top and bottom edges were covered by insulation, thus only a

3175 mm length of the 3810 mm long column was subjected to fire. The mechanical and thermal loading setup of Column 1582 is shown in Figure 5-77. The column was exposed to fire in the furnace with the maximum lateral displacement of 50 mm reached, which occurred at 120 minutes from the start of fire and lateral loading until failure.

The specimen experienced high levels of spalling along the entire tension side at around 26 minutes from the start of dire, and it failed after 180 minutes from the start of fire, when the axial load suddenly dropped to zero.

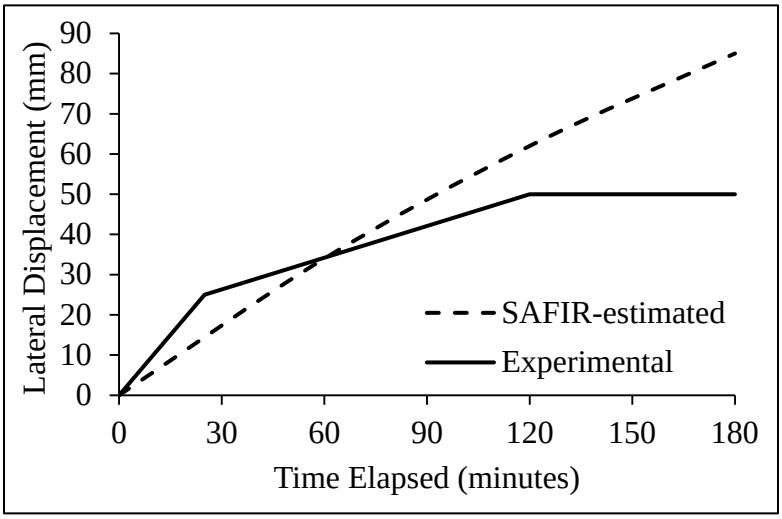

Figure 5-76 SAFIR-estimated and experimental lateral loading profile for NRC Column 1582

The finite element model created for the analysis of Columns 10, 11, and 12 could not be used for the analysis of Column 1582; the bending moment ensuing from the lateral loading required the entire depth of the column to be modelled. Therefore, half of the cross section was modelled, instead of the quarter cross section used for Columns 10, 11, and 12, using the finite element discretization as shown in Figure 5-78. Also, the limited parts of Columns 10, 11, and 12 that were modelled through their heights are inappropriate for the analysis of Column 1582, because the entire height is required to achieve the correct bending moment acting at the fixed base of the column. Therefore, the column was discretized into 75 elements with a height of 50.13 mm each, to achieve a total height of 3810 mm for the model. The 13 ties were modelled at 300 mm, instead of the actual 305 mm, in order to fit in the selected finite element discretization. This means that a tie was located at every sixth element along the height.

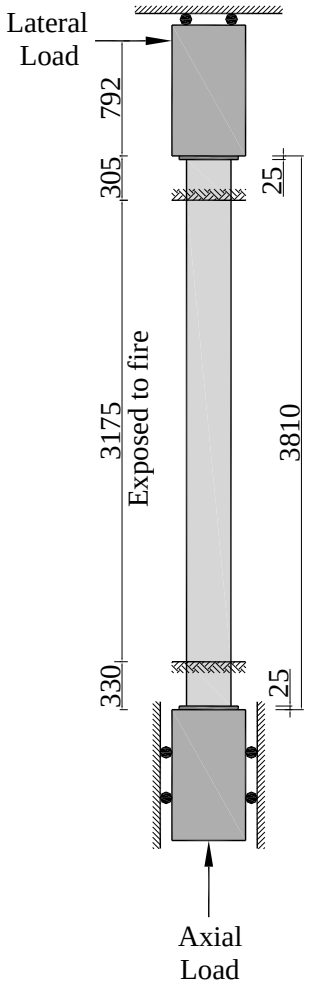

Figure 5-77 Mechanical and thermal loading setup of NRC Column 1582

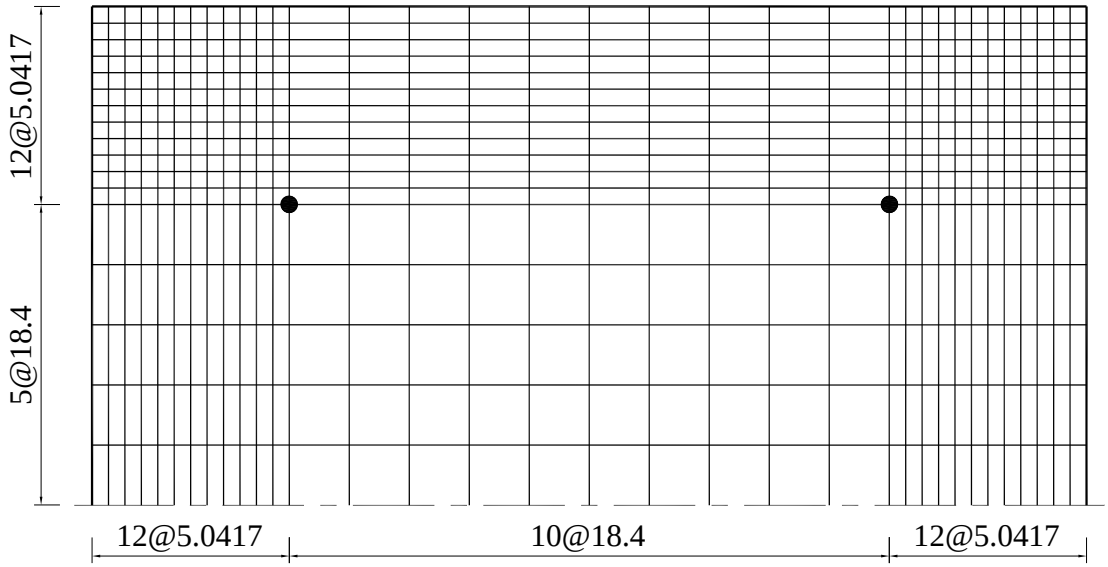

Figure 5-78 Finite element discretization of the cross section of NRC Column 1582 for structural analysis and the steel reinforcing bar location
(dimensions in mm)

A time step of 60 seconds was used for the analysis. The axial load of 1590 kN was applied prior to the start of fire at the top of the column as nodal loads, and the models provided by the current version of the Eurocode (EN 1992-1-2:2004, 2005) were used for the thermal analysis, as explained earlier. The exact same experimental lateral loading profile was applied at the top of the column in a displacement control loading regime until failure. The thermal loading of the fire and the lateral loading were started at the same time, resembling the experimental conditions.

Figures 5-79, 5-80, and 5-81 show the experimental results for the vertical displacement at the top of Column 1582 compared to the analytical results estimated using the models presented by the ASCE Manual of Practice (Structural Fire Protection by T. T. Lie, 1992), the former version of the Eurocode (ENV 1992-1-2:1995, 1996), and its current version (EN 1992-1-2:2004, 2005), respectively. Given the obviously significant role that geometric nonlinearity plays in this test with the P-Δ effects associated with the lateral load combined with axial loading, the results are shown for analyses where geometric nonlinearity effects were neglected for the sake of comparison. Figures 5-82, 5-83, and 5-84 present the same comparisons for the same models, but for the lateral load required for the predetermined lateral displacement, and Figures 5-85, 5-86, and 5-87 present lateral load-displacement curves for the same models.

It should be noted that the test results showed an initial lateral load of around 14 kN after applying the axial load and before the start of the fire or applying the lateral displacement. This initial lateral load might be a result of a slightly eccentric axial loading or some imperfections in the specimen construction or in the loading mechanism. In order to be able to compare the experimental results to the analytical results calculated by VecTor3, this initial lateral load has been deducted from all the lateral loads reported throughout the test.

One can notice from the results that all the models fail to accurately estimate the time of failure from the start of fire and simultaneous lateral loading. However, the models provided by the former version of the Eurocode (ENV 1992-1-2:1995, 1996), and the ones provided by its current version (EN 1992-1-2:2004, 2005) tend to be on the conservative side, with an analytical to experimental ratio of 0.76 and 0.82, respectively. On the other hand, the models provided by the ASCE Manual of Practice (Structural Fire

Protection by T. T. Lie, 1992) tend to estimate a fire resistance that is longer than the experimental fire resistance with an analytical to experimental ratio of 1.13. The results also show how neglecting geometric nonlinearities results in a less conservative fire resistance and lower values of contracting displacements. This can be attributed to the additional stresses applied through the height of the specimen due to the additional moment resulting from the P-Δ effects associated with the lateral load combined with axial loading

The models provided by the former version of the Eurocode (ENV 1992-1-2:1995, 1996) seem to generate the most accurate deformations with an analytical to experimental ratio of 0.96 for the maximum expansion displacement, followed by those provided by the current version (EN 1992-1-2:2004, 2005) with an analytical to experimental ratio of 0.95 for the same displacement, while the models provided ASCE Manual of Practice (Structural Fire Protection by T. T. Lie, 1992) tend to estimate significantly higher expansion displacements, with an analytical to experimental ratio of 1.68.

For the lateral stiffness represented in the load required for the predetermined lateral displacement profile described in Figure 5-76, all the models produce similar results, with an obviously higher resistance estimate when geometric nonlinearity effects are neglected. One interesting observation is how this lateral load crosses over to the negative side at around 60 minutes from the start of fire, meaning that the column is actually being pulled back to keep it at the desired lateral displacement. This effect is obviously caused by the additional moment resulting from the P-Δ effects. This is something that is missed when the geometric nonlinearity effects were neglected in the analysis whose results always showed a positive lateral load, and that is captured, to some extent, when geometric nonlinearity effects were considered, as shown in Figures 5-82, 5-83, and 5-84.

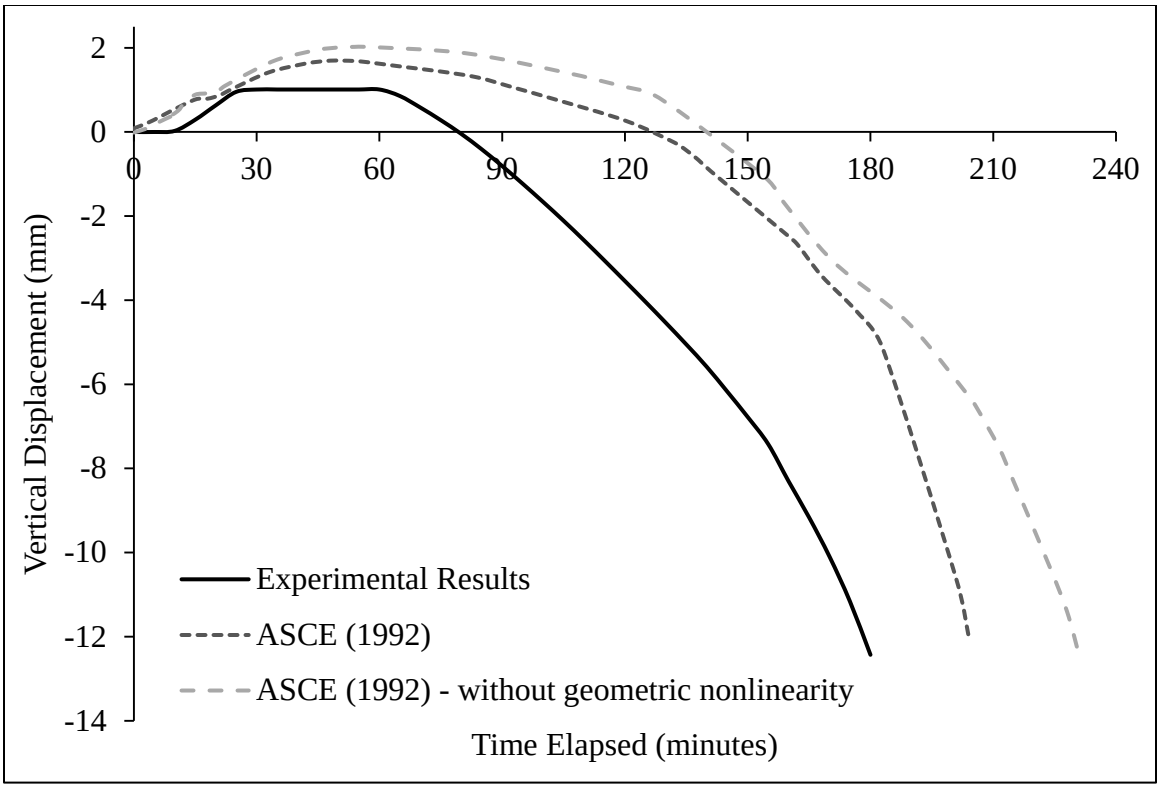

Figure 5-79 Vertical displacement at the top of NRC Column 1582 with time from the start of fire using the models presented by the ASCE Manual of Practice (1992)

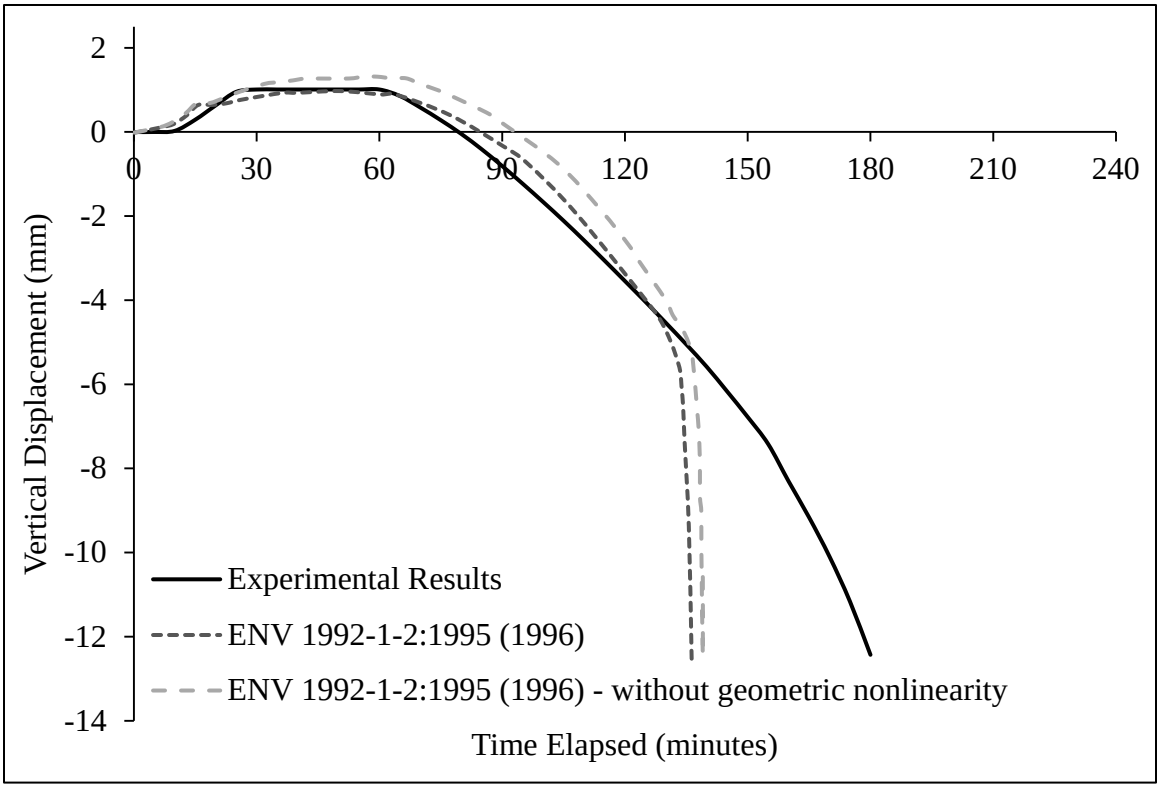

Figure 5-80 Vertical displacement at the top of NRC Column 1582 with time from the start of fire using the models presented by the Eurocode ENV 1992-1-2:1995 (1996)

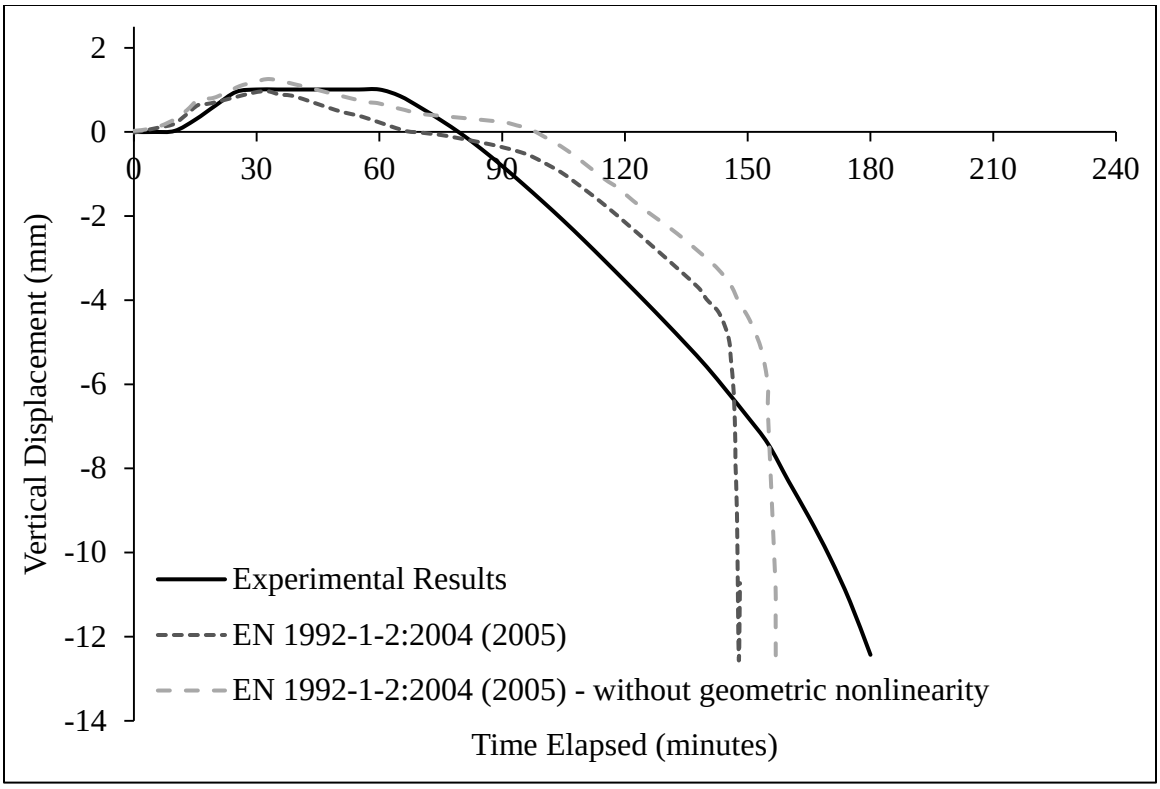

Figure 5-81 Vertical displacement at the top of NRC Column 1582 with time from the start of fire using the models presented by the Eurocode EN 1992-1-2:2004 (2005)

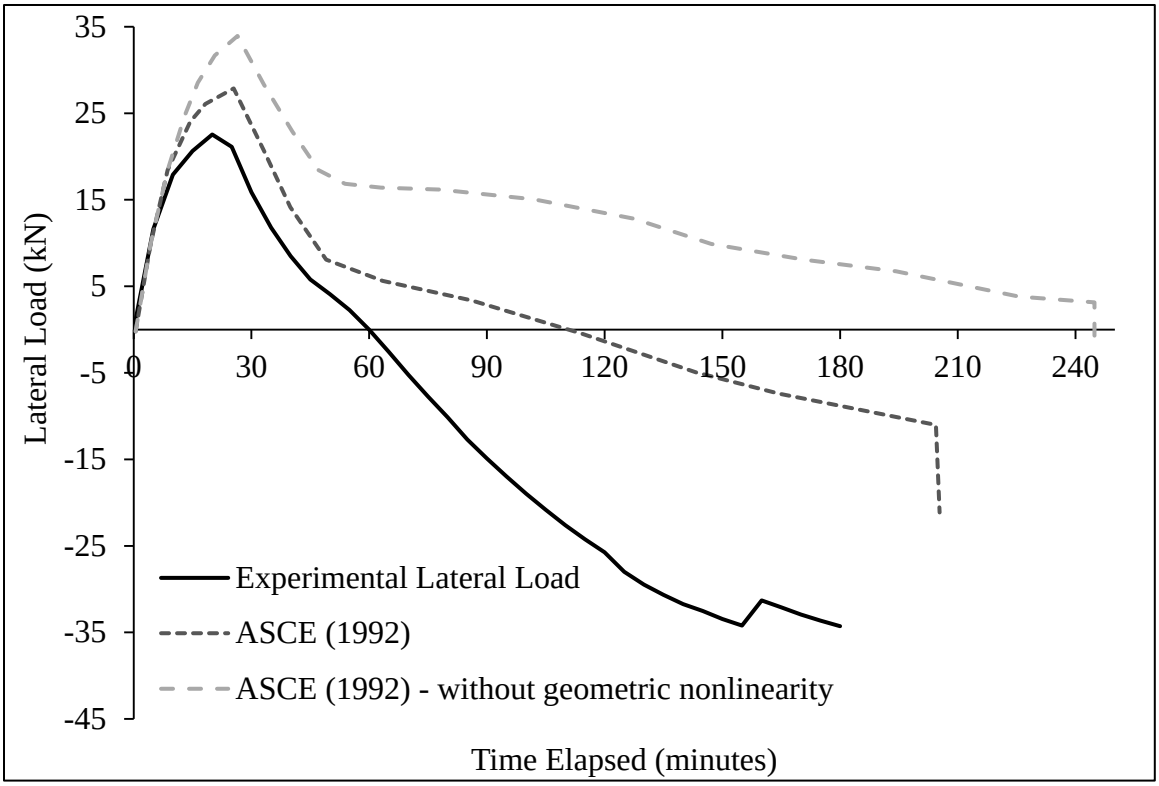

Figure 5-82 Lateral load at the top of NRC Column 1582 with time from the start of fire using the models presented by the ASCE Manual of Practice (1992)

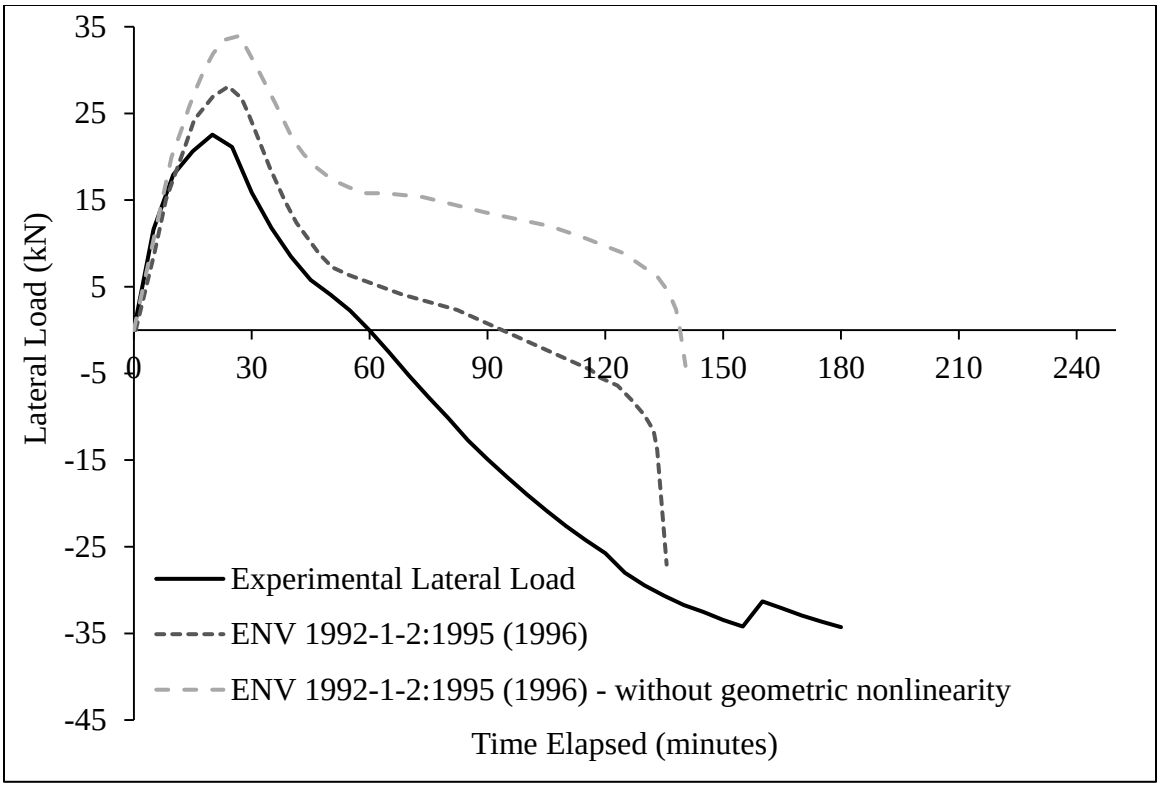

Figure 5-83 Lateral load at the top of NRC Column 1582 with time from the start of fire using the models presented by the Eurocode ENV 1992-1-2:1995 (1996)

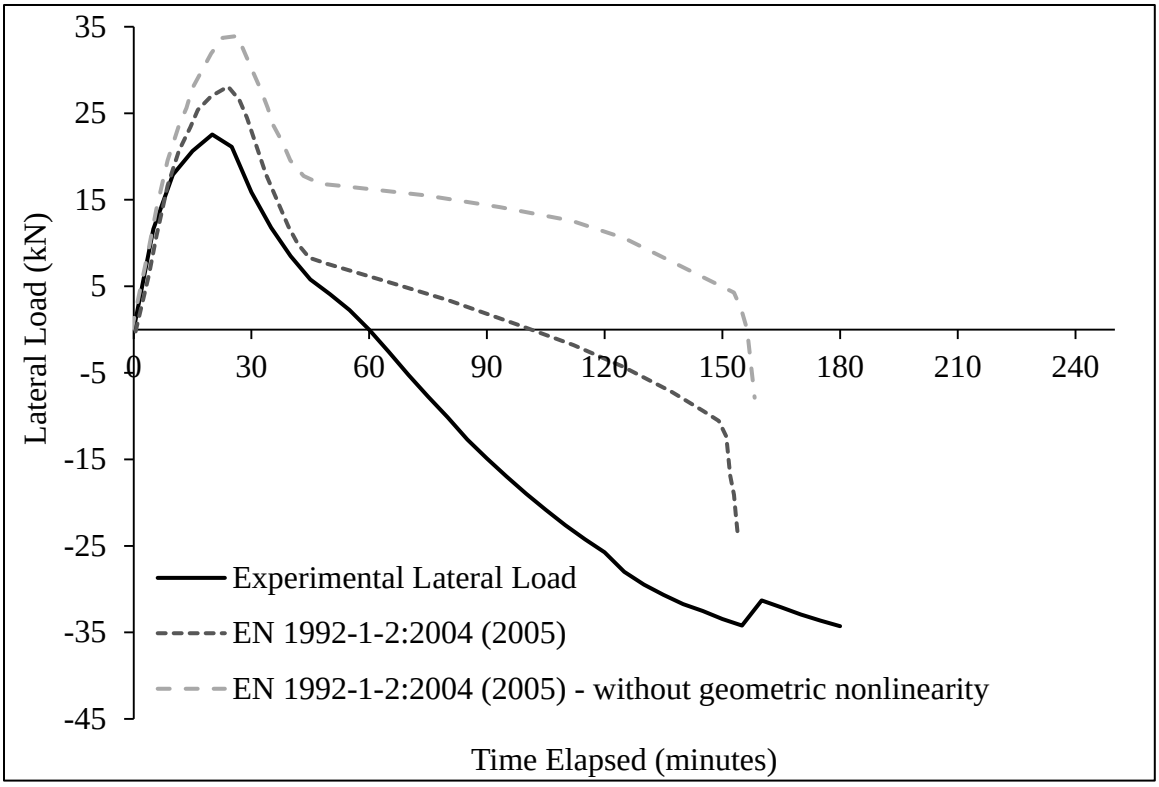

Figure 5-84 Lateral load at the top of NRC Column 1582 with time from the start of fire using the models presented by the Eurocode EN 1992-1-2:2004 (2005)

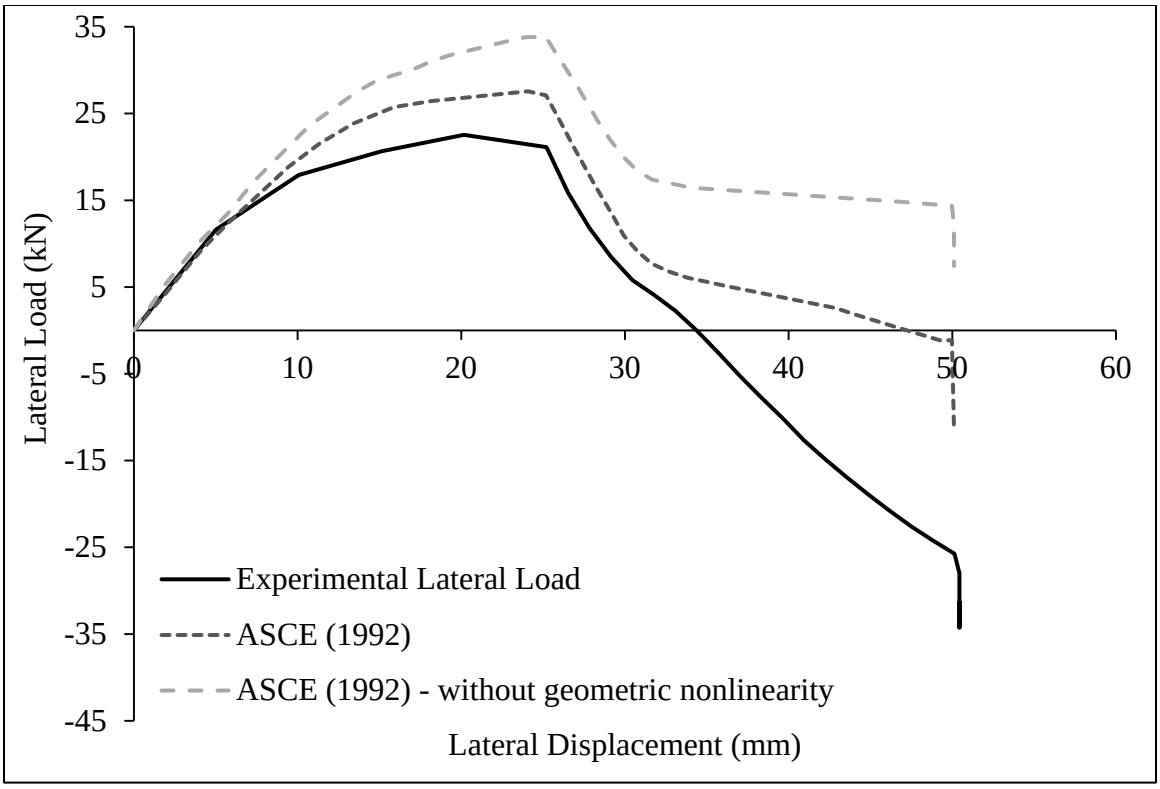

Figure 5-85 Lateral load-displacement curve at the top of NRC Column 1582 using the models presented by the ASCE Manual of Practice (1992)

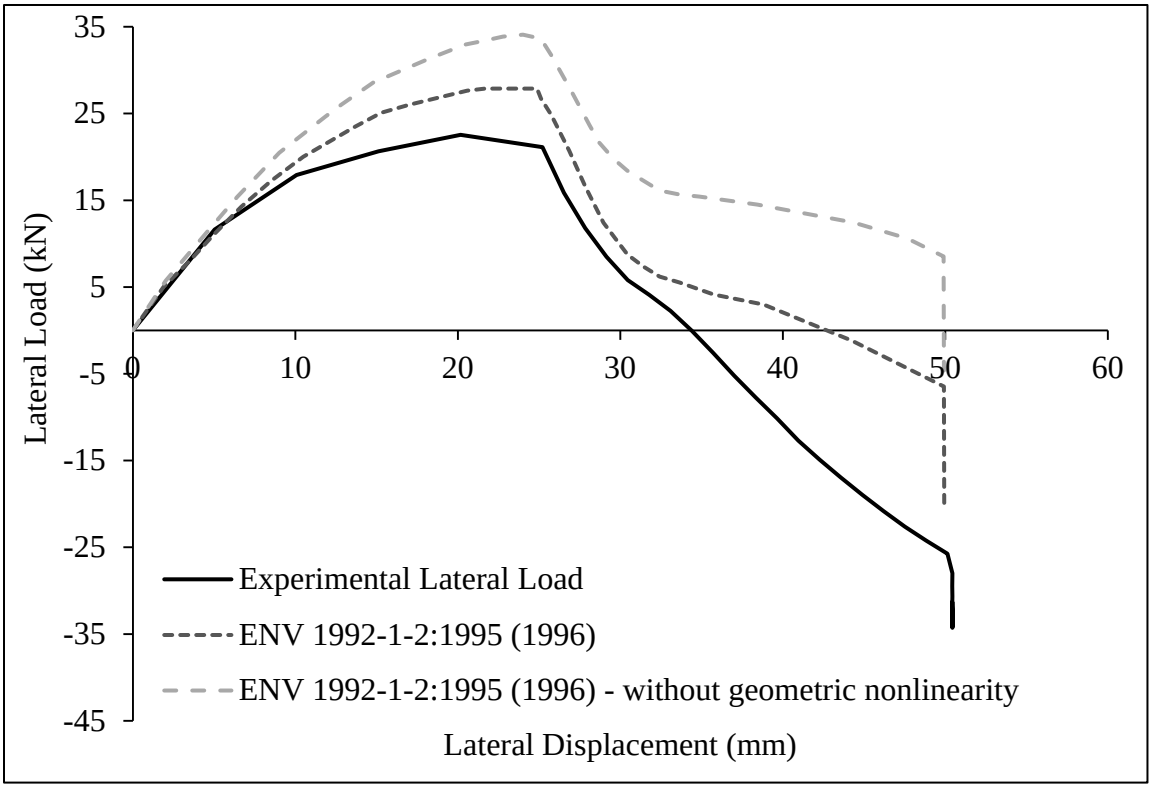

Figure 5-86 Lateral load-displacement curve at the top of NRC Column 1582 using the models presented by the Eurocode ENV 1992-1-2:1995 (1996)

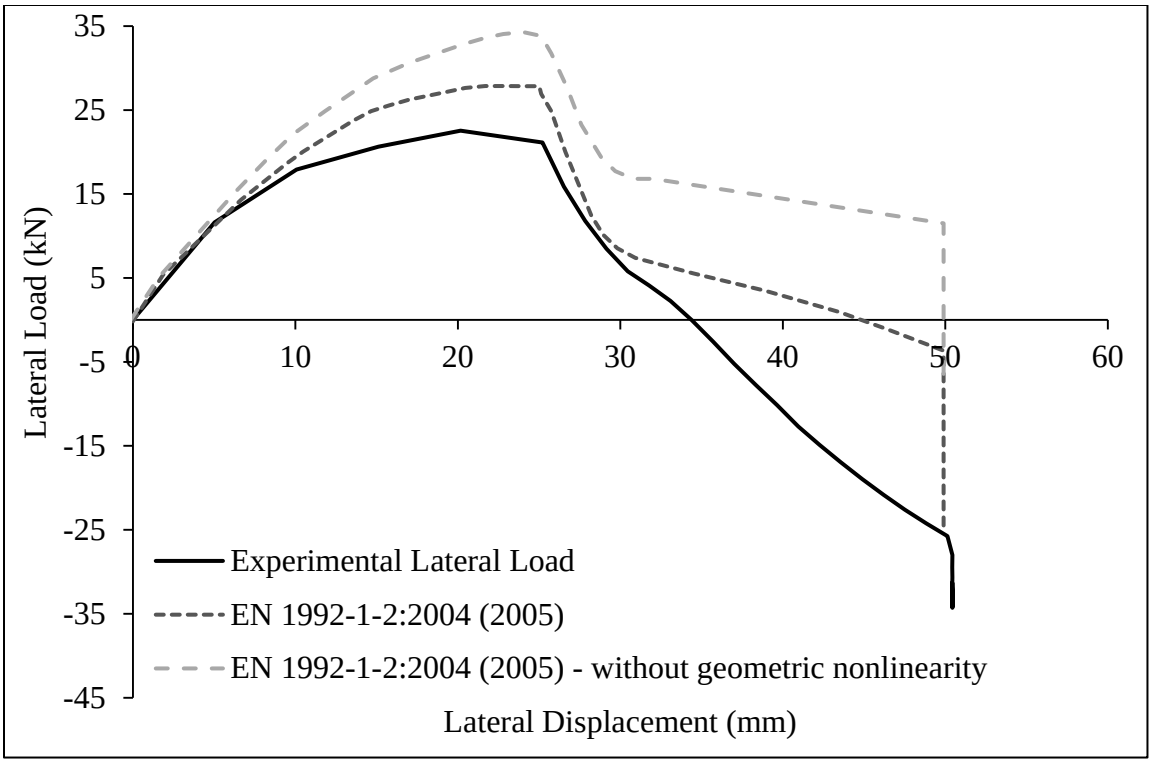

Figure 5-87 Lateral load-displacement curve at the top of NRC Column 1582 using the models presented by the Eurocode EN 1992-1-2:2004 (2005)

5.5.2.3 NRC Columns A and B

This experimental series, carried out by Lie et al. (1986), was aimed at assessing the residual strength of reinforced concrete columns after exposure to fire. The rationale for such an assessment is the determination of the feasibility of repair of fire-damaged structures. The experimental series included two columns, with typical properties as shown in Figures 5-37 and 5-38, and with the same steel reinforcement material properties. Column A and Column B were loaded under almost similar axial loads and were subjected to fire, following the CAN/ULC S101-07 (2007) standard temperature-fire curve, in the testing furnace for one hour and two hours, respectively. They were both allowed to cool naturally (in air at room temperature) for about twenty-four hours until they reached room temperature; then, they were axially loaded until failure.

The columns were constructed using siliceous aggregate. On the day of testing, the compressive strength of the concrete was 38.9 MPa for Column A and 41.8 MPa for Column B. Both columns were loaded axially one hour prior to the fire test; Column A

was loaded to 992 kN and Column B to 1022 kN. Based on monotonic loading analyses carried out using VecTor3 for the columns, these levels of loading amount to 22.0% and 21.4% of the axial capacity of Column A and Column B under normal temperatures, respectively.

The finite element model created for the analysis of Columns 10, 11, and 12, shown in Figure 5-69, was used in the analysis of Column A and Column B. The analysis was carried out to resemble the experimental conditions. A time step of 60 seconds was used, and the models provided by the current version of the Eurocode (EN 1992-1-2:2004, 2005) were used for the thermal analysis, as explained earlier. The models of Column A and Column B were loaded to their respective axial load, then subjected to the CAN/ULC S101-07 (2007) standard temperature-fire curve for one hour and two hours, respectively, after which the fire was allowed to decay, following the ISO 834-1:1999 (1999) standard temperature-fire curve for the descending temperature branch (fire decay phase). After around 24 hours, when the temperatures of the columns models were approximately 20 ºC, they were loaded to failure.

For the sake of comparison, the models provided by the ASCE Manual of Practice (Structural Fire Protection by T. T. Lie, 1992), the former version of the Eurocode (ENV 1992-1-2:1995, 1996), and its current version (EN 1992-1-2:2004, 2005) were used for the analysis. This analysis is different than the analysis of the Columns 10, 11, and 12, discussed in Section 5.5.2.1, and the analysis of Column 1582, discussed in Section 5.5.2.2, because these specimens were mixed using siliceous aggregates, hence, different models were tested here.

It should be noted that the literature presents models for the mechanical properties of concrete and steel at elevated temperatures during the event of fire and other models for the residual mechanical properties of concrete and steel after the event of fire. Yet, there is a void in the literature for the cooling period and the path that the mechanical properties follow going from their values at the maximum reached temperature to their values when they cool to room temperature (residual properties). Therefore, in this study, for the lack of a better experimentally-proven method, it has been assumed that the mechanical properties of concrete and steel change linearly moving between the values mentioned above.

Figures 5-88 and 5-89 present plots for the vertical displacements of Column A and Column B, respectively, from the start of the fire. The analytical results estimated using the three sets of models mentioned above are presented, together with the experimental results and an analytical estimate provided by Lie et al. (1986), denoted “NRC Estimate”. This analytical estimate was derived using the experimentally-measured temperatures of concrete at different depths from the surface to divide it into zones based on the maximum temperature reached. Then, the mechanical properties of these zones were determined using the available models for residual properties. Finally, a finite element analysis was undertaken for a model constructed with these residual mechanical properties and the failure load was determined.

While examining Figures 5-88 and 5-89, one should recall from Section 5.5.1.2 that the temperatures of concrete through the depths that were analytically calculated were always below the experimental ones. This might explain why the analytically-estimated displacements of Column A and Column B decreased at a steeper rate than the experimental displacements. Other reasons may be the limited data used to develop the models describing the post-fire properties and the approximate procedure adopted to fill the cooling phase properties void that was explained earlier.

Figure 5-88 shows that, for Column A, the ASCE Manual of Practice (1992) and ENV 1992-1-2:1995 (1996) accurately estimate the residual displacement after cooling, while EN 1992-1-2:2004 (2005) overestimates it. However, for Column B, all models seem to significantly underestimate the residual displacement, as can be seen in Figure 5-89. This is possibly due to localized plastic strains attained by the steel reinforcing bars at the cracks that are not accounted for. For both columns, the maximum expansion displacements are overestimated, with ENV 1992-1-2:1995 (1996) estimating significantly higher displacements.

The NRC estimate seems to capture the peak expansion displacements very accurately; yet, the residual displacements estimates are highly inaccurate. It is unclear why the NRC estimate for Column B estimated that the specimen expanded again while it was cooling, as can be seen in Figure 5-89.

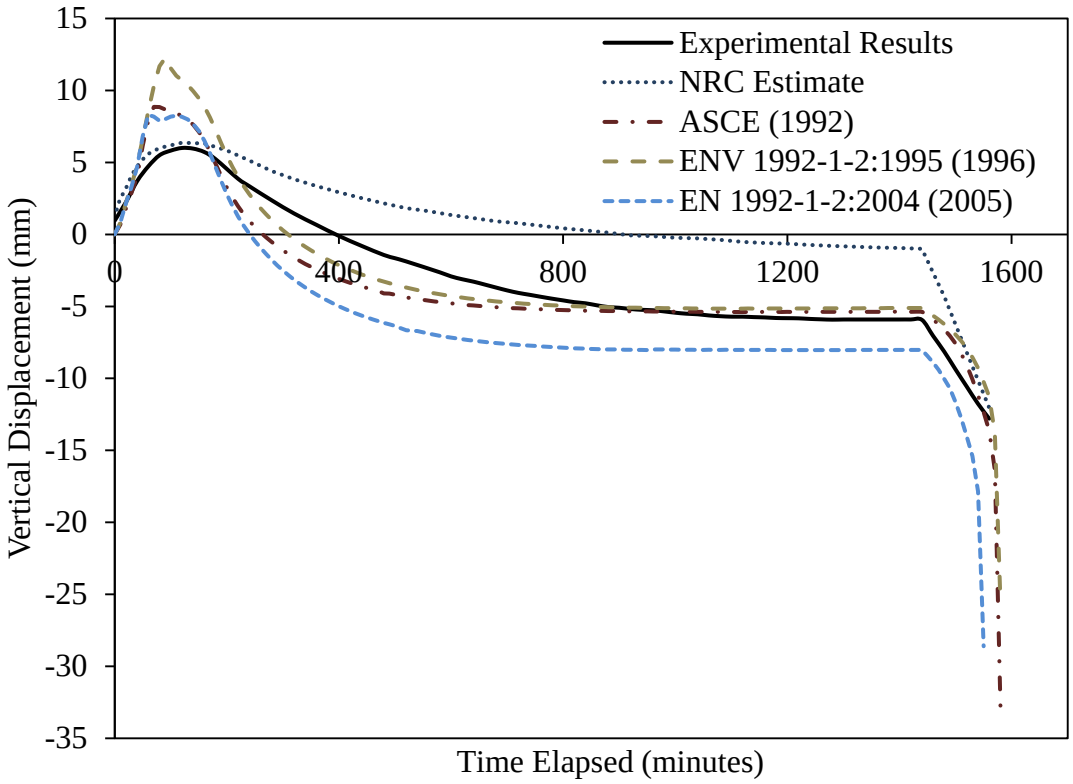

Figure 5-88 Vertical displacement of Column A from the start of fire to failure

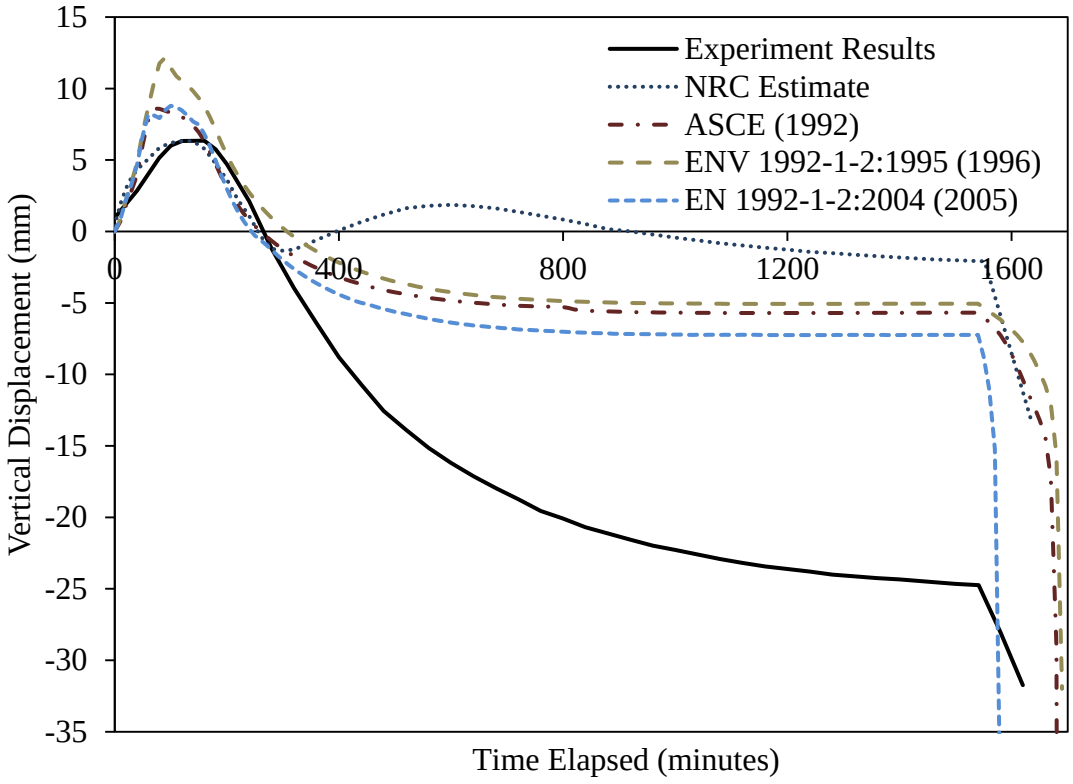

Figure 5-89 Vertical displacement of Column B from the start of fire to failure

Table 5-13 shows the experimentally-determined residual capacity of the columns and the analytically-estimated values, based on the different models. The column models that were analyzed using the models presented by the ASCE Manual of Practice (1992) produced a mean analytical to experimental value of 1.18. With the models presented by ENV 1992-1-2:1995 (1996), this value is 1.21. Finally, with the models presented by EN 1992-1-2:2004 (2005), this value comes to 1.13; hence, the models presented by EN 1992-1-2:2004 (2005) provide the most accurate results for concrete mixed using siliceous aggregates.

Table 5-13 Experimental and analytical residual capacities of Column A and Column B

Specimen	Experimental Results (kN)	ASCE Manual of Practice (1992) (kN)	ENV 1992-1-2:1995 (1996) (kN)	EN 1992-1-2:2004 (2005) (kN)
Column A	1987	2684	2686	2330
Column B	2671	2700	2830	2908

5.6 Coupled Heat and Moisture Transfer Analysis

In this section, the coupled heat and moisture transfer analysis theory and procedure are verified. Also, many of the phenomena associated with the heating of concrete, potentially causing explosive spalling, are shown and discussed. A unidirectional coupled heat and mass transfer analysis was carried out on a strip of concrete, which can represent any unidirectional coupled heat and mass flow through a concrete column, beam, slab, or any other concrete member. A unidirectional analysis was chosen in order to be able to clearly show the different phenomena the process experiences. However, a full three-dimensional procedure was implemented in VecTor3.

The procedure of the coupled heat and moisture transfer analysis discussed in Chapter 4 was used, employing the models, techniques, and material properties presented in Chapter 3, Chapter 4, Appendix A, and Appendix B. The solution involves a highly nonlinear iterative time-stepping procedure as shown in the flow chart presented in Figure C.1 and the step-by-step calculation scheme presented in Appendix C.

Figure 5-90 shows a typical strip of the unidirectional coupled heat and mass flow analyzed, discretized into finite elements with arbitrary lengths. Since the procedure is based on the assumption of homogeneous material properties for each element, the analysis is highly sensitive to the lengths of the elements. Many lengths have been tried and a length of 0.25 mm was chosen. A larger length would still produce reasonable results, but a smaller one was chosen in order to have a clear view of the phenomena and phases experienced by concrete subjected to fire. The width and depth of the elements are irrelevant, considering that the analysis is unidirectional. To achieve a good aspect ratio for a more stable analysis, the elements were modelled as perfect cubes of 0.25 mm sides.

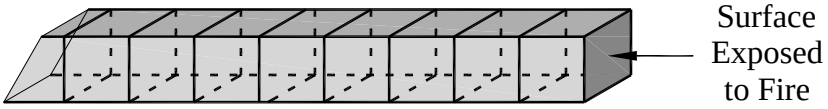

Figure 5-90 Finite element discretization for unidirectional coupled heat and moisture transfer analysis

The analyzed model consisted of 1600 elements, resulting in a total length of 400 mm. In order to impose a unidirectional flow, the four sides along the direction of the heat flow were assumed to be insulated, which means that no boundary conditions were applied to these surfaces. The boundary conditions of the ISO 834-1:1999 (1999) standard fire curve and normal atmospheric pressure were applied at the surface exposed to fire, as shown in Figure 5-90. The time step used in the analysis was 1 second. Although larger time steps were tried and worked reasonably well, with the high level of nonlinearity of the analysis, a small time step is crucial for its accuracy and stability.

For the properties of concrete that are inherent to each concrete mix, the initial porosity, ϕ_o, was set to a value of 0.08 in the analysis, and the initial mass of liquid water per unit volume of concrete, $\bar{\rho}_{L_{o,o}}$, was set to a value of 80 kg/m^3. The initial permeability, K_o, was assigned a value of 5×10^{-17} m^2, which is low enough to cause spalling according to Harmathy (1965). The specific heat capacity of concrete, c_{p_c}, and its conductivity, k, were calculated according to the current version of the Eurocode (EN 1992-1-2:2004, 2005).

Figure 5-91 presents a collective display of results for the temperature of concrete, T, the pressure of the gaseous mixture in concrete, P_G, the mass of the gaseous phases per unit volume of the gaseous mixture in concrete, $\tilde{\rho}_V$, the mass of water vapour per unit volume of concrete, $\bar{\rho}_V$ or $\varepsilon_G\tilde{\rho}_V$, and the mass of liquid water per unit volume of concrete, $\bar{\rho}_L$, through time from the start of fire. Conditions are shown at a depth of 10, 20, and 30 mm from the surface subjected to fire (a, b, c, d, and e) and through the depth of the concrete member at 10, 30, and 60 minutes from the start of the fire (f, g, h, i, and j).

Examining Figure 5-91 (a) to (e), one can observe many of the phenomena previously discussed. In Figure 5-91 (a), (b), and (c), the gradual increase in T, P_G, and $\tilde{\rho}_V$ at the different depths with the elapsing time can be seen. It can also be seen that T increases shortly after the start of fire, while P_G and $\tilde{\rho}_V$ do not, as they do not increase until the evaporation point of the water existing in concrete is reached at slightly higher than 100ºC.

The “moisture clog” or “saturation plug”, explained in Section 3.3.2.1, can be observed in Figure 5-91 as a shaded area with different tones for the three different plotted depths. In Figure 5-91 (e), $\bar{\rho}_L$ can be seen decreasing at the beginning due to the evaporation of liquid water. Then, due to the slower rate of migration of water vapour than the rate of evaporation of liquid water, the moisture clog happens and can be seen as an abrupt increase in $\bar{\rho}_L$. This introduces the next stage in the process, where the concrete is completely saturated for a certain period of time, marking the moisture clog, after which $\bar{\rho}_L$ drops to zero as all the liquid water is evaporated at this point in time. This happens suddenly because liquid water vanishes suddenly as it reaches its evaporation point.

In Figure 5-91 (d), a steeper increase in $\bar{\rho}_V$ can be observed through the time period of the occurrence of the moisture clog for all the depths shown, after which $\bar{\rho}_V$ experiences a sudden increase. Since $\bar{\rho}_L$ decreases abruptly just after the moisture clog ends as water reaches its evaporation point, a corresponding increase occurs in $\bar{\rho}_V$, as shown in Figure 5-91 (d). The logical explanation for this is that the mass lost in the liquid water phase due to evaporation is obviously added to the mass of the water vapour phase.

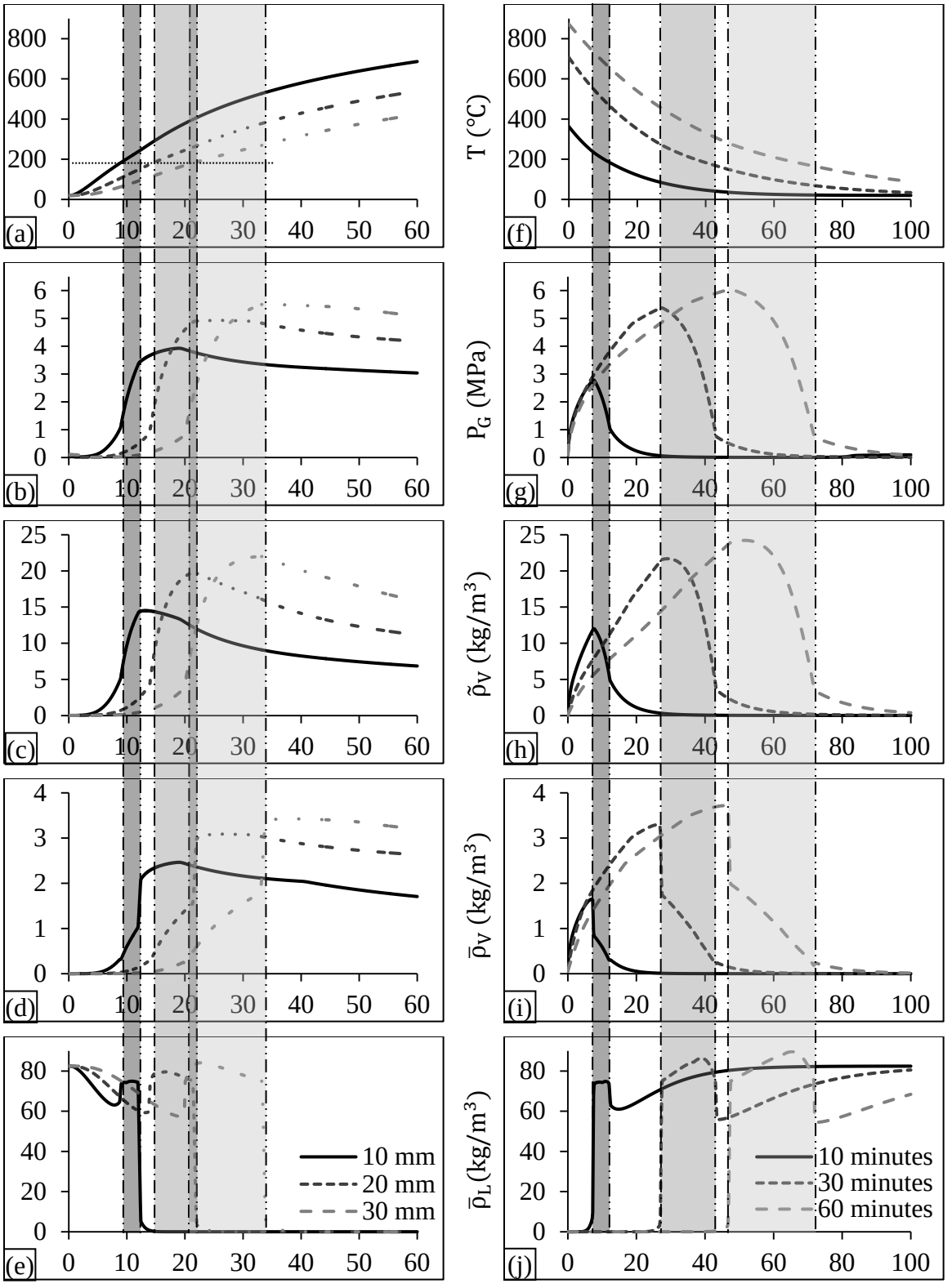

Figure 5-91 Temperature of concrete, T, pressure of the gaseous mixture in concrete, P_G, mass of the gaseous phases per unit volume of the gaseous mixture in concrete, $\tilde{\rho}_V$, mass of water vapour per unit volume of concrete, $\bar{\rho}_V$, and mass of liquid water per unit volume of concrete, $\bar{\rho}_L$, through the depth of concrete member and the time from the start of fire

The moisture clog can also be seen in Figure 5-91 (j) with respect to the distance from the surface exposed to fire. Figure 5-91 (j) also shows the different zones of concrete through the depth, where the outermost layer is completely dry with zero $\bar{\rho}_L$, followed by a sudden increase in $\bar{\rho}_L$, starting the moisture clog zone. In the zone behind the moisture clog, $\bar{\rho}_L$ increases gradually until it reaches its initial value at deeper layers of concrete. The start of the moisture clog zone as seen in Figure 5-91 (j) also marks the location of the maximum $\bar{\rho}_V$ and, more importantly, the maximum P_G, which would cause spalling to occur if high enough. These maximum values of $\bar{\rho}_V$ and P_G decrease abruptly behind the moisture clog because the clog hinders the migration of water vapour, which causes the pressure buildup in front of it and the low $\bar{\rho}_V$ and P_G behind it.

Among the other interesting observations in Figure 5-91 is the smooth increase in T as time elapses, compared to P_G and $\tilde{\rho}_V$, which experience sharp increases at a temperature around 180ºC for all the depths considered due to the moisture clog. It can also be seen that the maximum P_G for each depth occurs just when the moisture clog ends, which is the time at which spalling is most likely to happen. Also, the value of the maximum P_G reached increases as the depth increases. Figure 5-92 shows this value through time from the start of the fire and its corresponding location from the surface exposed to the fire. Theoretically, if P_G increased high enough to cause a stress that exceeds the cracking strength of concrete when combined with the mechanical tensile stress due to loading, spalling will occur. To determine the location of potential spalling, examining Figure 5-92, one can deduce that if spalling were to happen, this will occur at 10 to 30 minutes from the start of fire and at a depth ranging from 7 to 30 mm.

In conclusion, the procedure of coupled heat and moisture transfer analysis implemented in VecTor3 proved to be accurate and stable, and the various phases of water and the phenomena and stages which concrete experiences when subjected to fire were well captured. However, it should be noted that this type of analysis requires a very dense mesh to maintain accuracy and stability, as coarser meshes create unrealistic high pressure gradients between adjacent finite elements, resulting in erroneous results or instability of the analysis.

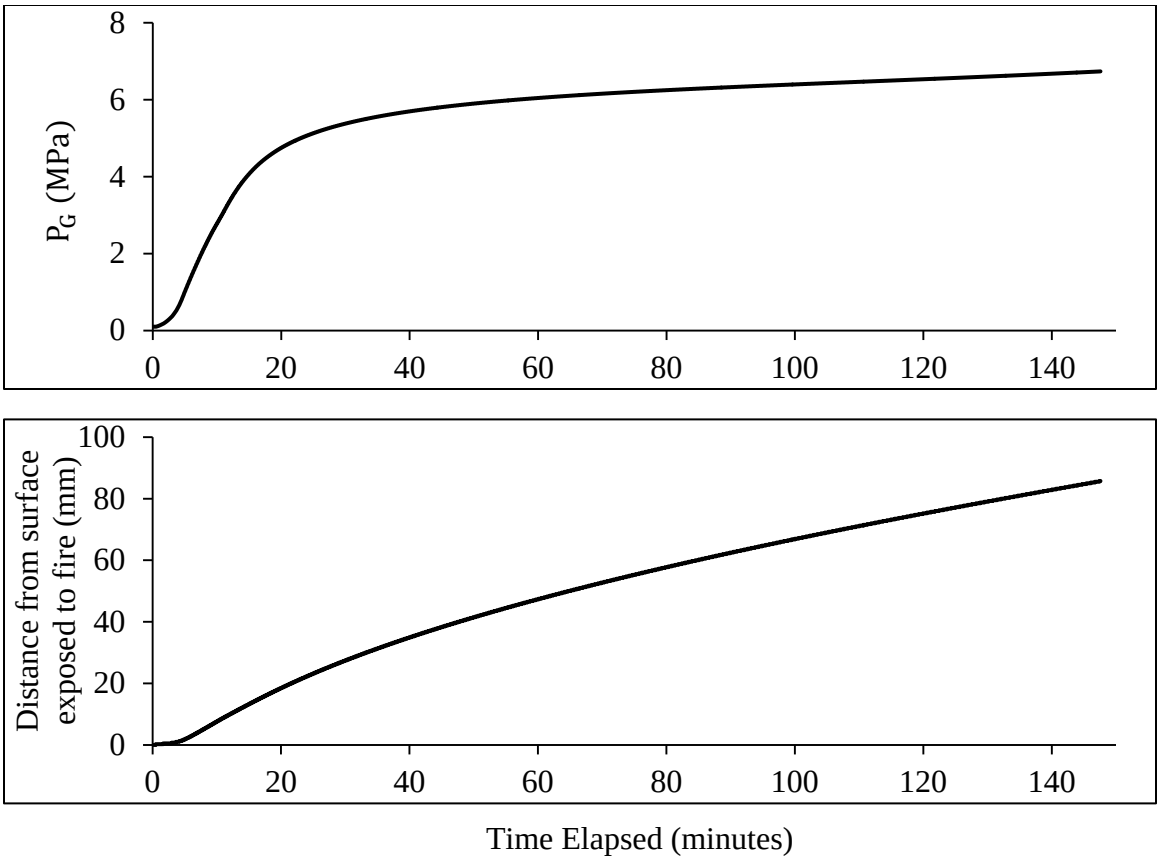

Figure 5-92 Maximum pressure of the gaseous mixture in concrete, P_G, through the time from the start of fire and its corresponding location

Chapter 6
Conclusion

6.1 Summary

The main objective of this study was to develop a structural analysis tool that is capable of modelling the advanced behaviour of concrete, handling a wide range of loading types and conditions, and modelling new material types. For this purpose, VecTor3, a finite element computer program previously developed at the University of Toronto for nonlinear analysis of three-dimensional reinforced concrete structures, was further developed to serve as the proposed tool.

VecTor3 originally employed the Modified Compression Field Theory (MCFT) (Vecchio and Collins, 1986); it was extended to include the more advanced Disturbed Stress Field Model (DSFM) (Vecchio, 2000), where shear slippage occurring on the surfaces of cracks is taken into account. In addition, more advanced material mechanisms for concrete and steel reinforcing bars were implemented in VecTor3, including dowel action and buckling of steel reinforcing bars, strain rate effects for dynamic loading, and the ability to link different nodes in the structure together in specific displacement relations to ensure uniformity of loading and stability of analysis.

The types of dynamic loads that can be handled by VecTor3 were extended to include earthquake ground acceleration spectra as well as impulse loads. Also, steel fibre-reinforced concrete (SFRC) analysis capabilities were added to VecTor3, using the newly developed Simplified Diverse Embedment Model (SDEM) (Lee et al., 2011a, 2011b, 2013a). Accompanying models for tension stiffening (Lee et al., 2013b) and average crack width (Deluce and Vecchio, 2013) of conventionally-reinforced SFRC were also implemented.

New eight-noded isoparametric hexahedral elements that can have arbitrary nodes without any limitations on their orientation with respect to each other were added to VecTor3, allowing for the modelling of a wider range of structures with more

complicated shapes and orientations, as well as accounting for the geometric nonlinearity effects (second-order analysis). Another new element type, the link element, was added for the modelling of the bond slippage between concrete and steel reinforcing bars. These link elements can model typical slippage of smooth and deformed steel reinforcing bars, as well as bonded and unbonded prestressing tendons for the analysis of prestressed concrete.

The new structural analysis capabilities make VecTor3 a more advanced structural analysis tool when added to the pre-existing structural and mechanical models and mechanisms. These mechanisms include compression softening, tension softening, tension stiffening, confinement effects, dilatation of concrete, creep, hysteretic response of both concrete and steel reinforcing bars, and structural damping for dynamic loading cases. However, new more advanced models were added for some of these mechanisms such as the hysteretic model provided by Palermo (2002).

The overall performance of VecTor3, with regards to the size of analytical models accommodated, convergence, stability, and speed of analysis, was significantly enhanced. Also, the amount of data required from the users was significantly reduced through updating the program to automatically determine many of the general properties of the structure. Among these properties are the depths of the different sections in all three directions (required for link elements modelling and for predicting cover splitting failures) and the presence of ties in the different sections to calculate the amount of confinement they provide.

The most significant addition to VecTor3 was the capability to analyze reinforced concrete structures subjected to fire. Two different algorithms were implemented. The first one undertakes heat transfer analysis, calculates the temperatures through the depth of each section, and uses the temperatures to determine thermal expansion strains and reduction factors for the various mechanical properties of concrete and steel reinforcing bars. These strains and updated mechanical properties are then transferred to the structural analysis procedure, where the external loads are also applied to the structure. Structural analysis evaluates the stresses and strains in concrete and steel reinforcing bars

at each time step, using the advanced concrete and steel models and mechanisms previously discussed.

The second algorithm undertakes coupled heat and moisture transfer analysis, which not only calculates the temperatures through the depth of each section as the first algorithm does, but also calculates the vapour pressure in the pores of concrete. As with the heat transfer analysis algorithm, the temperatures are used to determine thermal expansion strains and reduction factors for the various mechanical properties of concrete and steel reinforcing bars.

However, in this latter algorithm, the pore pressure is used to evaluate additional tensile stresses developed within the concrete. These stresses, together with the thermal expansion strains and the updated mechanical properties, are then transferred to the structural analysis procedure where the external loads are also applied to the structure. As with the heat transfer analysis algorithm, structural analysis then evaluates the stresses and strains in concrete and steel reinforcing bars at each time step, using the advanced models and mechanisms previously discussed. This algorithm has the special capability of predicting thermally-induced spalling in reinforced concrete structures subjected to fire, but it is more computationally expensive.

For the thermal and mechanical properties of concrete and steel reinforcing bars and their variation with the rise in temperature, numerous models presented by various studies, codes, and standards were incorporated in VecTor3. A parametric study was undertaken to compare the models presented by the ASCE Manual of Practice (Structural Fire Protection by T. T. Lie, 1992), the former version of the Eurocode (ENV 1992-1-2:1995, 1996), and its current version (EN 1992-1-2:2004, 2005) to each other and to experimental data for both the thermal and mechanical properties and to determine their performance in different fire scenarios.

The thermal properties required to be evaluated for the heat transfer analysis are limited to concrete only as steel reinforcing bars do not make a substantial contribution to the transfer of heat through reinforced concrete sections. These properties include the thermal conductivity, specific heat capacity, density, porosity, and permeability. For the mechanical properties that deteriorate with temperature and need to be evaluated for the

structural analysis, the compressive peak stress (compressive strength), the corresponding strain, the initial modulus of elasticity, and the overall compressive stress-strain constitutive model were investigated for concrete in compression. For concrete in tension, the tensile strength (cracking stress) and the overall tensile stress-strain constitutive model were investigated. The mechanical properties of steel reinforcing bars, represented by the yield and ultimate stresses and Young's modulus, were also investigated. Also, models presented in the literature for post-cooling behaviour of both concrete and steel reinforcing bars were presented. These models were compared to each other, showing their differences.

For the cooling phase of both concrete and steel reinforcing bars, there is a void in the literature in regards to the path that the mechanical properties follow in going from their values at the maximum reached temperature to their values when concrete and steel cool to room temperatures (residual properties). Therefore, for the lack of a better experimentally-proven method, it was assumed in this study that the mechanical properties of concrete and steel vary linearly with temperature moving between the values mentioned above.

One of the mechanisms that have been discussed and investigated in the literature, but neglected in this study, is the deterioration of the bond between concrete and steel reinforcing bars with the rise in temperature. The reason is that this deterioration is primarily attributed to the differential expansion between the two materials as the temperature rises. Since, the different coefficients of thermal expansion were explicitly modelled in this study, it was deemed unnecessary to include separate models for the deterioration of the bond; in fact, it may be erroneous to include them since the mechanism would be accounted for twice.

Also, the capacity to analyze a wider range of loading conditions was extended in VecTor3, where various types of dynamic loading can now be handled including seismic, impact, and blast loading. This is in addition to the pre-existing loading types, including monotonic load-controlled and displacement-controlled loading, support settlement, gravity loads, imposed preset elevated temperatures, concrete prestrains, and ingress pressures.

Finally, an extensive compilation of various analyses that cover a wide range of structural members and loading profiles carried out using VecTor3 was presented, aiming at verifying the models, mechanisms, and algorithms that were incorporated in VecTor3. The study showed generally strong agreement with the experimental results, where capacity, ductility, cracking pattern, failure mode, and resistance time in case of analyses involving fire exposure were all well estimated.

With this extensive development, VecTor3 was transformed into the desired powerful tool that is capable of performing accurate time-stepping structural analyses for almost any type of reinforced concrete structure under most typical and extreme types of loads. The applications for this tool are far-ranging. For example, one can analyze the residual seismic capacity of a structure that was subjected to fire while bearing typical static loads. One can also determine the capacity of a structure that was subjected to fire immediately after the occurrence of an earthquake, which is a commonly occurring incident.

6.2 Results and Findings

This study reached some major results and findings that can be summarized in the following points:

1. Generally, VecTor3 predicts well the response of various reinforced concrete members (two-way slabs, columns, and shear walls), various materials (plain reinforced concrete and conventionally-reinforced and unreinforced steel fibre-reinforced concrete), and various loading conditions (monotonic, cyclic, dynamic, and thermal), confirming the effectiveness of the employed models as well as the sound computer coding and modelling.

2. For all the analyses carried out, VecTor3 provided reasonable estimates of the failure loads (or failure time for thermal loading), ductility, cracking patterns, and failure modes.

3. The Simplified Diverse Embedment Model (SDEM) (Lee et al., 2011a, 2011b, 2013a) was found to accurately model the behaviour of steel fibre-reinforced concrete, together with the newly developed models for tension stiffening behaviour of concrete matrix in conventionally-reinforced SFRC (Lee et al., 2013b) and the average crack width in conventionally-reinforced SFRC (Deluce and Vecchio, 2013).

4. A punching shear failure mode was properly modelled for four specimens of steel fibre-reinforced concrete post-tensioned two-way slabs having no conventional reinforcement, where a mean analytical to experimental ratio of 0.96 was achieved for the peak load, with a coefficient of variation (COV) of 6%. The mid-point displacement at failure had a mean analytical to experimental ratio of 1.01, with a coefficient of variation (COV) of 11%.

5. The hysteretic response of wide-flanged squat shear walls was well modelled, capturing the peak load, post-peak behaviour, ductility, and failure mode. However, one of the analyzed wall models did not fail at the same displacement the specimen failed at in the experiment as it showed localized failure that occurred due to a possible construction defect.

6. Dynamic loading analyses, represented in the analysis of a two-way slab subjected to multiple blast shocks, showed good agreement with the experimental results. The periods and the peak mid-point displacements for the damaged and undamaged slab were well estimated, with a mean analytical to experimental ratio of 1.05 and a coefficient of variation (COV) of 6% for the period and a mean analytical to experimental ratio of 1.09 and a coefficient of variation (COV) of 2% for the peak mid-point displacement of the first cycle.

7. Residual deformations for dynamic loading cases were mostly reasonably estimated by VecTor3, except in the cases where significant damage occurred. This can be attributed to the fact that only the average plastic strains of steel reinforcing bars are considered in the analyses, and not the localized plastic strains of steel reinforcing bars crossing the surfaces of the cracks. This causes the localized plastic strains to be lost as the reinforced concrete member damps out and cracks close; hence, a part of the residual deformations is lost.

8. For heat transfer analysis, while VecTor3 performs the analysis accurately and efficiently, the models provided by the codes and standards for the thermal properties of concrete proved to be generally inadequate. Comparing the models provided by the ASCE Manual of Practice (Structural Fire Protection by T. T. Lie, 1992), the former version of the Eurocode (ENV 1992-1-2:1995, 1996), and its current version (EN 1992-1-2:2004, 2005), the models provided by the lattermost are the ones most capable of estimating accurate temperatures for concrete mixed with either siliceous or calcareous aggregates, given that the actual moisture content at the time of fire exposure is used in the analysis. This applies to the fire development phase and estimating the maximum temperatures reached through the depth of the member subjected to fire. However, for the cooling phase all models fail to estimate the correct temperatures.

9. For heat transfer analysis, the moisture content of concrete plays an important role in the calculation of the temperatures at different depths in the concrete members, due to its direct effect on the specific heat capacity of concrete. Therefore, moisture content of concrete should always be considered as a key part of the heat transfer analysis, as neglecting it will lead to significantly erroneous results.

10. Investigating the effect of the type of aggregate used in the concrete mix on its performance when exposed to fire show that calcareous aggregates are more preferable to siliceous aggregates. The reason is that calcareous aggregates are more chemically stable at higher temperatures; they have lower coefficients of thermal expansion and thermal conductivity. Finally, they experience less strength loss with the increase in temperature. However, some researchers reported that concrete mixed with calcareous aggregates performed poorer than that mixed with siliceous aggregates under tension.

11. The models available in the literature for the thermal and mechanical properties of concrete and steel reinforcing bars are alarmingly inadequate, especially for concrete. Most models provide general formulae for these properties, neglecting their dependence on loading levels, density, moisture content, porosity, permeability, aggregate type, and many other parameters that affect the microstructure of concrete

under elevated temperatures that cause microcracking to occur, hence affecting all its properties.

12. For coupled heat and structural analysis, the procedure followed by VecTor3 shows good stability and convergence, and VecTor3 managed to provide reasonable results for the fire resistance of reinforced concrete columns subjected to three different fire scenarios: exposure to fire under sustained axial loads until failure, exposure to fire under sustained axial loads and lateral displacements due to floor slab expansion until failure, and axial loading to failure after exposure to fire for a specific period of time then cooling in a natural environment.

13. For coupled heat and structural analysis, the comparison between the structural results produced by the models provided for the mechanical properties of concrete and steel by the ASCE Manual of Practice (Structural Fire Protection by T. T. Lie, 1992), the former version of the Eurocode (ENV 1992-1-2:1995, 1996), and its current version (EN 1992-1-2:2004, 2005) showed that the models provided by the lattermost are the ones most capable of accurately estimating the structural response for concrete constructed using either siliceous or calcareous aggregates.

14. The models provided by the ASCE Manual of Practice (Structural Fire Protection by T. T. Lie, 1992) for the mechanical properties of concrete and steel under elevated temperatures consistently led to an overstimulation of the fire resistance of reinforced concrete members, which renders these models unsafe for use in structural design.

15. Geometric nonlinearity effects (second-order analysis) were accurately modelled in VecTor3. Neglecting these effects resulted in a significant overestimation of the lateral capacity of the columns analyzed under concurrent fire and lateral loading.

16. The residual capacity of axially loaded columns after the exposure to fire for a specific period of time then cooling in a natural environment was reasonably well estimated by VecTor3. However, the residual deformation for the specimen that was subjected to fire for a longer period of time (two hours) was significantly underestimated. This is possibly due to the localized plastic strains attained by the steel reinforcing bars crossing the surfaces of the cracks that are not accounted for.

17. The procedure of coupled heat and moisture transfer analysis implemented in VecTor3 proved to be accurate and stable, and the various phases of water and the phenomena and stages which concrete experiences when subjected to fire were well captured.

18. Coupled heat and moisture transfer analyses require a very dense mesh to maintain their accuracy and stability, as coarser meshes create unrealistic high pressure gradient between adjacent finite elements, resulting in erroneous results or instability of the analysis.

6.3 Recommendations for Future Work

The objectives of this study were all achieved to high degree of success. VecTor3 was developed to provide the desired powerful and sophisticated structural analysis capacity. However, the capabilities of VecTor3 are still constrained by a number of issues related to computational limitations and the adequacy of the thermal and mechanicals models available in the literature for concrete and steel at elevated temperatures. These issues are presented in the following points as potential topics for future research having much room for investigation:

1. Extensive experimental programs on the behaviour of reinforced concrete members under elevated temperatures on both the material science and structural levels need to be undertaken to enrich the current sparse literature database.

2. Improved models for the thermal and mechanical properties of concrete and steel reinforcing bars under elevated temperatures need to be developed based on experimental results from more comprehensive experimental programs. As opposed to the existing models that merely consider the effect of the type of aggregate used in the concrete mix, the new models should take into account the numerous parameters that affect the behaviour, including, but not limited to, loading levels, density, moisture content, porosity, and permeability.

3. Due to the wide variation among the various models available in the literature that can be used to estimate the different thermal and mechanical properties of concrete and steel reinforcing bars subjected to fire, it is recommended that sensitivity analyses are undertaken prior to designing a reinforced concrete structure for a specific level of fire resistance. These sensitivity studies aim at estimating the effect of using different models describing each thermal or mechanical property on the global behaviour of the structure being analyzed.

4. The algorithm of the coupled heat and moisture transfer analysis is time costly due to the non-symmetric matrices involved in the solution, which calls for the development of better equation solver to be implemented in VecTor3.

5. Plastic strains occurring at the steel reinforcing bars crossing the surfaces of cracks need to be taken into account in order to achieve a better estimate for residual deformations.

6. Better computational capabilities need to be implemented in order to achieve faster and more efficient analyses. Three-dimensional analyses involve a large number of degrees of freedom in their solution procedure, and thus tend to be computationally expensive.

7. More comprehensive experimental programs need to be undertaken on the behaviour of steel fibre-reinforced concrete subjected to fire in order to develop more powerful models that can simulate the thermal and mechanical properties of this material type.

8. With the success in modelling the response of steel fibre-reinforced concrete using SDEM (Lee et al., 2011a, 2011b, 2013a), test programs need to be undertaken and models need to be developed for other type of materials, such as carbon and glass fibre-reinforced polymers (FRP). The models should be implemented in VecTor3 to provide a more comprehensive tool that is capable of analyzing more types of fibre-reinforced concrete.

9. Additional corroborative studies using VecTor3 need to be undertaken to verify its effectiveness in analyzing conventionally-reinforced and unreinforced steel fibre-reinforced concrete members under cyclic and dynamic loading.

References

Abaqus®, Release 6.12. (2013).

Abrahamsson, L., Haegglund, B., and Janzon, K. (1979). *HSLAB: An Interactive Program for One Dimensional Heat Flow Problems*. National Defence Research Institute of Sweden, Stockholm, Sweden, 47 p.

Abrams, M. S. (1971). Compressive strength of concrete at temperatures to 1600°F. *American Concrete Institute (ACI) Special Publication - SP25 - Temperature and Concrete*, 33-58.

Abrishami, H. H., and Mitchell, D. (1997). Influence of steel fibers on tension stiffening. *American Concrete Institute (ACI) Structural Journal, 94*(6), 769-776.

ACI Committee 216, Guide for Determining the Fire Endurance of Concrete Elements, ACI 216R-89, reapproved 1994. (1989). American Concrete Institute (ACI), Farmington Hills, Michigan.

ACI Committee 221, Guide for Use of Normal Weight Aggregates in Concrete, ACI 221R-96. (1996). American Concrete Institute (ACI), Farmington Hills, Michigan.

ACI Committee 213, Guide for Structural Lightweight-Aggregate Concrete, ACI 213R-03. (2003). American Concrete Institute (ACI), Farmington Hills, Michigan, 38 p.

Anderberg, Y. (1976). *Fire-Exposed Hyperstatic Concrete Structures - An Experimental and Theoretical Study, Bulletin 55*. Division of Structural Mechanics and Concrete Construction, Lund Institute of Technology (now Faculty of Engineering (LTH), Lund University), Lund, Sweden, 186 p.

Anderberg, Y. (1983). *Behaviour of Steel at High Temperatures*: Réunion Internationale des Laboratoires D'essais et de Recherche sur les Matériaux et les Constructions (RILEM), RILEM Technical Committee 44-PHT.

Anderberg, Y., and Thelandersson, S. (1976). *Stress and Deformation Characteristics of Concrete at High Temperatures, 2. Experimental Investigation and Material Behaviour Model, Bulletin 54*. Division of Structural Mechanics and Concrete Construction, Lund Institute of Technology (now Faculty of Engineering (LTH), Lund University), Lund, Sweden, 84 p.

Annerel, E., and Taerwe, L. (2007). *Approaches for the assessment of the residual strength of concrete exposed to fire*. International Workshop "Fire Design of Concrete Structures - From Materials Modelling to Structural Performance", Coimbra, Portugal.

Annerel, E., and Taerwe, L. (2008). *Approaches for the assessment of the residual strength of concrete exposed to fire*. Concrete Repair, Rehabilitation and Retrofitting II, Cape Town, South Africa.

ANSYS®, Release 14.5. (2013).

AS 1530.4—2005, Committee FP-018, Fire Safety, Methods for Fire Tests on Building Materials, Components and Structures - Part 4: Fire-Resistance Test of Elements of Construction. (2005). Standards Australia. Sydney, NSW, 151 p.

ASHRAE Handbook: Fundamentals. (1993). American Society of Heating, Refrigerating and Air-Conditioning Engineers (ASHRAE). Atlanta, GA.

Aslani, F., and Bastami, M. (2011). Constitutive relationships for normal- and high-strength concrete at elevated temperatures. *American Concrete Institute (ACI) Materials Journal, 108*(4), 355-364.

ASTM E119 – 12a, Standard Test Methods for Fire Tests of Building Construction and Materials. (2012). American Society for Testing and Materials (ASTM). West Conshohocken, PA, 34 p.

Balendran, R. V., Nadeem, A., Maqsood, T., and Leung, H. Y. (2003). Flexural and split cylinder strengths of HSC at elevated temperatures. *Fire Technology, 39*(1), 47-61.

Bangi, M. R., and Horiguchi, T. (2012). Effect of fibre type and geometry on maximum pore pressures in fibre-reinforced high strength concrete at elevated temperatures. *Cement and Concrete Research, 42*(2), 459–466.

Barnett, C. R. (2002). BFD curve: a new empirical model for fire compartment temperatures. *Fire Safety Journal, 37*(5), 437-463.

Baroghel-Bouny, V., Mainguy, M., Lassabatere, T., and Coussy, O. (1999). Characterization and identification of equilibrium and transfer moisture properties for ordinary and high-performance cementitious materials. *Cement and Concrete Research, 29*(8), 1225-1238.

Bary, B. (1996). *Etude du couplage hydraulique - mécanique dans le béton endommagé, Publication No. 11*. Laboratoire de Mécanique et Technologie, C.N.R.S. de Cachan, Université de Paris 6, Cachan, France, 156 p.

Bathe, K. J. (1982). *Finite Element Procedures in Engineering Analysis*. Englewood Cliffs, NJ: Prentice Hall.

Bauschinger, J. (1886). Über die veränderung der elastizitätsgrenze und der festigkeit des eisens und stahl durch strecken und quetschen, durch erwärmen und abkühlen und durch oftmal wiederholte beanspruchung. *Mittheilungen aus dem Mechanisch-Technischen Laboratorium der Königlichen Technischen Hochschule in München, 13*, 1-116.

Bažant, Z. P. (1997). *Analysis of Pore Pressure, Thermal Stress and Fracture in Rapidly Heated Concrete*. International Workshop on Fire Performance of High-Strength Concrete, NIST Special Publication No. 919, National Institute of Standards and Technology, Gaithersburg, MD.

Bažant, Z. P., and Chern, J. C. (1987). Stress-induced thermal and shrinkage strains in concrete. *Journal of Engineering Mechanics - American Society of Civil Engineers (ASCE), 113*(10), 1493-1511.

Bažant, Z. P., and Kaplan, M. F. (1996). *Concrete at High Temperatures: Material Properties and Mathematical Models*. Harlow: Longman.

Bažant, Z. P., and Thonguthai, W. (1978). Pore pressure and drying of concrete at high temperature. *Journal of the Engineering Mechanics Division, American Society of Civil Engineers (ASCE), 104*(5), 1059-1079.

Bentz, E. C. (2000). *Sectional Analysis of Reinforced Concrete Structures.* PhD Thesis, University of Toronto, Toronto, 184 p.

Bernoulli, J. (1692). Quadratura curvae, e cujus evolutione describitur inflexae laminae curvatura. *Die Werke von Jakob Bernoulli, Med. CLXX; L Ia 3, p. 211–212*.

Bilodeau, A., Malhotra, V. M., and Hoff, G. C. (1998). *Hydrocarbon fire resistance of high strength normal weight and light weight concrete incorporating polypropylene fibres*. International Symposium on High Performance and Reactive Powder Concretes, Sherbrooke, QC.

Biolzi, L., Cattaneo, S., and Rosati, G. P. (2008). Evaluating residual properties of thermally damaged concrete. *Cement and Concrete Composites, 30*(10), 907-916.

Birch, A. F., and Clark, H. (1940). The thermal conductivity of rocks and its dependence upon temperature and composition. *American Journal of Science, 238*(8), 529-558.

Blagojević, M. Dj., and Pešić, D. J. (2011). A new curve for temperature-time relationship in compartment fire. *Thermal Science, 15*(2), 339-352.

Bonnell, D. G. R. , and Harper, F. C. (1950). The Thermal Expansion of Concrete. *Journal of the ICE (Institution of Civil Engineers), 33*(4), 320-330.

Breitenbucker, R. (1996). *High strength concrete C105 with increased fire resistance due to polypropylene fibers*. Fourth International Symposium on the Utilization of High Strength/High Performance Concrete, Paris, France.

Bresler, B., Thielen, G., Nizamuddin, Z., and Iding, R. (1976). *Limit State Behavior of Reinforced Concrete Frames in Fire Environments*. Conference on Tall Buildings, Hong Kong.

Brockenbrough, R. L. (1970). Theoretical stresses and strains from heat curving. *Journal of the Structural Division - American Society of Civil Engineers (ASCE), 96*(7), 1421-1444.

BS 8110-2:1985 - Structural Use of Concrete — Part 2: Code of Practice for Special Circumstances. (1985). British Standards Institution (BSI). London, UK, 68 p.

BS 476-20:1987, Technical Committee FSM/1 (Fire Standards Committee), Fire Tests on Building Materials and Structures. Part 20: Method for Determination of the Fire Resistance of Elements of Construction (General Principles). (1987). British Standards Institution (BSI). London, UK, 42 p.

BS 5950-8:1990 - Structural Use of Steelwork in Building - Part 8: Code of Practice for Fire Resistant Design. (1990). British Standards Institution (BSI). London, UK, 26 p.

Campbell-Allen, D., and Desai, P. M. (1967). The influence of aggregate on the behaviour of concrete at elevated temperatures. *Nuclear Engineering and Design, 6*(1), 65-77.

CAN/ULC S101-07, Standard Methods of Fire Endurance Tests of Building Construction and Materials. (2007). Underwriters Laboratories of Canada. Toronto, ON, 85 p.

Carette, G. G., Painter, K. E., and Malhotra, V. M. (1982). Sustained high temperature effect on concretes made With normal portland cement, normal portland cement and slag, or normal portland cement and fly ash. *Concrete International, 4*(7), 16.

Carreira, D. J., and Chu, K. D. (1985). Stress-strain relationship for plain concrete in compression. *American Concrete Institute (ACI) Journal Proceedings, 82*(6), 797-804.

Cather, B. (2003). *Chapter 10: Concrete and fire exposure. In Advanced Concrete Technology: Concrete Properties* (Vol. 2). Oxford, UK: Butterworth-Heinemann.

CEB-FIP Model Code for Concrete Structures - Buletin D'Information No. 124/125. (1978). Comité Euro-International du Béton - Fédération Internationale De La Précontrainte (CEB-FIP), Lausanne, Switzerland, 348 p.

CEB-FIP Model Code 1990 - Buletin D'Information No. 213/214. (1993). Comité Euro-International du Béton - Fédération Internationale De La Précontrainte (CEB-FIP), Lausanne, Switzerland, 460 p.

CEB-FIP Working Party 4.3-1, Fire Design of Concrete Structures: Materials, Structures and Modelling: State-of-art Report, Bulletin 38. (2007). Fédération Internationale du Béton (fib), Comité Euro-International du Béton - Fédération Internationale De La Précontrainte (CEB-FIP), Lausanne, Switzerland. 97 p.

CEB-FIP Task Group 4.3, Fire Design of Concrete Structures - Structural Behaviour and Assessment: State-of-art Report, Bulletin 46. (2008). Fédération Internationale du

Béton (fib), Comité Euro-International du Béton - Fédération Internationale De La Précontrainte (CEB-FIP), Lausanne, Switzerland. 209 p.

CEB1988, Concrete Structures under Impact and Impulsive Loading, Bulletin D'Information No. 187. (1988). Comité Euro-International du Béton, Lausanne, Switzerland. 184 p.

Çengel, Y. A. (1998). *Heat Transfer: A Practical Approach*. New York, NY: McGraw-Hill.

Centre Technique Industriel de la Construction Métallique (CTICM , Saint-Aubin, France), Méthode de Prévision par le Calcul du Comportement au Feu des Structures en Acier, Construction Métallique, No. 3. (1982).

Chan, Y. N., Peng, G. F., and Anson, M. (1999). Residual strength and pore structure of high-strength concrete and normal strength concrete after exposure to high temperatures. *Cement and Concrete Composites, 21*(1), 23-27.

Chang, C. H., and Jau, W.-C. (2001). *Study of Fired Concrete Strengthened with Confinement.* M.Sc. Thesis, National Chiao Tung University, Hsinchu, Taiwan.

Chang, Y. F., Chen, Y. H., Sheu, M. S., and Yao, G. C. (2006). Residual stress–strain relationship for concrete after exposure to high temperatures. *Cement and Concrete Research, 36*(10), 1999-2005.

Chapman, D. A. (1976). *A study of the movement of Moisture in and from Concrete at Elevated and Non-uniform Temperatures.* PhD Thesis, King's College London (University of London), London, UK, 930 p.

Chapman, D. A., and England, G. L. (1977). *Effects of moisture migration on shrinkage, pore pressure and other concrete properties (Paper H5/3)*. the Fourth International Conference on Structural Mechanics in Reactor Technology (SMiRT 4), San Francisco, CA.

Cheng, F.-P., Kodur, V. K. R., and Wang, T.-C. (2004). Stress-strain curves for high strength concrete at elevated temperatures. *Journal of Materials in Civil Engineering, 16*(1), 84-90.

Cheung, F. B., and Baker, J. (1976). *Transient Dehydration Model for Concrete*. Reactor Analysis and Safety Division, Argonne National Laboratory, Lemont, IL.

Chiaia, B., Fantilli, A., and Vallini, P. (2009). Evaluation of crack width in FRC structures and application to tunnel linings. *Materials and Structures, 42*(3), 339-351.

Chilton, T. H., and Colburn, A. P. (1934). Mass transfer (absorption) coefficients prediction from data on heat transfer and fluid friction. *Industrial & Engineering Chemistry, 26*(11), 1183-1187.

Chowdhury, S. H., and Loo, Y.-C. (2001). A new formula for prediction of crack widths in reinforced and partially prestressed concrete beams. *Advances in Structural Engineering, 4*(2), 101-110.

Clark, A. P. (1956). Cracking in reinforced concrete flexural members. *American Concrete Institute (ACI) Journal Proceedings, 52*(4), 851-862.

Clayton, N., and Lennon, T. (2000). *Effect of Polypropylene Fibres on High Grade Concrete*. Watford, UK: Building Research Establishment (BRE).

Collet, Y., and Tavernier, E. (1976). *Etude des Propriétés du Béton Soumis à des Températures Élevées*. Groupe de Travail, Comportement du Matériau Béton en Fonction de la Température, Brussels, Belgium, 32 p.

Collins, M. P., and Mitchell, D. (1987). *Prestressed Concrete Basics*: Canadian Prestressed Concrete Institute.

Collins, M. P., and Porasz, A. (1989). Shear design for high strength concrete. *Bulletin d'Information No. 193 - Design Aspects of High Strength Concrete, Comité Euro-International du Béton (CEB),* 75-83.

Concrete Manual, 7th Ed. (1963). U.S. Bureau of Reclamation. Denver, CO.

Connolly, R. J. (1995). *The Spalling of Concrete in Fires.* PhD Thesis, Aston University, Birmingham, UK, 294 p.

Copier, W. J. (1983). The spalling of normal weight and lightweight concrete exposed to fire. *American Concrete Institute (ACI) Special Publication - SP80 - Fire Safety of Concrete Structures*, 219-236.

Copier, W.J. (1979). The Spalling of Normalweight and Lightweight Concrete on Exposure to Fire. *Heron, 24*(2), 1-92.

Coulomb, C. A. (1776). Essai sur une application des régles de maximis et minimis à quelques problèmes de statique, relatifs à l'architecture. *Mémoires de Mathématique et de Physique, présentés à l'Académie Royale des Sciences, par divers savans, et lûs dans ses assemblée, 7*, 343-382.

Crisfield, A. (1991). *Non-linear Finite Element Analysis of Solids and Structures: Essentials*. West Sussex, England: John Wiley & Sons.

Crook, R. N. (1980). *The Elevated Temperature Properties of Reinforced Concrete.* PhD Thesis, University of Aston in Birmingham, Birmingham, UK, 218 p.

Cross, H. C., McMaster, R. C., Simmons, W. F ., and Van Echo, J. A. (1948). *Short Time, High Temperature Properties of Heat-Resisting Alloy Sheet - Report RA-15077*. Project Rand (United States Air Force (USAF) Project MX-791) - Douglas Aircraft Company, Inc., Santa Monica, CA, 91 p.

CSA23.3-04 Design of Concrete Structures. (2004). Mississauga, Canada, 214 p.

Custer, R. L. P., and Meacham, B. J. (2000). *SFPE Engineering Guide to Performance-Based Fire Protection Analysis and Design of Buildings*. National Fire Protection Association, Society of Fire Protection Engineers, Bethesda, MD, 260 p.

Darcy, H. (1856). *Les Fontaines Publiques de la Ville de Dijon. Exposition et Application des Principes à Suivre et des Formules à Employer dans les Questions de Distribution D'eau*. Paris, France: Dalmont.

Davie, C. T., Pearce, C. J., and Bicanic, N. (2006). Coupled heat and moisture transport in concrete at elevated temperatures - effects of capillary pressure and adsorbed water. *Numerical Heat Transfer Part A: Applications, 49*(8), 733-763.

Deluce, J. R. (2011). *Cracking Behaviour of Steel Fibre Reinforced Concrete Containing Conventional Steel Reinforcement.* M.A.Sc. Thesis, University of Toronto, Toronto, Ontario, 469 p.

Deluce, J. R., Lee, S.C., and Vecchio, F. J. (expected 2013). Crack model for SFRC members containing conventional reinforcement. *American Concrete Institute (ACI) Structural Journal (accepted for publication).*

Deluce, J. R., and Vecchio, F. J. (2013). Cracking behavior of steel fiber-reinforced concrete members containing conventional reinforcement. *American Concrete Institute (ACI) Structural Journal, 110*(3), 481-490.

Dhakal, R. P., and Maekawa, K. (2002). Modeling for postyield buckling of reinforcement. *Journal of Structural Engineering - American Society of Civil Engineers (ASCE), 128*(9), 1139-1147.

Diederichs, U. (1987). *Modelle zur Beschreibung der Betonverformung bei Instationären Temperaturen*. "Bauwerke unter Brandeinwirkung" Conference : 19th-20th March 1987, Braunschweig, Germany.

Diederichs, U., Jumppanen, U. M., and Schneider, U. (1995). *High temperature properties and spalling behavior of high-strength concrete*. The Fourth Weimar Workshop on High-Strength Concrete: Material Properties and Design, Weimar, Germany.

Dorn, J. E. (1954). Some fundamental experiments on high temperature creep. *Journal of the Mechanics and Physics of Solids, 3*(2), 85-116.

Dounas, S., and Golrang, B. (1982). *Ståls Mekaniska Egenskaper vid Höga Temperaturer*. Division of Building Fire and Safety, Lund Institute of Technology (now Faculty of Engineering (LTH), Lund University), Lund, Sweden.

Dulacska, H. (1972). Dowel action of reinforcement crossing cracks in concrete. *American Concrete Institute (ACI) Journal Proceedings, 69*(12), 754-757.

Dupont, D., and Vandewalle, L. (2003). *Calculation of crack widths with the σ-ε method*. International RILEM Workshop on Test and Design Methods for Steel Fibre Reinforced Concrete - Background and Experiences, Bochum, Germany.

Dwaikat, M. B., and Kodur, V. K. R. (2009). Hydrothermal model for predicting fire-induced spalling in concrete structural systems. *Fire Safety Journal, 44*(3), 425-434.

Dwaikat, M. B., and Kodur, V. K. R. (2010). Fire induced spalling in high strength concrete beams. *Fire Technology, 46*(1), 251-274.

Edwards, W. T., and Gamble, W. L. (1986). Strength of grade 60 reinforcing bars after exposure to fire temperatures. *Concrete International, 8*(10), 17-19.

Eligehausen, R., Popov, E. P., and Bertero, V. V. (1983). *Local bond stress-slip relationships of deformed bars under generalized excitations: Experimental results and analytical model*. Earthquake Engineering Research Center, University of California, Berkeley., 169 p.

EN 1991-1-2:1992 - Eurocode 1: Actions on Structures - Part 1-2: General Actions - Actions on Structures Exposed to Fire. (1993). European Committee for Standardization (CEN), Brussels, Belgium, 59 p.

EN 1992-1-2:2004 - Eurocode 2: Design of Concrete Structures - Part 1-2: General Rules. Structural Fire Design. (2005). European Committee for Standardization (CEN), Brussels, Belgium, 97 p.

England, G. L., and Khoylou, N. (1995). Moisture flow in concrete under steady state non-uniform temperature states: experimental observations and theoretical modelling. *Nuclear Engineering and Design, 156*(1-2), 83-107.

England, G. L., and Ross, A. D. (1972). Shrinkage, moisture, and pore pressures in heated concrete. *American Concrete Institute (ACI) Special Publication - SP34 - Concrete for Nuclear Reactors*, 883-907.

ENV 1992-1-1:1992 - Eurocode 2: Design of Concrete Structures - Part 1-1: General Rules for Buildings. (1992). European Committee for Standardization (CEN), Brussels, Belgium, 274 p.

ENV 1992-1-2:1996 - Eurocode 2: Design of Concrete Structures - Part 1-2: General Rules. Structural Fire Design. (1996). European Committee for Standardization (CEN), Brussels, Belgium, 63 p.

European Convention for Constructional Steelwork (ECCS, Brussels, Belgium) – Technical Committee 3 – Fire Safey of Steel Structures, European Recommendations for the Fire Safety of Steel Structures - Calculation of the Fire Resistance of Load Bearing Elements and Structural Assemblies Exposed to the Standard Fire. (1983). Amsterdam, Netherlands. Elsevier, 106 p.

Fahmi, H. M., Polivka, M., and Bresler, B. (1972). Effects of sustained and cyclic elevated temperature on creep of concrete. *Cement and Concrete Research, 2*(5), 591-606.

Faiyadh, F. I., and Al-Ausi, M. A. (1989). Effect of elevated temperature on splitting tensile strength of fibre concrete. *International Journal of Cement Composites and Lightweight Concrete, 11*(3), 175-178.

Fares, H., Noumowé, A., and Remond, S. (2009). Self-consolidating concrete subjected to high temperature: Mechanical and physicochemical properties. *Cement and Concrete Research, 39*(12), 1230-1238.

Felicetti, R., Gambarova, P. G., and Meda, A. (2009). Residual behavior of steel rebars and R/C sections after a fire. *Construction and Building Materials, 23*(12), 3546-3555.

Felicetti, R., Gambarova, P. G., Rosati, G. P., Corsi, F., and Giannuzzi, G. (1996). *Residual mechanical properties of high-strength concretes subjected to high temperature cycles*. Fourth International Symposium on Utilization of High-Strength/High-Performance Concrete, Paris, France.

fib Model Code 2010 - Final Draft, Bulletin No. 66. (2012). Fédération Internationale du Béton (fib), Lausanne, Switzerland. 370 p.

Fick, A. (1855). Ueber Diffusion. *Annalen der Physik, 170*(1), 59-86.

Fischer, R. (1970). *Über das Verhalten von Zementmörtel und Beton bei höheren Temperaturen, Heft 214 (On the Behaviour of Cement Mortar and Concrete at high Temperatures, Nr. 214)*. Deutscher Ausschuss für Stahlbeton (German Committee for Reinforced Concrete), Berlin, Germany, 74 p.

Forsyth, P. A., and Simpson, R. B. (1991). A two-phase, two-component model for natural convection in a porous medium. *International Journal for Numerical Methods in Fluids, 12*(7), 665-682.

Fourier, J. B. J. (1822). *Théorie Analytique de la Chaleur*. Paris: Chez Firmin Didot, père et fils.

Franssen, J.-M. (2003). *SAFIR. A thermal/structural program modelling structures under fire*. North American Steel Construction Conference (NASCC), American Institute of Steel Construction (AISC), Baltimore, MD.

Franssen, J.-M. (2005). *Functionalities of the Software SAFIR*. Mécanique des Matériaux & Structures, Génie Civil et Géologie, Faculté des Sciences Appliquées, University of Liège, Liège, Belgium, 3 p.

Franssen, J.-M. (2011a). *User's Manual for SAFIR 2011 - A Computer Program For Analysis Of Structures Submitted To The Fire* Mécanique des Matériaux &

Structures, Génie Civil et Géologie, Faculté des Sciences Appliquées, University of Liège, Liège, Belgium, 57 p.

Franssen, J.-M. (2011b). *SAFIR: Users Manual Version 2011.a.0*. Mécanique des Matériaux & Structures, Génie Civil et Géologie, Faculté des Sciences Appliquées, University of Liège, Liège, Belgium, 70 p.

Frosch, R. J. (1999). Another look at cracking and crack control in reinforced concrete. *American Concrete Institute (ACI) Structural Journal, 96*(3), 437-442.

Furumura, F. (1966). The stress-strain curve of concrete at high temperatures: No. 1 (In Japanese). *Paper No. 7004 for the Annual Meeting of the Architectural Institute of Japan, 41*, 686-686.

Furumura, F. (1970). Studies On the Stress-Strain Relationship in Compression of Concrete at High Temperatures (No. 2). *Transactions of the Architectural Institute of Japan, 173*, 17-24.

Furumura, F., Abe, T., and Shinohara, Y. (1995). *Mechanical properties of high strength concrete at high temperatures*. Fourth Weimar Workshop on High Peiformance Concrete: Material Properties and Design, Hochschule für Architektur und Bauwesen (HAB), Weimar, Germany.

Gajda, J., VanGeem, M. G., and Dombrowski, K. (1997). Thermal properties of commercially available high-strength concretes. *Journal of Cement, Concrete and Aggregates (CCA), 19*(1), 38-54.

Galek, A., Moser, H., Ring, T., Zeiml, M., and Eberhardsteiner, J. (2010). Mechanical and transport properties of concrete at high temperatures. *Applied Mechanics and Materials, 24-25*, 1-11.

Galerkin, B. G. (1915). Rods and plates. Series occurring in various questions concerning the elastic equilibrium of rods and plates (in Russian). *Engineers Bulletin (Vestnik Inzhenerov), 19*, 897-908.

Gan, Y. (2000). *Bond Stress and Slip Modeling in Nonlinear Finite Element Analysis of Reinforced Concrete Structures.* M.A.Sc. Thesis, University of Toronto, 251 p.

Gary, M. (1916). *Fire tests on reinforced concrete buildings (in German)*, Germany.

Gauss, C. F. (1814). Methodus nova integralium valores per approximationem inveniendi. *Societati Regiae Scientarum Exhibita*, 40.

Gawin, D., Majorana, C. E., and Schrefler, B. A. (1999). Numerical analysis of hygro-thermal behaviour and damage of concrete at high temperature. *Mechanics of Cohesive-frictional Materials, 4*(1), 37-74.

Gawin, D., Pesavento, F., and Schrefler, B. A. (2002). Simulation of damage–permeability coupling in hygro-thermo-mechanical analysis of concrete at high

temperature. *Communications in Numerical Methods in Engineering, 18*(2), 113-119.

Gergely, P., and Lutz, L. A. (1968). Maximum crack width in reinforced concrete flexural members. *Causes, Mechanism, and Control of Cracking in Concrete, SP-20, American Concrete Institute*, 87-117.

Gernay, T., and Franssen, J.-M. (2011). *A comparison between explicit and implicit modelling of transient creep strain in concrete uniaxial constitutive relationships*. Fire and Materials 2011 Conference, London, UK.

Griffith, J. H. (1936). *Thermal Expansion of Typical American Rocks, Bulletin 128, Iowa Engineering Experiment Station*: Iowa State College of Agriculture and Mechanic Arts.

Grün, R., and Beckmann, H. (1930). The behaviour of cement, aggregates and concrete at high temperatures. *Mitteilungen aus dem Forschungs-Institut der Hüttenzement-Industrie, Nr. 108 (Proceedings of the Research Institute of Industrial blast-furnace cement, No. 108), from Cement and Cement Manufacture*, 35 p.

Guo, J., and Waldron, P. (2000). Deterioration of PCPV concrete. *Nuclear Engineering and Design, 198*(3), 211-226.

Haddad, R. H., Al-Saleh, R. J., and Al-Akhras, N. M. (2008). Effect of elevated temperature on bond between steel reinforcement and fiber reinforced concrete. *Fire Safety Journal, 43*(5), 334-343.

Hansen, A. S., and Davies, D. (1990). Fibres et Matiere Contenant ces Fibres. World Intellectual Property Organization Patent No. WO/1990/006902. Danaklon A/S.

Hansen, T. C., and Eriksson, L. (1966). Temperature change effect on behavior of cement paste, mortar, and concrete under load. *American Concrete Institute (ACI) Journal Proceedings, 63*(4), 489-504.

Harada, T., Takeda, T., Yamane, S., and Furumura, F. (1972). Strength, elasticity and thermal properties of concrete subjected to elevated temperatures. *American Concrete Institute (ACI) Special Publication - SP34 - Concrete for Nuclear Reactors*, 377-406.

Harajli, M.H., and Mukaddam, M.A. (1988). Slip of steel bars in concrete joints under cyclic loading. *Journal of Structural Engineering - American Society of Civil Engineers (ASCE), 114*(9), 2017-2035.

Harmathy, T. Z. (1965). Effect of moisture on the fire endurance of building materials. *American Society for Testing and Materials (ASTM) Special Technical Publication - STP385 - Moisture in Materials in Relation to Fire Tests*, 74–95.

Harmathy, T. Z. (1967). A comprehensive creep model. *Journal of basic engineering, American Society of Mechanical Engineers (ASME), 89*(3), 496-502.

Harmathy, T. Z. (1970). Thermal properties of concrete at elevated temperatures. *American Society for Testing and Materials (ASTM) Journal of Materials, 5*(1), 47–74.

Harmathy, T. Z. (1983). *Properties of Building Materials at Elevated Temperatures*. DBR Paper No. 1080, Division of Building Research, National Research Council of Canada (NRC), Ottawa, ON, 74 p.

Harmathy, T. Z., and Allen, L. W. (1973). Thermal properties of selected masonry unit concretes. *American Concrete Institute (ACI) Journal Proceedings, 70*(2), 132-142.

Harmathy, T. Z., and Berndt, J. E. (1966). Hydrated Portland Cement and Lightweight Concrete at Elevated Temperatures. *American Concrete Institute (ACI) Journal Proceedings, 63*(1), 93-112.

Harmathy, T. Z., and Stanzak, W. W. (1970). Elevated-temperature tensile and creep properties of some structural and prestressing steels. *American Society for Testing and Materials (ASTM) Special Technical Publication - STP464 - Fire Test Performance*, 186-208.

Heikal, M. (2008). Effect of elevated temperature on the physico-mechanical and microstructural properties of blended cement pastes. *Building Research Journal, 56*(2), 157-172.

Hertz, K. D. (1980). *Betonkonstruktioners brandtekniske egenskaber (Fire properties of concrete constructions) - Part 1 - BYG Rapport No. R-141*. PhD Thesis, Technical University of Denmark (DTU), Lyngby, Denmark, 174 p.

Hertz, K. D. (1984). *Heat Induced Explosion of Dense Concretes (Report No. 166)*. Institute of Building Design, Technical University of Denmark, Lyngby, Denmark, 20 p.

Hertz, K. D. (1991). *Danish investigations on silica fume concretes at elevated temperatures*. Concrete in the 21st Century, American Concrete Institute (ACI), Boston, MA.

Hertz, K. D. (1992). Danish investigations on silica fume concretes at elevated temperatures. *American Concrete Institute (ACI) Materials Journal, 89*(4), 345-347.

Hertz, K. D. (2003). Limits of spalling of fire-exposed concrete. *Fire Safety Journal, 38*(2), 103–116.

Hertz, K. D. (2005). Concrete strength for fire safety design. *Magazine of Concrete Research, 57*(8), 445–453.

Hetényi, M. (1946). *Beams on Elastic Foundation: Theory with Applications in the Fields of Civil and Mechanical Engineering*. Ann Arbor, Michigan: University of Michigan Press.

Hildenbrand, G., Peeks, M., Skokan, A., and Reimann, M. (1978). *Untersuchung der Wechselwirkung von Kernschmelze und Reaktorbeton. Abschlußbericht des Förderungvorhabens BMFT RS 154*. KWU, Erlangen, Germany, 10 p.

Hognestad, E. (1951). *A Study of Combined Bending and Axial Load in Reinforced Concrete Members*. University of Illinois, Engineering Experiment Station, Urbana, USA, 128 p.

Høj, N.P., Wageneder, J., Fellinger, J. H. H., Foit, W., Hejny, H., Breunese, A. J., Brekelmans, J. W. P. M., Schwenzfeier, A., and Feron, C. (2008). *Critical Structural and Functional Components - Work Package 4: Fire Effects and Tunnel Performance: System Structural Response*. UPTUN (UPgrading Methods for Fire Safety in existing TUNnels), Delft, Netherlands, 43 p.

Holmes, M. A., Cook, R. D., and Crtok, G. M. (1982). The effect of elevated temperatures on the strength properties of reinforcing and prestressing steels. *Structural Engineer, Part B, 60*(1), 7-13.

Hordijk, D. A. (1991). *Local Approach to Fatigue of Concrete*. PhD Thesis, Delft University of Technology, Delft, 210 p.

Hoshikuma, J., Kawashima, K., Nagaya, K., and Taylor, A.W. (1997). Stress-strain model for confined reinforced concrete in bridge piers. *Journal of Structural Engineering - American Society of Civil Engineers (ASCE), 123*(5), 624-633.

Huang, H. C., and Usmani, A. S. (1994). *Finite Element Analysis for Heat Transfer: Theory and Software* (1 ed.): Finite Element Analysis for Heat Transfer: Theory and Software.

Huang, Z., and Tan, K. (2003). Analytical Fire Resistance of Axially Restrained Steel Columns. *Journal of Structural Engineering, 129*(11), 1531-1537.

Huebner, K. H., Dewhirst, D. L., Smith, D. E., and Byrom, T. G. (2001). *The Finite Element Method for Engineers* (4 ed.). Hoboken, NJ: John Wiley & Sons.

Hult, J. A. H. (1966). *Creep in Engineering Structures*. Waltham, MA: Blaisdell Publishing Company.

Hundt, J. (1976). Wärme- und feuchtigkeitsleitung in beton unter einwirkung eines temperaturgefälles. *Deutscher Ausschuss für Stahlbeton (DAfStB) (German Committee for Structural Concrete), 256*.

Iding, R., Bresler, B., and Nizamuddin, Z. (1996). *FIRES-T3: A Computer Program for the Fire Response of Structure-Thermal (Three-Dimensional Version), NIST GCR*

95-682; UCB FRG 77-15. Building and Fire Research Laboratory, National Institute of Standards and Technology (NIST), Gaithersburg, Maryland, 178 p.

Illston, J. M., and Sanders, P. D. (1973). The effect of temperature change upon the creep of mortar under torsional loading. *Magazine of Concrete Research, 25*(84), 136-144.

Incropera, F. P., and DeWitt, D. P. (1990). *Fundamentals of Heat and Mass Transfer* (3rd ed.). Hoboken, NJ: John Wiley & Sons.

InfoGraph. (2013). *InfoCad 13: User Manual*. InfoGraph: Ingenieurgesellschaft für graphisch unterstützte Datenverarbeitung GmbH, Aachen, Germany, 814 p.

ISO 834-1:1999, Fire-Resistance Tests - lements of Building Construction - Part 1: General Requirements. (1999). International Organization for Standardization (ISO). Geneva, Switzerland, 25 p.

Izumo, J., Shin, H., Maekawa, K., and Okarnura, H. (1991). *An analytical model for RC panels subjected to in-plane stresses*. Concrete Shear in Earthquake, University of Houston, Texas, USA.

Jacques, E. (2011). *Blast Retrofit of Reinforced Concrete Walls and Slabs.* M.A.Sc. Thesis, University of Ottawa, Ottawa, ON, 196 p.

Kalifa, P., Chene, G., and Galle, C. (2001). High-temperature behaviour of HPC with polypropylene fibres: From spalling to microstructure. *Cement and Concrete Research, 31*(10), 1487–1499.

Kent, D. C., and Park, R. (1971). Flexural members with confined concrete. *Journal of the Structural Division - American Society of Civil Engineers (ASCE), 97*(7), 1969–1990.

Khoury, G. A. (1983). *Transient Thermal Creep of Nuclear Reactor Pressure Vessel Type Concretes.* PhD Thesis, University of London, London, UK, Vol. 1: 1126 p., Vol. 2: 418 p., Vol. 3: 895 p.

Khoury, G. A. (2000). Effect of fire on concrete and concrete structures. *Progress in Structural Engineering and Materials, 2*(4), 429-447.

Khoury, G. A. (2008). Passive fire protection of concrete structures. *Proceedings of the Institution of Civil Engineers (ICE) - Structures and Buildings, 161*(SB3), 135-145.

Khoury, G. A., and Anderberg, Y. (2000). *Concrete Spalling Review*. Fire Safety Design AB, Malmö, Sweden, 60 p.

Khoury, G. A., Grainger, B. N., and Sulivan, G. P. E. (1985a). Transient thermal strain of concrete: literature review, conditions within specimen and behaviour of individual constituents. *Magazine of Concrete Research, 37*(132), 131-144.

Khoury, G. A., Grainger, B. N., and Sulivan, G. P. E. (1985b). Strain of concrete during first heating to 600°C under load. *Magazine of Concrete Research, 37*(133), 195-215.

Khoury, G. A., Majorana, C. E., Pesavento, F., and Schrefler, B. A. . (2002). Modelling of heated concrete. *Magazine of Concrete Research, 54*(2), 77-101.

Kluge, R. W., Sparks, M. M., and Tuma, E. C. (1949). Lightweight aggregate concrete. *American Concrete Institute (ACI) Journal Proceedings, 45*(5), 625-642.

Kodur, V. K. R. (1999). Fibre-reinforced concrete for enhancing the structural fire resistance of columns. *American Concrete Institute (ACI) Special Publication - SP182 - Fibre-Structural Applications of Fibre-Reinforced Concrete*, 215-234.

Kodur, V. K. R., and Khaliq, W. (2011). Effect of Temperature on Thermal Properties of Different Types of High-Strength Concrete. *Journal of Materials in Civil Engineering, 23*(6), 793-801.

Kodur, V. K. R., and Sultan, M. A. (1998). *Structural behaviour of high strength concrete columns exposed to fire*. International Symposium on High Performance and Reactive Powder Concrete, Sherbrooke, Quebec.

Kodur, V. K. R., and Sultan, M. A. (2003). Effect of Temperature on Thermal Properties of High-Strength Concrete. *Journal of Materials in Civil Engineering, 15*(2), 101-107.

Kodur, V. K. R., Wang, T.-C., and Cheng, F.-P. (2004). Predicting the fire resistance behaviour of high strength concrete columns. *Cement & Concrete Composites, 26*(2), 141–153.

Kollegger, J., and Mehlhorn, G. (1990). *Experimentelle Untersuchungen zur Bestimmung der Druckfestigkeit des gerissenen Stahlbetons bei einer Querzugbeanspruchung*. Deutscher Ausschuss Für Stahlbeton, Berlin, Germany, 132 p.

Komonen, J., and Penttala, V. (2003). Effects of High Temperature on the Pore Structure and Strength of Plain and Polypropylene Fiber Reinforced Cement Pastes. *Fire Technology, 39*(1), 23-34.

Kopp, H. (1864). Ueber die spezifische wärme der starren körper (About the the specific heat of the rigid body). *Annalen der Chemie und Pharmacie, Supplementband III - Drittes Heft (Annals of Chemistry and Pharmacy, Supplement 3(3))*, 289-342.

Kupfer, H., Hilsdorf, H.K., and Rusch, H. (1969). Behavior of concrete under biaxial stress. *American Concrete Institute (ACI) Journal, 87*(2), 656-666.

Kwon, M., and Spacone, E. (2002). Three-dimensional finite element analyses of reinforced concrete columns. *Computers & Structures, 8*(2), 199–212.

Lankard, D. R. , Birkimer, D. L. , Fondriest, F. F. , and Snyder, M. J. (1971). Effects of moisture content on the structural properties of portland cement concrete exposed to temperatures up to 500°F. *American Concrete Institute (ACI) Special Publication - SP25 - Temperature and Concrete, 25*, 59-102.

Larson, F. R., and Miller, J. (1952). A time-temperature relationship for rupture and creep stress. *Transactions of American Society of Mechanical Engineers (ASME), 74*, 765-775.

Lea, F.C. (1920). The effect of temperature on some of the properties of materials. *Engineering, 110, NR. 2852*, 293-298.

Lea, F.C., and Stradling, R. E. (1922a). The resistance to fire of concrete and reinforced concrete. *Engineering, 114, No. 2959*(341-344).

Lea, F.C., and Stradling, R. E. (1922b). The resistance to fire of concrete and reinforced concrete. *Engineering, 114, No. 2960*(380-382).

Lee, S.-C., Cho, J.-Y., and Vecchio, F.J. (2011a). Diverse embedment model for steel fibre reinforced concrete in tension: model development. *American Concrete Institute (ACI) Materials Journal, 108*(5), 516-525.

Lee, S.-C., Cho, J.-Y., and Vecchio, F.J. (2011b). Diverse embedment model for steel fibre reinforced concrete in tension: model verification. *American Concrete Institute (ACI) Materials Journal, 108*(5), 526-535.

Lee, S.-C., Cho, J.-Y., and Vecchio, F.J. (2013a). Simplified diverse embedment model for steel fiber- reinforced concrete elements in tension. *American Concrete Institute (ACI) Materials Journal, 110*(4), 403-412.

Lee, S.-C., Cho, J.-Y., and Vecchio, F.J. (2013b). Tension stiffening model for steel fiber-reinforced concrete containing conventional reinforcement. *American Concrete Institute (ACI) Structural Journal, 110*(4), 639-648.

Lennon, T., Bailey, C., and Clayton, N. (2002). *The performance of high grade concrete columns in fire*. The sixth International Symposium on Utilization of High Strength / High Performance Concrete, Leipzig, Germany.

Li, L., and Purkiss, J.A. (2005). Stress-strain constitutive equations of concrete material at elevated temperatures. *Fire Safety Journal, 40*, 669-686.

Li, M., Qian, C., and Sun, W. (2004). Mechanical properties of high-strength concrete after fire. *Cement and Concrete Research, 34*(6), 1001-1005.

Li, W., and Guo, Z. (1993). Experimental investigation on strength and deformation of concrete under high temperature (in Chinese). *Journal of Building Structures, 14*(1), 8-16.

Lie, T. T. (1978). Calculation of the Fire Resistance of Composite Concrete Floor and Roof Slabs. *Fire Technology, 14*(1), 28-45.

Lie, T. T. (1992). *Structural Fire Protection (ASCE Manuals and Reports on Engineering Practice No. 78)*. New York, NY: American Society of Civil Engineers (ASCE).

Lie, T. T., and Allen, D. E. (1972). *Calculations of the Fire Resistance of Reinforced Concrete Columns*. NRCC 12797, Division of Building Research, National Research Council of Canada, Ottawa, ON.

Lie, T. T., and Kodur , V. K. R. (1996). Thermal and mechanical properties of steel-fibre-reinforced concrete at elevated temperatures. *Canadian Journal of Civil Engineering, 23*(4), 511-517.

Lie, T. T., and Lin, T. D. (1985). Fire performance of reinforced concrete columns. *American Society for Testing and Materials (ASTM) Special Technical Publication - STP882 - Fire Safety: Science and Engineering*, 176-205.

Lie, T. T., and Lin, T. D. (1983). *Fire Tests on Reinforced Concrete Columns, Specimens No. 1-12*. 12 NRC Publications - DBR Internal Reports No. 478 - 489, Division of Building Research, National Research Council of Canada (NRC), Ottawa, ON.

Lie, T. T., Lin, T. D., Allen, D. E., and Abrams, M. S. (1984). *Fire Resistance of Reinforced Concrete Columns*. DBR Paper No. 1167, Division of Building Research, National Research Council of Canada (NRC), Ottawa, ON, 20 p.

Lie, T. T., Rowe, T. J., and Lin, T. D. (1986). Residual strength of fire-exposed reinforced concrete columns. *American Concrete Institute (ACI) Special Publications - SP92 - Evaluation and Repair of Fire Damage to Concrete*, 153-174.

Lie, T. T., and Stanzak, W. W. (1974). Empirical method for calculating fire resistance of protected steel columns. *Engineering Journal (Transactions of the Canadian Society for Civil Engineering), 57*(5/6), 73-80.

Lion, M., Skoczylas, F., Lafhaj, Z., and Sersar, M. (2005). Experimental study on a mortar. Temperature effects on porosity and permeability. Residual properties or direct measurements under temperature. *Cement and Concrete Research, 35*(10), 1937-1942.

Liu, G.-R., and Quek, S. S. (2003). *The Finite Element Method: A Practical Course* (1st ed.). Maine: Butterworth-Heinemann.

Liu, X., Ye, G., De Schutter, G., Yuan, Y., and Taerwe, L. (2008). On the mechanism of polypropylene fibres in preventing fire spalling in self-compacting and high-performance cement paste. *Cement and Concrete Research, 38*(4), 487-499.

LS-DYNA®, Version R7.0.0. (2013).

Lu, Z. (1989). *A Research on Fire Response of Reinforced Concrete Beams (in Chinese).* PhD Thesis, Tongji University.

Luckner, L., Van Genuchten, M. Th, and Nielsen, D. R. (1989). A consistent set of parametric models for the two-phase flow of immiscible fluids in the subsurface. *Water Resources Research, 25*(10), 2187-2193.

Luo, X., Sun, W., and Chan, S. Y. N. (2000). Effect of heating and cooling regimes on residual strength and microstructure of normal strength and high-performance concrete. *Cement and Concrete Research, 30*(3), 379-383.

Magnusson, S. E., and Thelandersson, S. (1970). *Temperature-Time Curves of Complete Process of Fire Development, Theoretical Study of Wood Fuel Fires in Enclosed Spaces*. Acta Polytechnica Scandinavia, Civil Engineering and Building Construction, Series No. 65, Stockholm, Sweden, 181 p.

Majumdar, P., Gupta, A., and Marchertas, A. (1995). Moisture propagation and resulting stress in heated concrete walls. *Nuclear Engineering and Design, 156*(1–2), 147-158.

Malhotra, H. L. (1956). The effect of temperature on the compressive strength of concrete. *Magazine of Concrete Research, 23*(8), 85 - 94.

Malhotra, H. L. (1982a). *Design of Fire-Resisting Structures*. Guildford, UK: Surrey University Press.

Malhotra, H. L. (1982b). Report on the work of technical committee 44-PHT "Properties of materials at high temperatures". *Materials and Structures, 15*(2), 161-170.

Malhotra, H. L. (1984). *Spalling of Concrete in Fires - Technical Report No. 118*. Construction Industry Research and Information Association (CIRIA), London, UK, 36 p.

Mander, J. B. (1983). *Seismic Design of Bridge Piers.* PhD Thesis, University of Canterbury, Christchurch, New Zealand, 442 p.

Mander, J. B., Priestley, M. J. N., and R., Park. (1988). Theoretical stress-strain model for confined concrete. *Journal of Structural Engineering - American Society of Civil Engineers (ASCE), 114*(8), 1804-1826.

Marrero, T. R., and Mason, E. A. (1972). Gaseous diffusion coefficients. *Journal of Physical and Chemical Reference Data, 1*(1), 3-118.

Mason, E. A., and Monchick, L. (1965). Survey of the equation of state and transport properties of moist gases. In Wexler, A. (Ed.), *Humidity and Moisture Measurement and Control in Science and Industry (International Symposium on Humidity and Moisture, Washington, D.C., 1963)*. New York, NY: Reinhold.

Mayer, J. R., Joule, J. P., and Carnot, S. (1929). The discovery of the law of conservation of energy. *Isis, 13*(1), 18-44.

Meyer-Ottens, C. . (1974a). Behaviour of concrete structural members in fire conditions. *Beton, 4*, 133–136.

Meyer-Ottens, C. . (1974b). Behaviour of concrete structural members in fire conditions (in German). *Beton, 5*, 133–136.

Miller, A. (1989). Sätt att Armera Betongmassa med Stålfibrer. Sweden Patent No. SE460118. Institutet för Innovationsteknik AB.

Miyahara, T., Kawakami, T., and and Maekawa, K. (1987). Nonlinear behavior of cracked reinforced concrete plate element under uniaxial compression. *Proceedings of Japan Society of Civil Engineers (JSCE), No.378/V-6*, 306-319.

Miyahara, T., Kawakami, T., and and Maekawa, K. (1988). Nonlinear behavior of cracked reinforced concrete plate element under uniaxial compression. *Concrete Library International, Japan Society of Civil Engineers (JSCE), 11*, 131-144.

Moffatt, K. (2001). *Analyse de dalles de pont avec armature réduite et béton de fibres métalliques.* M.A.Sc. Thesis, École Polytechnique de Montréal, Montréal, Québec, 248 p.

Moftah, M. (2008). *Numerical Modelling and Performance of Reinforced Concrete Members under Fire Condition.* PhD Thesis, University of Western Ontario, Waterloo, ON, 286 p.

Mohamedbhai, G. T. G. (1983). Residual strength of concrete subjected to elevated temperatures. *Concrete (London), 17*(12), 22-27.

Mohr, C. O. (1900). Welche Umstände bedingen die Elastizitätsgrenze und den Bruch eines Materials? *Zeitschrift des Vereins Deutscher Ingenieure, 24*, 1524−1530 and 1572–1577.

Montoya, E. (2003). *Behaviour and Analysis of Confined Concrete.* PhD Thesis, University of Toronto, Toronto, 297 p.

Morita, S., and Fujii, S. (1982). *Bond capacity of deformed bars due to splitting of surrounding concrete*. Bond in concrete: Proceedings of the International Conference on Bond in Concrete, Paisley College of Technology, Scotland.

Morita, T., Saito, H., and Kumagai, H. (1992). *Residual mechanical properties of high strength concrete members exposed to high temperature—Part 1. Test on material properties (in Japanese)*. Summaries of Technical Papers of Annual Meeting, Architectural Institute of Japan, Niigata, Japan.

Mostafaei, H., Leroux, P., and Lafrance, P.-S. (2012). *Fire Endurance Of A Reinforced Concrete Column Under Both Axial And Lateral Loads*. NRC Report IRC-RR-327, National Research Council Canada (NRC), Ottawa, ON, 31 p.

Mostafaei, H., Vecchio, F. J., Gauvreau, P., and Semelawy, M. (2011). Punching shear behavior of externally prestressed concrete slabs. *Journal of Structural Engineering - American Society of Civil Engineers (ASCE), 137*(1), 100-108.

Mualem, Y. (1976). A new model for predicting the hydraulic conductivity of unsaturated porous media. *Water Resources Research, 12*(3), 513-522.

Na, C., and Kwak, H.-G. (2011). A numerical tension-stiffening model for ultra high strength fiber-reinforced concrete beams. *Computers and Concrete, 8*(1), 1-22.

Naaman, A. E., and Najm, H. (1991). Bond-slip mechanisms of steel fibers in concrete. *American Concrete Institute (ACI) Materials Journal, 88*(2), 135-145.

Nagao, K., and Nakane, S. (1991). *Influences of various factors on physical properties of concretes heated to high temperatures (Paper H03/1)*. Eleventh International Conference on Structural Mechanics in Reactor Technology (SMiRT 11), Tokyo, Japan.

Nassif, A. Y. (2002). Postfiring stress-strain hysteresis of concrete subjected to various heating and cooling regimes. *Fire and Materials, 26*(3), 103-109.

Nassif, A. Y., Burley, E., and Rigden, S. (1995). A new quantitative damage to concrete method of assessing fire structures. *Magazine of Concrete Research, 47*(172), 271-278.

Naus, D. J. (2010). *A Compilation of Elevated Temperature Concrete Material Property Data and Information for Use in Assessments of Nuclear Power Plant Reinforced Concrete Structures (NUREG/CR-7031)*. United States Nuclear Regulatory Commission (U.S.NRC), Office of Nuclear Regulatory Research, Oak Ridge, TN, 328 p.

Neumann, F. E. (1831). Untersuchung über die specifische wärme der mineralien (Study of the specific heat of minerals). *Annalen Der Physik und Chemie (Annals of Physics and Chemistry), 99*(9), 1-39.

NFPA 251, Standard Methods of Tests of Fire Endurance of Building Construction and Materials. (2006). National Fire Protection Association. Quincy, MA.

Ngo, D., and Scordelis, A. C. (1967). Finite element analysis of reinforced concrete beams. *American Concrete Institute (ACI) Journal, 64*(3), 152-163.

Nishida, A., Yamazaki, N., Inoue, H., Schneider, U., and Diederichs, U. (1995). *Study on the properties of high strength concrete with short polypropylene fibre for spalling resistance (CONSEC'95)*. International Symposium on Concrete under Severe Conditions, Sapporo, Japan.

Nishizawa, N., and Okamura, H. (1970). *Strength and inelastic properties of concrete at elevated temperature*. International Seminar on Concrete for Nuclear Reactors, Berlin, F. R. Germany.

Nishizawa, N., and Okamura, H. (1972). Strength and inelastic properties of concrete at elevated temperature. *American Concrete Institute (ACI) Special Publication - SP34 - Concrete for Nuclear Reactors*, 407-422.

Norton, C. L. (1911). Some thermal properties of concrete. *National Association of Cement Users (now American Concrete Institute (ACI)) Journal Proceedings, 7*(12), 78-90.

Noumowé, A. N., Clastres, P., Debicki, G., and Costaz, J.-L. (1996). *Thermal stresses and water vapour pressure of high performance concrete at high temperature*. Fourth International Symposium on Utilization of High-Strength/High-Performance Concrete, Paris, France.

Noumowé, A., Siddique, R., and Ranc, G. (2009). Thermo-mechanical characteristics of concrete at elevated temperatures up to 310°C. *Nuclear Engineering and Design, 239*(3), 470-476.

NS 3473 E - Concrete Structures, Design Rules. (1992). Norwegian Council for Building Standardization. Oslo, Norway, 79 p.

Ödeen, K. (1968). *Fire Resistance of Prestressed Concrete Double T Units, Acta Polytechnica Scandinavica*. Ingenjörsvetenskapsakademien (IVA), Royal Swedish Academy of Engineering Sciences, Stockholm, Sweden, 75 p.

Ödeen, K., and Nordström, A. (1972). Termiska egenskaper hos betong vid höga temperaturer (in Swedish). *Cement och Betong, 1*.

Oh, J.-H. (2011). *Uniaxial Behavior of Steel Fiber Reinforced Concrete (in Korean).* Master's Thesis, Seoul National University, Seoul, South Korea, 122 p.

Okamura, H., and Maekawa, K. (1991). *Nonlinear Analysis and Constitutive Models of Reinforced Concrete*. Tokyo: Gihodo-Shuppan Co.

Ottosen, N. S. (1979). Constitutive model for short-time loading of concrete. *Journal of the Engineering Mechanics Division, American Society of Civil Engineers (ASCE), 105*(1), 127–141.

Palermo, D. (2002). *Behaviour and Analysis of Reinforced Concrete Walls Subjected to Reversed Cyclic Loading.* PhD Thesis, University of Toronto, Toronto, ON, 492 p.

Papayianni, J., and Valiasis, T. (1991). Residual mechanical properties of heated concrete incorporating different pozzolanic materials. *Materials and Structures, 24*(2), 115-121.

Park, R., Priestley, M. J. N., and Gill, W. D. . (1982). Ductility of square-confined concrete columns. *Journal of the Structural Division, American Society of Civil Engineers (ASCE), 108*(4), 929-950.

Peng, G.-F., Bian, S.-H., Guo, Z.-Q., Zhao, J., Peng, X.-L., and Jiang, Y.-C. (2008). Effect of thermal shock due to rapid cooling on residual mechanical properties of fiber concrete exposed to high temperatures. *Construction and Building Materials, 22*(5), 948-955.

Persson, B. (2003). *Self-Compacting Concrete at Fire Temperatures - TVBM-3110*. Division of Building Materials, Faculty of Engineering (LTH), Lund University (formerly Lund Institute of Technology), Lund, Sweden, 216 p.

Pettersson, O., Magnusson, S.E., and J., Thor. (1976). *Fire Engineering Design of Steel Structures, Publication No. 50*. SBI - Stålbyggnadsinstitutet (Swedish Institute of Steel Construction), Stockholm, Sweden, 232 p.

Petzold, A., and Röhrs, M. (1970). *Concrete for High Temperatures* (Phillips, A. B. & Turner, F. H., Trans. 2 ed.). London: McLaren and Sons.

Phan, L. T. (1996). *Fire Performance of High-Strength Concrete: A Report of the State-of-the-Art, NISTIR 5934*. Building and Fire Research Laboratory, National Institute of Standards and Technology (NIST), Gaithersburg, MD, 115 p.

Phan, L. T. (2007). *Spalling and mechanical properties of high strength concrete at high temperature*. Concrete under Severe Conditions: Environment & Loading (CONSEC'07), Tours, France.

Philleo, R. (1958). Some physical properties of concrete at high temperature. *American Concrete Institute (ACI) Journal Proceedings, 54*(4), 857-864.

Poh, K. W. (2001). Stress-strain-temperature relationship for structural steel. *Journal of Materials in Civil Engineering - American Society of Civil Engineers (ASCE), 13*(5), 371-379.

Popovics, S. (1973). A numerical approach to the complete stress-strain curve of concrete. *Cement and Concrete Research, 3*(5), 583-599.

Potha Raju, M., Shobha, M., and Rambabu, K. (2004). Flexural strength of fly ash concrete under elevated temperatures. *Magazine of Concrete Research, 56*(2), 83-88.

Price, W. H., and Cordon, W. A. (1949). Tests of lightweight-aggregate concrete designed for monolithic construction. *American Concrete Institute (ACI) Journal Proceedings, 45*(4), 581-600.

Purkiss, J. A. (1996). *Fire Safety Engineering Design of Structures*. Oxforf, UK: Butterworth-Heinemann.

Purkiss, J. A., and Bali, A. (1988). *The transient behaviour of concrete at tem-peratures up to 800°C*. Tenth Ibausil (International Conference on Building Materials), Hochschule für Architektur und Bauwesen, Weimar, Germany.

Purkiss, J. A., and Dougill, J. W. (1973). Apparatus for compression tests on concrete at high temperatures. *Magazine of Concrete Research, 25*(83), 102 –108.

Raghava, R., Caddell, R. M., and Yeh, G. S. Y. (1973). The macroscopic yield behaviour of polymers. *Journal of Materials Science, 8*(2), 225-232.

Ramberg, W., and Osgood, W. R. (1943). *Description of stress-strain curves by three parameters*. National Advisory Committee For Aeronautics, Washington, DC, 13 p.

Ravindrarajah, R. S., Lopez, R., and Reslan, H. (2002). *Effect of elevated temperature on the properties of high-strength concrete containing cement supplementary materials*. Ninth International Conference on Durability of Building Materials and Components, Brisbane, Australia.

Rayleigh, J. W. S. (1877). *The Theory of Sound, reissued in 1945, Vol. 1, 2nd ed.* Dover Publications, New York, NY, 480 p.

Reddy, J. N., and Gartling, D.K. (2010). *The Finite Element Method in Heat Transfer and Fluid Dynamics, Third Edition* (3 ed.): CRC Press.

Reid, R. C., Prausnitz, J. M., and Poling, B. E. (1987). *The Properties of Gases and Liquids*. New York, NY: McGraw-Hill.

Richart, F.E., Brandtzaeg, A., and Brown, R.L. (1928). *A Study of the Failure of Concrete under Combined Compressive Stresses*. University of Illinois Engineering Experimental Station, Urbana, Illinois, 104 p.

Rowley, F. B., and Algren, A. B. (1937). *Thermal Conductivity of Building Materials, Bulletin No. 12*. University of Minnesota: University of Minnesota Engineering Experiment Station.

Saab, H. A. (1990). *Non-linear Finite Element Analysis of Steel Frames in Fire Conditions.* PhD Thesis, University of Sheffield, Sheffield, England, 143 p.

Saad, M., Abo-El-Enein, S. A., Hanna, G. B., and Kotkata, M. F. (1996). Effect of temperature on physical and mechanical properties of concrete containing silica fume. *Cement and Concrete Research, 26*(5), 669-675.

Saatci, S. (2007). *Behaviour and Modelling of Reinforced Concrete Structures Subjected to Impact Loads.* PhD Thesis, University of Toronto, 288 p.

Saemann, J. C., and Washa, G. W. (1957). Variation of mortar and concrete properties with temperature. *American Concrete Institute (ACI) Journal Proceedings, 54*(11), 385-395.

Saenz, L. P. (1964). Discussion of ‘‘Equation for the stress-strain curve of concrete” by P. Desayi and S. Krishnan. *American Concrete Institute (ACI) Journal, 61*(9), 1229–1235.

Sato, Y., and Vecchio, F.J. (2003). Tension stiffening and crack formation in RC members with FRP sheets. *Journal of Structural Engineering - American Society of Civil Engineers (ASCE), 129*(6), 717-724.

Schaumann, P., and Kettner, F. (2003). *BOFIRE – A FEM-Programm for Non-Linear Analysis of Structural Members under Fire Conditions*. Institute for Steel Construction, University of Hannover, Hannover, Germany, 5 p.

Scheidegger, A. E. (1957). *The Physics of Flow Through Porous Media*: University of Toronto Press.

Schneider, U. (1973). *Zur Kinetik festigkeitsmindernder Reaktionen in Normalbeton bei hohen Temperaturen.* PhD Thesis, Technischen Universität Braunschweig, Braunschweig, Germany, 137 p.

Schneider, U. (1974). Zur Kinetik festigkeitsmindernder Reaktionen in Normalbeton bei hohen Temperaturen. *Schriftenreihe des Sonderforschungsbereichs 148: Brandverhalten von Bauteilen, Technischen Universität Braunschweig, 3*, 1-111.

Schneider, U. (1976). Behaviour of concrete under thermal steady state and non-steady state conditions. *Fire and Materials, 1*(3), 103-115.

Schneider, U. (1982). *Behavior of concrete at high temperatures*. Deutscher Ausschuss für Stahlbeton, Berlin, Germany, 122 p.

Schneider, U. (1986). Modeling of Concrete Behaviour at High Temperature. In Anchor, R. D., Malhotra, H. L. & Purkiss, J. A. (Eds.), *Design of Structures Against Fire (Proceedings of the International Conference on Design of Structures Against Fire, held at Aston University, Birmingham, UK on 15th and 16th April 1986).* London, UK: Elsevier Applied Science.

Schneider, U. (1988). Concrete at high temperatures - a general review. *Fire Safety Journal, 13,* 55-68.

Schneider, U., and Diederichs, U. (1981a). Physikalische eigenschaften von beton von 20 celsius grad bis zum shmelzen, Teil 1 (Physical properties of concrete from 20°C up to melting, Part 1). *Betonwerk und Fertigteil-Technik, 47*(3), 141-149.

Schneider, U., and Diederichs, U. (1981b). Physikalische eigenschaften von beton von 20 celsius grad bis zum shmelzen, Teil 2 (Physical properties of concrete from 20°C up to melting, Part 2). *Betonwerk und Fertigteil-Technik, 47*(4), 223-230.

Schneider, U., Diederichs, U., and Ehm, C. (1982). Effect of temperature on steel and concrete for PCRV's. *Nuclear Engineering and Design, 67*(2), 245-258.

Schneider, U., and Haksever, A. (1976). *Bestimmung der äquivalenten Branddauer von statisch bestimmt gelagerten Stahlbetonbalken bei natürlichen Bränden (Beitrag zum Berechnungsverfahren nach DIN 18 230 E): Untersuchung im Auftrag des Deutschen Instituts für Bautechnik, Berlin (Az.: IV/1 5 111/75 und IV/1 5 111 76)* Braunschweig, Germany: Institut für Baustoffkunde und Stahlbetonbau.

Schneider, U., and Herbst, H.-J. . (1989). Permeabilität und porosität von beton bei hohen temperaturen. *Deutscher Ausschuß für Stahlbeton (DAfStb), 403*, 52.

Seckin, M. (1981). *Hysteretic Behaviour of Cast-in-Place Exterior Beam-Column-Slab Subassemblies.* PhD Thesis, University of Toronto, Toronto, ON, 266 p.

Selby, R. G. (1990). *Nonlinear Finite Element Analysis of Reinforced Concrete Solids.* Master of Applied Science Thesis, University of Toronto, 144 p.

Semelawy, M. (2007). *Effects of Axial Prestress on the Punching Behaviour of Plain and Fibre Reinforced Concrete Slabs.* M.A.Sc. Thesis, University of Toronto, Toronto, ON, 180 p.

Sharples, R. (1987). *The Strength of Partially Exposed Steel Columns in Fire.* M.Phil. Thesis, University of Sheffield, Sheffield, England.

Shin, K.-Y., Kim, S.-B., Kim, J.-H., Chung, M., and Jung, P.-S. (2002). Thermo-physical properties and transient heat transfer of concrete at elevated temperatures. *Nuclear Engineering and Design, 212*(1–3), 233-241.

Shirai, S., and Noguchi, H. (1989). *Compressive deterioration of cracked concrete*. ASCE Structures Congress 1989: Design, Analysis and Testing, New York, NY.

Shuttleworth, P. (1997). *Fire performance of concrete for tunnel linings, Channel Tunnel Rail Link Technical Report*. Arup, London, UK, 9 p.

Sideris, K. K., Manita, P., and Chaniotakis, E. (2009). Performance of thermally damaged fibre reinforced concretes. *Construction and Building Materials, 23*(3), 1232-1239.

Simmons, W. F., and Cross, H. C. (1952). Report on the Elevated-Temperature Properties of Stainless Steels. *American Society for Testing and Materials (ASTM) - Special Technical Publication - STP124*, 119.

Smith, C. I., Kirby, B. R., Lapwood, D. G., Cole, K. J., Cunningham, A. P., and Preston, R. R. (1981). The reinstatement of fire damaged steel framed structures. *Fire Safety Journal, 4*(1), 21-62.

Smith, L. M. (1983). *The Assessment of Fire Damage to Concrete Structures.* PhD Thesis, Paisley College of Technology (now Pailey Campus of the University of the West of Scotland), Paisley, Scotland.

Song, Y., Zhang, Z., Qing, L., and Yu, C. (2007). Biaxial tensile-compressive experiment of concrete at high temperatures. *Frontiers of Architecture and Civil Engineering in China, 1*(1), 94-98.

Sullivan, P. J. E., and Sharshar, R. (1992). The performance of concrete at elevated temperatures (as measured by the reduction in compressive strength). *Fire Technology, 28*(3), 240-250.

Susetyo, J. (2009). *Fibre Reinforcement for Shrinkage Crack Control in Prestressed, Precast Segmental Bridges.* PhD Thesis, University of Toronto, Toronto, ON, 502 p.

Takeuchi, M., Hiramoto, M., Kumagai, N., Yamazaki, N., Kadaira, A., and Sugiyama, K. (1993). *Material properties of concrete and steel bars at elevated temperatures (Paper H04/4)*. the Twelfth International Conference on Structural Mechanics in Reactor Technology (SMiRT 12), Stuttgart, Germany.

Tanyildizi, H., and Coskun, A. (2008). Performance of lightweight concrete with silica fume after high temperature. *Construction and Building Materials, 22*(10), 2124-2129.

Tao, Z., Wang, X.-Q., and Uy, B. (2012). Stress-strain curves of structural steel and reinforcing steel after exposure to elevated temperatures. *Journal of Materials in Civil Engineering - American Society of Civil Engineers (ASCE), accepted for publication on September 4, 2012*.

Tapsell, H. J., and Clenshaw, W. J. (1927). *Properties of Materials at High Temperatures: 1. Mechanical Properties of Armco Iron, 0.17 Percent Carbon Steel, and 0.24 Percent Carbon Steel, with Special Reference to Creep, Special Report No. 1*. Great Britain Department of Scientific and Industrial Research, Engineering Research Board, 60 p.

Tenchev, R. T., Li, L. Y., and Purkiss, J. A. (2001). Finite element analysis of coupled heat and moisture transfer in concrete subjected to fire. *Numerical Heat Transfer, Part A: Applications, 39*(7), 685-710.

Terro, M. J. (1998). Numerical modeling of the behavior of concrete structures in fire. *American Concrete Institute (ACI) Structural Journal, 9*(2), 183-193.

Thelandersson, S. (1972). Effect of High Temperature on Tensile Strength of Concrete. *Nordisk Betong, 2*.

Thomas, H. R., and Sansom, M. R. (1995). Fully coupled analysis of heat, moisture, and air transfer in unsaturated soil. *Journal of Engineering Mechanics, 121*(3), 392-405.

Thor, J. (1973). *Deformation and Critical Loads of Steel Beams Under Fire Exposure Conditions, Document D16*. Swedish Council for Building Research, Stockholm, Sweden, 123 p.

Thorenfeldt, E., Tomaszewicz, A., and Jensen, J. J. (1987). *Mechanical properties of high-strength concrete and application in design*. Symposium "Utilization of High Strength Concrete", Stavanger, Norway.

Topçu, I. B., and Karakurt, C. (2008). Properties of reinforced concrete steel rebars exposed to high temperatures, Article ID 814137. *Research Letters in Materials Science, 2008*, 4.

Toumi, B., and Resheidat, M. (2010). Influence of high temperatures on surface cracking of concrete studied by image scanning technique. *Jordan Journal of Civil Engineering, 4*(2), 155-163.

Tsai, W. (1988). Uniaxial Compressional Stress-Strain Relation of Concrete. *Journal of Structural Engineering, 114*(9), 2133-2136.

Tsimbrovska, M. (1998). *Dégradation des Bétons à Hautes Performances Soumis à des Températures Élevées.* PhD Thesis, Université de Joseph Fourier – Grenoble, 207 p.

UL 263, Fire Tests of Building Construction and Materials. (2003). Underwriters Laboratories Inc. Northbrook, IL, 30 p.

Valore, R. C. (1980). Calculations of U-values of hollow concrete masonry. *Concrete International, 2*(2), 40-63.

Van Brakel, J., and Heertjes, P. M. (1974). Analysis of diffusion in macroporous media in terms of a porosity, a tortuosity and a constrictivity factor. *International Journal of Heat and Mass Transfer, 17*(9), 1093-1103.

van Genuchten, M. Th. (1980). A closed-form equation for predicting the hydraulic conductivity of unsaturated soils. *Soil Science Society of America Journal (SSSAJ), 44*(5), 892-898.

Vecchio, F. J. (1982). *The Response of Reinforced Concrete to In-Plane Shear and Normal Stresses.* Ph.D Thesis, University of Toronto, 332 p.

Vecchio, F. J. (1990). Reinforced concrete membrane element formulations. *Journal of Structural Engineering - American Society of Civil Engineers (ASCE), 116*(3), 730-750.

Vecchio, F. J. (1999). Towards cyclic load modeling of reinforced concrete. *American Concrete Institute (ACI) Structural Journal, 96*(2), 193-202.

Vecchio, F. J. (2000). Disturbed stress field model for reinforced concrete: formulation. *Journal of Structural Engineering - American Society of Civil Engineers (ASCE), 126*(8), 1070-1077.

Vecchio, F. J., and Collins, M. P. (1986). The modified compression field theory for reinforced concrete elements subjected to shear. *American Concrete Institute (ACI) Journal, 83*(2), 219-231.

Vecchio, F. J., and Collins, M. P. (1993). Compression response of cracked reinforced concrete. *Journal of Structural Engineering - American Society of Civil Engineers (ASCE), 119*(12), 3590-3610.

Vecchio, F. J., and DeRoo, A. (1995). Smeared-crack modeling of concrete tension splitting. *Journal of Engineering Mechanics - American Society of Civil Engineers (ASCE), 121*(6), 702-708.

Vecchio, F. J., and Lai, D. (2004). Crack shear-slip in reinforced concrete elements. *Journal of Advanced Concrete Technology, 2*(3), 289-300.

Vecchio, F. J., and Selby, R. G. (1991). Towards compression field analysis of reinforced concrete solids. *Journal of Structural Engineering - American Society of Civil Engineers (ASCE), 117*(6), 1740-1758.

Vintzeleou, E. N., and Tassios, T. P. (1987). Behavior of dowels under cyclic deformations. *American Concrete Institute (ACI) Structural Journal, 84*(1), 18-30.

Voo, J. Y. L., and Foster, S. J. (2003). *Variable engagement model for fibre reinforced concrete in tension*. School of Civil and Environmental Engineering, University of New South Wales, UNSW Sydney, Australia, 86 p.

Wade, C. A., and Lovatt, A. J. (1996). *User's Guide to BRANZ TR8. Software for Calculating Fire Resistance of Concrete Beams and Floor Systems*. Building Research Association of New Zealand, Judgeford, Porirua City, New Zealand, 12 p.

Wallo, E. M., Yuan, R. L., Lott, J. L., and Kesler, C. E. (1965). *Sixth Progress Report: Prediction of Creep in Structural Concrete from Short Time Tests - Report No. 658*. Urbana, IL: Department of Theoretical and Applied Mechanics, University of Illinois.

Walraven, J.C., and Reinhardt, H.W. (1981). Theory and experiments on the mechanical behaviour of cracks in plain and reinforced concrete subjected to shear loading. *Heron, 26*(1A), 1-68.

Watson, K. M. (1943). Thermodynamics of the liquid states, generalized prediction of properties. *Industrial & Engineering Chemistry Research, 35*(4), 398-406.

Weigler, H., and Fischer, R. (1968). Beton bei temperaturen von 100°C bis 750°C. *Beton, 2*, 33–46.

Weigler, H., and Fischer, R. (1972). Influence of high temperatures on strength and deformation of concrete. *American Concrete Institute (ACI) Special Publication - SP34 - Concrete for Nuclear Reactors*, 481-491.

Whinnett, R. H. (1978). *Assessment of Fire-Damaged Concrete Structures and Repair by Gunite : Report of a Concrete Society Working Party, Technical Report No. 15*. The Concrete Society, London, UK, 28 p.

Wickstrom, U. (1979). *TASEF 2 - A computer Program for Temperature Analysis of Structures Exposed to Fire, Report No. 79-2*. Lund Institute of Technology (now Faculty of Engineering (LTH), Lund University), Lund, Sweden, 112 p.

Wickström, U. (1985). *Application of the standard fire curve for expressing natural fires for design purposes*. Fire Safety: Science and Engineering, ASTM STP 882, Philadelphia, PA.

Wijayasinghe, M. (2011). *Fire Losses in Canada: Year 2007 and Selected Years*. Office of the Fire Commissioner, Public Safety Division, Alberta Municipal Affairs, Calgary, AB, 67 p.

Wong, P. S., Trommels, H., and Vecchio, F. J. (2013). *VecTor2 and FormWorks User's Manual, Second Edition*. Department of Civil Engineering, University of Toronto, 318 p.

Xiao, J., and König, G. (2004). Study on concrete at high temperature in China—an overview. *Fire Safety Journal, 39*(1), 89-103.

Xie, D., and Qian, Z. (1998). Research on bond and tension of concrete after high temperature (in Chinese). *Journal of Zhejiang University (Natural Science), 32*(5), 597–602.

Xu, Y., Wong, Y. L., Poon, C. S., and Anson, M. (2003). Influence of PFA on cracking of concrete and cement paste after exposure to high temperatures. *Cement and Concrete Research, 33*(12), 2009-2016.

Yamamoto, T. (1999). *Nonlinear Finite Element Analysis of Transverse Shear and Torsional Problems in Reinforced Concrete Shells.* M.A.Sc. Thesis, University of Toronto, 112 p.

Zadražil, T., Vodák, F., and Kapičková, O. (2004). Effect of temperature and age of concrete on strength – porosity relation. *Acta Polytechnica, 44*(1), 53-56.

Zeiml, M. (2004). *Analytical and Numerical Modeling of Heat and Water-Vapor Transport in Concrete Subjected to Fire Loading.* Master's Thesis, Technische Universität Wien (Vienna University of Technology), Vienna, Austria.

Zeiml, M.atthias, Lackner, R.oman, Leithner, D.avid, and Eberhardsteiner, J. (2008). Identification of residual gas-transport properties of concrete subjected to high temperatures. *Cement and Concrete Research, 38*(5), 699-716.

Zhang, B., Bicanic, N., Pearce, C. J., and Phillips, D. V. (2002). Relationship between brittleness and moisture loss of concrete exposed to high temperatures. *Cement and Concrete Research, 32*(3), 363-371.

Zheng, W., Hu, Q., and Zhang, H. (2007). Experimental research on the mechanical property of prestressing steel wire during and after heating. *Frontiers of Architecture and Civil Engineering in China, 1*(2), 247-254.

Zhukov, V. V., Robsman, V. A., Shevchenko, V. I., and Cyganova, L. P. . (1971). *Thermophysical analysis of structures of heat resistant concrete (Translated from Russian)*. The Research, Design and Technological Institute for Concrete and Reinforced Concrete (NIIZhB), Russia.

Zhukov, V. V., and Shevchenko, V. I. (1974). Investigation of causes of possible spalling and failure of heat-resistant concretes at drying, first heating and cooling (Translated from Russian). *Heat-Resistant Concrete (Translated from Russian)*, 32-45.

Zienkiewicz, O. C., and Cormeau, I. C. (1974). Visco-plasticity—plasticity and creep in elastic solids—a unified numerical solution approach. *International Journal for Numerical Methods in Engineering, 8*(4), 821-845.

Zoldners, N. G. (1960). Effect of high temperatures on concrete incorporating different aggregates. *American Society for Testing and Materials (ASTM) Proceedings, 60*, 1087-1108.

Appendix A
Elements of Finite Element Matrices

A.1 Introduction

This section presents lists of the elements comprising the various matrices derived for finite element procedures for the coupled heat and moisture transfer analysis for regular eight-noded hexahedral brick elements, as discussed in Chapter 4.

A.2 Elements of $\int_{\Omega}(N^{T}C_{E}N)d\Omega$

Matrix $\int_{\Omega}(N^{T}C_{E}N)d\Omega$, introduced in Equation (4.83), is a 24×24 matrix, with elements given the notation C_{i-j}, where i is the row number and j is the column number.

$$\int_{\Omega}(N^{T}C_{E}N)d\Omega = \int_{-1}^{1}\int_{-1}^{1}\int_{-1}^{1}(N^{T}C_{E}N)\det[J]d\eta\, d\zeta\, d\xi = C_{i-j} \qquad (A.1)$$

With C_{TT}, C_{TP}, C_{TV}, C_{AT}, C_{AP}, C_{AV}, C_{MT}, C_{MP}, and C_{MV} defined in Table 4-1, and V_C equals $\frac{abc}{216}$, where a, b and c are defined in Figure 4-1, C_{i-j} can be given as:

$C_{1-1} = 8C_{TT}V_C$	$C_{1-2} = 8C_{TP}V_C$	$C_{1-3} = 8C_{TV}V_C$	$C_{1-4} = 4C_{TT}V_C$
$C_{2-1} = 8C_{AT}V_C$	$C_{2-2} = 8C_{AP}V_C$	$C_{2-3} = 8C_{AV}V_C$	$C_{2-4} = 4C_{AT}V_C$
$C_{3-1} = 8C_{MT}V_C$	$C_{2-2} = 8C_{MP}V_C$	$C_{3-3} = 8C_{MV}V_C$	$C_{3-4} = 4C_{MT}V_C$
$C_{4-1} = 4C_{TT}V_C$	$C_{4-2} = 4C_{TP}V_C$	$C_{4-3} = 4C_{TV}V_C$	$C_{4-4} = 8C_{TT}V_C$
$C_{5-1} = 4C_{AT}V_C$	$C_{5-2} = 4C_{AP}V_C$	$C_{5-3} = 4C_{AV}V_C$	$C_{5-4} = 8C_{AT}V_C$
$C_{6-1} = 4C_{MT}V_C$	$C_{6-2} = 4C_{MP}V_C$	$C_{6-3} = 4C_{MV}V_C$	$C_{6-4} = 8C_{MT}V_C$
$C_{7-1} = 2C_{TT}V_C$	$C_{7-2} = 2C_{TP}V_C$	$C_{7-3} = 2C_{TV}V_C$	$C_{7-4} = 4C_{TT}V_C$
$C_{8-1} = 2C_{AT}V_C$	$C_{8-2} = 2C_{AP}V_C$	$C_{8-3} = 2C_{AV}V_C$	$C_{8-4} = 4C_{AT}V_C$
$C_{9-1} = 2C_{MT}V_C$	$C_{9-2} = 2C_{MP}V_C$	$C_{9-3} = 2C_{MV}V_C$	$C_{9-4} = 4C_{MT}V_C$
$C_{10-1} = 4C_{TT}V_C$	$C_{10-2} = 4C_{TP}V_C$	$C_{10-3} = 4C_{TV}V_C$	$C_{10-4} = 2C_{TT}V_C$
$C_{11-1} = 4C_{AT}V_C$	$C_{11-2} = 4C_{AP}V_C$	$C_{11-3} = 4C_{AV}V_C$	$C_{11-4} = 2C_{AT}V_C$
$C_{12-1} = 4C_{MT}V_C$	$C_{12-2} = 4C_{MP}V_C$	$C_{12-3} = 4C_{MV}V_C$	$C_{12-4} = 2C_{MT}V_C$
$C_{13-1} = 4C_{TT}V_C$	$C_{13-2} = 4C_{TP}V_C$	$C_{13-3} = 4C_{TV}V_C$	$C_{13-4} = 2C_{TT}V_C$
$C_{14-1} = 4C_{AT}V_C$	$C_{14-2} = 4C_{AP}V_C$	$C_{14-3} = 4C_{AV}V_C$	$C_{14-4} = 2C_{AT}V_C$
$C_{15-1} = 4C_{MT}V_C$	$C_{15-2} = 4C_{MP}V_C$	$C_{15-3} = 4C_{MV}V_C$	$C_{15-4} = 2C_{MT}V_C$

$C_{16-1} = 2C_{TT}V_C$ $C_{16-2} = 2C_{TP}V_C$ $C_{16-3} = 2C_{TV}V_C$ $C_{16-4} = 4C_{TT}V_C$
$C_{17-1} = 2C_{AT}V_C$ $C_{17-2} = 2C_{AP}V_C$ $C_{17-3} = 2C_{AV}V_C$ $C_{17-4} = 4C_{AT}V_C$
$C_{18-1} = 2C_{MT}V_C$ $C_{18-2} = 2C_{MP}V_C$ $C_{18-3} = 2C_{MV}V_C$ $C_{18-4} = 4C_{MT}V_C$
$C_{19-1} = C_{TT}V_C$ $C_{19-2} = C_{TP}V_C$ $C_{19-3} = C_{TV}V_C$ $C_{19-4} = 2C_{TT}V_C$
$C_{20-1} = C_{AT}V_C$ $C_{20-2} = C_{AP}V_C$ $C_{20-3} = C_{AV}V_C$ $C_{20-4} = 2C_{AT}V_C$
$C_{21-1} = C_{MT}V_C$ $C_{21-2} = C_{MP}V_C$ $C_{21-3} = C_{MV}V_C$ $C_{21-4} = 2C_{MT}V_C$
$C_{22-1} = 2C_{TT}V_C$ $C_{22-2} = 2C_{TP}V_C$ $C_{22-3} = 2C_{TV}V_C$ $C_{22-4} = C_{TT}V_C$
$C_{23-1} = 2C_{AT}V_C$ $C_{23-2} = 2C_{AP}V_C$ $C_{23-3} = 2C_{AV}V_C$ $C_{23-4} = C_{AT}V_C$
$C_{24-1} = 2C_{MT}V_C$ $C_{24-2} = 2C_{MP}V_C$ $C_{24-3} = 2C_{MV}V_C$ $C_{24-4} = C_{MT}V_C$

$C_{1-5} = 4C_{TP}V_C$ $C_{1-6} = 4C_{TV}V_C$ $C_{1-7} = 2C_{TT}V_C$ $C_{1-8} = 2C_{TP}V_C$
$C_{2-5} = 4C_{AP}V_C$ $C_{2-6} = 4C_{AV}V_C$ $C_{2-7} = 2C_{AT}V_C$ $C_{2-8} = 2C_{AP}V_C$
$C_{3-5} = 4C_{MP}V_C$ $C_{3-6} = 4C_{MV}V_C$ $C_{3-7} = 2C_{MT}V_C$ $C_{3-8} = 2C_{MP}V_C$
$C_{4-5} = 8C_{TP}V_C$ $C_{4-6} = 8C_{TV}V_C$ $C_{4-7} = 4C_{TT}V_C$ $C_{4-8} = 4C_{TP}V_C$
$C_{5-5} = 8C_{AP}V_C$ $C_{5-6} = 8C_{AV}V_C$ $C_{5-7} = 4C_{AT}V_C$ $C_{5-8} = 4C_{AP}V_C$
$C_{6-5} = 8C_{MP}V_C$ $C_{6-6} = 8C_{MV}V_C$ $C_{6-7} = 4C_{MT}V_C$ $C_{6-8} = 4C_{MP}V_C$
$C_{7-5} = 4C_{TP}V_C$ $C_{7-6} = 4C_{TV}V_C$ $C_{7-7} = 8C_{TT}V_C$ $C_{7-8} = 8C_{TP}V_C$
$C_{8-5} = 4C_{AP}V_C$ $C_{8-6} = 4C_{AV}V_C$ $C_{8-7} = 8C_{AT}V_C$ $C_{8-8} = 8C_{AP}V_C$
$C_{9-5} = 4C_{MP}V_C$ $C_{9-6} = 4C_{MV}V_C$ $C_{9-7} = 8C_{MT}V_C$ $C_{9-8} = 8C_{MP}V_C$
$C_{10-5} = 2C_{TP}V_C$ $C_{10-6} = 2C_{TV}V_C$ $C_{10-7} = 4C_{TT}V_C$ $C_{10-8} = 4C_{TP}V_C$
$C_{11-5} = 2C_{AP}V_C$ $C_{11-6} = 2C_{AV}V_C$ $C_{11-7} = 4C_{AT}V_C$ $C_{11-8} = 4C_{AP}V_C$
$C_{12-5} = 2C_{MP}V_C$ $C_{12-6} = 2C_{MV}V_C$ $C_{12-7} = 4C_{MT}V_C$ $C_{12-8} = 4C_{MP}V_C$
$C_{13-5} = 2C_{TP}V_C$ $C_{13-6} = 2C_{TV}V_C$ $C_{13-7} = C_{TT}V_C$ $C_{13-8} = C_{TP}V_C$
$C_{14-5} = 2C_{AP}V_C$ $C_{14-6} = 2C_{AV}V_C$ $C_{14-7} = C_{AT}V_C$ $C_{14-8} = C_{AP}V_C$
$C_{15-5} = 2C_{MP}V_C$ $C_{15-6} = 2C_{MV}V_C$ $C_{15-7} = C_{MT}V_C$ $C_{15-8} = C_{MP}V_C$
$C_{16-5} = 4C_{TP}V_C$ $C_{16-6} = 4C_{TV}V_C$ $C_{16-7} = 2C_{TT}V_C$ $C_{16-8} = 2C_{TP}V_C$
$C_{17-5} = 4C_{AP}V_C$ $C_{17-6} = 4C_{AV}V_C$ $C_{17-7} = 2C_{AT}V_C$ $C_{17-8} = 2C_{AP}V_C$
$C_{18-5} = 4C_{MP}V_C$ $C_{18-6} = 4C_{MV}V_C$ $C_{18-7} = 2C_{MT}V_C$ $C_{18-8} = 2C_{MP}V_C$
$C_{19-5} = 2C_{TP}V_C$ $C_{19-6} = 2C_{TV}V_C$ $C_{19-7} = 4C_{TT}V_C$ $C_{19-8} = 4C_{TP}V_C$
$C_{20-5} = 2C_{AP}V_C$ $C_{20-6} = 2C_{AV}V_C$ $C_{20-7} = 4C_{AT}V_C$ $C_{20-8} = 4C_{AP}V_C$
$C_{21-5} = 2C_{MP}V_C$ $C_{21-6} = 2C_{MV}V_C$ $C_{21-7} = 4C_{MT}V_C$ $C_{21-8} = 4C_{MP}V_C$
$C_{22-5} = C_{TP}V_C$ $C_{22-6} = C_{TV}V_C$ $C_{22-7} = 2C_{TT}V_C$ $C_{22-8} = 2C_{TP}V_C$
$C_{23-5} = C_{AP}V_C$ $C_{23-6} = C_{AV}V_C$ $C_{23-7} = 2C_{AT}V_C$ $C_{23-8} = 2C_{AP}V_C$
$C_{24-5} = C_{MP}V_C$ $C_{24-6} = C_{MV}V_C$ $C_{24-7} = 2C_{MT}V_C$ $C_{24-8} = 2C_{MP}V_C$

$C_{1-9} = 2C_{TV}V_C$ $C_{1-10} = 4C_{TT}V_C$ $C_{1-11} = 4C_{TP}V_C$ $C_{1-12} = 4C_{TV}V_C$
$C_{2-9} = 2C_{AV}V_C$ $C_{2-10} = 4C_{AT}V_C$ $C_{2-11} = 4C_{AP}V_C$ $C_{2-12} = 4C_{AV}V_C$
$C_{3-9} = 2C_{MV}V_C$ $C_{3-10} = 4C_{MT}V_C$ $C_{3-11} = 4C_{MP}V_C$ $C_{3-12} = 4C_{MV}V_C$
$C_{4-9} = 4C_{TV}V_C$ $C_{4-10} = 2C_{TT}V_C$ $C_{4-11} = 2C_{TP}V_C$ $C_{4-12} = 2C_{TV}V_C$
$C_{5-9} = 4C_{AV}V_C$ $C_{5-10} = 2C_{AT}V_C$ $C_{5-11} = 2C_{AP}V_C$ $C_{5-12} = 2C_{AV}V_C$
$C_{6-9} = 4C_{MV}V_C$ $C_{6-10} = 2C_{MT}V_C$ $C_{6-11} = 2C_{MP}V_C$ $C_{6-12} = 2C_{MV}V_C$

$C_{7-9} = 8C_{TV}V_C$ $C_{7-10} = 4C_{TT}V_C$ $C_{7-11} = 4C_{TP}V_C$ $C_{7-12} = 4C_{TV}V_C$
$C_{8-9} = 8C_{AV}V_C$ $C_{8-10} = 4C_{AT}V_C$ $C_{8-11} = 4C_{AP}V_C$ $C_{8-12} = 4C_{AV}V_C$
$C_{9-9} = 8C_{MV}V_C$ $C_{9-10} = 4C_{MT}V_C$ $C_{9-11} = 4C_{MP}V_C$ $C_{9-12} = 4C_{MV}V_C$
$C_{10-9} = 4C_{TV}V_C$ $C_{10-10} = 8C_{TT}V_C$ $C_{10-11} = 8C_{TP}V_C$ $C_{10-12} = 8C_{TV}V_C$
$C_{11-9} = 4C_{AV}V_C$ $C_{11-10} = 8C_{AT}V_C$ $C_{11-11} = 8C_{AP}V_C$ $C_{11-12} = 8C_{AV}V_C$
$C_{12-9} = 4C_{MV}V_C$ $C_{12-10} = 8C_{MT}V_C$ $C_{12-11} = 8C_{MP}V_C$ $C_{12-12} = 8C_{MV}V_C$
$C_{13-9} = C_{TV}V_C$ $C_{13-10} = 2C_{TT}V_C$ $C_{13-11} = 2C_{TP}V_C$ $C_{13-12} = 2C_{TV}V_C$
$C_{14-9} = C_{AV}V_C$ $C_{14-10} = 2C_{AT}V_C$ $C_{14-11} = 2C_{AP}V_C$ $C_{14-12} = 2C_{AV}V_C$
$C_{15-9} = C_{MV}V_C$ $C_{15-10} = 2C_{MT}V_C$ $C_{15-11} = 2C_{MP}V_C$ $C_{15-12} = 2C_{MV}V_C$
$C_{16-9} = 2C_{TV}V_C$ $C_{16-10} = C_{TT}V_C$ $C_{16-11} = C_{TP}V_C$ $C_{16-12} = C_{TV}V_C$
$C_{17-9} = 2C_{AV}V_C$ $C_{17-10} = C_{AT}V_C$ $C_{17-11} = C_{AP}V_C$ $C_{17-12} = C_{AV}V_C$
$C_{18-9} = 2C_{MV}V_C$ $C_{18-10} = C_{MT}V_C$ $C_{18-11} = C_{MP}V_C$ $C_{18-12} = C_{MV}V_C$
$C_{19-9} = 4C_{TV}V_C$ $C_{19-10} = 2C_{TT}V_C$ $C_{19-11} = 2C_{TP}V_C$ $C_{19-12} = 2C_{TV}V_C$
$C_{20-9} = 4C_{AV}V_C$ $C_{20-10} = 2C_{AT}V_C$ $C_{20-11} = 2C_{AP}V_C$ $C_{20-12} = 2C_{AV}V_C$
$C_{21-9} = 4C_{MV}V_C$ $C_{21-10} = 2C_{MT}V_C$ $C_{21-11} = 2C_{MP}V_C$ $C_{21-12} = 2C_{MV}V_C$
$C_{22-9} = 2C_{TV}V_C$ $C_{22-10} = 4C_{TT}V_C$ $C_{22-11} = 4C_{TP}V_C$ $C_{22-12} = 4C_{TV}V_C$
$C_{23-9} = 2C_{AV}V_C$ $C_{23-10} = 4C_{AT}V_C$ $C_{23-11} = 4C_{AP}V_C$ $C_{23-12} = 4C_{AV}V_C$
$C_{24-9} = 2C_{MV}V_C$ $C_{24-10} = 4C_{MT}V_C$ $C_{24-11} = 4C_{MP}V_C$ $C_{24-12} = 4C_{MV}V_C$

$C_{1-13} = 4C_{TT}V_C$ $C_{1-14} = 4C_{TP}V_C$ $C_{1-15} = 4C_{TV}V_C$ $C_{1-16} = 2C_{TT}V_C$
$C_{2-13} = 4C_{AT}V_C$ $C_{2-14} = 4C_{AP}V_C$ $C_{2-15} = 4C_{AV}V_C$ $C_{2-16} = 2C_{AT}V_C$
$C_{3-13} = 4C_{MT}V_C$ $C_{3-14} = 4C_{MP}V_C$ $C_{3-15} = 4C_{MV}V_C$ $C_{3-16} = 2C_{MT}V_C$
$C_{4-13} = 2C_{TT}V_C$ $C_{4-14} = 2C_{TP}V_C$ $C_{4-15} = 2C_{TV}V_C$ $C_{4-16} = 4C_{TT}V_C$
$C_{5-13} = 2C_{AT}V_C$ $C_{5-14} = 2C_{AP}V_C$ $C_{5-15} = 2C_{AV}V_C$ $C_{5-16} = 4C_{AT}V_C$
$C_{6-13} = 2C_{MT}V_C$ $C_{6-14} = 2C_{MP}V_C$ $C_{6-15} = 2C_{MV}V_C$ $C_{6-16} = 4C_{MT}V_C$
$C_{7-13} = C_{TT}V_C$ $C_{7-14} = C_{TP}V_C$ $C_{7-15} = C_{TV}V_C$ $C_{7-16} = 2C_{TT}V_C$
$C_{8-13} = C_{AT}V_C$ $C_{8-14} = C_{AP}V_C$ $C_{8-15} = C_{AV}V_C$ $C_{8-16} = 2C_{AT}V_C$
$C_{9-13} = C_{MT}V_C$ $C_{9-14} = C_{MP}V_C$ $C_{9-15} = C_{MV}V_C$ $C_{9-16} = 2C_{MT}V_C$
$C_{10-13} = 2C_{TT}V_C$ $C_{10-14} = 2C_{TP}V_C$ $C_{10-15} = 2C_{TV}V_C$ $C_{10-16} = C_{TT}V_C$
$C_{11-13} = 2C_{AT}V_C$ $C_{11-14} = 2C_{AP}V_C$ $C_{11-15} = 2C_{AV}V_C$ $C_{11-16} = C_{AT}V_C$
$C_{12-13} = 2C_{MT}V_C$ $C_{12-14} = 2C_{MP}V_C$ $C_{12-15} = 2C_{MV}V_C$ $C_{12-16} = C_{MT}V_C$
$C_{13-13} = 8C_{TT}V_C$ $C_{13-14} = 8C_{TP}V_C$ $C_{13-15} = 8C_{TV}V_C$ $C_{13-16} = 4C_{TT}V_C$
$C_{14-13} = 8C_{AT}V_C$ $C_{14-14} = 8C_{AP}V_C$ $C_{14-15} = 8C_{AV}V_C$ $C_{14-16} = 4C_{AT}V_C$
$C_{15-13} = 8C_{MT}V_C$ $C_{15-14} = 8C_{MP}V_C$ $C_{15-15} = 8C_{MV}V_C$ $C_{15-16} = 4C_{MT}V_C$
$C_{16-13} = 4C_{TT}V_C$ $C_{16-14} = 4C_{TP}V_C$ $C_{16-15} = 4C_{TV}V_C$ $C_{16-16} = 8C_{TT}V_C$
$C_{17-13} = 4C_{AT}V_C$ $C_{17-14} = 4C_{AP}V_C$ $C_{17-15} = 4C_{AV}V_C$ $C_{17-16} = 8C_{AT}V_C$
$C_{18-13} = 4C_{MT}V_C$ $C_{18-14} = 4C_{MP}V_C$ $C_{18-15} = 4C_{MV}V_C$ $C_{18-16} = 8C_{MT}V_C$
$C_{19-13} = 2C_{TT}V_C$ $C_{19-14} = 2C_{TP}V_C$ $C_{19-15} = 2C_{TV}V_C$ $C_{19-16} = 4C_{TT}V_C$
$C_{20-13} = 2C_{AT}V_C$ $C_{20-14} = 2C_{AP}V_C$ $C_{20-15} = 2C_{AV}V_C$ $C_{20-16} = 4C_{AT}V_C$
$C_{21-13} = 2C_{MT}V_C$ $C_{21-14} = 2C_{MP}V_C$ $C_{21-15} = 2C_{MV}V_C$ $C_{21-16} = 4C_{MT}V_C$
$C_{22-13} = 4C_{TT}V_C$ $C_{22-14} = 4C_{TP}V_C$ $C_{22-15} = 4C_{TV}V_C$ $C_{22-16} = 2C_{TT}V_C$
$C_{23-13} = 4C_{AT}V_C$ $C_{23-14} = 4C_{AP}V_C$ $C_{23-15} = 4C_{AV}V_C$ $C_{23-16} = 2C_{AT}V_C$
$C_{24-13} = 4C_{MT}V_C$ $C_{24-14} = 4C_{MP}V_C$ $C_{24-15} = 4C_{MV}V_C$ $C_{24-16} = 2C_{MT}V_C$

$C_{1-17} = 2C_{TP}V_C$ $C_{1-18} = 2C_{TV}V_C$ $C_{1-19} = C_{TT}V_C$ $C_{1-20} = C_{TP}V_C$
$C_{2-17} = 2C_{AP}V_C$ $C_{2-18} = 2C_{AV}V_C$ $C_{2-19} = C_{AT}V_C$ $C_{2-20} = C_{AP}V_C$
$C_{3-17} = 2C_{MP}V_C$ $C_{3-18} = 2C_{MV}V_C$ $C_{3-19} = C_{MT}V_C$ $C_{3-20} = C_{MP}V_C$
$C_{4-17} = 4C_{TP}V_C$ $C_{4-18} = 4C_{TV}V_C$ $C_{4-19} = 2C_{TT}V_C$ $C_{4-20} = 2C_{TP}V_C$
$C_{5-17} = 4C_{AP}V_C$ $C_{5-18} = 4C_{AV}V_C$ $C_{5-19} = 2C_{AT}V_C$ $C_{5-20} = 2C_{AP}V_C$
$C_{6-17} = 4C_{MP}V_C$ $C_{6-18} = 4C_{MV}V_C$ $C_{6-19} = 2C_{MT}V_C$ $C_{6-20} = 2C_{MP}V_C$
$C_{7-17} = 2C_{TP}V_C$ $C_{7-18} = 2C_{TV}V_C$ $C_{7-19} = 4C_{TT}V_C$ $C_{7-20} = 4C_{TP}V_C$
$C_{8-17} = 2C_{AP}V_C$ $C_{8-18} = 2C_{AV}V_C$ $C_{8-19} = 4C_{AT}V_C$ $C_{8-20} = 4C_{AP}V_C$
$C_{9-17} = 2C_{MP}V_C$ $C_{9-18} = 2C_{MV}V_C$ $C_{9-19} = 4C_{MT}V_C$ $C_{9-20} = 4C_{MP}V_C$
$C_{10-17} = C_{TP}V_C$ $C_{10-18} = C_{TV}V_C$ $C_{10-19} = 2C_{TT}V_C$ $C_{10-20} = 2C_{TP}V_C$
$C_{11-17} = C_{AP}V_C$ $C_{11-18} = C_{AV}V_C$ $C_{11-19} = 2C_{AT}V_C$ $C_{11-20} = 2C_{AP}V_C$
$C_{12-17} = C_{MP}V_C$ $C_{12-18} = C_{MV}V_C$ $C_{12-19} = 2C_{MT}V_C$ $C_{12-20} = 2C_{MP}V_C$
$C_{13-17} = 4C_{TP}V_C$ $C_{13-18} = 4C_{TV}V_C$ $C_{13-19} = 2C_{TT}V_C$ $C_{13-20} = 2C_{TP}V_C$
$C_{14-17} = 4C_{AP}V_C$ $C_{14-18} = 4C_{AV}V_C$ $C_{14-19} = 2C_{AT}V_C$ $C_{14-20} = 2C_{AP}V_C$
$C_{15-17} = 4C_{MP}V_C$ $C_{15-18} = 4C_{MV}V_C$ $C_{15-19} = 2C_{MT}V_C$ $C_{15-20} = 2C_{MP}V_C$
$C_{16-17} = 8C_{TP}V_C$ $C_{16-18} = 8C_{TV}V_C$ $C_{16-19} = 4C_{TT}V_C$ $C_{16-20} = 4C_{TP}V_C$
$C_{17-17} = 8C_{AP}V_C$ $C_{17-18} = 8C_{AV}V_C$ $C_{17-19} = 4C_{AT}V_C$ $C_{17-20} = 4C_{AP}V_C$
$C_{18-17} = 8C_{MP}V_C$ $C_{18-18} = 8C_{MV}V_C$ $C_{18-19} = 4C_{MT}V_C$ $C_{18-20} = 4C_{MP}V_C$
$C_{19-17} = 4C_{TP}V_C$ $C_{19-18} = 4C_{TV}V_C$ $C_{19-19} = 8C_{TT}V_C$ $C_{19-20} = 8C_{TP}V_C$
$C_{20-17} = 4C_{AP}V_C$ $C_{20-18} = 4C_{AV}V_C$ $C_{20-19} = 8C_{AT}V_C$ $C_{20-20} = 8C_{AP}V_C$
$C_{21-17} = 4C_{MP}V_C$ $C_{21-18} = 4C_{MV}V_C$ $C_{21-19} = 8C_{MT}V_C$ $C_{21-20} = 8C_{MP}V_C$
$C_{22-17} = 2C_{TP}V_C$ $C_{22-18} = 2C_{TV}V_C$ $C_{22-19} = 4C_{TT}V_C$ $C_{22-20} = 4C_{TP}V_C$
$C_{23-17} = 2C_{AP}V_C$ $C_{23-18} = 2C_{AV}V_C$ $C_{23-19} = 4C_{AT}V_C$ $C_{23-20} = 4C_{AP}V_C$
$C_{24-17} = 2C_{MP}V_C$ $C_{24-18} = 2C_{MV}V_C$ $C_{24-19} = 4C_{MT}V_C$ $C_{24-20} = 4C_{MP}V_C$

$C_{1-21} = C_{TV}V_C$ $C_{1-22} = 2C_{TT}V_C$ $C_{1-23} = 2C_{TP}V_C$ $C_{1-24} = 2C_{TV}V_C$
$C_{2-21} = C_{AV}V_C$ $C_{2-22} = 2C_{AT}V_C$ $C_{2-23} = 2C_{AP}V_C$ $C_{2-24} = 2C_{AV}V_C$
$C_{3-21} = C_{MV}V_C$ $C_{3-22} = 2C_{MT}V_C$ $C_{3-23} = 2C_{MP}V_C$ $C_{3-24} = 2C_{MV}V_C$
$C_{4-21} = 2C_{TV}V_C$ $C_{4-22} = C_{TT}V_C$ $C_{4-23} = C_{TP}V_C$ $C_{4-24} = C_{TV}V_C$
$C_{5-21} = 2C_{AV}V_C$ $C_{5-22} = C_{AT}V_C$ $C_{5-23} = C_{AP}V_C$ $C_{5-24} = C_{AV}V_C$
$C_{6-21} = 2C_{MV}V_C$ $C_{6-22} = C_{MT}V_C$ $C_{6-23} = C_{MP}V_C$ $C_{6-24} = C_{MV}V_C$
$C_{7-21} = 4C_{TV}V_C$ $C_{7-22} = 2C_{TT}V_C$ $C_{7-23} = 2C_{TP}V_C$ $C_{7-24} = 2C_{TV}V_C$
$C_{8-21} = 4C_{AV}V_C$ $C_{8-22} = 2C_{AT}V_C$ $C_{8-23} = 2C_{AP}V_C$ $C_{8-24} = 2C_{AV}V_C$
$C_{9-21} = 4C_{MV}V_C$ $C_{9-22} = 2C_{MT}V_C$ $C_{9-23} = 2C_{MP}V_C$ $C_{9-24} = 2C_{MV}V_C$
$C_{10-21} = 2C_{TV}V_C$ $C_{10-22} = 4C_{TT}V_C$ $C_{10-23} = 4C_{TP}V_C$ $C_{10-24} = 4C_{TV}V_C$
$C_{11-21} = 2C_{AV}V_C$ $C_{11-22} = 4C_{AT}V_C$ $C_{11-23} = 4C_{AP}V_C$ $C_{11-24} = 4C_{AV}V_C$
$C_{12-21} = 2C_{MV}V_C$ $C_{12-22} = 4C_{MT}V_C$ $C_{12-23} = 4C_{MP}V_C$ $C_{12-24} = 4C_{MV}V_C$
$C_{13-21} = 2C_{TV}V_C$ $C_{13-22} = 4C_{TT}V_C$ $C_{13-23} = 4C_{TP}V_C$ $C_{13-24} = 4C_{TV}V_C$
$C_{14-21} = 2C_{AV}V_C$ $C_{14-22} = 4C_{AT}V_C$ $C_{14-23} = 4C_{AP}V_C$ $C_{14-24} = 4C_{AV}V_C$
$C_{15-21} = 2C_{MV}V_C$ $C_{15-22} = 4C_{MT}V_C$ $C_{15-23} = 4C_{MP}V_C$ $C_{15-24} = 4C_{MV}V_C$
$C_{16-21} = 4C_{TV}V_C$ $C_{16-22} = 2C_{TT}V_C$ $C_{16-23} = 2C_{TP}V_C$ $C_{16-24} = 2C_{TV}V_C$
$C_{17-21} = 4C_{AV}V_C$ $C_{17-22} = 2C_{AT}V_C$ $C_{17-23} = 2C_{AP}V_C$ $C_{17-24} = 2C_{AV}V_C$
$C_{18-21} = 4C_{MV}V_C$ $C_{18-22} = 2C_{MT}V_C$ $C_{18-23} = 2C_{MP}V_C$ $C_{18-24} = 2C_{MV}V_C$

$C_{19-21} = 8C_{TV}V_C$	$C_{19-22} = 4C_{TT}V_C$	$C_{19-23} = 4C_{TP}V_C$	$C_{19-24} = 4C_{TV}V_C$
$C_{20-21} = 8C_{AV}V_C$	$C_{20-22} = 4C_{AT}V_C$	$C_{20-23} = 4C_{AP}V_C$	$C_{20-24} = 4C_{AV}V_C$
$C_{21-21} = 8C_{MV}V_C$	$C_{21-22} = 4C_{MT}V_C$	$C_{21-23} = 4C_{MP}V_C$	$C_{21-24} = 4C_{MV}V_C$
$C_{22-21} = 4C_{TV}V_C$	$C_{22-22} = 8C_{TT}V_C$	$C_{22-23} = 8C_{TP}V_C$	$C_{22-24} = 8C_{TV}V_C$
$C_{23-21} = 4C_{AV}V_C$	$C_{23-22} = 8C_{AT}V_C$	$C_{23-23} = 8C_{AP}V_C$	$C_{23-24} = 8C_{AV}V_C$
$C_{24-21} = 4C_{MV}V_C$	$C_{24-22} = 8C_{MT}V_C$	$C_{24-23} = 8C_{MP}V_C$	$C_{24-24} = 8C_{MV}V_C$

While the integration presented in Equation (A.1) produces the fully populated consistent matrix presented above, it has been found by Huebner et al. (2001) that for heat capacitance matrix, which matrix $\int_\Omega (N^T C_E N) d\Omega$ is equivalent to for coupled heat and moisture transfer analysis, consistent matrices require smaller time steps than lumped ones. Also, consistent matrices may cause unrealistic temperature oscillations. In addition, if the explicit method is used in the finite difference method for time discretization in the analysis, the lumped matrix is a must. For all these reasons, in this study, the consistent matrix $\int_\Omega (N^T C_E N) d\Omega$ has been converted to the lumped form by summing up the elements in each row and assigning the product to the diagonal while all the other elements of the matrix are set to zero, producing a block diagonal matrix with the following diagonal elements:

$$C_{1-1} = C_{4-4} = C_{7-7} = C_{10-10} = C_{13-13} = C_{16-16} = C_{19-19} = C_{22-22} = V_p C_{TT}$$

$$C_{2-1} = C_{5-4} = C_{8-7} = C_{11-10} = C_{14-13} = C_{17-16} = C_{20-19} = C_{23-22} = V_p C_{AT}$$

$$C_{3-1} = C_{6-4} = C_{9-7} = C_{12-10} = C_{15-13} = C_{18-16} = C_{21-19} = C_{24-22} = V_p C_{MT}$$

$$C_{1-2} = C_{4-5} = C_{7-8} = C_{10-11} = C_{13-14} = C_{16-17} = C_{19-20} = C_{22-23} = V_p C_{TP}$$

$$C_{2-2} = C_{5-5} = C_{8-8} = C_{11-11} = C_{14-14} = C_{17-17} = C_{20-20} = C_{23-23} = V_p C_{AP}$$

$$C_{3-2} = C_{6-5} = C_{9-8} = C_{12-11} = C_{15-14} = C_{18-17} = C_{21-20} = C_{24-23} = V_p C_{MP}$$

$$C_{1-3} = C_{4-6} = C_{7-9} = C_{10-12} = C_{13-15} = C_{16-18} = C_{19-21} = C_{22-24} = V_p C_{TV}$$

$$C_{2-3} = C_{5-6} = C_{8-9} = C_{11-12} = C_{14-15} = C_{17-18} = C_{20-21} = C_{23-24} = V_p C_{AV}$$

$$C_{3-3} = C_{6-6} = C_{9-9} = C_{12-12} = C_{15-15} = C_{18-18} = C_{21-21} = C_{24-24} = V_p C_{MV}$$

where V_p is the volume of the element divided by the number of nodes and is equal to $\frac{abc}{8}$, where a, b and c are defined in Figure 4-1.

A.3 Elements of $\int_\Omega(\nabla N^T K_E \nabla N)d\Omega$

Matrix $\int_\Omega(\nabla N^T K_E \nabla N)d\Omega$, introduced in Equation (4.86), is a 24×24 matrix, with elements given the notation K_{i-j}, where i is the row number and j is the column number.

$$\int_\Omega(\nabla N^T K_E \nabla N)d\Omega = \int_{-1}^{1}\int_{-1}^{1}\int_{-1}^{1}(\nabla N^T K_E \nabla N)\det[J]d\eta\, d\zeta\, d\xi = K_{i-j} \qquad (A.2)$$

With K_{TT}, K_{TP}, K_{TV}, K_{AT}, K_{AP}, K_{AV}, K_{MT}, K_{MP}, and K_{MV} defined in Table 4-1, and A equals $\frac{bc}{36a}$; B equals $\frac{ac}{36b}$; and C equals $\frac{ab}{36c}$, where a, b and c are defined in Figure 4-1, K_{i-j} can be given as:

$$\begin{aligned}
K_{1-1} &= 4AK_{TT} + 4BK_{TT} + 4CK_{TT} & K_{1-2} &= 4AK_{TP} + 4BK_{TP} + 4CK_{TP}\\
K_{2-1} &= 4AK_{AT} + 4BK_{AT} + 4CK_{AT} & K_{2-2} &= 4AK_{AP} + 4BK_{AP} + 4CK_{AP}\\
K_{3-1} &= 4AK_{MT} + 4BK_{MT} + 4CK_{MT} & K_{3-2} &= 4AK_{MP} + 4BK_{MP} + 4CK_{MP}\\
K_{4-1} &= 2AK_{TT} + 2BK_{TT} - 4CK_{TT} & K_{4-2} &= 2AK_{TP} + 2BK_{TP} - 4CK_{TP}\\
K_{5-1} &= 2AK_{AT} + 2BK_{AT} - 4CK_{AT} & K_{5-2} &= 2AK_{AP} + 2BK_{AP} - 4CK_{AP}\\
K_{6-1} &= 2AK_{MT} + 2BK_{MT} - 4CK_{MT} & K_{6-2} &= 2AK_{MP} + 2BK_{MP} - 4CK_{MP}\\
K_{7-1} &= -2AK_{TT} + BK_{TT} - 2CK_{TT} & K_{7-2} &= -2AK_{TP} + BK_{TP} - 2CK_{TP}\\
K_{8-1} &= -2AK_{AT} + BK_{AT} - 2CK_{AT} & K_{8-2} &= -2AK_{AP} + BK_{AP} - 2CK_{AP}\\
K_{9-1} &= -2AK_{MT} + BK_{MT} - 2CK_{MT} & K_{9-2} &= -2AK_{MP} + BK_{MP} - 2CK_{MP}\\
K_{10-1} &= -4AK_{TT} + 2BK_{TT} + 2CK_{TT} & K_{10-2} &= -4AK_{TP} + 2BK_{TP} + 2CK_{TP}\\
K_{11-1} &= -4AK_{AT} + 2BK_{AT} + 2CK_{AT} & K_{11-2} &= -4AK_{AP} + 2BK_{AP} + 2CK_{AP}\\
K_{12-1} &= -4AK_{MT} + 2BK_{MT} + 2CK_{MT} & K_{12-2} &= -4AK_{MP} + 2BK_{MP} + 2CK_{MP}\\
K_{13-1} &= 2AK_{TT} - 4BK_{TT} + 2CK_{TT} & K_{13-2} &= 2AK_{TP} - 4BK_{TP} + 2CK_{TP}\\
K_{14-1} &= 2AK_{AT} - 4BK_{AT} + 2CK_{AT} & K_{14-2} &= 2AK_{AP} - 4BK_{AP} + 2CK_{AP}\\
K_{15-1} &= 2AK_{MT} - 4BK_{MT} + 2CK_{MT} & K_{15-2} &= 2AK_{MP} - 4BK_{MP} + 2CK_{MP}\\
K_{16-1} &= AK_{TT} - 2BK_{TT} - 2CK_{TT} & K_{16-2} &= AK_{TP} - 2BK_{TP} - 2CK_{TP}\\
K_{17-1} &= AK_{AT} - 2BK_{AT} - 2CK_{AT} & K_{17-2} &= AK_{AP} - 2BK_{AP} - 2CK_{AP}\\
K_{18-1} &= AK_{MT} - 2BK_{MT} - 2CK_{MT} & K_{18-2} &= AK_{MP} - 2BK_{MP} - 2CK_{MP}\\
K_{19-1} &= -AK_{TT} - BK_{TT} - CK_{TT} & K_{19-2} &= -AK_{TP} - BK_{TP} - CK_{TP}\\
K_{20-1} &= -AK_{AT} - BK_{AT} - CK_{AT} & K_{20-2} &= -AK_{AP} - BK_{AP} - CK_{AP}\\
K_{21-1} &= -AK_{MT} - BK_{MT} - CK_{MT} & K_{21-2} &= -AK_{MP} - BK_{MP} - CK_{MP}\\
K_{22-1} &= -2AK_{TT} - 2BK_{TT} + CK_{TT} & K_{22-2} &= -2AK_{TP} - 2BK_{TP} + CK_{TP}\\
K_{23-1} &= -2AK_{AT} - 2BK_{AT} + CK_{AT} & K_{23-2} &= -2AK_{AP} - 2BK_{AP} + CK_{AP}\\
K_{24-1} &= -2AK_{MT} - 2BK_{MT} + CK_{MT} & K_{24-2} &= -2AK_{MP} - 2BK_{MP} + CK_{MP}
\end{aligned}$$

$$\begin{aligned}
K_{1-3} &= 4AK_{TV} + 4BK_{TV} + 4CK_{TV} & K_{1-4} &= 2AK_{TT} + 2BK_{TT} - 4CK_{TT}\\
K_{2-3} &= 4AK_{AV} + 4BK_{AV} + 4CK_{AV} & K_{2-4} &= 2AK_{AT} + 2BK_{AT} - 4CK_{AT}\\
K_{3-3} &= 4AK_{MV} + 4BK_{MV} + 4CK_{MV} & K_{3-4} &= 2AK_{MT} + 2BK_{MT} - 4CK_{MT}
\end{aligned}$$

$$K_{4-3} = 2AK_{TV} + 2BK_{TV} - 4CK_{TV} \qquad K_{4-4} = 4AK_{TT} + 4BK_{TT} + 4CK_{TT}$$
$$K_{5-3} = 2AK_{AV} + 2BK_{AV} - 4CK_{AV} \qquad K_{5-4} = 4AK_{AT} + 4BK_{AT} + 4CK_{AT}$$
$$K_{6-3} = 2AK_{MV} + 2BK_{MV} - 4CK_{MV} \qquad K_{6-4} = 4AK_{MT} + 4BK_{MT} + 4CK_{MT}$$
$$K_{7-3} = -2AK_{TV} + BK_{TV} - 2CK_{TV} \qquad K_{7-4} = -4AK_{TT} + 2BK_{TT} + 2CK_{TT}$$
$$K_{8-3} = -2AK_{AV} + BK_{AV} - 2CK_{AV} \qquad K_{8-4} = -4AK_{AT} + 2BK_{AT} + 2CK_{AT}$$
$$K_{9-3} = -2AK_{MV} + BK_{MV} - 2CK_{MV} \qquad K_{9-4} = -4AK_{MT} + 2BK_{MT} + 2CK_{MT}$$
$$K_{10-3} = -4AK_{TV} + 2BK_{TV} + 2CK_{TV} \qquad K_{10-4} = -2AK_{TT} + BK_{TT} - 2CK_{TT}$$
$$K_{11-3} = -4AK_{AV} + 2BK_{AV} + 2CK_{AV} \qquad K_{11-4} = -2AK_{AT} + BK_{AT} - 2CK_{AT}$$
$$K_{12-3} = -4AK_{MV} + 2BK_{MV} + 2CK_{MV} \qquad K_{12-4} = -2AK_{MT} + BK_{MT} - 2CK_{MT}$$
$$K_{13-3} = 2AK_{TV} - 4BK_{TV} + 2CK_{TV} \qquad K_{13-4} = AK_{TT} - 2BK_{TT} - 2CK_{TT}$$
$$K_{14-3} = 2AK_{AV} - 4BK_{AV} + 2CK_{AV} \qquad K_{14-4} = AK_{AT} - 2BK_{AT} - 2CK_{AT}$$
$$K_{15-3} = 2AK_{MV} - 4BK_{MV} + 2CK_{MV} \qquad K_{15-4} = AK_{MT} - 2BK_{MT} - 2CK_{MT}$$
$$K_{16-3} = AK_{TV} - 2BK_{TV} - 2CK_{TV} \qquad K_{16-4} = 2AK_{TT} - 4BK_{TT} + 2CK_{TT}$$
$$K_{17-3} = AK_{AV} - 2BK_{AV} - 2CK_{AV} \qquad K_{17-4} = 2AK_{AT} - 4BK_{AT} + 2CK_{AT}$$
$$K_{18-3} = AK_{MV} - 2BK_{MV} - 2CK_{MV} \qquad K_{18-4} = 2AK_{MT} - 4BK_{MT} + 2CK_{MT}$$
$$K_{19-3} = -AK_{TV} - BK_{TV} - CK_{TV} \qquad K_{19-4} = -2AK_{TT} - 2BK_{TT} + CK_{TT}$$
$$K_{20-3} = -AK_{AV} - BK_{AV} - CK_{AV} \qquad K_{20-4} = -2AK_{AT} - 2BK_{AT} + CK_{AT}$$
$$K_{21-3} = -AK_{MV} - BK_{MV} - CK_{MV} \qquad K_{21-4} = -2AK_{MT} - 2BK_{MT} + CK_{MT}$$
$$K_{22-3} = -2AK_{TV} - 2BK_{TV} + CK_{TV} \qquad K_{22-4} = -AK_{TT} - BK_{TT} - CK_{TT}$$
$$K_{23-3} = -2AK_{AV} - 2BK_{AV} + CK_{AV} \qquad K_{23-4} = -AK_{AT} - BK_{AT} - CK_{AT}$$
$$K_{24-3} = -2AK_{MV} - 2BK_{MV} + CK_{MV} \qquad K_{24-4} = -AK_{MT} - BK_{MT} - CK_{MT}$$

$$K_{1-5} = 2AK_{TP} + 2BK_{TP} - 4CK_{TP} \qquad K_{1-6} = 2AK_{TV} + 2BK_{TV} - 4CK_{TV}$$
$$K_{2-5} = 2AK_{AP} + 2BK_{AP} - 4CK_{AP} \qquad K_{2-6} = 2AK_{AV} + 2BK_{AV} - 4CK_{AV}$$
$$K_{3-5} = 2AK_{MP} + 2BK_{MP} - 4CK_{MP} \qquad K_{3-6} = 2AK_{MV} + 2BK_{MV} - 4CK_{MV}$$
$$K_{4-5} = 4AK_{TP} + 4BK_{TP} + 4CK_{TP} \qquad K_{4-6} = 4AK_{TV} + 4BK_{TV} + 4CK_{TV}$$
$$K_{5-5} = 4AK_{AP} + 4BK_{AP} + 4CK_{AP} \qquad K_{5-6} = 4AK_{AV} + 4BK_{AV} + 4CK_{AV}$$
$$K_{6-5} = 4AK_{MP} + 4BK_{MP} + 4CK_{MP} \qquad K_{6-6} = 4AK_{MV} + 4BK_{MV} + 4CK_{MV}$$
$$K_{7-5} = -4AK_{TP} + 2BK_{TP} + 2CK_{TP} \qquad K_{7-6} = -4AK_{TV} + 2BK_{TV} + 2CK_{TV}$$
$$K_{8-5} = -4AK_{AP} + 2BK_{AP} + 2CK_{AP} \qquad K_{8-6} = -4AK_{AV} + 2BK_{AV} + 2CK_{AV}$$
$$K_{9-5} = -4AK_{MP} + 2BK_{MP} + 2CK_{MP} \qquad K_{9-6} = -4AK_{MV} + 2BK_{MV} + 2CK_{MV}$$
$$K_{10-5} = -2AK_{TP} + BK_{TP} - 2CK_{TP} \qquad K_{10-6} = -2AK_{TV} + BK_{TV} - 2CK_{TV}$$
$$K_{11-5} = -2AK_{AP} + BK_{AP} - 2CK_{AP} \qquad K_{11-6} = -2AK_{AV} + BK_{AV} - 2CK_{AV}$$
$$K_{12-5} = -2AK_{MP} + BK_{MP} - 2CK_{MP} \qquad K_{12-6} = -2AK_{MV} + BK_{MV} - 2CK_{MV}$$
$$K_{13-5} = AK_{TP} - 2BK_{TP} - 2CK_{TP} \qquad K_{13-6} = AK_{TV} - 2BK_{TV} - 2CK_{TV}$$
$$K_{14-5} = AK_{AP} - 2BK_{AP} - 2CK_{AP} \qquad K_{14-6} = AK_{AV} - 2BK_{AV} - 2CK_{AV}$$
$$K_{15-5} = AK_{MP} - 2BK_{MP} - 2CK_{MP} \qquad K_{15-6} = AK_{MV} - 2BK_{MV} - 2CK_{MV}$$
$$K_{16-5} = 2AK_{TP} - 4BK_{TP} + 2CK_{TP} \qquad K_{16-6} = 2AK_{TV} - 4BK_{TV} + 2CK_{TV}$$
$$K_{17-5} = 2AK_{AP} - 4BK_{AP} + 2CK_{AP} \qquad K_{17-6} = 2AK_{AV} - 4BK_{AV} + 2CK_{AV}$$
$$K_{18-5} = 2AK_{MP} - 4BK_{MP} + 2CK_{MP} \qquad K_{18-6} = 2AK_{MV} - 4BK_{MV} + 2CK_{MV}$$
$$K_{19-5} = -2AK_{TP} - 2BK_{TP} + CK_{TP} \qquad K_{19-6} = -2AK_{TV} - 2BK_{TV} + CK_{TV}$$
$$K_{20-5} = -2AK_{AP} - 2BK_{AP} + CK_{AP} \qquad K_{20-6} = -2AK_{AV} - 2BK_{AV} + CK_{AV}$$
$$K_{21-5} = -2AK_{MP} - 2BK_{MP} + CK_{MP} \qquad K_{21-6} = -2AK_{MV} - 2BK_{MV} + CK_{MV}$$

$$K_{22-5} = -AK_{TP} - BK_{TP} - CK_{TP} \qquad K_{22-6} = -AK_{TV} - BK_{TV} - CK_{TV}$$
$$K_{23-5} = -AK_{AP} - BK_{AP} - CK_{AP} \qquad K_{23-6} = -AK_{AV} - BK_{AV} - CK_{AV}$$
$$K_{24-5} = -AK_{MP} - BK_{MP} - CK_{MP} \qquad K_{24-6} = -AK_{MV} - BK_{MV} - CK_{MV}$$

$$K_{1-7} = -2AK_{TT} + BK_{TT} - 2CK_{TT} \qquad K_{1-8} = -2AK_{TP} + BK_{TP} - 2CK_{TP}$$
$$K_{2-7} = -2AK_{AT} + BK_{AT} - 2CK_{AT} \qquad K_{2-8} = -2AK_{AP} + BK_{AP} - 2CK_{AP}$$
$$K_{3-7} = -2AK_{MT} + BK_{MT} - 2CK_{MT} \qquad K_{3-8} = -2AK_{MP} + BK_{MP} - 2CK_{MP}$$
$$K_{4-7} = -4AK_{TT} + 2BK_{TT} + 2CK_{TT} \qquad K_{4-8} = -4AK_{TP} + 2BK_{TP} + 2CK_{TP}$$
$$K_{5-7} = -4AK_{AT} + 2BK_{AT} + 2CK_{AT} \qquad K_{5-8} = -4AK_{AP} + 2BK_{AP} + 2CK_{AP}$$
$$K_{6-7} = -4AK_{MT} + 2BK_{MT} + 2CK_{MT} \qquad K_{6-8} = -4AK_{MP} + 2BK_{MP} + 2CK_{MP}$$
$$K_{7-7} = 4AK_{TT} + 4BK_{TT} + 4CK_{TT} \qquad K_{7-8} = 4AK_{TP} + 4BK_{TP} + 4CK_{TP}$$
$$K_{8-7} = 4AK_{AT} + 4BK_{AT} + 4CK_{AT} \qquad K_{8-8} = 4AK_{AP} + 4BK_{AP} + 4CK_{AP}$$
$$K_{9-7} = 4AK_{MT} + 4BK_{MT} + 4CK_{MT} \qquad K_{9-8} = 4AK_{MP} + 4BK_{MP} + 4CK_{MP}$$
$$K_{10-7} = 2AK_{TT} + 2BK_{TT} - 4CK_{TT} \qquad K_{10-8} = 2AK_{TP} + 2BK_{TP} - 4CK_{TP}$$
$$K_{11-7} = 2AK_{AT} + 2BK_{AT} - 4CK_{AT} \qquad K_{11-8} = 2AK_{AP} + 2BK_{AP} - 4CK_{AP}$$
$$K_{12-7} = 2AK_{MT} + 2BK_{MT} - 4CK_{MT} \qquad K_{12-8} = 2AK_{MP} + 2BK_{MP} - 4CK_{MP}$$
$$K_{13-7} = -AK_{TT} - BK_{TT} - CK_{TT} \qquad K_{13-8} = -AK_{TP} - BK_{TP} - CK_{TP}$$
$$K_{14-7} = -AK_{AT} - BK_{AT} - CK_{AT} \qquad K_{14-8} = -AK_{AP} - BK_{AP} - CK_{AP}$$
$$K_{15-7} = -AK_{MT} - BK_{MT} - CK_{MT} \qquad K_{15-8} = -AK_{MP} - BK_{MP} - CK_{MP}$$
$$K_{16-7} = -2AK_{TT} - 2BK_{TT} + CK_{TT} \qquad K_{16-8} = -2AK_{TP} - 2BK_{TP} + CK_{TP}$$
$$K_{17-7} = -2AK_{AT} - 2BK_{AT} + CK_{AT} \qquad K_{17-8} = -2AK_{AP} - 2BK_{AP} + CK_{AP}$$
$$K_{18-7} = -2AK_{MT} - 2BK_{MT} + CK_{MT} \qquad K_{18-8} = -2AK_{MP} - 2BK_{MP} + CK_{MP}$$
$$K_{19-7} = 2AK_{TT} - 4BK_{TT} + 2CK_{TT} \qquad K_{19-8} = 2AK_{TP} - 4BK_{TP} + 2CK_{TP}$$
$$K_{20-7} = 2AK_{AT} - 4BK_{AT} + 2CK_{AT} \qquad K_{20-8} = 2AK_{AP} - 4BK_{AP} + 2CK_{AP}$$
$$K_{21-7} = 2AK_{MT} - 4BK_{MT} + 2CK_{MT} \qquad K_{21-8} = 2AK_{MP} - 4BK_{MP} + 2CK_{MP}$$
$$K_{22-7} = AK_{TT} - 2BK_{TT} - 2CK_{TT} \qquad K_{22-8} = AK_{TP} - 2BK_{TP} - 2CK_{TP}$$
$$K_{23-7} = AK_{AT} - 2BK_{AT} - 2CK_{AT} \qquad K_{23-8} = AK_{AP} - 2BK_{AP} - 2CK_{AP}$$
$$K_{24-7} = AK_{MT} - 2BK_{MT} - 2CK_{MT} \qquad K_{24-8} = AK_{MP} - 2BK_{MP} - 2CK_{MP}$$

$$K_{1-9} = -2AK_{TV} + BK_{TV} - 2CK_{TV} \qquad K_{1-10} = -4AK_{TT} + 2BK_{TT} + 2CK_{TT}$$
$$K_{2-9} = -2AK_{AV} + BK_{AV} - 2CK_{AV} \qquad K_{2-10} = -4AK_{AT} + 2BK_{AT} + 2CK_{AT}$$
$$K_{3-9} = -2AK_{MV} + BK_{MV} - 2CK_{MV} \qquad K_{3-10} = -4AK_{MT} + 2BK_{MT} + 2CK_{MT}$$
$$K_{4-9} = -4AK_{TV} + 2BK_{TV} + 2CK_{TV} \qquad K_{4-10} = -2AK_{TT} + BK_{TT} - 2CK_{TT}$$
$$K_{5-9} = -4AK_{AV} + 2BK_{AV} + 2CK_{AV} \qquad K_{5-10} = -2AK_{AT} + BK_{AT} - 2CK_{AT}$$
$$K_{6-9} = -4AK_{MV} + 2BK_{MV} + 2CK_{MV} \qquad K_{6-10} = -2AK_{MT} + BK_{MT} - 2CK_{MT}$$
$$K_{7-9} = 4AK_{TV} + 4BK_{TV} + 4CK_{TV} \qquad K_{7-10} = 2AK_{TT} + 2BK_{TT} - 4CK_{TT}$$
$$K_{8-9} = 4AK_{AV} + 4BK_{AV} + 4CK_{AV} \qquad K_{8-10} = 2AK_{AT} + 2BK_{AT} - 4CK_{AT}$$
$$K_{9-9} = 4AK_{MV} + 4BK_{MV} + 4CK_{MV} \qquad K_{9-10} = 2AK_{MT} + 2BK_{MT} - 4CK_{MT}$$
$$K_{10-9} = 2AK_{TV} + 2BK_{TV} - 4CK_{TV} \qquad K_{10-10} = 4AK_{TT} + 4BK_{TT} + 4CK_{TT}$$
$$K_{11-9} = 2AK_{AV} + 2BK_{AV} - 4CK_{AV} \qquad K_{11-10} = 4AK_{AT} + 4BK_{AT} + 4CK_{AT}$$
$$K_{12-9} = 2AK_{MV} + 2BK_{MV} - 4CK_{MV} \qquad K_{12-10} = 4AK_{MT} + 4BK_{MT} + 4CK_{MT}$$

$$K_{13-9} = -AK_{TV} - BK_{TV} - CK_{TV} \qquad K_{13-10} = -2AK_{TT} - 2BK_{TT} + CK_{TT}$$
$$K_{14-9} = -AK_{AV} - BK_{AV} - CK_{AV} \qquad K_{14-10} = -2AK_{AT} - 2BK_{AT} + CK_{AT}$$
$$K_{15-9} = -AK_{MV} - BK_{MV} - CK_{MV} \qquad K_{15-10} = -2AK_{MT} - 2BK_{MT} + CK_{MT}$$
$$K_{16-9} = -2AK_{TV} - 2BK_{TV} + CK_{TV} \qquad K_{16-10} = -AK_{TT} - BK_{TT} - CK_{TT}$$
$$K_{17-9} = -2AK_{AV} - 2BK_{AV} + CK_{AV} \qquad K_{17-10} = -AK_{AT} - BK_{AT} - CK_{AT}$$
$$K_{18-9} = -2AK_{MV} - 2BK_{MV} + CK_{MV} \qquad K_{18-10} = -AK_{MT} - BK_{MT} - CK_{MT}$$
$$K_{19-9} = 2AK_{TV} - 4BK_{TV} + 2CK_{TV} \qquad K_{19-10} = AK_{TT} - 2BK_{TT} - 2CK_{TT}$$
$$K_{20-9} = 2AK_{AV} - 4BK_{AV} + 2CK_{AV} \qquad K_{20-10} = AK_{AT} - 2BK_{AT} - 2CK_{AT}$$
$$K_{21-9} = 2AK_{MV} - 4BK_{MV} + 2CK_{MV} \qquad K_{21-10} = AK_{MT} - 2BK_{MT} - 2CK_{MT}$$
$$K_{22-9} = AK_{TV} - 2BK_{TV} - 2CK_{TV} \qquad K_{22-10} = 2AK_{TT} - 4BK_{TT} + 2CK_{TT}$$
$$K_{23-9} = AK_{AV} - 2BK_{AV} - 2CK_{AV} \qquad K_{23-10} = 2AK_{AT} - 4BK_{AT} + 2CK_{AT}$$
$$K_{24-9} = AK_{MV} - 2BK_{MV} - 2CK_{MV} \qquad K_{24-10} = 2AK_{MT} - 4BK_{MT} + 2CK_{MT}$$

$$K_{1-11} = -4AK_{TP} + 2BK_{TP} + 2CK_{TP} \qquad K_{1-12} = -4AK_{TV} + 2BK_{TV} + 2CK_{TV}$$
$$K_{2-11} = -4AK_{AP} + 2BK_{AP} + 2CK_{AP} \qquad K_{2-12} = -4AK_{AV} + 2BK_{AV} + 2CK_{AV}$$
$$K_{3-11} = -4AK_{MP} + 2BK_{MP} + 2CK_{MP} \qquad K_{3-12} = -4AK_{MV} + 2BK_{MV} + 2CK_{MV}$$
$$K_{4-11} = -2AK_{TP} + BK_{TP} - 2CK_{TP} \qquad K_{4-12} = -2AK_{TV} + BK_{TV} - 2CK_{TV}$$
$$K_{5-11} = -2AK_{AP} + BK_{AP} - 2CK_{AP} \qquad K_{5-12} = -2AK_{AV} + BK_{AV} - 2CK_{AV}$$
$$K_{6-11} = -2AK_{MP} + BK_{MP} - 2CK_{MP} \qquad K_{6-12} = -2AK_{MV} + BK_{MV} - 2CK_{MV}$$
$$K_{7-11} = 2AK_{TP} + 2BK_{TP} - 4CK_{TP} \qquad K_{7-12} = 2AK_{TV} + 2BK_{TV} - 4CK_{TV}$$
$$K_{8-11} = 2AK_{AP} + 2BK_{AP} - 4CK_{AP} \qquad K_{8-12} = 2AK_{AV} + 2BK_{AV} - 4CK_{AV}$$
$$K_{9-11} = 2AK_{MP} + 2BK_{MP} - 4CK_{MP} \qquad K_{9-12} = 2AK_{MV} + 2BK_{MV} - 4CK_{MV}$$
$$K_{10-11} = 4AK_{TP} + 4BK_{TP} + 4CK_{TP} \qquad K_{10-12} = 4AK_{TV} + 4BK_{TV} + 4CK_{TV}$$
$$K_{11-11} = 4AK_{AP} + 4BK_{AP} + 4CK_{AP} \qquad K_{11-12} = 4AK_{AV} + 4BK_{AV} + 4CK_{AV}$$
$$K_{12-11} = 4AK_{MP} + 4BK_{MP} + 4CK_{MP} \qquad K_{12-12} = 4AK_{MV} + 4BK_{MV} + 4CK_{MV}$$
$$K_{13-11} = -2AK_{TP} - 2BK_{TP} + CK_{TP} \qquad K_{13-12} = -2AK_{TV} - 2BK_{TV} + CK_{TV}$$
$$K_{14-11} = -2AK_{AP} - 2BK_{AP} + CK_{AP} \qquad K_{14-12} = -2AK_{AV} - 2BK_{AV} + CK_{AV}$$
$$K_{15-11} = -2AK_{MP} - 2BK_{MP} + CK_{MP} \qquad K_{15-12} = -2AK_{MV} - 2BK_{MV} + CK_{MV}$$
$$K_{16-11} = -AK_{TP} - BK_{TP} - CK_{TP} \qquad K_{16-12} = -AK_{TV} - BK_{TV} - CK_{TV}$$
$$K_{17-11} = -AK_{AP} - BK_{AP} - CK_{AP} \qquad K_{17-12} = -AK_{AV} - BK_{AV} - CK_{AV}$$
$$K_{18-11} = -AK_{MP} - BK_{MP} - CK_{MP} \qquad K_{18-12} = -AK_{MV} - BK_{MV} - CK_{MV}$$
$$K_{19-11} = AK_{TP} - 2BK_{TP} - 2CK_{TP} \qquad K_{19-12} = AK_{TV} - 2BK_{TV} - 2CK_{TV}$$
$$K_{20-11} = AK_{AP} - 2BK_{AP} - 2CK_{AP} \qquad K_{20-12} = AK_{AV} - 2BK_{AV} - 2CK_{AV}$$
$$K_{21-11} = AK_{MP} - 2BK_{MP} - 2CK_{MP} \qquad K_{21-12} = AK_{MV} - 2BK_{MV} - 2CK_{MV}$$
$$K_{22-11} = 2AK_{TP} - 4BK_{TP} + 2CK_{TP} \qquad K_{22-12} = 2AK_{TV} - 4BK_{TV} + 2CK_{TV}$$
$$K_{23-11} = 2AK_{AP} - 4BK_{AP} + 2CK_{AP} \qquad K_{23-12} = 2AK_{AV} - 4BK_{AV} + 2CK_{AV}$$
$$K_{24-11} = 2AK_{MP} - 4BK_{MP} + 2CK_{MP} \qquad K_{24-12} = 2AK_{MV} - 4BK_{MV} + 2CK_{MV}$$

$$K_{1-13} = 2AK_{TT} - 4BK_{TT} + 2CK_{TT} \qquad K_{1-14} = 2AK_{TP} - 4BK_{TP} + 2CK_{TP}$$
$$K_{2-13} = 2AK_{AT} - 4BK_{AT} + 2CK_{AT} \qquad K_{2-14} = 2AK_{AP} - 4BK_{AP} + 2CK_{AP}$$
$$K_{3-13} = 2AK_{MT} - 4BK_{MT} + 2CK_{MT} \qquad K_{3-14} = 2AK_{MP} - 4BK_{MP} + 2CK_{MP}$$

$$K_{4-13} = AK_{TT} - 2BK_{TT} - 2CK_{TT} \qquad K_{4-14} = AK_{TP} - 2BK_{TP} - 2CK_{TP}$$
$$K_{5-13} = AK_{AT} - 2BK_{AT} - 2CK_{AT} \qquad K_{5-14} = AK_{AP} - 2BK_{AP} - 2CK_{AP}$$
$$K_{6-13} = AK_{MT} - 2BK_{MT} - 2CK_{MT} \qquad K_{6-14} = AK_{MP} - 2BK_{MP} - 2CK_{MP}$$
$$K_{7-13} = -AK_{TT} - BK_{TT} - CK_{TT} \qquad K_{7-14} = -AK_{TP} - BK_{TP} - CK_{TP}$$
$$K_{8-13} = -AK_{AT} - BK_{AT} - CK_{AT} \qquad K_{8-14} = -AK_{AP} - BK_{AP} - CK_{AP}$$
$$K_{9-13} = -AK_{MT} - BK_{MT} - CK_{MT} \qquad K_{9-14} = -AK_{MP} - BK_{MP} - CK_{MP}$$
$$K_{10-13} = -2AK_{TT} - 2BK_{TT} + CK_{TT} \qquad K_{10-14} = -2AK_{TP} - 2BK_{TP} + CK_{TP}$$
$$K_{11-13} = -2AK_{AT} - 2BK_{AT} + CK_{AT} \qquad K_{11-14} = -2AK_{AP} - 2BK_{AP} + CK_{AP}$$
$$K_{12-13} = -2AK_{MT} - 2BK_{MT} + CK_{MT} \qquad K_{12-14} = -2AK_{MP} - 2BK_{MP} + CK_{MP}$$
$$K_{13-13} = 4AK_{TT} + 4BK_{TT} + 4CK_{TT} \qquad K_{13-14} = 4AK_{TP} + 4BK_{TP} + 4CK_{TP}$$
$$K_{14-13} = 4AK_{AT} + 4BK_{AT} + 4CK_{AT} \qquad K_{14-14} = 4AK_{AP} + 4BK_{AP} + 4CK_{AP}$$
$$K_{15-13} = 4AK_{MT} + 4BK_{MT} + 4CK_{MT} \qquad K_{15-14} = 4AK_{MP} + 4BK_{MP} + 4CK_{MP}$$
$$K_{16-13} = 2AK_{TT} + 2BK_{TT} - 4CK_{TT} \qquad K_{16-14} = 2AK_{TP} + 2BK_{TP} - 4CK_{TP}$$
$$K_{17-13} = 2AK_{AT} + 2BK_{AT} - 4CK_{AT} \qquad K_{17-14} = 2AK_{AP} + 2BK_{AP} - 4CK_{AP}$$
$$K_{18-13} = 2AK_{MT} + 2BK_{MT} - 4CK_{MT} \qquad K_{18-14} = 2AK_{MP} + 2BK_{MP} - 4CK_{MP}$$
$$K_{19-13} = -2AK_{TT} + BK_{TT} - 2CK_{TT} \qquad K_{19-14} = -2AK_{TP} + BK_{TP} - 2CK_{TP}$$
$$K_{20-13} = -2AK_{AT} + BK_{AT} - 2CK_{AT} \qquad K_{20-14} = -2AK_{AP} + BK_{AP} - 2CK_{AP}$$
$$K_{21-13} = -2AK_{MT} + BK_{MT} - 2CK_{MT} \qquad K_{21-14} = -2AK_{MP} + BK_{MP} - 2CK_{MP}$$
$$K_{22-13} = -4AK_{TT} + 2BK_{TT} + 2CK_{TT} \qquad K_{22-14} = -4AK_{TP} + 2BK_{TP} + 2CK_{TP}$$
$$K_{23-13} = -4AK_{AT} + 2BK_{AT} + 2CK_{AT} \qquad K_{23-14} = -4AK_{AP} + 2BK_{AP} + 2CK_{AP}$$
$$K_{24-13} = -4AK_{MT} + 2BK_{MT} + 2CK_{MT} \qquad K_{24-14} = -4AK_{MP} + 2BK_{MP} + 2CK_{MP}$$

$$K_{1-15} = 2AK_{TV} - 4BK_{TV} + 2CK_{TV} \qquad K_{1-16} = AK_{TT} - 2BK_{TT} - 2CK_{TT}$$
$$K_{2-15} = 2AK_{AV} - 4BK_{AV} + 2CK_{AV} \qquad K_{2-16} = AK_{AT} - 2BK_{AT} - 2CK_{AT}$$
$$K_{3-15} = 2AK_{MV} - 4BK_{MV} + 2CK_{MV} \qquad K_{3-16} = AK_{MT} - 2BK_{MT} - 2CK_{MT}$$
$$K_{4-15} = AK_{TV} - 2BK_{TV} - 2CK_{TV} \qquad K_{4-16} = 2AK_{TT} - 4BK_{TT} + 2CK_{TT}$$
$$K_{5-15} = AK_{AV} - 2BK_{AV} - 2CK_{AV} \qquad K_{5-16} = 2AK_{AT} - 4BK_{AT} + 2CK_{AT}$$
$$K_{6-15} = AK_{MV} - 2BK_{MV} - 2CK_{MV} \qquad K_{6-16} = 2AK_{MT} - 4BK_{MT} + 2CK_{MT}$$
$$K_{7-15} = -AK_{TV} - BK_{TV} - CK_{TV} \qquad K_{7-16} = -2AK_{TT} - 2BK_{TT} + CK_{TT}$$
$$K_{8-15} = -AK_{AV} - BK_{AV} - CK_{AV} \qquad K_{8-16} = -2AK_{AT} - 2BK_{AT} + CK_{AT}$$
$$K_{9-15} = -AK_{MV} - BK_{MV} - CK_{MV} \qquad K_{9-16} = -2AK_{MT} - 2BK_{MT} + CK_{MT}$$
$$K_{10-15} = -2AK_{TV} - 2BK_{TV} + CK_{TV} \qquad K_{10-16} = -AK_{TT} - BK_{TT} - CK_{TT}$$
$$K_{11-15} = -2AK_{AV} - 2BK_{AV} + CK_{AV} \qquad K_{11-16} = -AK_{AT} - BK_{AT} - CK_{AT}$$
$$K_{12-15} = -2AK_{MV} - 2BK_{MV} + CK_{MV} \qquad K_{12-16} = -AK_{MT} - BK_{MT} - CK_{MT}$$
$$K_{13-15} = 4AK_{TV} + 4BK_{TV} + 4CK_{TV} \qquad K_{13-16} = 2AK_{TT} + 2BK_{TT} - 4CK_{TT}$$
$$K_{14-15} = 4AK_{AV} + 4BK_{AV} + 4CK_{AV} \qquad K_{14-16} = 2AK_{AT} + 2BK_{AT} - 4CK_{AT}$$
$$K_{15-15} = 4AK_{MV} + 4BK_{MV} + 4CK_{MV} \qquad K_{15-16} = 2AK_{MT} + 2BK_{MT} - 4CK_{MT}$$
$$K_{16-15} = 2AK_{TV} + 2BK_{TV} - 4CK_{TV} \qquad K_{16-16} = 4AK_{TT} + 4BK_{TT} + 4CK_{TT}$$
$$K_{17-15} = 2AK_{AV} + 2BK_{AV} - 4CK_{AV} \qquad K_{17-16} = 4AK_{AT} + 4BK_{AT} + 4CK_{AT}$$
$$K_{18-15} = 2AK_{MV} + 2BK_{MV} - 4CK_{MV} \qquad K_{18-16} = 4AK_{MT} + 4BK_{MT} + 4CK_{MT}$$
$$K_{19-15} = -2AK_{TV} + BK_{TV} - 2CK_{TV} \qquad K_{19-16} = -4AK_{TT} + 2BK_{TT} + 2CK_{TT}$$
$$K_{20-15} = -2AK_{AV} + BK_{AV} - 2CK_{AV} \qquad K_{20-16} = -4AK_{AT} + 2BK_{AT} + 2CK_{AT}$$
$$K_{21-15} = -2AK_{MV} + BK_{MV} - 2CK_{MV} \qquad K_{21-16} = -4AK_{MT} + 2BK_{MT} + 2CK_{MT}$$

$$K_{22-15} = -4AK_{TV} + 2BK_{TV} + 2CK_{TV} \qquad K_{22-16} = -2AK_{TT} + BK_{TT} - 2CK_{TT}$$
$$K_{23-15} = -4AK_{AV} + 2BK_{AV} + 2CK_{AV} \qquad K_{23-16} = -2AK_{AT} + BK_{AT} - 2CK_{AT}$$
$$K_{24-15} = -4AK_{MV} + 2BK_{MV} + 2CK_{MV} \qquad K_{24-16} = -2AK_{MT} + BK_{MT} - 2CK_{MT}$$

$$K_{1-17} = AK_{TP} - 2BK_{TP} - 2CK_{TP} \qquad K_{1-18} = AK_{TV} - 2BK_{TV} - 2CK_{TV}$$
$$K_{2-17} = AK_{AP} - 2BK_{AP} - 2CK_{AP} \qquad K_{2-18} = AK_{AV} - 2BK_{AV} - 2CK_{AV}$$
$$K_{3-17} = AK_{MP} - 2BK_{MP} - 2CK_{MP} \qquad K_{3-18} = AK_{MV} - 2BK_{MV} - 2CK_{MV}$$
$$K_{4-17} = 2AK_{TP} - 4BK_{TP} + 2CK_{TP} \qquad K_{4-18} = 2AK_{TV} - 4BK_{TV} + 2CK_{TV}$$
$$K_{5-17} = 2AK_{AP} - 4BK_{AP} + 2CK_{AP} \qquad K_{5-18} = 2AK_{AV} - 4BK_{AV} + 2CK_{AV}$$
$$K_{6-17} = 2AK_{MP} - 4BK_{MP} + 2CK_{MP} \qquad K_{6-18} = 2AK_{MV} - 4BK_{MV} + 2CK_{MV}$$
$$K_{7-17} = -2AK_{TP} - 2BK_{TP} + CK_{TP} \qquad K_{7-18} = -2AK_{TV} - 2BK_{TV} + CK_{TV}$$
$$K_{8-17} = -2AK_{AP} - 2BK_{AP} + CK_{AP} \qquad K_{8-18} = -2AK_{AV} - 2BK_{AV} + CK_{AV}$$
$$K_{9-17} = -2AK_{MP} - 2BK_{MP} + CK_{MP} \qquad K_{9-18} = -2AK_{MV} - 2BK_{MV} + CK_{MV}$$
$$K_{10-17} = -AK_{TP} - BK_{TP} - CK_{TP} \qquad K_{10-18} = -AK_{TV} - BK_{TV} - CK_{TV}$$
$$K_{11-17} = -AK_{AP} - BK_{AP} - CK_{AP} \qquad K_{11-18} = -AK_{AV} - BK_{AV} - CK_{AV}$$
$$K_{12-17} = -AK_{MP} - BK_{MP} - CK_{MP} \qquad K_{12-18} = -AK_{MV} - BK_{MV} - CK_{MV}$$
$$K_{13-17} = 2AK_{TP} + 2BK_{TP} - 4CK_{TP} \qquad K_{13-18} = 2AK_{TV} + 2BK_{TV} - 4CK_{TV}$$
$$K_{14-17} = 2AK_{AP} + 2BK_{AP} - 4CK_{AP} \qquad K_{14-18} = 2AK_{AV} + 2BK_{AV} - 4CK_{AV}$$
$$K_{15-17} = 2AK_{MP} + 2BK_{MP} - 4CK_{MP} \qquad K_{15-18} = 2AK_{MV} + 2BK_{MV} - 4CK_{MV}$$
$$K_{16-17} = 4AK_{TP} + 4BK_{TP} + 4CK_{TP} \qquad K_{16-18} = 4AK_{TV} + 4BK_{TV} + 4CK_{TV}$$
$$K_{17-17} = 4AK_{AP} + 4BK_{AP} + 4CK_{AP} \qquad K_{17-18} = 4AK_{AV} + 4BK_{AV} + 4CK_{AV}$$
$$K_{18-17} = 4AK_{MP} + 4BK_{MP} + 4CK_{MP} \qquad K_{18-18} = 4AK_{MV} + 4BK_{MV} + 4CK_{MV}$$
$$K_{19-17} = -4AK_{TP} + 2BK_{TP} + 2CK_{TP} \qquad K_{19-18} = -4AK_{TV} + 2BK_{TV} + 2CK_{TV}$$
$$K_{20-17} = -4AK_{AP} + 2BK_{AP} + 2CK_{AP} \qquad K_{20-18} = -4AK_{AV} + 2BK_{AV} + 2CK_{AV}$$
$$K_{21-17} = -4AK_{MP} + 2BK_{MP} + 2CK_{MP} \qquad K_{21-18} = -4AK_{MV} + 2BK_{MV} + 2CK_{MV}$$
$$K_{22-17} = -2AK_{TP} + BK_{TP} - 2CK_{TP} \qquad K_{22-18} = -2AK_{TV} + BK_{TV} - 2CK_{TV}$$
$$K_{23-17} = -2AK_{AP} + BK_{AP} - 2CK_{AP} \qquad K_{23-18} = -2AK_{AV} + BK_{AV} - 2CK_{AV}$$
$$K_{24-17} = -2AK_{MP} + BK_{MP} - 2CK_{MP} \qquad K_{24-18} = -2AK_{MV} + BK_{MV} - 2CK_{MV}$$

$$K_{1-19} = -AK_{TT} - BK_{TT} - CK_{TT} \qquad K_{1-20} = -AK_{TP} - BK_{TP} - CK_{TP}$$
$$K_{2-19} = -AK_{AT} - BK_{AT} - CK_{AT} \qquad K_{2-20} = -AK_{AP} - BK_{AP} - CK_{AP}$$
$$K_{3-19} = -AK_{MT} - BK_{MT} - CK_{MT} \qquad K_{3-20} = -AK_{MV} - BK_{MV} - CK_{MV}$$
$$K_{4-19} = -2AK_{TT} - 2BK_{TT} + CK_{TT} \qquad K_{4-20} = -2AK_{TP} - 2BK_{TP} + CK_{TP}$$
$$K_{5-19} = -2AK_{AT} - 2BK_{AT} + CK_{AT} \qquad K_{5-20} = -2AK_{AP} - 2BK_{AP} + CK_{AP}$$
$$K_{6-19} = -2AK_{MT} - 2BK_{MT} + CK_{MT} \qquad K_{6-20} = -2AK_{MV} - 2BK_{MV} + CK_{MV}$$
$$K_{7-19} = 2AK_{TT} - 4BK_{TT} + 2CK_{TT} \qquad K_{7-20} = 2AK_{TP} - 4BK_{TP} + 2CK_{TP}$$
$$K_{8-19} = 2AK_{AT} - 4BK_{AT} + 2CK_{AT} \qquad K_{8-20} = 2AK_{AP} - 4BK_{AP} + 2CK_{AP}$$
$$K_{9-19} = 2AK_{MT} - 4BK_{MT} + 2CK_{MT} \qquad K_{9-20} = 2AK_{MV} - 4BK_{MV} + 2CK_{MV}$$
$$K_{10-19} = AK_{TT} - 2BK_{TT} - 2CK_{TT} \qquad K_{10-20} = AK_{TP} - 2BK_{TP} - 2CK_{TP}$$
$$K_{11-19} = AK_{AT} - 2BK_{AT} - 2CK_{AT} \qquad K_{11-20} = AK_{AP} - 2BK_{AP} - 2CK_{AP}$$
$$K_{12-19} = AK_{MT} - 2BK_{MT} - 2CK_{MT} \qquad K_{12-20} = AK_{MV} - 2BK_{MV} - 2CK_{MV}$$

$$K_{13-19} = -2AK_{TT} + BK_{TT} - 2CK_{TT} \qquad K_{13-20} = -2AK_{TP} + BK_{TP} - 2CK_{TP}$$
$$K_{14-19} = -2AK_{AT} + BK_{AT} - 2CK_{AT} \qquad K_{14-20} = -2AK_{AP} + BK_{AP} - 2CK_{AP}$$
$$K_{15-19} = -2AK_{MT} + BK_{MT} - 2CK_{MT} \qquad K_{15-20} = -2AK_{MV} + BK_{MV} - 2CK_{MV}$$
$$K_{16-19} = -4AK_{TT} + 2BK_{TT} + 2CK_{TT} \qquad K_{16-20} = -4AK_{TP} + 2BK_{TP} + 2CK_{TP}$$
$$K_{17-19} = -4AK_{AT} + 2BK_{AT} + 2CK_{AT} \qquad K_{17-20} = -4AK_{AP} + 2BK_{AP} + 2CK_{AP}$$
$$K_{18-19} = -4AK_{MT} + 2BK_{MT} + 2CK_{MT} \qquad K_{18-20} = -4AK_{MV} + 2BK_{MV} + 2CK_{MV}$$
$$K_{19-19} = 4AK_{TT} + 4BK_{TT} + 4CK_{TT} \qquad K_{19-20} = 4AK_{TP} + 4BK_{TP} + 4CK_{TP}$$
$$K_{20-19} = 4AK_{AT} + 4BK_{AT} + 4CK_{AT} \qquad K_{20-20} = 4AK_{AP} + 4BK_{AP} + 4CK_{AP}$$
$$K_{21-19} = 4AK_{MT} + 4BK_{MT} + 4CK_{MT} \qquad K_{21-20} = 4AK_{MV} + 4BK_{MV} + 4CK_{MV}$$
$$K_{22-19} = 2AK_{TT} + 2BK_{TT} - 4CK_{TT} \qquad K_{22-20} = 2AK_{TP} + 2BK_{TP} - 4CK_{TP}$$
$$K_{23-19} = 2AK_{AT} + 2BK_{AT} - 4CK_{AT} \qquad K_{23-20} = 2AK_{AP} + 2BK_{AP} - 4CK_{AP}$$
$$K_{24-19} = 2AK_{MT} + 2BK_{MT} - 4CK_{MT} \qquad K_{24-20} = 2AK_{MV} + 2BK_{MV} - 4CK_{MV}$$

$$K_{1-21} = -AK_{TV} - BK_{TV} - CK_{TV} \qquad K_{1-22} = -2AK_{TT} - 2BK_{TT} + CK_{TT}$$
$$K_{2-21} = -AK_{AV} - BK_{AV} - CK_{AV} \qquad K_{2-22} = -2AK_{AT} - 2BK_{AT} + CK_{AT}$$
$$K_{3-21} = -AK_{MV} - BK_{MV} - CK_{MV} \qquad K_{3-22} = -2AK_{MT} - 2BK_{MT} + CK_{MT}$$
$$K_{4-21} = -2AK_{TV} - 2BK_{TV} + CK_{TV} \qquad K_{4-22} = -AK_{TT} - BK_{TT} - CK_{TT}$$
$$K_{5-21} = -2AK_{AV} - 2BK_{AV} + CK_{AV} \qquad K_{5-22} = -AK_{AT} - BK_{AT} - CK_{AT}$$
$$K_{6-21} = -2AK_{MV} - 2BK_{MV} + CK_{MV} \qquad K_{6-22} = -AK_{MT} - BK_{MT} - CK_{MT}$$
$$K_{7-21} = 2AK_{TV} - 4BK_{TV} + 2CK_{TV} \qquad K_{7-22} = AK_{TT} - 2BK_{TT} - 2CK_{TT}$$
$$K_{8-21} = 2AK_{AV} - 4BK_{AV} + 2CK_{AV} \qquad K_{8-22} = AK_{AT} - 2BK_{AT} - 2CK_{AT}$$
$$K_{9-21} = 2AK_{MV} - 4BK_{MV} + 2CK_{MV} \qquad K_{9-22} = AK_{MT} - 2BK_{MT} - 2CK_{MT}$$
$$K_{10-21} = AK_{TV} - 2BK_{TV} - 2CK_{TV} \qquad K_{10-22} = 2AK_{TT} - 4BK_{TT} + 2CK_{TT}$$
$$K_{11-21} = AK_{AV} - 2BK_{AV} - 2CK_{AV} \qquad K_{11-22} = 2AK_{AT} - 4BK_{AT} + 2CK_{AT}$$
$$K_{12-21} = AK_{MV} - 2BK_{MV} - 2CK_{MV} \qquad K_{12-22} = 2AK_{MT} - 4BK_{MT} + 2CK_{MT}$$
$$K_{13-21} = -2AK_{TV} + BK_{TV} - 2CK_{TV} \qquad K_{13-22} = -4AK_{TT} + 2BK_{TT} + 2CK_{TT}$$
$$K_{14-21} = -2AK_{AV} + BK_{AV} - 2CK_{AV} \qquad K_{14-22} = -4AK_{AT} + 2BK_{AT} + 2CK_{AT}$$
$$K_{15-21} = -2AK_{MV} + BK_{MV} - 2CK_{MV} \qquad K_{15-22} = -4AK_{MT} + 2BK_{MT} + 2CK_{MT}$$
$$K_{16-21} = -4AK_{TV} + 2BK_{TV} + 2CK_{TV} \qquad K_{16-22} = -2AK_{TT} + BK_{TT} - 2CK_{TT}$$
$$K_{17-21} = -4AK_{AV} + 2BK_{AV} + 2CK_{AV} \qquad K_{17-22} = -2AK_{AT} + BK_{AT} - 2CK_{AT}$$
$$K_{18-21} = -4AK_{MV} + 2BK_{MV} + 2CK_{MV} \qquad K_{18-22} = -2AK_{MT} + BK_{MT} - 2CK_{MT}$$
$$K_{19-21} = 4AK_{TV} + 4BK_{TV} + 4CK_{TV} \qquad K_{19-22} = 2AK_{TT} + 2BK_{TT} - 4CK_{TT}$$
$$K_{20-21} = 4AK_{AV} + 4BK_{AV} + 4CK_{AV} \qquad K_{20-22} = 2AK_{AT} + 2BK_{AT} - 4CK_{AT}$$
$$K_{21-21} = 4AK_{MV} + 4BK_{MV} + 4CK_{MV} \qquad K_{21-22} = 2AK_{MT} + 2BK_{MT} - 4CK_{MT}$$
$$K_{22-21} = 2AK_{TV} + 2BK_{TV} - 4CK_{TV} \qquad K_{22-22} = 4AK_{TT} + 4BK_{TT} + 4CK_{TT}$$
$$K_{23-21} = 2AK_{AV} + 2BK_{AV} - 4CK_{AV} \qquad K_{23-22} = 4AK_{AT} + 4BK_{AT} + 4CK_{AT}$$
$$K_{24-21} = 2AK_{MV} + 2BK_{MV} - 4CK_{MV} \qquad K_{24-22} = 4AK_{MT} + 4BK_{MT} + 4CK_{MT}$$

$$K_{1-23} = -2AK_{TP} - 2BK_{TP} + CK_{TP} \qquad K_{1-24} = -2AK_{TV} - 2BK_{TV} + CK_{TV}$$
$$K_{2-23} = -2AK_{AP} - 2BK_{AP} + CK_{AP} \qquad K_{2-24} = -2AK_{AV} - 2BK_{AV} + CK_{AV}$$
$$K_{3-23} = -2AK_{MP} - 2BK_{MP} + CK_{MP} \qquad K_{3-24} = -2AK_{MV} - 2BK_{MV} + CK_{MV}$$

$$
\begin{aligned}
K_{4-23} &= -AK_{TP} - BK_{TP} - CK_{TP} & K_{4-24} &= -AK_{TV} - BK_{TV} - CK_{TV}\\
K_{5-23} &= -AK_{AP} - BK_{AP} - CK_{AP} & K_{5-24} &= -AK_{AV} - BK_{AV} - CK_{AV}\\
K_{6-23} &= -AK_{MP} - BK_{MP} - CK_{MP} & K_{6-24} &= -AK_{MV} - BK_{MV} - CK_{MV}\\
K_{7-23} &= AK_{TP} - 2BK_{TP} - 2CK_{TP} & K_{7-24} &= AK_{TV} - 2BK_{TV} - 2CK_{TV}\\
K_{8-23} &= AK_{AP} - 2BK_{AP} - 2CK_{AP} & K_{8-24} &= AK_{AV} - 2BK_{AV} - 2CK_{AV}\\
K_{9-23} &= AK_{MP} - 2BK_{MP} - 2CK_{MP} & K_{9-24} &= AK_{MV} - 2BK_{MV} - 2CK_{MV}\\
K_{10-23} &= 2AK_{TP} - 4BK_{TP} + 2CK_{TP} & K_{10-24} &= 2AK_{TV} - 4BK_{TV} + 2CK_{TV}\\
K_{11-23} &= 2AK_{AP} - 4BK_{AP} + 2CK_{AP} & K_{11-24} &= 2AK_{AV} - 4BK_{AV} + 2CK_{AV}\\
K_{12-23} &= 2AK_{MP} - 4BK_{MP} + 2CK_{MP} & K_{12-24} &= 2AK_{MV} - 4BK_{MV} + 2CK_{MV}\\
K_{13-23} &= -4AK_{TP} + 2BK_{TP} + 2CK_{TP} & K_{13-24} &= -4AK_{TV} + 2BK_{TV} + 2CK_{TV}\\
K_{14-23} &= -4AK_{AP} + 2BK_{AP} + 2CK_{AP} & K_{14-24} &= -4AK_{AV} + 2BK_{AV} + 2CK_{AV}\\
K_{15-23} &= -4AK_{MP} + 2BK_{MP} + 2CK_{MP} & K_{15-24} &= -4AK_{MV} + 2BK_{MV} + 2CK_{MV}\\
K_{16-23} &= -2AK_{TP} + BK_{TP} - 2CK_{TP} & K_{16-24} &= -2AK_{TV} + BK_{TV} - 2CK_{TV}\\
K_{17-23} &= -2AK_{AP} + BK_{AP} - 2CK_{AP} & K_{17-24} &= -2AK_{AV} + BK_{AV} - 2CK_{AV}\\
K_{18-23} &= -2AK_{MP} + BK_{MP} - 2CK_{MP} & K_{18-24} &= -2AK_{MV} + BK_{MV} - 2CK_{MV}\\
K_{19-23} &= 2AK_{TP} + 2BK_{TP} - 4CK_{TP} & K_{19-24} &= 2AK_{TV} + 2BK_{TV} - 4CK_{TV}\\
K_{20-23} &= 2AK_{AP} + 2BK_{AP} - 4CK_{AP} & K_{20-24} &= 2AK_{AV} + 2BK_{AV} - 4CK_{AV}\\
K_{21-23} &= 2AK_{MP} + 2BK_{MP} - 4CK_{MP} & K_{21-24} &= 2AK_{MV} + 2BK_{MV} - 4CK_{MV}\\
K_{22-23} &= 4AK_{TP} + 4BK_{TP} + 4CK_{TP} & K_{22-24} &= 4AK_{TV} + 4BK_{TV} + 4CK_{TV}\\
K_{23-23} &= 4AK_{AP} + 4BK_{AP} + 4CK_{AP} & K_{23-24} &= 4AK_{AV} + 4BK_{AV} + 4CK_{AV}\\
K_{24-23} &= 4AK_{MP} + 4BK_{MP} + 4CK_{MP} & K_{24-24} &= 4AK_{MV} + 4BK_{MV} + 4CK_{MV}
\end{aligned}
$$

A.4 Elements of $\int_\Gamma \left(N^T K_E F_{K_E} N\right) d\Gamma$ and $\int_\Gamma \left(N^T K_E F_{\infty_E}\right) d\Gamma$

Matrix $\int_\Gamma \left(N^T K_E F_{K_E} N\right) d\Gamma$, introduced in Equation (4.86), is a 24×24 matrix with elements given the notation $K_{F_{i-j}}$ and matrix $\int_\Gamma \left(N^T K_E F_{\infty_E} N\right) d\Gamma$, introduced in Equation (4.87), is a 24×1 vector with elements given the notation F_{i-j}, where i is the row number and j is the column number. The elemental area $d\Gamma$ is evaluated according to the surface with the boundary conditions (i.e. the surface exposed to fire), so that:

For $\eta = -1$ and $\eta = +1$: $$d\Gamma = \det[J_s] d\zeta d\xi \quad \text{(A.3)}$$

For $\zeta = -1$ and $\zeta = +1$: $$d\Gamma = \det[J_s] d\eta d\xi \quad \text{(A.4)}$$

For $\xi = -1$ and $\xi = +1$: $$d\Gamma = \det[J_s] d\eta d\zeta \quad \text{(A.5)}$$

where J_s is the Jacobian matrix of the coordinate transformation, and where $\det[J_s]$ is evaluated as the area of the surface subjected to fire divided by 4.

In order to evaluate the values of $K_{F_{i-j}}$ and F_{i-j}, the following terms need to be defined.

$$A_1 = C_A h \frac{K_{TT}K_{MV} - K_{TV}K_{MT}}{K_{TT}K_{MV}} \qquad A_2 = C_A h \frac{K_{AT}K_{MV} - K_{AV}K_{MT}}{K_{TT}K_{MV}} \qquad A_3 = C_A h \frac{K_{MT}K_{MV} - K_{MV}K_{MT}}{K_{TT}K_{MV}},$$

$$B_1 = C_A \beta \frac{K_{TV}}{K_{MV}} \qquad B_2 = C_A \beta \frac{K_{AV}}{K_{MV}} \qquad B_3 = C_A \beta \frac{K_{MV}}{K_{MV}}$$

Where K_{TT}, K_{TV}, K_{AT}, K_{AV}, K_{MT}, and K_{MV} are defined in Table 4-1; h is the combined convective and radiative heat transfer coefficients on the boundary surface, as shown in Equation (4.74); and C_A is a function of the dimensions of the surface with the boundary conditions and will be defined for each of the following six cases of boundary surfaces.

A.4.1 For $\eta = -1$

$$\int_{\Gamma} \left(N^T K_E F_{K_E} N\right) d\Gamma = \int_{-1}^{1}\int_{-1}^{1} \left(N^T K_E F_{K_E} N\right) \det[J_s]\, d\zeta\, d\xi \Bigg|^{\eta=-1} = K_{F_{i-j}} \qquad (A.6)$$

and

$$\int_{\Gamma} \left(N^T K_E F_{\infty_E}\right) d\Gamma = \int_{-1}^{1}\int_{-1}^{1} \left(N^T K_E F_{\infty_E}\right) \det[J_s]\, d\zeta\, d\xi \Bigg|^{\eta=-1} = F_{i-j} \qquad (A.7)$$

In this case, C_A will be equal to $\frac{bc}{4}$, where b and c are defined in Figure 4-1. The non-zero elements are given as:

$K_{F_{1-1}} = 4A_1/9$	$K_{F_{1-3}} = 4B_1/9$	$K_{F_{1-4}} = 2A_1/9$	$K_{F_{1-6}} = 2B_1/9$
$K_{F_{2-1}} = 4A_2/9$	$K_{F_{2-3}} = 4B_2/9$	$K_{F_{2-4}} = 2A_2/9$	$K_{F_{2-6}} = 2B_2/9$
$K_{F_{3-1}} = 4A_3/9$	$K_{F_{3-3}} = 4B_3/9$	$K_{F_{3-4}} = 2A_3/9$	$K_{F_{3-6}} = 2B_3/9$
$K_{F_{4-1}} = 2A_1/9$	$K_{F_{4-3}} = 2B_1/9$	$K_{F_{4-4}} = 4A_1/9$	$K_{F_{4-6}} = 4B_1/9$
$K_{F_{5-1}} = 2A_2/9$	$K_{F_{5-3}} = 2B_2/9$	$K_{F_{5-4}} = 4A_2/9$	$K_{F_{5-6}} = 4B_2/9$
$K_{F_{6-1}} = 2A_3/9$	$K_{F_{6-3}} = 2B_3/9$	$K_{F_{6-4}} = 4A_3/9$	$K_{F_{6-6}} = 4B_3/9$
$K_{F_{13-1}} = 2A_1/9$	$K_{F_{13-3}} = 2B_1/9$	$K_{F_{13-4}} = A_1/9$	$K_{F_{13-6}} = B_1/9$
$K_{F_{14-1}} = 2A_2/9$	$K_{F_{14-3}} = 2B_2/9$	$K_{F_{14-4}} = A_2/9$	$K_{F_{14-6}} = B_2/9$
$K_{F_{15-1}} = 2A_3/9$	$K_{F_{15-3}} = 2B_3/9$	$K_{F_{15-4}} = A_3/9$	$K_{F_{15-6}} = B_3/9$
$K_{F_{16-1}} = A_1/9$	$K_{F_{16-3}} = B_1/9$	$K_{F_{16-4}} = 2A_1/9$	$K_{F_{16-6}} = 2B_1/9$
$K_{F_{17-1}} = A_2/9$	$K_{F_{17-3}} = B_2/9$	$K_{F_{17-4}} = 2A_2/9$	$K_{F_{17-6}} = 2B_2/9$
$K_{F_{18-1}} = A_3/9$	$K_{F_{18-3}} = B_3/9$	$K_{F_{18-4}} = 2A_3/9$	$K_{F_{18-6}} = 2B_3/9$

$$
\begin{array}{llllllll}
K_{F_{1-13}} = 2A_1/9 & K_{F_{1-15}} = 2B_1/9 & K_{F_{1-16}} = A_1/9 & K_{F_{1-18}} = B_1/9 \\
K_{F_{2-13}} = 2A_2/9 & K_{F_{2-15}} = 2B_2/9 & K_{F_{2-16}} = A_2/9 & K_{F_{2-18}} = B_2/9 \\
K_{F_{3-13}} = 2A_3/9 & K_{F_{3-15}} = 2B_3/9 & K_{F_{3-16}} = A_3/9 & K_{F_{3-18}} = B_3/9 \\
K_{F_{4-13}} = A_1/9 & K_{F_{4-15}} = B_1/9 & K_{F_{4-16}} = 2A_1/9 & K_{F_{4-18}} = 2B_1/9 \\
K_{F_{5-13}} = A_2/9 & K_{F_{5-15}} = B_2/9 & K_{F_{5-16}} = 2A_2/9 & K_{F_{5-18}} = 2B_2/9 \\
K_{F_{6-13}} = A_3/9 & K_{F_{6-15}} = B_3/9 & K_{F_{6-16}} = 2A_3/9 & K_{F_{6-18}} = 2B_3/9 \\
K_{F_{13-13}} = 4A_1/9 & K_{F_{13-15}} = 4B_1/9 & K_{F_{13-16}} = 2A_1/9 & K_{F_{13-18}} = 2B_1/9 \\
K_{F_{14-13}} = 4A_2/9 & K_{F_{14-15}} = 4B_2/9 & K_{F_{14-16}} = 2A_2/9 & K_{F_{14-18}} = 2B_2/9 \\
K_{F_{15-13}} = 4A_3/9 & K_{F_{15-15}} = 4B_3/9 & K_{F_{15-16}} = 2A_3/9 & K_{F_{15-18}} = 2B_3/9 \\
K_{F_{16-13}} = 2A_1/9 & K_{F_{16-15}} = 2B_1/9 & K_{F_{16-16}} = 4A_1/9 & K_{F_{16-18}} = 4B_1/9 \\
K_{F_{17-13}} = 2A_2/9 & K_{F_{17-15}} = 2B_2/9 & K_{F_{17-16}} = 4A_2/9 & K_{F_{17-18}} = 4B_2/9 \\
K_{F_{18-13}} = 2A_3/9 & K_{F_{18-15}} = 2B_3/9 & K_{F_{18-16}} = 4A_3/9 & K_{F_{18-18}} = 4B_3/9
\end{array}
$$

and

$$
\begin{aligned}
F_{1-1} &= A_1 T_\infty + B_1 \tilde{\rho}_{V_\infty} \\
F_{2-1} &= A_2 T_\infty + B_2 \tilde{\rho}_{V_\infty} \\
F_{3-1} &= A_3 T_\infty + B_3 \tilde{\rho}_{V_\infty} \\
F_{4-1} &= A_1 T_\infty + B_1 \tilde{\rho}_{V_\infty} \\
F_{5-1} &= A_2 T_\infty + B_2 \tilde{\rho}_{V_\infty} \\
F_{6-1} &= A_3 T_\infty + B_3 \tilde{\rho}_{V_\infty} \\
F_{13-1} &= A_1 T_\infty + B_1 \tilde{\rho}_{V_\infty} \\
F_{14-1} &= A_2 T_\infty + B_2 \tilde{\rho}_{V_\infty} \\
F_{15-1} &= A_3 T_\infty + B_3 \tilde{\rho}_{V_\infty} \\
F_{16-1} &= A_1 T_\infty + B_1 \tilde{\rho}_{V_\infty} \\
F_{17-1} &= A_2 T_\infty + B_2 \tilde{\rho}_{V_\infty} \\
F_{18-1} &= A_3 T_\infty + B_3 \tilde{\rho}_{V_\infty}
\end{aligned}
$$

A.4.2 For $\eta = +1$

$$\int_{\Gamma} \left(N^T K_E F_{K_E} N\right) d\Gamma = \int_{-1}^{1}\int_{-1}^{1} \left(N^T K_E F_{K_E} N\right) \det[J_s]\, d\zeta\, d\xi \Bigg|^{\eta=+1} = K_{F_{i-j}} \qquad (A.8)$$

and

$$\int_{\Gamma} \left(N^T K_E F_{\infty_E}\right) d\Gamma = \int_{-1}^{1}\int_{-1}^{1} \left(N^T K_E F_{\infty_E}\right) \det[J_s]\, d\zeta\, d\xi \Bigg|^{\eta=+1} = F_{i-j} \qquad (A.9)$$

In this case, C_A will be equal to $\frac{bc}{4}$, where b and c are defined in Figure 4-1. The non-zero elements are given as:

$$
\begin{array}{llllllll}
K_{F_{7-7}} = 4A_1/9 & K_{F_{7-9}} = 4B_1/9 & K_{F_{7-10}} = 2A_1/9 & K_{F_{7-12}} = 2B_1/9 \\
K_{F_{8-7}} = 4A_2/9 & K_{F_{8-9}} = 4B_2/9 & K_{F_{8-10}} = 2A_2/9 & K_{F_{8-12}} = 2B_2/9 \\
K_{F_{9-7}} = 4A_3/9 & K_{F_{9-9}} = 4B_3/9 & K_{F_{9-10}} = 2A_3/9 & K_{F_{9-12}} = 2B_3/9 \\
K_{F_{10-7}} = 2A_1/9 & K_{F_{10-9}} = 2B_1/9 & K_{F_{10-10}} = 4A_1/9 & K_{F_{10-12}} = 4B_1/9 \\
K_{F_{11-7}} = 2A_2/9 & K_{F_{11-9}} = 2B_2/9 & K_{F_{11-10}} = 4A_2/9 & K_{F_{11-12}} = 4B_2/9 \\
K_{F_{12-7}} = 2A_3/9 & K_{F_{12-9}} = 2B_3/9 & K_{F_{12-10}} = 4A_3/9 & K_{F_{12-12}} = 4B_3/9 \\
K_{F_{19-7}} = 2A_1/9 & K_{F_{19-9}} = 2B_1/9 & K_{F_{19-10}} = A_1/9 & K_{F_{19-12}} = B_1/9 \\
K_{F_{20-7}} = 2A_2/9 & K_{F_{20-9}} = 2B_2/9 & K_{F_{20-10}} = A_2/9 & K_{F_{20-12}} = B_2/9 \\
K_{F_{21-7}} = 2A_3/9 & K_{F_{21-9}} = 2B_3/9 & K_{F_{21-10}} = A_3/9 & K_{F_{21-12}} = B_3/9 \\
K_{F_{22-7}} = A_1/9 & K_{F_{22-9}} = B_1/9 & K_{F_{22-10}} = 2A_1/9 & K_{F_{22-12}} = 2B_1/9 \\
K_{F_{23-7}} = A_2/9 & K_{F_{23-9}} = B_2/9 & K_{F_{23-10}} = 2A_2/9 & K_{F_{23-12}} = 2B_2/9 \\
K_{F_{24-7}} = A_3/9 & K_{F_{24-9}} = B_3/9 & K_{F_{24-10}} = 2A_3/9 & K_{F_{24-12}} = 2B_3/9
\end{array}
$$

$$
\begin{array}{llllllll}
K_{F_{7-19}} = 2A_1/9 & K_{F_{7-21}} = 2B_1/9 & K_{F_{7-22}} = A_1/9 & K_{F_{7-24}} = B_2/9 \\
K_{F_{8-19}} = 2A_2/9 & K_{F_{8-21}} = 2B_2/9 & K_{F_{8-22}} = A_2/9 & K_{F_{8-24}} = B_3/9 \\
K_{F_{9-19}} = 2A_3/9 & K_{F_{9-21}} = 2B_3/9 & K_{F_{9-22}} = A_3/9 & K_{F_{9-24}} = 2B_1/9 \\
K_{F_{10-19}} = A_1/9 & K_{F_{10-21}} = B_1/9 & K_{F_{10-22}} = 2A_1/9 & K_{F_{10-24}} = 2B_2/9 \\
K_{F_{11-19}} = A_2/9 & K_{F_{11-21}} = B_2/9 & K_{F_{11-22}} = 2A_2/9 & K_{F_{11-24}} = 2B_3/9 \\
K_{F_{12-19}} = A_3/9 & K_{F_{12-21}} = B_3/9 & K_{F_{12-22}} = 2A_3/9 & K_{F_{12-24}} = \\
K_{F_{19-19}} = 4A_1/9 & K_{F_{19-21}} = 4B_1/9 & K_{F_{19-22}} = 2A_1/9 & K_{F_{19-24}} = 2B_1/9 \\
K_{F_{20-19}} = 4A_2/9 & K_{F_{20-21}} = 4B_2/9 & K_{F_{20-22}} = 2A_2/9 & K_{F_{20-24}} = 2B_2/9 \\
K_{F_{21-19}} = 4A_3/9 & K_{F_{21-21}} = 4B_3/9 & K_{F_{21-22}} = 2A_3/9 & K_{F_{21-24}} = 2B_3/9 \\
K_{F_{22-19}} = 2A_1/9 & K_{F_{22-21}} = 2B_1/9 & K_{F_{22-22}} = 4A_1/9 & K_{F_{22-24}} = 4B_1/9 \\
K_{F_{23-19}} = 2A_2/9 & K_{F_{23-21}} = 2B_2/9 & K_{F_{23-22}} = 4A_2/9 & K_{F_{23-24}} = 4B_2/9 \\
K_{F_{24-19}} = 2A_3/9 & K_{F_{24-21}} = 2B_3/9 & K_{F_{24-22}} = 4A_3/9 & K_{F_{24-24}} = 4B_3/9
\end{array}
$$

and

$$
\begin{aligned}
F_{7-1} &= A_1 T_\infty + B_1 \tilde{\rho}_{V_\infty} \\
F_{8-1} &= A_2 T_\infty + B_2 \tilde{\rho}_{V_\infty} \\
F_{9-1} &= A_3 T_\infty + B_3 \tilde{\rho}_{V_\infty} \\
F_{10-1} &= A_1 T_\infty + B_1 \tilde{\rho}_{V_\infty} \\
F_{11-1} &= A_2 T_\infty + B_2 \tilde{\rho}_{V_\infty} \\
F_{12-1} &= A_3 T_\infty + B_3 \tilde{\rho}_{V_\infty} \\
F_{19-1} &= A_1 T_\infty + B_1 \tilde{\rho}_{V_\infty}
\end{aligned}
$$

$$F_{20-1} = A_2 T_\infty + B_2 \tilde{\rho}_{V_\infty}$$
$$F_{21-1} = A_3 T_\infty + B_3 \tilde{\rho}_{V_\infty}$$
$$F_{22-1} = A_1 T_\infty + B_1 \tilde{\rho}_{V_\infty}$$
$$F_{23-1} = A_2 T_\infty + B_2 \tilde{\rho}_{V_\infty}$$
$$F_{24-1} = A_3 T_\infty + B_3 \tilde{\rho}_{V_\infty}$$

A.4.3 For $\zeta = -1$

$$\int_\Gamma \left(N^T K_E F_{K_E} N\right) d\Gamma = \int_{-1}^{1}\int_{-1}^{1} \left(N^T K_E F_{K_E} N\right) \det[J_s] d\eta\, d\xi \Big|^{\zeta=-1} = K_{F_{i-j}} \qquad (A.10)$$

and

$$\int_\Gamma \left(N^T K_E F_{\infty_E}\right) d\Gamma = \int_{-1}^{1}\int_{-1}^{1} \left(N^T K_E F_{\infty_E}\right) \det[J_s] d\eta\, d\xi \Big|^{\zeta=-1} = F_{i-j} \qquad (A.11)$$

In this case, C_A will be equal to $\frac{ac}{4}$, where a and c are defined in Figure 4-1. The non-zero elements are given as:

$$K_{F_{1-1}} = 4A_1/9 \quad K_{F_{1-3}} = 4B_1/9 \quad K_{F_{1-4}} = 2A_1/9 \quad K_{F_{1-6}} = 2B_1/9$$
$$K_{F_{2-1}} = 4A_2/9 \quad K_{F_{2-3}} = 4B_2/9 \quad K_{F_{2-4}} = 2A_2/9 \quad K_{F_{2-6}} = 2B_2/9$$
$$K_{F_{3-1}} = 4A_3/9 \quad K_{F_{3-3}} = 4B_3/9 \quad K_{F_{3-4}} = 2A_3/9 \quad K_{F_{3-6}} = 2B_3/9$$
$$K_{F_{4-1}} = 2A_1/9 \quad K_{F_{4-3}} = 2B_1/9 \quad K_{F_{4-4}} = 4A_1/9 \quad K_{F_{4-6}} = 4B_1/9$$
$$K_{F_{5-1}} = 2A_2/9 \quad K_{F_{5-3}} = 2B_2/9 \quad K_{F_{5-4}} = 4A_2/9 \quad K_{F_{5-6}} = 4B_2/9$$
$$K_{F_{6-1}} = 2A_3/9 \quad K_{F_{6-3}} = 2B_3/9 \quad K_{F_{6-4}} = 4A_3/9 \quad K_{F_{6-6}} = 4B_3/9$$
$$K_{F_{7-1}} = A_1/9 \quad K_{F_{7-3}} = B_1/9 \quad K_{F_{7-4}} = 2A_1/9 \quad K_{F_{7-6}} = 2B_1/9$$
$$K_{F_{8-1}} = A_2/9 \quad K_{F_{8-3}} = B_2/9 \quad K_{F_{8-4}} = 2A_2/9 \quad K_{F_{8-6}} = 2B_2/9$$
$$K_{F_{9-1}} = A_3/9 \quad K_{F_{9-3}} = B_3/9 \quad K_{F_{9-4}} = 2A_3/9 \quad K_{F_{9-6}} = 2B_3/9$$
$$K_{F_{10-1}} = 2A_1/9 \quad K_{F_{10-3}} = 2B_1/9 \quad K_{F_{10-4}} = A_1/9 \quad K_{F_{10-6}} = B_1/9$$
$$K_{F_{11-1}} = 2A_2/9 \quad K_{F_{11-3}} = 2B_2/9 \quad K_{F_{11-4}} = A_2/9 \quad K_{F_{11-6}} = B_2/9$$
$$K_{F_{12-1}} = 2A_3/9 \quad K_{F_{12-3}} = 2B_3/9 \quad K_{F_{12-4}} = A_3/9 \quad K_{F_{12-6}} = B_3/9$$

$$K_{F_{1-7}} = A_1/9 \quad K_{F_{1-9}} = B_1/9 \quad K_{F_{1-10}} = 2A_1/9 \quad K_{F_{1-12}} = 2B_1/9$$
$$K_{F_{2-7}} = A_2/9 \quad K_{F_{2-9}} = B_2/9 \quad K_{F_{2-10}} = 2A_2/9 \quad K_{F_{2-12}} = 2B_2/9$$
$$K_{F_{3-7}} = A_3/9 \quad K_{F_{3-9}} = B_3/9 \quad K_{F_{3-10}} = 2A_3/9 \quad K_{F_{3-12}} = 2B_3/9$$
$$K_{F_{4-7}} = 2A_1/9 \quad K_{F_{4-9}} = 2B_1/9 \quad K_{F_{4-10}} = A_1/9 \quad K_{F_{4-12}} = B_1/9$$

$K_{F_{5-7}} = 2A_2/9 \quad K_{F_{5-9}} = 2B_2/9 \quad K_{F_{5-10}} = A_2/9 \quad K_{F_{5-12}} = B_2/9$
$K_{F_{6-7}} = 2A_3/9 \quad K_{F_{6-9}} = 2B_3/9 \quad K_{F_{6-10}} = A_3/9 \quad K_{F_{6-12}} = B_3/9$
$K_{F_{7-7}} = 4A_1/9 \quad K_{F_{7-9}} = 4B_1/9 \quad K_{F_{7-10}} = 2A_1/9 \quad K_{F_{7-12}} = 2B_1/9$
$K_{F_{8-7}} = 4A_2/9 \quad K_{F_{8-9}} = 4B_2/9 \quad K_{F_{8-10}} = 2A_2/9 \quad K_{F_{8-12}} = 2B_2/9$
$K_{F_{9-7}} = 4A_3/9 \quad K_{F_{9-9}} = 4B_3/9 \quad K_{F_{9-10}} = 2A_3/9 \quad K_{F_{9-12}} = 2B_3/9$
$K_{F_{10-7}} = 2A_1/9 \quad K_{F_{10-9}} = 2B_1/9 \quad K_{F_{10-10}} = 4A_1/9 \quad K_{F_{10-12}} = 4B_1/9$
$K_{F_{11-7}} = 2A_2/9 \quad K_{F_{11-9}} = 2B_2/9 \quad K_{F_{11-10}} = 4A_2/9 \quad K_{F_{11-12}} = 4B_2/9$
$K_{F_{12-7}} = 2A_3/9 \quad K_{F_{12-9}} = 2B_3/9 \quad K_{F_{12-10}} = 4A_3/9 \quad K_{F_{12-12}} = 4B_3/9$

and

$F_{1-1} = A_1T_\infty + B_1\tilde{\rho}_{V_\infty}$
$F_{2-1} = A_2T_\infty + B_2\tilde{\rho}_{V_\infty}$
$F_{3-1} = A_3T_\infty + B_3\tilde{\rho}_{V_\infty}$
$F_{4-1} = A_1T_\infty + B_1\tilde{\rho}_{V_\infty}$
$F_{5-1} = A_2T_\infty + B_2\tilde{\rho}_{V_\infty}$
$F_{6-1} = A_3T_\infty + B_3\tilde{\rho}_{V_\infty}$
$F_{7-1} = A_1T_\infty + B_1\tilde{\rho}_{V_\infty}$
$F_{8-1} = A_2T_\infty + B_2\tilde{\rho}_{V_\infty}$
$F_{9-1} = A_3T_\infty + B_3\tilde{\rho}_{V_\infty}$
$F_{10-1} = A_1T_\infty + B_1\tilde{\rho}_{V_\infty}$
$F_{11-1} = A_2T_\infty + B_2\tilde{\rho}_{V_\infty}$
$F_{12-1} = A_3T_\infty + B_3\tilde{\rho}_{V_\infty}$

A.4.4 For $\zeta = +1$

$$\int_\Gamma \left(N^T K_E F_{K_E} N\right) d\Gamma = \int_{-1}^{1}\int_{-1}^{1} \left(N^T K_E F_{K_E} N\right) \det[J_s]\, d\eta\, d\xi \Bigg|^{\zeta=+1} = K_{F_{i-j}} \qquad (A.12)$$

and

$$\int_\Gamma \left(N^T K_E F_{\infty_E}\right) d\Gamma = \int_{-1}^{1}\int_{-1}^{1} \left(N^T K_E F_{\infty_E}\right) \det[J_s]\, d\eta\, d\xi \Bigg|^{\zeta=+1} = F_{i-j} \qquad (A.13)$$

In this case, C_A will be equal to $\frac{ac}{4}$, where a and c are defined in Figure 4-1. The non-zero elements are given as:

$K_{F_{13-13}} = 4A_1/9 \quad K_{F_{13-15}} = 4B_1/9 \quad K_{F_{13-16}} = 2A_1/9 \quad K_{F_{13-18}} = 2B_1/9$

$K_{F_{14-13}} = 4A_2/9$ $K_{F_{14-15}} = 4B_2/9$ $K_{F_{14-16}} = 2A_2/9$ $K_{F_{14-18}} = 2B_2/9$
$K_{F_{15-13}} = 4A_3/9$ $K_{F_{15-15}} = 4B_3/9$ $K_{F_{15-16}} = 2A_3/9$ $K_{F_{15-18}} = 2B_3/9$
$K_{F_{16-13}} = 2A_1/9$ $K_{F_{16-15}} = 2B_1/9$ $K_{F_{16-16}} = 4A_1/9$ $K_{F_{16-18}} = 4B_1/9$
$K_{F_{17-13}} = 2A_2/9$ $K_{F_{17-15}} = 2B_2/9$ $K_{F_{17-16}} = 4A_2/9$ $K_{F_{17-18}} = 4B_2/9$
$K_{F_{18-13}} = 2A_3/9$ $K_{F_{18-15}} = 2B_3/9$ $K_{F_{18-16}} = 4A_3/9$ $K_{F_{18-18}} = 4B_3/9$
$K_{F_{19-13}} = A_1/9$ $K_{F_{19-15}} = B_1/9$ $K_{F_{19-16}} = 2A_1/9$ $K_{F_{19-18}} = 2B_1/9$
$K_{F_{20-13}} = A_2/9$ $K_{F_{20-15}} = B_2/9$ $K_{F_{20-16}} = 2A_2/9$ $K_{F_{20-18}} = 2B_2/9$
$K_{F_{21-13}} = A_3/9$ $K_{F_{21-15}} = B_3/9$ $K_{F_{21-16}} = 2A_3/9$ $K_{F_{21-18}} = 2B_3/9$
$K_{F_{22-13}} = 2A_1/9$ $K_{F_{22-15}} = 2B_1/9$ $K_{F_{22-16}} = A_1/9$ $K_{F_{22-18}} = B_1/9$
$K_{F_{23-13}} = 2A_2/9$ $K_{F_{23-15}} = 2B_2/9$ $K_{F_{23-16}} = A_2/9$ $K_{F_{23-18}} = B_2/9$
$K_{F_{24-13}} = 2A_3/9$ $K_{F_{24-15}} = 2B_3/9$ $K_{F_{24-16}} = A_3/9$ $K_{F_{24-18}} = B_3/9$

$K_{F_{13-19}} = A_1/9$ $K_{F_{13-21}} = B_1/9$ $K_{F_{13-22}} = 2A_1/9$ $K_{F_{13-24}} = 2B_1/9$
$K_{F_{14-19}} = A_2/9$ $K_{F_{14-21}} = B_2/9$ $K_{F_{14-22}} = 2A_2/9$ $K_{F_{14-24}} = 2B_2/9$
$K_{F_{15-19}} = A_3/9$ $K_{F_{15-21}} = B_3/9$ $K_{F_{15-22}} = 2A_3/9$ $K_{F_{15-24}} = 2B_3/9$
$K_{F_{16-19}} = 2A_1/9$ $K_{F_{16-21}} = 2B_1/9$ $K_{F_{16-22}} = A_1/9$ $K_{F_{16-24}} = B_1/9$
$K_{F_{17-19}} = 2A_2/9$ $K_{F_{17-21}} = 2B_2/9$ $K_{F_{17-22}} = A_2/9$ $K_{F_{17-24}} = B_2/9$
$K_{F_{18-19}} = 2A_3/9$ $K_{F_{18-21}} = 2B_3/9$ $K_{F_{18-22}} = A_3/9$ $K_{F_{18-24}} = B_3/9$
$K_{F_{19-19}} = 4A_1/9$ $K_{F_{19-21}} = 4B_1/9$ $K_{F_{19-22}} = 2A_1/9$ $K_{F_{19-24}} = 2B_1/9$
$K_{F_{20-19}} = 4A_2/9$ $K_{F_{20-21}} = 4B_2/9$ $K_{F_{20-22}} = 2A_2/9$ $K_{F_{20-24}} = 2B_2/9$
$K_{F_{21-19}} = 4A_3/9$ $K_{F_{21-21}} = 4B_3/9$ $K_{F_{21-22}} = 2A_3/9$ $K_{F_{21-24}} = 2B_3/9$
$K_{F_{22-19}} = 2A_1/9$ $K_{F_{22-21}} = 2B_1/9$ $K_{F_{22-22}} = 4A_1/9$ $K_{F_{22-24}} = 4B_1/9$
$K_{F_{23-19}} = 2A_2/9$ $K_{F_{23-21}} = 2B_2/9$ $K_{F_{23-22}} = 4A_2/9$ $K_{F_{23-24}} = 4B_2/9$
$K_{F_{24-19}} = 2A_3/9$ $K_{F_{24-21}} = 2B_3/9$ $K_{F_{24-22}} = 4A_3/9$ $K_{F_{24-24}} = 4B_3/9$

and

$$F_{13-1} = A_1 T_\infty + B_1 \tilde{\rho}_{V_\infty}$$
$$F_{14-1} = A_2 T_\infty + B_2 \tilde{\rho}_{V_\infty}$$
$$F_{15-1} = A_3 T_\infty + B_3 \tilde{\rho}_{V_\infty}$$
$$F_{16-1} = A_1 T_\infty + B_1 \tilde{\rho}_{V_\infty}$$
$$F_{17-1} = A_2 T_\infty + B_2 \tilde{\rho}_{V_\infty}$$
$$F_{18-1} = A_3 T_\infty + B_3 \tilde{\rho}_{V_\infty}$$
$$F_{19-1} = A_1 T_\infty + B_1 \tilde{\rho}_{V_\infty}$$
$$F_{20-1} = A_2 T_\infty + B_2 \tilde{\rho}_{V_\infty}$$
$$F_{21-1} = A_3 T_\infty + B_3 \tilde{\rho}_{V_\infty}$$
$$F_{22-1} = A_1 T_\infty + B_1 \tilde{\rho}_{V_\infty}$$
$$F_{23-1} = A_2 T_\infty + B_2 \tilde{\rho}_{V_\infty}$$
$$F_{24-1} = A_3 T_\infty + B_3 \tilde{\rho}_{V_\infty}$$

A.4.5 For $\xi = -1$

$$\int_{\Gamma}\left(N^{T}K_{E}F_{K_{E}}N\right)d\Gamma = \int_{-1}^{1}\int_{-1}^{1}\left(N^{T}K_{E}F_{K_{E}}N\right)\det[J_{s}]d\zeta\, d\xi\Big|^{\xi=-1} = K_{F_{i-j}} \qquad (A.14)$$

and

$$\int_{\Gamma}\left(N^{T}K_{E}F_{\infty_{E}}\right)d\Gamma = \int_{-1}^{1}\int_{-1}^{1}\left(N^{T}K_{E}F_{\infty_{E}}\right)\det[J_{s}]d\zeta\, d\xi\Big|^{\xi=-1} = F_{i-j} \qquad (A.15)$$

In this case, C_A will be equal to $\frac{ab}{4}$, where a and b are defined in Figure 4-1. The non-zero elements are given as:

$K_{F_{1-1}} = 4A_1/9$	$K_{F_{1-3}} = 4B_1/9$	$K_{F_{1-10}} = 2A_1/9$	$K_{F_{1-12}} = 2B_1/9$
$K_{F_{2-1}} = 4A_2/9$	$K_{F_{2-3}} = 4B_2/9$	$K_{F_{2-10}} = 2A_2/9$	$K_{F_{2-12}} = 2B_2/9$
$K_{F_{3-1}} = 4A_3/9$	$K_{F_{3-3}} = 4B_3/9$	$K_{F_{3-10}} = 2A_3/9$	$K_{F_{3-12}} = 2B_3/9$
$K_{F_{10-1}} = 2A_1/9$	$K_{F_{10-3}} = 2B_1/9$	$K_{F_{10-10}} = 4A_1/9$	$K_{F_{10-12}} = 4B_1/9$
$K_{F_{11-1}} = 2A_2/9$	$K_{F_{11-3}} = 2B_2/9$	$K_{F_{11-10}} = 4A_2/9$	$K_{F_{11-12}} = 4B_2/9$
$K_{F_{12-1}} = 2A_3/9$	$K_{F_{12-3}} = 2B_3/9$	$K_{F_{12-10}} = 4A_3/9$	$K_{F_{12-12}} = 4B_3/9$
$K_{F_{13-1}} = 2A_1/9$	$K_{F_{13-3}} = 2B_1/9$	$K_{F_{13-10}} = A_1/9$	$K_{F_{13-12}} = B_1/9$
$K_{F_{14-1}} = 2A_2/9$	$K_{F_{14-3}} = 2B_2/9$	$K_{F_{14-10}} = A_2/9$	$K_{F_{14-12}} = B_2/9$
$K_{F_{15-1}} = 2A_3/9$	$K_{F_{15-3}} = 2B_3/9$	$K_{F_{15-10}} = A_3/9$	$K_{F_{15-12}} = B_3/9$
$K_{F_{22-1}} = A_1/9$	$K_{F_{22-3}} = B_1/9$	$K_{F_{22-10}} = 2A_1/9$	$K_{F_{22-12}} = 2B_1/9$
$K_{F_{23-1}} = A_2/9$	$K_{F_{23-3}} = B_2/9$	$K_{F_{23-10}} = 2A_2/9$	$K_{F_{23-12}} = 2B_2/9$
$K_{F_{24-1}} = A_3/9$	$K_{F_{24-3}} = B_3/9$	$K_{F_{24-10}} = 2A_3/9$	$K_{F_{24-12}} = 2B_3/9$

$K_{F_{1-13}} = 2A_1/9$	$K_{F_{1-15}} = 2B_1/9$	$K_{F_{1-22}} = A_1/9$	$K_{F_{1-24}} = B_1/9$
$K_{F_{2-13}} = 2A_2/9$	$K_{F_{2-15}} = 2B_2/9$	$K_{F_{2-22}} = A_2/9$	$K_{F_{2-24}} = B_2/9$
$K_{F_{3-13}} = 2A_3/9$	$K_{F_{3-15}} = 2B_3/9$	$K_{F_{3-22}} = A_3/9$	$K_{F_{3-24}} = B_3/9$
$K_{F_{10-13}} = A_1/9$	$K_{F_{10-15}} = B_1/9$	$K_{F_{10-22}} = 2A_1/9$	$K_{F_{10-24}} = 2B_1/9$
$K_{F_{11-13}} = A_2/9$	$K_{F_{11-15}} = B_2/9$	$K_{F_{11-22}} = 2A_2/9$	$K_{F_{11-24}} = 2B_2/9$
$K_{F_{12-13}} = A_3/9$	$K_{F_{12-15}} = B_3/9$	$K_{F_{12-22}} = 2A_3/9$	$K_{F_{12-24}} = 2B_3/9$
$K_{F_{13-13}} = 4A_1/9$	$K_{F_{13-15}} = 4B_1/9$	$K_{F_{13-22}} = 2A_1/9$	$K_{F_{13-24}} = 2B_1/9$
$K_{F_{14-13}} = 4A_2/9$	$K_{F_{14-15}} = 4B_2/9$	$K_{F_{14-22}} = 2A_2/9$	$K_{F_{14-24}} = 2B_2/9$
$K_{F_{15-13}} = 4A_3/9$	$K_{F_{15-15}} = 4B_3/9$	$K_{F_{15-22}} = 2A_3/9$	$K_{F_{15-24}} = 2B_3/9$
$K_{F_{22-13}} = 2A_1/9$	$K_{F_{22-15}} = 2B_1/9$	$K_{F_{22-22}} = 4A_1/9$	$K_{F_{22-24}} = 4B_1/9$
$K_{F_{23-13}} = 2A_2/9$	$K_{F_{23-15}} = 2B_2/9$	$K_{F_{23-22}} = 4A_2/9$	$K_{F_{23-24}} = 4B_2/9$
$K_{F_{24-13}} = 2A_3/9$	$K_{F_{24-15}} = 2B_3/9$	$K_{F_{24-22}} = 4A_3/9$	$K_{F_{24-24}} = 4B_3/9$

and

$$
\begin{aligned}
F_{1-1} &= A_1 T_\infty + B_1 \tilde{\rho}_{V_\infty} \\
F_{2-1} &= A_2 T_\infty + B_2 \tilde{\rho}_{V_\infty} \\
F_{3-1} &= A_3 T_\infty + B_3 \tilde{\rho}_{V_\infty} \\
F_{10-1} &= A_1 T_\infty + B_1 \tilde{\rho}_{V_\infty} \\
F_{11-1} &= A_2 T_\infty + B_2 \tilde{\rho}_{V_\infty} \\
F_{12-1} &= A_3 T_\infty + B_3 \tilde{\rho}_{V_\infty} \\
F_{13-1} &= A_1 T_\infty + B_1 \tilde{\rho}_{V_\infty} \\
F_{14-1} &= A_2 T_\infty + B_2 \tilde{\rho}_{V_\infty} \\
F_{15-1} &= A_3 T_\infty + B_3 \tilde{\rho}_{V_\infty} \\
F_{22-1} &= A_1 T_\infty + B_1 \tilde{\rho}_{V_\infty} \\
F_{23-1} &= A_2 T_\infty + B_2 \tilde{\rho}_{V_\infty} \\
F_{24-1} &= A_3 T_\infty + B_3 \tilde{\rho}_{V_\infty}
\end{aligned}
$$

A.4.6 For $\xi = +1$

$$\int_\Gamma \left(N^T K_E F_{K_E} N\right) d\Gamma = \int_{-1}^{1}\int_{-1}^{1} \left(N^T K_E F_{K_E} N\right) \det[J_s] d\zeta\, d\xi \Bigg|^{\xi=+1} = K_{F_{i-j}} \qquad (A.16)$$

and

$$\int_\Gamma \left(N^T K_E F_{\infty_E}\right) d\Gamma = \int_{-1}^{1}\int_{-1}^{1} \left(N^T K_E F_{\infty_E}\right) \det[J_s] d\zeta\, d\xi \Bigg|^{\xi=+1} = F_{i-j} \qquad (A.17)$$

In this case, C_A will be equal to $\frac{ab}{4}$, where a and b are defined in Figure 4-1. The non-zero elements are given as:

$$
\begin{array}{llllllll}
K_{F_{4-4}} = 4A_1/9 & K_{F_{4-6}} = 4B_1/9 & K_{F_{4-7}} = 2A_1/9 & K_{F_{4-9}} = 2B_1/9 \\
K_{F_{5-4}} = 4A_2/9 & K_{F_{5-6}} = 4B_2/9 & K_{F_{5-7}} = 2A_2/9 & K_{F_{5-9}} = 2B_2/9 \\
K_{F_{6-4}} = 4A_3/9 & K_{F_{6-6}} = 4B_3/9 & K_{F_{6-7}} = 2A_3/9 & K_{F_{6-9}} = 2B_3/9 \\
K_{F_{7-4}} = 2A_1/9 & K_{F_{7-6}} = 2B_1/9 & K_{F_{7-7}} = 4A_1/9 & K_{F_{7-9}} = 4B_1/9 \\
K_{F_{8-4}} = 2A_2/9 & K_{F_{8-6}} = 2B_2/9 & K_{F_{8-7}} = 4A_2/9 & K_{F_{8-9}} = 4B_2/9 \\
K_{F_{9-4}} = 2A_3/9 & K_{F_{9-6}} = 2B_3/9 & K_{F_{9-7}} = 4A_3/9 & K_{F_{9-9}} = 4B_3/9 \\
K_{F_{16-4}} = 2A_1/9 & K_{F_{16-6}} = 2B_1/9 & K_{F_{16-7}} = A_1/9 & K_{F_{16-9}} = B_1/9 \\
K_{F_{17-4}} = 2A_2/9 & K_{F_{17-6}} = 2B_2/9 & K_{F_{17-7}} = A_2/9 & K_{F_{17-9}} = B_2/9 \\
K_{F_{18-4}} = 2A_3/9 & K_{F_{18-6}} = 2B_3/9 & K_{F_{18-7}} = A_3/9 & K_{F_{18-9}} = B_3/9 \\
K_{F_{19-4}} = A_1/9 & K_{F_{19-6}} = B_1/9 & K_{F_{19-7}} = 2A_1/9 & K_{F_{19-9}} = 2B_1/9 \\
K_{F_{20-4}} = A_2/9 & K_{F_{20-6}} = B_2/9 & K_{F_{20-7}} = 2A_2/9 & K_{F_{20-9}} = 2B_2/9
\end{array}
$$

$K_{F_{21-4}} = A_3/9 \quad K_{F_{21-6}} = B_3/9 \quad K_{F_{21-7}} = 2A_3/9 \quad K_{F_{21-9}} = 2B_3/9$

$K_{F_{4-16}} = 2A_1/9 \quad K_{F_{4-18}} = 2B_1/9 \quad K_{F_{4-19}} = A_1/9 \quad K_{F_{4-21}} = B_1/9$
$K_{F_{5-16}} = 2A_2/9 \quad K_{F_{5-18}} = 2B_2/9 \quad K_{F_{5-19}} = A_2/9 \quad K_{F_{5-21}} = B_2/9$
$K_{F_{6-16}} = 2A_3/9 \quad K_{F_{6-18}} = 2B_3/9 \quad K_{F_{6-19}} = A_3/9 \quad K_{F_{6-21}} = B_3/9$
$K_{F_{7-16}} = A_1/9 \quad K_{F_{7-18}} = B_1/9 \quad K_{F_{7-19}} = 2A_1/9 \quad K_{F_{7-21}} = 2B_1/9$
$K_{F_{8-16}} = A_2/9 \quad K_{F_{8-18}} = B_2/9 \quad K_{F_{8-19}} = 2A_2/9 \quad K_{F_{8-21}} = 2B_2/9$
$K_{F_{9-16}} = A_3/9 \quad K_{F_{9-18}} = B_3/9 \quad K_{F_{9-19}} = 2A_3/9 \quad K_{F_{9-21}} = 2B_3/9$
$K_{F_{16-16}} = 4A_1/9 \quad K_{F_{16-18}} = 4B_1/9 \quad K_{F_{16-19}} = 2A_1/9 \quad K_{F_{16-21}} = 2B_1/9$
$K_{F_{17-16}} = 4A_2/9 \quad K_{F_{17-18}} = 4B_2/9 \quad K_{F_{17-19}} = 2A_2/9 \quad K_{F_{17-21}} = 2B_2/9$
$K_{F_{18-16}} = 4A_3/9 \quad K_{F_{18-18}} = 4B_3/9 \quad K_{F_{18-19}} = 2A_3/9 \quad K_{F_{18-21}} = 2B_3/9$
$K_{F_{19-16}} = 2A_1/9 \quad K_{F_{19-18}} = 2B_1/9 \quad K_{F_{19-19}} = 4A_1/9 \quad K_{F_{19-21}} = 4B_1/9$
$K_{F_{20-16}} = 2A_2/9 \quad K_{F_{20-18}} = 2B_2/9 \quad K_{F_{20-19}} = 4A_2/9 \quad K_{F_{20-21}} = 4B_2/9$
$K_{F_{21-16}} = 2A_3/9 \quad K_{F_{21-18}} = 2B_3/9 \quad K_{F_{21-19}} = 4A_3/9 \quad K_{F_{21-21}} = 4B_3/9$

and

$F_{4-1} = A_1 T_\infty + B_1 \tilde{\rho}_{V_\infty}$
$F_{5-1} = A_2 T_\infty + B_2 \tilde{\rho}_{V_\infty}$
$F_{6-1} = A_3 T_\infty + B_3 \tilde{\rho}_{V_\infty}$
$F_{7-1} = A_1 T_\infty + B_1 \tilde{\rho}_{V_\infty}$
$F_{8-1} = A_2 T_\infty + B_2 \tilde{\rho}_{V_\infty}$
$F_{9-1} = A_3 T_\infty + B_3 \tilde{\rho}_{V_\infty}$
$F_{16-1} = A_1 T_\infty + B_1 \tilde{\rho}_{V_\infty}$
$F_{17-1} = A_2 T_\infty + B_2 \tilde{\rho}_{V_\infty}$
$F_{18-1} = A_3 T_\infty + B_3 \tilde{\rho}_{V_\infty}$
$F_{19-1} = A_1 T_\infty + B_1 \tilde{\rho}_{V_\infty}$
$F_{20-1} = A_2 T_\infty + B_2 \tilde{\rho}_{V_\infty}$
$F_{21-1} = A_3 T_\infty + B_3 \tilde{\rho}_{V_\infty}$

A.5 Elements of $\int_\Omega \left({N_T}^T \rho_c c_{p_c} N_T \right) d\Omega$

Matrix $\int_\Omega \left({N_T}^T \rho_c c_{p_c} N_T \right) d\Omega$, introduced in Equation (4.109), is an 8×8 symmetric matrix, with elements given the notation $C_{T_{i-j}}$, where i is the row number and j is the column number. $\rho_c c_{p_c}$ is the heat capacity of completely dry concrete.

$$\int_{\Omega}\left(N_T{}^T\,\rho_c c_{p_c} N_T\right)d\Omega = \int_{-1}^{1}\int_{-1}^{1}\int_{-1}^{1}\left(N_T{}^T\,\rho_c c_{p_c} N_T\right)\det[J]\,d\eta\,d\zeta\,d\xi = C_{T_{i-j}} \quad (A.18)$$

With $V_C = \frac{abc}{216}$, where a, b and c are defined in Figure 4-1, and , $C_{T_{i-j}}$ can be given as:

$$C_{T_{i-j}} = \rho_c c_{p_c} V_C \begin{bmatrix} 8 & 4 & 2 & 4 & 4 & 2 & 1 & 2 \\ & 8 & 4 & 2 & 2 & 4 & 2 & 1 \\ & & 8 & 4 & 2 & 2 & 4 & 2 \\ & & & 8 & 2 & 1 & 2 & 4 \\ & & & & 8 & 4 & 2 & 4 \\ & & & & & 8 & 4 & 2 \\ & & \text{Symmetric} & & & & 8 & 4 \\ & & & & & & & 8 \end{bmatrix} \quad (A.19)$$

As previously mentioned, the lumped matrix is used in lieu of the consistent one presented in Equation (A.19), thus with $V_p = \frac{abc}{8}$,

$$C_{T_{i-j}} = \rho_c c_{p_c} V_p \begin{bmatrix} 1 & 0 & 0 & 0 & 0 & 0 & 0 & 0 \\ & 1 & 0 & 0 & 0 & 0 & 0 & 0 \\ & & 1 & 0 & 0 & 0 & 0 & 0 \\ & & & 1 & 0 & 0 & 0 & 0 \\ & & & & 1 & 0 & 0 & 0 \\ & & & & & 1 & 0 & 0 \\ & & \text{Symmetric} & & & & 1 & 0 \\ & & & & & & & 1 \end{bmatrix} \quad (A.20)$$

A.6 Elements of $\int_{\Omega}\left(\nabla N_T{}^T K_{TE} \nabla N_T\right)d\Omega$

Matrix $\int_{\Omega}\left(\nabla N_T{}^T K_{TE} \nabla N_T\right)d\Omega$, introduced in Equations (4.110) and (4.112), is an 8×8 symmetric matrix, with elements given the notation $K_{T_{i-j}}$, where i is the row number and j is the column number. Matrix K_{TE} is defined in Equation (4.114).

$$\int_{\Omega}\left(\nabla N_T{}^T K_{TE} \nabla N_T\right)d\Omega = \int_{-1}^{1}\int_{-1}^{1}\int_{-1}^{1}\left(\nabla N_T{}^T K_{TE} \nabla N_T\right)\det[J]\,d\eta\,d\zeta\,d\xi = K_{T_{i-j}} \quad (A.21)$$

With A equals $\frac{bc}{36a}$, B equals $\frac{ac}{36b}$, and C equals $\frac{ab}{36c}$, where a, b and c are defined in Figure 4-1.

$$
\begin{bmatrix}
4A+4B+4C & 2A+2B-4C & -2A+B-2C & -4A+2B+2C & 2A-4B+2C & A-2B-2C & -A-B-C & -2A-2B+C \\
 & 4A+4B+4C & -4A+2B+2C & -2A+B-2C & A-2B-2C & 2A-4B+2C & -2A-2B+C & -A-B-C \\
 & & 4A+4B+4C & 2A+2B-4C & -A-B-C & -2A-2B+C & 2A-4B+2C & A-2B-2C \\
 & & & 4A+4B+4C & -2A-2B+C & -A-B-C & A-2B-2C & 2A-4B+2C \\
 & & & & 4A+4B+4C & 2A+2B-4C & -2A+B-2C & -4A+2B+2C \\
 & & \text{Symmetric} & & & 4A+4B+4C & -4A+2B+2C & -2A+B-2C \\
 & & & & & & 4A+4B+4C & 2A+2B-4C \\
 & & & & & & & 4A+4B+4C
\end{bmatrix}
$$

$$K_{T_{1-1}} = 4A+4B+4C$$
$$K_{T_{2-1}} = 2A+2B-4C$$
$$K_{T_{3-1}} = -2A+B-2C$$
$$K_{T_{4-1}} = -4A+2B+2C$$
$$K_{T_{5-1}} = 2A-4B+2C$$
$$K_{T_{6-1}} = A-2B-2C$$
$$K_{T_{7-1}} = -A-B-C$$
$$K_{T_{8-1}} = -2A-2B+C$$

$$K_{T_{1-2}} = K_{T_{2-1}}$$
$$K_{T_{2-2}} = 4A+4B+4C$$
$$K_{T_{3-2}} = -4A+2B+2C$$
$$K_{T_{4-2}} = -2A+B-2C$$
$$K_{T_{5-2}} = A-2B-2C$$
$$K_{T_{6-2}} = 2A-4B+2C$$
$$K_{T_{7-2}} = -2A-2B+C$$
$$K_{T_{8-2}} = -A-B-C$$

$$K_{T_{1-3}} = K_{T_{3-1}}$$
$$K_{T_{2-3}} = K_{T_{3-2}}$$
$$K_{T_{3-3}} = 4A+4B+4C$$
$$K_{T_{4-3}} = 2A+2B-4C$$
$$K_{T_{5-3}} = -A-B-C$$
$$K_{T_{6-3}} = -2A-2B+C$$
$$K_{T_{7-3}} = 2A-4B+2C$$
$$K_{T_{8-3}} = A-2B-2C$$

$$K_{T_{1-4}} = K_{T_{4-1}}$$
$$K_{T_{2-4}} = K_{T_{4-2}}$$
$$K_{T_{3-4}} = K_{T_{4-3}}$$
$$K_{T_{4-4}} = 4A+4B+4C$$
$$K_{T_{5-4}} = -2A-2B+C$$
$$K_{T_{6-4}} = -A-B-C$$
$$K_{T_{7-4}} = A-2B-2C$$
$$K_{T_{8-4}} = 2A-4B+2C$$

$$K_{T_{1-5}} = K_{T_{5-1}}$$
$$K_{T_{2-5}} = K_{T_{5-2}}$$
$$K_{T_{3-5}} = K_{T_{5-3}}$$
$$K_{T_{4-5}} = K_{T_{5-4}}$$
$$K_{T_{5-5}} = 4A+4B+4C$$
$$K_{T_{6-5}} = 2A+2B-4C$$
$$K_{T_{7-5}} = -2A+B-2C$$
$$K_{T_{8-5}} = -4A+2B+2C$$

$$K_{T_{1-6}} = K_{T_{6-1}}$$
$$K_{T_{2-6}} = K_{T_{6-2}}$$
$$K_{T_{3-6}} = K_{T_{6-3}}$$
$$K_{T_{4-6}} = K_{T_{6-4}}$$
$$K_{T_{5-6}} = K_{T_{6-5}}$$
$$K_{T_{6-6}} = 4A+4B+4C$$
$$K_{T_{7-6}} = -4A+2B+2C$$
$$K_{T_{8-6}} = -2A+B-2C$$

$$K_{T_{1-7}} = K_{T_{7-1}}$$
$$K_{T_{2-7}} = K_{T_{7-2}}$$

$$K_{T_{1-8}} = K_{T_{8-1}}$$
$$K_{T_{2-8}} = K_{T_{8-2}}$$

$K_{T_{3-7}} = K_{T_{7-3}}$ $K_{T_{3-8}} = K_{T_{8-3}}$
$K_{T_{4-7}} = K_{T_{7-4}}$ $K_{T_{4-8}} = K_{T_{8-4}}$
$K_{T_{5-7}} = K_{T_{7-5}}$ $K_{T_{5-8}} = K_{T_{8-5}}$
$K_{T_{6-7}} = K_{T_{7-6}}$ $K_{T_{6-8}} = K_{T_{8-6}}$
$K_{T_{7-7}} = 4A + 4B + 4C$ $K_{T_{7-8}} = K_{T_{8-7}}$
$K_{T_{8-7}} = 2A + 2B - 4C$ $K_{T_{8-8}} = 4A + 4B + 4C$

A.7 Elements of $\int_\Gamma (N_T{}^T h N_T) d\Gamma$ and $\int_\Gamma (N_T{}^T h T_\infty) d\Gamma$

Matrix $\int_\Gamma (N_T{}^T h N_T) d\Gamma$, introduced in Equation (4.112), is an 8×8 symmetric matrix, with elements given the notation $K_{F_{T_{i-j}}}$ and matrix $\int_\Gamma (N_T{}^T h T_\infty) d\Gamma$, introduced in Equation (4.113), is an 8×1 vector with elements given the notation $F_{T_{i-j}}$, where i is the row number and j is the column number. h is the combined convective and radiative heat transfer coefficients on the boundary surface, as shown in Equation (4.74). The elemental area dΓ is evaluated the same way as explained in Section A.4.

A.7.1 For $\eta = -1$

$$\int_\Gamma (N_T{}^T h N_T) d\Gamma = \int_{-1}^{1}\int_{-1}^{1} (N_T h N_T) \det[J_s] d\zeta\, d\xi \Big|^{\eta=-1} = K_{F_{T_{i-j}}} \quad (A.22)$$

and

$$\int_\Gamma (N_T{}^T h T_\infty) d\Gamma = \int_{-1}^{1}\int_{-1}^{1} (N_T{}^T h T_\infty) \det[J_s] d\zeta\, d\xi \Big|^{\eta=-1} = F_{T_{i-j}} \quad (A.23)$$

In this case, $\det[J_s]$ will be equal to $\frac{bc}{4}$, where b and c are defined in Figure 4-1. Hence, with D_1 defined as $h\frac{bc}{4}$ the non-zero elements are given as:

$K_{F_{T_{1-1}}} = 4D_1/9$ $K_{F_{T_{1-2}}} = K_{F_{T_{2-1}}}$ $K_{F_{T_{1-5}}} = K_{F_{T_{5-1}}}$ $K_{F_{T_{1-6}}} = K_{F_{T_{6-1}}}$
$K_{F_{T_{2-1}}} = 2D_1/9$ $K_{F_{T_{2-2}}} = 4D_1/9$ $K_{F_{T_{2-5}}} = K_{F_{T_{5-2}}}$ $K_{F_{T_{2-6}}} = K_{F_{T_{6-2}}}$
$K_{F_{T_{5-1}}} = 2D_1/9$ $K_{F_{T_{5-2}}} = D_1/9$ $K_{F_{T_{5-5}}} = 4D_1/9$ $K_{F_{T_{5-6}}} = K_{F_{T_{6-5}}}$
$K_{F_{T_{6-1}}} = D_1/9$ $K_{F_{T_{6-2}}} = 2D_1/9$ $K_{F_{T_{6-5}}} = 2D_1/9$ $K_{F_{T_{6-6}}} = 4D_1/9$

and

$$F_{T_{1-1}} = F_{T_{2-1}} = F_{T_{5-1}} = F_{T_{6-1}} = D_1 T_\infty$$

A.7.2 For $\eta = +1$

$$\int_\Gamma \left(N_T{}^T h N_T\right) d\Gamma = \int_{-1}^{1}\int_{-1}^{1} (N_T h N_T) \det[J_s]\, d\zeta\, d\xi \Bigg|^{\eta=+1} = K_{F_{T_{i-j}}} \qquad (A.24)$$

and

$$\int_\Gamma \left(N_T{}^T h T_\infty\right) d\Gamma = \int_{-1}^{1}\int_{-1}^{1} \left(N_T{}^T h T_\infty\right) \det[J_s]\, d\zeta\, d\xi \Bigg|^{\eta=+1} = F_{T_{i-j}} \qquad (A.25)$$

In this case, $\det[J_s]$ will be equal to $\frac{bc}{4}$, where b and c are defined in Figure 4-1. Hence, with D_1 defined as $h\frac{bc}{4}$ the non-zero elements are given as:

$$\begin{array}{llllllll}
K_{F_{T_{3-3}}} = 4D_1/9 & K_{F_{T_{3-4}}} = K_{F_{T_{4-3}}} & K_{F_{T_{3-7}}} = K_{F_{T_{7-3}}} & K_{F_{T_{3-8}}} = K_{F_{T_{8-3}}} \\
K_{F_{T_{4-3}}} = 2D_1/9 & K_{F_{T_{4-4}}} = 4D_1/9 & K_{F_{T_{4-7}}} = K_{F_{T_{7-4}}} & K_{F_{T_{4-8}}} = K_{F_{T_{8-4}}} \\
K_{F_{T_{7-3}}} = 2D_1/9 & K_{F_{T_{7-4}}} = D_1/9 & K_{F_{T_{7-7}}} = 4D_1/9 & K_{F_{T_{7-8}}} = K_{F_{T_{8-7}}} \\
K_{F_{T_{8-3}}} = D_1/9 & K_{F_{T_{8-4}}} = 2D_1/9 & K_{F_{T_{8-7}}} = 2D_1/9 & K_{F_{T_{8-8}}} = 4D_1/9
\end{array}$$

and

$$F_{T_{3-1}} = F_{T_{4-1}} = F_{T_{7-1}} = F_{T_{8-1}} = D_1 T_\infty$$

A.7.3 For $\zeta = -1$

$$\int_\Gamma \left(N_T{}^T h N_T\right) d\Gamma = \int_{-1}^{1}\int_{-1}^{1} (N_T h N_T) \det[J_s]\, d\eta\, d\xi \Bigg|^{\zeta=-1} = K_{F_{T_{i-j}}} \qquad (A.26)$$

and

$$\int_\Gamma \left(N_T{}^T h T_\infty\right) d\Gamma = \int_{-1}^{1}\int_{-1}^{1} \left(N_T{}^T h T_\infty\right) \det[J_s]\, d\eta\, d\xi \Bigg|^{\zeta=-1} = F_{T_{i-j}} \qquad (A.27)$$

In this case, $\det[J_s]$ will be equal to $\frac{ac}{4}$, where a and c are defined in Figure 4-1. Hence, with D_2 defined as $h\frac{ac}{4}$ the non-zero elements are given as:

$$\begin{array}{llllllll}
K_{F_{T_{1-1}}} = 4D_2/9 & K_{F_{T_{1-2}}} = K_{F_{T_{2-1}}} & K_{F_{T_{1-3}}} = K_{F_{T_{3-1}}} & K_{F_{T_{1-4}}} = K_{F_{T_{4-1}}} \\
K_{F_{T_{2-1}}} = 2D_2/9 & K_{F_{T_{2-2}}} = 4D_2/9 & K_{F_{T_{2-3}}} = K_{F_{T_{3-2}}} & K_{F_{T_{2-4}}} = K_{F_{T_{4-2}}} \\
K_{F_{T_{3-1}}} = D_2/9 & K_{F_{T_{3-2}}} = 2D_2/9 & K_{F_{T_{3-3}}} = 4D_2/9 & K_{F_{T_{3-4}}} = K_{F_{T_{4-3}}} \\
K_{F_{T_{4-1}}} = 2D_2/9 & K_{F_{T_{4-2}}} = D_2/9 & K_{F_{T_{4-3}}} = 2D_2/9 & K_{F_{T_{4-4}}} = 4D_2/9
\end{array}$$

and

$$F_{T_{1-1}} = F_{T_{2-1}} = F_{T_{3-1}} = F_{T_{4-1}} = D_2 T_\infty$$

A.7.4 For $\zeta = +1$

$$\int_\Gamma \left(N_T{}^T h N_T\right) d\Gamma = \int_{-1}^{1}\int_{-1}^{1} (N_T h N_T) \det[J_s] d\eta\, d\xi \Bigg|^{\zeta=+1} = K_{F_{T_{i-j}}} \qquad (A.28)$$

and

$$\int_\Gamma \left(N_T{}^T h T_\infty\right) d\Gamma = \int_{-1}^{1}\int_{-1}^{1} \left(N_T{}^T h T_\infty\right) \det[J_s] d\eta\, d\xi \Bigg|^{\zeta=+1} = F_{T_{i-j}} \qquad (A.29)$$

In this case, $\det[J_s]$ will be equal to $\frac{ac}{4}$, where a and c are defined in Figure 4-1. Hence, with D_2 defined as $h\frac{ac}{4}$ the non-zero elements are given as:

$$\begin{array}{llllllll}
K_{F_{T_{5-5}}} = 4D_2/9 & K_{F_{T_{5-6}}} = K_{F_{T_{6-5}}} & K_{F_{T_{5-7}}} = K_{F_{T_{7-5}}} & K_{F_{T_{5-8}}} = K_{F_{T_{8-5}}} \\
K_{F_{T_{6-5}}} = 2D_2/9 & K_{F_{T_{6-6}}} = 4D_2/9 & K_{F_{T_{6-7}}} = K_{F_{T_{7-6}}} & K_{F_{T_{6-8}}} = K_{F_{T_{8-6}}} \\
K_{F_{T_{7-5}}} = D_2/9 & K_{F_{T_{7-6}}} = 2D_2/9 & K_{F_{T_{7-7}}} = 4D_2/9 & K_{F_{T_{7-8}}} = K_{F_{T_{8-7}}} \\
K_{F_{T_{8-5}}} = 2D_2/9 & K_{F_{T_{8-6}}} = D_2/9 & K_{F_{T_{8-7}}} = 2D_2/9 & K_{F_{T_{8-8}}} = 4D_2/9
\end{array}$$

and

$$F_{T_{5-1}} = F_{T_{6-1}} = F_{T_{7-1}} = F_{T_{8-1}} = D_2 T_\infty$$

A.7.5 For $\xi = -1$

$$\int_{\Gamma} \left(N_T{}^T h N_T\right) d\Gamma = \int_{-1}^{1}\int_{-1}^{1} \left(N_T{}^T h N_T\right) \det[J_s]\, d\zeta\, d\xi \Bigg|^{\xi=-1} = K_{F_{T_{i-j}}} \qquad (A.30)$$

and

$$\int_{\Gamma} \left(N_T{}^T h T_\infty\right) d\Gamma = \int_{-1}^{1}\int_{-1}^{1} \left(N_T{}^T h T_\infty\right) \det[J_s]\, d\zeta\, d\xi \Bigg|^{\xi=-1} = F_{T_{i-j}} \qquad (A.31)$$

In this case, $\det[J_s]$ will be equal to $\frac{ab}{4}$, where a and b are defined in Figure 4-1. Hence, with D_3 defined as $h\frac{ab}{4}$ the non-zero elements are given as:

$$\begin{array}{llllllllll}
K_{F_{T_{1-1}}} = 4D_2/9 & K_{F_{T_{1-4}}} = K_{F_{T_{4-1}}} & K_{F_{T_{1-5}}} = K_{F_{T_{5-1}}} & K_{F_{T_{1-8}}} = K_{F_{T_{8-1}}} \\
K_{F_{T_{4-1}}} = 2D_2/9 & K_{F_{T_{4-4}}} = 4D_2/9 & K_{F_{T_{4-5}}} = K_{F_{T_{5-4}}} & K_{F_{T_{4-8}}} = K_{F_{T_{8-4}}} \\
K_{F_{T_{5-1}}} = 2D_2/9 & K_{F_{T_{5-4}}} = D_2/9 & K_{F_{T_{5-5}}} = 4D_2/9 & K_{F_{T_{5-8}}} = K_{F_{T_{8-5}}} \\
K_{F_{T_{8-1}}} = D_2/9 & K_{F_{T_{8-4}}} = 2D_2/9 & K_{F_{T_{8-5}}} = 2D_2/9 & K_{F_{T_{8-8}}} = 4D_2/9
\end{array}$$

and

$$F_{T_{1-1}} = F_{T_{4-1}} = F_{T_{5-1}} = F_{T_{8-1}} = D_3 T_\infty$$

A.7.6 For $\xi = +1$

$$\int_{\Gamma} \left(N_T{}^T h N_T\right) d\Gamma = \int_{-1}^{1}\int_{-1}^{1} \left(N_T{}^T h N_T\right) \det[J_s]\, d\zeta\, d\xi \Bigg|^{\xi=+1} = K_{F_{T_{i-j}}} \qquad (A.32)$$

and

$$\int_{\Gamma} \left(N_T{}^T h T_\infty\right) d\Gamma = \int_{-1}^{1}\int_{-1}^{1} \left(N_T{}^T h T_\infty\right) \det[J_s]\, d\zeta\, d\xi \Bigg|^{\xi=+1} = F_{T_{i-j}} \qquad (A.33)$$

In this case, $\det[J_s]$ will be equal to $\frac{ab}{4}$, where a and b are defined in Figure 4-1. Hence, with D_3 defined as $h\frac{ab}{4}$ the non-zero elements are given as:

$$K_{FT_{2-2}} = 4D_2/9 \quad K_{FT_{2-3}} = K_{FT_{3-2}} \quad K_{FT_{2-6}} = K_{FT_{6-2}} \quad K_{FT_{2-7}} = K_{FT_{7-2}}$$
$$K_{FT_{3-2}} = 2D_2/9 \quad K_{FT_{3-3}} = 4D_2/9 \quad K_{FT_{3-6}} = K_{FT_{6-3}} \quad K_{FT_{3-7}} = K_{FT_{7-3}}$$
$$K_{FT_{6-2}} = 2D_2/9 \quad K_{FT_{6-3}} = D_2/9 \quad K_{FT_{6-6}} = 4D_2/9 \quad K_{FT_{6-7}} = K_{FT_{7-6}}$$
$$K_{FT_{7-2}} = D_2/9 \quad K_{FT_{7-3}} = 2D_2/9 \quad K_{FT_{7-6}} = 2D_2/9 \quad K_{FT_{7-7}} = 4D_2/9$$

and

$$F_{T_{2-1}} = F_{T_{3-1}} = F_{T_{6-1}} = F_{T_{7-1}} = D_3 T_\infty$$

Appendix B
Material Properties Affecting Heat and Moisture Transfer

B.1 Introduction

This appendix presents the material properties that affect the coupled heat and moisture transfer through concrete, which was discussed in Chapter 4. Properties of cement, water in its various states, air, and concrete as a homogeneous material will be discussed. While some of these properties are constant, others tend to vary significantly with temperature, as shown in the following sections. The properties are divided into three main groups: one deals with the properties of concrete, another deals with the properties of liquid water, water vapour and air in concrete, and the last deals with the properties of the surrounding atmosphere and concrete boundary surface.

B.2 Properties of Concrete

The heat capacity of concrete, $\rho_T c_T$, can be calculated according to the Neumann-Kopp law (Neumann, 1831; Kopp, 1864) as suggested by Harmathy (1970). The law is a generalized experimental finding that the heat capacity of a substance can be approximated by the sum of the heat capacities of its constituents, weighted by their contribution to the total composition. Applying the law to concrete with all its constituents under elevated temperatures (dry skeleton, liquid water, water vapour and air), its heat capacity can be calculated as follows:

$$\rho_T c_T = \rho_c c_{p_c} + \bar{\rho}_L c_{p_L} + \varepsilon_G \tilde{\rho}_V c_{p_V} + \varepsilon_G \tilde{\rho}_A c_{p_A} \tag{B.1}$$

where c_{p_c}, c_{p_L}, c_{p_V}, and c_{p_A} are the specific heat capacities of the dry skeleton of concrete, liquid water, water vapour, and air, respectively. ρ_c is the density of concrete, $\bar{\rho}_L$ is the mass of liquid water phase per unit volume of concrete, and $\tilde{\rho}_V$ and $\tilde{\rho}_A$ are the

masses of the water vapour phase and the air per unit volume of the gaseous mixture, respectively. ε_G is the volume fraction of the gaseous mixture.

B.3 Properties of Liquid Water, Water Vapour and Air in Concrete

The mass of the liquid water phase per unit volume of concrete at a certain condition of temperature and pore pressure, $\bar{\rho}_L$, can be determined using the semi-empirical sorption isotherms presented in Equation (B.2) and plotted in Figure B.1(a). These curves were originally developed by Bažant and Thonguthai (1978) for determining the mass of water in any state (liquid or vapour) per unit volume of concrete at a certain condition of temperature and pressure (denoted $\bar{\rho}_w$). They were based on theoretical results together with the curve fitting of the experimental results presented by England and Ross (1972), Zhukov et al. (1971), and Zhukov and Shevchenko (1974). The value of this mass is dependent on the temperature of concrete, T, the cement content (mass of anhydrous cement per unit volume of concrete), $\bar{\rho}_c$, and the relative pore humidity, h_p, which is equal to the ratio between the partial pressure of water, P_w, and the saturation pressure of water, P_{sat}, at the respective temperature.

While a distinction between the unsaturated state of concrete and the saturated state is due for temperatures below the critical point of water (T_{crit} = 374.15ºC), such a distinction does not exist for higher temperatures, because the liquid state of water no longer exists regardless of the value of the pressure beyond this point (Bažant and Kaplan, 1996). Due to the significant difference between these states, the theoretical results propose an abrupt increase in the mass of water in concrete as concrete shifts from the unsaturated to the saturated state (i.e., from $P_w/P_{sat} < 1$ to $P_w/P_{sat} > 1$). However, according to Bažant and Thonguthai (1978), a sudden transition between the unsaturated and the saturated states cannot exist in reality, due to the wide range of the sizes of pores existing in concrete and the slow water exchange between large and small pores. Therefore, Bažant and Thonguthai (1978) introduced an empirical transition zone, where they assumed the formula of the unsaturated state to govern until a relative pore humidity of P_w/P_{sat} = 0.96, and the formula of the saturated state to govern starting from a relative

pore humidity of $P_w/P_{sat} = 1.04$. For the transition zone where $0.96 < P_w/P_{sat} < 1.04$, Bažant and Thonguthai (1978) assumed a straight line connecting $\bar{\rho}_W$ at $P_w/P_{sat} = 0.96$, denoted as $\bar{\rho}_{W_{0.96}}$ and $\bar{\rho}_W$ at $P_w/P_{sat} = 1.04$, denoted as $\bar{\rho}_{W_{1.04}}$, as shown in Equation (B.2).

$$\bar{\rho}_W = \begin{cases} \bar{\rho}_c \left(\dfrac{\bar{\rho}_{W_{o,o}}}{\bar{\rho}_c} \dfrac{P_w}{P_{sat}} \right)^{1/m(T)} & \text{for } \dfrac{P_w}{P_{sat}} \leq 0.96 \\ \bar{\rho}_{W_{0.96}} + \left(\dfrac{P_w}{P_{sat}} - 0.96 \right) \dfrac{\bar{\rho}_{W_{1.04}} - \bar{\rho}_{W_{0.96}}}{0.08} & \text{for } 0.96 < \dfrac{P_w}{P_{sat}} < 1.04 \\ \bar{\rho}_{W_o} \left[1 + 0.12 \left(\dfrac{P_w}{P_{sat}} - 1.04 \right) \right] & \text{for } \dfrac{P_w}{P_{sat}} \geq 1.04 \end{cases} \quad \text{(B.2)}$$

where
$$m(T) = 1.04 - \frac{(T+10)^2}{(T+10)^2 + 22.34(T_o + 10)^2} \quad \text{(B.3)}$$

where $\bar{\rho}_{W_{o,o}}$ is the mass of water per unit volume of concrete at the initial temperature, T_o (20°C), and initial pressure, P_{w_o}, which is equal to the atmospheric pressure (0.1 MPa). $\bar{\rho}_{W_o}$ is the mass of water per unit volume of concrete at initial pressure, P_{w_o}, at any temperature. T is the temperature in °C.

The difference between $\bar{\rho}_{W_{o,o}}$ and $\bar{\rho}_{W_o}$ lies in the fact that, for the state of saturated concrete, where for $P_w/P_{sat} \geq 1.04$, the mass of water per unit volume of concrete at any temperature, $\bar{\rho}_{W_o}$, is dictated by the porosity of concrete as the water (liquid or vapour) is assumed to fill all the pores. On the other hand, for the state of unsaturated concrete, the initial mass of water per unit volume of concrete, $\bar{\rho}_{W_{o,o}}$, is almost independent of the porosity of concrete as it depends on the initial relative humidity of concrete.

However, in this study, liquid water and water vapour are treated as two separate phases as opposed to the one single phase used in the development of the original curves. Therefore, as advised by Tenchev et al. (2001), the term '$\bar{\rho}_W$' is substituted by the term '$\bar{\rho}_L$', where the subscript 'L' denotes the liquid water phase only. Accordingly, for the

saturated state, where $P_V/P_{sat} \geq 1.04$, it cannot be assumed that the mass of liquid water per unit volume of concrete at any temperature (now denoted as $\bar{\rho}_L$) is dictated by the porosity of concrete as the pores can be filled with either liquid water or water vapour. Therefore, it will be taken as the initial mass of liquid water per unit volume of concrete, $\bar{\rho}_{L_{o,o}}$. This effectively renders the mass of liquid water per unit volume of concrete independent of temperature for the saturated condition of concrete, as shown in Figure B.1(b), except for the change in the value of the saturation pressure of water vapour, P_{sat}, with temperature.

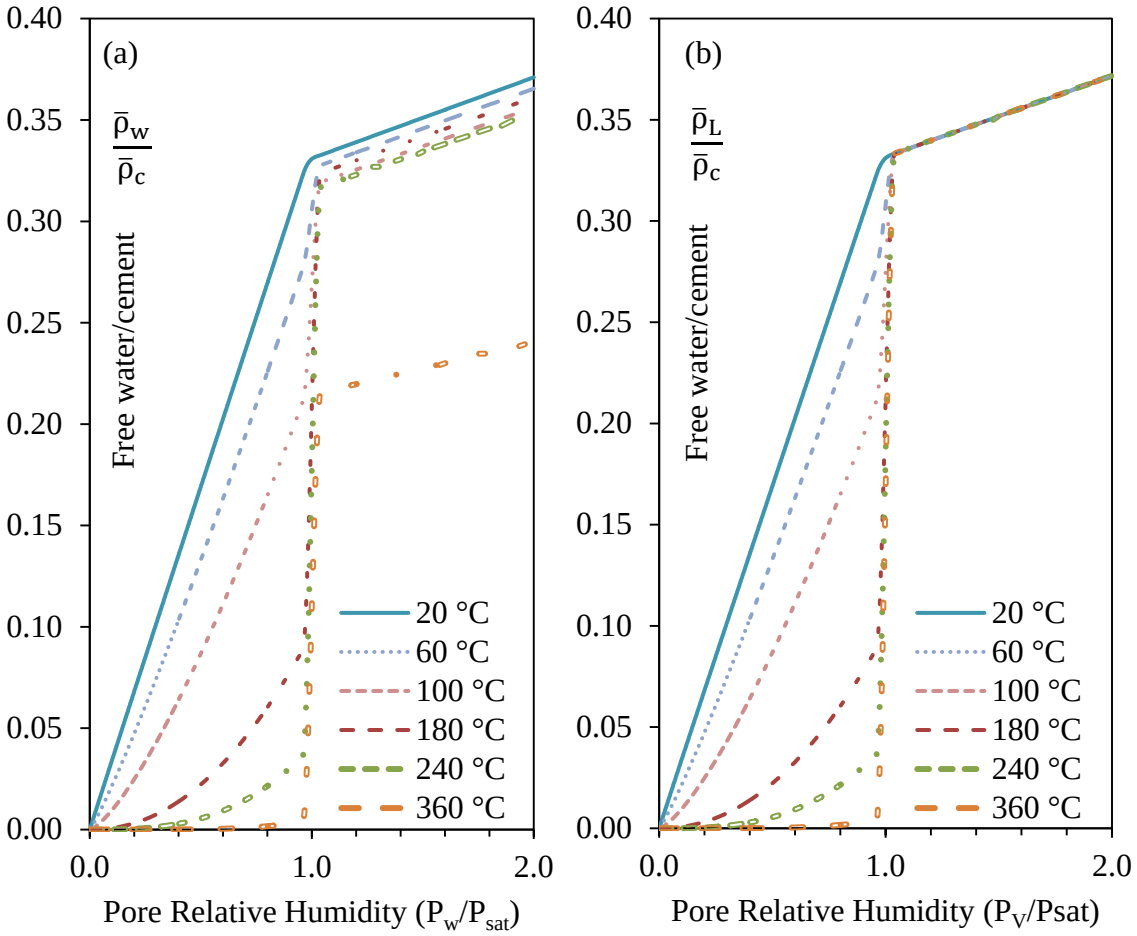

Figure B.1 (**a)** Original sorption isotherms (Bažant and Thonguthai, 1978) and **(b)** Modified sorption isotherms in this study

Therefore, the new format of the sorption isotherms becomes as follows:

$$\bar{\rho}_L = \begin{cases} \bar{\rho}_c \left(\dfrac{\bar{\rho}_{L_o}}{\bar{\rho}_c} \dfrac{P_V}{P_{sat}} \right)^{1/m(T)} & \text{for } \dfrac{P_V}{P_{sat}} \leq 0.96 \\ \bar{\rho}_{L_{0.96}} + \left(\dfrac{P_V}{P_{sat}} - 0.96 \right) \dfrac{\bar{\rho}_{L_{1.04}} - \bar{\rho}_{L_{0.96}}}{0.08} & \text{for } 0.96 < \dfrac{P_V}{P_{sat}} < 1.04 \\ \bar{\rho}_{L_o} \left[1 + 0.12 \left(\dfrac{P_V}{P_{sat}} - 1.04 \right) \right] & \text{for } \dfrac{P_V}{P_{sat}} \geq 1.04 \end{cases} \quad \text{(B.4)}$$

where $\bar{\rho}_{L_o}$ is the initial mass of liquid water per unit volume of concrete at ambient temperature, T_o (20°C). Temperature, T, is in ºC and any $\bar{\rho}$ is in kg/m^3. The value of $\bar{\rho}_{L_o}$ depends on the initial level of saturation of concrete prior to the rise in temperature. For absolutely dry concrete, it will be equal to 0, while for completely saturated concrete, it will be equal to the density of water at ambient temperature ($1000\,kg/m^3$) multiplied by the volume of the pores, i.e., directly depends on the porosity of concrete. For intermediate states, this value will be calculated according to the relative humidity of concrete at ambient temperature, T_o (20°C). The value of the mass of anhydrous cement per unit volume of concrete, $\bar{\rho}_c$, can be determined from the proportions of the concrete mix (normally estimated as $300\,kg/m^3$).

Values of the saturation pressure of water vapour, P_{sat}, were tabulated at different temperatures by Çengel (1998) but, for convenience, Davie et al. (2006) introduced the following equation by curve-fitting the tabulated data.

$$P_{sat} = aT^6 + bT^5 + cT^4 + dT^3 + eT^2 + fT + g \quad \text{(B.5)}$$

where T is the temperature in °K ($T(°C) + 273.15$), P_{sat} is in Pa, $a = -1.4374 \times 10^{-9}$, $b = 4.4244 \times 10^{-6}$, $c = -3.9281 \times 10^{-3}$, $d = 1.5910$, $e = -3.2589 \times 10^{2}$, $f = 3.2148 \times 10^{4}$, and $g = -1.1547 \times 10^{6}$.

The inflection points occurring at the beginning and the end of the fictitious transition stage in the sorption isotherms in Equation (B.4) impose computational complications and instability. This is why Majumdar et al. (1995) substituted the straight line adopted by Bažant and Thonguthai (1978) for this stage by the smoother and more accurate S-shaped equation presented in Equation (B.6).

$$\text{For } 0.96 < \frac{P_V}{P_{sat}} < 1.04 \qquad \bar{\rho}_L = \sum_{i=1}^{4} \alpha_i x^{i-1} \tag{B.6}$$

where
$$\alpha_1 = \bar{\rho}_{L_{0.96}} - x_1 \frac{{x_1}^2 S_{21} - x_1 x_2 (3S_{21} - S_2) + {x_2}^2 S_1}{(x_2 - x_1)^2} \tag{B.7}$$

$$\alpha_2 = \frac{{x_1}^2 S_2 - 2x_1 x_2 (3S_{21} - S_1 - S_2) + {x_2}^2 S_1}{(x_2 - x_1)^2} \tag{B.8}$$

$$\alpha_3 = \frac{x_1 (3S_{21} - S_1 - 2S_2) + x_2 (3S_{21} - 2S_1 - S_2)}{(x_2 - x_1)^2} \tag{B.9}$$

$$\alpha_4 = -\frac{2S_{21} - S_1 - S_2}{(x_2 - x_1)^2} \tag{B.10}$$

where x is P_V/P_{sat}, x_1 is 0.96, x_2 is 1.04, S_1 is the slope at the point $(x_1, \bar{\rho}_{L_{0.96}})$, S_2 is the slope at the point $(x_2, \bar{\rho}_{L_{1.04}})$, and $S_{21} = (\bar{\rho}_{L_{1.04}} - \bar{\rho}_{L_{0.96}})/(x_2 - x_1)$.

The derivatives of the mass of liquid water per unit volume of concrete with respect to both temperature and the mass of the water vapour phase per unit volume of the gaseous mixture, $\tilde{\rho}_V$, are also required to be evaluated for the calculation procedure of coupled heat and moisture transfer through concrete as shown in 3.6. These derivatives have been provided by Dwaikat and Kodur (2009) as follows:

$$\frac{\partial \bar{\rho}_L}{\partial P_V} = \begin{cases} \dfrac{\bar{\rho}_{L_o}}{m(T) P_{sat}} \left(\dfrac{\bar{\rho}_{L_o}}{\bar{\rho}_c} \dfrac{P_V}{P_{sat}} \right)^{\frac{1}{m(T)} - 1} & \text{for } \dfrac{P_V}{P_{sat}} \le 0.96 \\ \dfrac{\bar{\rho}_{L_{1.04}} - \bar{\rho}_{L_{0.96}}}{0.08 P_{sat}} & \text{for } 0.96 < \dfrac{P_V}{P_{sat}} < 1.04 \\ 0.12 \dfrac{\bar{\rho}_{L_o}}{P_{sat}} & \text{for } \dfrac{P_V}{P_{sat}} \ge 1.04 \end{cases} \tag{B.11}$$

and employing Equation (4.26): $$\frac{\partial \bar{\rho}_L}{\partial \tilde{\rho}_V} = R_V T \left(\frac{\partial \bar{\rho}_L}{\partial P_V} \right) \tag{B.12}$$

$$\frac{\partial \bar{\rho}_L}{\partial T} = \begin{cases} -\bar{\rho}_L \left[\dfrac{dm(T)/dT}{\left(m(T)\right)^2} \ln\left(\dfrac{\bar{\rho}_{L_o}}{\bar{\rho}_c}\dfrac{P_V}{P_{sat}}\right) + \dfrac{dP_{sat}/dT}{m(T)P_{sat}} \right] & \text{for } \dfrac{P_V}{P_{sat}} \le 0.96 \\ \dfrac{d\bar{\rho}_{L_{0.96}}}{dT} - \dfrac{P_V(dP_{sat}/dT)}{{P_{sat}}^2}\left(\dfrac{\bar{\rho}_{L_{1.04}} - \bar{\rho}_{L_{0.96}}}{0.08P_{sat}}\right) + X & \text{for } 0.96 < \dfrac{P_V}{P_{sat}} < 1.04 \\ \dfrac{d\bar{\rho}_{L_o}}{dT}\left[1 + 0.12\left(\dfrac{P_V}{P_{sat}} - 1.04\right)\right] - 0.12\dfrac{\bar{\rho}_{L_o}P_V(dP_{sat}/dT)}{{P_{sat}}^2} & \text{for } \dfrac{P_V}{P_{sat}} \ge 1.04 \end{cases} \quad \text{(B.13)}$$

where $$\frac{dm(T)}{dT} = -\frac{2(T+10)[(T+10)^2 + 22.34(T_o+10)^2] - 2(T+10)^3}{[(T+10)^2 + 22.34(T_o+10)^2]^2} \quad \text{(B.14)}$$

$$X = \left(\frac{P_V}{P_{sat}} - 0.96\right)\frac{\left(d\bar{\rho}_{L_{1.04}}/dT\right) - \left(d\bar{\rho}_{L_{0.96}}/dT\right)}{0.08} \quad \text{(B.15)}$$

$$\frac{d\bar{\rho}_{L_{0.96}}}{dT} = -\bar{\rho}_{L_{0.96}}\frac{\ln\left(0.96\,\bar{\rho}_{L_o}/\bar{\rho}_c\right)(dm(T)/dT)}{\left(m(T)\right)^2} \quad \text{(B.16)}$$

and in this study $$\frac{d\bar{\rho}_{L_{1.04}}}{dT} = 0 \quad \text{(B.17)}$$

Due to the complexity of these calculations, some researchers (Tenchev et al., 2001) chose to calculate $\partial\bar{\rho}_L/\partial P_V$ and $\partial\bar{\rho}_L/\partial T$ as follow:

$$\frac{\partial \bar{\rho}_L}{\partial \tilde{\rho}_V} = \frac{\bar{\rho}_{L_{\tilde{\rho}_V+\Delta\tilde{\rho}_V}} - \bar{\rho}_{L_{\tilde{\rho}_V}}}{\Delta\tilde{\rho}_V} \quad \text{(B.18)}$$

$$\frac{\partial \bar{\rho}_L}{\partial T} = \frac{\bar{\rho}_{L_{T+\Delta T}} - \bar{\rho}_{L_T}}{\Delta T} \quad \text{(B.19)}$$

where $\bar{\rho}_{L_{\tilde{\rho}_V}}$ is $\bar{\rho}_L$ at a pressure P_V equal to $R_V\tilde{\rho}_V T$ (see Equation (4.26)) and $\bar{\rho}_{L_{\tilde{\rho}_V+\Delta\tilde{\rho}_V}}$ is $\bar{\rho}_L$ at a pressure P_V equal to $R_V(\tilde{\rho}_V + \Delta\tilde{\rho}_V)T$ and the same temperature T. $\bar{\rho}_{L_T}$ is $\bar{\rho}_L$ at a temperature T and $\bar{\rho}_{L_{T+\Delta T}}$ is $\bar{\rho}_L$ at a temperature $T + \Delta T$ and the same pressure P_V. With small values for ΔT and $\Delta\tilde{\rho}_V$, this approximation was found to be acceptable. Tenchev et al. (2001) recommended a value of $0.1 \times 10^{-3}T$ for ΔT and a value of $0.1 \times 10^{-3}\tilde{\rho}_V$ for $\Delta\tilde{\rho}_V$.

For the mass of liquid water resulting from the dehydration of the water chemically bound in the cement paste of concrete, $\bar{\rho}_D$, Bažant and Kaplan (1996) proposed using the experimentally measured concrete weight loss at elevated temperatures as a measure for the mass of dehydrated water. They suggested using the results provided by Fischer (1970), Harmathy (1970), and Harmathy and Allen (1973). Two attempts were made to develop expressions for the mass of dehydrated water following this approach. The first one was made by Tenchev et al. (2001) and is presented in Equation (B.20), while the second one was developed by Dwaikat and Kodur (2009) and is presented in Equation (B.21). The two expressions significantly vary from each other; examining the experimental results, the latter expressions evidently provide better correlation.

$$\bar{\rho}_D = \bar{\rho}_c \times \begin{cases} 0.00 & \text{for } T \leq 200℃ \\ 7.00 \times 10^{-4}(T - 200) & \text{for } 200℃ < T \leq 300℃ \\ 0.40 \times 10^{-4}(T - 300) + 0.07 & \text{for } 300℃ < T \leq 800℃ \\ 0.09 & \text{for } T > 800℃ \end{cases} \tag{B.20}$$

or

$$\bar{\rho}_D = \bar{\rho}_c \times \begin{cases} 0.00 & \text{for } T \leq 100℃ \\ 0.04\dfrac{T - 100}{100} & \text{for } 100℃ < T \leq 700℃ \\ 0.24 & \text{for } T > 700℃ \end{cases} \tag{B.21}$$

where $\bar{\rho}_D$ is in kg/m^3.

The values of the specific heat capacities of liquid water c_{p_L}, water vapour, c_{p_V}, and dry air, c_{p_A}, were tabulated at different temperatures by Çengel (1998) but, for convenience, Davie et al. (2006) introduced the following formulae by curve-fitting the tabulated data.

$$c_{p_L} = \begin{cases} 2.4768T + 3368.2 + \left(\dfrac{aT}{513.15}\right)^b & \text{for } T \leq T_{crit} \\ 24515.0 & \text{for } T > T_{crit} \end{cases} \tag{B.22}$$

where $a = 1.0854$ and $b = 31.4448$.

$$c_{p_V} = \begin{cases} 7.1399T + 443 + \left(\frac{aT}{513.15}\right)^b & \text{for } T \leq T_{crit} \\ 45821.04 & \text{for } T > T_{crit} \end{cases} \quad \text{(B.23)}$$

where $a = 1.1377$ and $b = 29.4435$.

$$c_{p_A} = aT^6 + bT^5 + cT^4 + d \quad \text{(B.24)}$$

where $a = -9.8494 \times 10^{-8}$, $b = 3.5644 \times 10^{-4}$, $c = -0.1216$, $d = 1.0125 \times 10^3$.

where c_{p_L}, c_{p_V}, and, c_{p_A} are all in J/kg℃ and T in Equations (B.22), (B.23), and (B.24) is in °K.

For the dynamic viscosity of liquid water, μ_L, Thomas and Sansom (1995) presented Equation (B.25). Gawin et al. (1999) compared it to the test results provided by Reid et al. (1987) and Incropera and DeWitt (1990) and reported good correlation. Davie et al. (2006) also compared it to the values tabulated at different temperatures by Çengel (1998) and also reported good correlation.

$$\mu_L = 661.2(T - 229)^{-1.562} \times 10^{-2} \quad \text{(B.25)}$$

where μ_L is in $kg/m.sec$ and T is in °K.

For the dynamic viscosity of the total gaseous mixture consisting of water vapour and air, Gawin et al. (1999) used the test results provided by the ASHRAE Handbook (1993) and Mason and Monchick (1965) to develop the formula shown in Equation (B.26) for the dynamic viscosity of the total gaseous mixture.

$$\mu_G = \mu_V + (\mu_A - \mu_V)\left(\frac{P_A}{P_G}\right)^{0.608} \quad \text{(B.26)}$$

where $$\mu_V = 8.85 \times 10^{-6} + 5.53 \times 10^{-8}(T - T_o) \quad \text{(B.27)}$$

and $$\mu_A = 17.17 \times 10^{-6} + 4.73 \times 10^{-8}(T - T_o) - 2.22 \times 10^{-11}(T - T_o) \quad \text{(B.28)}$$

where μ_G, μ_V, and μ_A are in $kg/m.sec$ and T is in °K.

Davie et al. (2006) also compared the formulae of μ_V from Equation (B.27) and μ_A from Equation (B.28) to the values tabulated at different temperatures by Çengel (1998) and reported good correlation.

However, Tenchev et al. (2001) proposed a weighted averaging scheme between the dynamic viscosity of air and water vapour based on their contribution to the total composition, i.e., their masses per unit volume of the gaseous mixture, as shown in Equation (B.29).

$$\mu_G = \begin{cases} \dfrac{\tilde{\rho}_A \mu_A + \tilde{\rho}_V \mu_V}{\tilde{\rho}_A + \tilde{\rho}_V} & \text{for } \tilde{\rho}_A + \tilde{\rho}_V > 0 \\ 0 & \text{for } \tilde{\rho}_A + \tilde{\rho}_V = 0 \end{cases} \tag{B.29}$$

For the values of μ_V and μ_A, Tenchev et al. (2001) proposed using the values tabulated at different temperatures by Çengel (1998).

For the mass diffusivity (or diffusion coefficient) of air or water vapour in concrete, D_{AV}, Van Brakel and Heertjes (1974) proposed the expression presented in Equation (B.30), where they introduced two reduction factors to the diffusion coefficient of free fluid in order to calculate the corresponding value for the diffusion in cement paste. The first factor is the constrictivity, δ, which accounts for the non-uniformity of the cross section of the diffusion paths, where they can become very constricted at certain points. The second one is the tortuosity, τ, which accounts for the fact that, in cement paste, the diffusion paths are tortuous compared to diffusion in free fluids.

$$D_{AV} = D\frac{\delta}{\tau^2} \tag{B.30}$$

While tortuosity can be defined in terms of porosity, and constrictivity by the pore radius (Nagao and Nakane, 1991), Tenchev et al. (2001) suggested using an approximate value of 3 for tortuosity and 0.5 for constrictivity.

Marrero and Mason (1972) recommended using the following formula for the diffusion coefficient of free fluid, D:

$$D = \begin{cases} 1.87 \times 10^{-5} \dfrac{T^{2.072}}{P_G} & \text{for } 280°K < T \leq 450°K \\ 2.75 \times 10^{-4} \dfrac{T^{1.632}}{P_G} & \text{for } 450°K < T \leq 1070°K \end{cases} \quad \text{(B.31)}$$

where D is in m^2/sec and T is in °K.

For the specific heat of evaporation of water, λ_E, the expression presented in Equation (B.32) was proposed by Gawin et al. (1999), based on Watson's empirical formula (Watson, 1943). The expression was reached by dividing the expression presented by Forsyth and Simpson (1991) for the enthalpy of evaporation by the molar mass of water.

$$\lambda_E = 2.672 \times 10^5 (T_{crit} - T)^{0.38} \quad \text{(B.32)}$$

where λ_E is in J/kg and T is in °K. Davie et al. (2006) compared the expression to the values tabulated at different temperatures by Çengel (1998) and reported good correlation.

As for the specific heat of dehydration of chemically-bound water in concrete, λ_D, a constant value was proposed by Bažant and Thonguthai (1978) based on the assumption of Cheung and Baker (1976) that the release of the latent heat of dehydration of chemically-bound water occurs suddenly at a temperature slightly above 100ºC. This constant value was assumed to be 2400×10^3 J/kg by Tenchev et al. (2001) and 796×10^3 J/kg by Zeiml (2004).

Finally, the values of the density of water, ρ_L, at atmospheric pressure were tabulated by Çengel (1998) for different temperatures up to the critical point of water (T_{crit} = 374.15ºC).

B.4 Properties of the Surrounding Atmosphere and Concrete Boundary Surface

For the convective heat transfer coefficients of concrete, h_q, the Eurocode (EN 1991-1-2:1992, 1993) suggested a value of $25\ W/m^{2}°C$, should its standard temperature-time curve be used.

For estimating the radiative heat transfer coefficients of concrete, h_r, the basis of Stefan–Boltzmann law is normally used as shown in Equation (B.33) (Çengel, 1998). Stefan–Boltzmann law was originally developed by Slovene/Austrian physicist Jožef Stefan in 1879, but was extended by his Austrian student Ludwig Boltzmann in 1883.

$$h_r = e\sigma(T^2 + T_\infty^2)(T + T_\infty) \tag{B.33}$$

where e is the emissivity of concrete, given a value of 0.7 by the Eurocode (EN 1992-1-2:2004, 2005), and σ is the Stefan–Boltzmann constant ($5.67\times10^{-8}\ W/m^{2}°C^{4}$).

Çengel (1998) provided the formula presented in Equation (B.34) for calculating the water vapour transfer coefficient, β, based on the Chilton-Colburn analogy (Chilton and Colburn, 1934); an analogy that takes advantage of the similarities among the transport of momentum, mass, and energy.

$$\beta = \frac{h_q}{\rho_{A_\infty} c_{p_{A_\infty}}} \frac{D_{AV_{T_\infty}}}{\alpha_{A_\infty}} \tag{B.34}$$

where ρ_{A_∞}, $c_{p_{A_\infty}}$, α_{A_∞}, $D_{AV_{T_\infty}}$ are the density, specific heat capacity, thermal diffusivity, and mass diffusivity (or diffusion coefficient) of air at the temperature of the surrounding atmosphere, T_∞. The values of ρ_{A_∞} and α_{A_∞} at different temperatures were tabulated by Çengel (1998).

Appendix C
Calculation Sequence for Heat and Moisture Transfer Analysis

C.1 Introduction

This section explains the main steps of the calculation procedure of the coupled heat and moisture transfer analysis discussed in Chapter 4, employing the models, techniques, and material properties presented in Chapter 3, Chapter 4, Appendix A, and Appendix B. The solution involves a highly nonlinear iterative time-stepping procedure that is performed prior to the structural analysis as shown in the flow chart presented in Figure C.1, which explains the main steps of the solution procedure followed by VecTor3 for a typical analysis.

The driving factor of the coupled heat and moisture transfer analysis is the increase in temperature of the concrete boundary surface, while the target output variables are the temperature, T, the pressure of the gaseous mixture in the pores of concrete, P_G, and the mass of water vapour phase per unit volume of the gaseous mixture, $\tilde{\rho}_V$, through the depth of concrete.

In the context of the finite element solution procedure, these output variables are generated for the nodes of the structure at predefined time steps, while the properties of the structure need to be assigned to the elements, not the nodes, to determine their thermal and mechanical properties. Therefore, depending on the type of the element used and the number of nodes comprising it, its properties are determined as an average of the output variables of these nodes.

A sequential list of the steps to be followed for the coupled heat and moisture transfer analysis follows. For the analysis of the transfer of heat only, the same steps and the same flow chart are to be followed, but the procedure presented in Section 4.4 is used instead, where the output variable is the temperature, T, only, and no additional stresses due to the pore pressure are considered in the concrete.

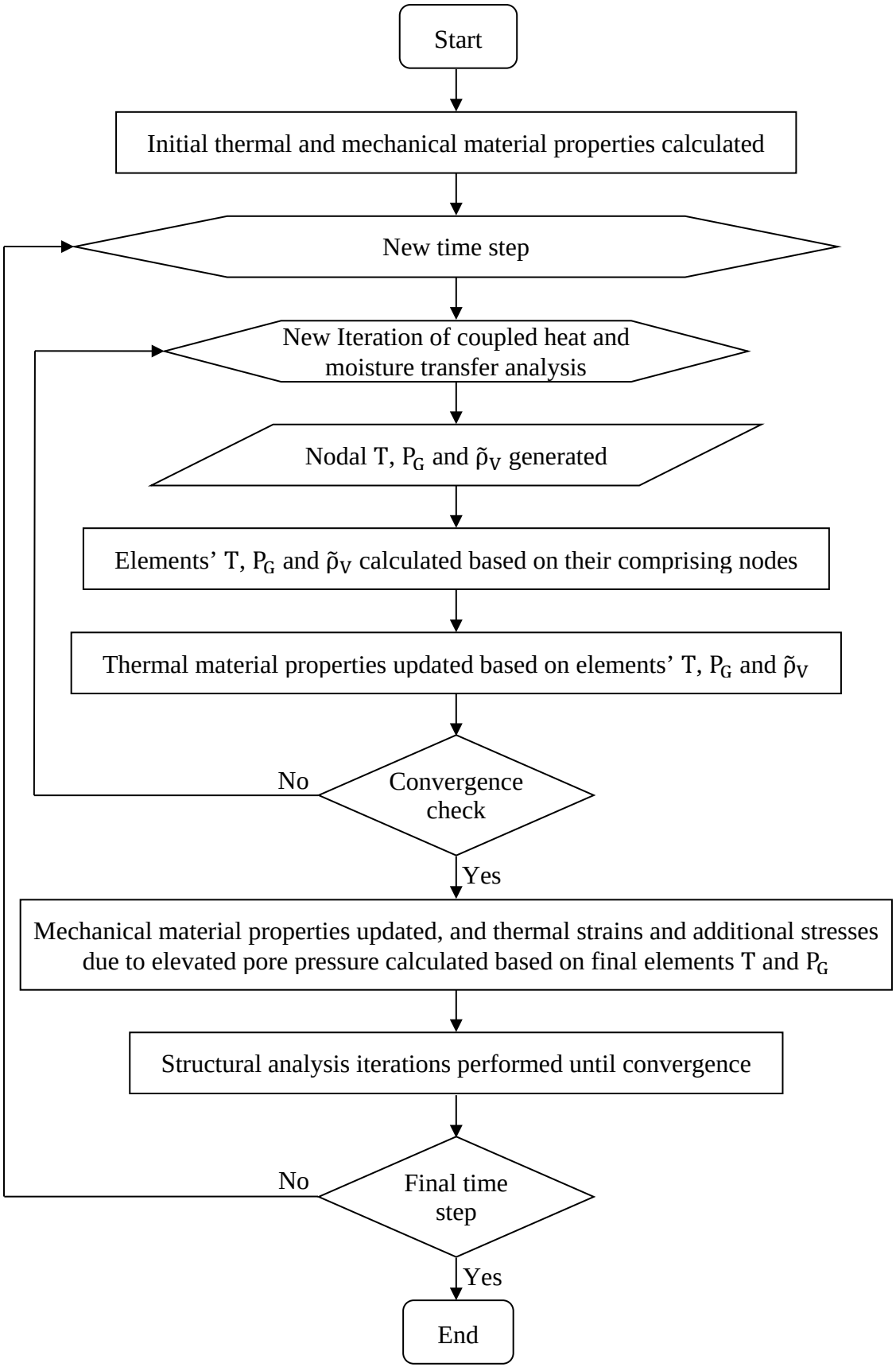

Figure C.1 Flow chart of the time-stepping procedure for coupled heat and moisture transfer analysis followed by VecTor3

C.2 Step I

The first step in the analysis is determining the initial conditions and material properties involved in the analysis.

For the initial values of the output variables T, P_G, and $\tilde{\rho}_V$,

Initial temperature: $$T_o = T_{\infty_o} = 20℃ \quad \text{(C.1)}$$

Initial pressure of gaseous mixture: $$P_{G_o} = P_\infty = 0.1\ \text{MPa} \quad \text{(C.2)}$$

Initial mass of water vapour phase per unit volume of the gaseous mixture from Equation (4.26): $$\tilde{\rho}_{V_o} = \frac{P_{V_o}}{R_V T_o} \quad \text{(C.3)}$$

where T_{∞_o} is the initial temperature of the surrounding atmosphere and P_∞ is the pressure at the boundary surface of concrete (i.e., atmospheric pressure). P_{G_o} is the initial pressure of the gaseous mixture in the pores of concrete. P_{V_o} is the initial partial pressure of water vapour phase, which can be assumed to be equal to the saturation pressure of water vapour at the initial temperature (T_o), $P_{sat_{T_o}}$, since concrete is assumed to be at a saturated state at the beginning of the analysis.

For the values of the variables acting on the boundary surfaces, the value of the temperature of the surrounding atmosphere, T_∞, is set to follow any of the temperature-time curves discussed in Section 3.2. The mass of water vapour phase per unit volume of the gaseous mixture on the boundary surface, $\tilde{\rho}_{V_\infty}$, is set to be constant throughout the analysis. This value is equal to the mass of water vapour phase per unit volume of the gaseous mixture at saturation multiplied by the relative humidity of the atmosphere, as shown in Equation (C.4).

$$\tilde{\rho}_{V_\infty} = \varphi \frac{P_{sat_{T_o}}}{R_V T_{\infty_o}} = \varphi \tilde{\rho}_{V_o} \quad \text{(C.4)}$$

where φ is the relative humidity of atmosphere, suggested to be taken as 0.8 by Tenchev et al. (2001).

This step is not an iterative step and is only performed once at the beginning of the analysis, except for the determination of the value of the temperature of the surrounding atmosphere, T_∞, which is done at the beginning of every time step.

C.3 Step II

This step involves the determination of the various properties of concrete, liquid water, water vapour, and air, based on the values of the temperature, T, the pressure of gaseous mixture, P_G, and the mass of water vapour phase per unit volume of the gaseous mixture, $\tilde{\rho}_V$. These values are calculated from the previous iteration or the previous time step for the solution of the first iteration, or calculated from the initial values for the solution of the first iteration of the first time step. As previously explained, T, P_G, and $\tilde{\rho}_V$ of an element are determined as an average of T, P_G, and $\tilde{\rho}_V$ of the nodes comprising it.

A sequence of the properties to be calculated for each element is as follows (Gawin et al., 1999; Tenchev et al., 2001; Davie et al., 2006):

1. P_V: from Equation (4.26), based on the values of T and $\tilde{\rho}_V$.
2. P_{sat}: from Equation (B.5), based on the value of T.
3. $\bar{\rho}_L$: from Equation (B.4) , based on the values of T, P_V, and P_{sat}.
4. $\frac{\partial \bar{\rho}_L}{\partial \tilde{\rho}_V}$: from Equation (B.11) and Equation (B.12), based on the values of T, P_V, and P_{sat}, or from Equation (B.18), based on the value of $\bar{\rho}_L$.
5. $\frac{\partial \bar{\rho}_L}{\partial T}$: from Equation (B.13), based on the values of T, P_V, and P_{sat}, or from Equation (B.19), based on the value of $\bar{\rho}_L$.
6. $\bar{\rho}_D$: from Equation (B.20) or Equation (B.21), based on the value of T.
7. k: as shown in Section 3.4.1.1, based on the value of T.
8. ϕ: from Equation (3.87) or Equation (3.88), based on the value of T.
9. K: from Equation (3.89) or Equation (3.90), based on the values of T and P_G, or from Equation (3.91), based on the value of ϕ.
10. $\rho_c c_{p_c}$ as shown in Section 3.4.1.3, or ρ_c and c_{p_c} separately, as shown in Section 0 and Section 3.4.1.3, respectively, all based on the value of T.

11. P_A: from Equation (4.9), based on the values of P_G and P_V.
12. ρ_L: from the tables presented by Çengel (1998), based on the value of T.
13. ε_L: from Equation (4.13), based on the values of $\bar{\rho}_L$ and ρ_L.
14. ε_G: from Equation (4.14), based on the values of ϕ and ε_L.
15. $\tilde{\rho}_A$: from Equation (4.27), based on the values of T and P_A.
16. $\tilde{\rho}_G$: from Equation (4.10), based on the values of $\tilde{\rho}_V$ and $\tilde{\rho}_A$.
17. c_{p_L}, c_{p_V}, and, c_{p_A}: from Equation (B.22), Equation (B.23), and Equation (B.24), respectively, based on the value of T.
18. μ_L, μ_V, and μ_A: from Equation (B.25), Equation (B.27), and Equation (B.28), respectively, based on the value of T.
19. μ_G: from Equation (B.26) or Equation (B.29), based on the values of μ_V and μ_A.
20. $\rho_T c_T$: from Equation (B.1), based on the values of ρ_c, $\bar{\rho}_L$, $\tilde{\rho}_V$, $\tilde{\rho}_A$, c_{p_c}, c_{p_L}, c_{p_V}, c_{p_A}, and ε_G.
21. s: from Equation (3.93), based on the values of ε_L and ϕ.
22. K_G: from Equation (3.92) or Equation (3.96), based on the value of s.
23. K_L: from Equation (3.94) or Equation (3.95), based on the value of s.
24. λ_E: from Equation (B.32), based on the value of T.
25. h_r: from Equation (B.33), based on the value of T.
26. D: from Equation (B.31), based on the values of T and P_G.
27. D_{AV}: from Equation (B.30), based on the value of D.
28. D_{T_∞}: from Equation (B.31), based on the values of T_∞ and P_∞.
29. $D_{AV_{T_\infty}}$: from Equation (B.30), based on the value of D_{T_∞}.
30. ρ_{A_∞}: from the tables presented by Çengel (1998), based on the value of T_∞.
31. $c_{p_{A_\infty}}$: from Equation (B.24), based on the value of T_∞.
32. α_{A_∞}: from the tables presented by Çengel (1998), based on the value of T_∞.
33. β: from Equation (B.34), based on the values of $D_{AV_{T_\infty}}$, ρ_{A_∞}, $c_{p_{A_\infty}}$, and α_{A_∞}.
34. C_{TT}, C_{TP}, C_{TV}, C_{AP}, C_{AV}, C_{MT}, C_{MP}, C_{MV}, K_{TT}, K_{TP}, K_{TV}, K_{AT}, K_{AP}, K_{AV}, K_{MT}, K_{MP}, and K_{MV}: according to the expressions presented in Table 4-1.
35. C_E and K_E: from Equation (4.72) and its clarification in Equation (4.71).
36. F_{K_e}: from Equation (4.88).

37. F_{∞_e}: from Equation (4.89).
38. $\int_{\Omega}(N^T C_E N)d\Omega$: Section A.2 directly presents the matrix elements for regular eight-noded hexahedral brick elements.
39. $\int_{\Omega}(\nabla N^T K_E \nabla N)d\Omega$: Section A.3 directly presents the matrix elements for regular eight-noded hexahedral brick elements.
40. $\int_{\Gamma}(N^T K_E F_{K_E} N)d\Gamma$ and $\int_{\Gamma}(N^T K_E F_{\infty_E})d\Gamma$: Section A.4 directly presents the matrix elements for regular eight-noded hexahedral brick elements.

C.4 Step III

With the matrices of all the elements compiled, the finite element solution can be performed starting by assembling the matrices of all the elements into the global matrices **C**, **K**, and **F** according to Equation (4.83), Equation (4.84) or Equation (4.85), and Equation (4.86), respectively. These matrices are then inserted into Equation (4.82) and the finite difference method is used for time discretization to solve the differential equation, using one of the techniques discussed in Section 4.5. The solution generates matrix **x**, defined in Equation (4.87), containing new values for T, P_G, and $\tilde{\rho}_V$ for all the nodes of the model at the new time step.

C.5 Step IV

Since the solution is highly nonlinear, iterations are required until a solution is reached. This step presents checks for determining whether a solution has been reached or another iteration is required, by specifying certain criteria that assume a solution has been reached once met. Following similar finite element solution procedures, these criteria are:

1. Convergence criterion, which involves tracking the diminishing difference between the output variables generated from successive iterations until it reaches a certain limit (tolerance). This gives definition to a convergence factor, ψ_j, that can be

compared to an arbitrary tolerance, tol. This factor can take numerous forms, but the one used in this study has the following form:

$$\psi_j = \frac{\sum_{i=1}^{n}\left(\mathbf{x_{j-1}} - \mathbf{x_j}\right)^2}{\sum_{i=1}^{n}\left(\mathbf{x_j}\right)^2} \tag{C.5}$$

where ψ_j is the convergence factor for time step number j, i is the node number, and n is the total number of nodes. $\mathbf{x_j}$ is the solution matrix, defined in Equation (4.87), for time step number j and $\mathbf{x_{j-1}}$ is that of the previous time step.

2. Number of iterations criterion, where an arbitrary maximum number of iterations is defined in order to keep the solution efficient.

If ψ_j is less than tol and the iteration number is less than the maximum number of iterations allowed, T, P_G, and $\tilde{\rho}_V$ generated from the last iteration are used for the next iteration and Step II to Step IV are repeated. Once ψ_j reaches a value less than the value of tol, or the maximum number of iterations allowed is reached, the current time step solution is finalized and the values of T, P_G, and $\tilde{\rho}_V$ at the final iteration are proclaimed as the output variables of time step number j. The next time step is then started, where the final values of T, P_G, and $\tilde{\rho}_V$ from time step number j are used to determine the material properties for the first iteration of time step number $j + 1$. This procedure carries on until the last time step, after which the solution is terminated.